Helium escaping exoplanets
pp. 1360, 1384, & 1388

Intimacy in the age of artificial intelligence *p. 1365*

Marine protected areas need better protection *p. 1403*

Science

$15
21 DECEMBER 2018
sciencemag.org

AAAS

2018

BREAKTHROUGH *of the* YEAR

E-mail : info@axion-research.com
www.axionr.com/eng/

AXiR Engine® tells you the risk of future disease in your body.

Until today we' ve been ignoring small signal in our body if we feel that the pain is a split second or very short period. In Japan we see the number of deaths by cancer like 370,000 people and the number is similar in the past 6 years. Maybe the fatalities number will be similar in 2018 and this causes the next guess like that the next year candidate 370,000 are waiting for cancer death order because of invisible reason today.
The total number of individuals affected by cancer in Japan is about 1,000,000 and the number means 37% people might be going to die. Medical doctor is focusing on patients who are clearly suffering from actual diseases like cancer. AXiON Research Inc., we assume the invisible path to reach those diseases and some reason with scientific background must be there to meet the numbers repeated every year. In The "Compass to Healthy Life" Research Complex Program organized by RIKEN and supported by JST, in July 2018, AXiON Research Inc. shows the performance of Replica Generator III to increase data of healthcare on 415 people data up to 4,150.
It' s really good result and succeeded in increase of 4 initial disease risk categories up to 7 ones after the data generation with keeping the original statistical feature and accuracy. It also keeps the probability density, the dispersion and the distribution of the original data increasing the number per different age and gender. It contributes the future analysis of 10,000 people data and analyzes health indices and invisible disease risk prediction for pre-disease state.

AXiR Engine

P-HARP
PRECISION HEALTH ANALYSIS RESEARCH PLATFORM

AXiON Research Inc. is introducing new methodology to identify the health indices / position in pre-disease state group and how quickly getting worse by checking autonomic nerves activities or up / down parameters related to individual immunity. Heatmap of health condition/disease risk level helps the identification of the risk and vector-map of disease risk level works how much, how quickly getting worse or shifting the next stage of future diseases.
The challenge started a few years ago and various technologies / research results are accelerating the analysis process and its accuracy. Today medical service is often using X-ray, MRI, CT or PET and it can identify the disease itself at very high rate. However, it does usually work as an answer like you have no problem at all, at least today. Some of pre-disease state people might be waiting for new technology to make some advice or estimation of future disease risk at very early stage. We introduce AXiR Engine® for how much healthy you are or we are. We' re going to the next pre-service stage with strategic partners to run the service into the real world and commercial service.

Business Model

AXiON Research provides AXiR Engine and P-HARP customized services for the customers and partners. Healthcare Services are built in various application. We' re interested in strategic alliance partners to accelerate the market adoption.

Global Partnership

AXiON Research is building global partnership with AR/VR and robotics companies targeting healthcare industry. We' re also looking for worldwide business partners.

Fund Raising

We' re seeking the next fundraising Series A in 2019. Series A 1st will be between Jan. and Apr. 2019. Series A 2nd will be between June and Oct. 2019. Welcome, Early Entries.

AXION RESEARCH INC.

Apply for our exciting research Prize!

SCIENCE-PINS PRIZE FOR NEUROMODULATION

SCIENCE-PINS

$25, 000 Grand Prize!
Get published in *Science*!

The *Science*-PINS Prize is a highly competitive international prize that honors scientists for their excellent contributions to neuromodulation research. For purposes of the Prize, neuromodulation is any form of alteration of nerve activity through the delivery of physical (electrical, magnetic, or optical) stimulation or chemical agents to targeted sites of the nervous system.

For full details, judging criteria and eligibility requirements, visit:

www.sciencemag.org/prizes/pins

Submission Deadline: March 15, 2019

Science AAAS

PINS 品驰

Science Translational Medicine AAAS

Beautiful Campus, Beautiful Minds:

Celebrating Wuhan University's Past, Present, and Future

Trees of Wuhan University

Xiankang Dou

Wuhan University is often described as having one of China's most beautiful campuses. In the spring, lotus flowers pop up on its small, central lake, and cherry blossoms line an avenue running below the imposing stone buildings of the Old Dormitory. If you're willing to climb the steep stairs past this structure—fondly called "Cherry Blossom Castle" by faculty—you can gaze across to the main administrative building, and the hill covered in sun-dappled trees behind it.

But, says Wuhan University president Xiankang Dou, there's more to the university than just pleasant scenery.

"When you come to Wuhan University, you'll see that it's beautiful and we have a great history. But that's not enough," he says, sitting in the main administrative building. "We are creating an environment and atmosphere where we respect knowledge and hard work."

Wuhan University was founded 125 years ago in Wuhan, a city of around 10 million located in China's central, landlocked Hubei Province. In a sense, the campus is a smaller version of the city itself—Wuhan is also centered around a series of lakes, including the enormous East Lake. When the university was founded, it was a little different from other universities in China. At the time, most universities focused on a single discipline, whereas Wuhan University offered accounting, business, physics, and foreign languages. That remains true today, and the university now boasts Lei Jun, the founder of smartphone-maker Xiaomi, and a former prime minister of Kazakhstan, among its alumni.

"[Wuhan University] is a comprehensive university, so we have many interdisciplinary discussions. These create the uniqueness of our school. Here, the social scientist can talk with the life scientist—this kind of mixture generates more creativity," Dou says. "I'm really proud of our glorious past, our flourishing present, and our bright future."

Over its lifetime, the university has undergone many iterations: different names, different buildings—and, of course, different students and faculty. But one thing that's stayed constant is the university's emphasis on taking care of its students, says Dou.

Dou points to how past presidents at Wuhan University made special efforts to look after their scholars. In the 1930s, the country was beset by the Second Sino-Japanese war (1937–1945), resulting in great hardship and extreme loss of life for the Chinese people. Nevertheless, the university continued to house its scholars in grand cottages on Luojia Hill, the sunny knoll behind the administrative building. "[It was] to show our values and attitudes toward these professors, that we wanted to continue to strengthen the foundation of our university and excel academically," he says.

Dou, who became president in 2016, has had an impressive academic career in his own right. He studied space physics at the University of Science and Technology of China (USTC), a prestigious research university in eastern Anhui Province. He admits that at the time, he didn't know exactly what he was getting into. "When I was a child, I didn't know the difference between astrophysics and space physics," he explains. "I liked to think about outer space, and that's why I chose space physics." He focused much of his research on the earth's atmosphere, namely, the stratosphere and mesosphere. In the following decades, he won numerous awards and accolades—last year he was honored by being selected as a member of the Chinese Academy of Sciences.

During his tenure as university president, Dou's focus has been firmly back on earth. He's making it his mission to attract top talent to the university and turn it into a world-class research institution. For him, that requires focusing on two main goals: improving the teaching faculty and enhancing the academic options and living conditions for students. Meeting the latter objective means allowing students to choose their courses, as well as ensuring they have a good studying environment. "The goal of the university is to foster young talent who can

PHOTOS: (FROM TOP) ZHANG RAN, 2012; WUHAN UNIVERSITY

Center of Humanities and Hall of Sciences

Cherry Blossoms at Wuhan University

better serve society. As such, we put the students' goals and requirements as our utmost priority," says Dou, who personally monitors the condition of the students' living quarters.

Although Dou says he's proud of Wuhan University, he has plans to make it even better. "I have a dream," he says. "Today, the competition between universities is really fierce. In the next decade, I believe and hope that we can continue to bring high-level teaching faculty to our school. This will help us to build a first-class university, respected nationally and internationally."

Of course, part of achieving that goal will be getting more papers published in top academic journals, says Dou. But that's only one aspect of what he is hoping for from his academic staff. "We also believe that our faculty can focus more on the growth of our country, the development of our society, and the improvement of our economy," Dou says.

Dou is also keen to encourage and attract more international students—particularly those from developing countries. That's partly to increase trust and partnerships between China and the countries in question, but also to provide students from those countries with tools they can take back with them to advance the developing medical and legal systems in their homelands, he says, pointing to Africa and Southeast Asia as areas of particular interest. Already, Wuhan has large numbers of international students as compared to other universities in China. To Dou, this is impressive—after all, Wuhan doesn't have the glitzy, big-city romance of Shanghai, or the grand, historical significance of Beijing. "We are in the hinterlands of China, but we still attract an impressive number of students. That is quite unique," he says proudly.

And unsurprisingly, given Dou's background, the university is pouring millions into developing better facilities across the sciences. According to him, Wuhan University is already one China's strongest for space science, and in the coming years he wants to attract more exceptional students there and to increase cooperation with researchers in the United States and United Kingdom.

But one thing Dou won't be trying to do is increase student admissions. "Because I come from the smallest university in China," he says, referring to USTC, "I don't really have any interest in increasing the number of students at our university." Instead, he just wants to focus on attracting the right people and making sure they are supported and encouraged adequately. "We want to turn them into the top thinkers in their fields—it's about quality, not quantity," he says.

Although Wuhan University has grand plans for its future and is certainly more than just a beautiful campus, the fact that the surroundings are aesthetically pleasing certainly doesn't hurt. Students can wander leisurely there, taking in the last rays of the sun, or stay active by running around the sports track. When Dou is asked about his favorite place in the university, he responds without hesitation: Cherry Blossom Boulevard, of course.

Looking nostalgic, he recalls watching a coming-of-age film called "Girls' Dormitory," as a college student at USTC in the 1980s, when there were few movies available in China. The film told the story of five first-year students who lived in Wuhan University's Old Dormitory next to Cherry Blossom Boulevard. Even now, that cherry-blossom-lined avenue beside the dormitories reminds him of watching that film, and in turn, of being a young college student himself. The Old Dormitory exhibits a combination of Western and Chinese architectural styles, which to Dou represent both the university's glorious history and its modern spirit of openness and tolerance.

"[Standing] on this boulevard, we can feel the history of Wuhan University," Dou says, referring to the generations of students and teachers who have walked there before. "We see the past, the present, and the future of this university."

武漢大學
WUHAN UNIVERSITY

PHOTOS: (FROM LEFT) PENG MIN, 2016; YANG ZIQING, 2018

Researchers in an experimental field, Saldaña, Colombia

Aerial photo of rice fields, Ibagué, Colombia

Sustainable agriculture supported by IoT

Agricultural productivity, sustainable careers, and environmental conservation are global issues in agriculture. Colombia is no exception, and a project to provide solutions to such issues using the internet of things (IoT) has started in cooperation with the governments of Colombia and Japan in January 2018 *(1)*.

The joint project is conducting small-scale experimental research that aims to develop a knowledge platform that increases rice production and conserves the environment by reducing methane emission and nitrification in farming through better input management (irrigation and nitrogen fertilizer). The project's partners include, from Japan, the Ministry of Internal Affairs and Communications (MIC), which is also funding the project, and from Colombia, the Ministry of Information Technology and Communication (MINTIC) , the Ministry of Agriculture and Rural Development (MADR) and the National Rice Growers Association (FEDEARROZ) in close collaboration with the International Center for Tropical Agriculture (CIAT).

e-kakashi, a knowledge platform for agriculture

PS Solutions is providing such a platform with **e-kakashi**. **e-kakashi** consists of three units: a gateway unit that functions as an interface between the other two units, a sensor node unit that obtains measurements from each sensor, and a cloud system unit that includes AI capability and receives all the collected data. AI trained with plant science and agricultural know-how integrates the acquired data and visualizes them as graphs, enabling users to easily analyze the data in the context of good farming practices and plant science.

In the current project, collected data include rice plant conditions (or growth), environment factors, and collective farming experiences. At the test fields of CIAT and FEDEARROZ, environmental data are collected by sensors *(2)* integrated to the **e-kakashi** cloud system unit. By giving scientific feedback from FEDEARROZ and CIAT about farming techniques and know-how, **e-kakashi's** AI will compare and integrate the field data to provide farmers with cultivation recipes (or **ek-recipes**) including actions for better crop management. **e-kakashi** will benefit Colombian agricultural practices as well as the environment by enabling the practical exchange of farming techniques to optimize farming processes and improve product quality and quantity.

FEDEARROZ's Technical Manager, Myriam Patricia Guzman, comments, "**e-kakashi** with real-time information analysis will provide farmers with tools to make optimal crop management decisions. The ICT (information and communication technology) utilized in this project will be integrated as part of the monitoring platform for crop conditions to improve crop management. The rice farming methods tested and practiced in the project will be disseminated through the FEDEARROZ AMTEC program (Massive Adaptation Technology Extension Program), which integrates climate services, site-specific agriculture and precision agriculture for the benefit of farmers."

Educating the next generation of farmers

In addition to providing solutions to agricultural productivity and environmental issues, the project deals with issues of employment in Colombia through IoT and agricultural education. To maximize **e-kakashi** for farming, training will be done through lectures, practical field training and workshops for participants from FEDEARROZ including member farmers and other stakeholders in rice production. During the training, farmers and technicians will familiarize themselves with IoT and science-based agriculture. This education is particularly useful to FEDEARROZ farmers who seek sustainable agriculture. Sustainable agricultural practice will bring stable employment to generations of farmers.

Scientific research and smart agriculture made easy with e-kakashi

The current project is a test case for how **e-kakashi** can contribute to improving agricultural practices in general. Its small-scale will show how common agricultural problems can be solved by measuring key environmental parameters. Ultimately, by using **e-kakashi**, scientific hypotheses can be tested for plant growth in any field anywhere in the world.

Dr. Takashi Togami, the developer of **e-kakashi**, imagines **e-kakashi** and its **ek-recipes** solving food sustainability and stable employment around the world. "Environmentally sound sustainable agriculture is needed to save our planet and ourselves," he says.

(1) http://www.soumu.go.jp/main_sosiki/joho_tsusin/eng/Releases/-Telecommunications/2018_01_12_02.html
In January 2018, the Colombian government and the Japanese government agreed to cooperate in the area of agricultural IoT to resolve the challenges Colombia is facing in agriculture, such as sustainable farming and food production.

(2) One of the sensors used to measure water depth is provided by Tokyo Electron Device Limited. With a built-in mobile unit, it communicates directly to the cloud system. PS Solutions foresees that all sensors will come with this communication capability in the near future, which would eliminate the gateway and sensor nodes units, allowing for easier and more economic data collection at more collection points in the fields.

CONTENTS

1362
Next-generation wargames

21 DECEMBER 2018 • VOLUME 362 • ISSUE 6421

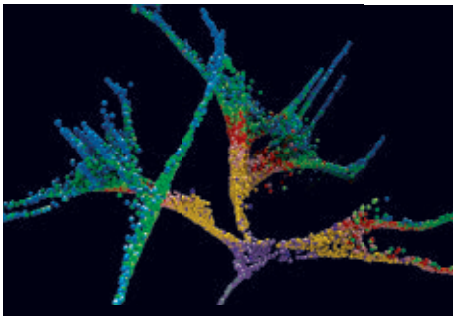

BREAKTHROUGH *of the* YEAR

ON THE COVER

A zebrafish embryo at an early stage of development. Fluorescent markers highlight cells expressing genes involved in determining the type of cell they will become. The ability to track development in stunning detail by marking early embryonic cells to trace their lineage, isolating thousands of cells during development, and sequencing their RNA cell by cell, is *Science*'s 2018 Breakthrough of the Year. See page 1344. *Image: Jeffrey Farrell, Schier Lab/Harvard University*

NEWS

INSIGHTS

MICROBES WITHIN THE HOST
IN HEALTH AND DISEASE

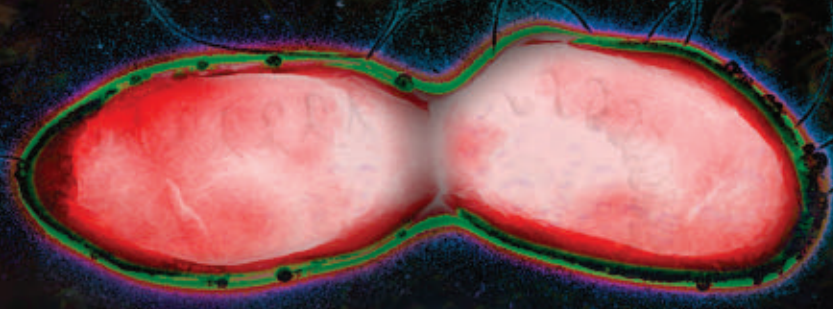

13th Annual Salk/Fondation Ipsen/Science Symposium on Biological Complexity

January 22 - 24, 2019 • Salk Institute for Biological Studies, La Jolla, CA

THE SYDNEY BRENNER NOBEL LECTURE JEFFREY GORDON *WASHINGTON UNIVERSITY IN ST. LOUIS*

KEYNOTE LECTURE
MARGARET MCFALL-NGAI *UNIVERSITY OF HAWAII AT MANOA*

SESSION 1: GUT-BRAIN AXIS
JANELLE AYRES (Chair) *SALK INSTITUTE FOR BIOLOGICAL STUDIES*
SARKIS MAZMANIAN *CALIFORNIA INSTITUTE OF TECHNOLOGY*
ROSA KRAJMALNIK-BROWN *ARIZONA STATE UNIVERSITY*
JOHN CRYAN *UNIVERITY COLLEGE CORK, IE*

SESSION 2: IMMUNOMETABOLISM
SUSAN PRESCOTT (Chair) *UNIVERSITY OF WESTERN AUSTRALIA, AS*
RUSLAN MEDZHITOV *YALE UNIVERSITY*
LUKE O'NEILL *TRINITY COLLEGE DUBLIN, IE*
RUTH LEY *MAX PLANCK INSTITUTE, GE*

SESSION 3: CANCER AND CANCER THERAPIES
LAURENCE ZITVOGEL (Chair) *GUSTAVE ROUSSY, FR*
CINDY SEARS *JOHNS HOPKINS MEDICAL INSTITUTE*
OMER YILMAZ *MASSACHUSETTS INSTITUTE OF TECHNOLOGY*
THOMAS GAJEWSKI *UNIVERSITY OF CHICAGO*

SESSION 4: HOST-PATHOGEN INTERACTIONS
DENISE MONAK (Chair) *STANFORD UNIVERSITY*
ANDREAS BÄUMIER *UNIVERSITY OF CALIFORNIA, DAVIS*
THAD STAPPENBECK *WASHINGTON UNIVERSITY IN ST. LOUIS*
HERBERT "SKIP" VIRGIN *WASHINGTON UNIVERSITY IN ST. LOUIS*

SESSION 5: IMMUNE-MICROBE INTERACTIONS
LORA HOOPER (Chair) *UNIVERSITY OF TEXAS SOUTHWESTERN MEDICAL CENTER*
GREGORY BARTON *UNIVERSITY OF CALIFORNIA, BERKELEY*
ANDREW MACPHERSON *UNIVERISTY OF BERN, SW*
YASMIN BELKAID *NATIONAL INSTITUTE OF HEALTH, NIAID*

SESSION 6: MICROBIAL COMMUNITIES IN HEALTH AND DISEASE
MARTY BLASER (Chair) *NEW YORK UNIVERSITY*
SUSAN LYNCH *UNIVERSITY OF CALIFORNIA, SAN FRANCISCO*
DAN LITTMAN *NEW YORK UNIVERSITY*
MICHAEL FISCHBACH *STANFORD UNIVERSITY*

ORGANIZING COMMITTEE: JANELLE AYRES · JAMES LEVINE · VALDA VINSON

SCIENTIFIC PROGRAM COMMITTEE: JANELLE AYRES (CHAIR) · RON EVANS · MICHAEL KARIN · ROB KNIGHT · MANUELA RAFFATELLU · INDER VERMA (PAST CHAIR) · VALDA VINSON · CAROLINE ASH

ONLINE REGISTRATION and INFORMATION: www.salk.edu/SFIS2019
CONTACT: events@salk.edu
#SFIS2019

ABSTRACT SUBMISSION DEADLINE: December 19, 2018 **REGISTRATION DEADLINE:** January 4, 2019

Poster design by Jamie Simon, Salk Institute

FONDATION IPSEN

salk® Where cures begin.

Science AAAS

CONTENTS

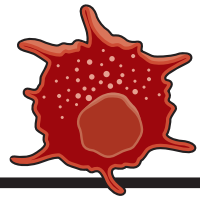

1355 & 1416
Hunting senescent tumor cells

21 DECEMBER 2018 • VOLUME 362 • ISSUE 6421

CREDITS: (TOP TO BOTTOM) A. KITTERMAN/*SCIENCE*; ISTOCK.COM/ALLGORD

SCIENCE (ISSN 0036-8075) is published weekly on Friday, except last week in December, by the American Association for the Advancement of Science, 1200 New York Avenue, NW, Washington, DC 20005. Periodicals mail postage (publication No. 484460) paid at Washington, DC, and additional mailing offices. Domestic individual membership, including subscription (12 months): $165 ($74 allocated to subscription). Domestic institutional subscription (51 issues): $1808; Foreign postage extra: Mexico, Caribbean (surface mail) $55; other countries (air assist delivery): $89. First class, airmail, student, and emeritus rates on request. Canadian rates with GST available upon request, GST #125488122. Publications Mail Agreement Number 1069624. **Printed in the U.S.A.**
Change of address: Allow 4 weeks, giving old and new addresses and 8-digit account number. **Postmaster:** Send change of address to AAAS, P.O. Box 96178, Washington, DC 20090–6178. **Single-copy sales:** $15 each plus shipping and handling; bulk rate on request. *Science* is indexed in the *Reader's Guide to Periodical Literature* and in several specialized indexes.

Science
AAAS
1200 New York Avenue, NW, Washington, DC 20005
Clarendon House, Clarendon Road, Cambridge, UK CB2 8FH

SUBSCRIPTION SERVICES For change of address, missing issues, new orders and renewals, and payment questions: 866-434-AAAS (2227) or 202-326-6417, FAX 202-842-1065. Mailing addresses: AAAS, P.O. Box 96178, Washington, DC 20090-6178 or AAAS Member Services, 1200 New York Avenue, NW, Washington, DC 20005

INSTITUTIONAL SITE LICENSES 202-326-6730 **REPRINTS:** Author Inquiries 800-635-7181 **COMMERCIAL INQUIRIES** 803-359-4578 **PERMISSIONS** 202-326-6765, permissions@aaas.org **AAAS Member Central Support** 866-434-2227 www.aaas.org/membercentral.

INFORMATION FOR AUTHORS See **www.sciencemag.org/authors/science-information-authors**

IAS conference attendees. (From left) Professor Jacob Huang, Professor Li Tatsien, Professor Jean Salençon, Professor Sir John Ball, Professor Serge Haroche, Professor Philippe G. Ciarlet, Mr. Alexandre Giorgini, Professor Jean-Marie Lehn, Professor Way Kuo, Professor Pierre-Louis Lions, Professor Lu Jian, Vice-President (Research and Technology), and Professor Alex Jen Kwan-yue, Provost.

Professor Kuo (right) and Mr. Giorgini.

Professor Jean-Marie Lehn (left) and Professor Philippe G. Ciarlet (right).

Sharing ideas across borders

International lecture series promotes collaboration

The spirit of international collaboration continues to thrive at the City University of Hong Kong (CityU), a fact that was highlighted last month during an important conference honoring the 80th birthday of Professor Philippe G. Ciarlet. During his career, the renowned mathematician has pioneered research into the finite element method, differential geometry, and the theories of elasticity, plates, and shells. Ciarlet joined CityU in 2002, and has been a senior fellow with the **Institute for Advanced Study (IAS)** at CityU since its inception in 2015. He has devoted himself to connecting its students and faculty with some of France's greatest minds.

Over the past 15 years, Ciarlet has organized a lecture series that has welcomed high-ranking members of the French Academy of Sciences to CityU. The series has introduced many notable French scientists to the CityU campus, including Fields Medalists and Nobel laureates. Speakers have included Nobel prize winners Serge Haroche, a physicist whose team was rewarded for its work on quantum systems in 2012, and chemist Jean-Marie Lehn, who in 1987 shared the Nobel Prize in Chemistry as part of a research group working in the field of supramolecular chemistry, pioneering the discovery and application of synthetic cyclic compounds known as cryptands.

Jacob Huang, executive director of IAS and chair professor of materials science at CityU, says that this unique research partnership between France and Hong Kong has helped foster high-level academic discussions between the two scientific communities.

"This dialogue has helped us further improve our international network and collaboration with global talent, which in turn helps to promote the cross-fertilization of ideas and the creation of new knowledge," he explains.

On November 12, IAS held a conference, "Celebrating France–Hong Kong Scientific Cooperation in Honour of Professor G. Ciarlet's 80th Birthday," to highlight Ciarlet's important contributions to the university's research environment and to reaffirm the values of international cooperation and high-level conversation that have come to underpin the work of IAS. The institute opened three years ago to promote innovative research in Hong Kong by world-renowned scholars.

Present were Nobel Prize-winners Haroche and Lehn as well as members of the French Academy of Sciences and Senior Fellows of IAS, including mathematicians Sir John Ball, Tatsien Li, Fields Medalist Pierre-Louis Lions, and physicist Jean Salençon.

Way Kuo, president of CityU, opened the one-day conference with a speech underlining the importance of the university's working relationship with French institutions. Over the years, he said, these partnerships have helped ensure that students and faculty at CityU put scientific excellence at the forefront of their research and teaching, and have kept the university at the heart of the international academic community.

In his follow-up remarks, Alexandre Giorgini, Consul General of France in Hong Kong and Macau, highlighted the importance of the research collaboration for France. He praised Ciarlet as an "*honnête homme,*" an 18th-century term for an enlightened man who "wants to understand the basic truths of the functions of the universe." He also commended Ciarlet for being an ambassador by using science as a "unifying language" to help create a common bond between France and Hong Kong.

Following the opening speeches, conference attendees enjoyed a day-long program of carefully curated talks by invited delegates on subjects as wide-ranging as the impact of Italian physicist and astronomer Galileo on modern science; quantum physics; and developments in game theory.

"We were deeply honored that six eminent scholars joined together on the CityU campus to present a series of lectures and disseminate knowledge in their research areas among the scientific community," says Huang. "We hope these kinds of events will further raise the global profile of the science and engineering community at CityU and other academic institutions in Hong Kong and Greater China."

The IAS intends to become a leader in interdisciplinary research that benefits society and to be recognized as both a regional and global intellectual center, adds Huang.

CityU 香港城市大學 City University of Hong Kong
Professional · Creative For The World

City University of Hong Kong Institute for Advanced Study

Institute for Advanced Study, CityU ■ www.ias.cityu.edu.hk

SCIENCE TRANSCENDING BOUNDARIES

AAAS | ANNUAL MEETING
Washington, DC | Feb. 14–17, 2019

visit aaas.org/meetings

BE A PART OF THE CONVERSATION

Artificial Intelligence | Astrophysics | Genomics | Sustainability
Science Diplomacy | Food Security | Digital Privacy | Infection Control
Public Engagement | Climate Change | Diversity | Big data

and more...

Advance registration rates are available now through January 22, 2019

Visit the online program and discover more information: aaas.org/meetings
Mobile app will be released in early January

EDITORIAL

Exploring organisms cell by cell

Editor-in-Chief, Science Journals.
jberg@aaas.org

In an imaginary universe, you have discovered a set of planets, each with its own complex civilization with many culturally distinct nations. You face the daunting task of exploring each planet, mapping national boundaries, and characterizing different cultural features. In discussing this challenge with your colleagues, you come up with an alternative plan. You can divide each planet into small sectors, tag each sector for identification, send out many small probes to land in random locations and send back data, and then use the tagging information to computationally assemble the information into detailed atlases and travel guides. *Science*'s Breakthrough of the Year recognizes the application of this tag-analyze-assemble approach to one of the most fundamental and fascinating processes in biology—the seemingly miraculous transformation of single cells into complex organisms—providing rich information about cell-type inventories and laying the foundation for many future studies.

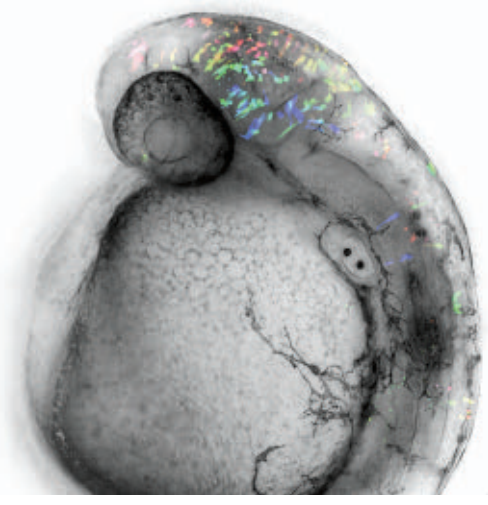

A zebrafish embryo, 30 hours postfertilization, reveals descendants (fluorescently labeled) of cells that were transplanted 22 hours earlier.

This achievement builds on the 2002 Nobel Prize–winning work of John Sulston and colleagues who had mapped the development of the roundworm *Caenorhabditis elegans* by painstakingly watching larvae mature cell by cell through microscopes. This revealed the sequence of cell divisions that resulted in elaborate structures, which led to the characterization of important processes. With today's technologies, especially massively parallel DNA sequencing and advanced fluorescence microscopy, the cells that comprise *C. elegans* have been mapped again using tag-analyze-assemble methods based on gene expression patterns within each cell. The same approaches have been used to map the cellular anatomy of organisms of increasing complexity and size. An additional benefit is that the gene expression signals that define each cell type also provide fundamental information about the biochemistry and biology of each cell. The large and rich datasets that have been generated, and the techniques that will produce more, constitute exciting breakthroughs in developmental biology.

Nucleic acid–based technologies also underlie some of this year's runners-up, including advanced methods in forensics that combine sequence and other databases, elucidation of the breeding habits of earlier hominids, and long-awaited advances in RNA-based therapies. A range of technologies has also led to important conceptual advances in the organizational principles within cells. Technologies that elucidated large biological molecular structures have been applied to smaller molecules, resulting in a remarkable advance in analytical chemistry. Exploration has revealed insights into the ancient history of our planet. Strange lifeforms, known from fossils hundreds of millions of years old, now appear to be ancestors of modern animals rather than lines that went extinct. A crater discovered under the ice in Greenland likely resulted from a large meteorite impact. One source of other cosmic visitors, high-energy neutrinos, has been found to be types of galaxies with a massive black hole at their centers.

Other events have highlighted cultural issues. The #MeTooSTEM movement has brought much needed attention to sexual harassment within the scientific community. Further progress is essential to allow individuals of all genders to pursue their training and careers without dealing with the realities of substantially unchecked harassment. The announcement of the birth of babies with genomes that had been intentionally modified in a manner that appears to violate many long-standing ethical principles reminds us that scientific results, no matter how exciting and full of potential, must be applied with appropriate care and respect for ethical international norms. Finally, we are challenged by the changing climate of our own planet. Powerful storms associated with large amounts of rainfall and other events are occurring with increasing frequency, illustrating the considerable urgency for appropriate actions. We must work together across global borders and cultures to drive effective steps to arrest harmful climate change.

–Jeremy Berg

10.1126/science.aaw3633

NEWS

IN BRIEF

Edited by **Catherine Matacic**

Scientists may be making Antarctica's birds sick

You can give your cat the flu. You can also pass pneumonia to a chimpanzee or tuberculosis to a bird. This kind of human-to-animal disease transmission, known as reverse zoonosis, has been seen on every continent except one: Antarctica. Now, human-linked pathogens in bird poop reveal, for the first time, that even animals on this isolated, ice-bound landmass can pick up a bug from tourists or visiting scientists. At four Southern Ocean locations—including Livingston Island off the Antarctic Peninsula—researchers collected fecal samples from 666 adult birds from 24 different species, including rockhopper penguins, Atlantic yellow-nosed albatrosses, giant petrels, and skuas. Bacterial species in the samples were a close match for those circulating in humans and domestic animals, based on their DNA. Among the matches: *Campylobacter jejuni*, which causes food poisoning; an antimicrobial-resistant strain of *C. lari*; and certain strains of *Salmonella*. That suggests humans—including scientists and tourists—may be passing their bacteria on to local seabirds, either directly or through migrating birds, the researchers report online in *Science of the Total Environment*. This newly identified infection route could have devastating consequences for some Antarctic bird colonies.

Paris agreement lives on

CLIMATE | After 2 weeks of all-night bargaining sessions, representatives of nearly 200 countries agreed to the "rules of the road" that will govern the Paris agreement on climate change, which seeks to limit the world's rise in global temperatures to 2°C by 2100. The new rules lay out how nations should track and report their carbon dioxide emissions—with the same requirements for both developed and developing countries. Other contentious issues, including the role of international carbon markets and whether long-polluting nations should pay others climate "reparations," were pushed off to later meetings of the United Nations group. But the world will need to take "unprecedented" action by 2030 in order to hit the Paris targets, scientists warned in an October report of the Intergovernmental Panel on Climate Change.

Lawsuit targets trial reporting

CLINICAL TRIALS | The U.S. Food and Drug Administration (FDA), the National Institutes of Health, and the Department of Health and Human Services have failed to ensure that researchers report clinical trial results as federal law requires, according to a lawsuit filed this month in a U.S. district court in New York. The plaintiffs are Peter Lurie, a physician and former associate FDA commissioner, and Charles Seife, a journalism professor at New York University in New York City (who has written for *Science*). In a 2007 law, Congress required researchers conducting clinical trials to report results both publicly and to the federal government, but in a 2016 rule, the agencies relieved some of the reporting obligations for trials completed before 18 January 2017. Lurie and Seife say that part of the rule is inconsistent with the law and should be struck down.

PHOTO: MINT IMAGES/AURORA PHOTOS

Probe kisses the sun

SPACE SCIENCE | NASA's Parker Solar Probe has made its first dip into the sun's atmosphere, providing scientists with longed-for data such as the image below of a solar streamer, a blast of particles from an area of high solar activity. (The bright spot in the center is Mercury.) Launched in August (*Science*, 3 August, p. 441), Parker will make 24 close flybys over 6 years, probing the sun's atmosphere, or corona, and an outward particle flow known as the solar wind. Its first flyby, from 31 October to 11 November, has already broken records for the highest speed for a spacecraft, at 343,000 kilometers per hour, and the closest approach to the sun, at 24 million kilometers. But those records won't last long as Parker's orbits become closer and faster.

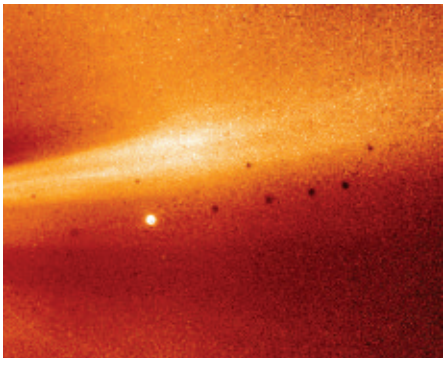

Particle flows from the sun snapped by the Parker Solar Probe in its first flyby.

CREDITS: (IMAGE) NASA/NRL/PARKER SOLAR PROBE; (GRAPH) J. BRAINARD/*SCIENCE*; (DATA) S. A. GALLO *ET AL.*, BIORXIV 10.1101/479816 (2018)

NIH urged to guard research

GRANT MANAGEMENT | An advisory panel to the director of the National Institutes of Health (NIH) has recommended that U.S. universities receiving NIH funding consider vetting the activities of foreign scientists before they are hired. Last week's report on "foreign influences" also suggests that NIH expand the definition of scientific misconduct to include "material nondisclosures" of any ties to other governments, companies, and individuals. The recommendations reflect concerns that academic researchers are unwittingly allowing China and other governments to steal research findings and other intellectual property that belong to the U.S. government. A senior Federal Bureau of Investigation official told Congress last week that it has investigated "thousands" of such attempts, and that U.S. universities must do more to thwart them. Preventing reviewers from downloading research proposals could be another way to prevent information from falling into unauthorized hands, the report suggests.

Australia cuts future funding

RESEARCH FUNDING | Funding for graduate research and education in Australia will be virtually flat for the next 4 years, the government said this week. A midyear budget adjustment requires the elimination of AU$328 million ($236 million) in planned increases, according to a 17 December announcement. "Economic growth and prosperity will not be achieved by cutting research," John Shine, president of the Australian Academy of Science in Canberra, said in a statement. Scientists hope to get the money at least partially restored in the next full-year budget, which will be adopted in the spring and take effect on 1 July 2019.

New immune system institute

BIOMEDICINE | The Allen Institute for Immunology was launched last week in Seattle, Washington. The effort will use a $125 million donation from the late Microsoft co-founder Paul Allen to better define how the immune system works and why it falters in certain illnesses, including cancer and autoimmune conditions. "We want to do a very detailed view of the immune system over time," says Executive Director Thomas Bumol, an immunologist and former senior vice president at Lilly Research Laboratories. Researchers will track the immune function of three groups of people—4-year-olds, adults in their 20s and 30s, and people between 55 and 65. The institute joins Allen-funded efforts exploring cell biology, the brain, and artificial intelligence.

A few grant reviewers do a lot

PEER REVIEW | A small cadre of seasoned researchers performs a disproportionately large share of the peer reviews that help U.S. science agencies award grants in the biological sciences, a study has found. Survey responses from 874 researchers showed that a subset served on seven or more funding panels over 3 years and spent an average of nearly 17 days on the task annually, according to a preprint paper published 28 November on bioRxiv. These reviewers made up 23% of respondents who sat on at least one panel, but they served on 40% of all panels reported. Frequent reviewers also reported spending nearly three times more hours on proposal reviews than less frequent reviewers, close to what they considered the maximum time available for such work.

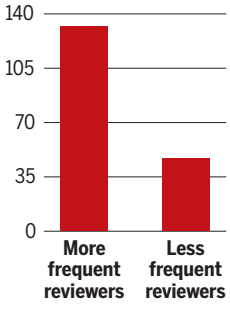

Mars's methane mystery deepens

SPACE SCIENCE | Mars's methane has gone missing. For 2 decades, spacecraft monitoring the martian atmosphere, including NASA's Curiosity rover, have hinted at the presence of the gas, which on Earth is primarily a byproduct of life. Last week, at a meeting of the American Geophysical Union in Washington, D.C., scientists reported that the European Space Agency's Trace Gas Orbiter (TGO), which arrived at Mars in 2016, has failed to detect methane in the atmosphere down to 50 parts per trillion. That's well below levels seen by Curiosity, which has detected small seasonal swings in the gas from its perch in Gale Crater. The TGO will run until at least 2022, long enough to capture any methane surges over several martian years.

Zinke exits Interior

CONSERVATION | U.S. Secretary of the Interior Ryan Zinke announced last week that he will leave the post by the end of the year. Many environmental groups

THREE QS

Monsoon memories

This year, India's monsoon rains, critical to the harvest and water supply, were below average for the 13th time in just 18 years. Alarm spreads when the rains don't come, says Sunil Amrith, a historian at Harvard University who has just released a new book—*Unruly Waters: How Rains, Rivers, Coasts, And Seas Have Shaped Asia's History*—which documents the long scientific quest to understand one of Asia's most important weather patterns. *Science* spoke to Amrith about his work.

Q: Why write about the monsoon?
A: Like many scholars, I sort of took the monsoon for granted. The cliché is that India is always just one bad monsoon away from disaster. But as I learned about all the people who had tried to figure out what makes the monsoon tick and why it varies from year to year, I realized we hadn't explored all of the implications. [The monsoon] is connected to so many things—food, floods, dams, climate change, sustainability.

Q: How has water engineering shaped the history of South Asia?
A: They often faced either too little or too much water. Sometimes you have both at the same time—flooding in [wet regions], drought in places that are among the most arid in the world. ... Eventually, [in India] you see the emergence of this idea that the nation needs to be liberated from climate.

Q: But now you're worried about how climate change—and new dam-building projects in the Himalayas—might affect water supplies. Why?
A: The historical record shows that relying on large-scale projects ... is a mistake and raises new risks. Dams in the Himalayas are particularly worrying. Until the 1980s, it was not viable to dam the rivers that far upstream. That's changed, and the risks are enormous. This is a seismically active zone, and the downstream consequences of a dam collapse would be serious. [As for climate change,] you have melting glaciers, for instance. And there is an increasing body of work on how the monsoon is changing. Planetary warming is interacting with aerosol emissions and land use changes to make the monsoon very unpredictable.

SCIENCEMAG.ORG/NEWS
Read more news from *Science* online.

celebrated the news, saying Zinke, who is under investigation for allegedly violating federal ethics rules, had failed to uphold his department's mission to protect wildlife and public lands by pushing for greater mining, drilling, and grazing on federal property. But observers expect those policies to remain largely in place under any new secretary appointed by President Donald Trump.

A 'Farout' planet

SPACE SCIENCE | Astronomers this week announced the discovery of the solar system's most distant resident, a dwarf planet 120 times farther from the sun than Earth. The planet, nicknamed "Farout," is pinkish in hue, reflecting an icy composition. It is likely some 500 kilometers in diameter, similar to Saturn's icy moon Enceladus. The astronomers—Scott Sheppard at the Carnegie Institution for Science in Washington, D.C.; David Tholen of the University of Hawaii in Honolulu; and Chad Trujillo of Northern Arizona University in Flagstaff—spotted Farout with the Japanese Subaru 8-meter telescope atop Mauna Kea in Hawaii on 10 November. It was confirmed this month by the Giant Magellan Telescope at Las Campanas Observatory in Chile. Farout's orbit is not yet known, so the team can't say whether its path hints at gravitational tugs from a hypothesized ninth giant planet.

CORRECTION

The 7 December item headlined "Sample return probe arrives at asteroid" incorrectly reported that NASA's OSIRIS-REx mission to the asteroid Bennu would be the agency's first to return materials from space since the Apollo moon landings. NASA's Stardust mission brought back comet dust in 2006.

PHOTO: RGB VENTURES/SUPERSTOCK/ALAMY STOCK PHOTO

FACILITIES

European x-ray source shuts down for rebuild

Europe's premier x-ray source shut down last week for a 20-month upgrade that will boost the brightness of its beams by a factor of 100. Since 1994, the European Synchrotron Radiation Facility (ESRF) in Grenoble, France, has generated x-rays 100 billion times brighter than medical x-ray machines by sending beams of electrons around a circular accelerator. The ESRF has been a workhorse for materials science, condensed matter physics, and biology. The €180 million upgrade will greatly reduce the width of the electron beam, boosting the intensity of the x-rays. Meanwhile, the U.S. Department of Energy approved a plan and cost estimate for an $815 million rebuild of the ESRF's longtime rival, the Advanced Photon Source (APS) at Argonne National Laboratory in Lemont, Illinois. If all goes as planned, the ESRF will turn back on in 2020, and the APS upgrade will commence in 2022.

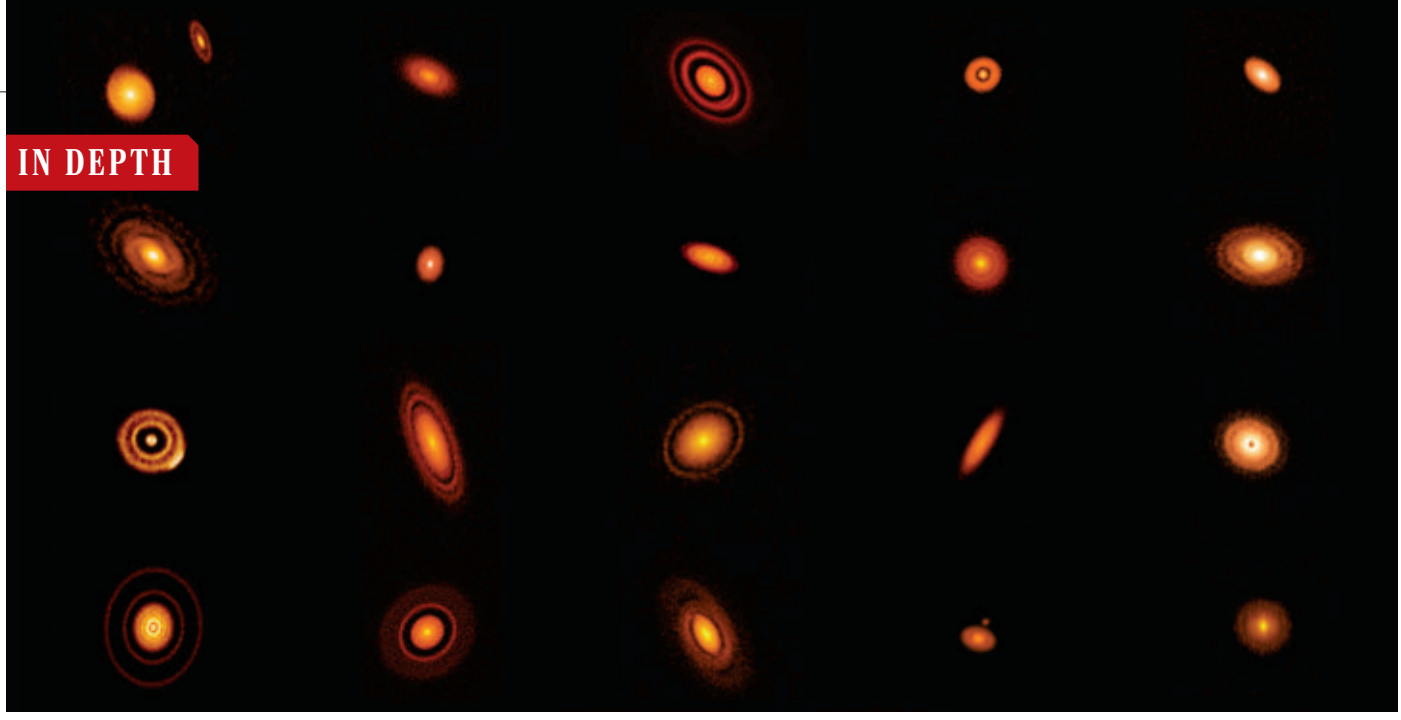

Gaps in disks of dust around young stars point to unseen planets sweeping them clear. Theorists had not expected planets to form so quickly.

ASTRONOMY

Hints of young planets puzzle theorists

Astronomical survey finds telltale gaps in dusty disks around newborn stars

By **Daniel Clery**

HL Tau, a mere stripling of a star no more than 1 million years old, was swaddled in a surprise. Four years ago, the Atacama Large Millimeter/submillimeter Array (ALMA) in Chile revealed gaps in a bright disk of dust around HL Tau—apparently swept clean by unseen planets that had formed millions of years earlier than astronomers thought possible. But now, an ALMA survey of 20 disks around nearby young stars suggests the precocious planets around HL Tau are no anomalies—a result that will keep theorists busy for years.

"It's spectacular," says Joshua Winn of Princeton University. "We will never think about disks in the same way."

Many theorists believe planets form by core accretion, which begins as dust particles collide and stick together. The clumps grow into pebbles, rocks, and, finally, large "cores" the size of small planets that can vacuum up remaining dust and gas through the pull of their gravity. The process is expected to be slow, taking millions of years to play out.

The new survey results, published in 10 papers last week in *The Astrophysical Journal Letters*, suggest a much tighter timescale. ALMA, an array of 64 movable dishes high in the Atacama Desert of northern Chile, captures the glow of dust particles at millimeter wavelengths, between the infrared and microwave bands. Once a year, the array is expanded to its widest extent, 15 kilometers across, to get the highest resolution. The survey team won a coveted "large program," which gave it 65 hours of high-resolution observing time, enough to find and study disks around 20 young stars.

The team was rewarded with a clear view of gaps, even around stars as young as 300,000 years old. Equally puzzling, many gaps lay far from their stars—much farther than Neptune's orbit—where a planet's slow orbital motion would make it even tougher to sweep up dust and gas and form planets by core accretion.

An alternative model relying on unstable ripples or clumps in the disk that collapse under their own gravity can make planets faster, especially large ones in distant orbits. But Marco Tazzari, of the Institute of Astronomy at the University of Cambridge in the United Kingdom, notes that the survey found few spiral arms—signs of disk instabilities—in the disks. "There are many structures we cannot account for," he says.

The new observations did reveal dense bands of material in the disks, which could alleviate one challenge for the core accretion model. Centimeter-size grains should experience drag from the surrounding gas and quickly fall in toward the star, depleting the disk of planet-forming material. But the dense bands could be acting as traps, Tazzari says, stopping grains from migrating inward and preserving them for planet growth.

The interpretations all assume unseen planets really are responsible for the gaps. But Roman Rafikov at Cambridge says they could have been created by pressure changes at snow lines, where gases such as water vapor freeze onto grains, or by magnetic fields in the disk, which can bunch up charged particles in bands. "What we see at work could be several mechanisms working simultaneously," he says.

To untangle these issues, astronomers need additional observations. ALMA and certain radio telescopes could spy on gas in the disks, which makes up 99% of their mass. That would allow astronomers to see whether the same bands and gaps exist in the gas and understand how gas and dust interact.

"The smoking gun," however, "would be finding the planets," Rafikov says. Large optical telescopes have captured images of a handful of exoplanets in distant orbits around young stars, but only once the deed is done and the disk has already dispersed.

Still, Tazzari says, results like the ALMA survey are transforming the field. "It's making planet formation an observational field, not just a theoretical one." ■

SCIENCE AND POLITICS

Universities 'held hostage' in Nicaragua's political crisis

Intensifying oppression paralyzes teaching and research

By **Lizzie Wade**

Molecular biologist Jorge Huete-Pérez, a professor at Central American University (UCA) in Managua, is one of many Nicaraguan academics whose life and work have been upended by an escalating political crisis. A longtime critic of Nicaraguan President Daniel Ortega, Huete-Pérez was inspired in April when demonstrations against a proposed cut to social security evolved into a new movement against Ortega's stranglehold on political power and his brutal repression of dissent. He felt a responsibility to support the students on the movement's front lines and joined their protests many times.

But on 14 October, about 2 weeks after the government outlawed political demonstrations, Huete-Pérez flinched. "I was about to open the [car] door to get out and join" another protest, he recalls, when police began to beat and arrest demonstrators close by. He slammed the door and sped away. "I literally felt like I was running for my life," he says. "I had not been that scared in a long time."

Many others, too, have recently stayed home in the face of an intensifying crackdown by Ortega, a leader of the Sandinista movement that overthrew a dictator in 1979. Ortega has become increasingly autocratic since beginning his second stint as president in 2007. More than 300 protesters have been killed and at least as many have been arrested, according to Amnesty International; some have been charged with terrorism. Tens of thousands more have gone into exile. Just last week, police raided offices of an independent newspaper and several nongovernmental organizations, including a leading human rights group.

The repression has struck particularly hard at Nicaragua's universities, where firings, arrests, and attacks on students have brought higher education and research to a virtual standstill. "It all started with university students, so universities have been the target of repression," says Huete-Pérez, who spoke at a 13 December meeting at UCA to discuss the crisis. The Inter-American Commission on Human Rights now considers students one of the most imperiled groups in the country. "The university system is being held hostage," says María Luisa Acosta, a human rights lawyer and president of the Nicaraguan Academy of Sciences (ACN) in Managua, which organized last week's meeting. (Acosta went into exile in June after being threatened by paramilitary forces.)

Students, seen here protesting in July, have been at the forefront of the opposition to President Daniel Ortega.

PHOTO: OSWALDO RIVAS/REUTERS

Critics say state universities have been coopted by the government, especially the National Autonomous University of Nicaragua (UNAN) in Managua, which fired more than 40 professors and expelled nearly 100 students who had demonstrated or expressed support for the movement. "We were fired because we spoke out against the silence and complicity that allowed the universities to permit students to be killed, repressed, and detained," says sociologist Freddy Quezada, another speaker at the meeting, who lost his job in July. (UNAN did not respond to *Science*'s interview requests.)

The crisis is also disrupting collaborations with foreign scientists. Huete-Pérez's department had to suspend the Nicaraguan Biotechnology Conference, which UCA organized every 2 years with scientists from Harvard University, the Massachusetts Institute of Technology, and other U.S. universities. Evolutionary biologist Axel Meyer of the University of Konstanz in Germany isn't sure whether he can continue his studies of fish evolution in Nicaragua's crater lakes this winter; Gerald Urquhart, a tropical ecologist at Michigan State University in East Lansing who has worked in Nicaragua for decades, has postponed fieldwork indefinitely and canceled his study abroad program in Nicaragua. "I am saddened by the limitations this places on my relationship with Nicaraguan colleagues," he says.

UCA, a private Jesuit university, is one of Nicaragua's last remaining bastions of free speech. In addition to publicly supporting the student movement, "They opened their doors to thousands of demonstrators" after the government fired on a protest in May, killing at least 17, says Carlos Tünnermann Bernheim, a former minister of education and UNAN rector. But teaching has been disrupted, as at most universities. "It's not safe enough to bring students to campus," Huete-Pérez says. He and others are holding classes online, but it's not the same, he says: "I teach biochemisty and biotechnology. You need a lab for that."

Now, UCA faces a more direct threat. The Nicaraguan legislature is considering a bill that would end the state funding the university receives under a law that designates its work as public service. "It's a direct aggression," says Josefina Vijil, a UCA education scientist and a member of ACN's leadership. Much of UCA's public funding goes to scholarships, "so if they do this, the ones who suffer are the students," Tünnermann Bernheim says.

Vijil especially worries about lasting psychological trauma to the researchers and students who lived through the crisis. Still, she and other participants in the UCA meeting spent time brainstorming for the day when students are back in classrooms, and made tentative plans for writing a book about university autonomy. "We need to start imagining—and articulating—the country we want in 50 years," Vijil says. ■

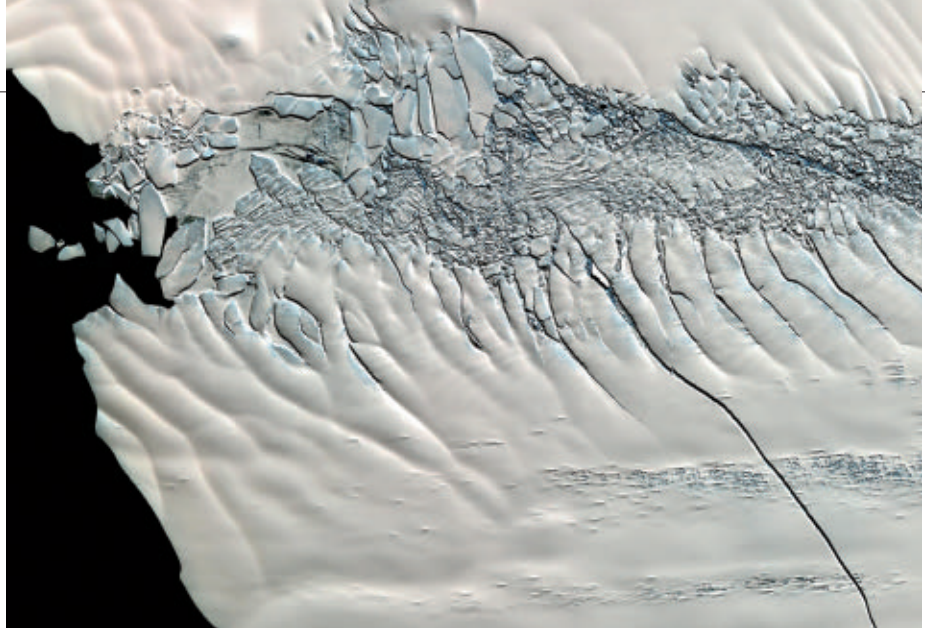

A 30-kilometer crack angles across the Pine Island Glacier, a vulnerable part of the West Antarctic Ice Sheet.

PHOTO: NASA/GSFC/METI/ERSDAC/JAROS, AND U.S./JAPAN ASTER SCIENCE TEAM/FLICKR

CLIMATE

Antarctic ice melt 125,000 years ago offers warning

Ice sheet apparently collapsed in a previous warm period

By **Paul Voosen**

Some 125,000 years ago, during the last brief warm period between ice ages, Earth was awash. Temperatures during this time, called the Eemian, were barely higher than in today's greenhouse-warmed world. Yet proxy records show sea levels were 6 to 9 meters higher than they are today, drowning huge swaths of what is now dry land.

Scientists have now identified the source of all that water: a collapse of the West Antarctic Ice Sheet. Glaciologists worry about the present-day stability of this formidable ice mass. Its base lies below sea level, at risk of being undermined by warming ocean waters, and glaciers fringing it are retreating fast. The discovery, teased out of a sediment core and reported last week at a meeting of the American Geophysical Union in Washington, D.C., validates those concerns, providing evidence that the ice sheet disappeared in the recent geological past under climate conditions similar to today's. "We had an absence of evidence," says Anders Carlson, a glacial geologist at Oregon State University in Corvallis, who led the work. "I think we have evidence of absence now."

If it holds up, the finding would confirm that "the West Antarctic Ice Sheet might not need a huge nudge to budge," says Jeremy Shakun, a paleoclimatologist at Boston College. That, in turn, suggests "the big uptick in mass loss observed there in the past decade or two is perhaps the start of that process rather than a short-term blip." If so, the world may need to prepare for sea level to rise farther and faster than expected: Once the ancient ice sheet collapse got going, some records suggest, ocean waters rose as fast as some 2.5 meters per century.

As an analogy for the present, the Eemian, from 129,000 to 116,000 years ago, is "probably the best there is, but it's not great," says Jacqueline Austermann, a geophysicist at Columbia University's Lamont-Doherty Earth Observatory. Global temperatures were some 2°C above preindustrial levels (compared with 1°C today). But the cause of the warming was not greenhouse gases, but slight changes in Earth's orbit and spin axis, and Antarctica was probably cooler than today. What drove the sea level rise, recorded by fossil corals now marooned well above high tide, has been a mystery.

Scientists once blamed the melting of Greenland's ice sheet. But in 2011, Carlson and colleagues exonerated Greenland after identifying isotopic fingerprints of its bedrock in sediment from an ocean core drilled off its southern tip. The isotopes showed ice continued to grind away at the bedrock through the Eemian. If the Greenland Ice Sheet didn't vanish and push up sea level, the vulnerable West Antarctic Ice Sheet was the obvious suspect. But the suspicion rested on little more than simple subtraction, Shakun says. "It's not exactly the most compelling or satisfying argument."

Carlson and his team set out to apply their isotope technique to Antarctica. First, they drew on archived marine sediment cores drilled from along the edge of the western ice sheet. Studying 29 cores, they identified geochemical signatures for three different bedrock source regions: the mountainous Antarctic Peninsula; the Amundsen province, close to the Ross Sea; and the area in between, around the particularly vulnerable Pine Island Glacier.

Armed with these fingerprints, Carlson's team then analyzed marine sediments from a single archived core, drilled farther offshore in the Bellingshausen Sea, west of the Antarctic Peninsula. A stable current runs along the West Antarctic continental shelf, picking up ice-eroded silt along the way. The current dumps much of this silt near the core's site, where it builds up fast and traps shelled microorganisms called foraminifera, which can be dated by comparing their oxygen isotope ratios to those in cores with known dates. Over a stretch of 10 meters, the core contained 140,000 years of built-up silt.

For most of that period, the silt contained geochemical signatures from all three of the West Antarctic bedrock regions, the team reported, suggesting continuous ice-driven erosion. But in a section dated to the early Eemian, the fingerprints winked out: first from the Pine Island Glacier, then from the Amundsen province. That left only silt from the mountainous peninsula, where glaciers may have persisted. "We don't see any sediments coming from the much larger West Antarctic Ice Sheet, which we'd interpret to mean that it was gone. It didn't have that erosive power anymore," Carlson says.

He concedes that the dating of the core is not precise, which means the pause in erosion may not have taken place during the Eemian. It is also possible that the pause itself is illusory—that ocean currents temporarily shifted, sweeping silt to another site.

More certainty is on the way. Next month, the International Ocean Discovery Program's *JOIDES Resolution* research ship will begin a 3-month voyage to drill at least five marine cores off West Antarctica. "That's going to be a great test," Carlson says. Meanwhile, he hopes to get his own study published in time to be included in the next United Nations climate report. In the 2001 and 2007 reports, West Antarctic collapse was not even considered in estimates of future sea level; only in 2013 did authors start to talk about an Antarctic surprise, he says. Research is due by December 2019. "We gotta beat that deadline." ■

This fossilized twig of a podocarp conifer dates back to the Permian, much earlier than expected.

EVOLUTION

Fossils push back origin of key plant groups millions of years

Finds from Middle East point to the dry tropics as cradle for plant evolution 250 million years ago

By **Elizabeth Pennisi**

Paleobotanists exploring a site near the Dead Sea have unearthed a startling connection between today's conifer forests in the Southern Hemisphere and an unimaginably distant time torn apart by a global cataclysm. Exquisitely preserved plant fossils show the podocarps, a group of ancient evergreens that includes the massive yellowwood of South Africa and the red pine of New Zealand, thrived in the Permian period, more than 250 million years ago. That's tens of millions of years earlier than thought, and it shows that early podocarps survived the "great dying" at the end of the Permian, the worst mass extinction the planet has ever known.

Reported on p. 1414, the fossils push back the origins not just of podocarps, but also of groups of seed ferns and cycadlike plants. Beyond altering notions of plant evolution, the discoveries lend support to a 45-year-old idea that the tropics serve as a "cradle" of evolution. "This is an exciting paper," says Douglas Soltis, a plant evolutionary biologist at the University of Florida (UF) in Gainesville. By revealing the richness of the Permian tropics, he adds, "The findings may also help researchers decide where to look for crucial fossil discoveries."

During the Permian, from 299 million to 251 million years ago, Earth's landmasses had merged to form a supercontinent, bringing a cooler, drier climate. Synapsids, thought to be ancient predecessors of mammals, and sauropsids, ancestors to reptiles and birds, roamed the landscape. Simple seed-bearing plants had already appeared on the scene. Family trees reconstructed from the genomes of living plants suggest more sophisticated plant groups might also have evolved during the Permian, but finding well-preserved plant fossils from that time has been difficult.

About 50 years ago, a German geologist described the Umm Irna formation, a series of sedimentary layers exposed along the Jordanian coast of the Dead Sea. Working at the site in the early 2000s, paleontologist Abdalla Abu Hamad, now with the University of Jordan in Amman, discovered some exquisitely preserved plants from Permian swamps and drier lowlands.

Freed from rock by a strong acid, this fossilized frond preserves enough detail to identify it as a seed fern.

After moving to the University of Münster in Germany for a Ph.D., he teamed up with paleobotanists there to analyze hundreds of newly collected plant fossils, including leaves, stems, and reproductive organs. Many of the fossils preserve the ancient plants' cuticle, a waxy surface layer that captures fine features, such as the leaf pores called stomata. That made it possible for the team to positively identify many of the plants.

"At first, we couldn't really believe our eyes," Benjamin Bomfleur, a study coauthor at the University of Münster, recalls. Many were plants thought have gotten their start later in the Mesozoic, the period when dinosaurs ruled. Along with the podocarps, they identified corystosperms, seed ferns common in the dinosaur age but extinct now, and cycadlike Bennettitales, another extinct group that had flowerlike reproductive structures.

Such finds could help resolve an ongoing debate about why the tropics have more species than colder latitudes do. Some have suggested that species originate at many latitudes but are more likely to diversify in the tropics, with its longer growing seasons, higher rainfall and temperatures, and other features. But another theory proposes that most plant—and animal—species actually got their start near the equator, making the low latitudes an evolutionary "cradle" from which some species migrate north and south. The new work "supports the idea of the evolution cradle," Bomfleur says. Philip Mannion, a paleontologist at Imperial College London agrees, but says the case is not fully settled. "Our sampling of the fossil record is extremely patchy throughout geological time and space," he cautions.

It's not clear how the newfound Permian plants made it through the great dying, a 100,000-year period when, for reasons that are still unclear, 90% of marine life and 70% of life on land disappeared. But their presence in the Permian raises the possibility that other plant groups thought to have later origins actually emerged then in the tropics, says UF plant evolutionary biologist Pamela Soltis. If these select plants survived the mass extinction, she says, "Perhaps the communities they supported may have been more stable as well." ■

PHOTOS: P. BLOMENKEMPER *ET AL*., *SCIENCE*, 362/1414 (2018)

NEUROLOGY

Link to Alzheimer's seen in nodding syndrome

Protein tangles hint that childhood illness is a degenerative disease of the brain

By **Laura Spinney**

A disease mystery with no shortage of leads now has an intriguing new one. Since the 1960s, thousands of children in poor, war-torn regions of East Africa have developed epilepsy-like seizures in which their heads bob to their chest; over time, the seizures worsen, cognitive problems develop, and the victims ultimately die. Researchers have proposed causes for nodding syndrome that include malnutrition, parasites, and viruses, but have not proved a clear link to any of them. Now, the first published examination of the brains of children who died after developing the condition suggests it has a key similarity to certain brain diseases of old age, such as Alzheimer's and Parkinson's: It leaves victims' brains riddled with fibrous tangles containing a protein called tau.

"Nodding syndrome is a tauopathy," concludes Michael Pollanen, a pathologist at the University of Toronto in Canada who is lead author of a report published last month in *Acta Neuropathologica*. Pollanen believes the finding "suggests a totally new line of investigation" into the syndrome. As significant as the discovery of the tangles may be what his group of Canadian and Ugandan researchers didn't find: any sign of the brain inflammation that might be triggered by a parasite or virus. "Our hypothesis is that nodding syndrome is a neurodegenerative disease, like Alzheimer's," Pollanen says.

Some who study the condition are skeptical, but the possibility excites researchers working on other tauopathies including Alzheimer's. Childhood forms of those diseases are exceedingly rare, but the nodding syndrome finding "means [tau deposition] is not an age-dependent problem," says John Hardy, of the UK Dementia Research Institute at University College London. Something else must have triggered the tauopathy in these children. And because nodding syndrome struck a small region of East Africa, over a specific time period—in Uganda, the condition appears to be vanishing—its trigger might be relatively easy to identify, and could shed light on the causes of diseases like Alzheimer's, Hardy and others say.

First, though, the researchers need to convince others who have studied nodding syndrome for years that they are right. Originally reported in Tanzania, the disease spread to what is now South Sudan in the 1990s and to northern Uganda after 1998. Uganda has reported 3000 cases, but no new ones since 2014. The current study was done on the brains of five Ugandan children who fell ill while living in camps for internally displaced persons between 2005 and 2010, when Joseph Kony's Lord's Resistance Army was terrorizing the region, and later died.

A 2012 image from Uganda shows an 11-year-old boy suffering from nodding syndrome.

PHOTO: JAMES AKENA/REUTERS

The brains are among a dozen obtained by U.S. and Ugandan researchers between 2014 and 2017, overcoming challenges such as persuading relatives, harvesting the organs promptly after death, and transporting them from remote areas in a tropical climate. Initial investigations done in the United States were never published—it's not clear why—and the brains were returned to Uganda, where Pollanen's group studied all 12. They hope to publish their analyses of the remaining seven soon.

The current paper is thin on detail and lacks important controls, cautions neurologist Avindra Nath of the U.S. National Institute of Neurological Disorders and Stroke in Bethesda, Maryland, who has studied nodding syndrome. It does not describe the brain pathology in children from the same population who died of other forms of epilepsy, for example.

Robert Colebunders, an infectious disease expert at the University of Antwerp in Belgium who has long worked on nodding syndrome, says he has still-unpublished postmortem findings from seven children who fell ill at the same time, in the same camps, but survived longer because they received better care and experienced fewer seizures. None of them shows tauopathy, he says. "My conclusion is that tau [deposition] is a consequence of seizures, not a cause."

Colebunders favors a long-standing theory that the ultimate cause of nodding syndrome is infection by a parasitic worm called *Onchocerca volvulus*, which is endemic to the same regions. There is no evidence that the worm itself penetrates the brain, but last year, Nath and others proposed that a protein in the worm triggers the production of antibodies that attack a similar protein on neurons, in a misdirected autoimmune response (*Science*, 17 February 2017, p. 678).

It's dangerous to propose that nodding syndrome is a neurodegenerative disease, Colebunders says, because it could divert resources away from much-needed efforts to eradicate the worm and to improve care for children with the illness. "With good care and nutrition, the epilepsy can be controlled and the children can go back to school without suffering any cognitive deficit," he says.

But Peter Spencer, a neurotoxicologist at Oregon Health & Science University in Portland, suspects the worm is a bystander. He suggests it opportunistically infects people who have another condition that also triggers seizures and tau deposition. How it all fits together is unclear, but tau gives investigators one more piece of the puzzle, Spencer says. "We have an opportunity here to discover the primary cause of this disease, and then to do primary prevention." Not only will that benefit affected children, Spencer adds, "It will potentially open up our understanding of other tauopathies, too." ■

Laura Spinney is a journalist in Paris.

In this submersible, two people can descend to 11,000 meters and gather samples with a robotic arm.

OCEAN SCIENCE

'Five Deeps' mission to explore mysterious ocean trenches

Crewed sub aims to spot new species and gather rocks

By **Erik Stokstad**

He scaled Mount Everest and the highest peaks on the six other continents. He skied to the North and South poles. Now, Victor Vescovo, the multimillionaire co-founder of a private equity company in Dallas, Texas, wants to be first person to visit the deepest point in each of the five oceans. This week, Vescovo was set to complete the first dive in the yearlong Five Deeps Expedition, piloting a titanium-alloy, 12.5-ton submersible down 8408 meters to the deepest part of the Atlantic Ocean, in the Puerto Rico Trench.

Five Deeps may look like a vanity project, but for scientists it is a rare opportunity to study inaccessible, mysterious places. "If there wasn't this rich guy, there is not any funding agency that would be willing to spend so much money to visit all those areas," says Ann Vanreusel, a deep-sea biologist at Ghent University in Belgium. The expedition will yield high-resolution maps that could offer clues about how ocean trenches form when tectonic plates plunge into the mantle. The dives are also sure to spot new species, which will give researchers a chance to compare the ecosystems that have evolved in these isolated, exotic habitats. "Great insights could come when we can start comparing these ultradeep sites," says Stuart Piertney, an evolutionary biologist at the University of Aberdeen in the United Kingdom.

The *HMS Challenger* Expedition, a pioneering voyage in the 1870s, showed that life exists across the deep ocean by trawling and dredging up creatures from as deep as 8000 meters. Since then, research trawls have netted cutthroat eels, snailfish, and other animals adapted to the cold and pressure. Some rely on bioluminescence to attract mates or prey in the darkness. Below 8000 meters, sea cucumbers and giant crustaceans called amphipods dominate.

Firsthand exploration of the trenches has been limited. People have reached the bottom of the Mariana Trench, the world's deepest trench, only twice: in 1960, in the bathyscaphe *Trieste*, and in 2012, when movie director James Cameron descended in an $8 million custom submersible. In 1964, a French submersible descended 8385 meters to what was then thought to be the deepest part of the Puerto Rico Trench. The other three deeps have never been visited, although trenches elsewhere have been probed with remotely operated submersibles and autonomous landers. Landers can make measurements, record images, and collect samples before returning to the surface, but can't be controlled or targeted.

Alan Jamieson, a marine ecologist at Newcastle University in the United Kingdom who designed some of these landers, now can visit multiple trenches himself, as the science leader for the Five Deeps Expedition. In March 2017, he received a cryptic phone call from Triton Submarines, a high-end manufacturer in Sebastian, Florida. After signing a nondisclosure agreement, Jamieson learned that Vescovo had bought a 68-meter-long research vessel from the U.S. government and commissioned Triton to build a submersible capable of diving to 11,000 meters. Designed for quick descents and ascents, the *Limiting Factor* has three acrylic portholes, leather seats for Vescovo and a passenger, and custom lithium batteries to power propellers for scooting along the sea floor. "When someone phones up and says, 'We have a multi-multi-multi-million-dollar submarine that can do things that your own gear can't,' it seems like a logical step forward," Jamieson says.

A rotating cast of 15 collaborators will join

Race to the bottoms

The Five Deeps Expedition aims to reach every ocean's deepest trench and seven other deep sites in 11 months.

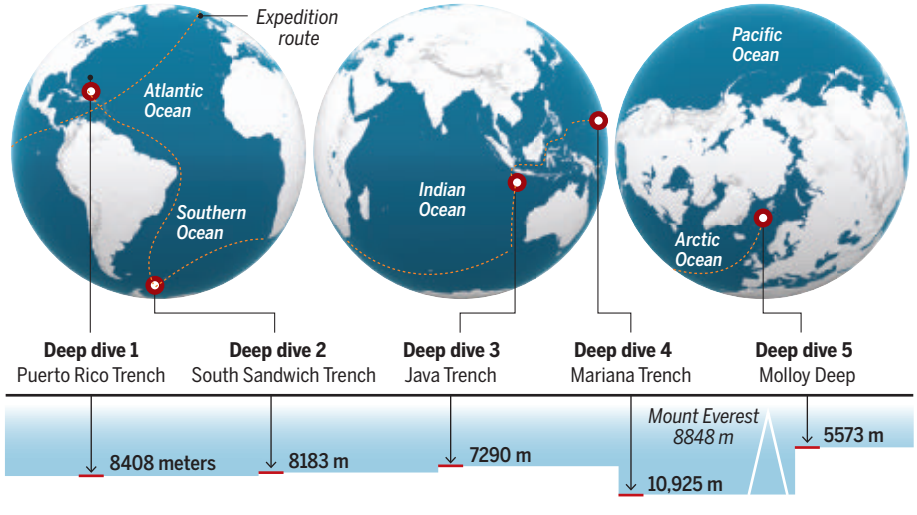

CREDITS: (PHOTO) THE FIVE DEEPS EXPEDITION; (MAP) A. CUADRA/*SCIENCE*; (DATA) FIVE DEEPS EXHIBITION

Jamieson on the mother ship, *Pressure Drop*. It has space for three scientists, a wet lab, and a $1.5 million multibeam sonar to map the sea floor and verify its deepest spots.

Once a dive site is chosen, Vescovo will plunge in the sub, following three landers dropped several kilometers apart. The landers, which contain cameras and baited traps, collect water and sediment samples. They also emit acoustic beacons for the sub to follow on its seafloor traverses. Along the way, it will record video with four wide-angle, low-light cameras. Floodlights will help the crew collect rocks or slow-moving organisms with a manipulator arm.

The sub can spend about a dozen hours at the bottom per dive, but the ship will linger only a few days at most sites. Even a cursory look could open windows on trench ecosystems. Examining specimens could reveal their adaptations, and genetic analysis back in Newcastle should yield evolutionary relationships of organisms from various trenches. Jamieson wants to know how species are influenced by temperature, depth, or the downward-drifting supply of food. He also wants to understand why fish in trenches seem to live shorter lives than those on the 6000-meter-deep abyssal plains. Jamieson thinks landslides and rockfalls in the steep-sided trenches may be taking a toll.

The new high-resolution maps could also yield insights into how tectonic forces created the deepest parts of the trenches—revealing cliffs created by faults, for example—says Heather Stewart, a geologist with the British Geological Survey in Edinburgh, who will be visiting at least the first two trenches. Sampled minerals could provide estimates of the water that subducting tectonic plates take into the mantle. These water-bearing minerals weaken the plates, perhaps reducing their potential for shallow earthquakes, and they also drive a deep water cycle in which water is swept into Earth's interior and returned to the surface in volcanic eruptions. Rocks collected from known locations should be more informative than those hauled up randomly in a trawl, says Lara Kalnins, a marine geophysicist at the University of Edinburgh. "They can take images and videos—all of this is context you ordinarily don't get."

After the team leaves Puerto Rico this week, it will head for the South Sandwich Trench, in the Southern Ocean near Antarctica. Then comes the Indian Ocean and the Pacific, and finally the Arctic. For the final leg of the expedition, in September 2019, *Pressure Drop* will sail up the Thames River to London, and Vescovo and Jamieson will give a lecture at the Royal Geographical Society. Then Vescovo hopes to sell *Pressure Drop*, the sub, and the landers, slightly used, for $48.2 million. ■

FUSION ENERGY

National Academies urges renewed commitment to fusion

U.S. should stick with ITER, build a power plant, panel says

By **Adrian Cho**

The United States should prepare to build its own prototype fusion power plant, according to leading energy scientists. The compact power plant (CPP), able to produce sustained electric power, would be a follow-up to ITER, an international megaproject under construction near Cadarache in France that aims to demonstrate that a fusion generator can produce more energy than it consumes. To be built in the 2030s, the CPP would be smaller and cheaper than ITER, says a report released last week by a committee of the National Academies of Sciences, Engineering, and Medicine. But it will depend on as yet unproven technologies and a long-shot infusion of money.

"The fundamental message is that the U.S. fusion program has to have an ambition to drive through and generate some kilowatts of power," says Steven Cowley, director of the Department of Energy's Princeton Plasma Physics Laboratory in New Jersey, who was not on the panel. "What's the point of having a fusion program if you don't have a goal to develop the first fusion power plant?"

> ***"What's the point of having a fusion program if you don't have a goal to develop the first fusion power plant?"***
>
> **Steven Cowley**, Princeton Plasma Physics Laboratory

In nuclear fusion, light nuclei fuse to form heavier ones and release energy. Physicists have struggled for decades to turn fusion into a practical source of power, generally by using intense magnetic fields in doughnut-shaped devices called tokamaks to confine and squeeze ionized gases, or plasmas, of deuterium and tritium so that the nuclei fuse to make helium. ITER will heat plasma to 150 million K and aims to be the first tokamak to realize a net gain in energy.

Researchers around the world have plans to build prototype power plants after ITER. For example, scientists in Europe want to build the Demonstration Power Station, a tokamak even bigger than ITER. In contrast, the CPP would generate more power in a device a fraction of ITER's size.

To shrink the CPP, physicists would ramp up its magnetic field to twice that of ITER's, Cowley says. That field would squeeze the plasma to a pressure four times greater than ITER's—and twice as great as the pressure in the ocean's 11-kilometer-deep Mariana Trench. The quadrupled pressure would quell turbulence and limit heat loss, so that the CPP could shrink to one-eighth the volume but crank out twice as much power. Whereas ITER's main magnet coils are 9 meters wide, the CPP's coils might be just 4 meters wide.

The CPP will require major advances in materials, computing, and plasma physics. For example, whereas ITER's main superconducting magnet coils consist of conventional niobium-tin wire, the CPP would use coils made from exotic high-temperature superconductors such as bismuth strontium calcium copper oxide. Those materials are relatively brittle ceramics. So far, researchers can fashion them into coils with bores just centimeters wide, not the meters needed for tokamak coils.

To build the CPP, researchers will also need the knowledge they'll gain from ITER, Cowley says. In the past, lawmakers in the U.S. Senate have called for the United States to withdraw from the project. But the report argues against a pullout, noting that the country would first have to build its own version of ITER before launching the CPP. "There is no shortcut" around ITER, says Michael Mauel, a fusion physicist at Columbia University and co-chair of the report panel.

To realize the committee's vision, the report also calls for increasing U.S. funding for fusion research by $200 million per year, a 35% increase over the current $564 million annual budget. "Adding $200 million [per year] for 2 decades is an extremely unlikely scenario," says William Madia, a vice president at Stanford University in Palo Alto, California. However, one Democratic staffer in the House of Representatives says, "I wouldn't say that these numbers are wildly out of step with what's possible." ■

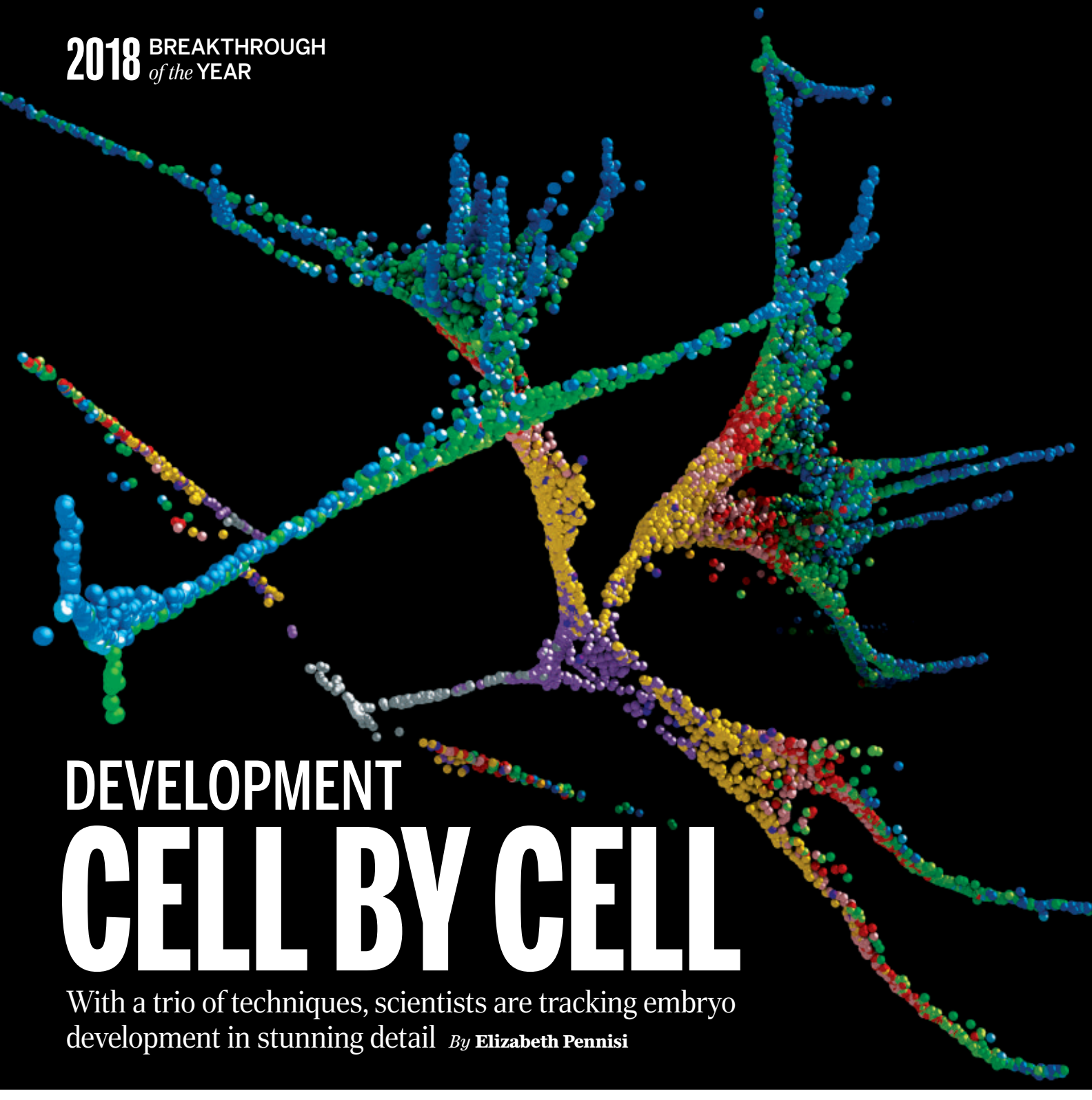

DEVELOPMENT
CELL BY CELL

With a trio of techniques, scientists are tracking embryo development in stunning detail *By* **Elizabeth Pennisi**

From at least the time of Hippocrates, biologists have been transfixed by the mystery of how a single cell develops into an adult animal with multiple organs and billions of cells. The ancient Greek physician hypothesized that moisture from a mother's breath helps shape a growing infant, but now we know it is DNA that ultimately orchestrates the processes by which cells multiply and specialize. Now, just as a music score indicates when strings, brass, percussion, and woodwinds chime in to create a symphony, a combination of technologies is revealing when genes in individual cells switch on, cueing the cells to play their specialized parts. The result is the ability to track development of organisms and organs in stunning detail, cell by cell and through time. *Science* is recognizing that combination of technologies, and its potential for spurring advances in basic research and medicine, as the 2018 Breakthrough of the Year.

Driving those advances are techniques for isolating thousands of intact cells from living organisms, efficiently sequencing expressed genetic material in each cell, and

IMAGE: JEFFREY FARRELL AND YIQUN WANG/SCHIER LAB/HARVARD UNIVERSITY

A representation of cell lineages in a zebrafish embryo, color-coded by time. The first cells are gray; by 6 hours (gold), three major branches have formed.

using computers, or labeling the cells, to reconstruct their relationships in space and time. That technical trifecta "will transform the next decade of research," says Nikolaus Rajewsky, a systems biologist at the Max Delbrück Center for Molecular Medicine in Berlin. This year alone, papers detailed how a flatworm, a fish, a frog, and other organisms begin to make organs and appendages. And groups around the world are applying the techniques to study how human cells mature over a lifetime, how tissues regenerate, and how cells change in diseases.

The ability to isolate thousands of individual cells and sequence each one's genetic material gives researchers a snapshot of what RNA is being produced in each cell at that moment. And because RNA sequences are specific to the genes that produced them, researchers can see which genes are active. Those active genes define what a cell does.

That combination of techniques, known as single-cell RNA-seq, has evolved over the past few years. But a turning point came last year, when two groups showed it could be done on a scale large enough to track early development. One group used single-cell RNA-seq to measure gene activity in 8000 cells extracted at one time point from fruit fly embryos. About the same time, another team profiled gene activity of 50,000 cells from one larval stage of the nematode *Caenorhabditis elegans*. The data indicated which proteins, called transcription factors, were guiding the cells to differentiate into specialized types.

This year, those researchers and others performed even more extensive analyses on vertebrate embryos. Using a variety of sophisticated computational methods, they linked single-cell RNA-seq readouts taken at different time points to reveal the turning on and off of sets of genes that defined the types of cells formed in those more complex organisms. One study uncovered how a fertilized zebrafish egg gives rise to 25 cell types; another monitored frog development through early stages of organ formation and determined that some cells begin to specialize earlier than previously thought. "The techniques have answered fundamental questions regarding embryology," says Harvard University stem cell biologist Leonard Zon.

Researchers interested in how some animals can regrow limbs or whole bodies have also turned to single-cell RNA-seq. Two groups studied gene expression patterns in aquatic flatworms called planaria—among biology's champion regenerators—after they had been cut into pieces. The scientists discovered new cell types and developmental trajectories that emerged as each piece regrew into a whole individual. Another group traced the genes that switched on and off in axolotls, a type of salamander, that had lost a forelimb. The researchers found that some mature limb tissue reverted to an embryonic, undifferentiated state and then underwent cellular and molecular reprogramming to build a new limb.

Because cells must be removed from an organism for single-cell sequencing, that technique alone can't show how those cells interact with their neighbors or identify the cells' descendants. But by engineering markers into early embryonic cells, researchers can now track cells and their progeny in living organisms. At least one team exposes early embryos to mobile genetic elements that carry genes for different colored fluorescent tags, which randomly settle into the cells, imparting different colors to each cell lineage. Other teams have harnessed the gene-editing technique called CRISPR to mark the genomes of individual cells with unique barcodelike identifiers, which are then passed on to all their descendants. The gene editor can make new mutations in progeny cells while retaining the original mutations, enabling scientists to track how lineages branch off to form new cell types.

ON OUR WEBSITE

For more on the Breakthrough of the Year, including a video and a podcast, go to: https://scim.ag/Breakthrough2018

By combining those techniques with single-cell RNA-seq, researchers can both monitor the behavior of individual cells and see how they fit into the organism's unfolding architecture. Using that approach, one team determined the relationships of more than 100 cell types in zebrafish brains. The researchers used CRISPR to mark early embryonic cells, then isolated and sequenced 60,000 cells at different time points to track gene activity as the fish embryo developed.

Other groups are applying similar techniques to track what happens in developing organs, limbs, or other tissues—and how those processes can go wrong, resulting in malformations or disease. "It's like a flight recorder, where you are watching what went wrong and not just looking at a snapshot at the end," says Jonathan Weissman, a stem cell biologist at the University of California, San Francisco. "We can ask questions at a resolution that was just not possible before."

Although those technologies cannot be used directly in developing human embryos, researchers are applying the approaches to human tissues and organoids to study gene activity cell by cell and characterize cell types. An international consortium called the Human Cell Atlas is 2 years into an effort to identify every human cell type, where each type is located in the body, and how the cells work together to form tissues and organs. Already, one project has identified most, if not all, kidney cell types, including ones that tend to become cancerous. Another effort has revealed the interplay between maternal and fetal cells that allows pregnancy to proceed. And a collaboration of 53 institutions and 60 companies across Europe, called the LifeTime consortium, is proposing to harness single-cell RNA-seq in a multipronged effort to understand what happens cell by cell as tissues progress toward cancer, diabetes, and other diseases.

High-resolution movies of development and disease will only get more compelling. Papers already posted online extend development studies to ever-more-complex organisms. And researchers hope to combine single-cell RNA-seq with new microscopy techniques to see where in each cell its distinctive molecular activity takes place and how neighboring cells affect that activity.

The single-cell revolution is just starting. ■

PEOPLE'S CHOICE

Our readers weigh in with their picks for the top breakthrough of 2018

Visitors to *Science*'s website are in agreement with the magazine's reporters and editors: Development cell by cell is the Breakthrough of the Year.

We invited online readers to vote on a dozen candidates for the breakthrough. The first round of voting narrowed the choices to four, and a second round, in which more than 12,000 votes were cast, determined the top People's Choice.

The combination of techniques that enables scientists to track development at the cellular level, in stunning detail and over time, was the clear winner. The approval of a gene-silencing drug after 20 years of development took second place, followed by the detection of a neutrino traced to a source outside our galaxy. The fourth contender, a set of images of the fruit fly brain showing individual synapses, just missed *Science*'s top 10.

1. Development cell by cell **35%**
2. RNAi drug approved **30%**
3. Neutrinos from a blazar **23%**
4. Fly brain revealed **12%**

A computer visualization of asteroid fragments falling toward Greenland.

IMAGE: NASA SCIENTIFIC VISUALIZATION STUDIO

Ice age impact

The asteroid slammed into northwestern Greenland like a fusillade of nuclear bombs, instantly vaporizing rock and sending shock waves across the Arctic. The scar it left—a 31-kilometer-wide impact crater called Hiawatha—is big enough to hold Washington, D.C. Scientists reported the startling discovery in November, after aircraft radar revealed the crater lurking beneath the kilometer-thick ice sheet.

Hiawatha crater is one of the 25 largest on Earth. Though not as cataclysmic as the dinosaur-killing Chicxulub impact, which carved out a 200-kilometer-wide crater in Mexico 66 million years ago, the Hiawatha impact could have had a powerful effect on the global climate. Meltwater from the impact, pouring into the north Atlantic Ocean, could have sent temperatures plunging by halting a conveyor belt of currents that brings warmth to northwest Europe.

The radar images suggest Hiawatha is exceptionally fresh, dating from the past 100,000 years. And a disturbance in the crater's deep ice hints that the asteroid may have struck as recently as 13,000 years ago. That would tie the impact to the Younger Dryas, a thousand-year global cooling event that began just as the world was thawing from the last ice age. It would also vindicate proponents of the controversial Younger Dryas impact theory. A decade ago, they proposed that extraterrestrial impacts could account for hints of mayhem in the archaeological and geological record. But they could never point to a crater.

The timing of this impact is far from settled. Ice cores elsewhere on Greenland, which record the past 100,000 years, contain no signs of impact debris. A firm answer will depend on painstaking work to tease dates from the radioactive clocks in tiny mineral crystals swept from under the ice.

If they show the Hiawatha impact did occur 13,000 years ago, it would have come just as humans were fanning across a new continent, chasing mastodons around North America. It is tempting to imagine their thoughts as they looked up to see the searing white orb of the impactor, four times brighter than the sun. —*Eric Hand*

An archaic human 'hybrid'

A fragment of bone from a woman who lived more than 50,000 years ago has revealed a startling connection between two extinct groups of archaic humans. Ancient DNA extracted from the bone, found in a cave in Siberia in 2012, showed the woman's mother was a Neanderthal and her father was a Denisovan, the mysterious group of ancient humans whose remains were discovered in the same cave in 2011.

Researchers knew Denisovans, Neanderthals, and modern humans interbred, at least occasionally, in ice age Europe and Asia. The genes of both types of archaic human are present in Asian and European people today. And other fossils found in the Siberian cave have shown members of all three groups lived there at different times. But the new finding is intimate testimony of an encounter between a Denisovan and a Neanderthal.

After sequencing DNA from the bone, researchers at the Max Planck Institute for Evolutionary Anthropology in Leipzig, Germany, found it came from a female, and that her genome matched those of Denisovans and Neanderthals in roughly equal measure. That could have been because her parents themselves had mixed ancestry. But her chromosome pairs harbored different variants—so-called heterozygous alleles—of nearly half her genes, suggesting the maternal and paternal chromosomes came from different kinds of humans. Her mitochondrial DNA, which is almost entirely inherited from the mother, was uniformly Neanderthal, so the researchers concluded she was a first generation hybrid of a Denisovan male and Neanderthal female. A closer look at the genome suggested her father also had some Neanderthal ancestry.

In another telltale finding, the woman's Neanderthal genes are closer to those of a Neanderthal found in Croatia than to those of earlier Neanderthal inhabitants of the Denisova Cave. That suggests, the authors say, that distinct groups of Neanderthals migrated back and forth between western Europe and Siberia multiple times. Along the way, apparently, they freely spread their genes to outsiders. Why did Denisovans and Neanderthals remain genetically distinct? Geographic barriers probably played a role, but researchers need more ancient DNA from different sites to understand the true influence of these prehistoric couplings. —*Gretchen Vogel*

A bone fragment found in a cave in the Denisova valley in Russia.

How cells marshal their contents

How do multiple actors inside a cell get together at the right place and time to perform critical functions? Often the answer, biologists are coming to realize, is liquid droplets. Unseen until recently, they are showing up everywhere in cells, organizing (and sometimes gumming up) the works.

Tens of thousands of proteins and other molecules populate the cytoplasm, the thick liquid that surrounds the cell nucleus, often jostling each other and reacting to perform the tasks of life, from breaking down nutrients to liberating energy to recycling waste. Beginning in 2009, researchers discovered that many proteins separate, or condense, into discrete droplets, concentrating their contents, especially when the cell is responding to stress. This "liquid-liquid phase separation," analogous to the "demixing" of oil and vinegar in a vinaigrette salad dressing, is now one of the hottest topics in cell biology, as evidence accumulates that it promotes critical biochemical reactions and appears to be a basic organizing principle of the cell.

Two 2017 papers in *Nature* had shown liquid protein droplets in the cell nucleus help compact regions of the genome, silencing the genes within. This year, three papers in *Science* pointed to an even bigger role for phase separation. They showed proteins that drive the transfer of the genetic code from DNA to RNA—the first step in making new proteins—can condense into droplets that attach to the DNA. Details remain to be worked out, but these studies reveal a role for phase separation in one of life's fundamental mysteries, the selective expression of genes.

Biophysicists are working out how these droplets form. Certain classes of proteins trail spaghettilike tails that interact to trigger the condensation. But when the process goes awry, what should be a liquid can become a gel, and a gel can solidify, forming the kinds of aggregates seen in neurodegenerative diseases such as amyotrophic lateral sclerosis. A March *Science* paper showed this happening when such proteins are improperly excluded from the cell nucleus. In April, four papers in *Cell* revealed possible measures for dissolving the toxic aggregates, and several labs are now trying to exploit this knowledge to discover drugs for treating neurodegenerative diseases. —*Ken Garber*

Ken Garber is a journalist in Ann Arbor, Michigan.

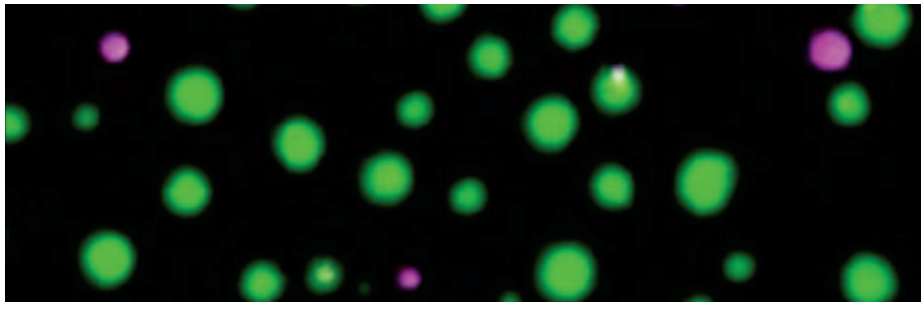

Liquid droplets formed from protein and RNA are emerging as a new form of cellular organization.

IMAGES: (TOP TO BOTTOM) THOMAS HIGHAM/UNIVERSITY OF OXFORD; E. M. LANGDON *ET AL.*, *SCIENCE* 2018

Forensic genealogy comes of age

In April, police announced they had arrested a suspect in one of the coldest of cold cases: a series of rapes and murders in California in the 1970s and 1980s. It was a stunning development, and so was the way investigators fingered the alleged Golden State Killer. They identified his relatives by uploading a profile of DNA recovered from one of the crime scenes to a public genealogy DNA database. Law enforcement agencies have since used this strategy to crack about 20 other cold cases, ushering in a new field: forensic genealogy.

Private DNA websites such as Ancestry and 23andMe contain millions of profiles that can be used to find a person's relatives from bits of shared DNA, but police need a court order to search them. In the Golden State Killer case, authorities turned to a public, no-frills online database called GEDMatch, run by two amateur genealogists in Texas and Florida, to which anyone can submit DNA test results. Investigators uploaded a DNA profile from a rape kit to the database, and found several distant relatives of the perpetrator. Working with a genealogist, they then used public records to construct large family trees and homed in on 73-year-old Joseph James DeAngelo, whose age and location fit some of the crimes. When tests showed the crime scene DNA matched DNA from DeAngelo's car door handle and a discarded tissue, they had their suspect.

This fall, geneticists reported that 60% of Americans of European descent (who make up most ancestry site users) would have a third cousin or closer match in a database with 1 million samples, about the size of GEDMatch. Once a database reaches 3 million profiles, more than 90% of white individuals could be found with similar methods—even if they have never had their DNA tested. All this has alarmed some ethicists and geneticists who see these familial searches as an invasion of privacy with a potential for misidentifying suspects. —*Jocelyn Kaiser*

Joseph James DeAngelo, the alleged Golden State Killer.

Molecular windows into primeval worlds

This year, scientists detected molecular traces from creatures that lived more than half a billion years ago, sharpening their picture of the mysterious world that gave rise to some of Earth's first animals and pushing such molecular paleontology back several hundred million years. They detected the signatures of fat molecules in some of the strangest fossils known, the enigmatic life forms called the Ediacarans, and molecular evidence of sponges from long before they appear in the fossil record.

For more than 70 years, scientists have puzzled over the bewildering shapes of Ediacaran fossils. Some resemble leaves or fronds; others look like no other organisms that have ever lived on Earth. Were the ancient ocean dwellers plants? Animals? Or some entirely separate form of life that failed to survive?

Researchers at Australian National University in Canberra wondered whether they could extract chemical clues from some exceptional fossils that, despite being 550 million years old, still preserve a film of what looks like organic material. These fossils come from a cliff on the shore of the White Sea in northwestern Russia, where the rocks have escaped the heat and pressure that can obliterate such molecular traces.

A fossil of *Dickinsonia* contained traces of cholesterol-like molecules, a signature of animal life.

Researchers first tested the idea on a collection of small, round Ediacaran fossils called *Beltanelliformis*. They removed the film from the rock, dissolved it, and used gas chromatography and mass spectrometry to look for preserved organic molecules. They found high levels of hopanes, molecules that suggested the balls were colonies of cyanobacteria, the researchers reported in January. That success gave them the nerve to try the technique on a fossil of a creature called *Dickinsonia*, one of the most famous Ediacaran species. Oval-shaped and about half a meter long, it resembles a quilted bath mat. In September, the team reported that the *Dickinsonia* fossil contained traces of cholesterol-like molecules, a signature of animal life. That fits with other evidence suggesting at least some Ediacarans were among the earliest animals on Earth.

In October, another team found traces of molecules that today are made only by sponges, in rock layers between 660 million and 635 million years old. The finding suggests sponges, another form of animal life, might have evolved 100 million years earlier than their oldest recognizable fossils. —*Gretchen Vogel*

PHOTOS: (TOP TO BOTTOM) PAUL KITAGAKI JR./*THE SACRAMENTO BEE* VIA AP/POOL; D. GRAZHDANKIN

2 PEOPLE'S CHOICE

Gene-silencing drug approved

A drug based on a gene-silencing mechanism called RNA interference (RNAi) won regulatory approval this year. The long-awaited step could be the harbinger of a new class of drugs targeting disease-causing genes.

Twenty years ago, two U.S. geneticists discovered that short RNA molecules can disrupt the translation of genes by attaching to the messenger RNA that carries a gene's message to the cell's proteinmaking machinery. The advance won them a Nobel Prize, but efforts to turn it into medicine quickly hit hurdles. Scientists struggled to keep the fragile RNA molecules intact and direct them to the right tissue. By 2008, researchers at Cambridge, Massachusetts–based Alnylam Pharmaceuticals thought they had a solution: a lipid nanoparticle that would protect the gene-silencing RNA and ferry it to the liver. There, they hoped, it could treat a rare disease called hereditary transthyretin amyloidosis by blocking the production of a misfolded protein that builds up and causes heart and nerve damage.

"We set off with great haste and enthusiasm," says Akshay Vaishnaw, Alnylam's president of R&D. But the new nanoparticle didn't release enough RNA into liver cells to knock down the problem gene effectively in all patients. A more potent formulation worked in human trials and became the intravenous drug Onpattro, which won clearance from U.S. and EU regulators this year and hit the market with a $450,000-per-year list price.

The approval, along with the 2016 approval of a different class of RNA-based drug, has invigorated the field, says Frank Slack, a developmental biologist at Beth Israel Deaconess Medical Center in Boston who studies another type of small RNA molecule. Many RNAi researchers are now shifting their attention to a newer delivery method: hooking chemically stabilized RNA onto a sugar molecule that homes in on the liver. Alnylam has developed a similar approach to target tissues beyond the liver, such as the eye and the central nervous system. Getting RNA to accumulate in certain tissues, including the heart, will be a challenge, says Slack, but Alnylam's success "has just opened the flood gates."
—*Kelly Servick*

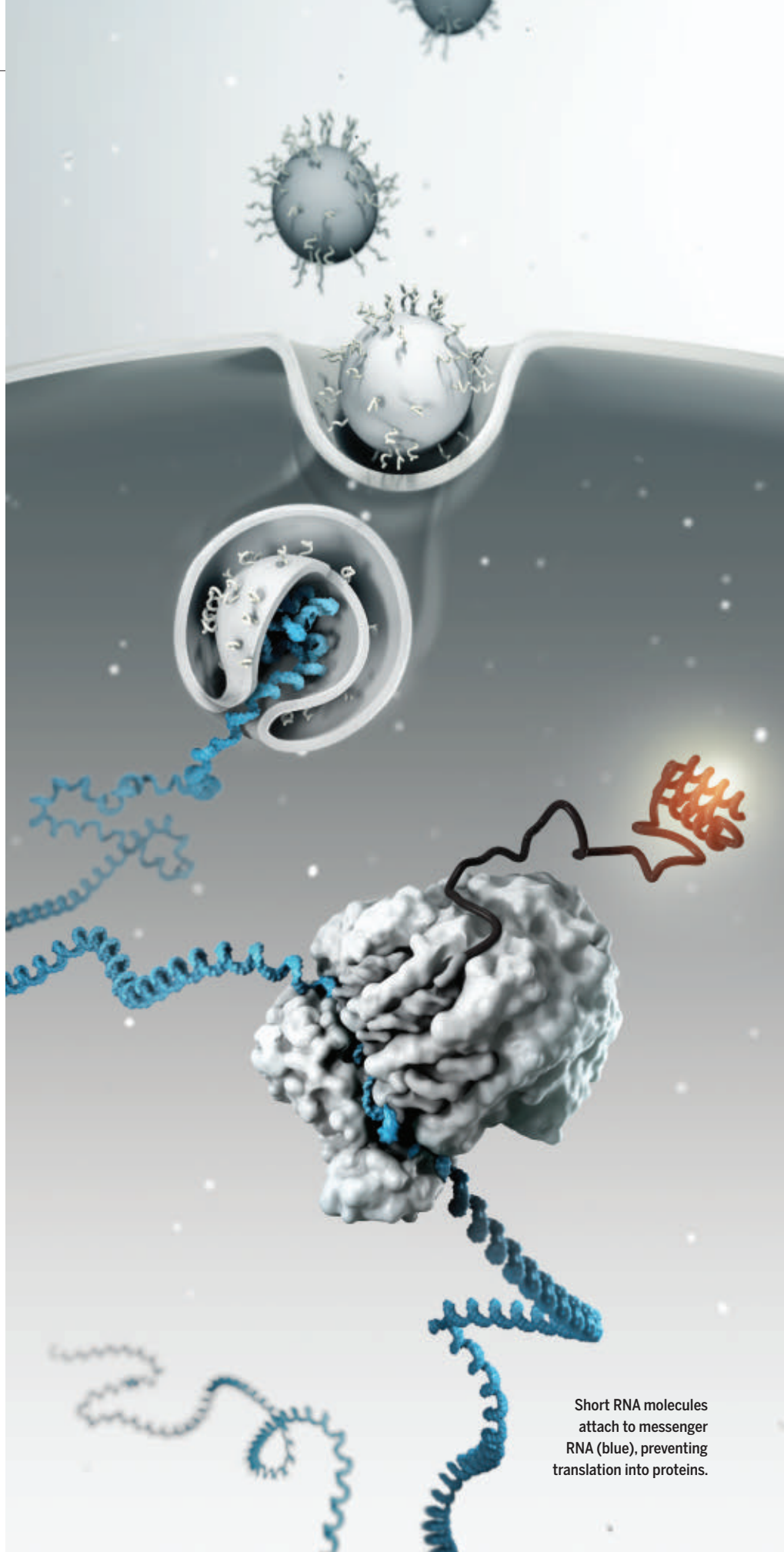

Short RNA molecules attach to messenger RNA (blue), preventing translation into proteins.

ILLUSTRATION: V. ALTOUNIAN/*SCIENCE*

An illustration of detectors buried in ice beneath the South Pole that record rare flashes triggered by neutrinos.

Molecular structures made simple

Two research teams simultaneously published papers in October revealing a new way to determine the molecular structures of small organic compounds in just minutes, rather than the days, weeks, or months required by traditional methods.

For decades, the gold standard for molecular mapping has been a technique known as x-ray crystallography, which involves firing a beam of x-rays at a crystal containing millions of copies of a molecule lined up in a common orientation. Researchers then track the way x-rays bounce off the crystal to identify individual atoms and assign them positions in the molecule. The structures are invaluable for understanding how biological molecules behave and how drugs interact with them. But the technique requires growing crystals about the size of a grain of sand, which can be a major hurdle for some substances.

In recent years, researchers have modified the diffraction technique by replacing the x-rays with an electron beam. The electron beam is aimed at a sheetlike 2D crystal of the target biomolecule, usually a protein. But in some cases, those sheets stack atop one another, creating a 3D crystal that doesn't work for ordinary electron diffraction and is too small for x-ray diffraction.

Two research teams—one in the United States, the other in Germany and Switzerland—found they could use such accidental crystals after all. They fired an electron beam at a tiny 3D crystal on a rotating stage and tracked how the diffraction pattern changed with each slight turn. The technique generated molecular structures in minutes—from microscopic crystals just one-billionth the size required for x-ray studies.

Well-suited for mapping small molecules such as hormones and potential drugs, the new technique should have a profound impact on fields ranging from the synthesis and discovery of new pharmaceuticals to the design of molecular probes to study and track diseases. —*Robert F. Service*

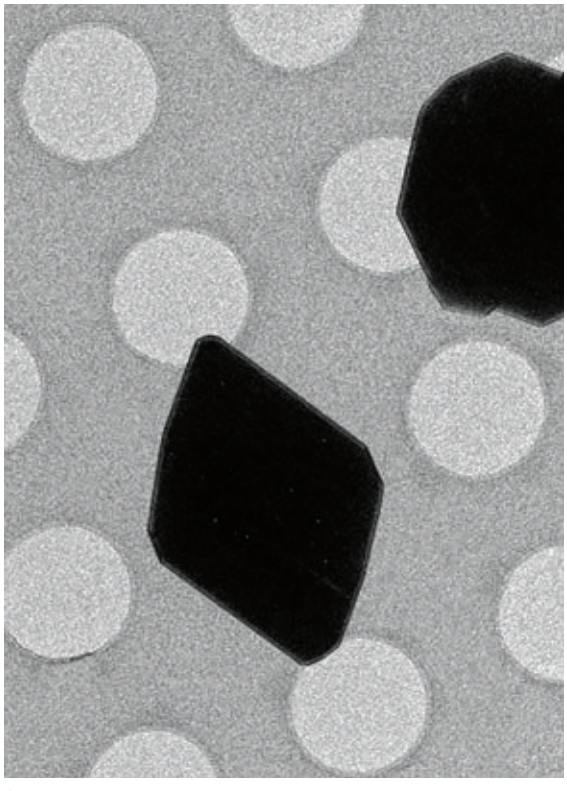

Structures can now be gleaned from micrometer-size crystals (black), seen here on an electron microscope slide.

IMAGES: (TOP TO BOTTOM) JAMIE YANG AND SAVANNAH GUTHRIE/ICECUBE/NSF; GONEN LAB

3 PEOPLE'S CHOICE

Messengers from a far-off galaxy

New kinds of messengers from the distant universe are joining the photons collected by telescopes—and revealing what light can't show. So-called multimessenger astrophysics got started with high-speed particles called cosmic rays and gravitational waves, the ripples in space-time first detected in 2015 that *Science* named Breakthrough of the Year in 2016. This year, another messenger has joined the party: neutrinos, tiny, almost massless particles that are extraordinarily hard to detect.

Snaring one of these extra-galactic will-o'-the-wisps took a cubic kilometer of ice deep below the South Pole, festooned with light detectors to record the faint flash triggered—very rarely—by a neutrino. Known as IceCube, the massive detector has logged many neutrinos before, some from outside the Milky Way, but none had been pinned to a particular cosmic source. Then, on 22 September 2017, a neutrino collided with a nucleus in the ice, and the light sensors got a good fix on the direction it had come from.

An alert sent out to other telescopes produced, after a few days, a match. As the researchers reported in July, NASA's Fermi Gamma-ray Space Telescope found an intensely bright source known as a blazar right where the neutrino appeared to come from. A blazar is the heart of a galaxy centered on a supermassive black hole, whose gravity heats up gas swirling around it, causing the material to glow brightly and fire jets of particles out of the maelstrom.

Researchers are pretty sure the blazar, which was flaring up at the time of the detection, is the source of the neutrino—making it the first time a neutrino telescope has identified an extra-galactic source. But the discovery is more than just a proof of principle. A blazar producing gamma rays and neutrinos is likely producing other high-energy particles, too, such as protons. These ultra–high-energy cosmic rays bombard Earth from time to time, but their source has been a mystery. Now, blazars are a suspect.

The IceCube team awaits more fleeting extra-galactic messengers. But having welcomed this first visitor, it is making its case for an enlarged detector enclosing 10 times the current volume of ice. —*Daniel Clery*

#MeToo makes a difference

Sexual harassment in science has been underreported and largely ignored until recently. But this year brought signs of change.

In June, the U.S. National Academies of Sciences, Engineering, and Medicine released a landmark report on sexual harassment of women in academic science, engineering, and medicine that could prove to be a watershed. It concluded, based on recent data from two large university systems, that more than 50% of female faculty and staff and 20% to 50% of students, depending on stage and field, have endured sexual harassment, including the most pervasive form—sexist hostility both verbal and nonverbal: putdowns, not come-ons. And this year, several institutions took action.

Some, prodded by news exposés or by formal complaints from harassed students and staff, fired or forced out prominent scientists after investigations upheld allegations of wrongdoing. Others announced policy changes.

In September, the U.S. National Science Foundation (NSF) in Alexandria, Virginia, said that, going forward, universities must tell it when a grantee is placed on leave during a harassment investigation or found guilty of sexual harassment—with the potential for "targeted and serious consequences" from NSF as a result, said Director France Córdova. Bemoaning the community's failure to protect harassment victims, Córdova declared: "This neglect must end." That same month, AAAS, which publishes *Science*, adopted a policy under which AAAS fellows proved to be sexual harassers can be stripped of this lifetime honor. And the presidents of the National Academies promised in May to explore how proven harassers could be ejected from their prestigious ranks.

The pace of change is not nearly fast enough for critics. BethAnn McLaughlin, a neuroscientist at Vanderbilt University in Nashville who this year founded the advocacy group #metooSTEM, notes, for example, that the National Institutes of Health (NIH) does not require universities to report grantees under investigation, or even disciplined, for sexual harassment. McLaughlin opens her public talks with 46 seconds of silence, "1 second for every year that NIH has given money to scientists and doctors and not asked if they have violated Title IX," a 1972 U.S. statute outlawing sexual harassment of students. She uses the silence, she says, "to honor the hundreds of women driven from our fields." —*Meredith Wadman*

ILLUSTRATION: DARIA KIRPACH/@SALZMANART

BREAKDOWNS OF THE YEAR

What went wrong in the world of science in 2018

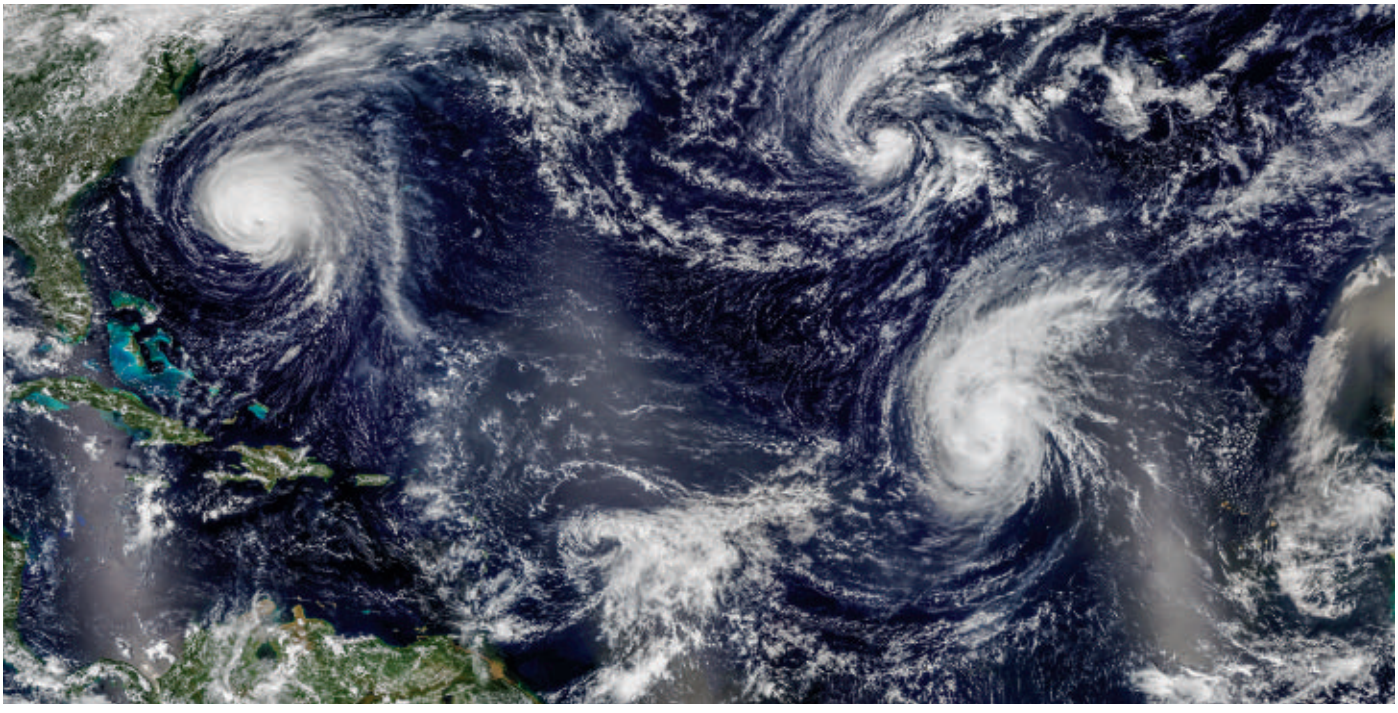

Four hurricanes churn in the Atlantic Ocean in September, the first such lineup in a decade.

Climate-fueled disasters rise, political action stalls

Devastating wildfires in the western United States and northern Europe. A record heat wave in southern Europe. Hurricanes, cyclones, and flooding in the Americas and the eastern Pacific Ocean. For many, this was the year climate change hit home. Climate-influenced disasters have grown stronger and lasted longer. As the latest iteration of the U.S. *National Climate Assessment* put it in November: "The evidence of human-caused climate change is overwhelming … [and] the impacts of climate change are intensifying across the country."

Several modern records will be broken this year, as they have been inexorably year after year. The overall temperature of the world's oceans—the best thermometer for the planet itself—is the highest it has been since record keeping began. Ocean levels are some 8 centimeters higher than in the 1990s—and the rise is accelerating. And global greenhouse gas emissions will again hit an all-time high, likely rising by more than 2% over last year.

Yet, as the evidence—enumerated in a series of alarming scientific reports this fall—has mounted, the gap between what the world needs to do and what it is doing seems wider and starker than ever. In the United States, President Donald Trump has disputed the science of human-driven climate change, sought to roll back most of the climate-focused policies that his predecessor enacted, and stood firm in his intent to pull the United States out of the Paris agreement, the international deal to curb greenhouse gas emissions. The White House even tried to downplay the *National Climate Assessment*, a report mandated by Congress and endorsed by government science agencies. "I do not believe it," Trump said when asked about estimated economic impacts; his spokesperson Sarah Sanders called the report "extreme" and "not based on facts." "The federal government is constructing an alternative reality," says Phil Duffy, president of the Woods Hole Research Center in Falmouth, Massachusetts. "They're in la-la land."

The United States is not alone. "Each year that goes by with lack of action and leadership in the U.S., more and more countries around the world have an excuse for stepping back," says Kelly Sims Gallagher, director of Tufts University's Center for International Environment & Resource Policy in Medford, Massachusetts. For example, Brazil's incoming president, Jair Bolsonaro, has promised to open Amazonian rainforest for development, potentially releasing a rush of carbon dioxide (CO_2) emissions. China is once again focusing more on problems such as clean air rather than carbon emissions, and even the European Union is distracted by internal upheavals.

The costs of decades of little or no action are becoming manifest as the "natural" is slowly drained from natural disasters. The consequences are worst where human influence on the climate slams into the human predilection to live in risk-prone places. Take the record wildfires in California, such as the Camp Fire, which killed at least 86 people and reduced the town of Paradise to ash. Warming temperatures and a downturn in summer rainfall are drying out the western United States, prolonging torrid droughts that turn forests and brush to tinder. Large wildfires there now burn twice the area they did in 1970; by mid-century, the area burned by all wildfires in the region is projected to increase as much as sixfold. "These bigger fires, fires that move faster, and a longer fire season—it's clearly, clearly here," Duffy says.

On the East Coast, low-lying cities such as Norfolk, Virginia, are experiencing flooding at high tide thanks to a combination of sea-level rise and subsidence linked to the long-ago retreat of the ice sheets. And when there's not sunny-day

PHOTO: NATIONAL OCEANIC AND ATMOSPHERIC ADMINISTRATION

flooding, there are storms: This year brought no reprieve from 2017's blockbuster hurricanes. Like Harvey, which devastated Houston, Texas, last year, this year's Hurricane Florence exhibited many telltale signs of global warming's influence: It intensified rapidly and dawdled over land, drowning the North Carolina coast with unprecedented rainfall.

Those effects don't stop at U.S. shores. Super Typhoon Mangkhut, the year's strongest storm, battered the Philippines, triggering landslides and killing at least 66 people. In the United Kingdom, human-driven warming has made debilitating summer heat waves 30 times more likely; by midcentury, such heat will grip the island once every 2 years. A similar heat wave in Canada this year killed more than 90 people. The recent spike in sea level, now at 3.9 millimeters a year, has put Pacific Island nations on edge, and studies this year suggested wave-driven overwash could make many of those islands uninhabitable within decades.

In October, the Intergovernmental Panel on Climate Change, a United Nations–sponsored group that includes hundreds of the world's leading climate scientists, released a grim look at the effects of a global temperature increase just 1.5°C above preindustrial levels—not much more than the 1°C the planet has already warmed. Among the findings: After another half-degree of warming, many of the world's coral reefs would be doomed. In some regions, drowning rains and scorching heat waves would grow more severe. Arctic sea ice would rapidly retreat. And holding the temperature increase to that level would require a stark drop in carbon emissions, along with steps to actively remove CO_2 from the atmosphere, the report said.

"We reach 1.5° by 2040. We've only got 2 or 3 decades," says Myles Allen, one of the report's lead authors and a climate dynamicist at the University of Oxford in the United Kingdom. Perhaps it's still theoretically possible, Duffy adds. "But to meet the goal, [the world] needs to change now. And I don't see that happening."

Even when global warming recaptures the world's attention, the problem will not be easy to solve. The world needs to weigh the costs and benefits of keeping the warming to 1.5°C rather than 2°C or higher, Allen says. "Politically the conversation has to move from now to how much a burden we impose on the next generation," he says. But Don Wuebbles, an atmospheric scientist at the University of Illinois in Urbana and a lead author of the *National Climate Assessment*, says the burden is already heavy. "I've been through Paradise," he says, "which no longer exists." —*Paul Voosen*

IMAGES: (TOP TO BOTTOM) MAURO PIMENTEL/AFP/GETTY IMAGES; MEDICALRF/SCIENCE SOURCE

Brazil's National Museum, following a devastating fire.

BRAZILIAN SCIENCE GUTTED

The fiery death of Brazil's 200-year-old National Museum in Rio de Janeiro was painfully symbolic of what many researchers fear is a looming demise of Brazilian science. The museum burned down on the night of 2 September, following years of underfunding and neglect by authorities. Public funds for science in most of the country have followed a similar trajectory. The budget of the federal science ministry shrank by more than 50% in the past 5 years, and an additional 10% cut is expected for 2019, despite scientists' many appeals to legislators in Brasília.

Fears deepened after the October election of far-right congressman Jair Bolsonaro as the next president of Brazil. Although he promises to triple the rate of investment in science, technology, and innovation to 3% of gross domestic product in the next 4 years—something many analysts say is not feasible—the former army captain is at odds with scientists on several issues. He has threatened to pull Brazil out of the 2015 Paris agreement on climate change and vowed to reduce funding for federal universities, where much of Brazil's science is conducted, claiming that Brazilian academia is dominated by "left ideology" and that many universities in Brazil represent "wasted money." —*Herton Escobar*

AN ETHICALLY FRAUGHT GENE-EDITING CLAIM

Humanity rewriting its own genetic code is no small feat. At another time, under different circumstances, germline gene editing might well have a shot at becoming *Science*'s Breakthrough of the Year. But a Chinese researcher's claim in November that he had created twin baby girls resistant to HIV using the gene-editing technique CRISPR doesn't qualify for that distinction.

Among scientists and ethicists, a consensus has emerged about the conditions under which such work might be acceptable in the future: if it is the only way to help parents conceive a healthy baby, if scientists have done everything possible to show the technique is safe, if the study has undergone careful ethical vetting, and if it is carried out transparently.

He Jiankui of the Southern University of Science and Technology in Shenzhen, China, appears to have met none of those criteria. As *Science* went to press, He had not published his findings, and there was no proof that two babies were born with altered genes for a protein exploited by HIV. It's unclear whether the edits would truly shield Lulu and Nana from HIV infection, or why the potential benefits were worth the risks given that other, proven methods exist to prevent HIV infection and the girls were not facing an unusually high risk of exposure to the virus. The study's ethical review seems murky at best, the work was shrouded in secrecy—a planned public relations campaign fell apart after a news leak—and He broke an international consensus on germline experiments as well as, it seems, Chinese regulations. Because of those many shortcomings, his claim counts as one of the science breakdowns of 2018. —*Martin Enserink*

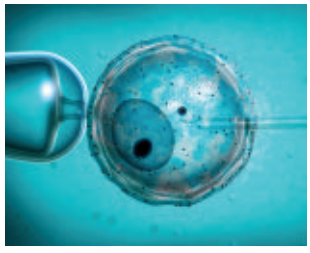

In vitro fertilization, the first step in gene editing.

QUASICRYSTALS

Tessellating tiny tetrahedrons

A tiling rule guides the formation of quasicrystalline superlattices of nanocrystals

By **Siyu Wu** *and* **Yugang Sun**

Tessellating tiles and bricks of well-defined geometric shapes can be traced back to the ancient age (~4000 BCE), when Sumerians used clay tiles to decorate building walls. Since 1619 when Johannes Kepler first wrote about tessellation, it has become a topic of interest in disciplines including pure mathematics, materials science, chemistry, art, architecture, and industrial design. Packing convex polygonal shapes into three-dimensional (3D) Euclidean space was conjectured by Ulam to form a more dense tessellation than spheres, but that conjecture was theoretically verified only recently for packing tetrahedrons in a quasicrystalline (QC) arrangement through shape-induced entropic interactions (*1*). Forming a QC superlattice of tetrahedrons with rotational symmetricity yet no transitional periodicity (*2*) has represented a grand experimental challenge. On page 1396 of this issue, Nagaoka *et al.* (*3*) report a "flexible polygon tiling rule" that guided the self-assembly of nanometer-sized tetrahedrons of cadmium chalcogenide (CdSe-CdS core-shell nanoparticles) to form a 10-fold QC superlattice at a liquid-air interface (see the figure).

The authors synthesized tetrahedral semiconductor nanocrystals (NCs) with two different types of surfaces, including three equivalent $\{10\bar{1}1\}$ facets (A type) and one {0002} facet (B type), which were covered with oleic acid and octadecylphosphonic acid, respectively. Such differentiation of surface chemistry promoted the selective facet-to-facet alignment and attachment (i.e., A-to-A and B-to-B) of neighboring tetrahedrons as they moved close together in the course of self-assembly. The preferred alignment of tetrahedral NCs led to the formation of decagon units with 10-fold symmetry, each of which contained a tetrahelix ring (*4*) surrounding a vertically stacked pair of tetrahedrons in the center.

Unlike clay bricks bonded with mortar, the tetrahelix rings of the decagon units were flexible, which allowed the entire system to gain additional stability through local configuration changes at the interfaces of packed decagon units (*5*). The flexible polygon tiling rule facilitated the tessellation of the decagon units into 10-fold QC superlattices of the nanosized tetrahedrons. This rule can be generalized to pack any polygon units with even numbers of edges n—for example, octagons, decagons, dodecagons, and tetradecagons—forming 3D QC tessellations. During packing, two neighboring polygons may overlap with only one or two edges. The two polygons need to remain intact when there is no edge or only one edge overlapping; when two edges overlap, the overlapped edges need to become flexible and transform into one straight edge (the flexible edge). Each polygon must have at least one flexible edge and at most $n/2$ flexible edges, and the generated tessellation pattern must have a QC order with an n-fold rotational symmetry.

When packing tetrahedral solids, external compressive force determines the packing order and density (*6*). Applying stronger compression forces to the tetrahedral NCs in the course of self-assembly prevented the formation of the tetrahelix polygon rings and QC tessellation at the liquid-air

Department of Chemistry, Temple University, Philadelphia, PA 19122, USA. Email: ygsun@temple.edu

IMAGE: SIYU WU AND YUGANG SUN

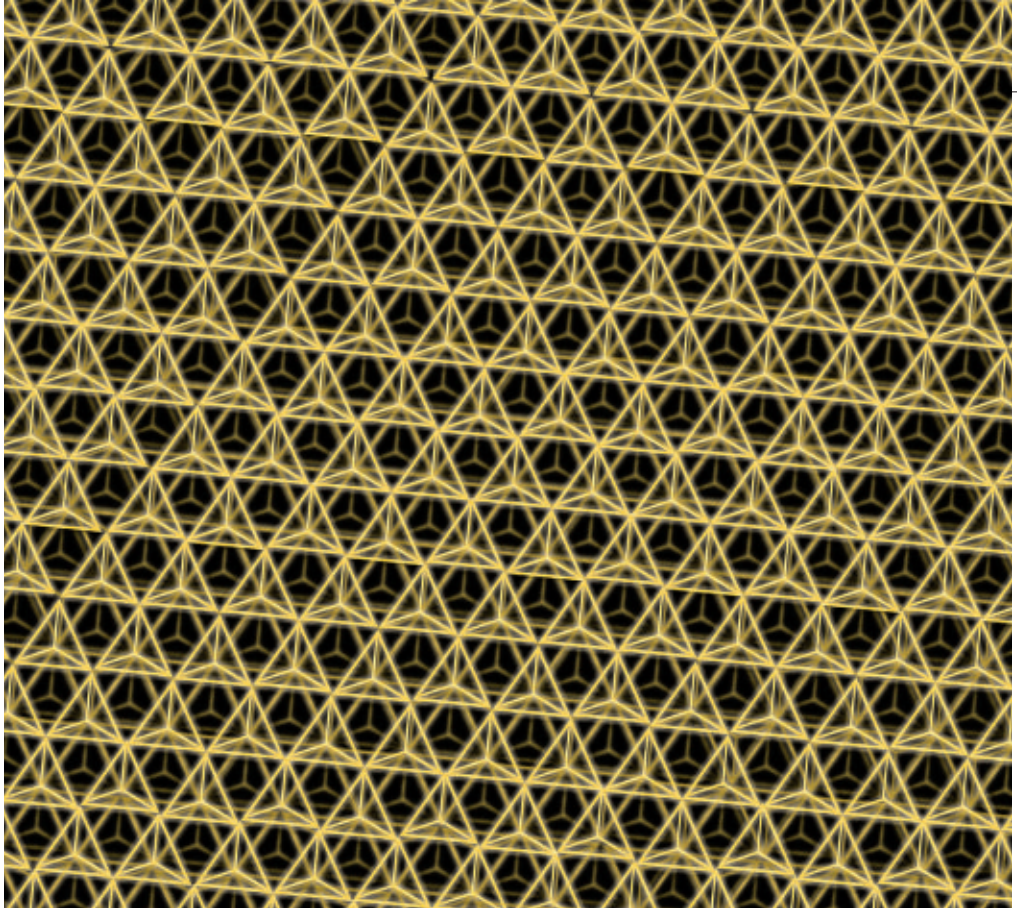

IMAGE: SIYU WU AND YUGANG SUN

interface (*3*). A stronger compression was realized by replacing the liquid subphase of ethylene glycol with diethylene glycol, which provided higher aliphatic hydrophobicity and increased the interfacial surface energy between the solvent (i.e., cyclohexane for dispersing the semiconductor NCs) and the substrate (i.e., diethylene glycol).

This change led to a smaller receding angle at the solidification front of assembled NCs. Thus, the assembled NCs lacked space to extend vertically and were firmly squeezed by the liquid surface to form 2D superlattices of hexagonal symmetry. However, the use of ethylene glycol as the substrate created a higher receding angle and provided sufficient space for selective facet-to-facet alignment of the semiconductor tetrahedrons and the corresponding QC superlattices.

The flexible polygon tiling rule, facilitated by both the anisotropic patchiness of surface chemistry and the appropriate pairing of solvent and liquid substrate used in the self-assembly process, led to the successful formation of QC tessellation of tetrahedral NCs. Although self-assembly of nanoparticles into dodecagonal (12-fold) QC orders had been demonstrated from the mixtures of spherical nanoparticles of two different types and sizes (*7*), the 10-fold QC order of tetrahedral NCs reported by Nagaoka *et al.* had been neither observed experimentally nor predicted in any simulated QC models.

This success demonstrates that controlling the geometrical and chemical anisotropy (in addition to size) of nanoparticle building blocks can enable their assembly into highly complicated (or even unexpected) superlattice symmetries. Unlike the commonly observed entropy maximization process, anisotropic patchiness favors directional enthalpic driving forces to promote the formation of new QC superlattices. The work of Nagaoka *et al.* will drive a wave of attention from matter assembly researchers, including the synthesis and use of different types of anisotropic building blocks to create unconventional superlattices and complex structures. Because the tessellation of tetrahedral and pyramidal shapes is a fascinating and challenging research topic in many research fields, including mathematics and computer simulation, this experimental discovery will likely stimulate other follow-up studies. ■

Packing nanosized tetrahedrons. Self-assembly of tetrahedral semiconductor nanoparticles normally forms a regular periodic Bragg lattice (this page). Nagaoka *et al.* show that packing at a liquid-air interface can create a quasicrystalline lattice (preceding page).

REFERENCES

1. A. Haji-Akbari *et al.*, *Nature* **462**, 773 (2009).
2. D. Shechtman, I. Blech, D. Gratias, J. W. Cahn, *Phys. Rev. Lett.* **53**, 1951 (1984).
3. Y. Nagaoka, H. Zhu, D. Eggert, O. Chen, *Science* **362**, 1396 (2018).
4. Y. Nagaoka *et al.*, *Nature* **561**, 378 (2018).
5. M. Engel, H.-R. Trebin, *Phys. Rev. Lett.* **98**, 225505 (2007).
6. S. Torquato, Y. Jiao, *Phys. Rev. E* **80**, 041104 (2009).
7. D. V. Talapin *et al.*, *Nature* **461**, 964 (2009).

10.1126/science.aav8597

CANCER IMMUNOTHERAPY

Chemotherapy and tumor immunity

Inducing senescence in tumor cells stimulates antitumor innate immune responses

By **Stéphanie Cornen**[1] *and* **Eric Vivier**[1,2,3]

A large increase in the incidence of cancers has been predicted for the coming years, with the number of cases worldwide rising from 15 million to 24 million between 2015 and 2035 (*1*). The current revolution in cancer treatment—cancer immunotherapy—is based on the mobilization of the immune system to target cancer cells and is opening new avenues for achieving cancer control. However, evidence suggests that immunotherapies in many cancers are most effective when combined with other treatments, such as surgery, radiotherapy, and chemotherapy. On page 1416 of this issue, Ruscetti *et al.* (*2*) show that a combination of chemotherapy drugs inhibiting MEK (mitogen-activated protein kinase kinase) and CDKs (cyclin-dependent kinases) induces tumor cell senescence, a type of cell growth arrest, that alerts the innate immune system by activating natural killer (NK) cells, leading to immune control of the cancer.

Therapies that enhance the development of an immune response against tumor cells are of high interest because the absence of antitumor immunity prior to treatment appears to be a major factor of resistance to immunotherapy. MEK and CDK inhibitors target the Ras-Raf-MEK-ERK (extracellular signal–regulated kinase) pathway, which is a key pathway in many cancers. CDKs act downstream from ERK to control the cell cycle, and hence their activity can promote tumor cell division. BRAF inhibitors, such as dabrafenib, have potent antitumor activity, particularly when combined with MEK inhibitors, such as trametinib, in the treatment of melanoma and non–small cell lung

[1]*Innate Pharma, Marseille, France.* [2]*Aix Marseille Université, INSERM, CNRS, Centre d'Immunologie de Marseille-Luminy, Marseille, France.* [3]*Service d'Immunologie, Marseille Immunopole, Hôpital de la Timone, Assistance Publique-Hôpitaux de Marseille, Marseille, France. Email: vivier@ciml.univ-mrs.fr*

cancer (*3*). The CDK4/6 inhibitors abemaciclib, ribociclib, and palbociclib have been approved for use in breast cancer (*4*). Ruscetti *et al.* screened several chemotherapy agents and identified MEK and CDK4/6 inhibitors as potent inducers of the senescent phenotype in the KP (Kras and p53) mouse model of lung adenocarcinoma.

Cellular senescence is a programmed change in cell state associated with permanent growth inhibition (*5*). It can be induced by stresses, such as DNA damage, shortening of telomeres (a biomarker of aging), oncogenic mutations, metabolic mitochondrial dysfunction, and inflammation. The senescence-associated secretory phenotype (SASP) is characterized by increased production of growth factors, proteases, and proinflammatory cytokines that recruit immune cells and stimulate them to clear the senescent cells. The precise mechanisms by which senescence is induced and the affected cells eliminated remain to be elucidated. Ruscetti *et al.* show that the treatment of tumor cells with MEK and CDK4/6 inhibitors selectively triggers the antitumor functions of NK cells.

NK cells are innate lymphoid cells (ILCs) with potent antitumor activities (*6*). The efficacy of some conventional anticancer agents, such as those used in chemotherapy, is not exclusively due to the direct killing of the tumor cells. Instead, some anticancer treatments can induce forms of cancer cell stress or death that alert the immune system, initiating an antitumor immune response (*7*). NK cells can be involved in these mechanisms. For instance, telomeric repeat–binding factor 2 (TRF-2) has been shown to induce a form of cellular stress that promotes the elimination of neoplastic cells in an NK cell–dependent manner (*8*). In addition, expression of ligands for NK cell–activating receptors, NKG2D and DNAM1, can be increased in cancer cells undergoing stress-induced senescent programs following treatment with chemotherapeutic agents, leading to NK cell activation (*9*). Senescent noncancer cells, such as decidual cells (*10*), fibroblasts (*11*), and hepatic stellate cells (*12*), can also trigger NK cell responses.

Given the dual potential of cellular senescence to halt the proliferation of tumor cells and recruit immune cells, interest in pro-senescence therapies for cancer treatment has been growing. However, several hurdles remain on the road to therapy-induced senescence as a means of treating cancer: optimization of the dose schedules and combinations required to induce cellular senescence and antitumor immunity, while overcoming the protumorigenic properties of senescent cells and the SASP. Indeed, the SASP has been described as a double-edged sword, because it can also induce tumor-promoting effects such as angiogenesis, epithelial-to-mesenchymal transition, and metastasis (*13*). It thus remains unclear whether it is preferable to induce senescence rather than cell death.

To date, attempts to make use of NK cells in cancer immunotherapy have focused on the initiation of a multilayered immune response culminating in protective and long-lasting antitumor immunity (*6*). Remarkably, Ruscetti *et al.* suggest that NK cells act as a natural senolytic, eliminating tumor cells rendered senescent by chemotherapy and controlling cancers without the assistance of other immune cell types. These findings raise important questions about the mechanisms by which senescent tumor cells are eliminated by NK cells and whether NK cells kill senescent tumor cells directly. Is the production of cytokines by NK cells, such as interferon-γ and GM-CSF (granulocyte-macrophage colony-stimulating factor), involved? Moreover, NK cells have many features in common with ILC1s (*14*). The selective involvement of NK cells in the control of KP tumors is striking, but its demonstration was based on the use of an NK1.1 monoclonal antibody that depletes both NK cells and ILC1s in mice. NK cells, ILC1s, and an intermediate subset (intILC1) can infiltrate mouse tumors and have opposing functions: NK cells favor tumor control, whereas intILC1s and ILC1s do not (*15*). Further dissection of the role of MEK and CDK4/6 inhibitors, and of other chemotherapy agents, in the composition and function of tumor-infiltrating ILCs is required. Does the recognition of senescent cells by NK cells initiate long-term protection against nonsenescent tumor cells? And most importantly, do these observations apply to human cancers?

Recent clinical results have supported the hypothesis that chemotherapy can boost immune responses and sensitize tumors to immunotherapies. However, we still know little about the underlying mechanisms, and more explorations are required to identify the most promising chemotherapy-immunotherapy combinations to further enhance clinical responses in cancer patients. The induction of senescence is one possible way in which chemotherapy and immunity may be able to join forces. ■

NK cells detect and eliminate senescent tumor cells

Pharmacological inhibition of MEK and CDK4/6 induces retinoblastoma (RB) protein–mediated cellular senescence and SASP, leading to the activation of NK cells, which detect and eliminate senescent tumor cells. Several questions remain to be addressed, as indicated.

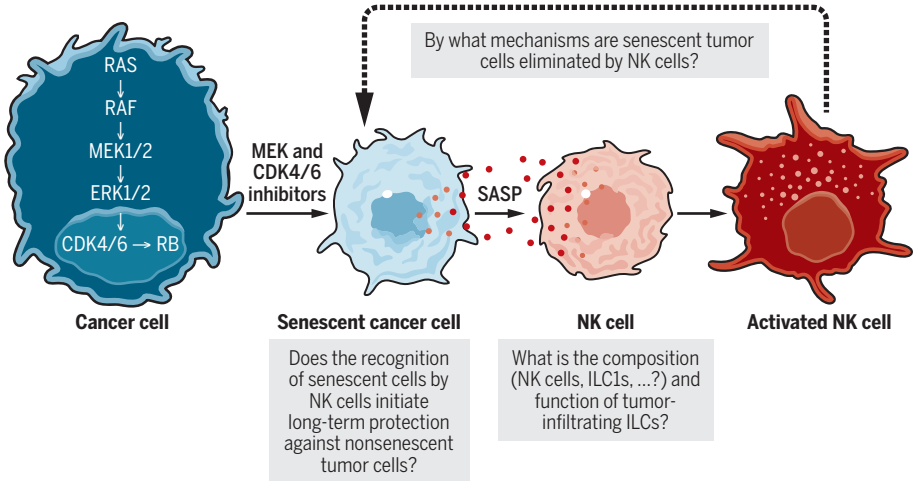

REFERENCES AND NOTES

1. Cancerprogressreport.org, American Association for Cancer Research (2018).
2. M. Ruscetti *et al.*, *Science* **362**, 1416 (2018).
3. J. J. Luke, K. T. Flaherty, A. Ribas, G. V. Long, *Nat. Rev. Clin. Oncol.* **14**, 463 (2017).
4. J. R.-E. Choo, S.-C. Lee, *Expert Opin. Drug Metab. Toxicol.* **14**, 1123 (2018).
5. S. He, N. E. Sharpless, *Cell* **169**, 1000 (2017).
6. L. Chiossone, P.-Y. Dumas, M. Vienne, E. Vivier, *Nat. Rev. Immunol.* **18**, 671 (2018).
7. L. Galluzzi *et al.*, *Cancer Cell* **28**, 690 (2015).
8. A. Biroccio *et al.*, *Nat. Cell Biol.* **15**, 818 (2013).
9. A. Soriani *et al.*, *Blood* **113**, 3503 (2009).
10. P. J. Brighton *et al.*, *eLife* **11**, 6 (2017).
11. A. Sagiv *et al.*, *Aging (Albany N.Y.)* **8**, 328 (2016).
12. H. Jin *et al.*, *Cell. Signal.* **33**, 79 (2017).
13. T. Saleh *et al.*, *Front. Oncol.* **8**, 164 (2018).
14. E. Vivier *et al.*, *Cell* **174**, 1054 (2018).
15. Y. Gao *et al.*, *Nat. Immunol.* **18**, 1004 (2017).

ACKNOWLEDGMENTS

E.V. receives funding from the European Research Council (TILC, no. 694502), the Agence Nationale de la Recherche, Equipe Labelisée "La Ligue," MSDAvenir, Innate Pharma, and institutional grants to CIML (INSERM, CNRS, and Aix-Marseille University) and to Marseille Immunopole. E.V. and S.C. are Innate Pharma employees.

10.1126/science.aav7871

GRAPHIC: A. KITTERMAN/*SCIENCE*

NETWORK ANALYSIS

Seeing a global web of connected systems

Social-ecological shifts may often be causally linked

By **Marten Scheffer** *and* **Egbert H. van Nes**

The Arab Spring, the invention of penicillin, and the recent mass bleaching of coral reefs are reminders that much of the change in nature and society happens in just a tiny portion of time. Understanding why and when such critical transitions happen remains notoriously difficult. On page 1379 of this issue, Rocha *et al.* (*1*) mine a database of shifts in social and ecological systems and conclude that about half of them may be causally linked on different scales. Their results highlight the importance of unraveling hidden connections in the web of ecological and social systems on which we depend.

It makes intuitive sense that the great Syrian exodus, the global financial crisis, Brexit, and the election of President Trump are not entirely unrelated. Yet, revealing the web of causalities behind such transitions remains difficult. Similarly, we have difficulties understanding connections between the fates of ice sheets, monsoons, tropical forests, and other tipping elements of Earth system that may shape the cascade of transitions toward a hothouse Earth (*2*). The challenge of seeing the bigger web of connections is a common thread in our struggle to understand transitions in complex systems. For example, after the collapse of the financial services firm Lehman Brothers, the global cascade of events ran through a network of connections between banks and other financial institutes that was largely hidden from the public eye (*3*). Another example is the Arab Spring, which precipitated from a complex web of drivers that encompassed social factors, climate-induced crop failures, and the rise of the biofuel market—these connections could be reconstructed only in hindsight (*4*).

This raises the question of what scientists can do to unravel the dazzling web of connections that weaves the biosphere and its human participants together. One approach is to use smart analytical techniques to mine the wealth of qualitative understanding of what affects what in the world (*5*, *6*). Rocha *et al.* took such an approach to analyze a database of transitions in intertwined socioecological systems (regime shifts) on the basis of more than 1000 scientific papers. They combined causes and effects of each of the regime shifts to build a larger web of potential links between them. They report that almost half of the theoretically possible links could plausibly be causal.

A major advantage of such a qualitative causal web analysis is that it allows the use of heterogeneous collections of narratives. One may, for instance, build a causality web simply from expert insights to analyze potential feedback loops and stability consequences (*7*). However, the use of qualitative information inevitably has limitations too. Most importantly, it can only provide a catalog of the possible. The actual stability properties and the net effects along causal chains depend critically on the relative strength of the different mechanisms involved. For example, snow cover reduces heat absorption, causing temperatures to drop; this allows more surface to freeze. However, a potential runaway of this destabilizing feedback toward a "snowball Earth" is prevented by counteracting forces. At the same time, even weak destabilizing feedbacks can produce a tipping point if they become aligned (*8*). Thus, although analyzing webs of qualitative insights can produce an inventory of the theoretically possible secondary effects and causal loops, there is the question of what we can do to reveal which of those are plausibly important.

The most obvious approach is to build quantitative simulation models to study the relative importance of different processes. This can help to constrain uncertainty in the vast catalog of the possible, showing, for example, that variation in solar activity has a negligible effect on recent warming (*9*). However, detailed models of complex systems remain difficult to verify and inevitably leave out potentially important processes (*9*). An emerging field of research therefore aims to complement the simulation approach by extracting causality directly from the increasing flood of time series data (*10*, *11*). This is tricky because of the problems of spurious correlations and the chicken-and-egg situations that are inherent in characterizing causal loops. For example, it may be tempting to interpret the observation that Earth's temperature started to rise somewhat before atmospheric CO_2 concentration started to increase as evidence that the first caused the latter at a glacial termination. However, such lags are meaningless in nonlinear dynamical systems in which only sophisticated approaches may help to probe the multiple simultaneous directions of causality (*12*).

There is no silver-bullet approach to unraveling the big scheme of things in nature and society, but that should not stop us from leaving our comfort zone and addressing the questions that matter. Understanding complex systems as a whole is crucial if we want to understand resilience and regime shifts, be it in the biosphere or in the human body (*13*). The way that Rocha *et al.* extracted insights from a web of qualitative narratives, and the emerging approaches to unravel causality from big data are reasons for optimism. ■

> ***"Understanding complex systems as a whole is crucial if we want to understand resilience and regime shifts, be it in the biosphere or in the human body."***

Department of Environmental Sciences, Wageningen Universiteit, 6708 PB Wageningen, Netherlands. Email: marten.scheffer@wur.nl

REFERENCES

1. J. C. Rocha *et al.*, *Science* **362**, 1379 (2018).
2. W. Steffen *et al.*, *Proc. Natl. Acad. Sci. U.S.A.* **115**, 8252 (2018).
3. S. Battiston *et al.*, *Science* **351**, 818 (2016).
4. J. Brownlee, T. Masoud, A. Reynolds, *Middle East Law and Governance* **7**, 3 (2015).
5. R. Levins, *Ann. N.Y. Acad. Sci.* **231**, 123 (1974).
6. G. Giordano, C. Altafini, *Sci. Rep.* **7**, 11378 (2017).
7. A. S. Downing *et al.*, *Ecol. Soc.* **19**, 31 (2014).
8. I. A. van de Leemput, T. P. Hughes, E. H. van Nes, M. Scheffer, *Coral Reefs* **35**, 857 (2016).
9. T. Stocker, *Climate Change 2013: The Physical Science Basis: Working Group I Contribution to the Fifth Assessment Report of the Intergovernmental Panel on Climate Change* (Cambridge Univ. Press, 2014).
10. J. Runge, *Chaos* **28**, 075310 (2018).
11. G. Sugihara *et al.*, *Science* **338**, 496 (2012).
12. E. H. van Nes *et al.*, *Nat. Clim. Chang.* **5**, 445 (2015).
13. M. Scheffer *et al.*, *Proc. Natl. Acad. Sci. U.S.A.* **115**, 11883 (2018).

10.1126/science.aav8478

PLANT BIOLOGY

Hydropatterning–how roots test the waters

Local water cues modulate auxin signaling to instruct root developmental decisions

By **Ricardo F. H. Giehl** *and* **Nicolaus von Wirén**

As sessile organisms, plants rely on their roots to acquire sufficient water and nutrients from the soil. Making the right choice about where to deploy new roots can determine survival, especially when soil resources are scarce and unevenly distributed. Recently, it was discovered that plant roots can respond to gradients of soil moisture by favoring the formation of lateral roots toward sites with available water (*1*). On page 1407 of this issue, Orosa-Puente *et al.* (*2*) show how growth along an air-water interface in the soil triggers asymmetric activation of a signaling module coordinated by the plant hormone auxin that biases lateral root initiation to the side in contact with water. These findings demonstrate how spatial environmental cues determine organ formation in higher plants.

The ability to generate new roots postembryonically confers plants a high degree of developmental plasticity. The formation of lateral roots starts deep in the parental root tissue. There, a specific number of cells of the pericycle, the tissue that delimits the root vasculature, are "primed" as lateral root founder cells at periodic intervals (*3*). Rather than progressing continuously, the initiation of lateral roots from primed pericycle cells can be stimulated or arrested at any developmental stage (*4*), allowing roots to adjust the number and spacing of lateral roots to the prevailing environmental conditions. This plasticity offers plants the opportunity to efficiently colonize regions of high resource availability, as long as root sensing mechanisms can precisely locate these sites.

In many plant species, low water availability can stimulate root expansion and steeper growth angles to improve water uptake from deeper soil layers (*5*, *6*). In soils that are not completely dry or flooded, an air-water interface develops between soil particles (see the figure). At this microscale, variations in water availability trigger abscisic acid–dependent hydrotropic growth to differentially modulate cell elongation, allowing roots to bend toward water (*7*, *8*). Additionally, tissue patterning is altered when roots are exposed to differential water availability on either side of the root. This adaptive response, termed hydropatterning, induces the formation of root hairs and aerenchyma (plant tissues containing enlarged gas-filled intercellular spaces) in the air-exposed side of roots, while positioning more lateral roots on the side that has direct contact with water (*1*). Although local water availability induces auxin biosynthesis and signaling (*1*), it has remained unknown how these changes are translated into asymmetrical lateral root formation across the root axis.

Orosa-Puente *et al.* found that mutations in the transcription factor AUXIN RESPONSE FACTOR 7 (ARF7), a key regulator of lateral root initiation (*9*), impaired the ability of plants to bias root branching toward moisture. Although LATERAL ORGAN BOUNDARIES-DOMAIN 16 (LBD16), a downstream target of ARF7, accumulates preferentially in lateral root founder cells on the water-exposed side, ARF7 is evenly expressed around the circumferential axis of the root. However, ARF7 can be posttranslationally modified with small ubiquitin modifier (SUMO). *Arabidopsis* plants lacking the SUMO proteases OVERLY TOLERANT TO SALT 1 (OTS1) and OTS2 (*10*), which promote deconjugation of SUMO from ARF7, exhibit a hydropatterning defect akin to ARF7 mutants. Intriguingly, SUMOylation does not affect the universal function of ARF7 to promote lateral root initiation but instead affects its capability to regulate the root branching pattern in response to water. ARF proteins can be inactivated by INDOLE-3-ACETIC ACID–INDUCIBLE (IAA) proteins in an auxin-dependent manner (*11*). This is also the case for ARF7, the DNA-binding activity of which is controlled by IAA3 and IAA14 at different stages of lateral root development (*12*, *13*). Orosa-Puente *et al.* identified that SUMOylation is specifically required for ARF7 recruitment and inactivation by IAA3 but is dispensable for the interaction with IAA14. These findings provide insights into how an environmental cue can fine-tune the function of common regulators of development to induce specific phenotypic plasticity.

Hydropatterning is conserved in many plant species and targets early stages of lateral root development, such as the positioning of founder cells along the main root axis (*1*). Developmental competence for hydropatterning is largely limited to the root zone undergoing active growth and is lost as cells mature (*14*). This has led to the hypothesis that water gradients are sensed near the root tip, leaving a positional imprint that triggers lateral root initiation further up in the root. In the growing root tip, cell expansion builds up a water potential gradient that increases hydraulic conductiv-

Shaped by water

Where there are small-scale differences in water availability around soil particles, water potential gradients are sensed in roots (red cells). Hydrotropism guides roots towards water, whereas hydropatterning alters the distribution of root hairs and lateral roots along the root circumference (not to scale). ARF7-dependent asymmetric LBD16 expression triggers lateral root initiation on the side in contact with water.

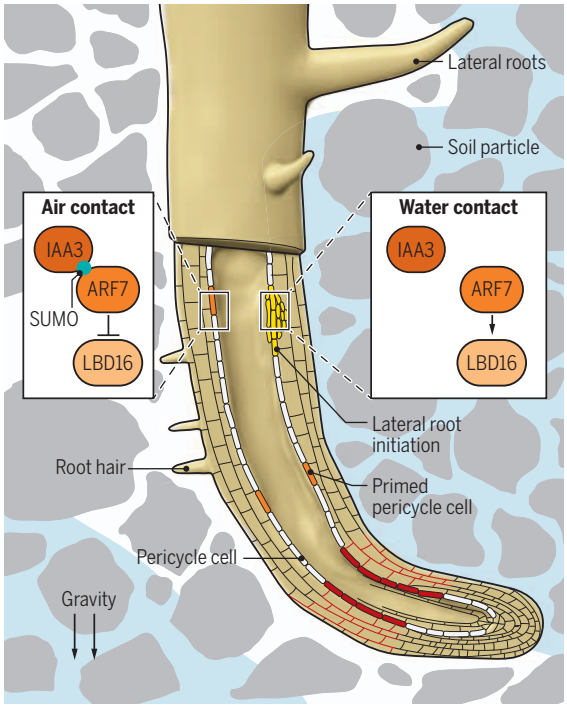

GRAPHIC: N. DESAI/*SCIENCE*

Department of Physiology and Cell Biology, Leibniz Institute of Plant Genetics and Crop Plant Research (IPK), 06466 Gatersleben, Germany. Email: vonwiren@ipk-gatersleben.de

ity (*14*). As water uptake rates are higher in expanding cells, differential access to water along the root circumference may generate sizable differences in water potential. Yet, experimentally demonstrating the existence of such gradients at this scale is very challenging. More research is necessary to uncover how root cells sense water potentials and how signals detected in outer cells are transmitted to inner root tissue. Interestingly, Orosa-Puente *et al.* observed that ARF7 SUMOylation occurs when roots are exposed to air, even though they have been unable to demonstrate if ARF7 is differentially SUMOylated in a root exposed to an air-water interface. Nonetheless, this finding suggests that the absence of water on its own serves as an informative cue for developmental decisions without depending on changes in cellular osmolarity.

Because water is such a critical resource for plant growth and development, it is not surprising that plants have evolved additional adaptive mechanisms. Although hydropatterning can increase root surface contact with water, the steering of growth direction by hydrotropism places this organ in water-available sites. Thus, if lateral roots primed by hydropatterning emerge at sites that become dry, hydrotropic growth allows them to maneuver toward water.

Considering the strong negative impact of precipitation variability on crop yield (*15*), breeding crops with a predefined root system architecture may be less appropriate than exploiting plasticity and sensing mechanisms to improve root adaptability to spatial and temporal variations of soil moisture. In this context, it will be interesting to determine the contribution of hydropatterning to water and nutrient uptake under challenging water regimes and to investigate how water and nutrient signals are integrated to shape root system architecture. Thus, manipulating the molecular mechanism uncovered by Orosa-Puente *et al.* and tapping into possible natural allelic variation for hydropatterning have potential for breeding crops that are better able to withstand environmental stresses. ■

REFERENCES AND NOTES

1. Y. Bao *et al.*, *Proc. Natl. Acad. Sci. U.S.A.* **111**, 9319 (2014).
2. B. Orosa-Puente *et al.*, *Science* **362**, 1407 (2018).
3. M. A. Moreno-Risueno *et al.*, *Science* **329**, 1306 (2010).
4. J. Lavenus *et al.*, *Trends Plant Sci.* **18**, 450 (2013).
5. Y. Uga *et al.*, *Nat. Genet.* **45**, 1097 (2013).
6. R. Rellán-Álvarez *et al.*, *eLife* **4**, e07597 (2015).
7. N. Takahashi *et al.*, *Planta* **216**, 203 (2002).
8. D. Dietrich *et al.*, *Nat. Plants* **3**, 17057 (2017).
9. Y. Okushima *et al.*, *Plant Cell* **19**, 118 (2007).
10. L. Conti *et al.*, *Plant Cell* **20**, 2894 (2008).
11. S. B. Tiwari *et al.*, *Plant Cell* **16**, 533 (2004).
12. H. Fukaku *et al.*, *Plant J.* **44**, 382 (2005).
13. K. Swarup *et al.*, *Nat. Cell Biol.* **10**, 946 (2008).
14. N. E. Robins II, J. R. Dinneny, *Proc. Natl. Acad. Sci. U.S.A.* **115**, E822 (2018).
15. D. K. Ray *et al.*, *Nat. Commun.* 6, 5989 (2015).

10.1126/science.aav9375

CARDIOLOGY

Unusual transcription factor protects against heart failure

Cleaved fragment of a cardiomyocyte structural protein moonlights as a transcription factor

By **Arun Padmanabhan**[1,2] *and* **Saptarsi M. Haldar**[1,2,3]

The heart pumps blood to the rest of the body in a coordinated and steadfast manner. This pumping function is achieved through synchronous contraction of billions of cardiomyocytes (heart muscle cells), which is governed by phasic increases in intracellular calcium. As such, cardiomyocytes have evolved intricate cellular structures that tightly couple external electrical impulses to the triggering of calcium ion release from intracellular stores and subsequent activation of force-producing proteins, a process termed excitation-contraction (E-C) coupling. A key component of this molecular ultrastructure is the cardiac dyad, a microdomain that juxtaposes the plasma membrane L-type calcium channel with the calcium-sensitive ryanodine receptor (RyR) channel complex, the molecular gatekeeper for the release of calcium ions from sarcoplasmic reticulum stores in cardiomyocytes. The cardiac dyad is physically stabilized by a membrane-associated scaffold protein called junctophilin-2 (JP2), which facilitates physiologic calcium release during E-C coupling. Excessive stress or injury to cardiomyocytes results in defective E-C coupling, reduced pumping capacity, and the clinical syndrome of heart failure, a leading cause of death worldwide. On page 1375 of this issue, Guo *et al.* (*1*) report the surprising discovery that during cardiac stress, a proteolytically cleaved fragment of JP2 can translocate to the cardiomyocyte nucleus and function as a transcription factor that can protect against heart failure pathogenesis. Thus, in addition to its "day job" as a structural protein, this suggest that JP2 can "moonlight" in the nucleus as part of a homeostatic feedback response to cardiac stress.

Heart failure, a syndrome in which pumping function cannot meet demand, is the final common clinical manifestation that results from diverse forms of cardiac injury, such as excessive mechanical stress, myocardial infarction, or exposure to toxins. This condition is typified by progressive structural remodeling of the geometry of the heart, activation of inflammatory and profibrotic pathways, cardiomyocyte hypertrophy, and abnormalities in cellular calcium homeostasis, E-C coupling, metabolism, and gene expression. During heart failure pathogenesis, JP2 is proteolytically cleaved by a family of intracellular calcium-dependent proteases called calpains, an event that compromises JP2 function and impairs E-C coupling (*2*, *3*). Mapping the precise cleavage site within JP2 revealed that this proteolytic event generated a novel N-terminal fragment, which the authors named JP2NT. It was initially thought that JP2NT was an inert by-product of the cleavage event and had no specific cellular function. However, Guo *et al.* found that JP2NT contains a functional nuclear localization sequence and a putative helix-turn-helix motif that confers DNA binding activity. These features suggested that JP2NT could function as a transcription factor that directly regulates cardiomyocyte gene expression.

Analyses of JP2NT-overexpressing cardiomyocytes revealed that JP2NT predominantly functions as a transcriptional repressor. JP2NT-repressed genes were enriched for those known to be activated in heart failure, including those that regulate cardiac hypertrophy, fibrosis, and inflammation. These unbiased analyses also revealed that JP2NT genomic binding sites strongly colocalized with binding sites for the MEF2 (myocyte enhancer factor 2) family of transcription factors, which are known drivers of heart failure pathogenesis (*4*, *5*). The study of Guo *et al.* supports a model in which JP2NT inhibits transcriptional function of MEF2, possibly via competitive binding for MEF2 DNA response elements.

The ability of JP2NT to transcriptionally repress MEF2 activity and inhibit heart failure–associated gene programs suggests that JP2NT might play a protective role in heart failure pathogenesis. Indeed, mice overexpressing JP2NT that were subjected to a widely used model of cardiac pressure overload (*6*) had improved cardiac function and reduced indices of heart failure, whereas

[1]*Gladstone Institutes, San Francisco, CA, USA.* [2]*Division of Cardiology, Department of Medicine, University of California San Francisco School of Medicine, San Francisco, CA, USA.* [3]*Cardiometabolic Disorders, Amgen, South San Francisco, CA, USA. Email: saptarsi.haldar@gladstone.ucsf.edu*

JP2NT functions as a cardiac transcription factor

Full-length JP2 is a scaffolding protein in cardiomyocytes that is essential for calcium homeostasis and E-C coupling. During cardiac stress, JP2 is proteolytically cleaved by calpain to release an N-terminal fragment (JP2NT), which translocates to the nucleus and functions as a transcription factor that represses MEF2 activity and protects against heart failure pathogenesis.

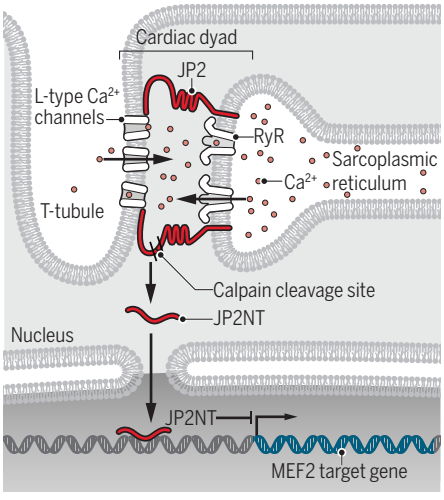

mice in which the JP2NT nuclear localization signal is ablated developed more severe heart failure. Together, these data support the idea that during cardiac stress, proteolytic release of JP2NT from the cardiac dyad in cardiomyocytes plays a protective role in heart failure pathogenesis, possibly by repressing MEF2 transcriptional activity (see the figure).

The paradigm that membrane-tethered precursor proteins can be proteolytically cleaved to unleash transcription factors is not new. Therefore, this newly discovered role for JP2NT must be considered alongside known cellular pathways that use this mechanism—for example, Notch signaling, the SREBP (sterol regulatory element–binding protein) pathway, and the ATF6 arm of the unfolded protein response. These examples share three notable features: a proximal physiological cue that triggers proteolysis, release of a cleaved fragment from its membrane-tethered parent protein, and a downstream transcriptional effector function that is homeostatically responsive to the proximal physiological cue. In canonical Notch signaling, plasma membrane Notch receptors are activated by cell-cell contact, prompting Notch receptor proteolysis and release of the Notch intracellular domain (NICD), which translocates into the nucleus and regulates expression of developmental gene programs that are appropriate for the type of cell contact (*7*, *8*). In the SREBP pathway, the upstream cue is cholesterol deprivation, which is sensed by the SREBP cleavage-activating protein complex in the endoplasmic reticulum, ultimately resulting in proteolytic release of SREBP transcription factors, which translocate to the nucleus to regulate gene programs that adapt to the low-cholesterol state (*9*, *10*). In the third example, unfolded proteins in the endoplasmic reticulum lead to transport of ATF6 to the Golgi membrane, where it is cleaved by Golgi-associated proteases, releasing a transcription factor that regulates gene programs involved in alleviating the stress caused by unfolded proteins (*11*).

In these three examples, the proteolytic cleavage of the parent protein reflects the primary cellular function of the pathway. By contrast, full-length JP2 is a professional scaffolding protein for the cardiac dyad that moonlights as a transcription factor during cardiac stress. In that case, what is the true physiological role of the JP2 cleavage pathway? Because full-length JP2 is in the cardiac dyad, we postulate that its cleavage might be a physiological transducer of local calcium excess, mechanical stretch, or oxidative stress. Although the characterization of JP2NT-overexpressing mice by Guo *et al.* is an important first step, more detailed phenotyping of their mice harboring an ablated JP2 nuclear localization signal will be required to better understand the physiological function of JP2NT. Similarly, the generation of cells or mice in which the endogenous JP2 cleavage site or DNA binding domain is inactivated will be informative. A more precise understanding of how calpain family members, or other endogenous proteases, are activated and targeted to the dyad will also provide essential clues to the homeostatic role of this cleavage event. Additionally, it will be critical to delineate the full spectrum of endogenous JP2NT transcriptional targets and interaction partners, as JP2NT is likely to have effects beyond regulating MEF2 function. It will also be important to solve the structure of JP2NT to elucidate the biophysical basis for DNA binding. Following up on these exciting findings by Guo *et al.* is certain to uncover new mechanisms of cardiac homeostasis; such knowledge may be harnessed to create much-needed therapies for heart failure. ■

REFERENCES

1. A. Guo *et al.*, *Science* **362**, 1375 (2018).
2. A. Guo *et al.*, *J. Biol. Chem.* **290**, 17946 (2015).
3. C. Y. Wu *et al.*, *J. Am. Heart Assoc.* **3**, e000527 (2014).
4. J. Xu *et al.*, *J. Biol. Chem.* **281**, 9152 (2006).
5. C. L. Zhang *et al.*, *Cell* **110**, 479 (2002).
6. H. A. Rockman *et al.*, *Proc. Natl. Acad. Sci. U.S.A.* **88**, 8277 (1991).
7. S. J. Bray, *Nat. Rev. Mol. Cell Biol.* **17**, 722 (2016).
8. R. Kopan, M. X. Ilagan, *Cell* **137**, 216 (2009).
9. M. S. Brown, J. L. Goldstein, *Cell* **89**, 331 (1997).
10. J. D. Horton *et al.*, *J. Clin. Invest.* **109**, 1125 (2002).
11. P. Walter, D. Ron, *Science* **334**, 1081 (2011).

10.1126/science.aav8956

ASTRONOMY

Escaping atmospheres of extrasolar planets

The study of helium absorption opens a new window on escaping exo-atmospheres

By **Matteo Brogi**

The atmospheres of planets orbiting other stars (exoplanets) are windows into their chemical composition and physical properties. For a planet that orbits closely to its star, the intense stellar irradiation can induce substantial atmospheric loss, a phenomenon that can be detected if the planet is transiting through an excess absorption of starlight by gas that is escaping the planet's atmosphere. On pages 1384 and 1388 of this issue, Allart *et al.* (*1*) and Nortmann *et al.* (*2*), respectively, report two independent measurements of planetary helium with remote, ground-based spectroscopy in the near-infrared. Their findings mark the first time that helium is detected from the ground and is unambiguously associated with the planet's orbital motion. The high spectral resolution of the observations allows direct tracking of helium's velocity and verifies that it trails the planet along its orbit.

The atmosphere of a close-in exoplanet can escape under the strong irradiation from the parent star (*3*, *4*). For a giant planet, the total mass loss over the lifetime of the system is negligible. However, for a small exoplanet, the entire atmospheric envelope can be stripped off, and this phenomenon may produce a gap in the occurrence of the exoplanet as a function of its distance from the parent star (or radius of its orbit) (*5*, *6*).

Most previous studies have focused on the detection of hydrogen escaping from exoplanets (*7*). Hydrogen is the most abundant chemical element in the Universe and it dominates the composition of giant

Department of Physics, University of Warwick, Coventry CV4 7AL, UK. Email: M.Brogi@warwick.ac.uk

GRAPHIC: VERONICA FALCONIERI/*SCIENCE*

exoplanets. As the lightest element, it can be stripped off very effectively, forming an extended cloud of gas around the planet, possibly with an elongated shape similar to cometary tails. If the planet transits its parent star as seen from Earth, this escaping gas can absorb substantially more starlight than the planet itself, revealing its presence during transit observations. This method has allowed scientists to detect massive "tails" of hydrogen around several exoplanets; the most dramatic example is the Neptune-size exoplanet GJ 436 b (*8*).

As neutral hydrogen absorbs at ultraviolet (UV) wavelengths, it is only possible to observe it from space, where UV light is not shielded by ozone in Earth's atmosphere. However, even at the altitude of the Hubble Space Telescope (about 568 km), hydrogen in Earth's exosphere (outermost region of the atmosphere) produces a contaminating signal (the so-called geo-coronal emission). Moreover, hydrogen gas permeates interstellar space, making it difficult to distinguish whether the absorption occurs around the planet or anywhere else along our line of sight. In addition, stellar activity alters the strength of hydrogen spectral lines, complicating the interpretation of variable absorption (*9*). As a result, only the "wings" of hydrogen spectral lines can be reliably associated with exoplanet mass loss. This corresponds to gas moving at tens to hundreds of kilometers per second, already quite far from the planet.

Helium is the second most abundant element in the atmospheres of giant planets, and it is still light enough to be easily stripped off. In the near infrared, around a wavelength of 10,830 Å, there is a particular helium spectral line that can form by absorbing radiation from a metastable state (a state where electrons decay but with very long time scales—hours in this case). Whereas this line can form at the temperatures and densities of planetary exospheres, interstellar helium absorption is 1000 times less likely than for hydrogen. This means that excess absorption due to a transiting planetary atmosphere can be sought even in the very core of the helium line, allowing small velocities to be probed. These give us direct access to the region where atmospheric escape originates.

Helium absorption was predicted at the dawn of exoplanet science (*10*). Absorptions up to a few percent in the core of the helium line—more than 10 times as strong as typical features in exoplanet spectra—were estimated for two well-known transiting exoplanets, the hot giant HD 209458 b and the hot Neptune-size GJ 436 b (*11*). Observations with the WFC3 instrument onboard the Hubble Space Telescope (*12*) detected helium in the transmission spectrum of the exoplanet WASP-107 b. However, owing to the low spectral resolution, this excess absorption could only be seen in one of the spectral channels, preventing the unambiguous identification of the planetary origin of the signal.

Fortunately, infrared radiation around 11,000 Å penetrates Earth's atmosphere and therefore helium measurements can be attempted with ground-based telescopes, leveraging larger mirrors and higher spectral resolution. Allart *et al.* and Nortmann *et al.* resolved the detailed shape of the helium spectral line and detected its changing velocity due to the radial component of the planet's orbital motion. This "Doppler" effect causes a shift in the characteristic absorption frequency of a spectral line for nonzero velocity.

Allart *et al.* used the line shape information to model the physical environment around the warm Neptune-size planet HAT-P-11 b. They derived a spherical shape for the cloud of helium around the planet, but no sizeable tail trailing the orbit. This is in stark contrast to the extended hydrogen comas such as the one detected around GJ 436 b, but in line with expectations from interactions with the stellar radiation field and winds. Nortmann *et al.* report a strong helium absorption surrounding the Saturn-size exoplanet WASP-69 b. By comparing their detection with a small sample of exoplanets, they propose that the presence of escaping helium depends on the intensity of x-rays and extreme-UV radiation from the parent star, which in turn regulates the population of the metastable state of helium responsible for the 10,830 Å line. Thus, only planets hosted by moderately active stars should show helium absorption, in line with observations to date.

The findings of Allart *et al.* and Nortmann *et al.* reinforce the importance of stellar environments in shaping the atmospheric evolution of exoplanets. Attention of the scientific community is turning toward potentially habitable planets around M-dwarf stars, which are particularly active. Studying atmospheric escape across a wide class of planetary systems will be crucial for assessing how habitability is influenced by energetic stellar radiation (*13*). The measurements presented by Allart *et al.* and Nortmann *et al.* were obtained with a new spectrograph called CARMENES (Calar Alto high-resolution search for M dwarfs with exoEarths with near-infrared and optical echelle spectrographs) originally designed to look at minute radial velocity variations of stars due to the gravitational influence of orbiting exoplanets, but also excelling in frontier atmospheric characterization. As more spectrographs like CARMENES will soon become available, it is expected that the synergy between space and ground-based observatories will intensify, with the ultimate aim of unveiling the atmospheres of temperate exoplanets in the not-too-distant future. ■

Escaping gases

Atmospheric hydrogen and helium gases of an exoplanet that orbits closely to its parent star can escape under strong irradiation. The escaping gas can absorb more starlight than the exoplanet and can be detected by remote, ground-based spectroscopy.

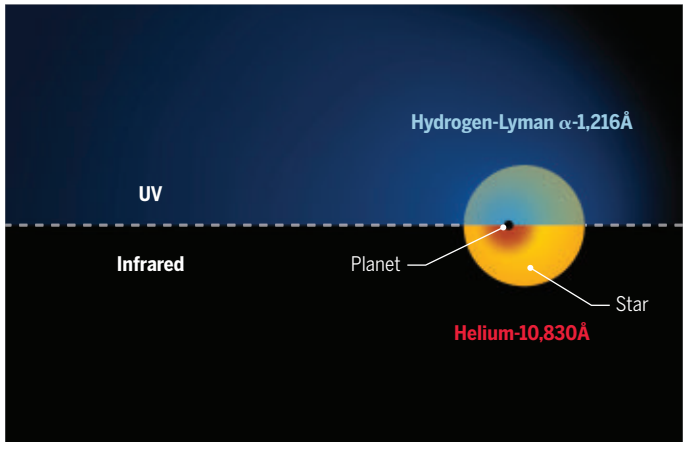

GRAPHIC: M. BROGI

REFERENCES

1. R. Allart *et al.*, *Science* **362**, 1384 (2018).
2. L. Nortmann *et al.*, *Science* **362**, 1388 (2018).
3. H. Lammer *et al.*, *Astrophys. J.* **598**, 121 (2003).
4. R. A. Murray-Clay, E. I. Chiang, N. Murray, *Astrophys. J.* **693**, 23 (2009).
5. B. J. Fulton *et al.*, *Astron. J.* **154**, 109 (2017).
6. J. E. Owen, Y. Wu, *Astrophys. J.* **847**, 29 (2017).
7. A. Vidal-Madjar *et al.*, *Nature* **422**, 143 (2003).
8. D. Ehrenreich *et al.*, *Nature* **522**, 459 (2015).
9. P. W. Cauley, S. Redfield, A. G. Jensen, *Astron. J.* **153**, 185 (2017).
10. S. Seager, D. D. Sasselov, *Astrophys. J.* **537**, 916 (2000).
11. A. Oklopčić, C. M. Hirata, *Astrophys. J.* **855**, L1 (2018).
12. J. J. Spake *et al.*, *Nature* **557**, 68 (2018).
13. S. Rugheimer, L. Kaltenegger, A. Segura, J. Linsky, S. Mohanty, *Astrophys. J.* **809**, 57 (2015).

10.1126/science.aav7010

POLICY FORUM

INTERNATIONAL SECURITY

Next-generation wargames

Technology enables new research designs, and more data

By **Andrew W. Reddie[1,2], Bethany L. Goldblum[3], Kiran Lakkaraju[4], Jason Reinhardt[4], Michael Nacht[5], Laura Epifanovskaya[4]**

Over the past century, and particularly since the outset of the Cold War, wargames (interactive simulations used to evaluate aspects of tactics, operations, and strategy) have become an integral means for militaries and policy-makers to evaluate how strategic decisions are made related to nuclear weapons strategy and international security (*1*). These methods have also been applied beyond the military realm, to examine phenomena as varied as elections, government policy, international trade, and supply-chain mechanics. Today, a renewed focus on wargaming combined with access to sophisticated and inexpensive drag-and-drop digital game development frameworks and new cloud computing architectures have democratized the ability to enable massive multiplayer gaming experiences. With the integration of simulation tools and experimental methods from a variety of social science disciplines, a science-based experimental gaming approach has the potential to transform the insights generated from gaming by creating human-derived, large-*n* datasets for replicable, quantitative analysis. In the following, we outline challenges associated with contemporary simulation and wargaming tools, investigate where scholars have searched for game data, and explore the utility of new experimental gaming and data analysis methods in both policy-making and academic settings.

THEORY RICH, DATA POOR

Increasingly, simulations have relied upon mathematical computer-based models to make inferences about real-world behavior regarding conflict and cooperation. However, in certain situations, observational data are limited or there are practical or ethical quandaries associated with producing them. This lack of data is a particularly salient problem for nuclear deterrence models, given the fortunate lack of observational data regarding nuclear weapon use. In such situations, these simplified, "toy" models used to explain phenomena as complicated as international cooperation or nuclear escalation patterns can fail to take into account the human factors that drive policy-making decisions. For example, model assumptions such as player rationality may not hold in conditions of crisis or when players have little time to make decisions.

To introduce human factors into simulations, policy-makers, economists, and social scientists have relied on exploratory simulation games, structured play environments that can be used to devise representations of real-world decision-making (*2*). Focus has traditionally been on analog games involving a limited player set and a single scenario. The constraints of the predigital environment restricted the complexity of the gameplay and largely prohibited the collection of sufficient data for generalizable inquiry, leading to wargaming being described as an "art rather than a science" (*3*). For example, the Sigma II-64 wargame created to strategize U.S. policy in Vietnam required more than 40 analysts and months of planning at the RAND Corporation to develop scenarios that involved upward of 35 players.

Among existing simulation game approaches, there are few experimental studies. Instead, both policy-makers and scholars have tended to focus upon process-oriented investigations of behavior inside of the game environment (for example, analyzing the dialogue between players to achieve exploratory insights) rather than utilizing each game as a unit of analysis for causal inference. These exploratory games may take a variety of forms—whether assessing what questions business executives might ask following a substantial drop in oil prices or examining military planners' decision-making processes related to the use of cyber weapons (*4*, *5*). These discussions can be particularly valuable when high-level policy-makers involved in real-world decision-making are engaged and provide their expertise and insights. The U.S. Naval War College and U.S. Strategic Command, for example, conduct the Deterrence and Escalation Game and Review series, a two-sided game to explore escalation dynamics during crises. These types of games also offer an opportunity to explore counterfactuals while allowing game designers to track the discussions.

Alternatively, structured exercises akin to board games offer designers increased control over game dynamics and the potential to increase the number of play-throughs for postexperiment analysis. For example, Karl Mueller at RAND has led an effort to create a tabletop exercise to explicitly address the challenge posed by a resurgent Russia in the Baltic region following the former's invasion of Ukraine in 2014 (*6*). The goal of this game, carried out with players from the U.S. Air Force and U.S. Army, is to inform the appropriate force composition necessary to defend North Atlantic Treaty Organization (NATO) members and deter adversaries in the region, given adversary capabilities. These insights into strategic decision-making have subsequently driven debate concerning the appropriate qualitative and quantitative force postures in the region.

Even with this type of game using stylized rules, players are subject to laboratory effects. For example, players sitting across from one another may hold back from aggressive maneuvers given the reputational costs associated with taking such an action amid their peers. Inferences related to structured exercises have also been called into question given the small number of players involved and the limited number of turns that may fail to capture real-world dynamics.

[1]*Department of Political Science, University of California, Berkeley, Berkeley, CA, USA.* [2]*Center for Global Security Research, Lawrence Livermore National Laboratory, Livermore, CA, USA.* [3]*Department of Nuclear Engineering, University of California, Berkeley, Berkeley, CA, USA.* [4]*Sandia National Laboratories, Albuquerque, NM, USA.* [5]*Goldman School of Public Policy, University of California, Berkeley, Berkeley, CA, USA. Email: areddie@berkely.edu*

PHOTO: CIRCUIT MEDIA, LLC

Scholars at play study the impact of weapons capabilities on conflict escalation using the Project on Nuclear Gaming's board game platform, SIGNAL.

The external validity of postgame analysis is also made difficult by the limited number of play-throughs of each game and the challenges associated with collecting data in a manner that allows for replication of the experiment. These difficulties combine to reduce the likelihood of statistical analysis and limit the production of generalizable insights. As a result, board wargame outcomes, like exploratory games, tend to be characterized by insights derived from game play rather than generalizable conclusions based on objective postgame analyses.

These exploratory approaches have also led to a focus on simulated games for training or educational purposes rather than experimentation. For example, the Apex Gold scenario-based discussion program designed by the National Nuclear Security Administration for senior-level policymakers tests how players work together and respond to a hypothetical nuclear terrorism threat. A series of questions and polls also drive the discussion between participants to emphasize the challenges associated with addressing nuclear security.

In sum, computer-based simulations, exploratory games, and structured exercises have led to a theory-rich, but data-poor, environment for scholarly inquiry.

THE SEARCH FOR EXISTING GAME DATA

There are a variety of ways to address this paucity of data by using experimental methods. A number of scholars are attempting to use archival material to reexamine past games for generalizable insights. For example, Reid Pauly uses material from the Massachusetts Institute of Technology (MIT) and the U.S. Department of Defense to collect notes and game outcomes from wargames designed by Lincoln Bloomfield and Thomas Schelling in the 1960s (*7*). Observing similar behavior across the collection of games, Pauly suggests that policymakers exhibit a generalizable pattern of behavior resulting in nuclear restraint during crises and in spite of provocation. Jacquelyn Schneider's recent project similarly examines longitudinal data created over 7 years of Naval War College wargames involving cyber weapons and finds that, contrary to statements from policy-makers, cyber capabilities do not appear to contribute to crisis instability (*8*).

Both projects mine collections of outcomes obtained from traditional wargaming approaches to provide quantitative insights not inferable from a single play-through. These approaches, however, present research design challenges, including being time intensive and having no potential for automation in terms of data collection or for adaptation to address alternative research questions that go beyond the original scenario for which the games were designed. There are also concerns about comparing apples to oranges as scenarios shift in terms of their framing, the identity and institutional affiliation of the players, and changes to the geopolitical context.

As well as using archival material from traditional wargames, scholars have looked to commercial games to provide natural experiments during the course of gameplay that are analogous to real-world settings—in spite of not explicitly being designed for research purposes (*9*). A famous example of commercial data providing a simulation of reality for scholars comes from the World of Warcraft, in which the first gamewide epidemic in a massive, multiplayer, online role-playing game led to 4 million player characters being affected by something not unlike a virus. Epidemiologists subsequently used the virus that spread from player to player throughout the game's "world" to model transmission rates and the chain of infection and compared these findings to real-world pandemics (*10*).

Over the past decade, numerous scientific disciplines have started to explore the use of commercial games for experimental inquiry. For example, virtual worlds have become a laboratory for ethnographic research concerning social behavior on platforms such as Second Life, where players have the potential to create entirely new identities and social relationships. Economists have been examining virtual currencies and financial systems in online games and their implications related to cryptocurrencies, decentralized finance, and blockchain banking. For war planners, battles such as the "Bloodbath of B-R5RB" on the Eve Online platform involving about 7500 human players, 20 million virtual soldiers, and 600 warships provide a virtual example to study the origins, conduct, and outcome of large-scale warfare in the absence of real-world corollaries (*11*).

However, these gaming environments are largely outside of researchers' control, which may limit the theories that can be tested. In an attempt to control an experimental environment using commercial software, social scientists have also created stand-alone "mods"—user-generated environments—in games such as World of Warcraft, Star Wars Galaxies, and Starcraft 2 to consider theories of human behavior, cooperation, and conflict from political science, economics, and sociology (*12*). One of the first of these efforts, NetLab, led to the creation of a variety of "collaboratories" in the early 2000s that sought to use the internet to field social and behavioral experiments (*13*). "Tribes," for example, modeled on intertribal rivalry in real-world Sudan measures the (artificially created) inter- and intragroup dynamics. Although these mods provide researchers with increased control over the structured play environment, they remain subject to the virtual world, characters, and player pools associated with the original game publisher.

BUILDING EXPERIMENTAL CONDITIONS

Now, scholars are increasingly able to build experimental settings from scratch with the goal of conducting replicable, quantitative analyses that focus on a particular real-

world policy decision. Building games from the ground up addresses the problem that researchers do not have control of the game setting and, subsequently, the treatments provided to game participants. Although this option was, until recently, prohibitively expensive, the production of online experiment-based games tailored to address particular questions of interest is becoming progressively accessible to researchers as low-cost gaming architectures and visual scripting systems proliferate.

With that said, game design and development presents its own challenges. At the outset, researchers need to decide what type of game to build—they range from simple to complex, turn-based to simultaneous, and vary in terms of the number of players, treatment variables, aesthetics, mechanics, and the interface that players interact with. Each of these features can affect the parsimony, internal validity, and external validity associated with the game. For example, maps in real-time strategy games can be designed to provide perfect information to all players or, alternatively, the moves of adversaries can be hidden under a "fog of war." The latter is more realistic but also more complicated to design and build into a gaming framework.

Although more research is needed to understand the optimal design and limitations of online experimental games, they do allow for replicable, structured rulesets, iterative turn-based play, and an increased number of play-throughs that overcome a number of challenges related to traditional wargaming methods. The online environment also provides access to a diverse set of research participants that traditional wargames do not engage with—Steam's gaming platform, for example, regularly hosts more than 10 million unique concurrent online gamers, whereas Amazon's Mechanical Turk provides an alternative source of experimental participants in online settings.

Our Project on Nuclear Gaming (PONG)—a collaboration between the University of California, Berkeley; Lawrence Livermore National Laboratory; and Sandia National Laboratories—and its SIGNAL game serves as a first execution of this large-scale, experimental gaming approach in an examination of nuclear deterrence and conflict escalation dynamics. SIGNAL provides a flexible gaming environment that can be used to explore a variety of research questions and mimic aspects of warfare. The platform also allows for large-*n*, quantitative analysis of game outcomes in a multiplayer context, tracks demographic data, and automatically collects player and game data in real time.

As new experimental gaming tools mature, they are well placed to take advantage of advances in data science and machine learning. For example, game data can be used as an input in machine learning algorithms to expand the amount of data available to create models of optimal behavior given particular experimental conditions (*14*).

These data might be leveraged to create autonomous agents that are representative of various player strategies in the training data as well as serve as venues for human-machine and machine-machine gameplay. Comparative analysis of these player models and their parameters may reveal insights about player "types" that can further augment our understanding of conflict strategies and crisis communications. Alternatively, inverse reinforcement learning methods can be applied to gameplay data to assess player perceptions of rewards, constraints, and optimal implementation strategies within a simulated environment.

METHODOLOGICAL CHALLENGES

Although the ability to build customizable online games that can be tailored to specific research questions offers a promising path toward experimental gaming, there are a number of methodological challenges that scholars must consider. First, game designers must address how the online game setting might lead to its own unique laboratory effects related to player behavior within the game environment. Might it, for example, make players more aggressive than they otherwise might be? Relatedly, the impact of using nonexperts rather than experts in the player pool is in need of further examination. Analyses are needed to compare expert to nonexpert players in the context of decision-making pertaining to national security settings.

Experimental gaming techniques that allow for large-*n* analysis using nonexpert players should also be compared against insights generated from traditional wargames involving experienced decision-makers. Addressing these challenges requires cross-method and cross-subject comparison. And although all gaming frameworks are predominantly focused on internal rather than external validity, more work is needed to further link game findings from online environments to real-world dynamics using observational data, where available.

As experimental gaming methods mature, its toolkit can be tailored to address extant questions being asked by the policy and defense communities—testing conventional wisdom and providing another data source for decision-makers. It may also offer a capability to analyze increasingly complex security dynamics that involve new types of actors and new domains of warfare, including space, cyber, and gray-zone operations. Already, government agencies, particularly those related to national security, are increasing their use of simulations in policy planning. Efforts are also underway to build data repositories such as the nascent Wargaming Repository created by the U.S. Office of the Secretary of Defense to pool insights, generate conclusions that might otherwise be hidden, and further refine existing wargaming methods—whether analog or digital.

Although an ability to reliably predict the actions of adversaries and the outcomes of conflict remains unlikely, new types of experimental tools have the potential to shed light on dynamics that have thus far existed only in theory. ■

REFERENCES AND NOTES

1. R. Work, "Wargaming and Innovation," Memorandum, Deputy Secretary of Defense (9 February 2015).
2. P. Sabin, *Simulating War: Studying Conflict Through Simulation Games* (Bloomsbury Academic, 2014).
3. P. Perla, *The Art of Wargaming: A Guide for Professionals and Hobbyists* (Naval Institute Press, 1990).
4. N. H. Barma, B. Durbin, E. Lorber, R. E. Whitlark, *Int. Stud. Perspect.* **17**, 117 (2015).
5. J. Schneider, "Cyber and crisis escalation: Insights from wargaming" (U.S. Naval War College, 2017); https://pacs.einaudi.cornell.edu/sites/pacs/files/Schneider.Cyber%20and%20Crisis%20Escalation%20Insights%20from%20Wargaming%20Schneider%20for%20Cornell.10-12-17.pdf.
6. K. Mueller, "Paper wargames and policy making: Filling the Baltic gap," *Battles Magazine*, No. 11 (May 2016); https://www.rand.org/content/dam/rand/pubs/external_publications/EP60000/EP66660/RAND_EP66660.pdf.
7. R. B. C. Pauly, *Int. Secur.* **43**, 151 (2018).
8. J. Schneider, "The information revolution and international stability: A multi-article exploration of computing, cyber, and incentives for conflict," thesis, The George Washington University, 2017.
9. W. S. Bainbridge, *The Warcraft Civilization: Social Science in a Virtual World* (MIT Press, 2012).
10. E. T. Lofgren, N. H. Fefferman, *Lancet Infect. Dis.* **7**, 625 (2007).
11. D. Fandino, in *Virtual Dark Tourism*, K. McDaniel, Ed. (Palgrave Macmillan, 2018).
12. A. M. Kaplan, M. Haenlein, *Bus. Horiz.* **52**, 563 (2009).
13. S. Teasley, S. Wolinsky, *Science* **292**, 2254 (2001).
14. G. N. Yannakakis, J. Togelius, *Artificial Intelligence and Games* (Springer, 2018).

ACKNOWLEDGMENTS

This work was supported by a grant from the Carnegie Corporation of New York through their International Peace and Security Program. The authors recognize support from the Nuclear Science and Security Consortium at the University of California, Berkeley, under contract DE-NA0003180; the Center for Global Security Research at Lawrence Livermore National Laboratory under contract DE-AC52-07NA27344; and Sandia National Laboratories, a multimission laboratory managed and operated by National Technology and Engineering Solutions of Sandia, LLC, a wholly owned subsidiary of Honeywell International Inc., for the U.S. Department of Energy's National Nuclear Security Administration under contract DE-NA0003525. The views and opinions of the authors expressed herein do not necessarily state or reflect those of the United States government; Lawrence Livermore National Security, LLC; or Sandia National Laboratories. The authors would also like to acknowledge members of the Project on Nuclear Gaming past and present and thank two anonymous reviewers for their helpful comments.

10.1126/science.aav2135

BOOKS *et al.*

An engineer makes an adjustment to a humanoid robot at a factory in Dalian, China.

PHOTO: FRED DUFOUR/CONTRIBUTOR/GETTY IMAGES

COMPUTER SCIENCE

The sex robots are here

Advances in robotics and AI bring new concerns to age-old questions about human intimacy

By **Lily Frank**

Sex robots are so hot right now. Robot brothels are popping up around the world, and the sex robot "Harmony" even has her own Tinder profile. (She reportedly matched with dozens of men within hours.) In *Turned On*, computer scientist Kate Devlin tackles the transition of sex-tech from novelty to just another feature of our technologically enabled environment.

The book is a highly readable romp through the history of computers, robots, and sex toys. In a journalistic and often humorous style, Devlin introduces the technical, social, historical, philosophical, and ethical issues surrounding humanoid sex robots, peppering these discussions with literary, historical, and pop culture references and personal anecdotes.

Turned On focuses on technologies that are currently available or in development. But sex robots are nothing new. They are part of a long history, as revealed in ancient myths, early literature, and archaeological and historical records. Here, Devlin introduces a central theme: the idea that humans have long been fascinated with amorous relations with inanimate objects.

Turned On
Science, Sex and Robots
Kate Devlin
Bloomsbury, 2018.
288 pp.

In chapter three, Devlin delves into the origins of the computer, interrogating some classic philosophical arguments about the nature of consciousness; the problem of other minds; and whether or not it might be possible for a machine to feel, think, or be conscious. She is, admittedly, not a philosopher and does not aim to offer more than a cursory discussion of these issues. But I found this somewhat unsatisfying because philosophical assumptions about mentality often inform nonphilosophers' speculation about artificial intelligence (AI) and robotics.

The book is at its best when explaining difficult technical concepts such as machine learning, artificial neural networks, and natural language processing. It also presents memorable examples of how biases are introduced into programmed systems.

After discussing the Turing test, "ELIZA" (the first conversational natural language processing program), and the Loebner Prize (an award given for programs that can fool humans into thinking they are interacting with another human), Devlin comes to a second major theme: that "[a] semblance of human-like behaviour can be enough for us to assume a degree of sentience."

Here, she launches into a discussion of love, sex, and attachment from psychological, physiological, anthropological, and neuroscientific perspectives. Canvassing vast swaths of history and anthropology, Devlin includes intriguing tidbits on sexual diversity and the taboos and mores of the past. (In case you ever wondered how many years of penance were required by the Bishop of Worms for the use of a dildo in 1008 AD, for example, the answer is three.) Humans, it seems, can become emotionally attached to all sorts of things—from fish to laptops—and we have no trouble anthropomorphizing and even empathizing with simple animated shapes.

In chapter five, Devlin takes the reader on a behind-the-scenes tour of the sex doll and robot industries, introducing us to designers, entrepreneurs, and avid users (lovers?). She meticulously describes various aspects of sex robot design, ranging from lifelike works of artistry to the mechanical, crude, and tinvoiced. From industry-compiled customer reports, she discovers that users are predominantly male and that they turn to these technologies for a variety of reasons, from sexual experimentation to coping with loneliness.

Next, Devlin engages with some scholarly philosophical works, including David Levy's 2007 book *Love and Sex with Robots*. What is love? What defines sex? Could human beings fall in love with machines? Should they?

There are also a range of normative issues surrounding sex robots, including what some perceive as their implicit sexism, concerns about how they might normalize violence against women and children, and questions about how they relate to prostitution and pornography. Here, Devlin raises a host of legal and ethical questions. Should sex robots be used to rehabilitate sex offenders? Should it be illegal to produce childlike sex robots? Do sex robots reinforce harmful stereotypes about women's bodies or their roles, or the importance of sexual consent? The book offers more questions than answers, leaving me somewhat dissatisfied, once again.

Devlin urges readers to "think outside the bot" in chapter 10, looking to the next generation of engineering and design of sex-tech more broadly. Here, she imagines a future in which a sex robot might have tentacles instead of arms or be molded from sensuous fabrics, rather than from silicone.

"The future of intimacy is not a bleak and isolated vision but a network of connected people who want, as humans have always wanted, to be together," Devlin writes. Regardless of how one feels about this optimistic attitude (I remain skeptical), *Turned On* provides the reader with an invitation to explore these topics further and a fascinating introduction to the state of sex-tech. ■

The reviewer is at the Department of Industrial Engineering and Innovation Sciences, Technical University of Eindhoven, 5612 AZ Eindhoven, Netherlands. Email: l.e.frank@tue.nl

10.1126/science.aav6001

SOCIOLOGY

Beyond blood

Strangers conceived via the same sperm donor reveal the role of choice in how we think about kin

Random Families
Genetic Strangers, Sperm Donor Siblings, and the Creation of New Kin
Rosanna Hertz and Margaret K. Nelson
Oxford University Press, 2018. 312 pp.

By **Sophie Zadeh**

In an age of direct-to-consumer DNA tests, conception from donated gametes that have crossed national borders, and connection websites for "genetic strangers," old questions seek new answers. What is family? What makes kin? And how far can genes alone generate relationships?

Random Families, Rosanna Hertz and Margaret Nelson explain, is a book about new forms of voluntary kinship. Unlike its own (academic) ancestors, it examines what people do with genetic connections that fall both within—and outside of—familiar familial repertoires. Concerned with connections that are created through choice but are genetic in origin, *Random Families* presents a timely sociological exploration of relationships between parents who have chosen the same sperm donor, and their children, who therefore share DNA.

Based on a virtual ethnography of existing online same-donor networks, and interviews conducted with 212 parents and 154 children, the book weaves extensive empirical insights together with compelling case studies that bring to life the diverse experiences of those who form, resist, and break apart from networks on the basis of same-donor status. Examining the networks formed across generations and documenting them over time, Hertz and Nelson's approach is a welcome addition to the scholarship on searching for genetic relations among donor-conceived people and their parents (*1*, *2*). For individuals conceived in earlier decades, the authors explain, searching for donors has led some to inadvertently discover "donor siblings." By contrast, the parents of today's donor-conceived infants may purposely seek out genetic connections on behalf of their children.

Hertz and Nelson's analysis brings into focus the combined role of personal preferences and intergroup dynamics in the formation and maintenance of same-donor networks. As the authors themselves admit, their findings will leave much to be desired for the reader looking for a straightforward story of how families connected by gametes relate to one another. Rather, *Random Families* is an intellectually honest account of the complexity, and diversity, of same-donor networks. Throughout the book, the narratives of those who do not ascribe meaning to genetic connections sit beautifully alongside those who emphasize the excitement of meeting individuals conceived using the same donor and of the long-lasting relationships that sometimes result.

Strikingly clear is the fact that these connections remain difficult to define. As the authors acknowledge, there is no rulebook for such relationships and no known nomenclature with which to describe them. Thus, for some participants, there are "families," "brothers," "sisters," or "cousins," whereas for others, there are "sperm siblings," "donor siblings," and "diblings." Within some networks, there are discrepancies in how individuals refer to one another and perceive their connections. Within others, such connections have nothing whatsoever to do with family.

Hertz and Nelson explain that they have used participants' terms to describe these connections where possible. Yet in their writing, they refer to one network as being "more like cousins," and at one point they describe parents who choose to bond with some network members and not others as "upending the hierarchy of nature over artifice." The researchers being no less immune from a traditional lexicon than their respondents, such examples would seem to suggest that same-donor networks pose as much of a conceptual challenge for the sociologist as they do for their members.

In many ways, the title of the book is a misnomer: Although the families described may be "random" at the outset, there is nothing random about the connections they ultimately make. Rather, Hertz and Nelson's study indicates just how deliberate the creation and maintenance of same-donor relationships can be. Ostensibly about new forms of voluntary kinship, then, *Random Families* ends up telling a familiar story about identity, intimacy, and choice in the 21st century.

This is not to say that Hertz and Nelson tell us nothing new. In fact, although many commentators have commended legislative moves across the world to make donors identifiable to offspring at the age of 18, few have considered the implications of this legislation in contemporary contexts. Same-donor networks—made up of children of different ages and of relations that may be close or distant and positive or negative—can circumvent these laws in ways that had not been anticipated and that may not be equitable. What becomes of these possibilities remains to be seen, but for bringing them to light, *Random Families* deserves recognition. ■

The reviewer is at the Centre for Family Research, University of Cambridge, Cambridge CB2 3RQ, UK. Email: sz255@cam.ac.uk

REFERENCES

1. T. Freeman, V. Jadva, W. Kramer, S. Golombok, *Hum. Reprod.* **24**, 505 (2009).
2. V. Jadva, T. Freeman, W. Kramer, S. Golombok, *Reprod. Biomed. Online* **20**, 523 (2010).

10.1126/science.aav6866

PHOTO: AFRICA STUDIO/SHUTTERSTOCK

PODCAST

2018: A Year of Great Books

From optimistic treatises on democracy and laboratory-grown meat to true-crime tales of start-ups behaving badly and natural history heists, we've covered more than a few memorable titles in our pages this year. This week on the *Science* podcast, Jennifer Golbeck and Valerie Thompson chat about their favorite books and interviews from 2018 and recommend some last-minute holiday gifts. sciencemag.org/podcasts

10.1126/science.aaw2584

2018 Swanson Award Winners

The M.J. Murdock Charitable Trust congratulates Dr. Kraig Wheeler, Hugh W. Johnston Professor of Chemistry at Whitworth University, as the 2018 recipient of the Lynwood W. Swanson Scientific Research Award and Dr. Moira Gresham, Associate Professor of Physics at Whitman College, recipient of the Lynwood W. Swanson Promise for Scientific Research Award.

For more information on the Murdock College Science Research Program and the Lynwood W. Swanson Awards, and how we are helping to inspire the next generation of researchers, please visit **murdocktrust.org**.

M.J. Murdock
CHARITABLE TRUST

College Science Research
A MURDOCK TRUST PROGRAM

LETTERS

Rising temperatures in the Himalayas (shown here) and Qinghai-Tibetan Plateau are causing environmental degradation.

Edited by **Jennifer Sills**

Protect Third Pole's fragile ecosystem

The Qinghai-Tibetan Plateau and its surrounding mountains, often termed the Third Pole, contain more ice than anywhere outside the Arctic and Antarctic (*1*). This region is also the source of the nine largest rivers in Asia, providing fresh water, food, and other ecosystem services to more than 1.5 billion people (*2*). Climate and topography vary greatly across the region, promoting rich biodiversity from species to ecosystems. Unfortunately, the Third Pole region is highly vulnerable to environmental changes (*2*).

In recent decades, air temperature at the Third Pole has warmed significantly faster than the global average (*3*). The effects of climate change in the region include increased precipitation (*3*), extensive glacial retreat (*4*), snow cover decline (*5*), shrinkage and expansion of lakes (*6*), permafrost loss (*7*), degradation of rangelands (*8*), and desertification (*9*). Meanwhile, intensive anthropogenic activities, such as overgrazing (*10*), deforestation (*11*), urbanization (*12*), and expansion of infrastructure projects such as construction of roads, dams, and electrical grids, are causing widespread landcover changes within the region (*12*).

Together, these changes are altering the Third Pole's biogeochemical cycles and pushing the fragile ecosystem toward degradation and possible collapse, which would cause irreversible harm on a regional and global scale. To avoid this, all nations must meet the standards laid out in the Paris Agreement. At the regional level, we strongly urge the relevant nations (including Afghanistan, Bhutan, China, India, Kyrgyzstan, Myanmar, Nepal, Pakistan, and Tajikistan) to cooperate in addressing these impending threats through systematic changes to management policies. Rapid and unprecedented coordination will be necessary, including a regional cooperation treaty and formation of a cross-border biodiversity conservation plan for the Third Pole region. Meanwhile, any infrastructure projects undertaken must be environmentally sustainable, and a practicable grazing management policy should be adopted. Finally, these countries should improve national policy coordination and increase efforts to raise environmental protection awareness among local communities, as well as enlist international assistance to effectively implement conservation plans.

Jie Liu[1,2], Richard I. Milne[3], Marc W. Cadotte[4], Zeng-Yuan Wu[2], Jim Provan[5], Guang-Fu Zhu[2], Lian-Ming Gao[1]*, De-Zhu Li[1,2,6]*

[1]CAS Key Laboratory for Plant Diversity and Biogeography of East Asia, Kunming Institute of Botany, Chinese Academy of Sciences, Kunming, Yunnan 650201, China. [2]Germplasm Bank of Wild Species, Kunming Institute of Botany, Chinese Academy of Sciences, Kunming, Yunnan 650201, China. [3]Institute of Molecular Plant Sciences, School of Biological Sciences, University of Edinburgh, Edinburgh EH9 3JH, UK. [4]Department of Biological Sciences, University of Toronto-Scarborough, Toronto, ON M1C 1A4, Canada. [5]Institute of Biological, Environmental and Rural Sciences, Aberystwyth University, Aberystwyth SY23 3DA, UK. [6]Kunming College of Life Sciences, University of Chinese Academy of Sciences, Kunming, Yunnan 650201, China.
*Corresponding authors.
Email: gaolm@mail.kib.ac.cn; dzl@mail.kib.ac.cn

REFERENCES

1. J. Qiu, *Nature* **454**, 393 (2008).
2. T. Yao *et al.*, *Environ. Dev.* **3**, 52 (2012).
3. B. Wang, Q. Bao, B. Hoskins, G. Wu, Y. Liu, *Geophys. Res. Lett.* **35**, L14702 (2008).
4. T. Yao *et al.*, *Nat. Clim. Change* **2**, 663 (2012).
5. W. Xu, L. Ma, M. Ma, H. Zhang, W. Yuan, *J. Clim.* **30**, 1521 (2017).
6. J. Sun *et al.*, *Earth-Sci. Rev.* **185**, 308 (2018).
7. Y. Ran, X. Li, G. Cheng, *Cryosphere* **12**, 595 (2018).
8. X. L. Li *et al.*, *Land Degrad. Dev.* **24**, 72 (2013).
9. M. Yang *et al.*, *Cold Reg. Sci. Technol.* **39**, 47 (2004).
10. X. Lu *et al.*, *Ecosphere* **8**, e01656 (2017).
11. X. Cui, H.-F. Graf, B. Langmann, W. Chen, R. Huang, *Earth Interact.* **11**, 1 (2007).
12. X. Cui, H.-F. Graf, *Clim. Change* **94**, 47 (2009).

10.1126/science.aaw0443

The freshwater biodiversity crisis

The 2018 Living Planet Index (LPI) (*1*) shows that populations of freshwater species have declined by an average of 83% since 1970, a far steeper drop than for terrestrial or marine species. Extinction rates for freshwater species are also exceptionally high (*2*). For example, freshwater fish extinction rates in the United States and Europe have been estimated to be more than 100 times their natural rates (*3*). Meanwhile, wetland loss is three times as high as forest loss (*4*). In 2006, the protection of freshwater biodiversity was noted as "the ultimate conservation challenge," requiring "immediate action" (*5*). The LPI underscores that actions taken since have been grossly inadequate.

Management of freshwater resources often focuses on human water security rather than natural ecosystem integrity (*6*). We urgently need effective policy solutions that can achieve both sets of objectives. Substantial advances have been made in understanding freshwater biodiversity distributions, trends, and patterns (*7*, *8*). Now, scientists must translate this science into recommendations for action for practitioners and policy-makers.

Many of the Convention on Biological Diversity's Aichi targets will not be met by 2020 (*9*, *10*). The post-2020 revision of the Aichi targets should better address freshwater biodiversity. Because freshwater biodiversity conservation must operate in partnership with the needs for socioeconomic development under a changing climate, revised Aichi targets should correspond to the UN Sustainable Development Goals and UN Framework Convention on Climate Change. The conservation community, as well as governments and international organizations that are shaping the broader post-2020 agenda for biodiversity and sustainable development, need to ensure that there is dedicated space in emerging policy frameworks to address the steep decline of freshwater species.

Ian Harrison[1,2]*, Robin Abell[2], William Darwall[1], Michele L. Thieme[3], David Tickner[4], Ingrid Timboe[5]

[1]IUCN, 1196 Gland, Switzerland. [2]Conservation International, Arlington, VA 22202, USA. [3]WWF-US, Washington, DC 20037, USA. [4]WWF-UK, Woking, Surrey GU21 4LL, UK. [5]Alliance for Global Water Adaptation, Salt Lake City, UT 84105, USA.
*Corresponding author.
Email: iharrison@conservation.org

REFERENCES

1. World Wildlife Foundation (WWF), "Living Planet Report—2018: Aiming Higher" (WWF, 2018).
2. A. J. Reid *et al.*, *Biol. Rev.*, 10.1111/brv.12480 (2018).
3. M.S. Dias *et al.*, *Ecol. Indic.* **79**, 37 (2017).
4. Ramsar Convention on Wetlands, "Global wetland outlook: State of the world's wetlands and their services to people" (Ramsar Convention Secretariat, 2018).
5. D. Dudgeon *et al.*, *Biol. Rev. Camb. Philos. Soc.* **81**, 163 (2006).
6. C. J. Vörösmarty *et al.*, *Ecohydrology and Hydrobiology*, 10.1016/j.ecohyd.2018.07.004 (2018).
7. B. Collen *et al.*, *Glob. Ecol. Biogeogr.* **23**, 40 (2014).
8. P. B. McIntyre *et al.*, *Proc. Natl. Acad. Sci. U.S.A.* **113**, 12880 (2016).
9. G. M. Mace *et al.*, *Nat. Sustain.* **1**, 448 (2018).
10. P. W. Leadley *et al.*, "Progress towards the Aichi Biodiversity Targets: An assessment of biodiversity trends, policy scenarios and key actions" (Technical Series 78, Secretariat of the Convention on Biological Diversity, 2014).

10.1126/science.aav9242

China's reopened rhino horn trade

On 29 October, China revoked its 1993 rhino horn trade ban (*1*) and reopened its domestic rhino horn trade under two conditions: Horns must be sourced sustainably, and the use of the horns must be limited to traditional Chinese medicine (TCM), medical research, the preservation of antique cultural artifacts, and educational materials (*2*). This policy reversal could have substantial consequences for rhino conservation. State agencies are working to determine regulatory details such as product certification and enforcement infrastructure. African and Asian rhino range states and conservationists should work with Beijing on the implementation of this directive to minimize risks and maximize conservation gains (*3*).

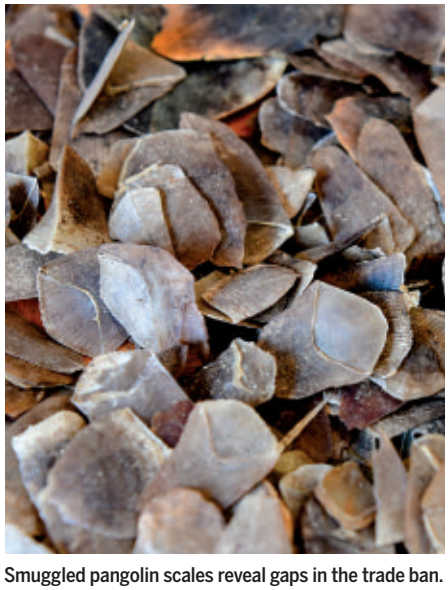

Smuggled pangolin scales reveal gaps in the trade ban. China's new rhino horn policy may have similar flaws.

Regulatory shortcomings in the pangolin scale trade can provide insight for implementing the horn trade. Although the pangolin scale trade has, at least on paper, been strictly controlled through a certification system since 2008, seizures of illegal pangolin products remain frequent nationwide (*4*, *5*). Demand far outweighs supply, and the volume of pangolin scales sold each year through designated, legal outlets exceeds annual quotas (*6*). Understanding consumer preferences (*7*) can help ensure that sustainably sourced rhino horn serves as a substitute for poached supplies (*8*). The pangolin trade's setbacks show that TCM practitioners, industry leaders, law enforcement agencies, and conservation stakeholders should participate in policymaking and that implementation details must be adequately publicized (*6*). Farmed animals should be genetically registered to make legal goods traceable and enable reliable identification of laundering.

Hubert Cheung[1]*, Yifu Wang[2], Duan Biggs[1,3,4]

[1]ARC Centre of Excellence for Environmental Decisions, Centre for Biodiversity & Conservation Science, University of Queensland, Brisbane, QLD 4072, Australia. [2]Department of Geography, University of Cambridge, Cambridge CB2 3EN, UK. [3]Environmental Futures Research Institute, Griffith University, Nathan, QLD 4111, Australia. [4]Department of Conservation Ecology and Entomology, Stellenbosch University, Matieland 7602, South Africa.
*Corresponding author.
Email: h.cheung@uqconnect.edu.au

REFERENCES

1. PRC State Council, State Council of the People's Republic of China, "Circular of the State Council on banning the trade of rhinoceros horns and tiger bones" (1993); www.lawinfochina.com/display.aspx?id=12109&lib=law.
2. PRC State Council, State Council of the People's Republic of China, "Circular of the State Council on strictly regulating the trade and use of rhinoceros horns and tiger bones and their products" (2018); www.gov.cn/zhengce/content/2018-10/29/content_5335423.htm [in Chinese].
3. D. Biggs *et al.*, *Science* **358,** 1378 (2017).
4. L. Xu, J. Guan, W. Lau, Y. Xiao, "An Overview of Pangolin Trade in China," *TRAFFIC Briefing Paper* (TRAFFIC, 2016).
5. W. Cheng, S. Xing, T. C. Bonebrake, *Conserv. Lett.* **10**, 757 (2017).
6. Y. Wang, N. Leader-Williams, S. Turvey, "How can we save pangolins? A case study from a market perspective in China" (European Congress of Conservation Biology, Jyväskylä, Finland, 2018).
7. H. Cheung, L. Mazerolle, H. P. Possingham, D. Biggs, *Trop. Conserv. Sci.* **11**, 1 (2018).
8. J. Phelps, L. R. Carrasco, E. L. Webb, *Conserv. Biol.* **28**, 244 (2014).

10.1126/science.aav9392

ERRATA

Erratum for the Research Article "Recombination initiation maps of individual human genomes" by F. Pratto *et al.*, *Science* **362**, eaav6294 (2018). Published online 19 October 2018; 10.1126/science.aav6294

PHOTO: IMAGINE CHINA/NEWSCOM

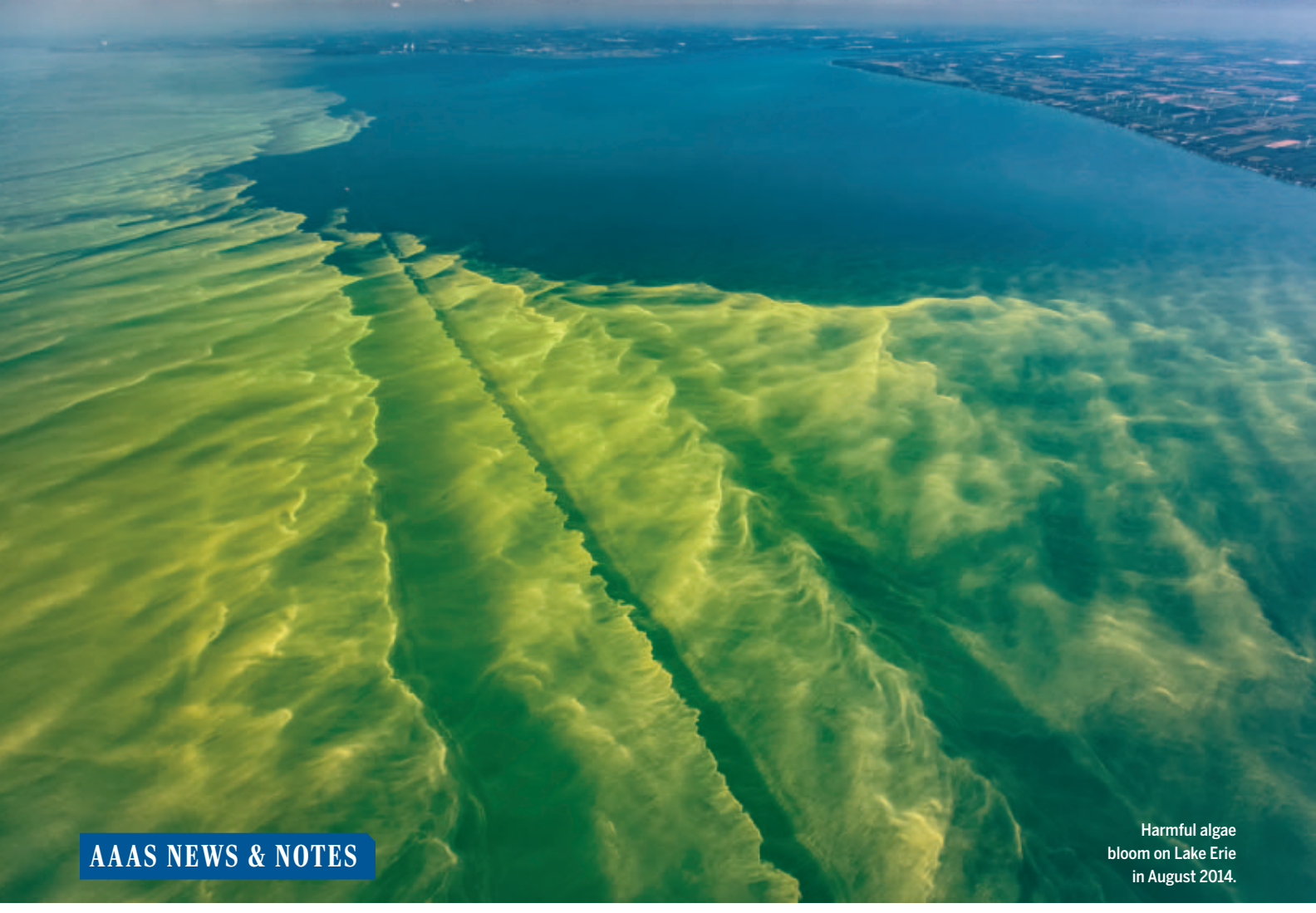

Harmful algae bloom on Lake Erie in August 2014.

PHOTO: ZACHARY HASLICK/AERIAL ASSOCIATES PHOTOGRAPHY, INC./NOAA GLERL/FLICKR

2018 AAAS Kavli Science Journalism Award winners named

The international competition drew entries from 54 countries

By **Earl Lane**

Stories on the long-sought pill for male contraception, the complicated legacy of a sexually proficient panda, and the environmental hazards posed by toxic algae and invasive mussels are among the winners of the 2018 AAAS Kavli Science Journalism Awards.

The judges also honored "Alive Inside," a series by *Houston Chronicle* reporter Mike Hixenbaugh on efforts by a local hospital to restore patients with severe brain injuries, and "The Farthest—Voyager in Space," a documentary written and directed by Irish filmmaker Emer Reynolds on NASA's ongoing mission to the outer planets and beyond.

The science journalism awards, administered by the American Association for the Advancement of Science (AAAS) since their inception in 1945, honor distinguished reporting for a general audience. The awards, endowed by The Kavli Foundation, are open to journalists worldwide. There were entries this year from 54 countries.

Independent panels of science journalists select the winners. A Gold Award ($5000) and a Silver Award ($3500) are presented in each of eight categories.

Emily Anthes, a freelancer for *Bloomberg Businessweek*, won a Gold Award in the magazine category for a story on the search for a male contraceptive. Maggie Koerth-Baker won a Gold Award for a lively online story for FiveThirtyEight about Pan Pan, the oldest known male panda at the time of his death in 2016.

Silver Award winners included Tony Bartelme in the small newspaper category for a report in *The Post and Courier* in Charleston, South Carolina, on the impact of destructive algae blooms and an audio team from Montana Public Radio for an ambitious report on the threat of invasive zebra and quagga mussels in Montana waters.

"These awards represent the highest quality in science journalism," said Rush Holt, AAAS chief executive officer. "Congratulations to the winners for their important and compelling stories." The awards will be presented at a 15 February ceremony held in conjunction with the 2019 AAAS Annual Meeting in Washington, D.C.

In addition to the annual awards, the AAAS Kavli program also brings past winners to college campuses for public lectures and workshops with journalism students. The speakers this fall were Sarah Holt, a three-time winner in the video category, who discussed the making of her new PBS NOVA documentary on addiction in a talk at Arizona State University on 23 October; Llewellyn Smith, a two-time video winner, who spoke at Howard University on 1 November about the relevance of science journalism for social justice; and freelancer Hillary Rosner, a two-time winner in print categories, who spoke at Northwestern University on 8 November about the challenges of covering conservation in an era of upheaval.

The winners are:

Large Newspaper (Circulation of 150,000 or more) Gold Award: Mike Hixenbaugh, *The Houston Chronicle,* for "Alive Inside" (series)—3 to 6 December 2017.

Large Newspaper Silver Award: Marc Hasse, *Hamburger Abendblatt* (Germany), for "Hamburgs nächste Elbphilharmonie?"—26 August 2017.

Small Newspaper (Circulation less than 150,000) Gold Award: Kale Williams, *The Oregonian* (Portland), for "The loneliest polar bear" (series)—16 to 20 October 2017.

Small Newspaper Silver Award: Tony Bartelme, *The Post and Courier* (Charleston, S.C.), for "Scum"—17 September 2017

Magazine Gold Award: Emily Anthes, *Bloomberg Businessweek*, for "What Do We Have to Do to Get the Male Pill?"—7 August 2017.

Magazine Silver Award: Nicola Twilley, *The New Yorker*, for "The Exercise Pill"—6 November 2017

Video Spot News/Feature Reporting (20 minutes or less) Gold Award: Joss Fong, David Seekamp, Rubab Shakir, and Laura Bult, Vox.com for Netflix, "Designer DNA, explained"—23 May 2018.

Video Spot News/Feature Reporting Silver Award: Jennifer Green and Jules Bartl, BBC World Service, for "How trees secretly talk to each other"—28 June 2018.

Video In-Depth Reporting (more than 20 minutes) Gold Award: Emer Reynolds, John Murray, Clare Stronge, John Rubin, and Sean B. Carroll, A Crossing the Line and HHMI Tangled Bank Studios Production for PBS, "The Farthest—Voyager in Space"—23 August 2017.

Video In-Depth Reporting Silver Award: Jamie Lochhead and Charlotte Hunt-Grubbe, Windfall Films for SVT2 (Sweden), Channel 4 (UK), and PBS, for "Ozone Hole: How We Saved the Planet"—21 May 2018 (SVT2).

Audio Gold Award: Cathy Edwards and Marnie Chesterton, BBC World Service, for "CrowdScience: Is Carbon Dioxide Higher Than Ever?"—6 October 2017.

Audio Silver Award: Nicky Ouellet, Eric Whitney, Josh Burnham, and Nora Saks, Montana Public Radio, for "SubSurface: Resisting Montana's Underwater Invaders" (series)—20 November, 24 November, 4 December, 10 December, and 18 December 2017.

Online Gold Award: Maggie Koerth-Baker, FiveThirtyEight, for "The Complicated Legacy of a Panda Who Was Really Good at Sex"—28 November 2017.

Online Silver Award: Sarah Zhang, The Atlantic.com, for "China Is Genetically Engineering Monkeys with Brain Disorders"— 8 June 2018.

Children's Science News Gold Award: Jeanne Miller, *Muse* magazine, for "Fighting to the End"—October 2017.

Children's Science News Silver Award: Anna Rothschild, "Science Magic Show Hooray" from *The Washington Post*, for "Why do we have butts?"—31 May 2018, and "Why am I so sweaty?"—12 July 2018.

Annual Meeting focuses on boundary-breaking research

Attendees of the 2019 Annual Meeting of the American Association for the Advancement of Science will celebrate three milestones that exemplify the 2019 meeting theme of science transcending boundaries. The 150th anniversary of the presentation of the periodic table of elements helped bridge the gap between chemistry, physics, and biology, while the 50th anniversary of Neil Armstrong's moonwalk and the first messages sent on the nascent internet erased the boundary between Earth and space and brought the world closer together than ever.

The 2019 annual meeting, to be held 14 to 17 February in Washington, D.C., will highlight research that brings together people, ideas, and solutions across boundaries in plenary and topical lectures, scientific sessions, career workshops, and public events such as Family Science Days. Among the topics to be discussed are the challenges of climate change, artificial intelligence, drug discovery, criminal justice, and more. Visit the Annual Meeting site at https://meetings.aaas.org for registration materials and a detailed program.

RESEARCH

Network analysis of ecosystem regime shifts

Rocha et al., *p. 1379*

IN *SCIENCE* JOURNALS

Edited by **Stella Hurtley**

PLANT SCIENCE

Rooting out the mechanism of asymmetry

Plant roots grow not in response to architectural blueprints but rather in search of scarce resources in the soil. Orosa-Puente *et al*. show why a new lateral root emerges on the damp side of a root rather than the dry side (see the Perspective by Giehl and von Wirén). The transcription factor ARF7 is found across the whole root but acquires a posttranslational modification on the dry side of the root, which represses its function. ARF7 on the damp side remains functional and is thus able to initiate the signaling cascade that leads to a new lateral root. —PJH

Science, this issue p. 1407; see also p. 1358

Computer-generated image of *Arabidopsis thaliana* root preferentially branching toward moist soil.

EXOPLANET ATMOSPHERES

Helium escaping from hot gas giants

Many gas giant exoplanets orbit so close to their host star that they are heated to high temperatures, causing atmospheric gases to escape. Gas giant atmospheres are mostly hydrogen and helium, which are difficult to observe. Two papers have now observed escaping helium in the near-infrared (see the Perspective by Brogi). Allart *et al*. observed helium in a Neptune-mass exoplanet and performed detailed simulations of its atmosphere, which put constraints on the escape rate. Nortmann *et al*. found that helium is escaping a Saturn-mass planet, trailing behind it in its orbit. They combined this with observations of several other exoplanets to show that atmospheres are being lost more quickly by exoplanets that are more strongly heated. —KTS

Science, this issue p. 1384, p. 1388; see also p. 1360

MOLECULAR MAGNETS

Breaking through the nitrogen ceiling

Single-molecule magnets could prove useful in miniaturizing a wide variety of devices. However, their application has been severely hindered by the need to cool them to extremely low temperature using liquid helium. Guo *et al*. now report a dysprosium compound that manifests magnetic hysteresis at temperatures up to 80 kelvin. The principles applied to tuning the ligands in this complex could point the way toward future architectures with even higher temperature performance. —JSY

Science, this issue p. 1400

QUASICRYSTALS

Quantum dots line up as a quasicrystal

Quasicrystals have rotational symmetry but no long-range order. Although several materials have quasicrystalline order, examples of quasicrystalline superlattices formed from different types of particles are rare. Nagaoka *et al*. discovered a type of 10-fold quasicrystalline superlattice formed from truncated tetrahedral quantum dots (see the Perspective by Wu and Sun). The order is driven by a "flexible polygon tiling rule," which explains the unique arrangement of the quantum dots. —BG

Science, this issue p. 1396; see also p. 1354

MARINE PROTECTED AREAS

Not as advertised

Marine protected areas (MPAs) have increasingly designated globally, with an associated

CREDITS: (TOP) ROCHA *ET AL*.; (BOTTOM) DANIEL VON WANGENHEIM

advertised percentage of area protected. However, recent research has made it clear that many MPAs are not actually protecting marine biodiversity. Dureuil *et al*. focused on European MPAs and found that trawling, one of the most damaging types of fishing, occurs widely in these areas. Furthermore, using sharks and rays as indicator species, they found that many MPAs are failing to protect vulnerable species. —SNV

Science, this issue p. 1403

SOCIAL NETWORKS

The strength of long-range ties

It seems reasonable that we would have the closest, strongest ties with people in our immediate social network and that the ties between networks would be weaker. However, Park *et al*. discovered strong ties that spanned extreme network (not geographic) distances in 11 culturally diverse population-scale networks on four continents—encompassing 56 million Twitter users and 58 million mobile phone subscribers. Although they are fairly rare, strong ties between networks could be important for the spreading of ideas or disease. —BJ and TSR

Science, this issue p. 1410

CANCER

Small molecules spark NK cell response

Immunotherapy is a powerful treatment for certain cancers. Yet for those patients that do not respond, simultaneous strategies that mobilize the immune system and directly target malignant cells may be more effective. Ruscetti *et al*. report that combining two clinically approved cancer drugs promoted immune surveillance and killing of KRAS-mutant lung tumors in mice (see the Perspective by Cornen and Vivier). The two small molecules—a mitogen-activated protein kinase inhibitor and a cyclin-dependent kinase 4/6 inhibitor—induced natural killer (NK) cell recruitment and elimination of senescent lung cancer cells, which did not occur when either agent was used alone. —PNK

Science, this issue p. 1416; see also p. 1355

NEUROSCIENCE

A safer way to probe for brain cancer

Needle biopsies of the brain are commonly used for diagnosing brain tumors but can cause intracerebral hemorrhage. Ramakonar *et al*. developed a high-resolution imaging needle that allows for improved visualization and differentiation of at-risk blood vessels in real time. They detected blood vessels with high sensitivity and specificity over a large field of view in both mouse brain and human brain tissue samples. Thus, optical imaging needles could reduce the occurrence of brain hemorrhages during biopsies and other neurosurgical procedures. —PJB

Sci. Adv. 10.1126/sciadv.aav4992 (2018).

ROBOTIC MANIPULATION

3D-printed, partially passive piano player

Our bodies are capable of a wide range of complex behaviors, but these abilities are limited by the specific anatomic and environmental conditions. Hughes *et al*. used this "conditional model" concept to test three-dimensionally (3D)–printed skeletal robot hands with ligaments of varied elasticity connecting rigid finger bones. Moving the base of the hand made the fingers play a piece of piano music. Varying ligament stiffness and hand movement enabled or restricted subsequent actions, such as a finger and thumb simultaneously pressing keys far apart. By changing these parameters, one hand could play three pieces of music that each required a different playing style. —RLK

Sci. Robot. **3**, eaau3098 (2018).

IN OTHER JOURNALS

Edited by **Caroline Ash** *and* **Michael Funk**

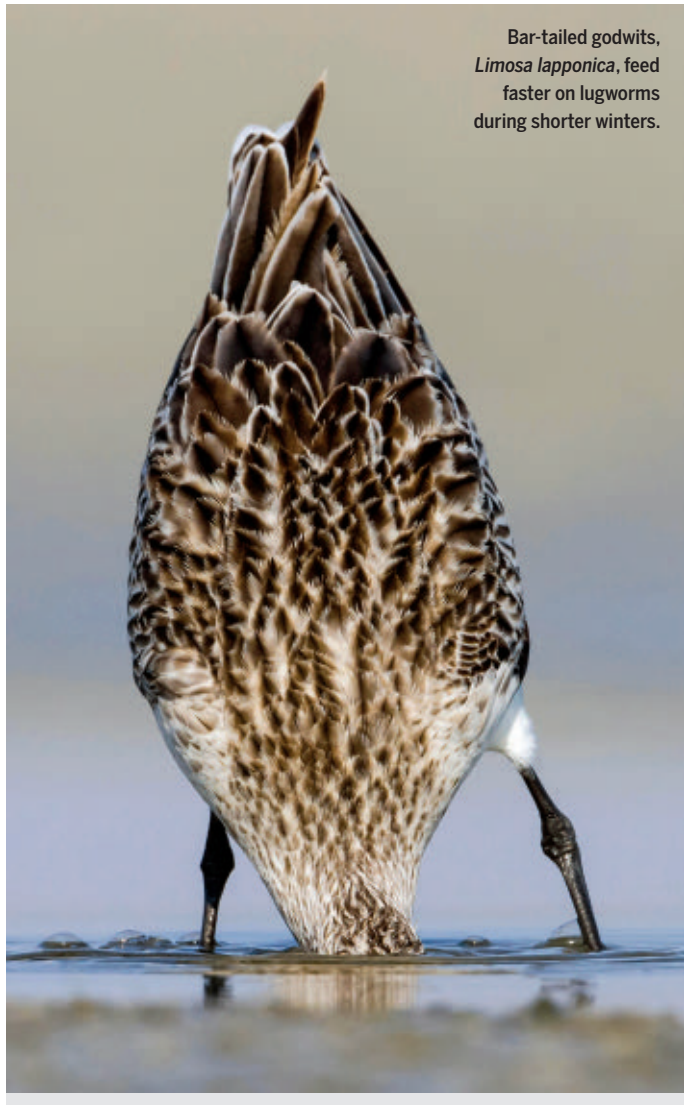

Bar-tailed godwits, *Limosa lapponica*, feed faster on lugworms during shorter winters.

MIGRATION

The importance of lugworms

As the climate warms, Arctic ice melts are occurring earlier in spring, and earlier ice melt means an early Arctic summer. For birds that migrate to the poles from temperate and tropical regions to breed, seasonal shifts represent a notable challenge to reproductive physiology. Rakhimberdiev *et al*. show that a wading bird called a bar-tailed godwit can arrive on the breeding grounds earlier in the year by shortening its over-wintering time by reducing the time it spends on the refueling grounds in the Wadden Sea of northwestern Europe. Increased rates of feeding, especially on lugworms, can compensate for a shorter feeding season. However, mortality is extensive if food sources become scarce, with one major factor being mechanized human harvest of lugworms in the Wadden Sea. —SNV

Nat. Comm. **9**, 4263 (2018).

PHOTO: AGAMI PHOTO AGENCY/ALAMY STOCK PHOTO

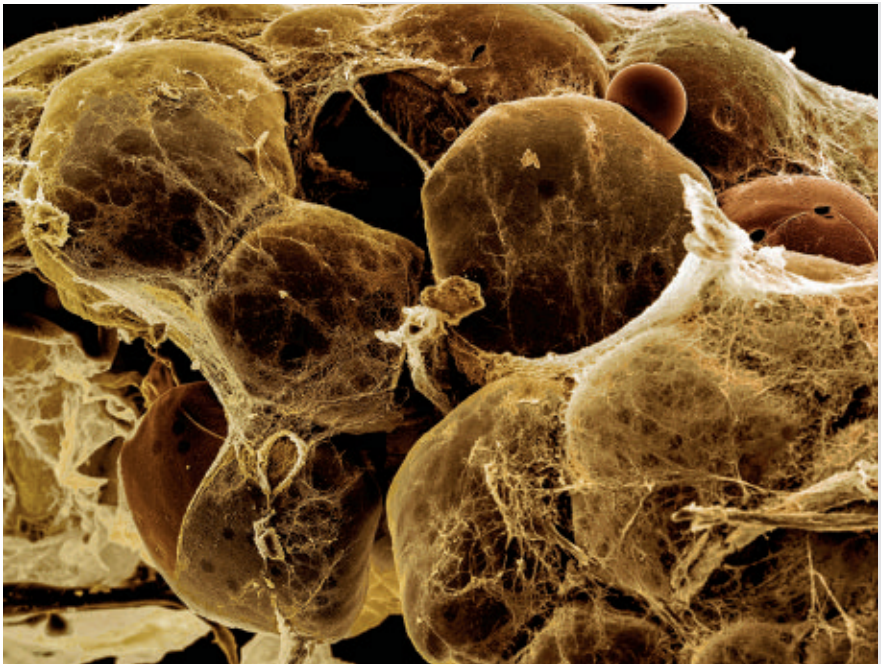

PHYSIOLOGY

Targeting brown fat to make less fat

Brown fat can release energy from food as heat instead of storing it and could thus help in battling obesity. Li *et al*. found that after a meal, brown fat in mice was stimulated to increase thermogenesis by direct action of the gut hormone secretin. The heat produced may be detected by the brain and thus induce a sense of satiety. This signaling relay may increase energy expenditure and decrease appetite, making it a potential target for therapies that attempt to control obesity. —LBR

Cell **175**, 1561 (2018).

Heat production by brown fat cells (shown) might reduce appetite.

IMMUNOLOGY

Lymph node mass transport

Cytokines are transported around the body via a network of lymph ducts and lymph nodes. Conduits within lymph nodes convey cytokines from the subcapsular sinus (SCS) into the deep parenchyma. From there, they discharge into high endothelial venules. In the SCS, sinus-lining cells prevent molecules greater than 70 kilodaltons from entering conduits. Nevertheless, Thierry *et al*. found that the massive 970-kilodalton pentamers of immunoglobulin M antibodies can cross into conduits. Transport is mediated by transient, activated, antigen-specific B cells, thus enabling rapid mobilization of the first wave of antibodies produced during an acute infection. —STS

J. Exp. Med. **215**, 2972 (2018).

VIROLOGY

Revelation in the gut virome

Some of the trillions of bacteria in the human gut are beginning to disclose their secrets. By contrast, we know little about the viruses other than that there are even more of them and most parasitize bacteria and other microbiota. Guerin *et al*. systematically investigated fecal DNA bacteriophages called crAssphages, which appear to infect Bacteroidetes. These phages are found in about half of individuals, constitute 90% of fecal DNA, and show differences in health and disease (for example, in malnourished infants). crAssphage genes tend not to match known sequences, but, through the use of a variety of methods on almost 100 complete circular genomes extracted from more than 700 human gut microbiota, four crAssphage subfamilies were found, each composed of 10 genera and with short-tailed icosahedral podovirus structures. —CA

Cell Host Microbe **24**, 653 (2018).

BIOORGANIC CHEMISTRY

Electrochemically clicking on tyrosine

Proteins are readily modified at lysine or cysteine residues, but for the other amino acids, general methods still need to be developed. For example, for electron-rich tyrosine, click methods have been developed based on cyclic diazodicarboxyamide anchors, but activation with chemical oxidants can also modify lysine residues or create products with limited aqueous stability. Alvarez-Dorta *et al*. show that tyrosine residues on proteins, including insulin and bovine serum albumin, can be targeted by electrochemically oxidizing phenyl urazoles without affecting amine or thiol groups of other amino acids. A reactive N=N species generated in the five-membered ring reacts with the C–H bonds adjacent to the tyrosine OH group. —PDS

J. Am. Chem. Soc. **140**, 17120 (2018).

MATERIALS SCIENCE

Connecting the dots

Much of the power of chemistry comes from the wide range of methods that can be used to connect atoms and molecules selectively at desired positions. Colloidal nanoparticles offer their own range of tunable properties that can be enhanced by connecting them together into superstructures through the bonding of their oligomeric surface ligands. Chen *et al*. developed a method using a block copolymer and solvent to selectively cover part of the nanoparticles, creating a mask for subsequent attachment of DNA. The coverage of the particles can be tuned by adjusting the ratio of hydrophilic to hydrophobic ligand, because this changes the way the ligands pack on the surface of the nanoparticles. —MSL

Nat. Mater. 10.1038/s41563-018-0231-1 (2018).

DIVERSITY IN STEM

With role models come persistence

Role model programs centered on women and underrepresented groups have been successful for early career scientists, but are they successful for undergraduate students? Hernandez *et al*. describe PROGRESS, a role modeling and mentoring program aimed at supporting undergraduate women in the geosciences, a historically male-dominated field. PROGRESS participants reported higher rates of persistence in geoscience-related majors, which was related to the number of female STEM career role models that they were able to identify; participants' odds of persisting in geoscience approximately doubled for each role model identified. The preliminary evidence suggests that presenting undergraduate students with successful female role models can encourage undergraduates to believe that they, too, can be successful scientists. —MMc

Geosphere **14**, 2585 (2018).

IMAGE: STEVE GSCHMEISSNER/SCIENCE SOURCE

ALSO IN *SCIENCE* JOURNALS

Edited by **Stella Hurtley**

CELL BIOLOGY

Protecting the heart

Excitation-contraction (E-C) coupling is fundamental to heart contraction. Junctophilin-2 is a structural protein required for formation of the E-C coupling machinery. During heart disease, stress-activated calpain cleaves junctophilin-2, disrupting the E-C coupling machinery and calcium ion signaling, which compromises cell contraction. Guo *et al*. found that under stress conditions, calpain-mediated cleavage converted full-length junctophilin-2 from a structural protein into a transcriptional regulator that shuttled to the nucleus (see the Perspective by Padmanabhan and Haldar). Furthermore, failing cardiomyocytes in stressed myocardium transduced mechanical information (E-C uncoupling) into transcriptional reprogramming. —BAP

Science, this issue p. 1375; see also p. 1359

STRUCTURAL BIOLOGY

Mechanism of promoter recognition

To start transcription, RNA polymerase II is recruited by the general transcription factor IID (TFIID) to the DNA promoter. Patel *et al*. used a combination of experimental approaches to elucidate the full molecular architecture of human TFIID and its complete conformational landscape during promoter recognition. They suggest exactly how TFIID is loaded onto the promoter, which involves defined steps—including promoter recognition and transcription initiation—and leads to regulated gene expression. —SYM

Science, this issue p. 1376

STRUCTURAL BIOLOGY

Architecture of the human TRPM2 channel

Adenosine diphosphate–ribose (ADPR) mediates calcium (Ca^{2+}) release by activating the transient receptor potential melastatin 2 (TRPM2) channel. Three structures now elucidate the conformational regulation mechanism of TRPM2 gating. Wang *et al*. describe cryo–electron microscopy structures of human TRPM2 in the apo, ADPR-bound, and ADPR- and Ca^{2+}-bound states. In the apo state, both intra- and intersubunit interactions appeared to lock TRPM2 into a closed and autoinhibited state. ADPR binding disrupted some interactions and dramatically altered the TRPM2 conformation. Binding of Ca^{2+} further primed the opening of the channel. —SYM

Science, this issue p. 1377

MOLECULAR MAGNETS

Cobalt unfettered by its ligand field

Applied magnetic fields induce a field in any compound with unpaired electrons. However, for the induced field to persist once the applied field is gone, the electrons must be configured to manifest orbital angular momentum. Generally, the influence of ligands severely restricts that property in transition metal complexes. Bunting *et al*. now show that a cobalt ion is just barely affected by two linearly coordinated carbon ligands and, as such, exhibits maximal orbital angular momentum. Although its magnetic properties mainly pertain at very low temperature, its structure offers a more general design principle. —JSY

Science, this issue p. 1378

CRITICAL TRANSITIONS

Cascading effects of regime shifts

The potential for regime shifts and critical transitions in ecological and Earth systems, particularly in a changing climate, has received considerable attention. However, the possibility of interactions between such shifts is poorly understood. Rocha *et al*. used network analysis to explore whether critical transitions in ecosystems can be coupled with each other, even when far apart (see the Perspective by Scheffer and van Nes). They report different types of potential cascading effects, including domino effects and hidden feedbacks, that can be prevalent in different systems. Such cascading effects can couple the dynamics of regime shifts in distant places, which suggests that the interactions between transitions should be borne in mind in future forecasts. —AMS and BJ

Science, this issue p. 1379; see also p. 1357

GUT MICROBES

Distinguishing two similar gut disorders

Inflammatory bowel disease and irritable bowel syndrome are two of the most common diseases of the gastrointestinal tract. Vich Vila *et al*. characterized the gut microbe composition of both disorders using shotgun metagenomic sequencing of stool samples from 1792 individuals. Bacterial taxonomy, metabolic functions, antibiotic resistance genes, virulence factors, and bacterial growth rates revealed key differences between these two gut disorders. —OMS

Sci. Transl. Med. **10**, eaap8914 (2018).

PLASMA ASTROPHYSICS

Reconnection in Earth's magnetotail

Magnetic fields in plasmas can rapidly rearrange themselves in a process known as magnetic reconnection, which releases energy and accelerates particles. Torbert *et al*. used the Magnetospheric Multiscale (MMS) mission to probe a reconnection event in Earth's magnetotail—the region of plasma downstream from the planet as it moves through the solar wind. MMS has previously studied reconnection in the upstream magnetopause, but a different orbit was used to study the magnetotail, where the symmetry of the process is different. The authors measured plasma properties on scales of the electron dynamics, leading to insights that will apply in other regions where magnetic reconnection occurs. —KTS

Science, this issue p. 1391

PALEOBOTANY

Late Permian seed-plant evolution

The great evolutionary expansion of seed plants took place in the Mesozoic era, which began after the Permian mass extinction 252 million years ago. Blomenkemper *et al*. report the discovery of seed-plant fossils from Late Permian (252-million- to 260-million-year-old) deposits on the margins of the Dead Sea in Jordan. This area represents an equatorial habitat with pronounced dry seasons. These fossils, which include the earliest records of conifers, push back the ages of several important seed-plant lineages. Some of these lineages appear to span the mass extinction event at the end of the Permian, which suggests that the communities they supported may have been more stable than expected over this transition. Thus, early evolutionary innovations can occur in drought-prone tropical habitats—which rarely offer the conditions needed for fossil preservation. —AMS

Science, this issue p. 1414

PAIN

A painful lipid in irritable bowel syndrome

Patients with irritable bowel syndrome (IBS) often experience abdominal pain. Bautzova *et al*. found that the abundance

of the polyunsaturated fatty acid 5-oxoETE was selectively increased in colonic biopsies from patients with a subtype of IBS characterized by constipation. They showed that 5-oxoETE increased pain sensitivity in mice without eliciting inflammation and stimulated both mouse and human pain-sensing neurons expressing the G protein–coupled receptor Mrgprd. Knockdown of Mrgprd in mice reduced the percentage of neurons that responded to 5-oxoETE and decreased pain sensitivity. —JFF

Sci. Signal. **11**, eaal2171 (2018).

CELL BIOLOGY

Membrane scission by ESCRTs

The ESCRT protein complexes are essential for cell division, the release of HIV from infected cells via budding, and other cell processes involving the scission of narrow membrane necks from their inner surface. The unusual inside-directed membrane cutting has made it hard to recapitulate this reaction and understand its mechanism. Schöneberg *et al*. encapsulated ESCRTs inside lipid vesicles and used optical tweezers to pull out membrane nanotubes. In the presence of adenosine triphosphate, clusters of ESCRTs generated force and constricted the nanotube, eventually severing it. This approach provides a window into the molecular mechanisms involved in the activities of ESCRTs. —SMH

Science, this issue p. 1423

TUMOR IMMUNOLOGY

γδ T cells come to the fore

Studies on T cells within the tumor microenvironment have largely focused on T cells that express γδ T cell receptors (TCRs). Benveniste *et al*. used an in vitro culture system to expand melanoma antigen–specific T cells and identified γδ T cells that recognize melanoma antigens in a class I major histocompatibility complex (MHC)–restricted manner. They then crystallized one of these γδ TCRs complexed with cognate peptide, MHC, and β2 microglobulin. T cell–centric therapies have been successful in treating certain cancers. These results should contribute toward a closer examination of the role of γδ T cells in the tumor microenvironment of melanomas and other cancers. —AB

Sci. Immunol. **3**, eaav4036 (2018).

RESEARCH ARTICLE SUMMARY

CELL BIOLOGY

E-C coupling structural protein junctophilin-2 encodes a stress-adaptive transcription regulator

Ang Guo, Yihui Wang, Biyi Chen, Yunhao Wang, Jinxiang Yuan, Liyang Zhang, Duane Hall, Jennifer Wu, Yun Shi, Qi Zhu, Cheng Chen, William H. Thiel, Xin Zhan, Robert M. Weiss, Fenghuang Zhan, Catherine A. Musselman, Miles Pufall, Weizhong Zhu, Kin Fai Au, Jiang Hong, Mark E. Anderson, Chad E. Grueter, Long-Sheng Song*

INTRODUCTION: Cardiac excitation-contraction (E-C) coupling refers to a cascade of Ca^{2+}-mediated events whereby membrane depolarization leads to cell contraction. At the subcellular level, E-C coupling occurs within a microdomain of the cardiomyocyte, termed the cardiac dyad. In various forms of heart disease, such as pathological hypertrophy and heart failure, the E-C coupling process is abnormal, in part because of ultrastructural remodeling. Abnormal Ca^{2+} homeostasis (as a result of failed E-C coupling) triggers maladaptive remodeling at the transcriptional level, contributing to pathological myocardial remodeling, hypertrophy, and heart failure. However, it remains unclear whether cardiomyocytes possess a self-protective or homeostatic mechanism that mitigates adverse myocardial remodeling.

RATIONALE: Junctophilin-2 (JP2) is a structural protein that organizes the E-C coupling ultrastructural machinery in cardiomyocytes. We previously showed that calpain-mediated proteolytic cleavage of JP2 is key to its downregulation in the diseased heart after cardiac stress. This cleavage contributes to loss of ultrastructural integrity at cardiac dyads, E-C uncoupling, and dysfunction of Ca^{2+} handling that results in heart failure. Computational analyses predicted that JP2 contains a nuclear localization signal (NLS), as well as an alanine-rich region (ARR) with characteristics of a helix-turn-helix structure, a DNA binding motif. We tested the hypothesis that JP2 encodes a stress-adaptive transcriptional regulator, which transduces mechanical information (E-C uncoupling) into transcriptional reprogramming in the myocardium in the setting of cardiac stress.

ON OUR WEBSITE

Read the full article at http://dx.doi.org/10.1126/science.aan3303

RESULTS: Biochemical, mutagenesis, and confocal imaging analyses revealed that stress-induced proteolysis of JP2 liberated an N-terminal fragment (JP2NT) that was imported into the nucleus through its NLS. Further biochemical and microarray assays showed that in the nucleus, JP2NT associated with chromatin and regulated transcription of a wide spectrum of genes via an evolutionarily conserved ARR located in the α-helix region of JP2. Chromatin immunoprecipitation sequencing (ChIP-seq) of JP2NT-overexpressing hearts revealed that it bound preferentially to the transcription start sites (TSSs) of genes, and gel shift studies defined the DNA binding motifs of JP2NT as the TATA box and a MEF2-response element (MRE). Elevation of JP2NT levels by JP2NT overexpression altered the in vivo genomic binding profile of TATA-box binding protein (TBP) and MEF2C. In addition, JP2NT suppressed the transcriptional activity of MEF2C by competing for MRE. Overexpression of JP2NT in mice led to reprogramming of the transcriptome in the setting of stress and attenuated hypertrophic remodeling and the progression of heart failure. Loss of JP2NT function by deletion of the JP2 NLS in mice accelerated the development of hypertrophy and heart failure after cardiac stress.

CONCLUSION: Our data reveal that calpain-mediated cleavage of JP2 transforms this E-C coupling structural protein into a transcriptional regulator that is shuttled into the nucleus and binds to promoters of target genes, inducing cardioprotective transcriptional reprogramming. These data reveal that cardiomyocytes possess a self-protective mechanism that counters pathological transcriptional remodeling after cardiac stress. Our findings also identify an intrinsic direct connection between ultrastructural remodeling and transcriptional reprogramming in the stressed heart. ■

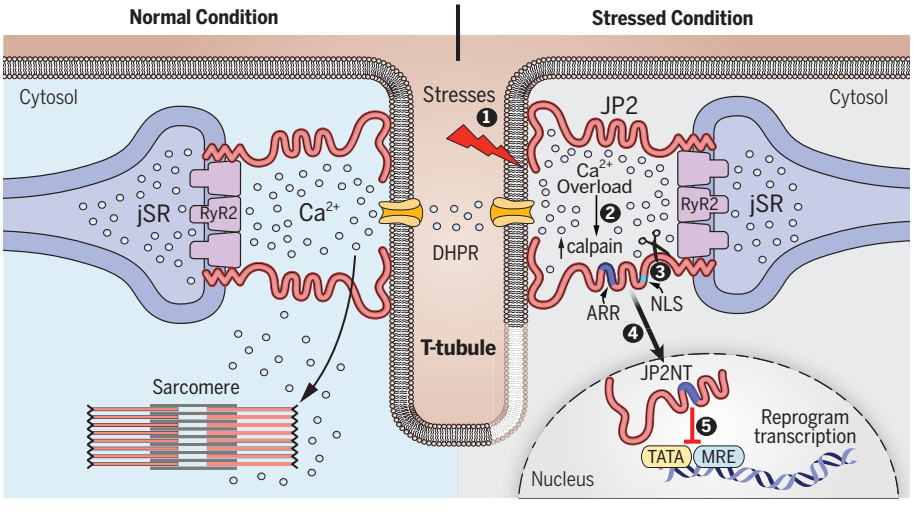

Schematic depiction of the mechanism by which JP2NT converts a mechanical stress signal to transcriptional reprogramming in the stressed heart. Left: E-C coupling under physiological conditions. Right: E-C coupling under pathologic conditions. Cardiac stress results in Ca^{2+} overload (1), promoting calpain activation (2). The resulting cleavage of JP2 liberates JP2NT from the T-tubule/sarcoplasmic reticulum junction, disrupting the ultrastructure of the E-C coupling machinery (3). JP2NT is shuttled into the nucleus via a conserved NLS (4). JP2NT binds to TATA-box elements via the ARR and associates with a MEF2 response element (MRE) to repress the transcription of genes that control deleterious cardiac remodeling (5).

The list of author affiliations is available in the full article online.
*Corresponding author. Email: long-sheng-song@uiowa.edu
Cite this article as A. Guo *et al.*, *Science* **362**, eaan3303 (2018). DOI: 10.1126/science.aan3303

RESEARCH ARTICLE

CELL BIOLOGY

E-C coupling structural protein junctophilin-2 encodes a stress-adaptive transcription regulator

Ang Guo[1], Yihui Wang[1,2], Biyi Chen[1], Yunhao Wang[1], Jinxiang Yuan[1], Liyang Zhang[3], Duane Hall[1], Jennifer Wu[1], Yun Shi[1], Qi Zhu[1,4], Cheng Chen[1,2], William H. Thiel[1], Xin Zhan[1], Robert M. Weiss[1], Fenghuang Zhan[1], Catherine A. Musselman[3], Miles Pufall[3], Weizhong Zhu[4], Kin Fai Au[1]*, Jiang Hong[2], Mark E. Anderson[5], Chad E. Grueter[1,6], Long-Sheng Song[1,6,7]†

Junctophilin-2 (JP2) is a structural protein required for normal excitation-contraction (E-C) coupling. After cardiac stress, JP2 is cleaved by the calcium ion–dependent protease calpain, which disrupts the E-C coupling ultrastructural machinery and drives heart failure progression. We found that stress-induced proteolysis of JP2 liberates an N-terminal fragment (JP2NT) that translocates to the nucleus, binds to genomic DNA, and controls expression of a spectrum of genes in cardiomyocytes. Transgenic overexpression of JP2NT in mice modifies the transcriptional profile, resulting in attenuated pathological remodeling in response to cardiac stress. Conversely, loss of nuclear JP2NT function accelerates stress-induced development of hypertrophy and heart failure in mutant mice. These data reveal a self-protective mechanism in failing cardiomyocytes that transduce mechanical information (E-C uncoupling) into salutary transcriptional reprogramming in the stressed heart.

Calcium ion (Ca^{2+}) signaling affects almost every aspect of cells (*1*). In heart muscle, excitation-contraction (E-C) coupling is a cascade of Ca^{2+}-mediated processes linking membrane depolarization to activation of cell contraction (*2*). At the cellular level, E-C coupling in working ventricular myocytes depends on precise communication between voltage-gated L-type Ca^{2+} channels located mainly on the transverse tubule (T-tubule) membrane and Ca^{2+}-sensitive ryanodine receptors (RyRs) on the terminal cisternae of the sarcoplasmic reticulum (SR) (*3*–*6*). Upon membrane depolarization, Ca^{2+} influx through the opening of voltage-gated L-type Ca^{2+} channels increases local Ca^{2+} concentration. This high concentration of Ca^{2+} sensitizes adjacent RyRs to release a much larger amount of Ca^{2+} from the SR. The SR-released Ca^{2+} together with Ca^{2+} influx activates myofilaments, resulting in myocyte contraction. This intermolecular Ca^{2+} crosstalk between L-type Ca^{2+} channels and RyRs takes place in a confined spatial microdomain, where T-tubules and terminal cisternae of SR form tight junctional couplings with a gap of 12 to 15 nm, termed "cardiac dyads" (*7*). Cardiac dyads provide the structural basis for E-C coupling and are established and maintained by junctophilin-2 (JP2) (*8*). JP2 contains eight N-terminal MORN (membrane occupation and recognition nexus) domains that mediate interactions with the T-tubule membrane, a space-spanning α helix that is thought to control the dyad distance, and a C-terminal transmembrane (TM) domain that anchors JP2 in the SR membrane (*8*, *9*). Genetic manipulation of JP2 by silencing, knockout, or overexpression authenticated its role as a structural protein responsible for the formation of cardiac dyads and maintenance of normal E-C coupling in the heart (*8*, *10*, *11*).

Defective E-C coupling is a hallmark of heart failure (*12*–*16*). Recent studies have provided compelling evidence that the expression level of JP2 is decreased in failing hearts of multiple etiologies including human heart failure, contributing to the loss of ultrastructural integrity of cardiac dyads and E-C coupling dysfunction (*16*–*22*). In particular, we discovered that JP2 proteolytic cleavage by calpain in response to cardiac stress represents a key mechanism of JP2 down-regulation, causing E-C uncoupling, Ca^{2+} mishandling, and heart failure (*23*–*25*). Abnormal Ca^{2+} homeostasis triggers maladaptive transcriptional remodeling, contributing to pathological myocardial remodeling and development of heart failure (*26*–*32*). However, it was not clear whether cardiomyocytes undergoing E-C uncoupling possess a self-protective or homeostatic mechanism that mitigates adverse myocardial remodeling. It was also unknown whether there is an intrinsic connection between cardiac ultrastructural remodeling at E-C coupling junctions and transcriptional reprogramming in stressed hearts.

Here, we show a mechanism in which a JP2 fragment, generated during cardiac stress and a marker of E-C uncoupling, serves as a negative feedback mechanism to antagonize maladaptive cardiac remodeling. This fragment translocates to the nucleus and represses transcriptional reprogramming, in part through regulating a key muscle transcription factor, MEF2 (myocyte enhancer factor 2). Specifically, we found that the α-helix domain of JP2 contains an evolutionarily conserved DNA binding domain. Under stress conditions, proteolytic processing of JP2 by calpain converts it from a structural protein to a transcriptional regulator, indicating an intrinsic connection between cardiomyocyte ultrastructural remodeling and transcriptional reprogramming in the heart.

Nuclear localization of JP2NT

We previously reported that JP2 is a substrate of calpain (calpain 1) and identified the primary calpain proteolysis site in the C-terminal region of JP2 between residues Arg^{565} and Thr^{566} (*24*). Calpain cleavage creates an N-terminal truncate (residues 1 to 565, termed JP2NT) that contains the plasma membrane–binding MORN motifs, and a C-terminal fragment containing the SR membrane–anchoring TM domain (Fig. 1A). We performed Western blotting with an antibody to an internal epitope of JP2, which is not destroyed by calpain cleavage of JP2 (fig. S1A). Analysis of subcellular fractions of mouse myocardium established that endogenous JP2NT (75 kDa) is present and predominantly enriched in nuclear fractions (Fig. 1B and fig. S1, B and C). Immunostainings of human and mouse myocardium sections using the same antibody also detected a JP2 product in nuclei (fig. S2, arrows). In contrast, an antibody to the C terminus of JP2 did not detect JP2 signals in the nucleus of myocardium sections (fig. S2). JP2NT was markedly increased in myocardium from mice with cardiac-specific overexpression of calpain1 and enriched in the nuclear fraction (Fig. 1C) [for calpain1-OE mice, see (*33*)]. In addition, treatment with micrococcal nuclease (MNASE), which cleaves DNA and releases chromatin-associated proteins, released JP2NT from the chromatin pellet (Fig. 1C); this result substantiates the nuclear localization of endogenous JP2NT in vivo and suggests that JP2NT is a chromatin-associated protein.

We hypothesized that pathological stresses that activate calpain (*34*) promote the generation

[1]Department of Internal Medicine, Abboud Cardiovascular Research Center, Carver College of Medicine, University of Iowa, Iowa City, IA 52242, USA. [2]Department of Emergency Medicine, Shanghai General Hospital, Shanghai Jiao Tong University School of Medicine, Shanghai 200080, China. [3]Department of Biochemistry, Carver College of Medicine, University of Iowa, Iowa City, IA 52242, USA. [4]Department of Pharmacology, School of Pharmacy, Nantong University, Nantong, Jiangsu 226001, China. [5]Department of Medicine, Johns Hopkins School of Medicine, Baltimore, MD 21205, USA. [6]Fraternal Order of Eagles Diabetes Research Center, Carver College of Medicine, University of Iowa, Iowa City, IA 52242, USA. [7]Iowa City Veterans Affairs Medical Center, Iowa City, IA 52242, USA.
*Present address: Department of Biomedical Informatics, Ohio State University, Columbus, OH 43210.
†Corresponding author. Email: long-sheng-song@uiowa.edu

and nuclear accumulation of JP2NT. Consistent with this notion, we found that both isoproterenol infusion (Fig. 1D and figs. S1B and S2A) and myocardial infarction (Fig. 1E, fig. S1C, and fig. S2, B and C) increased the amount of JP2NT in nuclei of stressed hearts relative to (sham) controls. Under pressure overload stress, nuclear accumulation of JP2NT reached its peak at 2 to 3 weeks after transaortic banding (TAB) surgery (Fig. 1F). Conversely, administration of the calpain inhibitor MDL-28170 significantly attenuated stress-induced elevation in nuclear JP2NT (Fig. 1, D to F), further supporting the idea that calpain-mediated proteolysis of full-length JP2 under cardiac stress results in accumulation of nuclear JP2NT.

These data led us to postulate that the post-translational removal of JP2 C terminus is sufficient to promote JP2NT translocation into the nucleus. To recapitulate the process by which calpain-mediated proteolysis is associated with

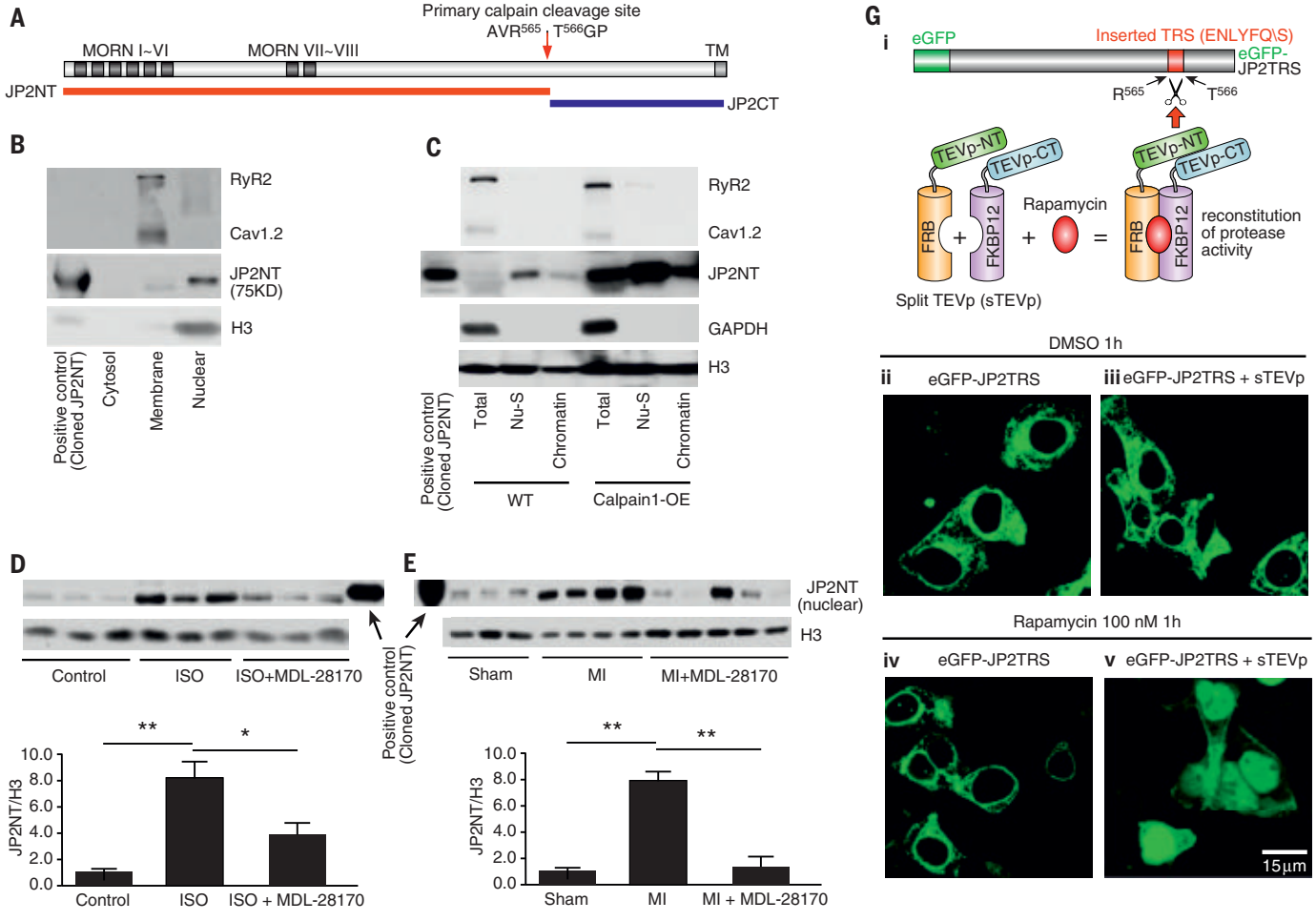

Fig. 1. JP2 N-terminal truncate (JP2NT) accumulates in the nucleus of stressed hearts. (**A**) Schematic of JP2 and JP2 truncates. (**B**) JP2NT is primarily present in nuclear fractions of murine heart lysates. H3, histone H3 (nuclear marker); $Ca_V1.2$, L-type Ca^{2+} channel (membrane marker); RyR2, ryanodine receptor type 2. (**C**) Increased endogenous JP2NT in soluble (Nu-S) and chromatin-containing (chromatin) nuclear fractions from 3 weeks postnatal calpain1–overexpressing (OE) hearts. The chromatin fraction was derived by treating a chromatin pellet with micrococcal nuclease (MNASE), which cleaves DNA and releases chromatin-associated proteins (see also Fig. 2C). (**D** to **F**) Increased endogenous JP2NT levels in chronic cardiac stress models: (D) isoproterenol (ISO, 1 week) minipump infusion; (E) myocardial infarction (MI, 1 week); (F) TAB-induced ventricular pressure overload. Calpain inhibitor MDL-28170 attenuated or abolished the elevation of nuclear JP2NT in all these models. JP2NT-OE, transgenic mouse with cardiac specific expression of JP2NT. The overexpression level of JP2NT is in the same order of magnitude of the peak level of endogenous JP2NT induced by TAB. $N = 3$ or 4 for each group; $^*P < 0.05$, $^{**}P < 0.01$ (t test or Kruskal-Wallis rank test when appropriate). (**G**) Analysis of JP2NT nuclear translocation using the rapamycin-inducible split tobacco etch virus protease (sTEVp) system. (i) Schematic of the sTEVp system. The N- and C-terminal fragments of TEV protease were fused to FRB and FKBP12, respectively. Rapamycin induces reconstitution of TEV protease through the FKBP12-rapamycin-FRB complex. A TEVp substrate recognition sequence (TRS) was inserted into the primary calpain cleavage site (Arg^{565}/Thr^{566}) of JP2 (eGFP-JP2TRS), allowing for inducible and site-specific rapid cleavage of substrates at the TRS. (ii to v) eGFP-JP2TRS was transfected into HEK293T cells alone (ii and iv) or with sTEVp system (iii and v), followed by treatment with DMSO control (ii and iii) or rapamycin (100 nM) for 1 hour (iv and v).

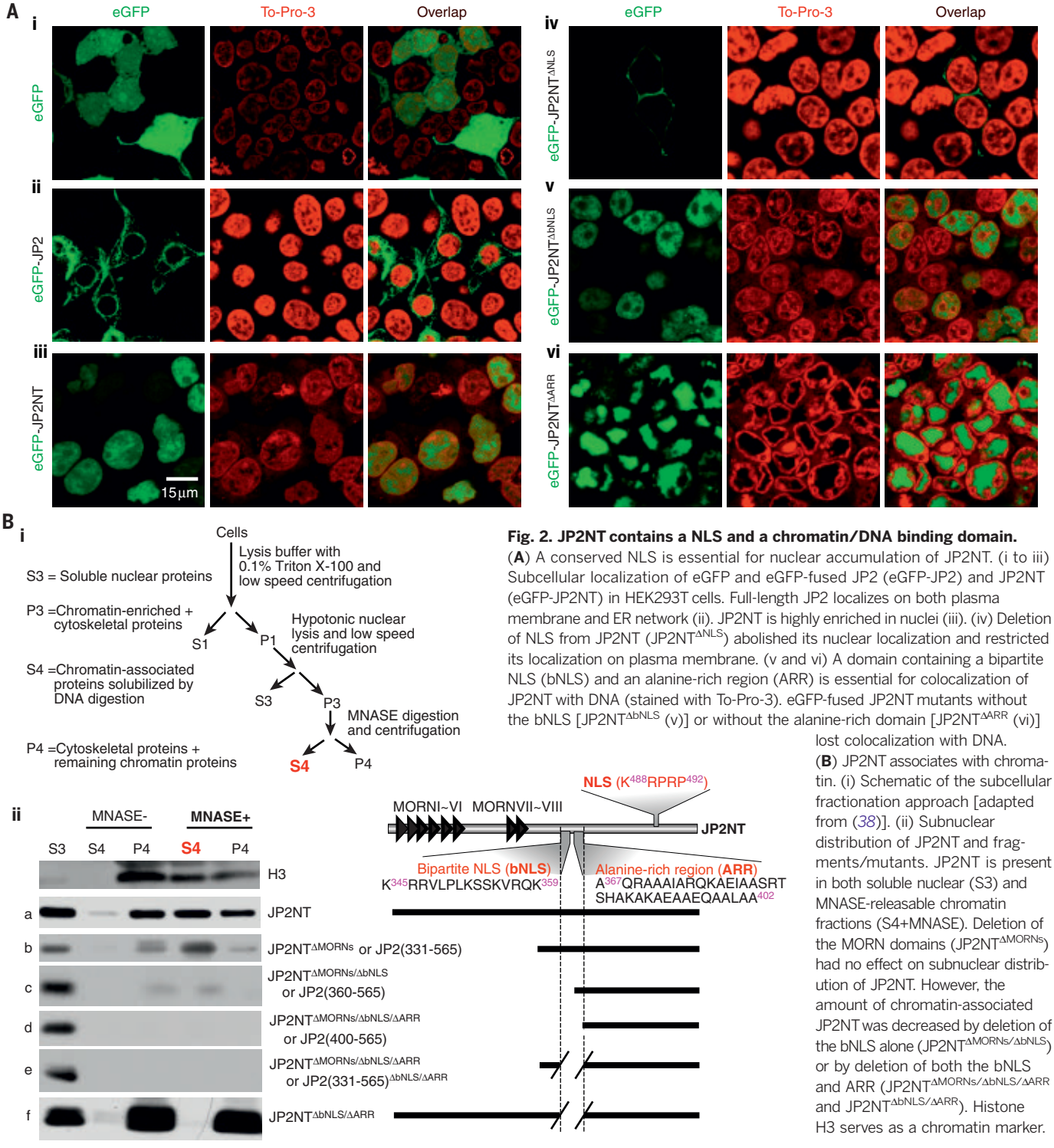

Fig. 2. JP2NT contains a NLS and a chromatin/DNA binding domain. (**A**) A conserved NLS is essential for nuclear accumulation of JP2NT. (i to iii) Subcellular localization of eGFP and eGFP-fused JP2 (eGFP-JP2) and JP2NT (eGFP-JP2NT) in HEK293T cells. Full-length JP2 localizes on both plasma membrane and ER network (ii). JP2NT is highly enriched in nuclei (iii). (iv) Deletion of NLS from JP2NT (JP2NT$^{\Delta NLS}$) abolished its nuclear localization and restricted its localization on plasma membrane. (v and vi) A domain containing a bipartite NLS (bNLS) and an alanine-rich region (ARR) is essential for colocalization of JP2NT with DNA (stained with To-Pro-3). eGFP-fused JP2NT mutants without the bNLS [JP2NT$^{\Delta bNLS}$ (v)] or without the alanine-rich domain [JP2NT$^{\Delta ARR}$ (vi)] lost colocalization with DNA. (**B**) JP2NT associates with chromatin. (i) Schematic of the subcellular fractionation approach [adapted from (*38*)]. (ii) Subnuclear distribution of JP2NT and fragments/mutants. JP2NT is present in both soluble nuclear (S3) and MNASE-releasable chromatin fractions (S4+MNASE). Deletion of the MORN domains (JP2NT$^{\Delta MORNs}$) had no effect on subnuclear distribution of JP2NT. However, the amount of chromatin-associated JP2NT was decreased by deletion of the bNLS alone (JP2NT$^{\Delta MORNs/\Delta bNLS}$) or by deletion of both the bNLS and ARR (JP2NT$^{\Delta MORNs/\Delta bNLS/\Delta ARR}$ and JP2NT$^{\Delta bNLS/\Delta ARR}$). Histone H3 serves as a chromatin marker.

JP2NT translocation, we adapted an inducible split tobacco etch virus protease (sTEVp) system (Fig. 1G, i) (*35*). A TEVp substrate recognition sequence (TRS) was inserted into an enhanced green fluorescent protein–JP2 fusion in the primary calpain cleavage site (Arg^{565}/Thr^{566}) (eGFP-JP2TRS; Fig. 1G, i). At baseline in human embryonic kidney (HEK) 293T cells, eGFP-JP2TRS was localized at the cell membrane and an intracellular network-like structure that is likely the endoplasmic reticulum (Fig. 1G, ii). In the absence of rapamycin, cotransfection of sTEVp did not affect eGFP-JP2TRS localization (Fig. 1G, iii). In cells expressing sTEVp, rapamycin treatment rapidly induced nuclear importation of eGFP-JP2TRS N terminus (Fig. 1G, v). These data show that JP2 C terminus anchors the intact JP2 protein at the dyad, and that removal of JP2 C terminus is sufficient to induce trafficking of the N-terminal fragment into nuclei.

JP2NT has a NLS and a chromatin/DNA binding region

To investigate the molecular mechanism of JP2NT nuclear importation, we performed in silico analysis (*36*). In JP2NT, we found a monopartite

nuclear localization signal (NLS) at positions 488 to 492 (Lys-Arg-Pro-Arg-Pro) and a bipartite NLS-like peptide (bNLS) at positions 345 to 359 (Lys-Arg-Arg-Val-Leu-Pro-Leu-Lys-Ser-Ser-Lys-Val-Arg-Gln-Lys), adjacent to an alanine-rich region (ARR; Ala^{367} to Ala^{402}) (fig. S3A) that shows characteristics of a helix-turn-helix structure [GYM 2.0 (*37*)]. These domains are evolutionarily conserved among species (fig. S3, B and C). Fusion of a short peptide containing this monopartite NLS to mCherry resulted in nuclear enrichment of the fusion proteins (fig. S3D). Deletion of this sequence ($JP2NT^{\Delta NLS}$) abolished nuclear localization of eGFP-JP2NT in HEK293T cells (Fig. 2A, iii and iv) and cardiomyocytes (fig. S3E), indicating that this NLS is indispensable for nuclear localization of JP2NT. A fusion protein containing mCherry and the bNLS peptide together with the ARR was imported into nuclei (fig. S3D). However, deletion of the bNLS sequence from JP2NT ($eGFP\text{-}JP2NT^{\Delta bNLS}$) did not prevent its nuclear importation in HEK293T cells (Fig. 2A, v) and cardiomyocytes (fig. S3E), indicating that this region is not necessary for nuclear importation of JP2NT. However, the subnuclear localization of $eGFP\text{-}JP2NT^{\Delta bNLS}$ was mutually exclusive from To-Pro-3 staining, which labels genomic DNA (Fig. 2A, v), suggesting physical dissociation of $eGFP\text{-}JP2NT^{\Delta bNLS}$ from genomic DNA. Deletion of the adjacent ARR from JP2NT ($eGFP\text{-}JP2NT^{\Delta ARR}$) induced greater separation of eGFP-JP2NT from DNA and was accompanied by accumulation of DNA at the nuclear periphery (Fig. 2A, vi). These data indicate that bNLS and ARR are involved in DNA or chromatin binding.

To further confirm the association of JP2NT with chromatin, we applied a biochemical fractionation procedure (*38*) (Fig. 2B, i). JP2NT was detected in both soluble (S3) and chromatin-containing insoluble (P4) nuclear fractions (Fig. 2B, ii, a). MNASE-mediated DNA digestion released JP2NT from the insoluble chromatin fraction (MNASE+/S4) (Fig. 2B, ii, a). Deletion of the eight

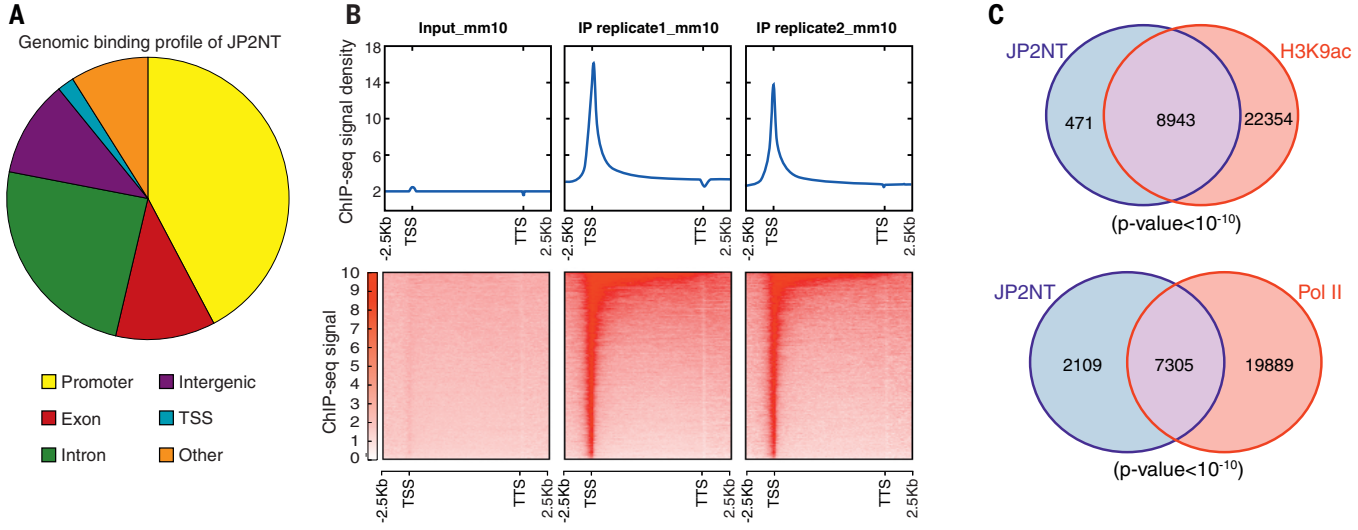

Fig. 3. JP2NT is a TATA-box binding protein enriched at transcription start sites and interacts with basic transcription machinery. (**A**) Genomic DNA binding profile of JP2NT in cardiomyocytes as revealed by ChIP-seq. (**B**) JP2NT is preferentially localized around transcription start sites (TSSs), as revealed by two replicates of ChIP-seq. (**C**) Overlap chart of DNA binding peaks of indicated proteins. (**D**) JP2NT binds to TATA box DNA sequences in vitro. (i and ii) Gel shift assays of purified GST-JP2NT binding to wild-type (WT) (i) or mutant TATA box–containing sequences (ii) derived from the cMyc promoter. (iii) Summary of the results of gel shift assays with various TATA box variants or mutants. Mutation of the core TATA sequences abolished the interaction with GST-JP2NT. (iv) Deletion of the ARR, but not the N-terminal MORN domains, eliminated JP2NT binding to the TATA box sequence. (v) The peptide $JP2^{331\text{-}405}$ containing the ARR specifically binds to the consensus TATA box sequence.

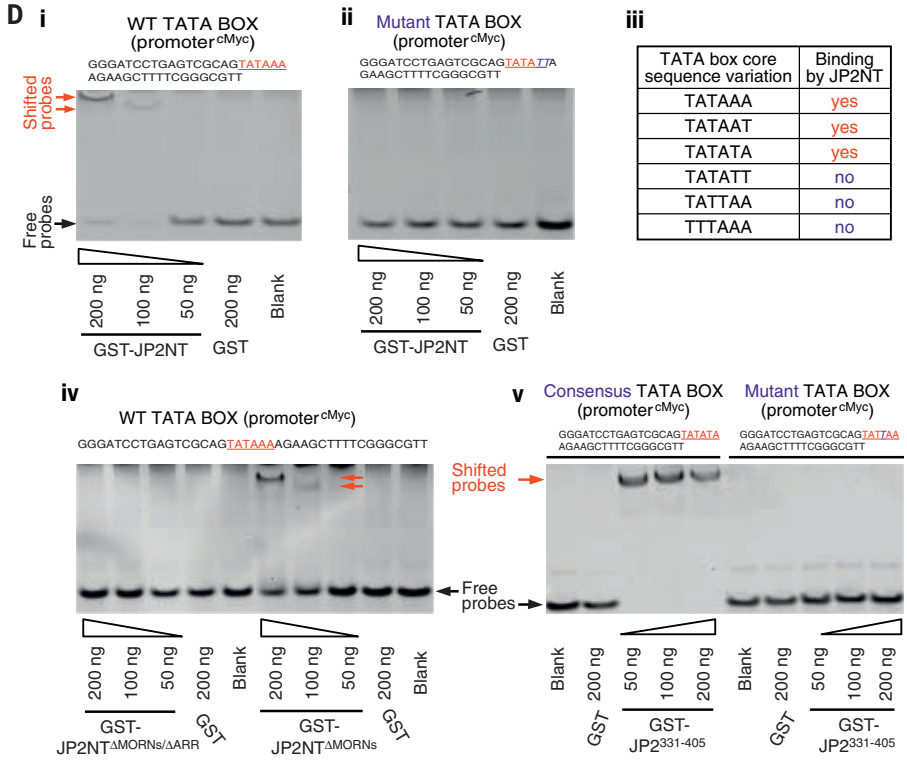

MORN domains from JP2NT (JP2NT$^{\Delta MORNs}$) did not influence its distribution in the nucleus or its association with chromatin (Fig. 2B, ii, b). In contrast, deletion of the bNLS-like sequence from this construct (JP2NT$^{\Delta MORNs/\Delta bNLS}$) significantly reduced the association of JP2NT with chromatin (Fig. 2B, ii, c). Deletion of the alanine-rich domain in combination with the bNLS (JP2NT$^{\Delta MORNs/\Delta bNLS/\Delta ARR}$ or JP2NT$^{\Delta bNLS/\Delta ARR}$) completely prevented presence of JP2NT in the MNASE-releasable chromatin fraction (Fig. 2B, ii, d to f). On the basis of these data, we conclude that JP2NT associates with chromatin via a domain located at residues ~345 to 402, which is highly evolutionarily conserved in mammalian species as well as in vertebrates such as fish and birds (fig. S3C).

JP2NT is enriched at transcription start sites

To systematically study the genomic targets of JP2NT, we generated transgenic mice with cardiac-specific overexpression of hemagglutinin (HA)–tagged JP2NT. In these mice, JP2NT is predominantly localized in the nuclei of cardiomyocytes (fig. S4A). The level of JP2NT transgene in nuclear fraction is of the same order of magnitude, relative to the peak level of endogenous JP2NT induced by TAB (Fig. 1F). Hearts of the JP2NT-overexpressing mice (JP2NT-OE) were subjected to chromatin immunoprecipitation sequencing (ChIP-seq) analysis using antibody to HA. Two replicates of ChIP-seq analyses were performed using different batches of JP2NT heart samples. Only the DNA peaks ($P < 10^{-10}$) that were detected in both replicates of ChIP-seq analyses were considered as JP2NT-binding DNA regions. We identified 9414 JP2NT-binding genomic DNA regions encompassing 7398 genes. The DNA binding profile revealed that JP2NT is concentrated in gene-enriched regions, especially the promoter and 5′ untranslated regions (Fig. 3A). Moreover, JP2NT is preferentially enriched at transcription start sites (Fig. 3B), a characteristic of transcription regulators. We

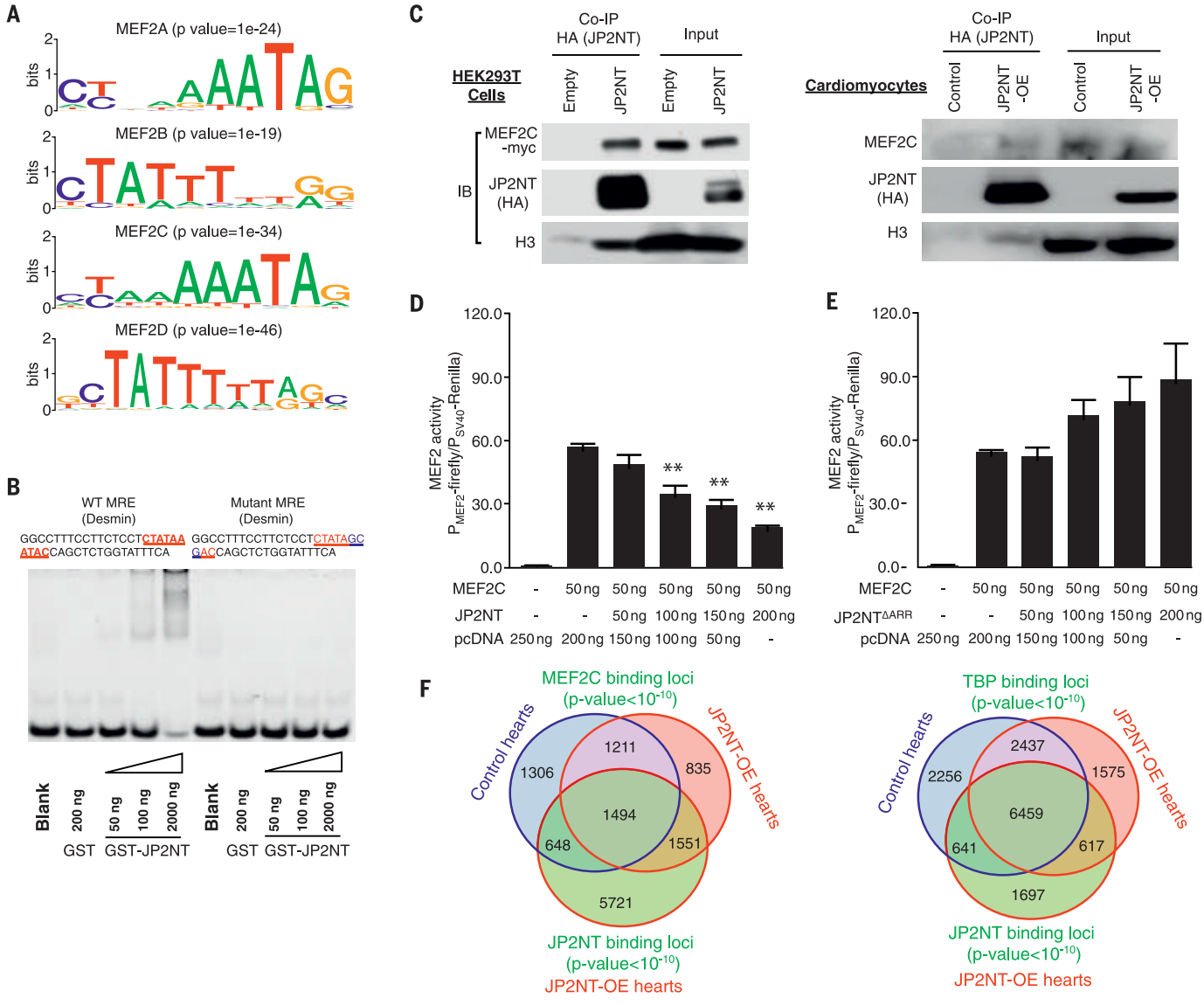

Fig. 4. JP2NT represses MEF2-mediated transcription by competing for the MEF2 response element (MRE). (**A**) Enrichment of MEF2 binding motifs in ChIP-seq dataset. (**B**) Gel shift assay of JP2NT binding to a desmin enhancer–derived DNA sequence containing a WT or mutant MRE in vitro. (**C**) Coimmunoprecipitation of HA-tagged JP2NT binding to MEF2C or Histone H3 in HEK293T cells transfected with JP2NT and MEF2C as well as in JP2NT-OE hearts (postnatal 2 weeks). (**D** and **E**) MEF2 activity assays in HEK293T cells cotransfected with P_{MEF2}-firefly, P_{SV40}-renilla, MEF2C, and WT JP2NT (D) or a mutant lacking the ARR (E, JP2NT$^{\Delta ARR}$) ($n \geq 3$ independent batches of experiments, three transfection replicates included in each batch; $^{**}P < 0.01$ versus MEF2C+empty pcDNA). (**F**) Overlap chart of MEF2C (left) and TBP (right) DNA binding peaks compared between control and JP2NT-OE hearts, as well as compared with JP2NT binding peaks from JP2NT-OE hearts.

compared JP2NT occupancy of genomic loci with that of cardiac polymerase II (Pol II) and acetylated histone H3 Lys[9] (H3K9ac, a marker for active promoters and enhancers) binding peaks from published data (*39*). We found that 95% of JP2NT peaks overlap with H3K9ac peaks and 78% overlap with Pol II peaks (Fig. 3C; example tracks shown in fig. S4B, a). These data strongly suggest that JP2NT regulates active cardiac transcription.

JP2NT is a TATA-box binding protein and interacts with transcription machinery

On the basis of these results, we hypothesized that JP2NT may directly associate with core cis-regulatory elements that regulate transcription initiation. Cross-linking reversal coimmunoprecipitation experiments in JP2NT transgenic cardiomyocytes demonstrated that JP2NT associates with RNA Pol II (RPB1) and TATA-box binding protein (TBP), both of which are components of the basic transcriptional machinery (fig. S5A). TBP specifically binds to TATA boxes, eukaryotic core cis-regulatory elements localized at transcription start sites. Subsequent in vitro analysis with purified recombinant glutathione *S*-transferase (GST)–JP2NT revealed that JP2NT directly binds to the TATA box or variants (TATAAA, TATAAT, and TATATA) from the cMyc (Fig. 3D, i, and fig. S5B) or the CMV promoter (fig. S5C). This interaction was abrogated by mutation of the TATA-box elements (Fig. 3D, ii, and fig. S5B). We conclude that JP2NT is a DNA binding protein, binding to the consensus TATA box represented as TATAA(A/T) or TATATA (Fig. 3D, iii).

Deletion of N-terminal MORN domains alone from JP2NT (GST-JP2NT$^{\Delta MORNs}$) did not alter the interaction of JP2NT with the TATA-box oligonucleotide (Fig. 3D, iv, and fig. S5C). However, deletion of the ARR from this construct (GST-JP2NT$^{\Delta MORNs/\Delta ARR}$) completely abrogated the association of JP2NT with TATA-box elements (Fig. 3D, iv, and fig. S5C). Conversely, a purified peptide containing the ARR (GST-JP2$^{331-405}$) specifically bound to the consensus but not the mutant TATA box (Fig. 3D, v, and fig. S5D). Together, these data indicate that the ARR is responsible for TATA-box binding.

JP2NT modulates MEF2-mediated transcription via competing for MEF2 binding sites

The MEF2 family, master regulators of hypertrophic genes in cardiomyocytes, binds to the A/T enriched consensus sequence (*C/T* TA(A/T)4TA *G/A*), which shares the same core sequence with the TATA box. Thus, we hypothesized that JP2NT directly interacts with the MEF2 response element (MRE). Consistent with this hypothesis, MEF2 binding motifs were significantly enriched in the ChIP-seq dataset (Fig. 4A and table S1). Gel shift assay demonstrated that purified JP2NT or purified DNA binding domain of JP2NT (GST-JP2$^{331-405}$) interacts with a MRE from the desmin enhancer (Fig. 4B and fig. S6A). The specificity of this interaction was further shown by mutant MRE oligos (Fig. 4B) and cold competitor assay

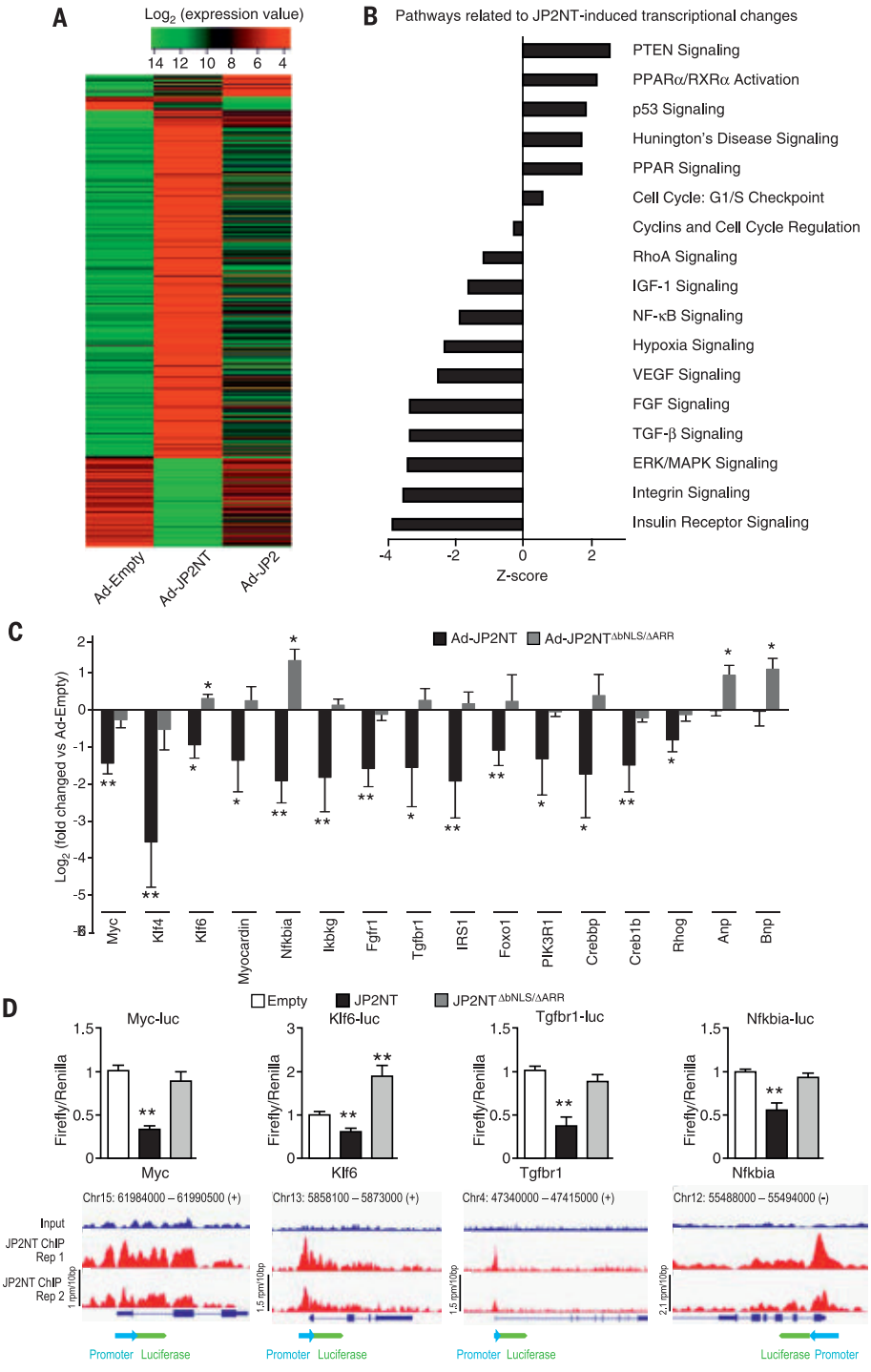

Fig. 5. JP2NT drives broad-spectrum transcriptional reprogramming in cultured cardiomyocytes. (**A**) Heat map of significantly altered genes in cultured adult murine cardiomyocytes expressing JP2 or JP2NT by adenovirus (Ad). (**B**) IPA pathway enrichment analysis of significantly altered transcripts induced by JP2NT. (**C**) RT-qPCR validation of genes that were significantly down-regulated by JP2NT as compared to Ad-Empty control. Note that deletion of the ARR (JP2NT$^{\Delta ARR}$) prevented JP2NT-mediated transcriptional repression. Data were calculated as the $\log_2$ fold change relative to cells transfected with Ad-Empty. Each transcript was assayed in $n \geq 4$ batches of cells. (**D**) Transcriptional activity assays in which luciferase is under the control of the indicated promoters [$n \geq 3$ independent batches of HEK293T cells, three transfection replications included in each batch; $^*P < 0.05$, $^{**}P < 0.01$ versus control (empty virus or plasmid)]. Under each bar graph are the JP2NT binding tracks at these gene loci and location of cloned promoters for luciferase construct, respectively.

(fig. S6B). Biotinylated oligo DNA pull-down assay confirmed that the JP2NT transgene as well as endogenous full-length JP2 from heart lysis can interact with MRE (fig. S6C). Coimmunoprecipitation of HEK293T cells transfected with Myc-tagged MEF2C and HA-tagged JP2NT demonstrated an interaction of the two proteins (Fig. 4C). The interaction of endogenous MEF2C with JP2NT transgene was confirmed in JP2NT transgenic hearts (Fig. 4C).

To examine whether JP2NT regulates MEF2-mediated transcription, we used a luciferase reporter system with firefly cDNA driven by desmin enhancer–derived MRE (P_{MEF2}-firefly) (*40*). Cotransfection of a plasmid expressing MEF2C and P_{MEF2}-firefly in HEK293T cells significantly increased the firefly luciferase signal relative to constitutive P_{SV40}-renilla (Fig. 4, D and E). Cotransfection of JP2NT attenuated the MEF2-responsive signal in a dose-dependent manner (Fig. 4D). By contrast, MEF2C-mediated transcriptional activity was not significantly altered in cells expressing a JP2NT construct lacking the ARR ($JP2NT^{\Delta ARR}$, Fig. 4E), which we found to be required for its association with chromatin and TATA box sequences. These data suggest that JP2NT competes with MEF2 for direct interaction with its consensus sequence at promoters to block MEF2-mediated transcription.

JP2NT alters DNA binding profiles of TBP and MEF2C in cardiomyocytes

To understand whether JP2NT influences DNA occupancy of MEF2 in cardiomyocytes, we analyzed the DNA binding profile of MEF2C in control and JP2NT-OE myocardium. ChIP-seq analyses revealed that JP2NT-OE suppressed MEF2C interactions at 42% of the endogenous MEF2C binding sites. JP2NT-OE created 2386 new MEF2C binding peaks that are absent in control hearts, and 65% of them overlap with JP2NT binding sites. In addition, 33% of the MEF2C binding peaks inhibited by JP2NT-OE overlap with JP2NT binding sites (Fig. 4F). ChIP-seq analyses of TBP revealed that ~25% of the endogenous TBP binding sites were suppressed by JP2NT-OE, and 22% of them overlap with JP2NT binding sites. JP2NT-OE created 2192 new TBP binding peaks, and 28% of them overlap with JP2NT binding sites (Fig. 4F; example tracks shown in fig. S4B, b to e). These data indicate that JP2NT can affect MEF2C and TBP DNA binding, either by competing for the endogenous binding sites or by recruiting MEF2C and TBP to new binding sites.

Overexpression of JP2NT in cultured cardiomyocytes induces profound changes in transcriptional profile

The association of JP2NT with DNA and transcription machinery led us to investigate whether JP2NT directly modulates the transcriptional profile in cardiomyocytes. Compared with cardiomyocytes infected with empty adenovirus (Ad-Empty control), Affymetrix GeneChip analysis revealed that the expression of 574 and 1996 known genes were significantly induced or repressed ($P < 0.01$), respectively, in JP2NT-expressing cardiomyocytes (Fig. 5A and fig. S7A; see table S2 for complete list of differentially expressed genes). Conversely, only 96 significantly induced and 264 significantly repressed genes were detected in cardiomyocytes with overexpression of full-length JP2 (Fig. 5A and fig. S7B). Of the differentially expressed genes induced by JP2NT, ~60% mapped to genomic loci where JP2NT was found to bind by ChIP-seq; this proportion is significantly larger than the ~46% ($P < 10^{-15}$) of JP2NT binding genes among those genes whose expression was detectable in cardiomyocytes but was not significantly influenced by JP2NT. Notably, the regulatory effect of JP2NT on gene expression appeared to be dependent on binding of JP2NT to gene loci: Among the differentially expressed genes for which JP2NT bound to the genomic loci, the vast majority (84%) were down-regulated in the presence of JP2NT overexpression; this percentage is decreased to 67% ($P < 10^{-15}$) in differentially expressed genes not bound by JP2NT. We interpret these findings to indicate that JP2NT represses transcription by binding to genomic regions, either directly through binding to TATA box and MRE or through interactions with transcription factors such as MEF2C and TBP.

Many of the JP2NT–down-regulated genes encode nuclear proteins (fig. S7C) and proteins that are functionally enriched in nuclear events such as transcriptional regulation and chromatin modification (fig. S7D). Ingenuity Pathway Analysis (IPA; Qiagen) of the differentially expressed genes induced by JP2NT identified pathways and regulators implicated in cardiac hypertrophy, fibrosis, cell growth, and differentiation as well as inflammation. Specifically, ERK/MAPK, NF-κB, TGF-β, and integrin signaling pathways were predicted to be inhibited in response to JP2NT overexpression (Fig. 5B and table S3). Confirming these GeneChip findings, reverse transcription quantitative polymerase chain reaction (RT-qPCR) revealed that mRNA levels of genes including those that encode KLF4, KLF6, Myc, TGFβR1, NFKBIA, FOXO1, and PI3KR1 were significantly decreased in cardiomyocytes expressing JP2NT relative to Ad-Empty infected cells (Fig. 5C). Deletion of the DNA binding region from JP2NT ($JP2NT^{\Delta bNLS/\Delta ARR}$) largely prevented the repressive effect of JP2NT (Fig. 5C). Notably, the cardiac hypertrophy markers ANP and BNP were not altered by JP2NT expression but were significantly increased by $JP2NT^{\Delta bNLS/\Delta ARR}$ (Fig. 5C).

To further test whether JP2NT regulates transcription of these genes, we constructed luciferase reporters controlled by promoters of Myc, KLF6, TGFβR1, and NFKBIA. For all genes, promoter activity was significantly attenuated by coexpression of JP2NT in HEK293T cells (Fig. 5D). Consistent with the changes in mRNA levels, expression of $JP2NT^{\Delta bNLS/\Delta ARR}$ either had no effect on baseline firefly luciferase signal or increased promoter activity as compared to empty vector control (Fig. 5D), supporting the idea that the DNA binding domain of JP2NT is important for its function as a transcriptional repressor.

JP2NT attenuates hypertrophic response and heart failure development in mice

Because JP2NT represses transcription of key regulators of hypertrophy, fibrosis, and inflammation, we predicted that JP2NT would exert a protective effect on stress-induced pathological cardiac remodeling. At baseline, JP2NT overexpression had no effect on cardiac morphology or function (Fig. 6, A to C). The E-C coupling function at the single-cell level (e.g., L-type Ca^{2+} channel densities, amplitude and kinetics of Ca^{2+} transients, SR Ca^{2+} content, and the gain function of E-C coupling) was not altered by the JP2NT transgene (fig. S8). Under stress conditions induced by TAB surgery to produce pressure overload hypertrophy and heart failure, JP2NT-OE mice had improved cardiac function (Fig. 6A), lower heart weight/body weight ratio (Fig. 6B), and reduced lung edema indicated by the lung weight/body weight ratio (Fig. 6C) relative to controls. These results suggest that JP2NT-OE protects the heart against stress-induced pathological remodeling.

RNA-seq demonstrated minor differences in the cardiac transcription profile of JP2NT-OE mice at baseline relative to control littermates (fig. S9A), with only 220 significantly altered genes ($P < 0.01$). TAB promoted a marked change in the transcriptome of control hearts as compared to sham surgery, with 4636 significantly altered transcripts derived from 3580 genes (fig. S8B). Overexpression of JP2NT significantly modified the transcriptional response to cardiac stress: We detected a significant difference in 1082 transcripts derived from 954 known genes based on a linear regression model ($P < 0.01$, Fig. 6D). Among these, 540 transcripts (mapped to 481 known genes) were negatively influenced and 542 transcripts (mapped to 476 known genes) positively influenced by JP2NT overexpression (see table S4), with a predicted inhibition of ERK, TGF-β, CREB, and NF-κB signaling pathways (Fig. 6E and table S5). These findings are in line with observations in cultured cardiomyocytes (Fig. 5B) and substantiate a pivotal role for JP2NT in the cardiac response to stress by inhibiting transcriptional reprogramming.

Loss of function of nuclear JP2NT exacerbates cardiac dysfunction in response to stress

To investigate the function of endogenous JP2NT, we developed a knock-in (KI) mouse line with NLS deleted in the JP2 coding sequence ($JP2^{\Delta NLS}$-KI) (fig. S10A). NLS deletion abolished the nuclear accumulation of JP2NT after cardiac stress (fig. S10B). The homozygous $JP2^{\Delta NLS}$-KI mice show no difference in cardiac morphology, contractile function, and cellular E-C coupling / Ca^{2+} handling function compared to wild-type littermates under baseline condition (Fig. 6, F to I, and fig. S10, C to E). However, when subjected to TAB, $JP2^{\Delta NLS}$-KI mice developed more severe cardiac hypertrophy and worsened heart function relative to wild-type littermates. Three weeks after TAB, echocardiography detected

larger myocardium mass (Fig. 6F), higher end diastolic volume (EDV) (Fig. 6H) and end systolic volume (ESV) (Fig. 6I), and lower ejection fraction (Fig. 6G) in JP2$^{\Delta NLS}$-KI mice than in wild-type littermates. These findings suggest that JP2NT functions as an endogenous cardiac protector against pathological challenges.

Discussion

Our study provides compelling evidence suggesting that an E-C coupling structural protein can also act as a transcriptional regulator. We have shown that regulated cleavage of JP2 converts it from a structural protein to a nuclear transcriptional regulator via an NLS and an ARR contained within JP2NT. JP2NT is enriched in the promoter region of genes in cardiomyocytes and primarily acts as a transcriptional repressor of genes implicated in cell growth and differentiation, hypertrophy, inflammation, and fibrosis, with evidence for a specific interaction with the transcription factor MEF2. Cardiac-specific transgenic overexpression of JP2NT attenuates pressure overload induced development of heart failure, identifying JP2NT generation as a self-protective homeostatic mechanism that safeguards against the deleterious effects of cardiac stress. These discoveries reveal a signaling pathway that transduces membrane stresses into transcriptome changes in the setting of E-C uncoupling after cardiac stress.

JP2 was initially discovered as a structural protein with dual membrane-anchoring domains

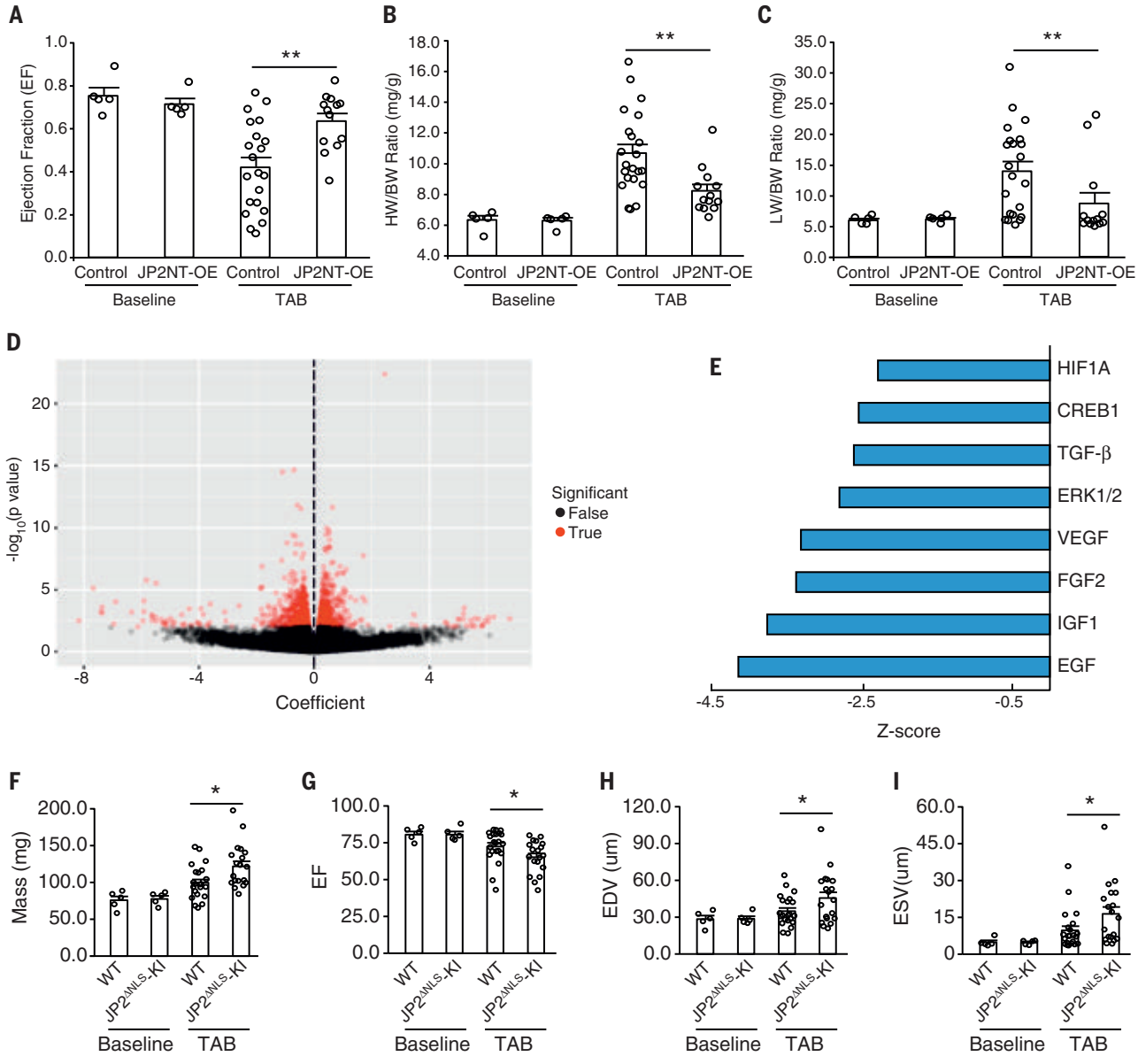

Fig. 6. JP2NT overexpression protects against pressure overload-induced hypertrophy and heart failure. (**A**) Cardiac specific overexpression of JP2NT (JP2NT-OE) preserved cardiac ejection fraction (EF) in mice 3 weeks after transverse aortic banding (TAB). (**B**) JP2NT overexpression attenuated TAB-induced cardiac hypertrophy as evidenced by a decreased heart weight/body weight (HW/BW) ratio. (**C**) Lung weight/body weight (LW/BW) ratio is significantly reduced in JP2NT-OE mice after TAB; *n* = 5, 5, 22, 13 for each group respectively. (**D**) Volcano plot of the effect of JP2NT overexpression on TAB-induced transcriptional remodeling. JP2NT-OE significantly changed the transcriptional response to TAB. Red dots indicate the transcripts whose response to TAB was significantly changed by JP2NT-OE. (**E**) IPA pathway enrichment analysis of significantly altered transcripts in JP2NT-OE mice after TAB as compared to littermate controls. (**F** to **I**) Echocardiogram measurement of heart mass (F), ejection fraction (G), EDV (H), and ESV (I) in WT and JP2$^{\Delta NLS}$-KI mice under baseline or TAB condition.

that connect T-tubules and the SR membrane (*8*). Here, we discovered that JP2 contains additional regulatory domains that extend beyond its role as a structural protein. An NLS in the N-terminal region of JP2 is necessary for nuclear import of the calpain-generated JP2NT truncate. Thus, under stress conditions, calpain-mediated cleavage of JP2 serves two purposes: (i) It impairs the bridging of T-tubules with the SR membrane [contributing to cardiomyocyte ultrastructural remodeling and E-C uncoupling (*23*)], and (ii) it liberates JP2NT, allowing JP2NT to translocate to the nucleus and mediate transcriptional reprogramming. In addition, we found that the α-helix region of JP2 contains a previously unappreciated DNA binding domain that mediates selective binding to canonical TATA box motifs and MRE. This DNA binding domain is evolutionarily conserved, suggestive of a dual function for JP2 as a structural protein and transcriptional regulator in other species.

The development and progression of heart failure involves diverse cellular and molecular mechanisms (*41*, *42*). Our ChIP-seq and transcriptomic profiling data suggest that JP2NT suppresses gene transcription by targeting multiple signaling pathways such as inflammatory responses, fibrosis, myocyte hypotrophy, and cell death among others. Taken with the protective effect of JP2NT overexpression in the setting of cardiac stress, this study indicates that JP2NT is an endogenous self-protective stress transducer that conveys the E-C uncoupling signal to the nucleus, regulates transcriptional reprogramming, and ultimately attenuates the progression of heart failure. As JP2 is abundant in all muscle cells (cardiac, skeletal, and smooth muscle), JP2NT may serve as a general protective mechanism antagonizing stress-induced pathological remodeling related to many diseases.

REFERENCES AND NOTES

1. D. E. Clapham, Calcium signaling. *Cell* **131**, 1047–1058 (2007). doi: 10.1016/j.cell.2007.11.028; pmid: 18083096
2. D. M. Bers, Cardiac excitation-contraction coupling. *Nature* **415**, 198–205 (2002). doi: 10.1038/415198a; pmid: 11805843
3. H. Cheng, W. J. Lederer, M. B. Cannell, Calcium sparks: Elementary events underlying excitation-contraction coupling in heart muscle. *Science* **262**, 740–744 (1993). doi: 10.1126/science.8235594; pmid: 8235594
4. M. B. Cannell, H. Cheng, W. J. Lederer, The control of calcium release in heart muscle. *Science* **268**, 1045–1049 (1995). doi: 10.1126/science.7754384; pmid: 7754384
5. J. R. López-López, P. S. Shacklock, C. W. Balke, W. G. Wier, Local calcium transients triggered by single L-type calcium channel currents in cardiac cells. *Science* **268**, 1042–1045 (1995). doi: 10.1126/science.7754383; pmid: 7754383
6. S. Q. Wang, L. S. Song, E. G. Lakatta, H. Cheng, Ca^{2+} signalling between single L-type Ca^{2+} channels and ryanodine receptors in heart cells. *Nature* **410**, 592–596 (2001). doi: 10.1038/35069083; pmid: 11279498
7. E. Page, M. Surdyk-Droske, Distribution, surface density, and membrane area of diadic junctional contacts between plasma membrane and terminal cisterns in mammalian ventricle. *Circ. Res.* **45**, 260–267 (1979). doi: 10.1161/01.RES.45.2.260; pmid: 376173
8. H. Takeshima, S. Komazaki, M. Nishi, M. Iino, K. Kangawa, Junctophilins: A novel family of junctional membrane complex proteins. *Mol. Cell* **6**, 11–22 (2000). pmid: 10949023
9. M. Nishi, A. Mizushima, Ki. Nakagawara, H. Takeshima, Characterization of human junctophilin subtype genes. *Biochem. Biophys. Res. Commun.* **273**, 920–927 (2000). doi: 10.1006/bbrc.2000.3011; pmid: 10891348
10. R. J. van Oort *et al*., Disrupted junctional membrane complexes and hyperactive ryanodine receptors after acute junctophilin knockdown in mice. *Circulation* **123**, 979–988 (2011). doi: 10.1161/CIRCULATIONAHA.110.006437; pmid: 21339484
11. A. Guo *et al*., Overexpression of junctophilin-2 does not enhance baseline function but attenuates heart failure development after cardiac stress. *Proc. Natl. Acad. Sci. U.S.A.* **111**, 12240–12245 (2014). doi: 10.1073/pnas.1412729111; pmid: 25092313
12. A. M. Gómez *et al*., Defective excitation-contraction coupling in experimental cardiac hypertrophy and heart failure. *Science* **276**, 800–806 (1997). doi: 10.1126/science.276.5313.800; pmid: 9115206
13. S. E. Litwin, D. Zhang, J. H. Bridge, Dyssynchronous Ca^{2+} sparks in myocytes from infarcted hearts. *Circ. Res.* **87**, 1040–1047 (2000). doi: 10.1161/01.RES.87.11.1040; pmid: 11090550
14. L. S. Song *et al*., Orphaned ryanodine receptors in the failing heart. *Proc. Natl. Acad. Sci. U.S.A.* **103**, 4305–4310 (2006). doi: 10.1073/pnas.0509324103; pmid: 16537526
15. M. Xu *et al*., Intermolecular failure of L-type Ca^{2+} channel and ryanodine receptor signaling in hypertrophy. *PLOS Biol.* **5**, e21 (2007). doi: 10.1371/journal.pbio.0050021; pmid: 17214508
16. A. Guo, C. Zhang, S. Wei, B. Chen, L. S. Song, Emerging mechanisms of T-tubule remodelling in heart failure. *Cardiovasc. Res.* **98**, 204–215 (2013). doi: 10.1093/cvr/cvt020; pmid: 23393229
17. S. Wei *et al*., T-tubule remodeling during transition from hypertrophy to heart failure. *Circ. Res.* **107**, 520–531 (2010). doi: 10.1161/CIRCRESAHA.109.212324; pmid: 20576937
18. M. Xu *et al*., Mir-24 regulates junctophilin-2 expression in cardiomyocytes. *Circ. Res.* **111**, 837–841 (2012). doi: 10.1161/CIRCRESAHA.112.277418; pmid: 22891046
19. H. D. Wu *et al*., Ultrastructural remodelling of Ca^{2+} signalling apparatus in failing heart cells. *Cardiovasc. Res.* **95**, 430–438 (2012). doi: 10.1093/cvr/cvs195; pmid: 22707157
20. M. Jiang *et al*., JPH-2 interacts with Ca_v-handling proteins and ion channels in dyads: Contribution to premature ventricular contraction-induced cardiomyopathy. *Heart Rhythm* **13**, 743–752 (2016). doi: 10.1016/j.hrthm.2015.10.037; pmid: 26538326
21. S. Minamisawa *et al*., Junctophilin type 2 is associated with caveolin-3 and is down-regulated in the hypertrophic and dilated cardiomyopathies. *Biochem. Biophys. Res. Commun.* **325**, 852–856 (2004). doi: 10.1016/j.bbrc.2004.10.107; pmid: 15541368
22. H. B. Zhang *et al*., Ultrastructural uncoupling between T-tubules and sarcoplasmic reticulum in human heart failure. *Cardiovasc. Res.* **98**, 269–276 (2013). doi: 10.1093/cvr/cvt030; pmid: 23405000
23. C. Y. Wu *et al*., Calpain-dependent cleavage of junctophilin-2 and T-tubule remodeling in a mouse model of reversible heart failure. *J. Am. Heart Assoc.* **3**, e000527 (2014). doi: 10.1161/JAHA.113.000527; pmid: 24958777
24. A. Guo *et al*., Molecular Determinants of Calpain-dependent Cleavage of Junctophilin-2 Protein in Cardiomyocytes. *J. Biol. Chem.* **290**, 17946–17955 (2015). doi: 10.1074/jbc.M115.652396; pmid: 26063807
25. Y. Wang *et al*., Targeting Calpain for Heart Failure Therapy: Implications From Multiple Murine Models. *JACC Basic Transl. Sci.* **3**, 503–517 (2018). doi: 10.1016/j.jacbts.2018.05.004; pmid: 30175274
26. J. D. Molkentin *et al*., A calcineurin-dependent transcriptional pathway for cardiac hypertrophy. *Cell* **93**, 215–228 (1998). doi: 10.1016/S0092-8674(00)81573-1; pmid: 9568714
27. N. Frey, T. A. McKinsey, E. N. Olson, Decoding calcium signals involved in cardiac growth and function. *Nat. Med.* **6**, 1221–1227 (2000). doi: 10.1038/81321; pmid: 11062532
28. R. Passier *et al*., CaM kinase signaling induces cardiac hypertrophy and activates the MEF2 transcription factor in vivo. *J. Clin. Invest.* **105**, 1395–1406 (2000). doi: 10.1172/JCI8551; pmid: 10811847
29. J. Backs, K. Song, S. Bezprozvannaya, S. Chang, E. N. Olson, CaM kinase II selectively signals to histone deacetylase 4 during cardiomyocyte hypertrophy. *J. Clin. Invest.* **116**, 1853–1864 (2006). doi: 10.1172/JCI27438; pmid: 16767219
30. X. Wu *et al*., Local InsP3-dependent perinuclear Ca^{2+} signaling in cardiac myocyte excitation-transcription coupling. *J. Clin. Invest.* **116**, 675–682 (2006). doi: 10.1172/JCI27374; pmid: 16511602
31. M. Colella *et al*., Ca^{2+} oscillation frequency decoding in cardiac cell hypertrophy: Role of calcineurin/NFAT as Ca^{2+} signal integrators. *Proc. Natl. Acad. Sci. U.S.A.* **105**, 2859–2864 (2008). doi: 10.1073/pnas.0712316105; pmid: 18287024
32. S. R. Houser, J. D. Molkentin, Does contractile Ca^{2+} control calcineurin-NFAT signaling and pathological hypertrophy in cardiac myocytes? *Sci. Signal.* **1**, pe31 (2008). doi: 10.1126/scisignal.125pe31; pmid: 18577756
33. A. S. Galvez *et al*., Cardiomyocyte degeneration with calpain deficiency reveals a critical role in protein homeostasis. *Circ. Res.* **100**, 1071–1078 (2007). doi: 10.1161/01.RES.0000261938.28365.11; pmid: 17332428
34. C. Patterson, A. L. Portbury, J. C. Schisler, M. S. Willis, Tear me down: Role of calpain in the development of cardiac ventricular hypertrophy. *Circ. Res.* **109**, 453–462 (2011). doi: 10.1161/CIRCRESAHA.110.239749; pmid: 21817165
35. D. J. Williams, H. L. Puhl 3rd, S. R. Ikeda, Rapid modification of proteins using a rapamycin-inducible tobacco etch virus protease system. *PLOS ONE* **4**, e7474 (2009). doi: 10.1371/journal.pone.0007474; pmid: 19830250
36. C. J. Sigrist *et al*., PROSITE: A documented database using patterns and profiles as motif descriptors. *Brief. Bioinform.* **3**, 265–274 (2002). doi: 10.1093/bib/3.3.265; pmid: 12230035
37. G. Narasimhan *et al*., Mining protein sequences for motifs. *J. Comput. Biol.* **9**, 707–720 (2002). doi: 10.1089/10665270276103414 5; pmid: 12487759
38. J. Wysocka, P. T. Reilly, W. Herr, Loss of HCF-1-chromatin association precedes temperature-induced growth arrest of tsBN67 cells. *Mol. Cell. Biol.* **21**, 3820–3829 (2001). doi: 10.1128/MCB.21.11.3820-3829.2001; pmid: 11340173
39. D. Sayed, M. He, Z. Yang, L. Lin, M. Abdellatif, Transcriptional regulation patterns revealed by high resolution chromatin immunoprecipitation during cardiac hypertrophy. *J. Biol. Chem.* **288**, 2546–2558 (2013). doi: 10.1074/jbc.M112.429449; pmid: 23229551
40. F. J. Naya, C. Wu, J. A. Richardson, P. Overbeek, E. N. Olson, Transcriptional activity of MEF2 during mouse embryogenesis monitored with a MEF2-dependent transgene. *Development* **126**, 2045–2052 (1999). pmid: 10207130
41. J. O. Mudd, D. A. Kass, Tackling heart failure in the twenty-first century. *Nature* **451**, 919–928 (2008). doi: 10.1038/nature06798; pmid: 18288181
42. J. H. van Berlo, M. Maillet, J. D. Molkentin, Signaling effectors underlying pathologic growth and remodeling of the heart. *J. Clin. Invest.* **123**, 37–45 (2013). doi: 10.1172/JCI62839; pmid: 23281408

ACKNOWLEDGMENTS

We thank M. J. Welsh, K. P. Campbell, E. D. Abel, B. London, L. Yang (University of Iowa), and S. R. W. Chen (University of Calgary) for reading the manuscript and providing constructive comments, S. R. Ikeda (NIAAA/NIH) for providing TEVp plasmids, and W. Kutschke for technique aids in animal surgery. **Funding:** This work was funded by NIH R01 HL090905, HL130346, VA 1I01BX002334 (L.S.S.), AHA 16SDG30820003 (A.G.); NIH R01 HL125436 (C.G.), OD019941 (B.W.), and China NSF 81570293 (J.H.). **Author contributions:** L.S.S. supervised the project; A.G. and L.S.S. designed the study; A.G., Y.W., B.C., J.Y., L.Y.Z., D.H., J.W., Y.S., Q.Z., C.C., R.W., and X.Z. performed the experiments and data analysis; Y.W. (Yunhao) and A.G. performed bioinformatics analyses; C.G., M.E.A, F.Z., K.F.A., C.M., M.P., W.Z., and J.H. participated in supervision of experiments, data analysis, interpretations and revision of the manuscript. A.G. and L.S.S. wrote the manuscript. All authors reviewed the results and edited and approved the final version of the manuscript. **Competing interests:** The authors have no conflicting financial interests. **Data and materials availability:** Microarray and Sequencing data are available at NCBI Gene Expression Omnibus (GEO) with accession numbers GSE121545, GSE121546, and GSE121547. All other data are available in the manuscript or the supplementary materials.

SUPPLEMENTARY MATERIALS

www.sciencemag.org/content/362/6421/eaan3303/suppl/DC1
Materials and Methods
Figs. S1 to S10
Tables S1 to S5
References (*43*–*55*)

8 April 2017; resubmitted 10 May 2018
Accepted 24 October 2018
Published online 8 November 2018
10.1126/science.aan3303

FORCEFORSCIENCE.ORG

STAND TOGETHER
Be a Force for Science

GET THE FACTS

Understand the science behind the issues that matter.

FOLLOW AAAS ADVOCACY

Champion public discussion and evidence-based policy.

TAKE ACTION

Learn ways you can become an advocate and stand up for science.

AMERICAN ASSOCIATION FOR THE ADVANCEMENT OF SCIENCE

AAAS

RESEARCH ARTICLE SUMMARY

STRUCTURAL BIOLOGY

Structure of human TFIID and mechanism of TBP loading onto promoter DNA

Avinash B. Patel*, Robert K. Louder*, Basil J. Greber, Sebastian Grünberg, Jie Luo, Jie Fang, Yutong Liu, Jeff Ranish, Steve Hahn, Eva Nogales†

INTRODUCTION: In eukaryotes, transcription initiation starts with the assembly of the transcription preinitiation complex (PIC) onto promoter DNA. The PIC comprises the general transcription factors and RNA polymerase II (Pol II). The general transcription factor IID (TFIID) is responsible for initially recognizing the core promoter. Human TFIID is a trilobed (lobes A, B, and C) complex composed of TATA box binding–protein (TBP) and 13 evolutionarily conserved TBP-associated factors (TAF1 to TAF13), with six TAFs present in two copies. Together, TBP and the TAF subunits of TFIID directly interact with promoter DNA with the assistance of TFIIA, forming a platform for the assembly of the rest of the PIC.

RATIONALE: A key challenge in understanding the molecular basis behind TFIID's recognition of promoter DNA is the lack of a complete structural depiction of the complex. We used cryo–electron microscopy (cryo-EM) to describe the various biochemical and/or conformational states of the complex, thus providing information on both the structure and dynamics of TFIID and its interaction with promoter DNA.

RESULTS: We report the cryo-EM structure of TFIID with a resolution of 4.3 Å for lobe C, 4.5 Å for lobe B, and 9.8 Å for lobe A. Together with chemical cross-linking mass spectrometry and structure prediction, we generated a complete structural model of the evolutionarily conserved core of TFIID. TFIID is built on a dimeric scaffold of TAFs, containing at its center a TAF6 dimer in lobe C that connects to lobes A and B. Lobes A and B are both organized around TAF4, -5, -6, -9, -10, and -12 but include additional subunits that result in distinct function (see the figure). Lobe A, which contains TAF11 and TAF13 interacting with TBP, keeps TBP inhibited unless TFIID is promoter bound, at which point it loads TBP onto DNA. Lobe B contains TAF8, which extends to hold lobes B and C together rigidly. Lobe B positions TAF4 in place to stabilize upstream DNA binding and recruits TFIIA. Lobe C, in addition to TAF6 and TAF8, contains TAF1, -2, and -7, which bind the downstream core promoter sequences.

ON OUR WEBSITE

Read the full article at http://dx.doi.org/10.1126/science.aau8872

Using computational sorting of cryo-EM images, we characterized the conformational landscape of apo-TFIID and TFIID in the presence of TFIIA and promoter DNA. Two major states for apo-TFIID (termed the canonical and extended states) were observed, and three additional states (termed the scanning, rearranged, and engaged states) were observed in the presence of TFIIA and core promoter DNA. Lobe A, which migrates 150 Å from its position near lobe C in the canonical state to near lobe B in the extended state, carries TBP in a repressed state that is only released in the context of promoter binding. Identification of distinct TFIID states allowed us to generate a mechanistic model for TFIID promoter binding (see the figure). We propose that TFIID first binds the downstream core promoter elements through TAF1 and TAF2. This binding and the flexible attachment of lobe A help position the upstream DNA in proximity to TBP. TBP then scans for a TATA box or its sequence variants. Engagement of upstream core promoter sequences by TBP is facilitated by TFIIA interacting with TAF4 and TAF12 within lobe B. When TBP finally binds the promoter, it releases from lobe A, opening the binding site for TFIIB, which can then recruit Pol II.

The structure of TFIID also allowed us to deduce the position of various regulatory domains of TFIID involved in contacts with transcriptional activators and active chromatin marks that are responsible for recruiting and modulating TFIID function.

CONCLUSION: Our studies lead to a mechanistic model of how TFIID prevents TBP from nonspecifically engaging with DNA outside of gene promoters, thus preventing aberrant PIC assembly and erroneous transcription initiation. Our model also suggests how TFIID loads TBP onto TATA-less promoters and how activators and chromatin marks may direct TFIID recruitment and PIC assembly. ■

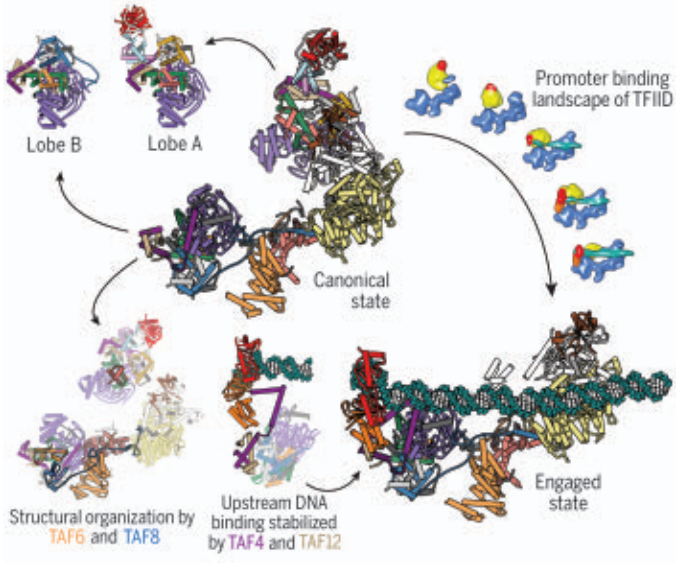

Structure of human TFIID. The structure of apo-TFIID is shown in the canonical state and that of promoter-bound TFIID is depicted in the engaged state. Lobes A and B in TFIID share a similar architecture that contains histone-fold domains organized in a manner that resembles a histone octamer. The TAF6 subunit of TFIID dimerizes the core set of TAFs. The TAF8 subunit rigidly tethers together lobes B and C. Five states of TFIID were observed in the process of promoter binding, leading to a mechanistic model of TBP loading onto the promoter DNA.

The list of author affiliations is available in the full article online.
*These authors contributed equally to this work.
†Corresponding author. Email: enogales@lbl.gov
Cite this article as A. B. Patel *et al.*, *Science* **362**, eaau8872 (2018). DOI: 10.1126/science.aau8872

RESEARCH ARTICLE

STRUCTURAL BIOLOGY

Structure of human TFIID and mechanism of TBP loading onto promoter DNA

Avinash B. Patel[1,2]*, Robert K. Louder[1,2]*†, Basil J. Greber[2,3], Sebastian Grünberg[4]‡, Jie Luo[5], Jie Fang[6], Yutong Liu[7], Jeff Ranish[5], Steve Hahn[4], Eva Nogales[1,2,6,8]§

The general transcription factor IID (TFIID) is a critical component of the eukaryotic transcription preinitiation complex (PIC) and is responsible for recognizing the core promoter DNA and initiating PIC assembly. We used cryo–electron microscopy, chemical cross-linking mass spectrometry, and biochemical reconstitution to determine the complete molecular architecture of TFIID and define the conformational landscape of TFIID in the process of TATA box–binding protein (TBP) loading onto promoter DNA. Our structural analysis revealed five structural states of TFIID in the presence of TFIIA and promoter DNA, showing that the initial binding of TFIID to the downstream promoter positions the upstream DNA and facilitates scanning of TBP for a TATA box and the subsequent engagement of the promoter. Our findings provide a mechanistic model for the specific loading of TBP by TFIID onto the promoter.

The regulation of transcription initiation is arguably the primary method by which the expression of genes is controlled. The transcription preinitiation complex (PIC) is responsible for the loading of RNA polymerase II (Pol II) onto DNA (*1*, *2*). The assembly of the PIC begins with the recognition of the core promoter by transcription factor IID (TFIID), aided by TFIIA (*3*). The TATA box–binding protein (TBP), a component of TFIID, recruits TFIIB, which then loads the Pol II–TFIIF complex (*4*). Lastly, the addition of TFIIE and TFIIH facilitates the opening of the transcription bubble (*5*). Whereas the stepwise assembly of a TBP-based PIC has been well characterized structurally (*6*), the process by which TFIID loads TBP onto the promoter is not well understood.

TFIID is a ~1.3-MDa complex that contains, in addition to TBP, 13 TBP-associating factors (TAFs), with six of them (TAF4, -5, -6, -9, -10, -12) present in two copies (*7*–*9*) (fig. S1). At low resolution, human TFIID is composed of three lobes (lobes A, B, and C), with a fairly rigid connection between lobes B and C and with lobe A more flexibly attached to this "BC core" (*10*). In previous work we showed that in a promoter-bound complex (IIDAS, which we will refer to here as IIDA-SCP) containing TFIID, TFIIA, and the super core promoter (SCP) (*11*), the promoter elements downstream of the transcription start site (TSS) are recognized by TAF1 and TAF2 in lobe C, whereas TBP binds the TATA box upstream of the TSS with the aid of TFIIA and lobe B (*12*).

Here we present cryo–electron microscopy (cryo-EM) structures of human TFIID, alone and in various stages of promoter binding. Together with chemical cross-linking–mass spectrometry (CX-MS) data and biochemical reconstitution, we were able to determine the complete structure of TFIID and the functional conformational landscape of the complex. Our studies lead to a mechanistic model of TBP loading onto the promoter by TFIID and TFIIA and provide insights into how TFIID may engage chromatin, respond to transcriptional activators, and serve as a scaffold for PIC assembly.

Overall structure of TFIID

The flexible nature of TFIID has long hampered a high-resolution structural description of the intact complex (*10*). In previous work, we showed how the distribution of positions of the flexibly attached lobe A shifts upon binding of promoter DNA and TFIIA (*10*). Lobe A in apo-TFIID exists in a bimodal but continuous distribution of states, with roughly equal occupancy of two distinct, major states referred to as the canonical and extended states. Whereas in the canonical state lobe A is near lobe C, in the extended state lobe A is between lobes B and C (Fig. 1A). The displacement of lobe A between these two states is ~100 Å. By sorting a large cryo-EM dataset of free TFIID into two predominant states, refining them independently, and then combining the refined regions, we were able to extend the resolution of the BC core to 4.5 Å (range of 4.2 to 6.5 Å) and to generate a three-dimensional (3D) reconstruction of lobe A at 9.5 Å (range of 8.5 to 15 Å) (Fig. 1B and figs. S2 and S3). We then used a combination of cryo-EM, CX-MS, and structure prediction to generate a complete model of the complex.

Compared with that of the IIDA-SCP structure (*12*), the density corresponding to the TAF1-TAF7 subcomplex within lobe C in apo-TFIID is poorly defined, indicating that this module is flexible in the unbound TFIID, but stabilized upon binding to promoter DNA (figs. S4 and S5). For the rest of lobe C, it was possible to dock into the density the model of the TAF6 HEAT repeat dimer, a segment from the C-terminal region of TAF8, and the TAF2 aminopeptidase-like domain (APD) from the previous IIDA-SCP structure (*12*), with adjustments and extensions made to fit the observed density (Fig. 1, C to E, and fig. S5).

Within lobe B, we were able to fit a homology model of the WD40 domain of TAF5, the crystal structures of the TAF5 NTD2 domain and the histone-fold domain (HFD) heterodimers of TAF6-TAF9, TAF4-TAF12, and TAF8-TAF10, as well as to extend the models where additional densities were present in the cryo-EM map (Fig. 1, C and D, and fig. S5). The resulting atomic model for lobe B is consistent with our CX-MS data (fig. S6) and in agreement with previous biochemical studies (*8*, *13*). To further validate our model, we heterologously coexpressed exclusively those segments of TAFs that we could directly model into the lobe B cryo-EM density, which comprised only 35% of the residues present in the full-length versions of the subunits (fig. S7). Three successive pulldowns using different affinity tags placed on TAF5, TAF4, and TAF8, followed by size exclusion chromatography, resulted in a pure, soluble complex containing stoichiometric amounts of all seven TAF fragments, supporting the formation of a stable complex from the components predicted by our structural model.

All of the TAFs in lobe B, except for TAF8, have been proposed to exist in two copies within TFIID (*8*, *14*), suggesting that a similar architecture could exist within the flexible lobe A. We used a computational strategy based on automated docking of different combinations of TFIID subunits into the lobe A cryo-EM density to generate a complete model of lobe A (fig. S5). The core of the structure is equivalent to lobe B, except for the replacement of TAF8 with TAF3 as the histone-fold partner of TAF10. Additionally, lobe A includes the TAF11-TAF13 HFD pair and TBP (Fig. 1, C and E). Our placement of TAF11-TAF13 adjacent to the TBP subunit is supported by the presence of chemical cross-links between TAF11 and TBP (fig. S6), as well as in vivo and

[1]Biophysics Graduate Group, University of California, Berkeley, CA 94720, USA. [2]Molecular Biophysics and Integrative Bio-Imaging Division, Lawrence Berkeley National Laboratory, Berkeley, CA 94720, USA. [3]California Institute for Quantitative Biology (QB3), University of California, Berkeley, CA 94720, USA. [4]Division of Basic Sciences, Fred Hutchinson Cancer Research Center, Seattle, WA 98109, USA. [5]Institute for Systems Biology, Seattle, WA 98109, USA. [6]Howard Hughes Medical Institute, University of California, Berkeley, CA 94720, USA. [7]Department of Chemical and Biomolecular Engineering, University of California, Berkeley, CA 94720, USA. [8]Department of Molecular and Cell Biology, University of California, Berkeley, CA 94720, USA.
*These authors contributed equally to this work. †Present address: Department of Biology, John Hopkins University, Baltimore, MD 21218, USA. ‡Present address: New England Biolabs, Ipswich, MA 01938, USA. §Corresponding author. Email: enogales@lbl.gov

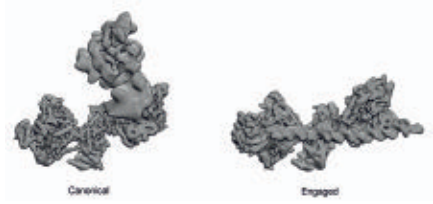

Movie 1. Structural models for the canonical and engaged states of human TFIID. The models are shown within the cryo-EM maps of the two estates aligned on the BC core (different regions of the maps were refined to different resolutions due to their different degrees of flexibility). Lobe A is shown only in the canonical state.

in vitro studies showing that the HFDs of TAF11-TAF13 constitute the bridge between TBP and the rest of TFIID (*15*). Altogether, our structure defines the full architecture of human TFIID, revealing the complete evolutionarily conserved regions of all TAFs and TBP (fig. S1 and Movie 1).

TFIID assembly around a dimeric subcomplex of TAFs

Our structure of human TFIID shows that the complex assembles around a dimeric yet asymmetric arrangement of TAFs (fig. S6). Two copies of interacting TAF6 HEAT repeat domains are found at the center of the BC core, where they form a dimer with a 3_1 screw axis symmetry that bridges lobes B and C (Fig. 2A). The N-terminal HFDs of each copy of TAF6 are then separated between lobes A and B, and thus, TAF6, through the flexible connection between its HFD and HEAT repeat domain, tethers the entire complex together. This TAF6 connection is maintained throughout the various conformational states of TFIID (Fig. 2A). The HFD of TAF6 forms a heterodimer with the HFD of TAF9, which interacts with the WD40 and NTD2 regions of TAF5. The TAF6-TAF9 HFD pair then forms a tetramer with the TAF4-TAF12 HFD pair, and together these five subunits (TAF5, -6, -9, -4, -12) define the TAF subcomplex that is present in two copies within TFIID (Fig. 2B and figs. S7 and S8), one each in lobes A and B. The existence of a dimeric TAF-containing subcomplex has been previously proposed on the basis of in vivo knockdown and in vitro biochemical studies (*8*, *16*). However, the structure within the native TFIID complex does not exhibit the symmetry previously proposed for a reconstituted subcomplex containing the same subunits, likely due to the presence of additional symmetry-breaking TAFs in the fully formed, native complex (*8*) (fig. S7).

The two sets of TAFs (-4, -5, -6, -9, -12) shared between lobes A and B act as a base for the assembly of the rest of each lobe. In lobe B, a hexamer of HFDs is formed by the TAF8-TAF10, TAF6-TAF9, and TAF4-TAF12 HFD pairs. In lobe A, the TAF3-TAF10 and TAF11-TAF13 HFD pairs form an octamer-like structure with the TAF6-TAF9 and TAF4-TAF12 HFD pairs (Fig. 2B and Movie 1). Though the presence of higher-order

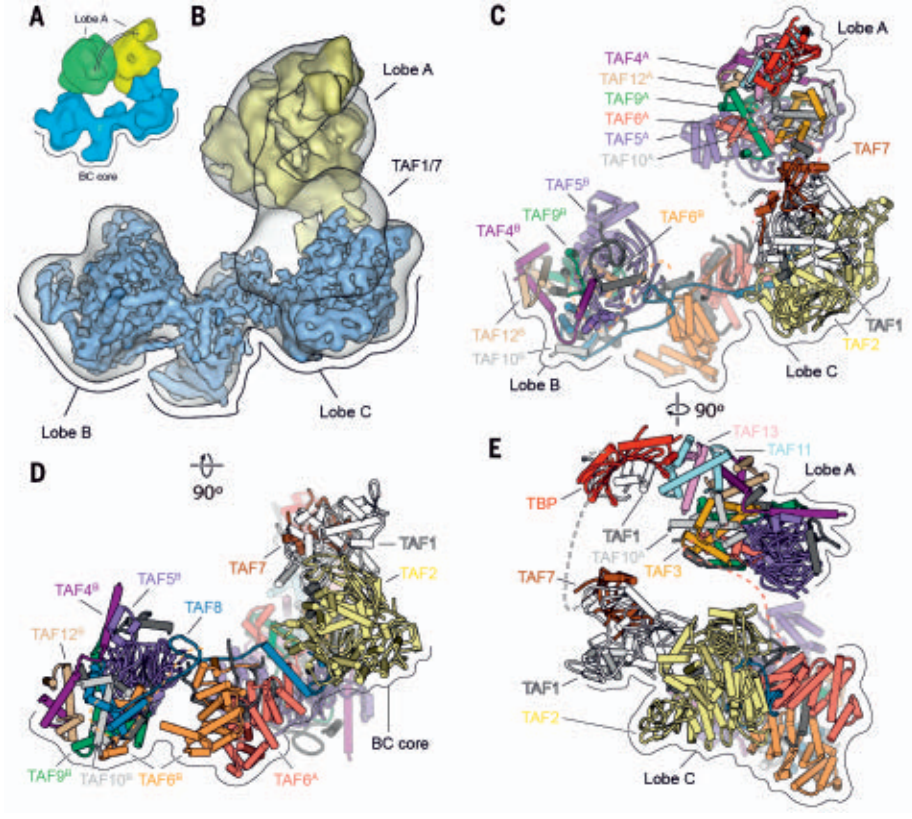

Fig. 1. Cryo-EM structure of TFIID. (**A**) Cryo-EM reconstructions of TFIID, with the BC core in blue and lobe A in yellow (canonical state) and green (extended state). (**B**) Transparent cryo-EM map of TFIID in the canonical state with fitted cryo-EM maps from focused refinements of the BC core and lobe A in solid blue and yellow, respectively. (**C** to **E**) TFIID structural model in front (C), top (D), and side views (E). See also Movie 1.

histone-fold assemblies had been predicted to exist within TFIID, such a structure had not been visualized until now (fig. S8). It has been proposed that these nucleosome corelike structures may be involved in interaction with DNA and promoter binding (*16*–*20*). However, the surfaces of lobes A and B lack the large positively charged patches observed in the nucleosomal histone octamer (fig. S8). The TAF6-TAF9 HFD pair that was proposed to interact with the downstream DNA (*20*, *21*) is actually located far from the DNA in the IIDA-SCP complex (fig. S8). We instead propose that HFDs serve as a structural scaffold within TFIID.

The difference in the flexibility of lobes A and B is likely due to the presence of TAF8 in lobe B, which stabilizes its connection with lobe C (Fig. 2C). In our model, the highly conserved middle region of TAF8 (residues 130 to 235) snakes through the BC core, interacting extensively with TAF2 and TAF6. Extending from its N-terminal HFD, the TAF6 interacting domain (6iD) of TAF8 forms a bridge between the WD40 of TAF5 in lobe B and the first of the HEAT repeats of TAF6 (Fig. 2D). The long helix of the TAF2-interacting domain (2iD) of TAF8 then bridges the second TAF6 HEAT repeat and TAF2, and then TAF8 folds onto the surface of the TAF2 APD, effectively anchoring TAF2 to the rest of the complex. This network of interactions among TAF8, TAF6, and TAF2 (Fig. 2E) is consistent with previous biochemical studies (*8*, *13*).

Role of lobe B in the stabilization of upstream DNA binding

Our structural studies indicate that the function of lobe B is to stabilize the upstream DNA and bind TFIIA. Both of these functions involve the highly conserved C terminus of TAF4 (Fig. 3A). The HFD of TAF4, comprising helices α1 and α2, is followed by a large loop and a helix (α3) that interacts with the WD40 of TAF5 (Fig. 3B). Docking of the lobe B structure into the IIDA-SCP map reveals that the highly conserved loop between α3 and a fourth helix in TAF4 (α4) contacts the promoter DNA just downstream of the TATA box (Fig. 3, C and D, and fig. S4). This loop has previously been shown to bind DNA in vitro (*20*), and in TAF4$^{-/-}$ human fibroblast cells, stable expression of a TAF4 mutant lacking this loop results in the down-regulation of a subset of genes (*22*). From there, α4 continues toward the TBP-TFIIA density and is likely involved in TFIIA recruitment and the stabilization of the TFIIA-TBP-DNA module, in agreement with previous data (*23*) (Fig. 3D). The docking of lobe B into the IIDA-SCP map also revealed that the four-helix bundle of TFIIA likely contacts the

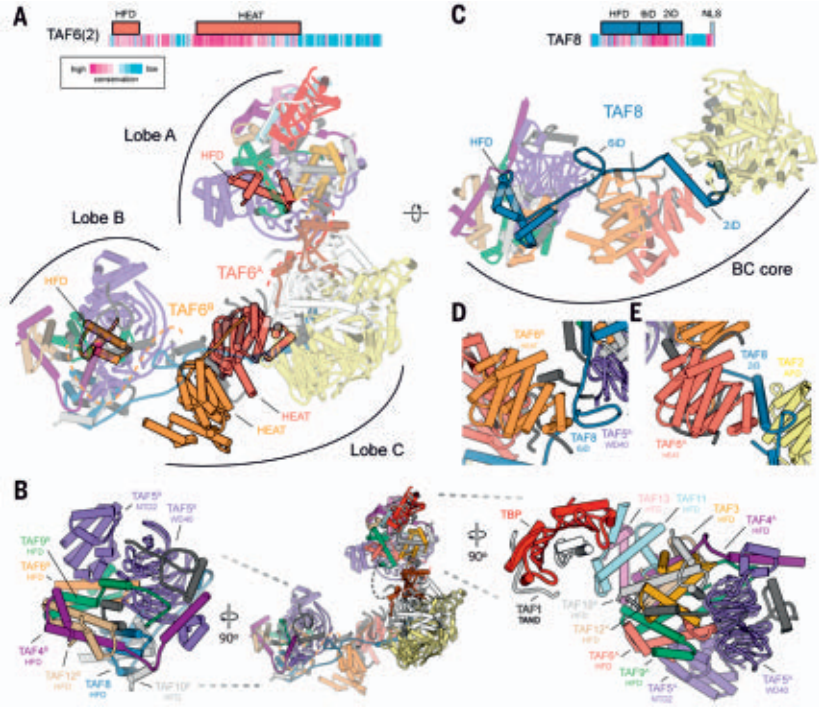

Fig. 2. Structural organization of human TFIID. (**A**) Domain organization of TAF6, with sequence conservation colored according to ConSurf (*69*) scores (top). Model of TFIID with the TAF6 dimer highlighted (bottom). The dimer of TAF6 HEAT repeats is centrally located within the complex. Dashed lines are shown connecting the TAF6 HEAT domains with their corresponding HFDs in lobes A and B. (**B**) Model of TFIID (center) and close-up views of lobe B (left) and lobe A (right). (**C**) Domain organization of TAF8, with sequence conservation colored according to ConSurf (*69*) scores (top). NLS, nuclear localization sequence. Model of the BC core of TFIID with TAF8 highlighted (bottom). (**D**) The 6iD (TAF6 interacting domain) of TAF8 bridges the WD40 domain of TAF5 in lobe B and the HEAT repeat of TAF6 in lobe C. (**E**) The 2iD (TAF2 interacting domain) of TAF8 bridges the HEAT repeat of TAF6 and the APD of TAF2 within lobe C. See also Movie 1.

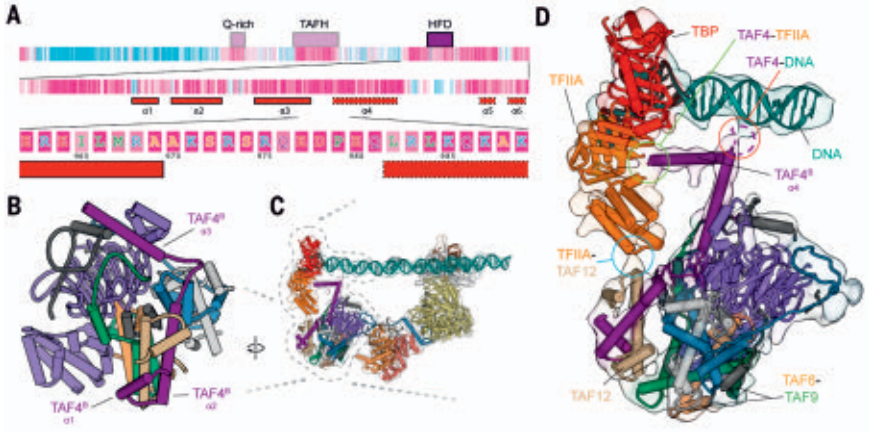

Fig. 3. Upstream promoter binding stabilized by lobe B. (**A**) Domain organization and sequence conservation of TAF4 according to ConSurf (*69*) scores. The first level shows the domain organization of TAF4. The second level zooms in on the C terminus and shows the secondary structure [solid outline corresponds to observed secondary structure and dashed outline to the predicted secondary structure based on PSIPRED (*70*) results (α4 is not visible in the apo-TFIID structure but becomes ordered upon interaction with the DNA)]. The third level shows the amino acid sequence of the loop between helices 3 and 4, which contain several conserved, positively charged residues that could be contacting the DNA. Single-letter abbreviations for the amino acid residues are as follows: A, Ala; C, Cys; D, Asp; E, Glu; F, Phe; G, Gly; H, His; I, Ile; K, Lys; L, Leu; M, Met; N, Asn; P, Pro; Q, Gln; R, Arg; S, Ser; T, Thr; V, Val; W, Trp; and Y, Tyr. (**B**) Structure of lobe B. (**C**) Model of TFIID docked into the IIDAS reconstruction. (**D**) Close-up view of part of (C), highlighting the loop between helices 3 and 4 as it contacts the DNA (circled in red), helix 4 continuing on toward the TFIIA and TBP (circled in green), and the interaction between the TFIIA and TAF12 (circled in blue).

first helix-turn-helix motif of the TAF12 HFD (Fig. 3D). Thus, we propose that TAF4 and TAF12 within lobe B act to promote the binding of TBP to the upstream DNA by directly contacting both the DNA and the TFIIA-TBP module. Therefore, the BC core of TFIID appears to act as a molecular ruler, placing TBP at a defined distance from the downstream promoter elements. This role suggests that maintaining a fairly rigid connection between lobes B and C is important for correctly positioning TBP with respect to the TSS, which in human core promoters are separated by ~30 base pairs (bp) (*24*, *25*) (fig. S8).

Our structure suggests a potential overlap between the contacts that TAF4 makes with the upstream promoter DNA in the IIDA-SCP complex and those established by the TFIIF winged-helix domain within the PIC (*6*, *26*) (fig. S9). Additionally, the downstream promoter binding regions of TAF1 and TAF2 were also found to clash with Pol II in the closed PIC complex, and the path of the downstream promoter in the closed PIC is bent compared with the more linear path observed in the IIDA-SCP complex (*12*) (fig. S9). Thus, significant structural rearrangements in TFIID must occur during PIC assembly and transcription initiation, opening the question of whether TFIID can remain promoter bound throughout the transcription initiation cycle.

Role of lobe A movement in TBP loading

To gain insight into potential intermediate states in the process of TFIID binding to promoter DNA, we carried out cryo-EM analysis of a sample containing TFIID, TFIIA, and SCP DNA that was a mixture of DNA-bound and unbound complexes. Extensive 3D sorting revealed the presence of five different states of TFIID that we propose correspond to different stages in its engagement with the promoter (Fig. 4, fig. S10, and Movie 2). We observed the same canonical

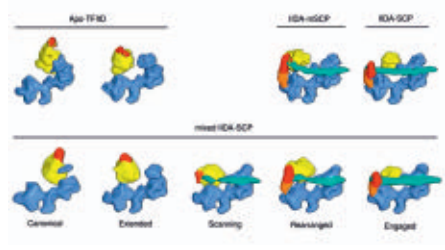

Movie 2. Functional states of TFIID during binding to core promoter DNA and TFIIA. Cryo-EM maps were obtained for apo-TFIID (canonical and extended); for purified mutant-SCP–bound TFIID-TFIIA (rearranged); for purified SCP-bound TFIID-TFIIA (engaged); and from a mixture of TFIID, TFIIA, and DNA (all states). Atomic models were fit into the cryo-EM structures of the canonical, extended, rearranged, and engaged state and then used to generate a model of how TFIID transitions structurally through the process of core promoter binding.

and extended states that we saw in the free TFIID sample (Figs. 1A and 4, A and B), as well as the "engaged" state we previously described for the promoter-purified IIDA-SCP complex (*12*) (Fig. 3C and 4E). Additionally, we identified a state in which lobe A is rotated toward lobe B, and TBP appears to occupy a conformation that would permit it to scan the DNA. We refer to this state, which includes only TFIID and DNA (no TFIIA), as the scanning state (Fig. 4C). The last state, called the rearranged state [described at low resolution in one of our previous studies (*10*)], resembles the scanning state, but with the presence of TFIIA constraining the motion of lobe A and TBP within it. In both the scanning and rearranged states, the downstream DNA is stably bound to TFIID, whereas the upstream region remains flexible, as indicated by the poor density observed for the upstream DNA (Fig. 4D).

By combining the mapping of TBP positions through the various states of promoter binding with previous biochemical and structural studies, we are able to propose a model of how TBP within TFIID would transition from being inhibited to being DNA engaged. We propose that in the canonical and extended states, TBP is bound by the TAND of TAF1 and by TAF11-TAF13 within lobe A, both of which have been found to inhibit TBP from binding DNA (*15*, *27*) (Fig. 4, A and B). The N terminus of the TAF1 TAND (TAND1) interacts with the DNA-binding cleft of TBP, whereas TAND2 binds the outer surface of TBP where a number of different TBP-interacting factors are known to interact, including TFIIA (*28*) (Fig. 4, A and B). In the scanning state, we propose that DNA displaces TAND1 and interacts with the cleft of TBP, but that the DNA remains in a linear, unbent form (Fig. 4C), owing to a lack of defined DNA-TBP interaction, in contrast with what is seen for the bent DNA-TBP interaction (Fig. 4E). In the rearranged state, TFIIA would displace TAND2, releasing the connection between TAF1 and TBP and stabilizing the connection between lobes A and B (*26*, *28*–*30*) (Fig. 4D). Finally, in the engaged state, TBP forms a stable complex with bent DNA, which causes the connection between TBP and TAF11 to break and TBP to release from lobe A (Fig. 4E). This last step of lobe A release is essential for recruitment of TFIIB and for the assembly of the PIC, as it opens up the surface on TBP for TFIIB binding (*31*) (Fig. 4F).

Though TBP binds the TATA box sequence with the highest affinity of any DNA sequence, it has been observed to be a relatively indiscriminate DNA binder (*32*, *33*). The mechanisms of TBP inhibition within lobe A effectively represent an important role of TFIID as a TBP chaperone, stopping TBP from nonspecifically engaging with DNA outside of gene promoters, and therefore preventing aberrant PIC assembly and erroneous transcription initiation (*33*). We propose that, at the same time, the architecture and dynamics of TFIID facilitate the proper loading of TBP at core promoters by progressively releasing those inhibitory interactions with TAFs, and, as explained below, strategically positioning TBP onto the upstream DNA.

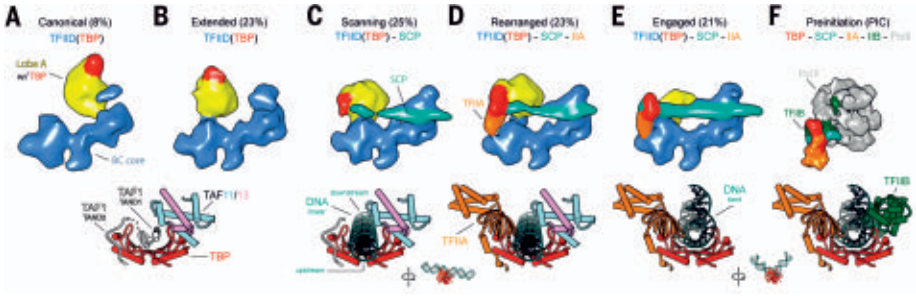

Fig. 4. Regulation of TBP DNA-binding activity by lobe A. Reconstructions of TFIID from the mixed dataset (which includes SCP and TFIIA), showing TFIID in the canonical (**A**), extended (**B**), scanning (**C**), rearranged (**D**), and engaged (**E**) states. (**F**) Human PIC cryo-EM map (EMD-2304) containing Pol II, TFIIA, TFIIB, TBP, and promoter DNA (*6*). Models for TBP (PIC: PDB 5IYA) and its interacting partners are shown below each corresponding reconstruction. See also Movie 2.

Fig. 5. Mechanism of TBP loading by TFIID. (**A**) Cryo-EM reconstructions of the canonical, extended, rearranged, and engaged states of TFIID superimposed onto the BC core to show the range of motion of lobe A and TBP. The TAF1-TAF7 module is positioned according to the engaged state reconstruction, and the DNA models for both the engaged and rearranged states are shown. (**B**) Cartoon schematic for the process of TBP loading onto promoter DNA by TFIID, with subsequent PIC recruitment, assembly, and progression to the elongation complex. See also Movie 2.

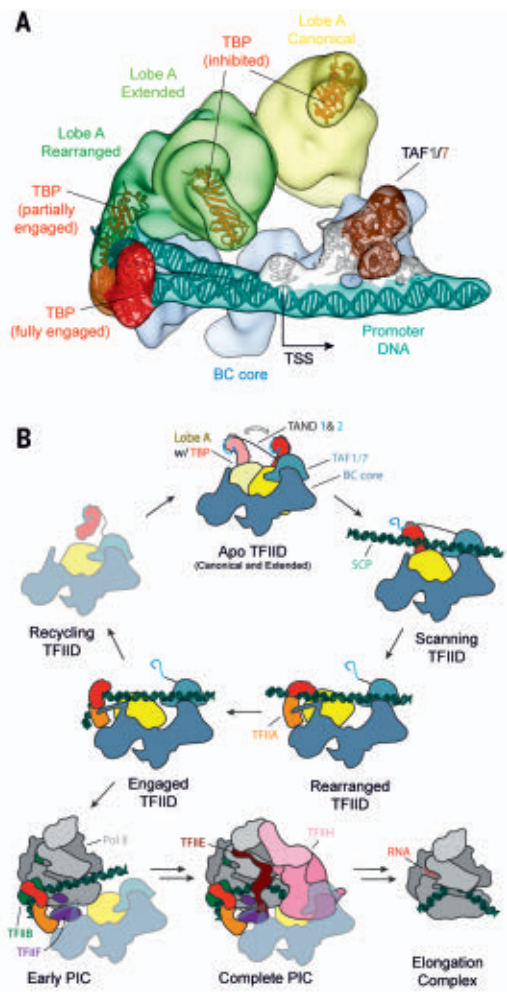

Proposed mechanism of TBP loading by TFIID and consequent PIC recruitment

Superposition of the five conformational states of TFIID—canonical, extended, scanning, rearranged, and engaged—illustrates the range of motion TBP experiences with respect to the BC core during the steps leading to full promoter engagement (Fig. 5A and Movie 2). The distance that TBP travels between these states is approximately 130, 40, 30, and 50 Å, respectively, and follows a curved path that directs TBP toward the upstream DNA. Taken together, these structures suggest a stepwise mechanism of TBP loading onto the promoter and the consequent recruitment of the rest of the PIC. In the first step, TAF1-TAF7 and TAF2 in lobe C bind to downstream DNA. This initial DNA binding facilitates the positioning of the TATA box where

it can be reached by TBP as it travels with the mobile lobe A, thus helping the upstream DNA outcompete the inhibitory TAND1 from the cleft of TBP. In the second step, TFIIA displaces TAND2 from TBP and likely stabilizes the upstream DNA through its interaction with lobe B. In this way, the rearranged state constrains the position of lobe A and facilitates TBP binding to the upstream DNA. In the third step, TBP fully engages the promoter DNA, bending it and simultaneously causing a steric clash between the DNA and TAF11 that results in the release of TBP from the rest of lobe A (Fig. 5B and Movie 2).

In the fourth step, TFIIB recognizes the fully engaged TBP-DNA complex and recruits with it Pol II-TFIIF. At this stage, the binding of the TFIIF winged-helix domain in Rap40 and Pol II would displace the TAF4 contact with upstream DNA and the interactions of lobe C with downstream core promoter sequences, respectively. This process could potentially result in the TAFs falling off of the PIC, unless the interaction between TFIIA and TAF4 was sufficient to keep TFIID bound or new contacts were to form between TFIID and the PIC at this stage of the assembly. Although a number of interactions have been reported between TFIID and other general transcription factors in vitro (*34*–*37*), it has been shown that upon the addition of Pol II-TFIIB-TFIIF, TFIID remains associated with the promoter only in the presence of activators (*38*, *39*). In this potential scenario, TFIID may not remain as part of the growing PIC but could instead bind another TBP to enable formation of a new active complex once the previous complex clears the promoter (Fig. 5B). Additional experiments will be required to test this model and determine the precise role of TFIID in PIC assembly after TBP loading.

Approximately 80% of eukaryotic promoters lack a canonical TATA box, yet loading of TBP is essential to initiate transcription for all protein genes (*40*). The mechanism of TBP loading by TFIID provides a way to promote TBP loading in the absence of a canonical TATA box and expands the potential for regulation through variation in the core promoter sequence. To structurally explore this concept, we assembled a promoter-bound complex by using a mutant SCP (mSCP) that lacked a consensus TATA sequence (ACTGCCGT replacing TATAAAAG). The resulting IIDA-mSCP complex was purified via a DNA-pulldown assay and resulted in a sample that still bound the promoter DNA but appeared trapped in the rearranged state with TBP constrained onto the promoter (fig. S11). We did not observe any complexes in the engaged state, consistent with previous DNase footprinting experiments that showed that TFIID is only able to weakly protect the TATA box by using purified components (*10*). However, both in vitro transcription assays containing nuclear extracts and in vivo reporter assays showed transcription from mSCP templates (*11*, *41*). Those results would indicate that other factors not present in the DNase footprinting experiments, but present in the nuclear extract, must be aiding TBP in the absence of a consensus TATA. Factors such as transcriptional activators, chromatin marks, or other coactivator complexes could play an essential role in allowing transcription from TATA-less promoters by facilitating the transition from the rearranged to the engaged states and thus the full engagement of TBP onto DNA.

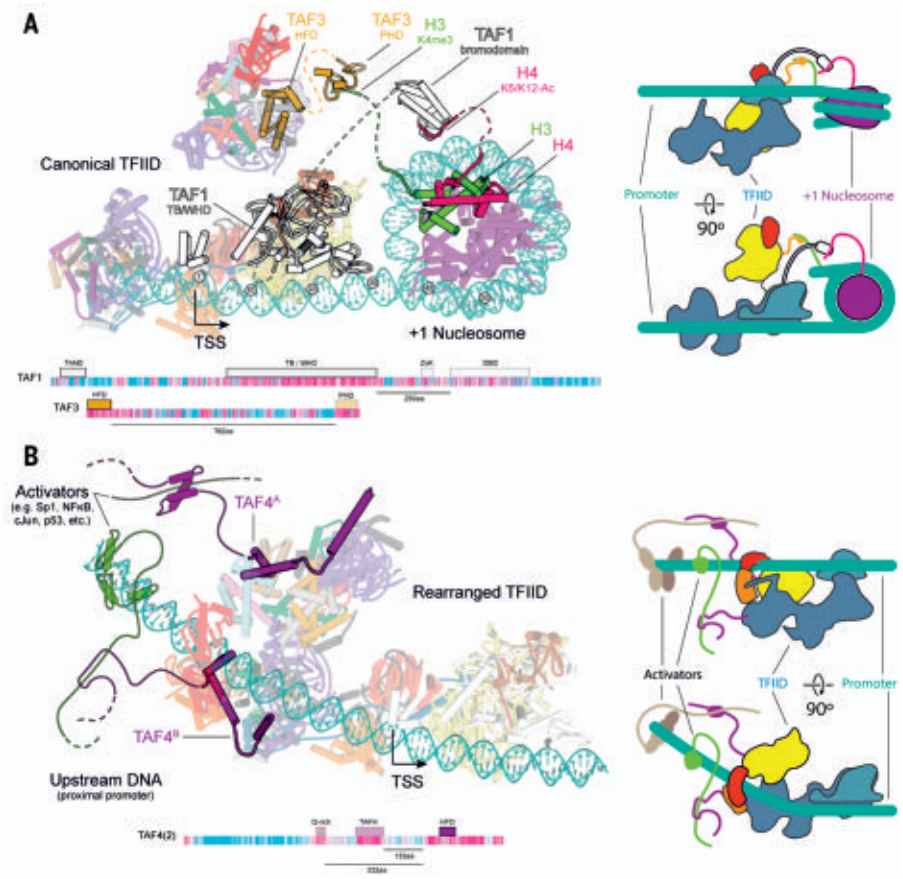

Fig. 6. Model of TFIID recruitment. (**A**) Model of TFIID bound to the promoter including a +1 nucleosome. The model is compatible with the binding of flexible histone tails of H3 and H4 to the PHD [PDB ID 2K17 (*47*)] of TAF3 and the bromodomain of BRD2 [PDB ID 2DVR (*49*)], a homolog of the DBD of TAF1, respectively. Dashed lines indicate the connections between domains contained in the models of TFIID or the nucleosome, with the flexible domains that bridge the two. Domain architecture maps of TAF1 and TAF3 showing the distance between the structured domains modeled within TFIID and the domains that contact chromatin. A cartoon model of TFIID binding to the +1 nucleosome is shown to the right. (**B**) Model of TFIID bound to the core promoter with bound activators at the upstream proximal promoter region. Activators are contacting the N terminus of TAF4 that contains activator interacting regions, like the glutamine-rich and TAFH domains. Domain maps of the highlighted TAFs illustrate the distance between the domains that were part of the TFIID model (solid) and those domains that were not observed (transparent). Distances between the conserved C terminus and the domains that contact activators (TAFH and glutamine-rich) are shown below the domain map. A cartoon model of TFIID binding to activators is shown on the right.

TFIID as a coactivator and chromatin reader

In vivo TFIID recruitment to the core promoter is aided by gene-specific activators and chromatin marks. Promoters are enriched in certain posttranslational modifications of histones and in histone variants that distinguish them from the rest of the genome (*42*). Trimethylation of lysine 4 on histone H3 (H3K4me3) and acetylation of H3 and H4 are especially enriched on the +1 nucleosome (the first nucleosome downstream of the TSS), located ~50 bp downstream of the TSS (*43*–*46*). TFIID recognizes H3K4me3 through the plant homeodomain (PHD) of TAF3 and the diacetylated H4 via the TAF1 double bromodomain (DBD) (*47*–*49*). A model of the downstream promoter extended with a +1 nucleosome shows how these domains, which our studies indicate are flexibly tethered to the core of TFIID, would be oriented toward the +1 nucleosome in the canonical state of TFIID, suggesting a mechanism of TFIID recruitment by the modified +1 nucleosomes of activated genes (Fig. 6A).

Transcriptional activators determine cellular fate by directing the transcription of genes controlling development, differentiation, stimulus response, growth, and maintenance of homeostatic

balance (*50*). Though many activators have been shown to interact with different TAFs, the strongest evidence has been shown for binding of activators through the conserved glutamine-rich and TAFH domains of TAF4 within its long and flexible N terminus (*51*–*53*). A model generated by extending the upstream DNA in the TFIID rearranged state shows how both copies of TAF4 are positioned toward the upstream proximal promoter [which is known to remain cleared of nucleosomes and act as a binding site for transcriptional activators (*45*)] so that they can interact with an activator via their flexible N-terminal domains. This model suggests that transcriptional activators may play a dual role in TFIID recruitment to the promoter, as well as in promoting TBP engagement by stabilizing the rearranged state of TFIID (Fig. 6B).

Implications for the structure and function of the SAGA transcription complex

The insights into the structure and mechanism of TFIID also shed light onto the possible function of the large transcription factor SAGA, as the two complexes share a number of similar components (*54*) (fig. S12A). SAGA contains four main modules of different function: a TBP-loading TAF-containing module, a histone acetyltransferase module, a histone deubiquitinase module, and an activator binding TRRAP module (*55*). In humans, the SAGA TAF module contains TAF9, -10, and -12, which are shared with TFIID, as well as the SAGA-specific TAF5L and TAF6L, which are paralogs to TAF5 and TAF6 in TFIID. In addition, SAGA also contains TADA1, which substitutes for TAF4 in forming a histone fold pair with TAF12; SUPT7, which can form a histone fold pair with TAF10; and SUPT3H, which contains two HFDs homologous to those in TAF11 and -13. Therefore, SAGA contains homologous proteins for all TAFs that make up the dimeric core of TFIID, but whether these exist in two copies within SAGA has not been determined. Using a model of lobe A, we aligned the common SAGA components with those in TFIID and were able to show that within the structurally modeled regions of TFIID, the homologous SAGA subunits are highly conserved (fig. S12B). We were also able to dock the TFIID-derived lobe A model containing only the SAGA homologous regions into the cryo-EM map of the *Pichia pastoris* SAGA complex (*56*), revealing its potential location within the complex (fig. S12C).

The TADA1 subunit of SAGA has a HFD similar to TAF4 but does not appear to retain the conserved C-terminal region that in TFIID interacts with DNA and TFIIA. The SUPT7L subunit of SAGA that could act as a replacement for TAF8 or TAF3 lacks strong sequence similarity to either of them outside of the HFD. The yeast ortholog of SUPT3H, Spt3, binds TBP but with much lower affinity than TAF11-TAF13, as demonstrated by the fact that TBP does not immunopurify with either human or yeast SAGA but can still bind TBP (*54*, *57*). The presence of SUPT3H in SAGA suggests that a lobe A–like module may exist within the complex, but whether such a module is involved in delivering TBP to promoters in vivo remains unclear. Existing models suggest that the activator-binding components within SAGA bring it to the promoter to load TBP (*58*, *59*).

Outlook

Our studies provide a full structural description of human TFIID and its conformational landscape and how these relate to core promoter engagement. The model we propose for TBP loading is likely conserved in eukaryotes as those regions that play critical roles in the process of TBP loading are all highly conserved (TAF1 and TAF2 downstream binding regions; TAF1 TAND, and TAF4 C-terminal regions). Notably, although the regions responsible for contacting the downstream promoter motifs in human TAF1 and TAF2 appear to be conserved in yeast, downstream promoter elements have not been identified in yeast despite a wealth of genomic data. Thus, it is likely that sequence-specific recognition plays a lesser role in downstream promoter binding in yeast TFIID and that other factors, such as activators and chromatin marks, may play a more substantial role in positioning TFIID. Our structures shed light on how TBP is regulated within TFIID to prevent it from nonspecifically binding DNA and starting aberrant transcription events, while simultaneously providing an explanation for how TFIID is able to load TBP onto both TATA and TATA-less promoters. Our structures also suggest how activators and chromatin marks may be directing TFIID recruitment and PIC assembly. Further studies will be needed to dissect the effects that these regulatory factors have on the mechanism of TBP loading and the details of TFIID dynamic rearrangements during PIC assembly.

Methods and materials summary

TFIID was immunopurified from HeLa cells as described previously (*10*). For CX-MS, 100 nM of TFIID was incubated with 150 nM TFIIA and 5 mM BS3 at room temperature for 2 hours and then quenched by the addition of 2.1 μM ammonium bicarbonate. The cross-linked proteins were precipitated with trichloroacetic acid and treated as described (*60*). Mass spectrometry and identification of BS3 cross-linked peptides was performed as described previously (*60*).

For the cryo-EM sample preparation of apo-TFIID, TFIID was cross-linked on ice for 5 min using 0.01% glutaraldehyde, and then 4 μl were applied to a C-flat CF 2/2 holey carbon gird (Protochips) to which a thin continuous carbon film coated with polyethylenimine had been applied to improve orientation distribution. For cryo-EM sample preparation of the mixed IIDA-SCP sample, TFIIA and SCP DNA were added at ~1.2× molar excess to TFIID and incubated for 3 min on ice followed by 2 min at 37°C and finally cross-linked on ice using 0.05% glutaraldehyde for 5 min before grid preparation. For cryo-EM sample preparation of the IIDA-mSCP complex was done as described in (*12*) except that the promoter DNA contained a mutated TATA box, with the sequence TATAAAAG in the original SCP being replaced by ACTGCCGT.

The grids for apo-TFIID and IIDA-mSCP were loaded into a Titan Low-base electron microscope (FEI) and those for mixed IIDA-SCP were loaded into a Titan Krios electron microscope (FEI), and both were operated at 300 keV of acceleration voltage and equipped with a K2 direct electron detector (Gatan). Collected movies were motion corrected using MotionCor2 (*61*), CTF fits were determined using Gctf (*62*), and particles were picked using Gautomatch (version 0.53, from K. Zhang, MRC-LMB, Cambridge). Data processing was performed using Relion (*63*, *64*), model building was carried out with O (*65*) and Coot (*66*), and model refinement was done using Phenix (*67*).

Depictions of molecular models were generated using PyMOL (The PyMOL Molecular Graphics System, version 1.8, Schrödinger) and the UCSF Chimera (*68*) package from the Computer Graphics Laboratory, University of California, San Francisco (supported by National Institutes of Health P41 RR-01081).

REFERENCES AND NOTES

1. D. Reinberg, M. Horikoshi, R. G. Roeder, Factors involved in specific transcription in mammalian RNA polymerase II. Functional analysis of initiation factors IIA and IID and identification of a new factor operating at sequences downstream of the initiation site. *J. Biol. Chem.* **262**, 3322–3330 (1987). pmid: 3818643
2. S. Buratowski, S. Hahn, L. Guarente, P. A. Sharp, Five intermediate complexes in transcription initiation by RNA polymerase II. *Cell* **56**, 549–561 (1989). doi: 10.1016/0092-8674(89)90578-3; pmid: 2917366
3. P. Cortes, O. Flores, D. Reinberg, Factors involved in specific transcription by mammalian RNA polymerase II: Purification and analysis of transcription factor IIA and identification of transcription factor IIJ. *Mol. Cell. Biol.* **12**, 413–421 (1992). doi: 10.1128/MCB.12.1.413; pmid: 1729613
4. O. Flores *et al.*, The small subunit of transcription factor IIF recruits RNA polymerase II into the preinitiation complex. *Proc. Natl. Acad. Sci. U.S.A.* **88**, 9999–10003 (1991). doi: 10.1073/pnas.88.22.9999; pmid: 1946469
5. F. C. Holstege, P. C. van der Vliet, H. T. Timmers, Opening of an RNA polymerase II promoter occurs in two distinct steps and requires the basal transcription factors IIE and IIH. *EMBO J.* **15**, 1666–1677 (1996). doi: 10.1002/j.1460-2075.1996.tb00512.x; pmid: 8612591
6. Y. He, J. Fang, D. J. Taatjes, E. Nogales, Structural visualization of key steps in human transcription initiation. *Nature* **495**, 481–486 (2013). doi: 10.1038/nature11991; pmid: 23446344
7. B. D. Dynlacht, T. Hoey, R. Tjian, Isolation of Coactivators Associated with the TATA-Binding Protein That Mediate Transcriptional Activation. *Cell* **66**, 563–576 (1991). doi: 10.1016/0092-8674(81)90019-2
8. C. Bieniossek *et al.*, The architecture of human general transcription factor TFIID core complex. *Nature* **493**, 699–702 (2013). doi: 10.1038/nature11791; pmid: 23292512
9. L. Tora, A unified nomenclature for TATA box binding protein (TBP)-associated factors (TAFs) involved in RNA polymerase II transcription. *Genes Dev.* **16**, 673–675 (2002). doi: 10.1101/gad.976402; pmid: 11963920
10. M. A. Cianfrocco *et al.*, Human TFIID binds to core promoter DNA in a reorganized structural state. *Cell* **152**, 120–131 (2013). doi: 10.1016/j.cell.2012.12.005; pmid: 23332750
11. T. Juven-Gershon, S. Cheng, J. T. Kadonaga, Rational design of a super core promoter that enhances gene expression. *Nat. Methods* **3**, 917–922 (2006). doi: 10.1038/nmeth937; pmid: 17124735
12. R. K. Louder *et al.*, Structure of promoter-bound TFIID and model of human pre-initiation complex assembly. *Nature* **531**, 604–609 (2016). doi: 10.1038/nature17394; pmid: 27007846
13. S. Trowitzsch *et al.*, Cytoplasmic TAF2-TAF8-TAF10 complex provides evidence for nuclear holo-TFIID assembly from preformed submodules. *Nat. Commun.* **6**, 6011 (2015). doi: 10.1038/ncomms7011; pmid: 25586196
14. S. L. Sanders, K. A. Garbett, P. A. Weil, Molecular characterization of Saccharomyces cerevisiae TFIID. *Mol. Cell. Biol.* **22**, 6000–6013 (2002). doi: 10.1128/MCB.22.16.6000-6013.2002; pmid: 12138208

15. K. Gupta *et al*., Architecture of TAF11/TAF13/TBP complex suggests novel regulation properties of general transcription factor TFIID. *eLife* **6**, e30395 (2017). doi: 10.7554/eLife.30395; pmid: 29111974
16. K. J. Wright, M. T. Marr 2nd, R. Tjian, TAF4 nucleates a core subcomplex of TFIID and mediates activated transcription from a TATA-less promoter. *Proc. Natl. Acad. Sci. U.S.A.* **103**, 12347–12352 (2006). doi: 10.1073/pnas.0605499103; pmid: 16895980
17. A. Hoffmann *et al*., A histone octamer-like structure within TFIID. *Nature* **380**, 356–359 (1996). doi: 10.1038/380356a0; pmid: 8598932
18. W. Selleck *et al*., A histone fold TAF octamer within the yeast TFIID transcriptional coactivator. *Nat. Struct. Biol.* **8**, 695–700 (2001). doi: 10.1038/90408; pmid: 11473260
19. C. Leurent *et al*., Mapping histone fold TAFs within yeast TFIID. *EMBO J.* **21**, 3424–3433 (2002). doi: 10.1093/emboj/cdf342; pmid: 12093743
20. H. Shao *et al*., Core promoter binding by histone-like TAF complexes. *Mol. Cell. Biol.* **25**, 206–219 (2005). doi: 10.1128/MCB.25.1.206-219.2005; pmid: 15601843
21. T. W. Burke, J. T. Kadonaga, The downstream core promoter element, DPE, is conserved from *Drosophila* to humans and is recognized by TAFII60 of *Drosophila*. *Genes Dev.* **11**, 3020–3031 (1997). doi: 10.1101/gad.11.22.3020; pmid: 9367984
22. K. Gazit *et al*., TAF4/4b x TAF12 displays a unique mode of DNA binding and is required for core promoter function of a subset of genes. *J. Biol. Chem.* **284**, 26286–26296 (2009). doi: 10.1074/jbc.M109.011486; pmid: 19635797
23. J. H. Layer, P. A. Weil, Direct TFIIA-TFIID protein contacts drive budding yeast ribosomal protein gene transcription. *J. Biol. Chem.* **288**, 23273–23294 (2013). doi: 10.1074/jbc.M113.486829; pmid: 23814059
24. A. O'Shea-Greenfield, S. T. Smale, Roles of TATA and initiator elements in determining the start site location and direction of RNA polymerase II transcription. *J. Biol. Chem.* **267**, 1391–1402 (1992). pmid: 1730658
25. P. Carninci *et al*., Genome-wide analysis of mammalian promoter architecture and evolution. *Nat. Genet.* **38**, 626–635 (2006). doi: 10.1038/ng1789; pmid: 16645617
26. Y. He *et al*., Near-atomic resolution visualization of human transcription promoter opening. *Nature* **533**, 359–365 (2016). doi: 10.1038/nature17970; pmid: 27193682
27. D. Liu *et al*., Solution structure of a TBP-TAF(II)230 complex: Protein mimicry of the minor groove surface of the TATA box unwound by TBP. *Cell* **94**, 573–583 (1998). doi: 10.1016/S0092-8674(00)81599-8; pmid: 9741622
28. M. Anandapadamanaban *et al*., High-resolution structure of TBP with TAF1 reveals anchoring patterns in transcriptional regulation. *Nat. Struct. Mol. Biol.* **20**, 1008–1014 (2013). doi: 10.1038/nsmb.2611; pmid: 23851461
29. T. Kokubo, M. J. Swanson, J. I. Nishikawa, A. G. Hinnebusch, Y. Nakatani, The yeast TAF145 inhibitory domain and TFIIA competitively bind to TATA-binding protein. *Mol. Cell. Biol.* **18**, 1003–1012 (1998). doi: 10.1128/MCB.18.2.1003; pmid: 9447997
30. S. Bagby *et al*., TFIIA-TAF regulatory interplay: NMR evidence for overlapping binding sites on TBP. *FEBS Lett.* **468**, 149–154 (2000). doi: 10.1016/S0014-5793(00)01213-8; pmid: 10692576
31. D. B. Nikolov *et al*., Crystal structure of a TFIIB-TBP-TATA-element ternary complex. *Nature* **377**, 119–128 (1995). doi: 10.1038/377119a0; pmid: 7675079
32. J. M. Wong, E. Bateman, TBP-DNA interactions in the minor groove discriminate between A:T and T:A base pairs. *Nucleic Acids Res.* **22**, 1890–1896 (1994). doi: 10.1093/nar/22.10.1890; pmid: 8208615
33. R. A. Coleman, B. F. Pugh, Evidence for functional binding and stable sliding of the TATA binding protein on nonspecific DNA. *J. Biol. Chem.* **270**, 13850–13859 (1995). doi: 10.1074/jbc.270.23.13850; pmid: 7775443
34. K. Hisatake *et al*., Evolutionary conservation of human TATA-binding-polypeptide-associated factors TAFII31 and TAFII80 and interactions of TAFII80 with other TAFs and with general transcription factors. *Proc. Natl. Acad. Sci. U.S.A.* **92**, 8195–8199 (1995). doi: 10.1073/pnas.92.18.8195; pmid: 7667268
35. S. Ruppert, R. Tjian, Human TAFII250 interacts with RAP74: Implications for RNA polymerase II initiation. *Genes Dev.* **9**, 2747–2755 (1995). doi: 10.1101/gad.9.22.2747; pmid: 7590250
36. V. Dubrovskaya *et al*., Distinct domains of hTAFII100 are required for functional interaction with transcription factor TFIIF beta (RAP30) and incorporation into the TFIID complex. *EMBO J.* **15**, 3702–3712 (1996). doi: 10.1002/j.1460-2075.1996.tb00740.x; pmid: 8758937
37. A. Gegonne *et al*., TFIID component TAF7 functionally interacts with both TFIIH and P-TEFb. *Proc. Natl. Acad. Sci. U.S.A.* **105**, 5367–5372 (2008). doi: 10.1073/pnas.0801637105; pmid: 18391197
38. N. Yudkovsky, J. A. Ranish, S. Hahn, A transcription reinitiation intermediate that is stabilized by activator. *Nature* **408**, 225–229 (2000). doi: 10.1038/35041603; pmid: 11089979
39. P. Yakovchuk, B. Gilman, J. A. Goodrich, J. F. Kugel, RNA polymerase II and TAFs undergo a slow isomerization after the polymerase is recruited to promoter-bound TFIID. *J. Mol. Biol.* **397**, 57–68 (2010). doi: 10.1016/j.jmb.2010.01.025; pmid: 20083121
40. P. C. FitzGerald, A. Shlyakhtenko, A. A. Mir, C. Vinson, Clustering of DNA sequences in human promoters. *Genome Res.* **14**, 1562–1574 (2004). doi: 10.1101/gr.1953904; pmid: 15256515
41. C. Y. Lim *et al*., The MTE, a new core promoter element for transcription by RNA polymerase II. *Genes Dev.* **18**, 1606–1617 (2004). doi: 10.1101/gad.1193404; pmid: 15231738
42. T. K. Barth, A. Imhof, Fast signals and slow marks: The dynamics of histone modifications. *Trends Biochem. Sci.* **35**, 618–626 (2010). doi: 10.1016/j.tibs.2010.05.006; pmid: 20685123
43. T. H. Kim *et al*., A high-resolution map of active promoters in the human genome. *Nature* **436**, 876–880 (2005). doi: 10.1038/nature03877; pmid: 15988478
44. N. D. Heintzman *et al*., Distinct and predictive chromatin signatures of transcriptional promoters and enhancers in the human genome. *Nat. Genet.* **39**, 311–318 (2007). doi: 10.1038/ng1966; pmid: 17277777
45. D. E. Schones *et al*., Dynamic regulation of nucleosome positioning in the human genome. *Cell* **132**, 887–898 (2008). doi: 10.1016/j.cell.2008.02.022; pmid: 18329373
46. T. N. Mavrich *et al*., Nucleosome organization in the *Drosophila* genome. *Nature* **453**, 358–362 (2008). doi: 10.1038/nature06929; pmid: 18408708
47. H. van Ingen *et al*., Structural insight into the recognition of the H3K4me3 mark by the TFIID subunit TAF3. *Structure* **16**, 1245–1256 (2008). doi: 10.1016/j.str.2008.04.015; pmid: 18682226
48. R. H. Jacobson, A. G. Ladurner, D. S. King, R. Tjian, Structure and function of a human TAFII250 double bromodomain module. *Science* **288**, 1422–1425 (2000). doi: 10.1126/science.288.5470.1422; pmid: 10827952
49. T. Umehara *et al*., Structural basis for acetylated histone H4 recognition by the human BRD2 bromodomain. *J. Biol. Chem.* **285**, 7610–7618 (2010). doi: 10.1074/jbc.M109.062422; pmid: 20048151
50. M. Levine, C. Cattoglio, R. Tjian, Looping back to leap forward: Transcription enters a new era. *Cell* **157**, 13–25 (2014). doi: 10.1016/j.cell.2014.02.009; pmid: 24679523
51. W.-L. Liu *et al*., Structures of three distinct activator-TFIID complexes. *Genes Dev.* **23**, 1510–1521 (2009). doi: 10.1101/gad.1790709; pmid: 19571180
52. E. Hibino *et al*., Identification of heteromolecular binding sites in transcription factors Sp1 and TAF4 using high-resolution nuclear magnetic resonance spectroscopy. *Protein Sci.* **26**, 2280–2290 (2017). doi: 10.1002/pro.3287; pmid: 28857320
53. X. Wang *et al*., Conserved region I of human coactivator TAF4 binds to a short hydrophobic motif present in transcriptional regulators. *Proc. Natl. Acad. Sci. U.S.A.* **104**, 7839–7844 (2007). doi: 10.1073/pnas.0608570104; pmid: 17483474
54. E. Martinez *et al*., Human STAGA complex is a chromatin-acetylating transcription coactivator that interacts with pre-mRNA splicing and DNA damage-binding factors in vivo. *Mol. Cell. Biol.* **21**, 6782–6795 (2001). doi: 10.1128/MCB.21.20.6782-6795.2001; pmid: 11564863
55. D. Helmlinger, L. Tora, Sharing the SAGA. *Trends Biochem. Sci.* **42**, 850–861 (2017). doi: 10.1016/j.tibs.2017.09.001; pmid: 28964624
56. G. Sharov *et al*., Structure of the transcription activator target Tra1 within the chromatin modifying complex SAGA. *Nat. Commun.* **8**, 1556 (2017). doi: 10.1038/s41467-017-01564-7; pmid: 29146944
57. Y. Han, J. Luo, J. Ranish, S. Hahn, Architecture of the *Saccharomyces cerevisiae* SAGA transcription coactivator complex. *EMBO J.* **33**, 2534–2546 (2014). doi: 10.15252/embj.201488638; pmid: 25216679
58. R. Belotserkovskaya *et al*., Inhibition of TATA-binding protein function by SAGA subunits Spt3 and Spt8 at Gcn4-activated promoters. *Mol. Cell. Biol.* **20**, 634–647 (2000). doi: 10.1128/MCB.20.2.634-647.2000; pmid: 10611242
59. E. Larschan, F. Winston, The S. cerevisiae SAGA complex functions in vivo as a coactivator for transcriptional activation by Gal4. *Genes Dev.* **15**, 1946–1956 (2001). doi: 10.1101/gad.911501; pmid: 11485989
60. L. M. Tuttle *et al*., Gcn4-Mediator Specificity Is Mediated by a Large and Dynamic Fuzzy Protein-Protein Complex. *Cell Rep.* **22**, 3251–3264 (2018). doi: 10.1016/j.celrep.2018.02.097; pmid: 29562181
61. S. Q. Zheng *et al*., MotionCor2: Anisotropic correction of beam-induced motion for improved cryo-electron microscopy. *Nat. Methods* **14**, 331–332 (2017). doi: 10.1038/nmeth.4193; pmid: 28250466
62. K. Zhang, Gctf: Real-time CTF determination and correction. *J. Struct. Biol.* **193**, 1–12 (2016). doi: 10.1016/j.jsb.2015.11.003; pmid: 26592709
63. S. H. W. Scheres, RELION: Implementation of a Bayesian approach to cryo-EM structure determination. *J. Struct. Biol.* **180**, 519–530 (2012). doi: 10.1016/j.jsb.2012.09.006; pmid: 23000701
64. D. Kimanius, B. O. Forsberg, S. H. Scheres, E. Lindahl, Accelerated cryo-EM structure determination with parallelisation using GPUs in RELION-2. *eLife* **5**, e18722 (2016). doi: 10.7554/eLife.18722; pmid: 27845625
65. T. A. Jones, Interactive electron-density map interpretation: From INTER to O. *Acta Crystallogr. D* **60**, 2115–2125 (2004). doi: 10.1107/S0907444904023509; pmid: 15572764
66. P. Emsley, B. Lohkamp, W. G. Scott, K. Cowtan, Features and development of Coot. *Acta Crystallogr. D* **66**, 486–501 (2010). doi: 10.1107/S0907444910007493; pmid: 20383002
67. P. D. Adams *et al*., *PHENIX*: A comprehensive Python-based system for macromolecular structure solution. *Acta Crystallogr. D* **66**, 213–221 (2010). doi: 10.1107/S0907444909052925; pmid: 20124702
68. E. F. Pettersen *et al*., UCSF Chimera—a visualization system for exploratory research and analysis. *J. Comput. Chem.* **25**, 1605–1612 (2004). doi: 10.1002/jcc.20084; pmid: 15264254
69. H. Ashkenazy, E. Erez, E. Martz, T. Pupko, N. Ben-Tal, ConSurf 2010: Calculating evolutionary conservation in sequence and structure of proteins and nucleic acids. *Nucleic Acids Res.* **38**, W529–W533 (2010). doi: 10.1093/nar/gkq399; pmid: 20478830
70. D. W. A. Buchan, F. Minneci, T. C. O. Nugent, K. Bryson, D. T. Jones, Scalable web services for the PSIPRED Protein Analysis Workbench. *Nucleic Acids Res.* **41**, W349–W357 (2013). doi: 10.1093/nar/gkt381; pmid: 23748958

ACKNOWLEDGMENTS

We thank S. Zheng for TAF4 monoclonal antibody; D. King for providing TAF4 antibody antigen peptide; A. Iavarone for performing in-gel mass spectrometry data collection and analysis; S. Gradia and Berkeley Macrolab facility for 438 series plasmids; P. Grob, S. Howes, R. Zhang, and L.-A. Carlson for electron microscopy support; A. Chintangal and T. Houweling for computing support; C. Lopez and C. Yoshioka at the OSHU Cryo-EM Facility for help with collecting Krios data; and D. Herbst for discussion. We acknowledge the use of the LAWRENCIUM computing cluster at Lawrence Berkeley National Laboratory and the resources of the National Energy Research Scientific Computing Center, a Department of Energy Office of Science user facility supported by the Office of Science of the U.S. Department of Energy under contract DE-AC02-05CH11231. **Funding:** This work was funded through NIGMS grants R01-GM63072 to E.N., R01-GM053451 to S.H., P50-GM076547 to J.R., and NCI grant R21-CA175849 to J.R. A.B.P. and R.K.L. were supported by an NIGMS Molecular Biophysics Training Grant (GM008295). B.J.G. was supported by fellowships from the Swiss National Science Foundation (projects P300PA_160983 and P300PA_174355). E.N. is a Howard Hughes Medical Institute investigator. **Author contributions:** J.F. purified TFIID. R.K.L. and Y.L. reconstituted lobe B. A.B.P. prepared, collected, and processed the apo-TFIID sample. R.K.L. reprocessed the purified IIDA-SCP sample and prepared, collected, and processed the mixed IIDA-SCP and IIDA-mSCP samples. A.B.P. and B.J.G. built and refined the atomic coordinate model. S.G., J.L., J.R., and S.H. performed cross-linking mass spectrometry analysis of the IIDA sample. A.B.P., R.K.L., and E.N. analyzed data and wrote the paper. **Competing interests:** The authors declare no competing interests. **Data and materials availability:** The cryo-EM maps and refined coordinate models reported here have been deposited in the Electron Microscopy Data Bank with accession codes EMD-9298 (BC core), EMD-9299 (lobe B), EMD-9300 (lobe C), EMD-9302 (lobe A canonical), EMD-9301 (lobe A extended), EMD-9305 (apo-TFIID canonical), and EMD-9306 (IIDA-SCP) and in the Protein Data Bank with accession codes PDB-6MZC (BC core), PDB-6MZD (lobe A), PDB-6MZL (apo-TFIID canonical), and 6MZM (IIDA-SCP engaged).

SUPPLEMENTARY MATERIALS

www.sciencemag.org/content/362/6421/eaau8872/suppl/DC1
Materials and Methods
Figs. S1 to S12
Tables S1 to S3
References (*71*–*95*)

24 July 2018; accepted 6 November 2018
Published online 15 November 2018
10.1126/science.aau8872

RESEARCH ARTICLE SUMMARY

STRUCTURAL BIOLOGY

Structures and gating mechanism of human TRPM2

Longfei Wang*, Tian-Min Fu*†, Yiming Zhou, Shiyu Xia, Anna Greka, Hao Wu†

INTRODUCTION: Transient receptor potential (TRP) melastatin 2 (TRPM2) is a Ca^{2+}-permeable, nonselective cation channel implicated in the development of many inflammatory and neurodegenerative diseases. Human TRPM2 has a C-terminal NUDT9H domain, which shares similarity to the NUDT9 enzyme that hydrolyzes adenosine diphosphate (ADP)–ribose (ADPR). Previous studies showed that TRPM2 is coactivated by ADPR and Ca^{2+}. However, the molecular mechanism of human TRPM2 activation remains elusive.

RATIONALE: To address the gating mechanism of human TRPM2, we aimed to resolve the structures of full-length human TRPM2 in different states. By optimizing expression and purification procedures, we obtained homogeneous recombinant TRPM2 samples from human embryonic kidney (HEK) 293F cells. With single-particle cryo–electron microscopy (cryo-EM), the structures of human TRPM2 alone, in complex with ADPR, and in complex with ADPR and Ca^{2+} were determined to 3.6-, 6.1-, and 6.4-Å resolution, respectively.

RESULTS: Human TRPM2 assembles into a tetramer with a three-tier architecture, which resembles other structures in the TRPM family (see the figure). The bottom tier is composed of the C-terminal NUDT9H domain, the N-terminal MHR1/2 and MHR3 domains, and the pole helix. The middle tier consists of the MHR4 domain and the rib helix, whereas the top tier comprises the S1 to S6 transmembrane helices and the TRP helices, including TRP H1.

One notable feature in the human TRPM2 apo structure is that the NUDT9H domain, which is responsible for sensing ADPR, as shown by binding affinity measurements, folds back to form extensive interactions with the TRPM2 N-terminal domains both in cis and in trans. Upon ADPR binding, the NUDT9H domain and the MHR1/2 domain undergo a 27° rigid-body rotation, which disrupts the trans interaction between NUDT9H and MHR and may prime the channel for opening. Compared with the ADPR-bound structure, the ADPR and Ca^{2+}–doubly bound TRPM2 undergoes a 15° rotation in the cytoplasmic domain, a tilt of the TRP helix, and a twist of the S6 gating helix to open the channel. The structures collectively provide a full depiction for the mechanism of human TRPM2 activation (see the figure).

ON OUR WEBSITE

Read the full article at http://dx.doi.org/10.1126/science.aav4809

In addition, our structures highlight several differences in the gating mechanism of TRPM2 across species. In contrast with our observation that the NUDT9H domain of human TRPM2 is required for channel coactivation by ADPR and Ca^{2+}, the open-state structure of zebrafish TRPM2 revealed an unexpected ADPR-binding site at the MHR1/2 domains. To resolve this inconsistency, we demonstrated that NUDT9H of human TRPM2 has a substantially higher affinity to ADPR than that of zebrafish TRPM2, and that mutation of MHR1/2 residues in human TRPM2 equivalent to the ADPR-binding residues in zebrafish TRPM2 does not compromise human TRPM2 channel opening. A second major difference is that the P loop of NUDT9H responsible for the trans interaction in human TRPM2 is absent in NUDT9H of zebrafish TRPM2, which does not closely associate with the MHR arm in the apo state. Moreover, in comparison with sea anemone TRPM2, in which the NUDT9H domain hydrolyzes ADPR but does not contribute to channel opening, NUDT9H of human TRPM2 binds ADPR to promote channel opening but does not degrade ADPR. Together, these species-specific features reflect functional and mechanistic complexity in TRPM2 and the TRP superfamily during evolution.

CONCLUSION: Structures of human TRPM2 alone, in complex with ADPR, and in complex with ADPR and Ca^{2+} elucidate the mechanism of TRPM2 gating and provide a framework for the understanding of TRPM2-associated diseases. Although it is conserved across species that TRPM2 is coactivated by ADPR and Ca^{2+}, the organization of the NUDT9H domain and how the orthologs respond to ADPR seem to diverge on the basis of our and previously resolved structures of TRPM2. Moreover, our structures reveal an important role of the TRP helix in TRPM2 gating, which may be universal in many other TRP channels. ■

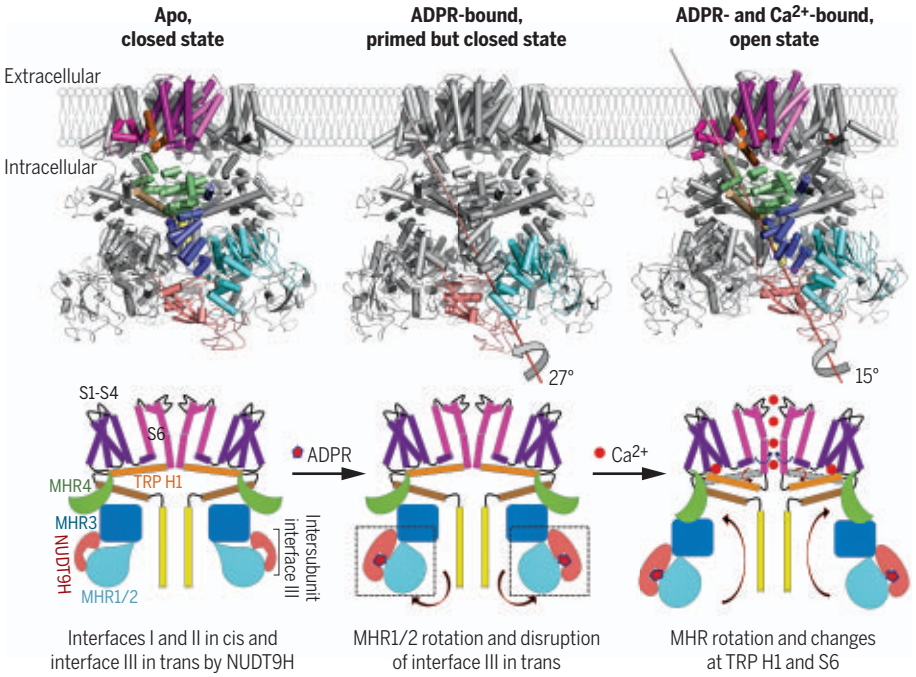

Activation mechanism of the human TRPM2 channel. Cryo-EM structures of full-length human TRPM2 in apo (closed), ADPR-bound (closed), and ADPR- and Ca^{2+}-bound (open) states and corresponding cartoons that illustrate the gating process of the channel.

The list of author affiliations is available in the full article online.
*These authors contributed equally to this work.
†Corresponding author. Email: tianmin.fu@childrens.harvard.edu (T.-M.F.); wu@crystal.harvard.edu (H.W.)
Cite this article as L. Wang *et al.*, *Science* **362**, eaav4809 (2018). DOI: 10.1126/science.aav4809

RESEARCH ARTICLE

STRUCTURAL BIOLOGY

Structures and gating mechanism of human TRPM2

Longfei Wang[1,2]*, Tian-Min Fu[1,2]*†, Yiming Zhou[3,4], Shiyu Xia[1,2], Anna Greka[3,4], Hao Wu[1,2]†

Transient receptor potential (TRP) melastatin 2 (TRPM2) is a cation channel associated with numerous diseases. It has a C-terminal NUDT9 homology (NUDT9H) domain responsible for binding adenosine diphosphate (ADP)–ribose (ADPR), and both ADPR and calcium (Ca^{2+}) are required for TRPM2 activation. Here we report cryo–electron microscopy structures of human TRPM2 alone, with ADPR, and with ADPR and Ca^{2+}. NUDT9H forms both intra- and intersubunit interactions with the N-terminal TRPM homology region (MHR1/2/3) in the apo state but undergoes conformational changes upon ADPR binding, resulting in rotation of MHR1/2 and disruption of the intersubunit interaction. The binding of Ca^{2+} further engages transmembrane helices and the conserved TRP helix to cause conformational changes at the MHR arm and the lower gating pore to potentiate channel opening. These findings explain the molecular mechanism of concerted TRPM2 gating by ADPR and Ca^{2+} and provide insights into the gating mechanism of other TRP channels.

The transient receptor potential melastatin (TRPM) family belongs to the superfamily of transient receptor potential (TRP) ion channels and is involved in multiple biological processes and diseases (*1*–*3*). In humans, there are eight TRPMs, which share sequence similarity but respond to different stimuli (*1*–*3*). TRPM family members share a core architecture that includes a large TRPM homology region (MHR1 to 4), a six-helix transmembrane (TM) domain, a conserved TRP helix region, a rib helix, and a pole helix (Fig. 1A). In addition to the core, some TRPMs have an additional enzyme domain that regulates gating and are sometimes classified as chanzymes (*1*). For example, TRPM2 has a C-terminal NUDT9 homology (NUDT9H) domain, which has a predicted fold belonging to the Nudix hydrolase family that catalyzes the conversion of adenosine diphosphate (ADP)–ribose (ADPR) to adenosine monophosphate (AMP) and ribose-5-phosphate (R5P). It has been debated whether the NUDT9H domain of TRPM2 has enzymatic activity (*4*, *5*).

TRPM2 forms a Ca^{2+}-permeable nonselective cation channel gated by ADPR and Ca^{2+} (*6*–*9*). ADPR is a metabolic product of nicotinamide adenine dinucleotide (NAD) and accumulates in cells upon oxidative stress. TRPM2 relays oxidative stress to Ca^{2+} signaling with many vital physiological roles (*10*–*13*). In particular, TRPM2 plays prominent functions in immunity and inflammation, which include chemokine production, inflammasome activation, and infection control (*8*, *14*–*18*). Under pathological conditions such as ischemia-reperfusion injury, inflammation, and Alzheimer's disease, TRPM2 can be activated by high levels of reactive oxygen species through ADPR accumulation and exacerbates the diseases (*19*, *20*). Therefore, TRPM2 is an attractive therapeutic target against chronic inflammatory and neurodegenerative diseases.

Recently reported cryo–electron microscopy (cryo-EM) structures of human TRPM4 (*21*–*24*), *Ficedula albicollis* TRPM8 (*25*), *Nematostella vectensis* TRPM2 (*nv*TRPM2) (*26*), and mouse TRPM7 (*27*) have shed light on the closed, inactive core architecture of TRPM family cation channels. Here we determined the cryo-EM structures of full-length human (*Homo sapiens*) TRPM2 (*hs*TRPM2) in apo, ADPR-bound, and ADPR- and Ca^{2+}-bound states. Instead of being flexibly linked to the C-terminal end as previously presumed (*26*), NUDT9H folds back onto the N-terminal domain to form extensive interactions with MHR through both intra- and intersubunit contacts. Upon ADPR binding, NUDT9H undergoes conformational changes that trigger the rotation of MHR1/2 and dislodging of the intersubunit interaction. This ADPR-induced "priming" effect may further allow Ca^{2+} binding to concertedly tilt the TRP helix, twist the MHR, and rotate the gating S6 helix to open the channel. Unexpectedly, the cryo-EM structure of zebrafish (*Danio rerio*) TRPM2 (*dr*TRPM2) in complex with ADPR and Ca^{2+} published recently shows ADPR binding at the MHR1/2 region (*28*). Our further experimental evidence confirmed the species-specific difference in ADPR binding and gating using NUDT9H for *hs*TRPM2 and MHR1/2 for *dr*TRPM2, respectively.

[1]Department of Biological Chemistry and Molecular Pharmacology, Harvard Medical School, Boston, MA 02115, USA. [2]Program in Cellular and Molecular Medicine, Boston Children's Hospital, Boston, MA 02115, USA. [3]Department of Medicine, Brigham and Women's Hospital and Harvard Medical School, Boston, MA 02115, USA. [4]Broad Institute of MIT and Harvard, Cambridge, MA 02142, USA.
*These authors contributed equally to this work.
†Corresponding author. Email: tianmin.fu@childrens.harvard.edu (T.-M.F.); wu@crystal.harvard.edu (H.W.)

Structure of full-length *hs*TRPM2 in the apo state

We expressed *hs*TRPM2 in human embryonic kidney (HEK) 293F cells and purified it in the absence of ADPR and Ca^{2+} (fig. S1). We then determined its fourfold symmetric cryo-EM structure at 3.6-Å resolution (figs. S2 and S3, and table S1). The initial cryo-EM density map was of sufficient quality for modeling the N-terminal cytosolic domains but not NUDT9H and the TM region. Using density subtraction and focused three-dimensional (3D) classification followed by local refinement, we improved the cryo-EM maps at these regions (figs. S2 and S3). The final map revealed a square-shaped structure with approximate dimensions of 150 Å by 100 Å by 100 Å, and the final model comprises all domains except the linker between the pole helix and the NUDT9H domain (Fig. 1, A and B).

The overall structure of *hs*TRPM2 is similar to that of *dr*TRPM2 (*28*) (fig. S4A), with NUDT9H prominently decorating the bottom corners of the large intracellular region of the tetramer (Fig. 1, B and C). In a three-tier description of the overall architecture that has been used for TRPM channels, NUDT9H resides on the bottom tier, which also comprises the N-terminal MHR1/2, MHR3, and the pole helix (Fig. 1, C to E). Surrounded by MHR1/2, the symmetric pole helices form a parallel tetrameric coiled coil at the fourfold axis. The middle tier of TRPM2 consists of the rib helix and the MHR4 domain; the latter provides stacked α helices to bridge the N-terminal cytosolic domain and the TM region. We call the entire MHR region the MHR arm (Fig. 1A). The top tier is composed of pre-S1, S1 to S6 TM domain helices, and the TRP helices. As in most classic six-pass cation channels, the TM region of TRPM2 is arranged in a domain-swapped architecture, where the S1-S4 voltage sensing–like domain (VSLD) of one subunit interacts with the S5-S6 pore domain of a neighboring subunit (fig. S4, B and C).

Cis and trans interactions between NUDT9H and MHRs

NUDT9H adopts a two-domain architecture, in which the N-terminal domain (NTD) is dominated by loops and short β strands, and the C-terminal domain (CTD) comprises a central β sheet surrounded by several α helices (Fig. 2A). NUDT9H resembles human NUDT9 (*29*), a mitochondrial ADPR pyrophosphatase, and has a conserved P loop that connects two β strands in the central β sheet of the NUDT9H CTD (Fig. 2, A and B). NUDT9H lies adjacent to MHR1/2 and MHR3 in the same subunit and also interacts with MHR1/2 of a neighboring subunit. We defined three contact areas: interfaces I, II, and III (Fig. 2C). Interfaces I and II mediate intrasubunit (cis) interactions of NUDT9H with MHR1/2 and MHR3, respectively (Fig. 2, D and E). Interface III enables intersubunit (trans)

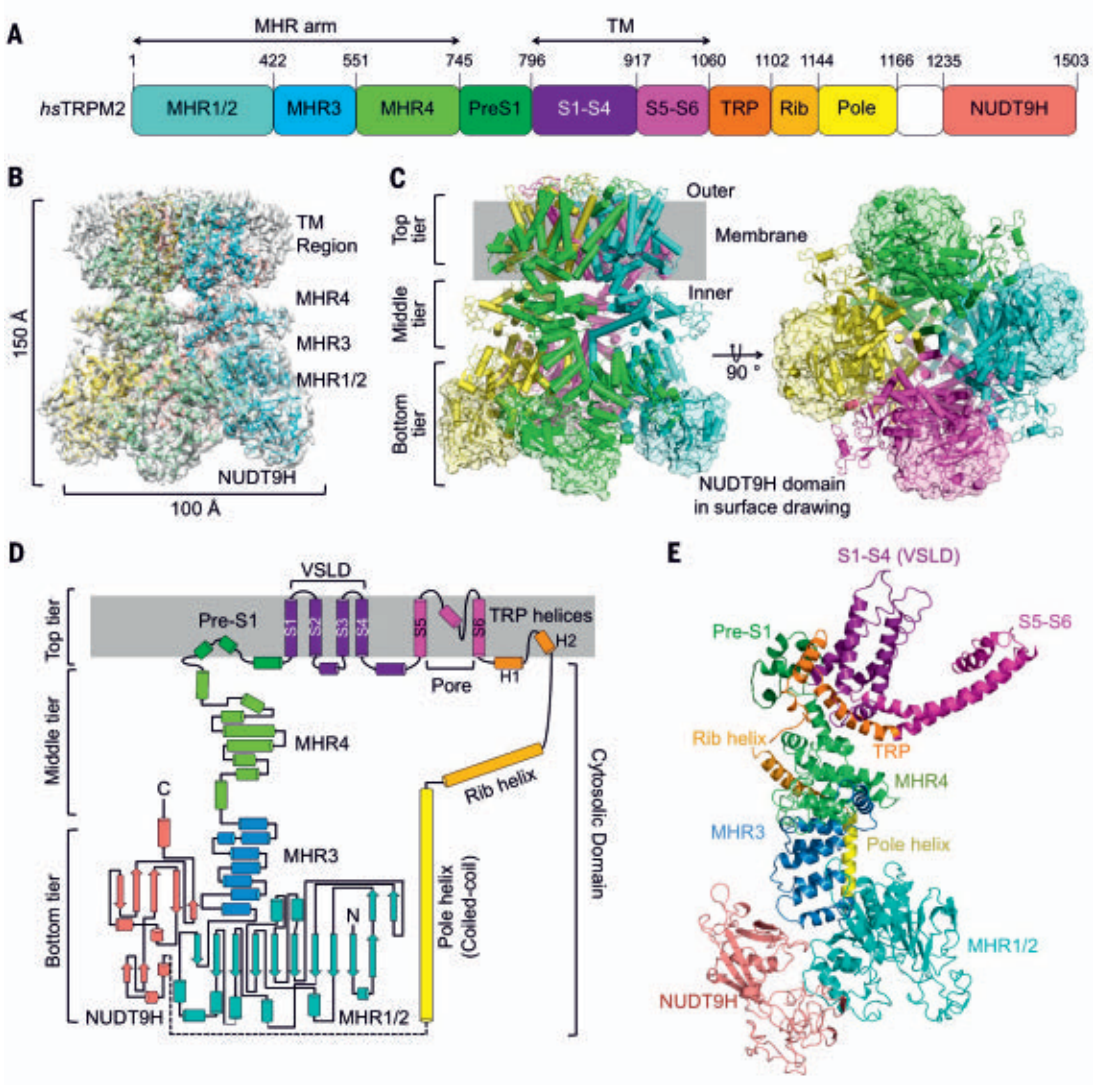

Fig. 1. Cryo-EM structure of *hs*TRPM2 in the apo, closed state. (**A**) Domain organization, with residue numbers indicated above. (**B**) Side view of the 3D cryo-EM density superimposed with the atomic model. Four subunits in the tetramer are colored in green, cyan, magenta, and yellow. The tetramer has estimated dimensions of 150 Å by 100 Å by 100 Å. (**C**) Ribbon diagrams with the subunits colored in green, cyan, magenta, and yellow and in two orthogonal views. The model is divided into three tiers, and the NUDT9H domain model is overlaid with a transparent surface representation. (**D**) Illustration of the major structural components and their spatial organization, shown in the same color scheme as in (A). (**E**) A ribbon diagram of a monomeric subunit, with domains labeled and colored according to the illustration in (D).

interactions between the P loop of NUDT9H in one subunit and MHR1/2 of a neighboring subunit (Fig. 2F). Through these interfaces, NUDT9H couples neighboring subunits by occupying the groove between two MHR arms, thereby restricting intersubunit movement and likely stabilizing the MHR arms in the absence of ADPR binding (Fig. 2C). Of note, despite the overall similarity in the subunit structure, this intersubunit interaction is absent in *dr*TRPM2 (fig. S4D), likely owing to the P-loop deletion in *dr*TRPM2 NUDT9H (fig. S4, E and F).

MHR1/2 rotation, MHR3 allosteric change, and dislodging of the intersubunit interface upon ADPR binding

To obtain a structure of TRPM2 in complex with ADPR, we first showed by surface plasmon resonance that the NUDT9H domain of *hs*TRPM2 directly interacts with ADPR with a measured affinity of ~15 μM (Fig. 3A), similar to the measured affinity of ~41 μM for ADPR binding to full-length *hs*TRPM2 (Fig. 3A) (*7*, *30*–*32*). The NUDT9H domain is also absolutely required for channel gating (fig. S5, A to C), and TRPM2 does not hydrolyze ADPR (*4*, *5*) (fig. S5, D and E). By contrast, the *dr*TRPM2 structure revealed functionally important ADPR binding at the MHR1/2 domain (*28*). To determine whether the ADPR-binding site at MHR1/2 is also important for *hs*TRPM2, we generated the double mutant R302A/R358A (Arg^{302}→Ala/Arg^{358}→Ala), whose equivalent in *dr*TRPM2 nearly abolished ADPR-induced current (*28*). We found by Ca^{2+} imaging that the mutant did not substantially affect channel gating by ADPR (fig. S5, B and C), suggesting that the ADPR-binding site observed in *dr*TRPM2 does not play an important role in *hs*TRPM2. We further expressed the NUDT9H domain of *dr*TRPM2 and found that its binding affinity to ADPR is close to millimolar, much reduced in comparison to the NUDT9H domain of *hs*TRPM2 (fig. S5, F and G), which is also consistent with the multiple mutations in *dr*TRPM2 at the proposed NUDT9H ADPR-binding site (*30*) (fig. S4F). These data collectively demonstrate that *dr*TRPM2 and *hs*TRPM2 use MHR1/2 and NUDT9H domains, respectively, for ADPR sensing.

We then purified TRPM2 in the presence of ADPR and EDTA to chelate Ca^{2+} and obtained a cryo-EM density map at 6.1-Å resolution (fig. S6 and table S1). Despite the limited resolution of this state, a comparison to the apo state reveals dramatic conformational changes at the bottom tier where NUDT9H, MHR1/2, and MHR3 reside (Fig. 3, B and C). In particular, interface III between NUDT9H of one subunit and the MHR1/2 domain of a neighboring subunit is lost upon ADPR engagement (Fig. 3B). MHR1/2 rotates about 27° toward NUDT9H, clockwise if viewed from the extracellular side, whereas the remainder of the TRPM2 subunit structure does not show large changes (Fig. 3, C to E). Although the change at the MHR1/2 region is mostly rigid-body movement (fig. S7A), the MHR3 region, especially the helical hairpin that interacts with the NUDT9H CTD on one side and MHR1/2 on the other side, exhibits substantial local conformational changes (fig. S7B).

To deduce conformational changes at NUDT9H upon ADPR binding, we fit the apo NUDT9H model as a rigid body into the cryo-EM density

of the ADPR-bound form (Fig. 3F). In the homologous NUDT9 crystal structure [Protein Data Bank (PDB) 1QVJ], the hydrolytic product R5P sits in a cleft between the NTD and CTD (*29*), and docking, molecular dynamics simulation, and mutagenesis identified the crevice between the NTD and CTD as an ADPR-binding site (*30*). We could not resolve the bound ADPR in our density but observed that the NTD-CTD crevice is smaller, consistent with direct ADPR binding (Fig. 3F). The density also suggests that the NTD needs to rotate relative to the CTD to fit better, likely leading to changes at the interface with MHRs. In addition, the P-loop region is considerably different, which may contribute to the

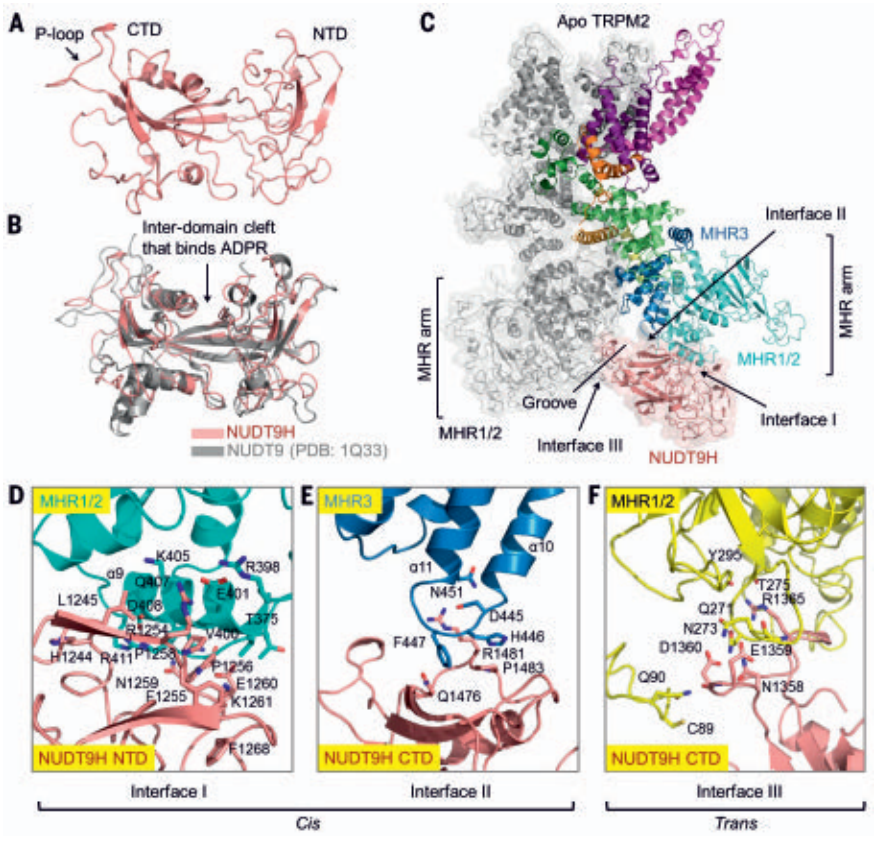

Fig. 2. NUDT9H and its interactions with the MHR1/2 and MHR3 domains. (**A**) Structure of NUDT9H in a two-domain architecture. The location of the P loop is labeled. (**B**) Structural comparison between NUDT9H and human NUDT9 (PDB 1Q33) (*29*). (**C**) Three interfaces mediated by NUDT9H that contact in cis the MHR1/2 and MHR3 domains and in trans the MHR1/2 domain of a neighboring subunit. (**D** to **F**) Depiction of the three interfaces in detail. At interface I (D), the NUDT9H NTD closely contacts helix α9 from MHR1/2, forming charge-charge interactions between R1254 and E401, hydrogen bonds between N1259 and Q407/D408 and between E1260 and Q407, and hydrophobic interactions among P1256, P1258, V400, and K405 and between F1255 and V400. The NUDT9H CTD and the α10-α11 region of MHR3 establish interface II (E), in which R1481 and E476 form charge-charge interactions while Q1476, P1483, F447, and H446 form hydrophobic interactions. Interface III (F) features mostly hydrophilic interactions formed by the P loop of one subunit and MHR1/2 of a neighboring subunit, such as those between D1360 and Q90, between E1359/N1358 and Q271, and between N273 and R1365. Single-letter abbreviations for the amino acid residues are as follows: A, Ala; C, Cys; D, Asp; E, Glu; F, Phe; G, Gly; H, His; I, Ile; K, Lys; L, Leu; M, Met; N, Asn; P, Pro; Q, Gln; R, Arg; S, Ser; T, Thr; V, Val; W, Trp; and Y, Tyr.

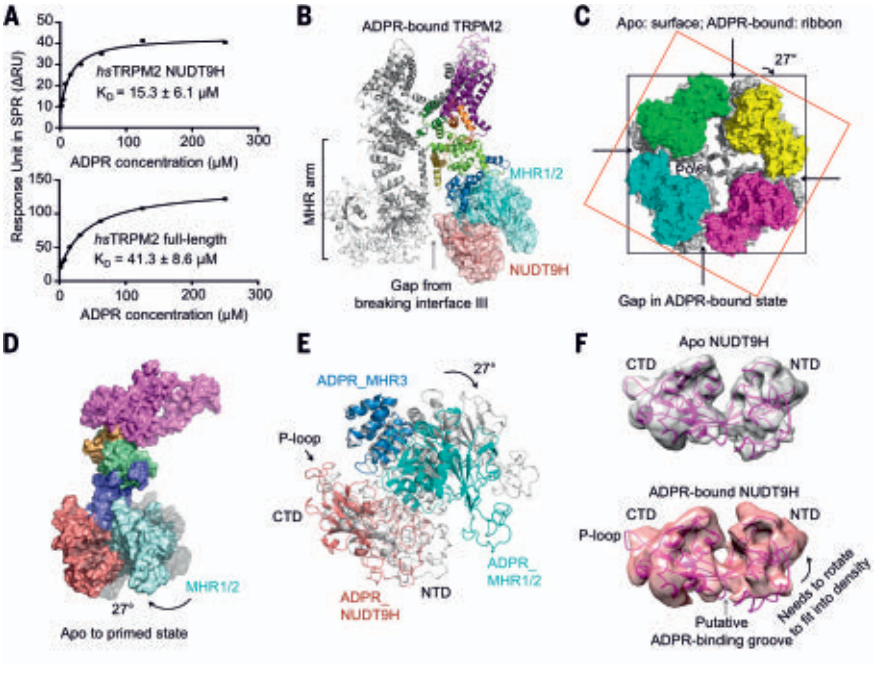

Fig. 3. TRPM2 priming by ADPR binding to NUDT9H. (**A**) ADPR binding affinities to NUDT9H (top) and full-length TRPM2 (bottom), as measured by surface plasmon resonance (SPR). ΔRU, change in response units; K_D, dissociation constant. (**B**) A ribbon diagram of ADPR-bound TRPM2 shown as a dimer, with one subunit in domain colors and the other subunit in gray. Disruption of the intersubunit interaction is indicated. (**C**) Top view of overlaid tetramers of TRPM2 in ADPR-bound state (colored surface) and in apo state (gray surface), showing a 27° rotation between subunits in the two states. Two squares help to indicate the rotation. (**D**) Side view of one subunit in surface representation, showing the conformational changes of TRPM2 from the apo state (gray) to the ADPR-bound state (colored). (**E**) Overlaid side-view ribbon diagrams, showing the rotation of NUDT9H, MHR1/2, and MHR3 domains from the apo state (gray) to the ADPR-bound state (colored). (**F**) Comparison of NUDT9H densities in the apo state (gray) and the ADPR-bound state (salmon). The NUDT9H model from the apo state (magenta) is fitted into the ADPR-bound state density as a rigid body. The P-loop region and the NTD that needs to be rotated are indicated.

disengagement of interface III between NUDT9H and MHR1/2 in trans. NUDT9H is likely bifunctional: It inhibits MHR movement in the absence of ADPR through intra- and intersubunit interactions and induces MHR rotation and dislodging of the intersubunit interaction in the presence of ADPR. As discussed below, these changes collectively "prime" TRPM2 for channel opening by Ca^{2+} binding, and we therefore named the ADPR-bound state the primed state.

Global conformational changes upon coactivation by ADPR and Ca^{2+}

It has been shown that although ADPR is required for TRPM2 opening, the channel remains closed until Ca^{2+} binds at the TM region (*9*). Using single-channel recording, we recapitulated the process of channel opening synergistically triggered by ADPR and Ca^{2+} (fig. S8). To elucidate coactivation by ADPR and Ca^{2+}, we purified *hs*TRPM2 in the presence of ADPR and Ca^{2+} and obtained a cryo-EM map at 6.4-Å resolution (fig. S9 and table S1). Although the structure is only at a modest resolution, the global

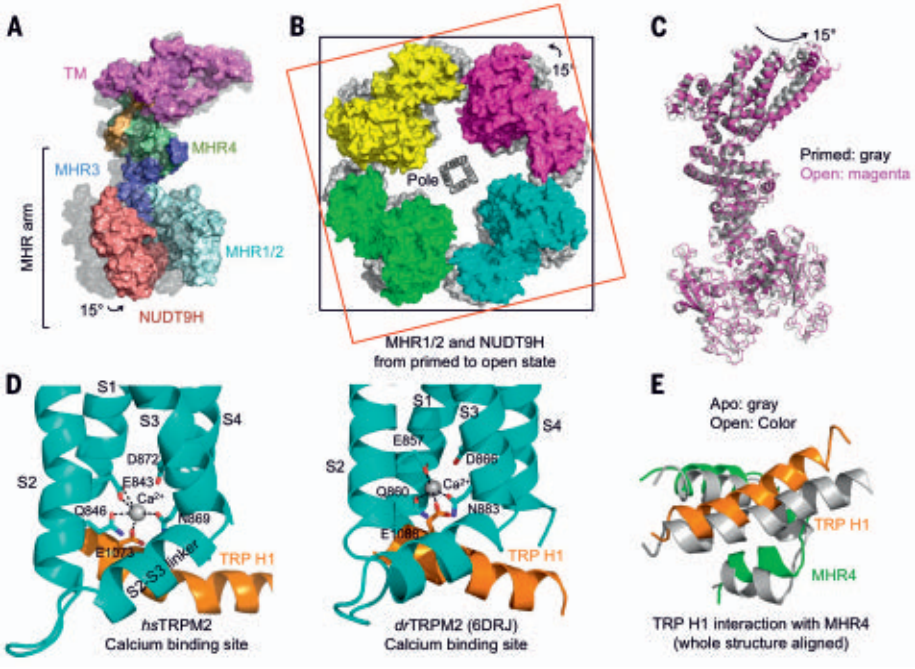

Fig. 4. Global conformational changes of *hs*TRPM2 during its opening. (**A**) Side view of one subunit in surface representation, showing a 15° rotation from the primed state (gray surface) to the open state (colored surface). The entire MHR arm moves. (**B**) Top view of overlaid tetramers in the open state (colored surface) and the primed state (gray surface). Two squares help to indicate the rotation. (**C**) Superimposed TRPM2 structures in the primed (gray) and open (magenta) states. (**D**) Coordination of Ca^{2+} by residues in TRP H1, S2, and S3 in both *hs*TRPM2 and *dr*TRPM2 (PDB 6DRJ) (*28*). (**E**) TRP H1 and MHR4 are positioned in close proximity via direct interactions, shown as a global superposition between the apo (gray) and open (colored) states. TRP H1 tilts as a consequence of Ca^{2+} binding, establishing a molecular coupling between TRP H1 and the cytosolic domain.

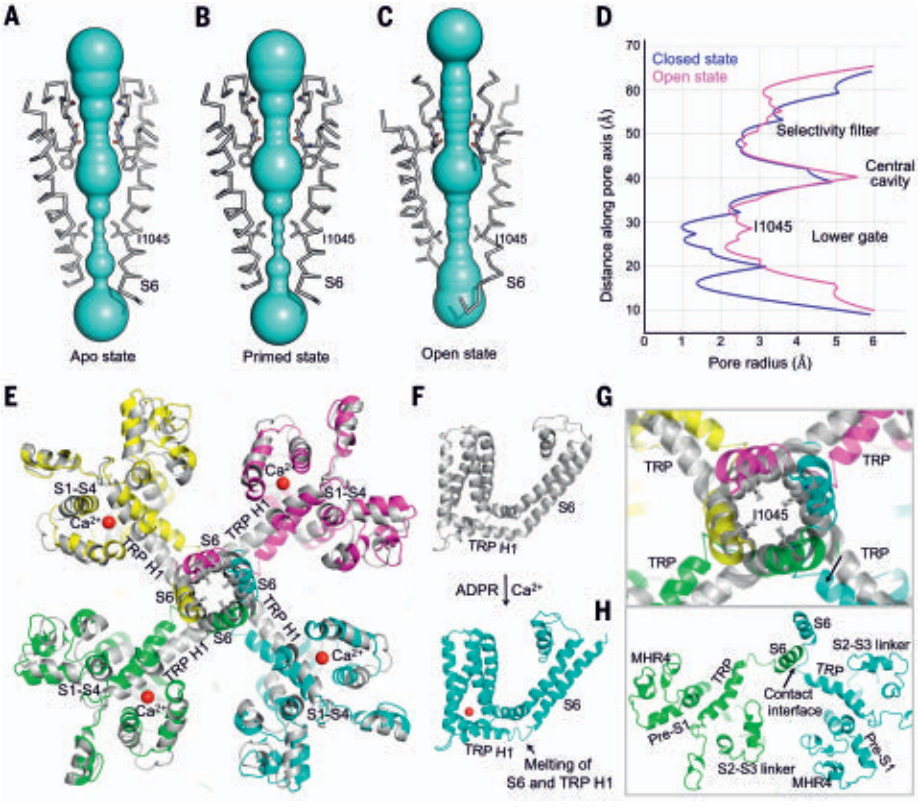

Fig. 5. Conformational changes of the ion permeation pore. (**A** to **C**) Pore-forming domain of TRPM2 in apo (A), ADPR-bound (B), and open (C) states, with key residues lining the pore shown as sticks. The pores are shown as space-filling models and were calculated using the HOLE program (*38*). (**D**) Pore radii of apo (blue) and open (magenta) states along the pore axis, calculated as in (A) to (C). (**E**) Comparison of the TM region in apo (gray) and open (colored) states. Bound Ca^{2+}, S6, TRP H1, and S1-S4 are labeled. (**F**) TM region of the apo (gray) and open (cyan) states, showing a partial melting of S6 and TRP H1 in the open state. (**G**) Enlarged view of the conformational change near residue I1045 at the lower gate. (**H**) The open state conformation may be stabilized by the trans interaction between S6 and the melted S6-TRP helix loop.

organization of the domains and the TM helices are well defined. In contrast to the clockwise rotation between the ADPR-bound state and the apo state (Fig. 3D), subunits in the open-state structure undergo counterclockwise rotation in comparison with the ADPR-bound state when viewed from outside the cell (Fig. 4, A and B). The subunit structure in the primed state is similar to that in the open state, suggesting that the rotation is largely rigid body in nature (Fig. 4C). Whereas the rotation from apo to primed involves mostly the bottom MHR arm, the rotation from primed to open involves both the middle and bottom tiers, as well as conformational adjustments in the TM region (Fig. 4A).

The Ca^{2+}-binding site is localized near the intracellular border of the channel, in between S2, S3, and the TRP H1 helix. Despite the modest resolution, the electron density was best interpreted as Ca^{2+} being coordinated by residues E843 and Q846 of S2, N869 of S3 and E1073 of TRP H1 (E, Glu; Q, Gln; and N, Asn) (Fig. 4D and fig. S10A). Involvement of the TRP helix in Ca^{2+} coordination has not been observed in structures of other TRP channels but is consistent with the coordination seen in the higher resolution *dr*TRPM2 structure (PDB 6DRJ) even though the authors did not point this out (*28*) (Fig. 4D). In the *nv*TRPM2 structure in the absence of ADPR, the TRP H1 residue equivalent to E1073 locates right below the observed Ca^{2+} site (fig. S10B), and mutagenesis on this residue also compromised Ca^{2+} sensitivity as it did on residues on S2 and S3 (*26*). Notably, E1073 of TRP H1 is highly conserved in different TRPM channels (fig. S10C). These data support a subtle, but notable, difference in Ca^{2+} coordination in the presence and absence of ADPR.

Binding of Ca^{2+} is associated with a tilt at TRP H1, which, in turn, is intimately associated with the cytosolic domain through its interaction with MHR4 using extensive hydrophobic and hydrogen-bonding interactions (Fig. 4E). We propose that this TRP-MHR coupling is responsible for the transmission of the Ca^{2+}-binding signal to the cytosolic domain. Superposition of just the TRP-MHR4 region between the closed and open states suggests that the coupling is mostly rigid body (fig. S10D). Because of the large dimensions of the MHR arm, a subtle conformational change at TRP H1 may be amplified to large movement at the bottom tier of the structure (Fig. 4A). We propose that neither Ca^{2+} binding nor ADPR binding alone provides a sufficient amount of energy to elicit the concerted conformational changes that involve MHR1/2 rotation, local changes at MHR3, and global rotation of the entire cytosolic domain. Instead, two binding events likely mutually prime each other to share the energetic cost required for the conformational changes. For *hs*TRPM2, these conformational changes may also be restricted by the intersubunit interaction exerted through the NUDT9H domain (Fig. 2C). Freeing the subunits from this intersubunit restriction through ADPR binding may then also facilitate any conformational changes required for regulation and gating.

Conformational changes at the pore region associated with TRPM2 channel gating

As in other TRP channels, the ion permeation pathway in TRPM2 is composed of a selectivity filter, a central cavity, and a lower gate (Fig. 5, A to D). The selectivity filter and the central cavity of TRPM2 are relatively invariant among the different states (Fig. 5, A to C). The lower gate, however, is highly restricted in the apo and primed states, with I1045 (I, Ile) of S6 forming the most constricted point to block ion flow (Fig. 5, A, B, and D). In the state doubly bound to ADPR and Ca^{2+}, the local region of S6 that includes I1045 and Q1053 tilts away from the central cavity, thereby dilating the lower gate to a similar radius as the selectivity filter, promoting channel-open probability (Fig. 5, C and D). This pore enlargement, however, is not sufficient to allow the passage of hydrated Ca^{2+} ions, which are ~4 Å in radius. Comparatively, the lower gate of the doubly bound state of *dr*TRPM2 is wider (fig. S10E). However, in this presumed open state, the selectivity filter of *dr*TRPM2 becomes the most constricted point in the ion conductive pathway (*28*), and its width is similar to that of the selectivity filter of *hs*TRPM2. Therefore, both *hs*TRPM2 and *dr*TRPM2 structures in complex with ADPR and Ca^{2+} may represent an intermediate state on the way to the fully open state; the latter may be quite transient, as shown by single-channel recordings (fig. S8).

Conformational changes at TRP H1 and the S6 gating helix accompany the widening of the lower gate to promote channel-opening probability. In a closed state, either apo or primed, TRP H1 connects to S6 via a continuous helix that bends at the junction (Fig. 5F). Upon Ca^{2+} binding to ADPR-primed TRPM2, the beginning part of TRP H1 and the ending part of S6 melt together into a loop, which likely releases the pull on S6 by TRP H1 and allows it to rotate and translate (Fig. 5, F and G), as also seen in the *dr*TRPM2 structure (*28*). Because TRP H1 directly binds to Ca^{2+}, we propose that it brings about Ca^{2+}-induced conformational changes at the S6 gating helix (Fig. 5, E to G). In this state, doubly bound to ADPR and Ca^{2+}, there is an additional contact between the melted S6-TRP connection and S6 of a neighboring subunit, which may stabilize the open conformation (Fig. 5H).

For some TRP channels, an α helix–to–π helix transition in a region of S6 has been proposed to cause gating (*33*, *34*). For TRPM2 structures from the different species presented here and published previously (*26*, *28*), the π-helix segment already exists in the closed conformation, suggesting that TRPM2 must be gated differently. Of note, many cation channels use the S4-S5 linker within the S1-S4 VSLD to cause a conformational change at the S6 gating helix (*35*). In *hs*TRPM2 and *dr*TRPM2 (*28*), TRP H1 sits adjacent to the S4-S5 linker, and it is possible that TRP H1 couples to S4-S5 to effect gating indirectly as well as through its direct connection to S6. Because TRP H1 consistently links to both the TM and the cytosolic domain through extensive interactions in available structures in the TRP family (fig. S11), we propose that the role of TRP H1 as an allosteric center to regulate gating, as revealed from the current study, may be more general than previously appreciated.

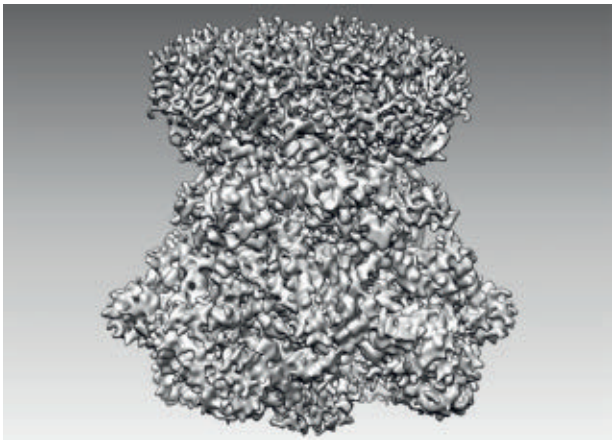

Movie 1. Conformational changes of *hs*TRPM2 during channel opening.

Discussion

Our cryo-EM structures of *hs*TRPM2 in the apo, ADPR-bound, and ADPR- and Ca^{2+}-bound states reveal conformational regulation of TRPM2 gating (Fig. 6 and Movie 1). In the apo state, the NUDT9H domain forms both intra- and intersubunit interactions, which may be important for locking TRPM2 in a closed state. Supporting this autoinhibition concept, small-molecule inhibitors for the related TRPM4 channel have been shown to bind at these interfaces (*22*, *23*). Specifically, adenosine triphosphate (ATP) binding at the subunit interface has an inhibitory role in TRPM4 activity (*22*), and, although more complex, one of the decavanadate molecules also nestles at a subunit interface (*23*). In addition to sensing Ca^{2+} and ADPR, *hs*TRPM2 has been shown to sense body temperature to limit the fever response (*11*, *12*). By contrast, *dr*TRPM2 lacks intersubunit interactions (*28*) and does not respond to heat or pH (*36*). We speculate that higher temperature, in the form of enhanced thermal motion, may overcome the intersubunit interactions in *hs*TRPM2 to modulate gating.

The apo conformation of TRPM2 is dramatically altered upon ADPR binding, with large

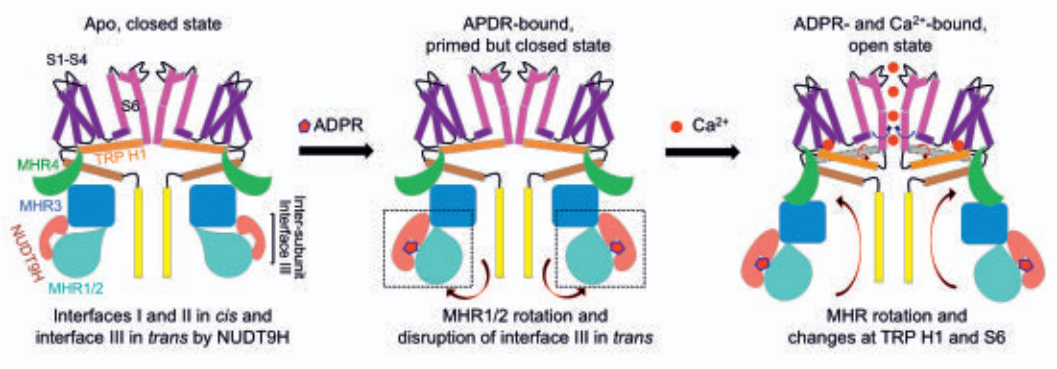

Fig. 6. A model for *hs*TRPM2 gating. In the apo state (left), the channel is in a closed conformation with S6 (magenta) forming the lower gate and NUDT9H (pink) interacting with MHR1/2 (cyan) and MHR3 (blue) in cis and MHR1/2 from a neighboring subunit in trans. Upon ADPR binding (middle), rotation of MHR1/2 and disengagement of the trans interaction prime the channel for opening. Binding of Ca^{2+} directly engages S2 and S3 helices (purple) and TRP H1 (orange), leading to a tilt at TRP H1 and partial melting at the S6-TRP junction to trigger S6 rotation and channel opening. In the open conformation cartoon (right), the gray helix represents TRP H1 in a closed state and is shown for comparison with TRP H1 in the open state (orange). Arrows indicate conformational transitions.

domain rotation in MHR1/2 and local changes in MHR3, as well as disengagement of the intersubunit interaction. This effect of ADPR may allow the cytosolic domain of each subunit to freely rotate when Ca^{2+} binds at S2, S3, and TRP H1. In contrast to ADPR, the priming conformational changes by Ca^{2+} may be more subtle, as suggested by the lack of gross conformational differences between the apo state of *hs*TRPM2 and the Ca^{2+}-bound state of *nv*TRPM2 (fig. S12). The tilt of TRP H1 and melting at the S6-TRP junction, as well as the proximity of the S4-S5 linker to TRP H1, may all help to twist the gating helix S6 to enhance the channel-opening probability. Because of its strategic location and coupling to both the TM and the cytosolic domain (fig. S11), TRP H1 appears to be especially important for gathering allosteric signals from various parts of the channel to effect gating, a hypothesis that may be further tested in multiple TRP channels. During the conformational transitions accompanying either priming or opening, the coiled coil formed by the pole helix remains unchanged, as if serving as a central spine to provide an anchor for movements at the periphery.

Intriguingly, the *dr*TRPM2 structure showed ADPR binding at MHR1/2 instead of at NUDT9H (*28*). Our experimental data demonstrate that this ADPR binding mode represents a true difference between *dr*TRPM2 and *hs*TRPM2, as NUDT9H of *dr*TRPM2 has affinity to ADPR in the millimolar range (fig. S5G), likely much higher than an inducible intracellular ADPR concentration, and mutations at MHR1/2 did not affect Ca^{2+} signaling by *hs*TRPM2 (fig. S5B). In this regard, previous studies showed that NUDT9H of *nv*TRPM2 degrades ADPR but plays no role in coactivation by ADPR and Ca^{2+} (*37*), whereas NUDT9H of *hs*TRPM2 binds ADPR to promote gating but does not have the ability to hydrolyze ADPR. Additional studies on species-specific aspects of TRPM2 structure and function are required to further tease out the complexity.

Materials and methods summary

Full-length *hs*TRPM2 with an N-terminal MBP tag was expressed in HEK293F cells and solubilized in 50 mM HEPES at pH 7.4, 150 mM NaCl, 2 mM TCEP, 2% glycerol, 1% LMNG, 0.1% CHS, and a protease inhibitor cocktail. TRPM2 was purified by amylose affinity resin followed by glycerol gradient and dialysis. For the cryo-EM study, 1 mg/ml TRPM2 was applied to grids and plunge-frozen using Vitrobot Mark IV. All the cryo-EM data were collected on a Titan Krios and processed using standard procedures.

REFERENCES AND NOTES

1. D. E. Clapham, TRP channels as cellular sensors. *Nature* **426**, 517–524 (2003). doi: 10.1038/nature02196; pmid: 14654832
2. K. Venkatachalam, C. Montell, TRP channels. *Annu. Rev. Biochem.* **76**, 387–417 (2007). doi: 10.1146/annurev.biochem.75.103004.142819; pmid: 17579562
3. D. Julius, TRP channels and pain. *Annu. Rev. Cell Dev. Biol.* **29**, 355–384 (2013). doi: 10.1146/annurev-cellbio-101011-155833; pmid: 24099085
4. B. Tóth, I. Iordanov, L. Csanády, Putative chanzyme activity of TRPM2 cation channel is unrelated to pore gating. *Proc. Natl. Acad. Sci. U.S.A.* **111**, 16949–16954 (2014). doi: 10.1073/pnas.1412449111; pmid: 25385633
5. I. Iordanov, C. Mihályi, B. Tóth, L. Csanády, The proposed channel-enzyme transient receptor potential melastatin 2 does not possess ADP ribose hydrolase activity. *eLife* **5**, e17600 (2016). doi: 10.7554/eLife.17600; pmid: 27383051
6. K. Nagamine *et al.*, Molecular cloning of a novel putative Ca^{2+} channel protein (TRPC7) highly expressed in brain. *Genomics* **54**, 124–131 (1998). doi: 10.1006/geno.1998.5551; pmid: 9806837
7. A. L. Perraud *et al.*, ADP-ribose gating of the calcium-permeable LTRPC2 channel revealed by Nudix motif homology. *Nature* **411**, 595–599 (2001). doi: 10.1038/35079100; pmid: 11385575
8. Y. Sano *et al.*, Immunocyte Ca^{2+} influx system mediated by LTRPC2. *Science* **293**, 1327–1330 (2001). doi: 10.1126/science.1062473; pmid: 11509734
9. L. Csanády, B. Törocsik, Four Ca^{2+} ions activate TRPM2 channels by binding in deep crevices near the pore but intracellularly of the gate. *J. Gen. Physiol.* **133**, 189–203 (2009). doi: 10.1085/jgp.200810109; pmid: 19171771
10. K. Uchida, M. Tominaga, TRPM2 modulates insulin secretion in pancreatic β-cells. *Islets* **3**, 209–211 (2011). doi: 10.4161/isl.3.4.16130; pmid: 21636972
11. K. Song *et al.*, The TRPM2 channel is a hypothalamic heat sensor that limits fever and can drive hypothermia. *Science* **353**, 1393–1398 (2016). doi: 10.1126/science.aaf7537; pmid: 27562954
12. C. H. Tan, P. A. McNaughton, The TRPM2 ion channel is required for sensitivity to warmth. *Nature* **536**, 460–463 (2016). doi: 10.1038/nature19074; pmid: 27533035
13. A. L. Perraud *et al.*, Accumulation of free ADP-ribose from mitochondria mediates oxidative stress-induced gating of TRPM2 cation channels. *J. Biol. Chem.* **280**, 6138–6148 (2005). doi: 10.1074/jbc.M411446200; pmid: 15561722
14. S. Yamamoto *et al.*, TRPM2-mediated Ca^{2+} influx induces chemokine production in monocytes that aggravates inflammatory neutrophil infiltration. *Nat. Med.* **14**, 738–747 (2008). doi: 10.1038/nm1758; pmid: 18542050
15. H. Knowles *et al.*, Transient receptor potential melastatin 2 (TRPM2) ion channel is required for innate immunity against *Listeria monocytogenes*. *Proc. Natl. Acad. Sci. U.S.A.* **108**, 11578–11583 (2011). doi: 10.1073/pnas.1010678108; pmid: 21709234
16. J. K. Tripathi *et al.*, Oxidant sensor cation channel TRPM2 regulates neutrophil extracellular trap formation and protects against pneumoseptic bacterial infection. *FASEB J.* 10.1096/fj.201800605 (2018). doi: 10.1096/fj.201800605; pmid: 29906250
17. N. L. Shakerley, A. Chandrasekaran, M. Trebak, B. A. Miller, J. A. Melendez, *Francisella tularensis* catalase restricts immune function by impairing TRPM2 Channel activity. *J. Biol. Chem.* **291**, 3871–3881 (2016). doi: 10.1074/jbc.M115.706879; pmid: 26679996
18. Z. Zhong *et al.*, TRPM2 links oxidative stress to NLRP3 inflammasome activation. *Nat. Commun.* **4**, 1611 (2013). doi: 10.1038/ncomms2608; pmid: 23511475
19. S. Yamamoto, S. Shimizu, Significance of TRP channels in oxidative stress. *Eur. J. Pharmacol.* **793**, 109–111 (2016). doi: 10.1016/j.ejphar.2016.11.007; pmid: 27838397
20. V. G. Ostapchenko *et al.*, The transient receptor potential melastatin 2 (TRPM2) channel contributes to β-amyloid oligomer-related neurotoxicity and memory impairment. *J. Neurosci.* **35**, 15157–15169 (2015). doi: 10.1523/JNEUROSCI.4081-14.2015; pmid: 26558786
21. H. E. Autzen *et al.*, Structure of the human TRPM4 ion channel in a lipid nanodisc. *Science* **359**, 228–232 (2018). doi: 10.1126/science.aar4510; pmid: 29217581
22. J. Guo *et al.*, Structures of the calcium-activated, non-selective cation channel TRPM4. *Nature* **552**, 205–209 (2017). pmid: 29211714
23. P. A. Winkler, Y. Huang, W. Sun, J. Du, W. Lü, Electron cryo-microscopy structure of a human TRPM4 channel. *Nature* **552**, 200–204 (2017). pmid: 29211723
24. J. Duan *et al.*, Structure of full-length human TRPM4. *Proc. Natl. Acad. Sci. U.S.A.* **115**, 2377–2382 (2018). doi: 10.1073/pnas.1722038115; pmid: 29463718
25. Y. Yin *et al.*, Structure of the cold- and menthol-sensing ion channel TRPM8. *Science* **359**, 237–241 (2018). doi: 10.1126/science.aan4325; pmid: 29217583
26. Z. Zhang, B. Tóth, A. Szollosi, J. Chen, L. Csanády, Structure of a TRPM2 channel in complex with Ca^{2+} explains unique gating regulation. *eLife* **7**, e36409 (2018). doi: 10.7554/eLife.36409; pmid: 29745897

27. J. Duan *et al*., Structure of the mammalian TRPM7, a magnesium channel required during embryonic development. *Proc. Natl. Acad. Sci. U.S.A.* **115**, E8201–E8210 (2018). doi: 10.1073/pnas.1810719115; pmid: 30108148
28. Y. Huang, P. A. Winkler, W. Sun, W. Lü, J. Du, Architecture of the TRPM2 channel and its activation mechanism by ADP-ribose and calcium. *Nature* **562**, 145–149 (2018). doi: 10.1038/s41586-018-0558-4; pmid: 30250252
29. B. W. Shen, A. L. Perraud, A. Scharenberg, B. L. Stoddard, The crystal structure and mutational analysis of human NUDT9. *J. Mol. Biol.* **332**, 385–398 (2003). doi: 10.1016/S0022-2836(03)00954-9; pmid: 12948489
30. P. Yu *et al*., Identification of the ADPR binding pocket in the NUDT9 homology domain of TRPM2. *J. Gen. Physiol.* **149**, 219–235 (2017). doi: 10.1085/jgp.201611675; pmid: 28108595
31. R. Fliegert *et al*., 2′-Deoxyadenosine 5′-diphosphoribose is an endogenous TRPM2 superagonist. *Nat. Chem. Biol.* **13**, 1036–1044 (2017). doi: 10.1038/nchembio.2415; pmid: 28671679
32. J. Starkus, A. Beck, A. Fleig, R. Penner, Regulation of TRPM2 by extra- and intracellular calcium. *J. Gen. Physiol.* **130**, 427–440 (2007). doi: 10.1085/jgp.200709836; pmid: 17893195
33. L. L. McGoldrick *et al*., Opening of the human epithelial calcium channel TRPV6. *Nature* **553**, 233–237 (2018). doi: 10.1038/nature25182; pmid: 29258289
34. A. K. Singh, L. L. McGoldrick, A. I. Sobolevsky, Structure and gating mechanism of the transient receptor potential channel TRPV3. *Nat. Struct. Mol. Biol.* **25**, 805–813 (2018). doi: 10.1038/s41594-018-0108-7; pmid: 30127359
35. W. A. Catterall, G. Wisedchaisri, N. Zheng, The chemical basis for electrical signaling. *Nat. Chem. Biol.* **13**, 455–463 (2017). doi: 10.1038/nchembio.2353; pmid: 28406893
36. H. Nam Tran *et al*., Functional charaterization of zebrafish transient receptor potential melastatin 2. *Biophys. J.* **114**, 641A–642A (2018). doi: 10.1016/j.bpj.2017.11.3463
37. F. Kühn, C. Kühn, A. Lückhoff, Different principles of ADP-ribose-mediated activation and opposite roles of the NUDT9 homology domain in the TRPM2 orthologs of man and sea anemone. *Front. Physiol.* **8**, 879 (2017). doi: 10.3389/fphys.2017.00879; pmid: 29163217
38. O. S. Smart, J. G. Neduvelil, X. Wang, B. A. Wallace, M. S. Sansom, HOLE: A program for the analysis of the pore dimensions of ion channel structural models. *J. Mol. Graph.* **14**, 354–360 (1996). doi: 10.1016/S0263-7855(97)00009-X; pmid: 9195488

ACKNOWLEDGMENTS

Cryo-EM data were collected with the assistance of H. Wei at the Simons Electron Microscopy Center and National Resource for Automated Molecular Microscopy located at the New York Structural Biology Center, supported by grants from the Simons Foundation (349247), NYSTAR, and the NIH National Institute of General Medical Sciences (GM103310). K. Song and C. Xu at the University of Massachusetts Cryo-EM Core Facility helped with grid screening. K. Arnett in the Center for Macromolecular Interactions at the Harvard Medical School helped with the binding assay. **Funding:** This work is supported by NIH grants DK095045, DK099465, and DK103658 to A.G. **Author contributions:** H.W., T.-M.F., and L.W. conceived the project. L.W., T.-M.F., and S.X. performed molecular cloning. L.W. and T.-M.F. purified TRPM2 and solved cryo-EM structures. L.W., T.-M.F., S.X., and H.W. analyzed the structures and designed experiments. Y.Z. and A.G. performed Ca^{2+} imaging and electrophysiological characterizations. H.W., L.W., T.-M.F., and S.X. wrote the manuscript. **Competing interests:** The authors declare no competing interests. **Data and materials availability:** All data needed to evaluate the conclusions in this paper are available in the main text and the supplementary materials. The coordinates and electron density maps are deposited in the Protein Data Bank and EMDB with the following accession numbers: 6MIX and EMD-9132 for apo TRPM2, 6MIZ and EMD-9133 for ADPR-bound TRPM2, and 6MJ2 and EMD-9134 for ADPR- and Ca^{2+}-bound TRPM2.

SUPPLEMENTARY MATERIALS

www.sciencemag.org/content/362/6421/eaav4809/suppl/DC1
Materials and Methods
Figs. S1 to S12
Table S1
References (*39*–*51*)

20 September 2018; accepted 10 November 2018
Published online 22 November 2018
10.1126/science.aav4809

RESEARCH ARTICLE SUMMARY

MOLECULAR MAGNETS

A linear cobalt(II) complex with maximal orbital angular momentum from a non-Aufbau ground state

Philip C. Bunting, Mihail Atanasov, Emil Damgaard-Møller, Mauro Perfetti, Iris Crassee, Milan Orlita, Jacob Overgaard, Joris van Slageren, Frank Neese, Jeffrey R. Long*

INTRODUCTION: The magnetic properties of a single metal center are determined by a combination of its total spin S and orbital angular momentum L. Orbital angular momentum gives rise to magnetic anisotropy, an essential property for applications such as information storage and high-coercivity magnets. Unquenched L arises from an odd number of electrons in degenerate orbitals and is typically observed only for free ions, as well as for complexes of the f elements. For the majority of transition metal ions, however, orbital angular momentum is quenched by the ligand field, which removes the requisite orbital degeneracies. Maximal L for a transition metal ($L = 3$) would require an odd number of electrons in two sets of degenerate orbitals. Such a species would entail a non-Aufbau configuration, wherein the electrons do not fill the d orbitals in the usual order of lowest to highest in energy, and likely exhibit a large magnetic anisotropy.

RATIONALE: Previous efforts have identified the utility of linear coordination environments for isolating iron complexes with unquenched orbital angular momentum and large magnetic anisotropies. Crucially, transition metals in this environment are unaffected by Jahn-Teller distortions that would otherwise remove orbital degeneracies in the case of partially filled d orbitals. Separately, cobalt atoms deposited on a MgO surface—for which one-coordination of the metal is achieved, provided a vacuum is maintained—were shown to have $L = 3$, giving rise to near-maximal magnetic anisotropy. Calculations on the hypothetical linear molecule $Co(C(SiMe_3)_3)_2$ (where Me is methyl) also predicted that this system would possess a ground state with $L = 3$. Empirically, maximal L in a transition metal complex thus requires both a linear coordination environment and a sufficiently weak ligand field strength to allow for non-Aufbau electron filling.

RESULTS: The strongly reducing nature of the carbanion ligand hinders isolation of dialkyl cobalt(II) complexes. However, reducing the basicity of the central carbanion through the use of electron-withdrawing aryloxide groups allowed for the synthesis of the dialkyl cobalt(II) complex $Co(C(SiMe_2ONaph)_3)_2$, where Naph is a naphthyl group. Ab initio calculations on this complex predict a ground state with $S = {}^3/_2$, $L = 3$, and $J = {}^9/_2$ arising from the non-Aufbau electron configuration $(d_{x^2-y^2}, d_{xy})^3(d_{xz}, d_{yz})^3(d_{z^2})^1$. Much as for lanthanide complexes, the ligand field is sufficiently weak that interelectron repulsion and spin-orbit coupling play the key roles in determining the electronic ground state. dc magnetic susceptibility measurements reveal a well-isolated $M_J = \pm{}^9/_2$ ground state, and simulations of the magnetic data from the calculations are in good agreement with the experimental data. Variable-field far-infrared (FIR) spectroscopy shows a magnetically active excited state at 450 cm^{-1} that, in combination with calculations and variable-temperature ac magnetic susceptibility experiments, is assigned to the $M_J = \pm{}^7/_2$ state. Modeling of experimental charge density maps also suggests a d-orbital filling with equally occupied $(d_{x^2-y^2}, d_{xy})$, and (d_{xz}, d_{yz}) orbital sets. As a consequence of its large orbital angular momentum, the molecule exhibits slow magnetic relaxation and, in a magnetically dilute sample, a coercive field of 600 Oe at 1.8 K.

ON OUR WEBSITE

Read the full article at http://dx.doi.org/10.1126/science.aat7319

CONCLUSION: Isolation of $Co(C(SiMe_2ONaph)_3)_2$ illustrates how an extreme coordination environment can confer an f-element–like electronic structure on a transition metal complex. The non-Aufbau ground state enables realization of maximal orbital angular momentum and magnetic anisotropy near the physical limit for a 3d metal. In this respect, the linear L–Co–L motif may prove useful in the design of new materials with high magnetic coercivity. ■

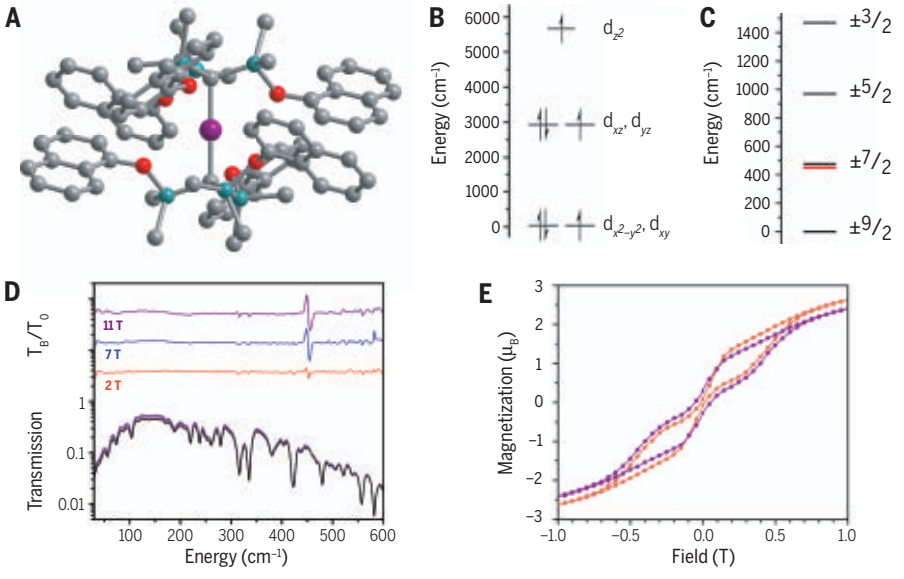

Linear dialkyl cobalt(II). (**A**) Molecular structure of $Co(C(SiMe_2ONaph)_3)_2$. Purple, gray, turquoise, and red spheres represent Co, C, Si, and O, respectively. Hydrogen atoms have been omitted for clarity. (**B**) Energy diagram depicting the energy and electron occupations of the 3d orbitals. (**C**) The calculated splitting of the ground $^4\Phi$ state by spin-orbit coupling. The red line is the experimentally determined energy of the $M_J = \pm{}^7/_2$ state. (**D**) Variable-field FIR spectra of $Co(C(SiMe_2ONaph)_3)_2$. The top section shows the applied-field spectra (T_B) divided by the zero-field spectrum (T_0). (**E**) Variable-field magnetization data for $Co(C(SiMe_2ONaph)_3)_2$ and $Co_{0.02}Zn_{0.98}(C(SiMe_2ONaph)_3)_2$ at 1.8 K. μ_B, bohr magnetons.

The list of author affiliations is available in the full article online.
*Corresponding author. Email: jrlong@berkeley.edu
Cite this article as P. C. Bunting *et al.*, *Science* 362, eaat7319 (2018). DOI: 10.1126/science.aat7319

RESEARCH ARTICLE

MOLECULAR MAGNETS

A linear cobalt(II) complex with maximal orbital angular momentum from a non-Aufbau ground state

Philip C. Bunting[1], Mihail Atanasov[2,3], Emil Damgaard-Møller[4], Mauro Perfetti[5], Iris Crassee[6], Milan Orlita[6,7], Jacob Overgaard[4], Joris van Slageren[5], Frank Neese[2], Jeffrey R. Long[1,8,9]*

Orbital angular momentum is a prerequisite for magnetic anisotropy, although in transition metal complexes it is typically quenched by the ligand field. By reducing the basicity of the carbon donor atoms in a pair of alkyl ligands, we synthesized a cobalt(II) dialkyl complex, $Co(C(SiMe_2ONaph)_3)_2$ (where Me is methyl and Naph is a naphthyl group), wherein the ligand field is sufficiently weak that interelectron repulsion and spin-orbit coupling play a dominant role in determining the electronic ground state. Assignment of a non-Aufbau $(d_{x^2-y^2}, d_{xy})^3(d_{xz}, d_{yz})^3(d_{z^2})^1$ electron configuration is supported by dc magnetic susceptibility data, experimental charge density maps, and ab initio calculations. Variable-field far-infrared spectroscopy and ac magnetic susceptibility measurements further reveal slow magnetic relaxation via a 450–wave number magnetic excited state.

All materials exhibiting a large magnetic anisotropy have nonzero orbital angular momentum L arising from an electronic structure of partially filled (but not half-filled) energetically degenerate orbitals. In trivalent lanthanide ions, the valence 4f orbitals are well-shielded and interact little with their coordination environment, allowing for a nonzero L that couples with the total spin S to give rise to a total angular momentum J of $|L - S| \leq J \leq |L + S|$ and potentially a large magnetic anisotropy. In the case of transition metals, however, the ligand field typically removes any orbital degeneracy, leading to quenching of the orbital angular momentum ($L = 0$) and an appropriate description of the ground state in terms of S only. When magnetic anisotropy is present in such complexes, it is generally a weak effect that arises from mixing of electronic ground and excited states induced by spin-orbit coupling. Creating unquenched orbital angular momentum in molecular transition metal–based systems requires an unusually weak ligand field and/or two or more orbitals that are nearly degenerate. In this context, perhaps the simplest experimental system is a one-coordinate cobalt atom: individual cobalt atoms on a MgO surface (referred to as adatoms) were recently shown by scanning probe microscopy to have a $J = {}^9/_2$ ($L = 3, S = {}^3/_2$) ground state and exhibit near-maximal magnetic anisotropy in a half-integer spin 3d system (*1*).

In the regime of molecules, complexes with linearly coordinated transition metal ions have garnered interest of late because they are energetically unaffected by Jahn-Teller distortions, allowing for the possibility of virtually unquenched orbital angular momentum (*2*). Analogously to lanthanide complexes, such transition metal systems with nonzero L are best described by a total angular momentum J, which is split by spin-orbit coupling and the ligand field into $2J + 1$ M_J states (where M_J is the projection of J along the magnetic axis). Two transition metal complexes that have been described by using this formalism are the iron(II) complex $Fe(C(SiMe_3)_3)_2$ (where Me is methyl) and the iron(I) complex $[Fe(C(SiMe_3)_3)_2]^-$ (*3*, *4*). Both complexes have ground states with $L = 2$ due to electronic configurations that place three electrons in the degenerate orbital pair $d_{x^2-y^2}$ and d_{xy}, which arise from linear combinations of the d orbitals with magnetic quantum number $m_l = \pm 2$. A notable consequence of these electronic structures is that both complexes exhibit relatively large energy separations between their ground and first excited M_J states, making them prone to single-molecule magnet behavior (*5*). ac magnetic susceptibility data revealed that both molecules exhibit slow magnetic relaxation (the former complex under an applied dc field and the latter in zero applied field) with effective spin-reversal barriers (U_{eff}) of 178 and 246 cm^{-1}, respectively (*6*)—values close to the calculated energy separations between their ground and first excited M_J states (*7*, *8*).

At first glance it may seem impossible to increase orbital angular momentum for a transition metal complex beyond $L = 2$. An $L = 3$ ground state requires two sets of degenerate orbitals, ($d_{x^2-y^2}$, d_{xy}) ($m_l = \pm 2$) and (d_{xz}, d_{yz}) ($m_l = \pm 1$), with an odd number of electrons in each. The Aufbau principle describes the manner in which electrons fill orbitals, typically from lowest to highest energy. A more rigorous consideration of electronic structure accounts for three main effects: ligand field stabilization, interelectron repulsion, and spin-orbit coupling. Ligand field effects typically dominate when considering transition metal complexes. When the ligand field stabilization and interelectron repulsion energies are similar in transition metal complexes, high-spin electronic configurations arise. For example, placing three electrons in the orbitals ($d_{x^2-y^2}$, d_{xy})(d_{xz}, d_{yz}) could give the low-spin configuration $(d_{x^2-y^2}, d_{xy})^3(d_{xz}, d_{yz})^0$ if the energy separation between orbital pairs is larger than the electron pairing energy, or the high-spin configuration $(d_{x^2-y^2}, d_{xy})^2(d_{xz}, d_{yz})^1$ if the orbital pairs are relatively close in energy. For six electrons, the expected Aufbau filling of these orbitals is $(d_{x^2-y^2}, d_{xy})^4(d_{xz}, d_{yz})^2$, and as the sixth electron must be paired in either orbital pair, there is no reason to assume there would be any stabilization from the non-Aufbau configuration, $(d_{x^2-y^2}, d_{xy})^3(d_{xz}, d_{yz})^3$.

Calculations on the hypothetical complex $Co(C(SiMe_3)_3)_2$ show a ground state with $L = 3$, which arises from a non-Aufbau 3d-orbital filling of $(d_{x^2-y^2}, d_{xy})^3(d_{xz}, d_{yz})^3(d_{z^2})^1$, and further predict a splitting between ground and first excited M_J states of 454 cm^{-1} (*9*). Efforts to synthesize this molecule both by our laboratory and by others (*10*) were unsuccessful. Moreover, although nearly 70 two-coordinate, paramagnetic transition metal complexes have been synthesized (*11*), the only such compounds with alkyl ligands are of the type $[M(C(SiMe_3)_3)_2]^{0/1-}$, where M is Fe(II) (*12*), Fe(I) (*4*), Mn(II) (*13*), and Mn(I) (*14*). Several approximately linear cobalt(II) complexes have been studied, however, and one such molecule, (sIPr)CoNDmp (where sIPr is an N-heterocyclic carbene and NDmp is an arylimido ligand), has a spin-reversal barrier of 413 cm^{-1}, more than 1.5 times that measured for $[Fe^I(C(SiMe_3)_3)_2]^-$, despite both molecules having the same total angular momentum of $J = {}^7/_2$ (*15*). Correspondingly, the increase in magnetic anisotropy for the Co(II) complex must arise from an increase in the spin-orbit coupling constant, a value which trends with effective nuclear charge. In another example, bent $[OCoO]^-$ anions inserted into the channels of an apatite-type structure were shown to have a spin-reversal barrier of 387 cm^{-1} (*16*). A semi-empirical model

[1]Department of Chemistry, University of California, Berkeley, CA 94720, USA. [2]Max-Planck-Insitut für Kohlenforschung, Mülheim an der Ruhr D-45470, Germany. [3]Institute of General and Inorganic Chemistry, Bulgarian Academy of Sciences, Academy Georgi Bontchev, Sofia 1113, Bulgaria. [4]Department of Chemistry and Centre for Materials Crystallography, Aarhus University, DK-8000 Aarhus C, Denmark. [5]Institut für Physikalische Chemie and Center for Integrated Quantum Science and Technology (IQST), Universität Stuttgart, Pfaffenwaldring 55, 70569 Stuttgart, Germany. [6]Laboratoire National des Champs Magnétiques Intenses, CNRS-UGA-UPS-INSA-EMFL, 25 rue des Martyrs, 38042 Grenoble, France. [7]Institute of Physics, Charles University, Ke Karlovu 5, 12116 Praha 2, Czech Republic. [8]Department of Chemical and Biomolecular Engineering, University of California, Berkeley, CA 94720, USA. [9]Materials Sciences Division, Lawrence Berkeley National Laboratory, Berkeley, CA 94720, USA.
***Corresponding author. Email: jrlong@berkeley.edu**

based on ligand field parameterization predicted that such a barrier could arise from a $J = {}^{9}/_{2}$ ground state, with increasing mixing of M_J states (and a concomitant diminishing of the barrier height) arising as the $[OCoO]^-$ anion becomes increasingly bent. In the extreme case of the cobalt adatoms mentioned above, a separation of 468 cm^{-1} was determined for the separation between $M_J = {}^{9}/_{2}$ and ${}^{7}/_{2}$ states (1).

Our motivations to isolate a dialkyl cobalt(II) complex were thus twofold: First, the proposed electronic structure violates the Aufbau principle and is analogous to what is commonly seen for lanthanides; second, realizing maximal orbital angular momentum should afford a very large magnetic anisotropy, a property that has important applications in the study of magnetism. Here, we present the synthesis and characterization of such a dialkyl cobalt(II) complex and confirm the proposed $J = {}^{9}/_{2}$ ground state through direct electronic and spectroscopic measurements, ab initio modeling, and magnetic susceptibility measurements. The energy separation between the $M_J = \pm{}^{9}/_{2}$ and $\pm{}^{7}/_{2}$ states leads to slow magnetic relaxation at temperatures as high as 70 K and low-temperature magnetic hysteresis.

Synthesis and structure of a linear cobalt dialkyl complex

Our attempts to synthesize $Co(C(SiMe_3)_3)_2$ from metathesis reactions of $[C(SiMe_3)_3]^-$ salts and CoX_2 (X = Cl, Br, or I) gave only intractable amorphous black solids. Similar reactivity with $[C(SiMe_3)_3]^-$ was reported previously, but after switching to $[C(SiMe_2Ph)_3]^-$ (where Ph is phenyl), we found it possible to isolate the dimer $[Co(C(SiMe_2Ph)_3)]_2$, a product formed by the in situ reduction of cobalt(II) (*10*). Thus, at least one challenge in isolating a dialkyl cobalt(II) complex is the strongly reducing nature of the carbanion. Others have shown that substituting electron-withdrawing alkoxides onto each silyl group substantially reduces the basicity and electron density of the carbanion (*17*, *18*). In an initial pursuit of this approach, we found that $[C(SiMe_2OPh)_3]^-$ did support a dialkyl cobalt(II) complex, $Co(C(SiMe_2OPh)_3)_2$, but long-range Co···O interactions led to a substantially bent C–Co–C axis (fig. S1). We next synthesized a number of $[C(SiMe_2OR)_3]^-$ derivatives (R = various alkyl or substituted phenyl groups) by following the general reaction scheme outlined in Fig. 1A. Smaller substituents did not readily yield isolable products, and larger substituents supported only dinuclear complexes of the type $(R_3CCo)_2(\mu\text{-}X)_2$ (where X is a halide), similar to the structure of $((PhMe_2Si)_3CZn)_2(\mu\text{-}Cl)_2$ (*19*). In an effort to reduce the nucleophilicity of the oxygen atom, we also tried using electron-withdrawing substituents such as perfluorophenyl but found these ligands to be susceptible to Si–O cleavage, a challenge also encountered in trying to metalate other $HC(SiMe_2OR)_3$ complexes with MeLi (*20*). Ultimately, we determined that only the naphthol (R = Naph = $C_{10}H_7$) derivative yielded the requisite linear geometry.

The reaction of two equivalents of KC(SiMe$_2$ONaph) with $CoBr_2$ in tetrahydrofuran (THF) at 60°C affords a green solution. After removal of the solvent in vacuo and redissolution into hexanes, dark red crystals of $Co(C(SiMe_2ONaph)_3)_2$ (**1**) emerged from the green solution over the course of several days at room temperature. Crystallization at −30°C formed green crystals that were not suitable for x-ray diffraction, but elemental analysis of the thoroughly dried crystals suggested the isolation of the solvated complex, $Co(C(SiMe_2ONaph)_3)_2(THF)$. Compound **1** is insoluble in common organic solvents, and exposure to THF led to the formation of a green solution that is likely the aforementioned solvated complex. The zinc congener, $Zn(C(SiMe_2ONaph)_3)_2$ (**2**), was obtained from the reaction of KC(SiMe$_2$ONaph) and $ZnBr_2$ in Et_2O (Et = ethyl). After removal of KBr by filtration, colorless crystals of **2** grew from the Et_2O solution over the course of several days. Using the same reaction conditions with a mixture of $ZnBr_2$ and $CoBr_2$(THF) further enabled the preparation of a magnetically dilute sample, $Co_{0.02}Zn_{0.98}(C(SiMe_2ONaph)_3)_2$ (**3**).

Single-crystal x-ray diffraction analysis revealed compounds **1** and **2** to be isostructural, crystallizing in space group *R*–3 (no. 148) and featuring a linear C–M–C axis imposed by the S_6 site symmetry (Fig. 1, B and C). The Co–C and Zn–C interatomic distances of 2.066(2) and 1.995(3) Å, respectively, are similar to the Fe–C separation of 2.0505(14) Å in $Fe(C(SiMe_3)_3)_2$ (*12*) and the Zn–C separation of 1.982(2) Å in $Zn(C(SiMe_3)_3)_2$ (*21*). In addition, the Co···O distance of 3.1051(11) Å and the Zn···O distance of 3.1240(16) Å are substantially longer than the sum of cobalt or zinc and oxygen ionic radii (~2.2 Å), suggesting minimal interactions. Instead, the staggered orientation of the ligands facilitates close sp^3-CH···π and sp^2-CH···π contacts of 2.692 and 2.822 Å, respectively (fig. S3), which are in the range of weak CH-π interactions (*22*). This suggests that interligand interactions may help stabilize **1**, consistent with reports of dispersion forces stabilizing other two-coordinate complexes (*23*).

Electronic structure calculations

Ab initio calculations performed on **1** by using the crystal structure geometry reveal that the ^{4}F free-ion state is split by the linear ligand field into three doubly-degenerate states, $^4\Phi$, $^4\Pi$, and $^4\Delta$, and one nondegenerate state, $^4\Sigma^-$ (here we employ $C_{\infty v}$ point group notation). Because of the weak ligand field, the seven states of ^{4}F parentage are split by less than 3000 cm^{-1}

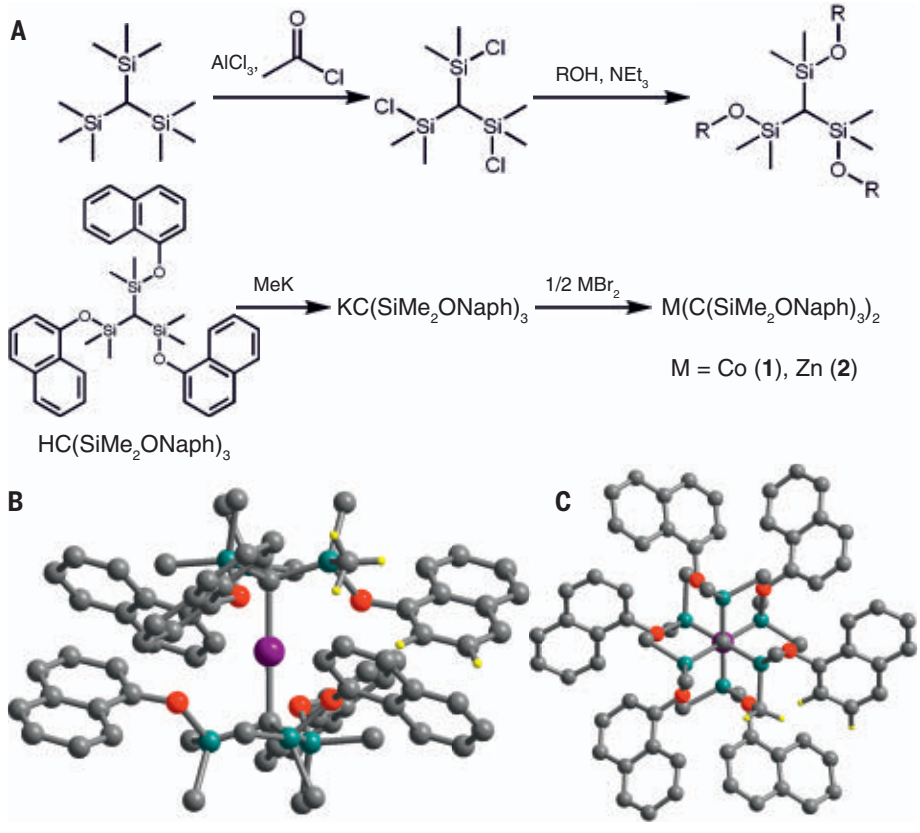

Fig. 1. Synthesis and structure of linear Co and Zn dialkyl complexes. (**A**) General synthetic scheme for ligands of the type $HC(SiMe_2OR)_3$ and synthesis of compounds **1** and **2**. (**B**) Molecular structure of $Co(C(SiMe_2ONaph)_3)_2$ (**1**). Purple, gray, turquoise, red, and yellow spheres represent Co, C, Si, O, and H atoms, respectively. Most hydrogen atoms have been omitted for clarity. Hydrogen atoms are shown on three carbons to illustrate the location of the CH-π interactions. (**C**) Molecular structure of $Co(C(SiMe_2ONaph)_3)_2$ viewed along the molecular *z* axis.

(accounting also for interelectron repulsion energy). This splitting is small even relative to that of other two-coordinate complexes; for example, the ^{5}D and ^{4}F free-ion states of $Fe(C(SiMe_3)_3)_2$ and $[Fe(C(SiMe_3)_3)_2]^-$ are split by 5000 and 6000 cm^{-1}, respectively (*3*, *4*, *7*). Excitations from the $^4\Phi$ ground state of **1** to the $^4\Sigma^-(^4P)$ and $^4\Pi(^4P)$ states were calculated to be spectroscopically accessible at 13,537 and 18,864 cm^{-1} and are observed in the ultraviolet-visible (UV-vis) diffuse reflectance spectrum at 12,000 and 15,000 cm^{-1} (fig. S4). The splitting of the $^4\Phi$ ground state due to spin-orbit coupling results in four sets of Kramers doublets, best described by $M_J = \pm^9/_2$, $\pm^7/_2$, $\pm^5/_2$, and $\pm^3/_2$, in order of increasing energy. The total splitting of $^4\Phi$ is 1469 cm^{-1}, whereas the calculated separation between just $M_J = \pm^9/_2$ and $M_J = \pm^7/_2$ is 476 cm^{-1}. Additional calculations performed on a truncated model molecule show that inclusion of the carbon σ-bonding electrons in the complete active space has only a very minor effect (less than 3%) on the energies of both the nonrelativistic and relativistic states (tables S10 and S11).

Ligand field analysis of the calculations revealed the $^4\Phi$ ground state to have the 3d-orbital filling $(d_{x^2-y^2}, d_{xy})^3(d_{xz}, d_{yz})^3(d_{z^2})^1$ (Fig. 2A), which deviates from the expected Aufbau orbital filling of $(d_{x^2-y^2}, d_{xy})^4(d_{xz}, d_{yz})^2(d_{z^2})^1$ ($^4\Sigma^-$) and can be explained by considering the competing effects of ligand-field stabilization and interelectron repulsion. In general, interelectronic repulsion is strongest for two electrons occupying the same orbital (necessarily with opposite spin). Two electrons with opposite spin in different orbitals alternatively experience medium-strong electron-electron repulsion, whereas two electrons with parallel spin (necessarily in different orbitals) repel each other least strongly, owing to the presence of the Fermi hole. Typically, only the electron-pairing energy component of interelectron repulsion is important for transition metal complexes, and whether a complex is high or low spin is determined by considering whether the ligand field strength is small or large compared with the pairing energy. In the case of **1**, the ligand field strength is so small that not only does the molecule display a high-spin state, but it also maximizes its orbital angular momentum in keeping with the Hund rule for free atoms and ions, thus leading to a non-Aufbau ground state configuration. Clearly, the $(d_{x^2-y^2}, d_{xy})^3(d_{xz}, d_{yz})^3(d_{z^2})^1$ configuration minimizes electron-electron repulsion relative to the alternative $(d_{x^2-y^2}, d_{xy})^4(d_{xz}, d_{yz})^2(d_{z^2})^1$ configuration that features an electronically crowded $(d_{x^2-y^2}, d_{xy})^4$ subshell. This stabilization is also reflected in the total orbital angular momentum of the ground state that is an approximately good quantum number in this system. Nonrelativistic ligand field calculations without interelectron repulsion show the expected ground state of $^4\Sigma^-$ (with $L = 0$). By using ligand field parameters from ab initio *n*-electron valence perturbation theory to second order (NEVPT2) calculations and ligand field expressions for the $S = {}^3/_2$ states under linear symmetry with interelectron repulsion, the high orbital angular momentum $^4\Phi$ state (with $L = 3$) is stabilized by 1300 cm^{-1} relative to the $^4\Sigma^-$ state (Fig. 2B and table S9). Spin-orbit coupling further stabilizes the $M_J = {}^9/_2$ component of the $^4\Phi$ ground state by 788 cm^{-1}.

This situation is completely distinct from that of established complexes with stronger ligand fields that can sometimes have electronic ground states with substantial contributions from non-Aufbau configurations. For example, the iron(II) metallophthalocyanine complex (FePc) has a ground state with nearly equal contributions from Aufbau and non-Aufbau configurations, wherein the non-Aufbau component arises from an accidental orbital near-degeneracy (*24*). The essential difference between complex **1** and FePc, however, is in ligand field strength, with the two molecules calculated to exhibit total d-orbital splittings of 6000 and 165,000 cm^{-1} (*24*), respectively. With the focus on the orbitals that give rise to the non-Aufbau states, the ($d_{x^2-y^2}$, d_{xy}) and (d_{xz}, d_{yz}) orbital pairs are separated by 2900 cm^{-1} in **1**, whereas for FePc the (d_{xz}, d_{yz}) orbital pair and d_{z^2} orbital are separated by 19,000 cm^{-1} (*24*). Our calculations show that interelectron repulsion in **1** easily overwhelms the ligand field stabilization energy associated with the Aufbau configuration, destabilizing the $^4\Sigma^-(^4P)$ state by 12,000 cm^{-1} relative to the $^4\Phi$ state. No similar calculations appear to have been reported for FePc, but it is clear that it would be impossible to observe a pure non-Aufbau ground state as long as the ligand field stabilization energy is of the same magnitude as interelectron repulsion. Once the ligand field requirement for a non-Aufbau ground state is met, it is also possible to observe maximal orbital angular momentum. The maximal orbital angular momentum of $L = 3$ for transition metals requires degenerate ($d_{x^2-y^2}$, d_{xy}) and (d_{xz}, d_{yz}) orbital pairs, and thus the molecule should also be linear to avoid Jahn-Teller distortions.

The ligand field analysis elucidates another challenge in isolating a dialkyl cobalt complex: Namely, the ligand field stabilization energy suggests that metal-ligand bond formation provides only a minor stabilizing effect of 4.8 kcal/mol (1700 cm^{-1}). This result is perhaps intuitively understood by considering that the formal Co–C bond order is approximately one-half, because the (d_{xz}, d_{yz}) orbitals have slight π-antibonding character and are destabilized primarily by electrostatic interactions. It is not until we consider transmetallic dispersion and electrostatic (CH···π) forces that **1** appears to be stable.

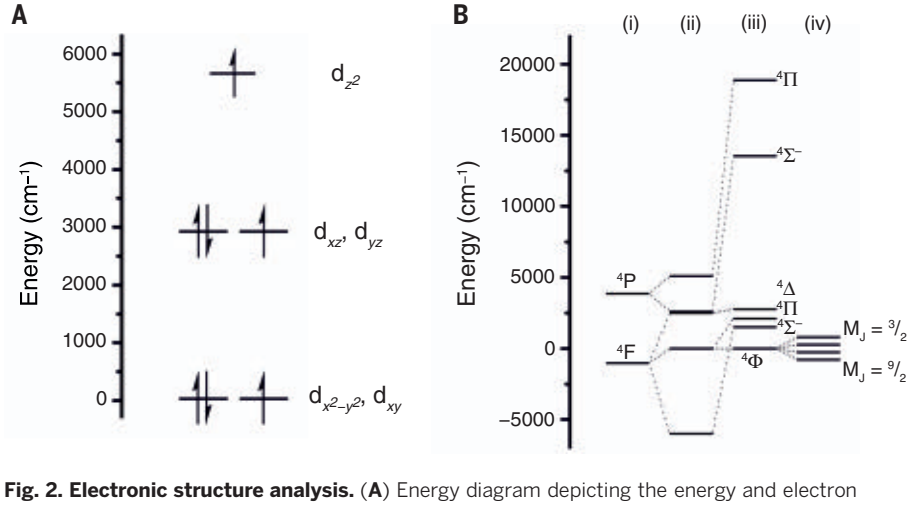

Fig. 2. Electronic structure analysis. (**A**) Energy diagram depicting the energy and electron occupations of the 3d orbitals on the basis of ligand field analysis of ab initio calculations. (**B**) Electronic structure of (i) a free Co(II) ion, (ii) $Co(C(SiMe_2ONaph)_3)_2$ (**1**) considering only ligand field interactions, (iii) $Co(C(SiMe_2ONaph)_3)_2$ considering both ligand field interactions and interelectron repulsion, and (iv) the splitting of the ground $^4\Phi$ state of $Co(C(SiMe_2ONaph)_3)_2$ because of spin-orbit coupling according to ab initio calculations. Term symbols are for $C_{\infty v}$ symmetry. The splitting between the ground $M_J = {}^9/_2$ and maximal excited $M_J = {}^3/_2$ states is 1469 cm^{-1}.

Charge density determination

The molecular charge density (CD) of **1** was obtained from multipolar refinement of single-crystal x-ray diffraction data measured at 20 K by using synchrotron radiation. A small amount of disorder (~6%) is present in the structure because of flipping of the naphthalene groups (also involving the O and Si atoms); however, a detailed description of this disorder was possible and allowed us to extract quantitative information pertinent to the magnetic properties (see methods for a detailed description of the experimental procedure).

The experimental temperature of 20 K is low enough that the CD represents primarily the electronic properties of the relativistic ground state. We used an atom-centered multipole formalism to describe the CD, and thus a complete set of spherical harmonic functions for each atom was used to quantify the deviations from a spherical density distribution. The use of this formalism enables estimation of 3d-orbital populations on the central cobalt atom, under the assumption that the density around the metal

originates solely from the atom itself (i.e., that no substantial covalent bonding occurs). The parameterized CD also enables an analysis in the framework of quantum theory of atoms in molecules (QTAIM) (*25*) and estimates of atomic charges and the strength of chemical bonding. With the local coordination axes defined such that the Co–C direction is along the *z* axis, the electron density of the cobalt valence shell is distributed in the following manner: 42.8% is in the ($d_{x^2-y^2}$) orbitals, 41.2% is in the (d_{xz}, d_{yz}) orbitals, and 16.0% is in the d_{z^2} orbital. Furthermore, the same distribution of electrons in the cobalt 3d orbitals was obtained regardless of the manner in which the naphthalene disorder was treated.

Variable-field far-infrared spectroscopy

We sought to confirm experimentally the magnitude of the separation between the ground and first excited magnetic states in **1** by using variable-field far-infrared (FIR) spectroscopy (*26*, *27*). Although such energy separations are more commonly determined by fitting low-temperature magnetization data or high-temperature magnetic relaxation data, these approaches give values that are sensitive to fitting procedures and provide only an indirect measure of the representative ground–to–excited-state energy separation. Additionally, given the calculated energy splitting of 476 cm^{-1} for the lowest M_J states, dc susceptibility measurements would provide limited information on the position of excited states, as the Boltzmann population of the ground state doublet is still 90% at 300 K. Thus, not only is spectroscopy a more direct measurement, but in this case, it is also necessary to gain information on the excited states. Transmission spectra in the 30- to 600-cm^{-1} energy range were collected at a temperature of 4.2 K under applied fields ranging from 0 to 11 T (Fig. 3A). Although absorption bands associated with magnetic dipole transitions are usually substantially weaker than those of electronic dipole transitions, a pronounced field dependence is immediately evident in the data upon dividing the applied-field spectra by the zero-field spectrum (Fig. 3B). The only peak visible in this energy range is at 450 cm^{-1} and is attributable to the transition from $M_J = \pm{}^9/_2$ to $\pm{}^7/_2$, in good agreement with the calculated separation of 476 cm^{-1}. A steadily increasing blue shift of the infrared (IR) absorption maximum is observed with increasing applied fields (fig. S5) and is in good agreement with a simulation of the spectral envelope magnetic dipole $M_J = \pm{}^9/_2$ to $\pm{}^7/_2$ transitions (fig. S6). In addition to the blue shift, there is a concomitant decrease in absorption intensity and peak broadening with increasing field, giving rise to the derivative shape observed in Fig. 3B.

Magnetic properties

Variable-temperature dc magnetic susceptibility data for **1** are shown in Fig. 4A. The gradual decrease in the product of the molar magnetic susceptibility and temperature ($\chi_M T$) with decreasing temperature is indicative of magnetic anisotropy, whereas the strong field dependence at low temperature arises from an increased Zeeman splitting at higher fields. The room temperature $\chi_M T$ value of 4.89 cm^3 K mol^{-1} is consistent with a well-isolated $M_J = {}^9/_2$ ground state (the theoretical $\chi_M T$ value for an isotropic $J = {}^9/_2$ ion is 5.47 cm^3 K mol^{-1}), and reduced magnetization plots (Fig. 4B) show a saturation magnetization of 3.00 bohr magnetons (μ_B). The simulated $\chi_M T$ and reduced magnetization data from ab initio calculations (solid lines, Fig. 4) are in close agreement with the experimental data, further corroborating the well-isolated $M_J = {}^9/_2$ ground state.

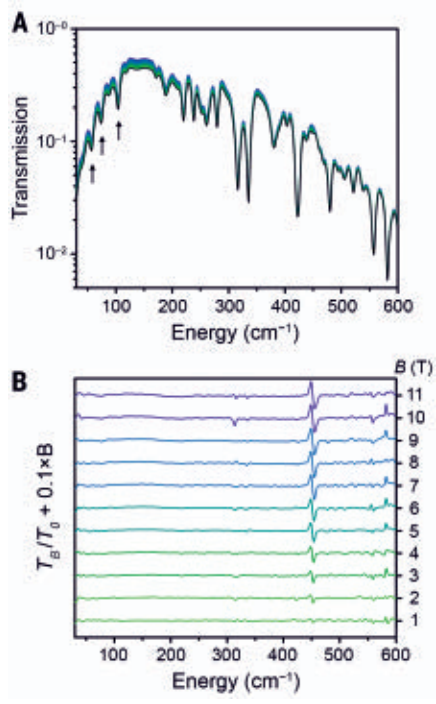

Fig. 3. Variable-field FIR spectroscopy. (**A**) Absolute transmission spectra for **1** collected at 4.2 K under applied fields ranging from 0 to 11 T. Phonon energies used in Eq. 2 to describe magnetic relaxation are marked with arrows. (**B**) Plots of applied-field spectra (T_B) divided by the zero-field spectrum (T_0), where B is the applied field. The peak at 450 cm^{-1} corresponds to the transition from $M_J = {}^9/_2$ to $M_J = {}^7/_2$. The spectra have been vertically offset for clarity.

ac susceptometry was used to probe magnetic relaxation in the range from 10^{-4} to 10^1 s (10^4 to 10^{-1} Hz). By fitting the in-phase (χ') and out-of-phase (χ'') susceptibility (figs. S8 to S11) to a generalized Debye model, we obtained relaxation times for **1**, as shown in the Arrhenius plot in Fig. 5A. The temperature dependence of the magnetic relaxation time (τ) in molecules exhibiting slow magnetic relaxation is typically described by the expression

$$\tau^{-1} = \frac{A_1}{1 + A_2 H^2} + BH^4 T + CT^n + \tau_0^{-1}\exp(-U/k_B T) \quad (1)$$

where the four terms represent quantum-tunneling, direct, Raman, and Orbach relaxation processes, respectively (*28*–*30*). However, we were unable to fit the relaxation data for **1** to the total sum of these processes. An alternative model for through-barrier relaxation has recently been proposed, wherein specific phonon modes may facilitate relaxation through direct doublet transitions (*31*, *32*). Building on the results of Lunghi and co-workers, we derived the expression

$$\tau^{-1} = \tau_{tunnel}^{-1} + \sum_\alpha \left(\frac{V_\alpha^2}{\hbar} \frac{\Delta_\alpha (2n_\alpha + 1)}{[\Delta_\alpha^2 + (\hbar\omega_\alpha)^2]} \right) + \tau_0^{-1}\exp(-U/k_B T) \quad (2)$$

where the first term represents quantum tunneling and the last term represents Orbach relaxation. The second term represents relaxation through the α-th phonon mode, V represents spin-phonon coupling, Δ is the phonon linewidth, n is the phonon occupation number, ω is the phonon frequency, and $\hbar$ is Planck's constant. Both Δ and n are dependent on both temperature and ω. Values for U and ω are taken from the variable-field FIR data, whereas τ_{tunnel}, V, and τ_0 are fit parameters (see eqs. S1 to S4 for details). From this equation, we were able to obtain reasonable fits (SE of the estimate = 0.17 and 0.21 for **1** and ***3***, respectively) to the relaxation data in Fig. 5A.

To further examine the effect of any tunneling relaxation process, we collected data under a 3000-Oe field. The lack of a temperature-independent region at low temperature under zero and applied field indicates that molecular quantum tunneling is not a dominant relaxation pathway above 4 K; however, the observed increase in relaxation times upon application of a dc field (Fig. 5A) demonstrates that it is a contributing factor. To some extent, the tunneling relaxation rate can be slowed through magnetic dilution (*33*), and a magnetically dilute sample prepared with a 1:49 ratio of cobalt to zinc (***3***) exhibits lower relaxation rates than **1** under zero field. The lack of a linear temperature dependence at the highest temperatures indicates that two-phonon Orbach relaxation (involving excitation to and relaxation from a real excited state) is not yet dominant at 70 K. By using the value of U = 450 cm^{-1} obtained from FIR spectroscopy, however, we determined an upper bound for τ_0 of 1.79 × 10^{-9} s, which is a reasonable value for a single-molecule magnet (*5*).

The low-temperature relaxation dynamics of **1** and ***3*** were also probed by using dc relaxation and magnetization experiments (Fig. 5B). The tunneling and direct relaxation terms introduced above were used in fits of the variable-field relaxation data and are discussed in detail in the methods. The relaxation times extracted at 1.8 K and zero applied field are 16.4 ± 0.7 and 48.2 ± 4.7 s for **1** and ***3***, respectively, and these values slow to 221 and 660 s at 1.8 K under a 1500-Oe applied field. These relaxation times suggest that magnetic hysteresis should be apparent in variable-field magnetization data, and

1 and **3** show waist-restricted hysteresis loops between −0.7 and 0.7 T up to 5 K. A sudden decline in the magnetization as the field approaches zero can be ascribed to rapid relaxation induced by tunneling of the magnetization (Fig. 5, C and D), and this decline results in small values of the remnant magnetization for **1** (0.08 μ_B) and **3** (0.28 μ_B) at 1.8 K that diminish to near zero at higher temperatures. Despite the relatively fast relaxation at zero field, **1** has a coercive field H_c of 180 Oe at 1.8 K, as measured with a field sweep rate of 32 Oe/s. Under the same conditions, the magnetically dilute sample, **3**, exhibits H_c = 600 Oe.

Outlook

These results have clear implications for technologies that require a large magnetic anisotropy. For a magnetic bit to retain its magnetization for information storage, the magnetic anisotropy energy must be substantially greater than the thermal energy. For the cobalt adatom on MgO, the separation between the ground ($M_J = \pm{}^9/_2$) and first excited ($M_J = \pm{}^7/_2$) states was determined to be 468 cm^{-1}, and it was suggested that this value was near a physical limit for magnetic anisotropy for 3d transition metals. This limit can be quantified by using the phenomenological spin-orbit coupling Hamiltonian, $H_{SOC} = \lambda \mathbf{LS} = ({}^{\zeta}/_{2S})\sum_i \mathbf{l}_i\mathbf{s}_i$, where λ is the effective spin-orbit coupling constant, ζ is the atomic spin-orbit coupling constant, and $\mathbf{L} = \Sigma_i \mathbf{l}_i$ and $\mathbf{S} = \Sigma_i \mathbf{s}_i$ are the operators for the orbital and spin-angular momenta, respectively (the index i sums over individual electrons). In systems with a doubly degenerate ground state, the energies (E) of the M_J states (where $M_J = M_S + M_L$) are given by $E(M_J) = ({}^{\zeta}/_{2S})M_L M_S$; the separation between lowest and highest M_J states is equal to $L\zeta$, and the separation between adjacent states is $({}^{L}/_{2S})\zeta$. Thus, the actual limit for the energy separation between ground and first excited states would be found in a system with $L = 3$ and $S = 1$. However, in order to maximize relaxation times, it is advantageous to use half-integer spin systems, as the crystal field cannot couple the two components of the lowest doublet and the tunneling relaxation pathway is therefore suppressed (*34*). The maximal total angular momentum for a transition metal with half-integer spin is $J = {}^9/_2$, exhibited by both the cobalt adatom and compound **1**. The magnetic M_J states of **1** span a substantial calculated energy range of 1469 cm^{-1}, and the separation between the ground ($M_J = \pm{}^9/_2$) and first excited ($M_J = \pm{}^7/_2$) states alone is 450 cm^{-1}. Within a rigorously linear geometry, it may be possible to further increase the magnetic anisotropy by changing the nature of the Co–L bond (L = ligand) and by increasing the spin-orbit coupling constant. However, at present the barrier of U_{eff} = 450 cm^{-1} determined here for **1** is the largest measured to date for any transition metal single-molecule magnet, with the second largest being U_{eff} = 413 cm^{-1} from the aforementioned (sIPr)CoNDmp complex (*15*). Given the similarity between the cobalt adatom and **1**, it is possible that this value is near the physical limit. Our calculations for the Co adatom on MgO indicate that the $^4\Phi(^4F)$ ground state is also well isolated in this system, suggesting that spin-orbit coupling is also the dominant factor determining the energies of the M_J states (table S13). Although information storage will certainly require longer zero-field relaxation times than observed here, magnetic relaxation times can be substantially affected by the molecular environment, as has been observed for terbium(III) bis(phthalocyaninato) molecules in bulk solids (*35*) and on a variety of surfaces (*36*–*41*). A comparison of the relaxation times of the cobalt adatom on MgO and those of compound **1** indicates that such an environmental effect is at play. The two cobalt centers have similar electronic structures, yet the relaxation time for the adatom at 0.6 K is on the order of 10^{-4} s, whereas a much longer relaxation time on the order of 10^1 s is observed for **1** at 1.8 K.

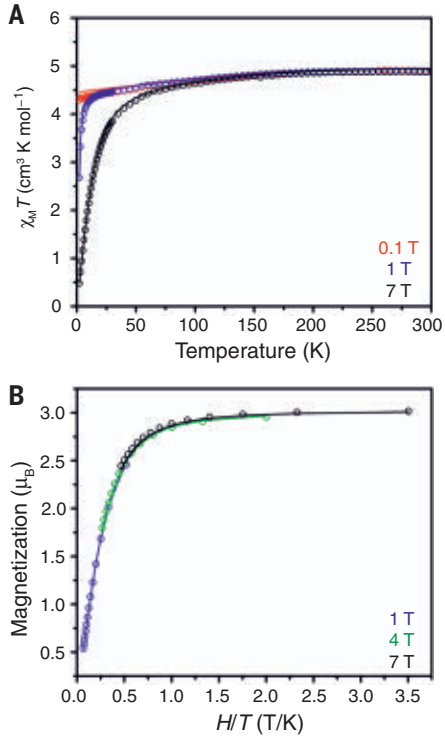

Fig. 4. Magnetic susceptibility and reduced magnetization analysis. (**A**) Variable-temperature molar magnetic susceptibility times temperature ($\chi_M T$) for **1** collected under dc fields (H) of 0.1, 1, and 7 T. Solid lines are simulated data from ab initio calculations. (**B**) Reduced magnetization data for **1** collected at temperatures from 2 to 15 K under dc fields of 1, 4, and 7 T. Solid lines are simulated data from ab initio calculations.

Beyond the implications for molecular magnetism, an intriguing potential use of the linear L–Co^{II}–L moiety is in the pursuit of lanthanide-free bulk magnets. Generally speaking, orbital angular momentum and spin-orbit coupling tie the magnetic moment to the lattice (*42*). In bulk magnetism, orbital angular momentum is responsible for magnetocrystalline anisotropy, the main determinant of magnetic coercivity, which is why the strongest magnets, such as $Nd_2Fe_{14}B$ and $SmCo_5$, feature lanthanide ions with unquenched orbital angular momentum. Our results show how linearly coordinated transition metal ions could provide a similar effect. For example, the extended solid $Li_2(Li_{1-x}Fe_x)N$ features linear iron(I) centers similar to those in $[Fe(C(SiMe_3)_3)_2]^-$, and in high concentration (x = 0.28), this material displays a large coercivity (H_c = 11.6 T at 2 K) (*43*). The magnetic anisotropy of compound **1** is nearly twice as large as that of $[Fe(C(SiMe_3)_3)_2]^-$, and incorporation of the L–Co^{II}–L moiety in an extended solid could therefore in principle lead to permanent magnets with an even greater coercivity.

Materials and methods

General considerations

Unless otherwise noted, all manipulations were carried out using standard air-free Schlenk line and glove box techniques under an argon atmosphere. Reagents were purchased from commercial vendors. Anhydrous $CoBr_2$ and $ZnBr_2$ were used as received, whereas 1-naphthol was sublimed and triethylamine (NEt_3) was dried over KOH and distilled prior to use. $HC(SiMe_2Cl)_3$ (*17*) and MeK (*44*) were prepared according to literature procedures. Solvents were dried by using a commercial solvent purification system designed by JC Meyer Solvent Systems. Elemental analysis was performed at the Microanalytical Laboratory of the University of California, Berkeley. Nuclear magnetic resonance (NMR) spectra were collected on a 500-MHz Bruker spectrometer; chemical shifts are reported in parts per million (ppm) referenced to residual protiated solvent.

Synthesis of $HC(SiMe_2OPh)_3$ and $HC(SiMe_2OC_{10}H_7)_3$

A 100-ml Schlenk flask containing a stir bar was charged with a THF solution (50 ml) of $HC(SiMe_2Cl)_3$ (3.73 g, 12.7 mmol) and NEt_3 (1.80 ml, 38.1 mmol). A separate 50-ml Schlenk flask was charged with a THF solution (25 ml) of 1-naphthol (5.58 g, 38.7 mmol). The 1-naphthol solution was added to the reaction flask over the course of several minutes with stirring, and a white precipitate immediately formed upon addition. The reaction mixture was stirred at room temperature for 3 hours, after which air-free techniques were no longer required. Water (20 ml) was added to the reaction flask, and the organic layer was collected. The water was extracted with 3×20 ml Et_2O, and the combined organic layers were dried with $MgSO_4$. The ether solvent was removed under reduced pressure, leaving a colorless residue. The residue was washed with MeOH (50 ml), and the resulting white solid, $HC(SiMe_2OC_{10}H_7)_3$ (5.15 g, 66%), was collected by filtration. Anal. calcd. for $C_{37}H_{40}O_3Si_3$: C, 72.03; H, 6.54. Found: C, 72.04; H, 6.75. ^{1}H NMR (500 MHz, THF-d8): δ 8.33 (3 H, d), 7.83 (3 H, d), 7.47 (3 H, d), 7.40 (6 H, m), 7.32 (3 H, t), 7.03 (3 H, d), 1.39 (1 H, s), 0.63 (18 H, s) ppm. ^{13}C NMR (500 MHz, THF-d8): δ 151.8, 136.0, 128.9, 128.3,

126.7, 126.4, 125.7, 123.4, 122.0, 114.4, 13.1, 2.9, 2.8 ppm.

The same method was used to synthesize $HC(SiMe_2OPh)_3$, which has been reported previously using a different synthetic method (*45*). The identity of $HC(SiMe_2OPh)_3$ was confirmed by ^1H NMR spectroscopy.

Synthesis of $(CH_3OCH_2CH_2OCH_3)_2KC(SiMe_2OPh)_3$

Solid MeK (0.11 g, 1.9 mmol) was slowly added to a stirring solution of **1** (0.91 g, 1.9 mmol) dissolved in Et_2O (10 ml) and dimethoxyethane (3 ml); bubbles evolved during the course of addition. The reaction mixture was then allowed to stir for 3 hours, during which time a white microcrystalline solid precipitated from solution. The solid was collected by filtration and dried under vacuum (0.65 g, 0.95 mmol, 49%). Anal. calcd. for $KC_{33}H_{53}O_7Si_3$: C, 57.85; H, 7.80. Found: C, 57.83; H, 7.60. ^1H NMR (500 MHz, THF-d8): δ 7.15 (6 H, t), 6.91 (6 H, d), 6.83 (3 H, t), 3.42 (8 H, s), 3.26 (12 H, s), 0.24 (18 H, s) ppm. ^{13}C NMR (500 MHz, THF-d8): δ 158.3, 129.7, 122.2, 121.0, 72.7, 58.9, 16.8, 15.7, 5.2 ppm.

Synthesis of $KC(SiMe_2OC_{10}H_7)_3$

$HC(SiMe_2OC_{10}H_7)_3$ (0.967 g, 1.57 mmol) was dissolved in THF (15 ml). Freshly prepared MeK (0.0850 g, 1.57 mmol) was added as a solid to the stirring reaction mixture; bubbles evolved from the mixture over the course of an hour. After 3 hours, the reaction mixture was filtered through diatomaceous earth and solvent was removed under reduced pressure, leaving a sticky colorless residue. Hexane was added to precipitate a white solid, $KC(SiMe_2OC_{10}H_7)_3$ (1.20 g, 76%), which was collected by filtration. Anal. calcd. for $KC_{37}H_{39}O_3Si_3$: C, 67.84; H, 6.00. Found: C, 67.59; H, 6.31. ^1H NMR (500 MHz, THF-d8): δ 8.42 (3 H, d), 7.71 (3 H, d), 7.49 (3 H, d), 7.28 (12 H, m), 0.38 (18 H, s) ppm. ^{13}C NMR (500 MHz, THF-d8): δ 154.8, 135.9, 129.7, 127.7, 126.9, 125.6, 124.4, 124.2, 118.7, 114.5, 16.2, 5.9, 5.8 ppm.

Synthesis of $Co(C(SiMe_2OPh)_3)_2$

Solid $CoCl_2$ (18.2 mg, 0.140 mmol) was added to a stirring THF solution (10 ml) of $(CH_3OCH_2CH_2OCH_3)_2KC(SiMe_2OPh)_3$ (200. mg, 0.290 mmol) at room temperature, and then the mixture was stirred for 2 hours at 60°C. The solvent was removed in vacuo, and the resulting blue-green solid was dissolved in hexanes. The hexanes solution was stirred at 60°C for 1 hour to form a yellow-green solution. The hexanes solution was filtered through diatomaceous earth and was concentrated in vacuo. Red-brown crystals of $Co(C(SiMe_2OPh)_3)_2$ (0.044 g, 39%) suitable for x-ray diffraction grew in 2 hours at −30°C. Anal. calcd. for $CoC_{50}H_{66}Si_6O_6$: C, 60.63; H, 6.72. Found: C, 60.98; H, 6.84.

Synthesis of $Co(C(SiMe_2OC_{10}H_7)_3)_2$ (1)

Solid $CoBr_2$ (41.6 mg, 0.190 mmol) was added to a stirring THF (8 ml) solution of $KC(SiMe_2OC_{10}H_7)_3$ (249 mg, 0.380 mmol) at room temperature. The reaction mixture was stirred for 4 hours at 60°C, after which time the solution had turned green. The reaction mixture was filtered through diatomaceous earth, and solvent was removed under reduced pressure, leaving a green solid. The green solid was dissolved in hexanes (20 ml) and filtered to give an emerald green solution, from which brown-red crystals of **1** (17.8 mg, 7%) suitable for x-ray diffraction grew over the course of 3 days. Compound **1** is insoluble in all common organic solvents except THF, in which it forms a green solution. Anal. calcd. for $CoC_{74}H_{78}O_6Si_6$: C, 68.85; H, 6.09. Found: C, 68.36; H, 6.03.

Cooling the green hexanes solution appears to favor precipitation of the THF solvate, $Co(C(SiMe_2OC_{10}H_7)_3)_2(THF)$. Green crystals not suitable for single-crystal x-ray diffraction were grown from the green hexanes solution over 1 day at −30°C, collected by filtration, and thoroughly dried in vacuo. Anal. calcd. for $CoC_{78}H_{86}O_7Si_6$: C, 68.74; H, 6.36. Found: C, 68.66; H, 6.52.

Synthesis of $Zn(C(SiMe_2OC_{10}H_7)_3)_2$ (2)

At room temperature, a solution of $ZnBr_2$ (35.1 mg, 0.155 mmol) dissolved in THF (2 ml) was added to a solution of $KC(SiMe_2OC_{10}H_7)_3$ (206 mg, 0.314 mmol) dissolved in THF (8 ml), and the mixture was stirred at room temperature for 12 hours. The reaction mixture was subsequently filtered through diatomaceous earth, and the THF solvent was removed under reduced pressure, leaving a white solid. The colorless solid was stirred in hexanes (20 ml) and filtered to give a pale-yellow solution, from which colorless crystals of **1** (36.7 mg, 9%) suitable for x-ray diffraction grew over the course of 1 day. Anal. calcd. for $ZnC_{74}H_{78}O_6Si_6$: C, 68.51; H, 6.06. Found: C, 68.14; H, 5.92.

Synthesis of $Co_{0.02}Zn_{0.98}(C(SiMe_2OC_{10}H_7)_3)_2$ (3)

Initially, $CoBr_2(THF)$ was prepared by dissolving $CoBr_2$ (6.2 mg, 0.028 mmol) in THF (5 ml) and then removing the solvent under reduced pressure. A suspension of $CoBr_2(THF)$ (0.028 mmol) and $ZnBr_2$ (57.4 mg, 25.5 mmol) was prepared in Et_2O (4 ml), and this suspension was added to a stirring solution of $KC(SiMe_2OC_{10}H_7)_3$ (371 mg, 0.567 mmol) dissolved in Et_2O (6 ml). The mixture was stirred for 1 hour at room temperature and then filtered through diatomaceous earth. A light pink powder was collected from the

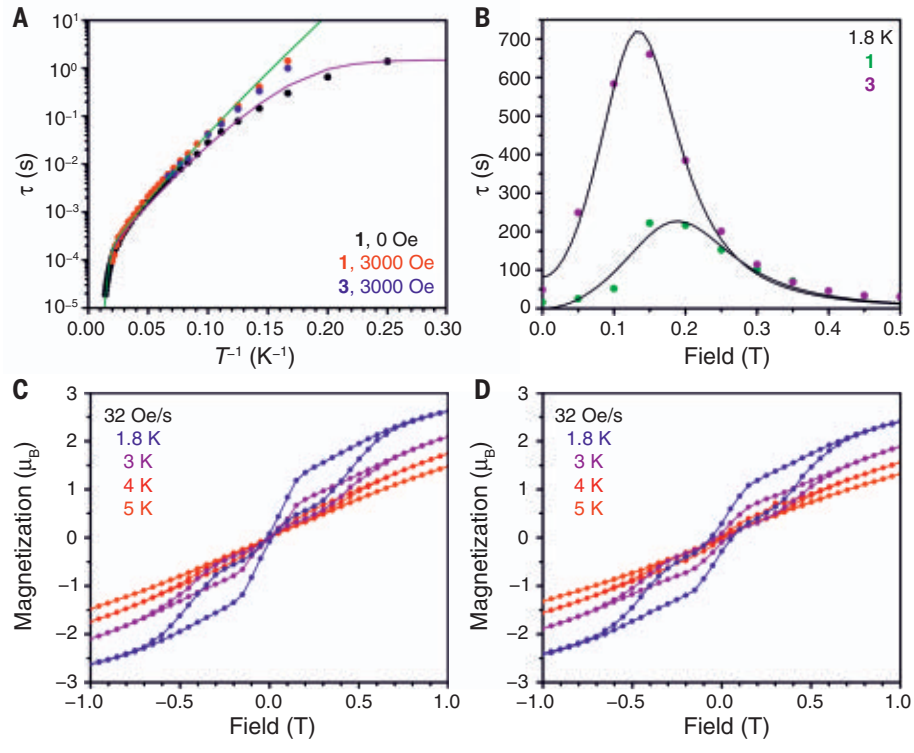

Fig. 5. Magnetic relaxation dynamics. (**A**) Arrhenius plot showing the natural log of relaxation time, τ, versus inverse temperature for **1** in the absence of an applied dc field (black circles), **1** under a 3000-Oe dc field (red circles), and **3** in the absence of an applied dc field (blue circles). Relaxation times are determined from fits of ac susceptibility measurements over the temperature range of 4 to 70 K. The purple and green lines represent fits of the relaxation data for **1** under 0 and 3000 Oe, respectively. (**B**) dc relaxation and magnetization times for **1** (green circles) and **3** (purple circles). The solid lines are from fits describing relaxation via tunneling and direct relaxation processes as described in the text and methods. (**C**) Variable-field magnetization data for **1** collected at temperatures ranging from 1.8 to 5 K at a field sweep rate of 32 Oe/s. (**D**) Variable-field magnetization data for **3** collected at temperatures ranging from 1.8 to 5 K at a field sweep rate of 32 Oe/s.

reaction mixture and the resulting light green Et_2O filtrate was put in a 20-ml vial. Crystallization tubes were added to the vial to increase the amount of crystallization surfaces, and Et_2O was added to fill the vial. Light pink crystals of **3** (63.9 mg, 9%) suitable for x-ray diffraction grew over the course of 4 days. Successful dilution was confirmed by determination of a unit cell consistent with pure **1** and **2**, and the metal composition was determined from comparison of molar magnetization data for the pure and diluted samples.

Single-crystal x-ray diffraction

In an argon-filled glove box, crystals of $Co(C(SiMe_2OPh)_3$, **1**, **2**, and **3** were coated in Paratone-N oil in individual vials, which were then sealed and remained sealed until immediately prior to mounting. Crystals were mounted on Kaptan loops and cooled under a stream of N_2. Data were collected using a Bruker QUAZAR diffractometer equipped with a Bruker MICROSTAR x-ray source of Mo Kα radiation (λ = 0.71073 Å) and an APEX-II detector. Raw data were integrated and corrected for Lorentz and polarization effects by using Bruker Apex3 v. 2016.5. Absorption corrections were applied by using SADABS (*46*). The space group was determined by examination of systematic absences, analysis of E-statistics, and successive refinement of the structure. The crystal structure was solved with ShelXT (*47*) and further refined with ShelXL (*48*) operated in the Olex2 software (*49*). The crystal did not show any substantial decay during data collection. Thermal parameters were refined anisotropically for all nonhydrogen atoms. Hydrogen atoms were placed in ideal positions and refined by using a riding model for all structures. A checkCIF report for **1** gave rise to a B-level alert regarding the ratio of maximum/minimum residual density. The maximum residual density for **1** lies in the napthyl ring. In the case of the low-temperature synchrotron data used for CD modeling, disorder in the naphthyl ring was successfully modeled. For the data collected at 100 K used for the generation of the CIFs for **1** and **2**, we were unable to fully model this disorder; however, it is likely that the same disorder is responsible for the relatively large residual density.

UV-vis near-IR diffuse reflectance

UV-vis near-IR diffuse reflectance spectra were collected by using a CARY 5000 spectrophotometer interfaced with Varian Win UV software. The samples were prepared in a glove box and held in a Praying Mantis air-free diffuse reflectance cell. Powdered $BaCO_3$ was used as a nonabsorbing matrix. The spectra were collected in $F(R)$ versus wave number, where $F(R)$ is the Kubelka-Munk conversion $F(R) = (1 - R)^2/2R$ and R is reflectance.

Magnetometry

All magnetic measurements were carried out by using a Quantum Design MPMS-XL SQUID magnetometer, with the exception of those for the high-frequency ac magnetic susceptibility data. High-frequency data (up to 10,000 Hz) were collected at the Quantum Design facility in San Diego, CA, by using a 9T PPMS instrument equipped with the ACMSII measurement option to probe the ac moment at frequencies above 1000 Hz. For the measurements using the MPMS instrument, polycrystalline samples of **1** (32.1 mg) and **3** (49.7 mg) were loaded into quartz tubes (5 mm i.d., 7 mm o.d.) with a raised quartz platform. Solid eicosane was then added on top of the samples (32.0 and 61.2, respectively) to prevent crystallite torqueing and provide good thermal contact between the sample and the cryogenic bath. The tubes were fitted with Teflon sealable adapters, evacuated by using a glove box vacuum pump, and sealed under static vacuum by using an H_2/O_2 flame. Following flame sealing, the solid eicosane was melted in a water bath held at 40°C. When not in the magnetometer, the sealed samples were stored at −30°C. dc magnetic susceptibility data were collected for each sample from 2 to 300 K under dc fields ranging from 0 to 7 T. ac magnetic susceptibility data collected by using the MPMS instrument were obtained by using a 6-Oe switching field; data from the PPMS instrument were collected by using a 10-Oe switching field. All data were corrected for diamagnetic contributions of the eicosane and the individual samples by using Pascal's constants (*50*).

The ac susceptibility data were fit by using a generalized Debye model, which accounts for relaxation time (τ), attempt time (τ_0), isothermal susceptibility (χ_T), adiabatic susceptibility (χ_S), and the presence of a distribution of relaxation times (α) (*51*). Data for **1** collected under zero applied field and below 7 K exhibited high-frequency shoulders in χ'', and fits to the data yielded very large α values, suggesting that a second, faster relaxation process might be operating at low temperatures. This second process may be related to the disordered molecules in the crystal. Data from 4 to 10 K were fit with two relaxation processes. Once the minor relaxation process moved out of the frequency range of the magnetometer (0.1 to 1488 Hz), a one-process fit was sufficient. The two fitting procedures gave only modestly different τ values for the 4 and 5 K data. The data for **3** and the applied-field data for **1** were fit sufficiently well with one process. Data collected by using the PPMS instrument (50 to 70 K, 100 to 10,000 Hz) gave some negative values for χ' at high frequency. Presumably, this result is due to the fact that the PPMS sample consisted of less material (6.9 mg of **1**, 29.0 mg of eicosane) and, especially at high temperatures, exhibited a smaller paramagnetic response relative to the diamagnetic response. The negative values did not affect the extraction of relaxation times, however. The method for fitting the relaxation data from 4 to 70 K is given in detail in the supplementary materials.

dc relaxation measurements were implemented with the hysteresis mode of the MPMS magnetometer by using small magnetizing fields such that the time to set the field was in the 10- to 30-s range; measurements were made every ~4 s. We found that the relaxation times had a small dependence on the magnetizing field for **1** and a larger dependence for **3** (tables S19 and S20); the times reported in the main text are averages of those times. The relaxation times were determined by using a stretched exponential of the form $M_t = M_0\exp[-(t/\tau)^n]$, where M_0 is the magnetization of the first data point measured, once the field was set, and n is a free variable (*52*).

dc magnetization experiments were implemented by applying a field to a sample at zero magnetization and measuring the magnetization until it became constant. Relaxation times were determined by using the equation $M_t = M_{sat} - (M_{sat} - M_0)\exp[-(t/\tau)^n]$, where M_{sat} is the saturation magnetization, M_0 is the magnetization of the first data point measured once the field was set, and n is a free variable. Magnetization times for **1** and **3** for each field are given in tables S20 and S21; the main text reports the average of these values (16.4 and 48.2 s, respectively) and their SD (0.7 and 4.7, respectively).

Variable-field FIR spectroscopy

FIR spectra were recorded on a Bruker IFS 66v/s FTIR spectrometer with a globar source and a composite bolometer detector element located inside an 11 T magnet directly below the sample. Approximately 5 mg of **1** was diluted in eicosane (1:10 ratio) and pressed in the shape of a 5-mm pellet. The sample was prepared and measured under an inert atmosphere. The sample was cooled to 4.2 K and irradiated with FIR light. Transmission spectra were recorded both in the absence and in the presence of a magnetic field (0 to 11 T).

CD modeling

Crystals of **1** are rather air sensitive, and thus all crystal manipulation was carried out inside of a glove box under an Ar atmosphere. A triangularly shaped single crystal with a maximum dimension of 0.10 mm was selected, and it was mounted by using cryo-protecting oil on a precentered glass fiber and then rapidly inserted into a cold He stream with a temperature of 20 K to minimize any risk of air exposure and subsequent crystal decay.

The crystal was mounted on the goniometer of beamline BL02B1 at the SPring8 synchrotron in Japan. The x-ray energy was fixed to 40 keV, corresponding to a wavelength of 0.30988 Å. We have previously experienced substantial crystal decay due to radiation damage, and this high energy was chosen in an attempt to avoid this detrimental effect. As shown in fig. S17, the frame scale factor, which accurately captures any crystal decay (as well as other systematic effects, such as beam intensity fluctuations), is scattered relatively close to 1.0 and does not drop off systematically, indicating that there is no substantial crystal decay.

The data were collected on a Fuji IP system by using 36 ω-scans with a width of 5° and an overlap of 0.5° for a total of 180° with a scan speed of 1 min/degree. Given the high symmetry of the compound, this protocol provided a complete dataset with sufficient redundancy. The

diffraction data ceased to be significant already at $\sin(\theta)/\lambda = 0.9$ Å^{-1}. As we explain below, there is substantial dynamic disorder in the crystal structure, which likely results in the lack of high-angle data.

The diffraction data were integrated by using dedicated Rigaku software RAPID AUTO v2.41, which integrates only the intensity of reflections estimated to be fully present on one frame, i.e., having been rotated fully through the Ewald sphere during one of the 5° rotations. This estimation obviously depends on the mosaicity of the crystal and the desired box size for integration. We experimented with these values in order to optimize the integration results, and those presented herein used mosaicity of 0.7° and a box size of 13 × 13 pixels. The raw images were scaled to accommodate the different sensitivities of the photomultiplier tubes, an effect which was uncovered in the summer of 2018.

The integration and subsequent scaling in RAPID AUTO provided a total of 43,260 reflections, which were then averaged by using the point group symmetry –3. These averaged data were reduced to 9008 unique reflections with an average redundancy of 4.8 and a completeness of 99.5% by using the program SORTAV. During refinement, it was noticed that the ratio of F(obs) to F(calc) varied systematically, and thus we decided to include 10 resolution-dependent scale factors that helped to alleviate this problem, as shown in fig. S19.

These data were used to solve the crystal structure by using SHELXT within the Olex2 interface. The structure solution was found to contain a minor, but clearly visible, disordered component, and the disorder is solely in the naphthalene moiety (see fig. S18). The disorder is perhaps best explained as resulting from a mirror symmetry in the plane defined by C(1) (bonded to Co) and partially by Si(1) and O(1). This plane also very nearly includes C(2) [carbon bonded to O(1)]. The occupation of the disordered parts is 4.8%, and including this disorder in the model leads to a substantial improvement of the refinement.

Despite the substantial disorder (one of the consequences of which is that some atoms in the structure are nearly overlapping), we decided to attempt multipole-based CD modeling. The independent-atom model (IAM) structure from ShelX was exported to the program XD, which is based on the Hansen-Coppens multipole formalism. Herein, we kept the extent of disorder fixed on the values obtained from ShelX and furthermore used isotropic thermal parameters for the disordered atoms. We did not apply multipole parameters to the disordered atoms, which were kept spherical. Given the nearly whole-molecule disorder, it is imperative to be extremely careful during the refinement procedure. Thus, we used constraints to avoid overfitting, which otherwise is a possibility in such a disordered system. The use of isotropic and spherical disordered atoms helps with this as well.

The final multipole model consists of hexadecapoles on Co and octopoles on all other non-H atoms (except the disordered atoms), whereas H atoms were refined by using one common monopole and bond-directed dipole. The model was reached after several refinements, in which the level of multipoles was increased by one for each step. Both neutral and ionic scattering factors were tested for Co. In the final model, a neutral scattering factor was used.

In the final refinement, the largest residuals were, as expected, near the Si and the Co atoms. The largest residuals were positive [the largest is around 1.2 eÅ^{-3} (where eÅ is electrons per cubic angstrom) and is close to the Co] and notably larger than the most negative residual density peaks, which were around –0.55 eÅ^{-3}. Such large discrepancy between the positive and negative residuals may indicate that the disorder was not fully accounted for. The Co atom sits on a special position in the space group with a multiplicity of 6, and it is possible that the high residual density at this position is also a result of this high symmetry. The residual near Co does not indicate that the atom sits off-centered. However, it may be related to the disorder, and perhaps it does not sit in a harmonic potential. We tried to refine anharmonic thermal parameters, but this refinement had no effect on the residual density.

The residual density distribution, interpreted by using the fractal dimensionality plots as first presented by Meindl and Henn (fig. S19) (*53*), shows a somewhat distorted parabola, with a slight tendency to increase more toward the positive residuals. However, this increase is much smaller than expected from the substantial residuals near Co and Si and suggests that despite the disorder, the multipole model may be quantitatively useful.

Co sits on a –3 crystallographic position, and therefore only four multipole parameters are symmetry-allowed. The most important parameter in this respect is the quadrupole along the z axis. However, in the least-squares refinement, this parameter correlates strongly with the thermal parameters, including U33, which represents the atomic vibration along the same z direction. To avoid this correlation, we separated the refinement of multipole parameters from the refinement of atomic positions and vibrations. We first attempted a high-angle refinement of the atomic vibrations and positions, but the resulting refinement of multipole parameters led to unphysical values—for instance, atomic charges derived from monopole values of more than +2 and κ-parameters deviating by more than 20% from unity. Instead, we chose to use the full dataset to independently refine the atomic positions and vibrations of all atoms, subsequently fixing these values and refining the multipole parameters until convergence. This approach represented the final model, from which we extracted the d-orbital population ratios. In the final model, the charge on Co was determined to be +1.3.

REFERENCES AND NOTES

1. I. G. Rau *et al*., Reaching the magnetic anisotropy limit of a *3d* metal atom. *Science* **344**, 988–992 (2014). doi: 10.1126/science.1252841; pmid: 24812206
2. W. M. Reiff, A. M. LaPointe, E. H. Witten, Virtual free ion magnetism and the absence of Jahn-Teller distortion in a linear two-coordinate complex of high-spin iron(II). *J. Am. Chem. Soc.* **126**, 10206–10207 (2004). doi: 10.1021/ja030632w; pmid: 15315408
3. J. M. Zadrozny *et al*., Slow magnetization dynamics in a series of two-coordinate iron(II) complexes. *Chem. Sci.* **4**, 125–138 (2013). doi: 10.1039/C2SC20801F
4. J. M. Zadrozny *et al*., Magnetic blocking in a linear iron(I) complex. *Nat. Chem.* **5**, 577–581 (2013). doi: 10.1038/nchem.1630; pmid: 23787747
5. D. Gatteschi, R. Sessoli, J. Villain, *Molecular Nanomagnets* (Oxford Univ. Press, 2006).
6. J. M. Zadrozny *et al*., Mössbauer spectroscopy as a probe of magnetization dynamics in the linear iron(I) and iron(II) complexes $[Fe(C(SiMe_3)_3)_2]^{1-/0}$. *Inorg. Chem.* **52**, 13123–13131 (2013). doi: 10.1021/ic402013n; pmid: 24175913
7. M. Atanasov, J. M. Zadrozny, J. R. Long, F. Neese, A theoretical analysis of chemical bonding, vibronic coupling, and magnetic anisotropy in linear iron(II) complexes with single-molecule magnet behavior. *Chem. Sci.* **4**, 139–156 (2013). doi: 10.1039/C2SC21394J
8. The term "spin-reversal barrier" is somewhat ambiguous in the single-molecule magnet literature. In the systems described here, we define it as the separation between ground and first excited M_J (or M_S) states. Thus, "over-barrier" relaxation refers to excitation from $M_J = +J$ to $M_J = +(J - 1)$ states followed by relaxation to the $M_J = -J$ state (an Orbach mechanism). "Through-barrier" relaxation mechanisms are any that allow the system to go from $M_J = +J$ to $M_J = -J$ without excitation to the $M_J = +(J - 1)$ state.
9. M. Atanasov *et al*., First principles approach to the electronic structure, magnetic anisotropy and spin relaxation in mononuclear 3d-transition metal single molecule magnets. *Coord. Chem. Rev.* **289–290**, 177–214 (2015). doi: 10.1016/j.ccr.2014.10.015
10. P. Zhao *et al*., Synthesis and structural characterization of a dimeric cobalt(I) homoleptic alkyl and an iron(II) alkyl halide complex. *Organometallics* **33**, 1917–1920 (2014). doi: 10.1021/om500180u
11. P. P. Power, Stable two-coordinate, open-shell (d^1-d^9) transition metal complexes. *Chem. Rev.* **112**, 3482–3507 (2012). doi: 10.1021/cr2004647; pmid: 22480221
12. T. Viefhaus, W. Schwarz, K. Hübler, K. Locke, J. Weidlein, Das unterschiedliche Reaktionsverhalten von basefreiem Tris (trimethylsilyl)methyl-Lithium gegenüber den Trihalogeniden der Erdmetalle und des Eisens. *Z. Anorg. Allg. Chem.* **627**, 715 (2001). doi: 10.1002/1521-3749(200104)627:4<715::AID-ZAAC715>3.0.CO;2-0
13. N. H. Buttrus, C. Eaborn, P. B. Hitchcock, J. D. Smith, A. C. Sullivan, Preparation and crystal structure of a two-coordinate manganese compound, bis[(tris(trimethyl) silylmethyl)]manganese. *J. Chem. Soc. Chem. Commun.* **1985**, 1380–1381 (1985). doi: 10.1039/c39850001380
14. C.-Y. Lin *et al*., Salts of the two-coordinate homoleptic manganese(I) dialkyl anion $[Mn\{C(SiMe_3)_3\}_2]^-$ with quenched orbital magnetism. *Chem. Commun.* **51**, 13275–13278 (2015). doi: 10.1039/C5CC05166E; pmid: 26178861
15. X.-N. Yao *et al*., Two-coordinate Co(II) imido complexes as outstanding single-molecule magnets. *J. Am. Chem. Soc.* **139**, 373–380 (2017). doi: 10.1021/jacs.6b11043; pmid: 27936686
16. P. E. Kazin *et al*., A Co-based single-molecule magnet confined in a barium phosphate apatite matrix with a high energy barrier for magnetization relaxation. *Chem. Commun.* **53**, 5416–5419 (2017). doi: 10.1039/C7CC02453C; pmid: 28453011
17. H. Li *et al*., A zwitterionic carbanion frustrated by boranes—dihydrogen cleavage with weak Lewis acids via an "inverse" frustrated Lewis pair approach. *J. Am. Chem. Soc.* **135**, 16066–16069 (2013). doi: 10.1021/ja409330h; pmid: 24124979
18. H. Li, A. J. A. Aquino, D. B. Cordes, W. L. Hase, C. Krempner, Electronic nature of zwitterionic alkali metal methanides, silanides, and germanides—a combined experimental and computational approach. *Chem. Sci.* **8**, 1316–1328 (2017). doi: 10.1039/c6sc02390h
19. S. S. Al-Juaid *et al*., The preparation and crystal structures of the compounds $(Ph_2MeSi)_3CMCl$ (M = Zn, Cd, or Hg). *J. Organomet. Chem.* **462**, 45–55 (1993). doi: 10.1016/0022-328X(93)83340-2
20. S. S. Al-Juaid *et al*., Tris(triorganosilyl)methyl derivatives of potassium and lithium bearing dimethylamino or methoxy

substituents at silicon. Crystal structures of $KC(SiMe_3)_2$ ($SiMe_2NMe_2$), $KC(SiMe_2NMe_2)_3$ and $[LiC(SiMe_3)(SiMe_2OMe)_2]_2$. *J. Chem. Soc. Dalton Trans.* **1999**, 3267–3273 (1999). doi: 10.1039/a904043i
21. M. Westerhausen, B. Rademacher, W. Poll, Trimethylsilyl-substituierte Derivate des Dimethylzinks—Synthese, spektroskopische Charakterisierung und Struktur. *J. Organomet. Chem.* **421**, 175–188 (1991). doi: 10.1016/0022-328X(91)86402-C
22. M. Nishio, The CH/π hydrogen bond in chemistry. Conformation, supramolecules, optical resolution and interactions involving carbohydrates. *Phys. Chem. Chem. Phys.* **13**, 13873–13900 (2011). doi: 10.1039/c1cp20404a; pmid: 21611676
23. C.-Y. Lin *et al*., Dispersion force stabilized two-coordinate transition metal–amido complexes of the –$N(SiMe_3)$Dipp (Dipp = C_6H_3-2,6-Pr^i_2) ligand: Structural, spectroscopic, magnetic, and computational studies. *Inorg. Chem.* **52**, 13584–13593 (2013). doi: 10.1021/ic402105m
24. A. J. Wallace, B. E. Williamson, D. L. Crittenden, CASSCF-based explicit ligand field models clarify the ground state electronic structures of transition metal phthalocyanines (MPc; M = Mn, Fe, Co, Ni, Cu, Zn). *Can. J. Chem.* **94**, 1163–1168 (2016). doi: 10.1139/cjc-2016-0264
25. R. F. W. Bader, *Atoms in Molecules: A Quantum Theory* (Clarendon Press, 1990).
26. R. Marx *et al*., Spectroscopic determination of crystal field splittings in lanthanide double deckers. *Chem. Sci.* **5**, 3287–3293 (2014). doi: 10.1039/c4sc00751d
27. Y. Rechkemmer *et al*., A four-coordinate cobalt(II) single-ion magnet with coercivity and a very high energy barrier. *Nat. Commun.* **7**, 10467 (2016). doi: 10.1038/ncomms10467; pmid: 26883902
28. D. Gatteschi, R. Sessoli, Quantum tunneling of magnetization and related phenomena in molecular materials. *Angew. Chem. Int. Ed.* **42**, 268–297 (2003). doi: 10.1002/anie.200390099; pmid: 12548682
29. K. N. Shrivastava, Theory of spin-lattice relaxation. *Phys. Status Solidi B* **117**, 437–458 (1983). doi: 10.1002/pssb.2221170202
30. R. Orbach, Spin-lattice relaxation in rare-earth salts. *Proc. R. Soc. London Ser. A* **264**, 458 (1961).
31. A. Lunghi, F. Totti, R. Sessoli, S. Sanvito, The role of anharmonic phonons in under-barrier spin relaxation of single molecule magnets. *Nat. Commun.* **8**, 14620 (2017). doi: 10.1038/ncomms14620; pmid: 28262663
32. A. Lunghi, F. Totti, S. Sanvito, R. Sessoli, Intra-molecular origin of the spin-phonon coupling in slow-relaxing molecular magnets. *Chem. Sci.* **8**, 6051–6059 (2017). doi: 10.1039/C7SC02832F; pmid: 28989635
33. S.-D. Jiang, B.-W. Wang, G. Su, Z.-M. Wang, S. Gao, A mononuclear dysprosium complex featuring single-molecule-magnet behavior. *Angew. Chem. Int. Ed.* **49**, 7448–7451 (2010). doi: 10.1002/anie.201004027; pmid: 20803599
34. H. A. Kramers, A general theory of paramagnetic rotation in crystals. *Proc. R. Acad. Sci. Amsterdam* **33**, 959 (1930).
35. M. Gonidec, E. S. Davies, J. McMaster, D. B. Amabilino, J. Veciana, Probing the magnetic properties of three interconvertible redox states of a single-molecule magnet with magnetic circular dichroism spectroscopy. *J. Am. Chem. Soc.* **132**, 1756–1757 (2010). doi: 10.1021/ja9095895; pmid: 20099818
36. L. Margheriti *et al*., X-ray detected magnetic hysteresis of thermally evaporated terbium double-decker oriented films. *Adv. Mater.* **22**, 5488–5493 (2010). doi: 10.1002/adma.201003275; pmid: 20949539
37. M. Gonidec *et al*., Surface supramolecular organization of a terbium(III) double-decker complex on graphite and its single molecule magnet behavior. *J. Am. Chem. Soc.* **133**, 6603–6612 (2011). doi: 10.1021/ja109296c; pmid: 21486019
38. D. Klar *et al*., Hysteretic behaviour in a vacuum deposited submonolayer of single ion magnets. *Dalton Trans.* **43**, 10686–10689 (2014). doi: 10.1039/C4DT01005A; pmid: 24875369
39. M. Mannini *et al*., Magnetic behaviour of $TbPc_2$ single-molecule magnets chemically grafted on silicon surface. *Nat. Commun.* **5**, 4582 (2014). doi: 10.1038/ncomms5582; pmid: 25109254
40. J. Dreiser *et al*., Exchange interaction of strongly anisotropic tripodal erbium single-ion magnets with metallic surfaces. *ACS Nano* **8**, 4662–4671 (2014). doi: 10.1021/nn500409u; pmid: 24645922
41. C. Wäckerlin *et al*., Giant hysteresis of single-molecule magnets adsorbed on a nonmagnetic insulator. *Adv. Mater.* **28**, 5195–5199 (2016). doi: 10.1002/adma.201506305; pmid: 27159732
42. M. Getzlaff, *Fundamentals of Magnetism* (Springer-Verlag, 2008).
43. A. Jesche *et al*., Giant magnetic anisotropy and tunnelling of the magnetization in $Li_2(Li_{1-x}Fe_x)N$. *Nat. Commun.* **5**, 3333 (2014). doi: 10.1038/ncomms4333; pmid: 24566374
44. C. J. Schaverien, A. G. Orpen, Chemistry of (octaethylporphyrinato)lutetium and -yttrium complexes: Synthesis and reactivity of (OEP)MX derivatives and the selective activation of O_2 by (OEP)Y(.mu.-Me)$_2$AlMe$_2$. *Inorg. Chem.* **30**, 4968–4978 (1991). doi: 10.1021/ic00026a023
45. K. D. Safa, S. Tofangdarzadeh, H. H. Ayenadeh, Reactions of tris(dimethylsilyl)methane and polymers containing Si–H groups with various hydroxy compounds under aerobic and mild conditions. *Heteroatom Chem.* **19**, 365–376 (2008). doi: 10.1002/hc.20440
46. G. M. Sheldrick, SADABS, version 2.03 (Bruker Analytical X-Ray Systems, 2000).
47. G. M. Sheldrick, SHELXT – integrated space-group and crystal-structure determination. *Acta Crystallogr. A* **71**, 3–8 (2015). doi: 10.1107/S2053273314026370; pmid: 25537383
48. G. M. Sheldrick, Crystal structure refinement with SHELXL. *Acta Crystallogr. C* **71**, 3–8 (2015). doi: 10.1107/S0108767307043930; pmid: 25567568
49. O. V. Dolomanov, L. J. Bourhis, R. J. Gildea, J. A. K. Howard, H. Puschmann, OLEX2: A complete structure solution, refinement and analysis program. *J. Appl. Crystallogr.* **42**, 339–341 (2009). doi: 10.1107/S0021889808042726
50. G. A. Bain, J. F. Berry, Diamagnetic corrections and Pascal's constants. *J. Chem. Educ.* **85**, 532 (2008). doi: 10.1021/ed085p532
51. K. S. Cole, R. H. Cole, Dispersion and absorption in dielectrics I. Alternating current characteristics. *J. Chem. Phys.* **9**, 341–351 (1941). doi: 10.1063/1.1750906
52. C. Sangregorio, T. Ohm, C. Paulsen, R. Sessoli, D. Gatteschi, Quantum tunneling of the magnetization in an iron cluster nanomagnet. *Phys. Rev. Lett.* **78**, 4645–4648 (1997). doi: 10.1103/PhysRevLett.78.4645
53. K. Meindl, J. Henn, Foundations of residual-density analysis. *Acta Crystallogr. A* **64**, 404–418 (2008).doi: 10.1107/S0108767308006879

ACKNOWLEDGMENTS

We thank K. R. Meihaus for editorial assistance. **Funding:** This work was funded by NSF grant CHE-1464841 (P.C.B., J.R.L.), Max-Planck Gesellschaft (M.A., F.N.), DNRF93 and Danscatt (E.D.-M., J.O.), and DFG SL104/5-1 (M.P., J.V.S.). **Author contributions:** Synthesis, magnetic characterization, and analysis were performed by P.C.B. and J.R.L. Ab initio calculations and analysis were performed by M.A. and F.N. Applied-field FIR spectra were collected and analyzed by M.P., I.C., M.O., and J.V.S. CD data collection and modeling were performed by E.D.-M. and J.O. **Competing interests:** The authors have no competing interests to claim. **Data and materials availability:** Crystallographic data for **1**, **2**, and $Co(C(SiMe_2OPh)_3)_2$ are freely available from the Cambridge Crystallographic Data Centre under CCDC numbers 1872361, 1872361, and 1872363, respectively. The supplementary materials include details on the fitting of magnetic relaxation data, as well as computational methods.

SUPPLEMENTARY MATERIALS

www.sciencemag.org/content/362/6421/eaat7319/suppl/DC1
Materials and Methods
Figs. S1 to S19
Tables S1 to S22
References (*54*–*70*)

28 March 2018; resubmitted 2 August 2018
Accepted 1 November 2018
Published online 15 November 2018
10.1126/science.aat7319

RESEARCH ARTICLE

CRITICAL TRANSITIONS

Cascading regime shifts within and across scales

Juan C. Rocha[1,2]*, Garry Peterson[1], Örjan Bodin[1], Simon Levin[1,2,3,4]

Regime shifts are large, abrupt, and persistent critical transitions in the function and structure of ecosystems. Yet, it is unknown how these transitions will interact, whether the occurrence of one will increase the likelihood of another or simply correlate at distant places. We explored two types of cascading effects: Domino effects create one-way dependencies, whereas hidden feedbacks produce two-way interactions. We compare them with the control case of driver sharing, which can induce correlations. Using 30 regime shifts described as networks, we show that 45% of regime shift pairwise combinations present at least one plausible structural interdependence. The likelihood of cascading effects depends on cross-scale interactions but differs for each type. Management of regime shifts should account for potential connections.

Regime shifts occur across a wide range of social-ecological systems (*1*–*3*). They are difficult to predict and reverse (*4*, *5*) and often produce sustained shifts in the availability of ecosystems services (*6*). When a system undergoes a regime shift, it moves from one set of self-reinforcing processes and structures to another (*2*, *7*–*9*). Changes in a key variable (for example, temperature in coral reefs) often make a system more susceptible to shifting regimes when exposed to shock events (such as hurricanes) or the action of external drivers (such as fishing) (*10*). More than 30 different regime shifts in social-ecological systems have been documented (*3*), and similar nonlinear dynamics are seen across societies, finance, language, neurological diseases, and climate (*11*, *12*). As humans increase their pressure on the planet, regime shifts are likely to occur more often and more severely (*13*–*15*).

An emergent challenge for science and practice is that regime shifts can potentially lead to subsequent regime shifts. We define a regime shift as cascading when its occurrence may affect the occurrence of another regime shift. A variety of causal pathways connecting regime shifts have been identified (table S1). For example, eutrophication is often reported as a regime shift preceding hypoxia or dead zones in coastal areas (*16*). Similarly, hypoxic events have been reported to affect the resilience of coral reefs to warming and other stressors in the tropics (*17*). If, why, and how a regime shift somewhere in the world could affect the occurrence of another regime shift remain largely open questions and a key frontier of research (*18*, *19*).

Research on regime shifts is often confined to well-defined branches of science, reflecting empirical, theoretical (*20*), or predictive approaches (*10*, *21*). These approaches require a deep knowledge of the causal structure of the system or a high quality of spatiotemporal data. Hence, research on regime shifts has generally focused on the analysis of individual types of regime shifts rather than potential interactions across systems. We took another approach and instead explored potential cascading effects among a large set of regime shifts. We investigated two types of interconnections: domino effects and hidden feedbacks. Domino effects occur when the feedback processes of one regime shift affect the drivers of another regime shift, creating a one-way dependency (*10*, *19*, *22*). A feedback mechanism is a self-amplifying or -dampening process

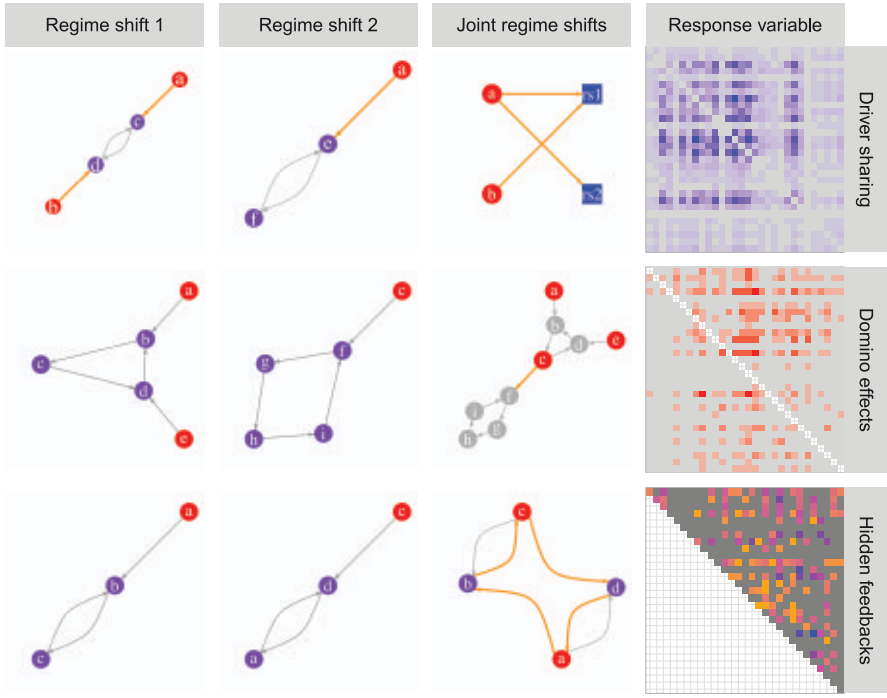

Fig. 1. Method scheme. Pairs of regime shift causal networks were merged to create a response variable matrix that accounted for drivers shared, domino effects, or hidden feedbacks. In all examples, two minimal regime shifts are depicted as causal diagrams, drivers are red, and variables belonging to feedbacks are purple. For driver sharing, the joint network is simplified as a two-mode network that allows us to study the co-occurrence of drivers (in red) across regime shifts (in blue). Driver a is shared by regime shifts 1 and 2, but driver b is not. The response variable matrix counts the number of drivers shared by all pairwise combinations of regime shifts. For domino effects, two regime shift networks are joined together, where driver c in regime shift 2 is also part of a feedback process in regime shift 1, creating a one-way dependency (orange link) between the two regime shifts. The response variable matrix counts all the one-way causal pathways between pairwise combinations of regime shifts. For hidden feedbacks, two minimal regime shifts, when joined together, give rise to a new unidentified feedback (orange circular pathway). The response variable matrix counts all hidden feedbacks that arise when merging pairwise combinations of regime shifts. The 30 causal networks used and the labeled matrices of the resulting response variables are shown in figs. S1 and S3.

characterized by a pathway of causal processes that return to its origin, creating a cycle. Two-way interactions arise when two regime shifts combine to generate new feedbacks that cannot be identified in the separated regime shifts (*18*, *22*) and, if strong enough, can amplify or dampen the coupled dynamics. We call them "hidden feedbacks" because they only show when two regime shift networks are combined. We contrast these cascading effects, in which the occurrence of a regime shift gives rise to subsequent regime shifts, with the potentially multiplying albeit different effect of two regime shifts being caused by common drivers. Driver sharing is likely to increase correlation in time or space among regime shifts but not necessarily interdependence (*13*, *19*).

Hypotheses of cascading effects

In analyzing individual regime shifts, bifurcation theory often treats drivers as slow variables, which assumes that their change is relatively slower than changes in variables that describe the state of the system (*1*, *2*, *11*, *12*, *23*, *24*). Applying the same logic to pairs of regime shifts, we first expect that domino effects will be dominated by connections from regime shifts occurring at larger spatial scales and slower temporal dynamics than regime shifts receiving the connection (*25*, *26*). Second, hidden feedbacks are expected to occur when scales match in space and time because for a new feedback to emerge, regime shifts need to be somewhat aligned in the scale at which their process operates. Third, regime shifts occurring in similar ecosystem types or land uses will be subject to relatively similar sets of drivers, and thus, we expect driver sharing to be context-specific (*13*, *19*).

We tested the three hypotheses by analyzing regime shifts as networks of drivers and feedback processes. These directed signed graphs allowed us to explore driver co-occurrence, directional pathways, and emergent feedback cycles of coupled regime shift networks (*27*). The empirical basis for our investigation draws from the regime shifts database (figs. S1 and S2) (*3*), which offers syntheses of more than 30 types of regime shifts, and >300 case studies based on literature review of >1000 scientific papers. The database describes regime shifts in terms of their alternative regimes, drivers, feedback mechanisms, impacts on ecosystem services, and management options. It provides a set of 75 categorical variables about impacts, scales, and evidence types used to test our expectations (*27*). The database consistently encodes regime shifts into causal diagrams as a graphical summary of the drivers and underlying feedbacks of each regime shift (fig. S1). Causal diagrams for each regime shift were converted into a network by creating the adjacency matrix A, where $A_{i,j}$ is 1 if there is a connection or 0 if not (*27*). A link between two nodes in these networks means that there is at least one scientific paper reviewed in the database providing some evidence for a causal relationship (*3*, *13*).

Three response variables matrices were created by merging pairs of regime shift networks (Fig. 1): (i) For driver sharing, it is the number of common drivers; (ii) for domino effects, it is the number of directed pathways that connect two regime shifts; and (iii) for hidden feedbacks, it is the number of new cycles that emerge when joining two regime shift networks (*27*). We tested the hypotheses using exponential random graph models (*27*). In this framework, our research question can be rephrased as "What is the likelihood of a link between regime shifts in the response variable matrix, and what features change this likelihood?" As explanatory variables, we used the regime shift database categorical variables, focusing on how similar two regime shifts are and whether the similarity increases the likelihood of having a link on the response variable matrices (*27*). The specification for the model follows a Poisson reference distribution (*28*), given that the response variables contain weighted links of count data—how many domino effects, hidden feedbacks, or shared drivers link pairs of regime shifts.

Results

Regime shifts can be structurally interdependent (Fig. 2). The three response variables combined show that ~45% of the regime shift couplings analyzed present structural dependencies in the form of one-way interactions for the domino effect or two-way interactions for hidden feedbacks. Whereas ~5 and ~2% of the couplings present only domino effects and hidden feedbacks, respectively, ~28% of the pairwise combinations are linked through two different types of connections, and ~9% are linked by all three of them. Only for 19% of the pairwise combinations can we be certain with the current dataset that there are no cascading effects. However, the discovery of new drivers or feedback mechanisms underlying these dynamics could reduce this estimate.

Driver sharing is the most common type of connection found (Fig. 2). Regime shifts can correlate in time and space because of common drivers, but they do not necessarily become interdependent (*13*, *19*)—that is, the occurrence of one does not affect the probability of the second occurring. Of all pairwise regime shift combinations, 36% were coupled only by driver sharing. The resulting matrix for driver sharing describes the co-occurrence patterns of 77 drivers across the 30 regime shifts analyzed. In our sample, aquatic regime shifts tend to have and share more drivers, although the driver sharing is not exclusively with other aquatic regime shifts (Figs. 3A and 4B). The highest driver co-occurrence was found between regime shifts in kelps, marine eutrophication, and the collapse of fisheries. Terrestrial and polar regime shifts tended to have fewer and more specific sets of drivers. Large-scale regime shifts in polar and subcontinental areas (such as monsoon weakening) have fewer

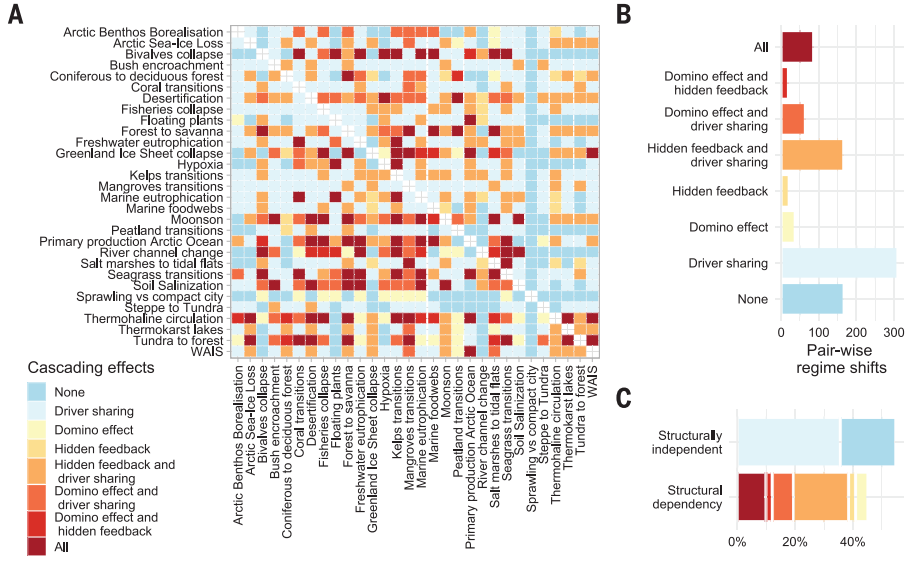

Fig. 2. Potential structural dependencies between regime shifts. (**A**) The three response variables combined show eight different possibilities in which regime shifts can interact through cascading effects. (**B**) Driver sharing is the most common type found. (**C**) Domino effects and hidden feedbacks alone or in combination account for ~45% of all regime shift couplings analyzed, implying structural dependence.

[1]Stockholm Resilience Centre, Stockholm University, Kräftriket 2B, 10691 Stockholm, Sweden. [2]Beijer Institute, Swedish Royal Academy of Sciences, Lilla Frescativägen 4A, 104 05 Stockholm, Sweden. [3]Department of Ecology and Evolutionary Biology, Princeton University, 106A Guyot Hall, Princeton, NJ 08544-1003, USA. [4]Resources for the Future, Washington, DC 20036, USA.
***Corresponding author. Email: juan.rocha@su.se**

drivers but are hotspots of sharing, typically including climate-related drivers. Drivers that co-occurred most frequently were related to food production, climate change, and urbanization, yet none of them is ubiquitous in our sample (Fig. 3B).

In line with our expectations, regime shifts were more likely to share drivers when they occurred in similar land uses but not necessarily under the same ecosystem types ($P \ll 0.001$) (Fig. 4 and table S3). We did not expect cross-scale interactions in driver sharing, yet we found that driver sharing is more likely in dynamics that are faster in time (from weeks to years) and when spatial scales match. Regime shift impacts on ecosystem services and human well-being were related to driver sharing. We found that affecting similar regulating and provisioning services increases the likelihood of common drivers.

Evidence of cross-scale interactions for domino effects was only found in time but not in space. As expected, regime shifts that produce domino effects have slow temporal dynamics and larger spacial scales. These regime shifts include Earth system–tipping elements such as monsoon weakening, thermohaline circulation collapse, and Greenland ice sheet collapse (Fig. 3C). On the other hand, regime shifts influenced by domino effects were often marine and occurred over shorter times and more localized spaces, including mangrove transitions, kelp transitions, and transitions from salt marshes to tidal flats. The statistical models support this observation for temporal scales (Fig. 4 and table S4), but we did not find evidence for spatial ones. Having domino effects was significantly associated with affecting similar regulating and provisioning services ($P < 0.001$), but the size of the effects are dwarfed by its rarity. The sparse response variable matrix (Fig. 1) and the negative coefficient on the sum term in the statistical models (table S4) show that domino effects are not common. When they do occur, it is only through a few pathways between regime shifts (maximum of four in our sample). Key variables involved in domino effects were related to climate, nutrients, and water transport (Fig. 3D).

Hidden feedbacks were expected to arise when regime shift dynamics matched scales in space and time. The statistical analysis supports our hypothesis: Regime shifts that occur on the range of decades to centuries and at national scale are more likely to have hidden feedbacks (Fig. 4 and table S5). We found fewer hidden feedbacks than one would expect by chance, but when hidden feedbacks did occur, they tended to couple regime shifts through multiple feedbacks. Most hidden feedbacks in our sample occurred in terrestrial and Earth systems (Figs. 3E and 4). The regime shifts with higher numbers of connections (15 to 18 out of 30 possible) are thermohaline circulation, primary productivity of the Arctic Ocean, forest to savanna, monsoon weakening, and the Greenland ice sheet collapse. Key variables belonging to many

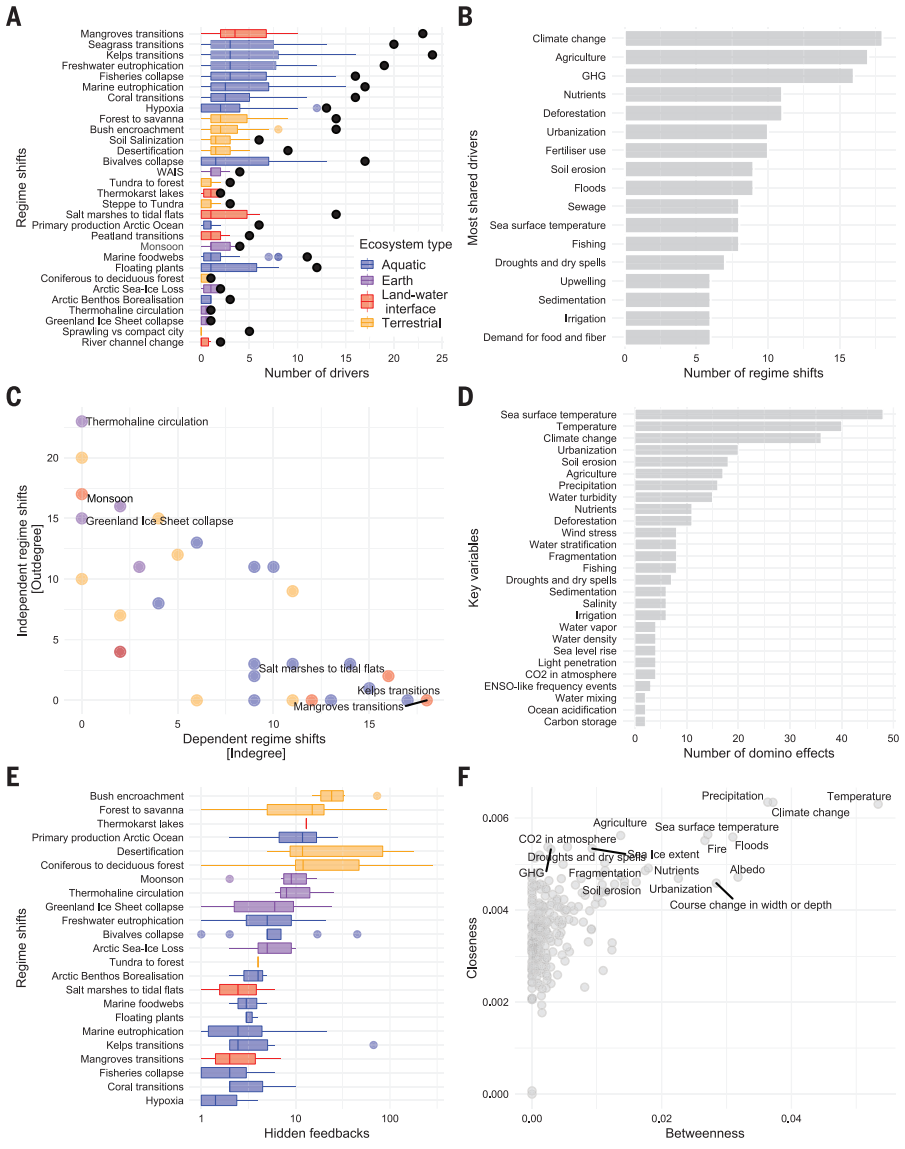

Fig. 3. Patterns of cascading effects. (**A**, **C**, and **E**) Regime shifts are ranked according to their role in (A) driver sharing, (C) domino effect, and (E) hidden feedbacks. (**B**, **D**, and **F**) Key variables involved in cascading effects are shown for (B) driver sharing, (D) domino effects, and (F) hidden feedbacks. The distribution of drivers shared per regime shift (A) with respect to the number of drivers each one has (black points) shows that regime shifts in aquatic environments tend to have and share more drivers. WAIS, West Antarctica Ice Sheet collapse. Regime shifts that produce most domino effects (high outdegree) are Earth system tipping points, whereas the regime shifts that receive the most (high indegree) occur in aquatic and land-water interface (C); labels are plotted only for regime shifts in which the maximum number of domino effects (four) is found. Most variables associated with domino effects are related to climate and transport mechanisms (D). These variables are part of a feedback mechanism in one regime shift that are in turn drivers in another regime shift. Hidden feedbacks occur typically in terrestrial and Earth system regime shifts. The distribution of hidden feedbacks (E) is organized by higher to lower mean number of feedbacks. Boxplots are shown in log-scale after zero values have been removed. The variables most often involved in hidden feedbacks have high betweenness and closeness centralities (F) calculated on the network of all regime shifts in our sample (n = 30). These measures reveal the variables (labeled) that lie on most shorter pathways from all other variables in the network.

Fig. 4. Cascading effects across scales. (**A**) Summary of the statistical results. Only models with the lower Akaike information criteria were included on the figure. The figure is complemented by tables S3 to S5, with alternative models fitted. (**B** to **J**) Circular plots showing the mixing matrices of cascading effects [driver sharing, (B), (E), and (H); domino effects, (C), (F), and (I); and hidden feedbacks, (D), (G), and (J)] according to ecosystem type [(B), (C), and (D)], spatial scales [(E), (F), and (G)], and temporal scales [(H), (I), and (J)].

hidden feedbacks were related to climate, fires, agriculture, and urbanization (Fig. 3F).

Discussion and conclusions

Regime shifts are ubiquitous in nature, yet how they can interact has remained an unexplored question. Although this question is fundamental for scientists to forecast the dynamics of ecosystems, the answers are relevant for policymakers and managers because regime shifts can affect ecosystem services and human well-being and hence undermine the achievement of sustainable development goals. Domino effects and hidden feedbacks are often disregarded because research on regime shifts is divided by disciplines that focus on one system at a time. Consequently, data collection and hypothesis testing for coupled systems have largely remained unexplored (*18*, *19*). Although few studies have investigated cascading effects by looking at temperature-driven tipping points in the climate systems (*15*, *25*, *29*), a growing body of literature has started to offer hypotheses on how different regime shifts can be interconnected (table S1). We have developed a network-based method that allows us to systematically identify potential cascading effects and differentiate whether a regime shift coupling is expected to create structural dependencies in the form of domino effects or hidden feedbacks (Fig. 2).

Our findings align with previous results on the type of variables and processes that can couple regime shifts (table S1), highlighting the role of climate, agriculture, and transport mechanisms for nutrients and water (Fig. 3). Recent literature (table S1, references) reports potential linkages between eutrophication and hypoxia, hypoxia and coral transitions, shifts in coral reefs and mangrove transitions, or climate interactions. Other examples in the terrestrial realm report potential increase in Arctic warming from higher fire frequency in boreal forest or permafrost thawing. Regime shifts in the Arctic can affect any temperature-driven regime shift in and outside the Arctic (*30*), including the weakening of the thermohaline circulation. Moisture recycling is a key underlying feedback on the shift from forest to savanna or the Indian monsoon but also has the potential to couple ecosystems beyond the forest that depend on moisture recycling as an important water source. Changes in moisture recycling can affect mountain forests in the Andes, nutrient cycling in the ocean by affecting sea surface temperature, and therefore regime shifts in marine food webs or exacerbation of dry land–related regime shifts. Not all cascading effects reported in the literature and our results are expected to amplify each other. For example, it has been reported that climate-tipping points can regulate each other and reduce the probability of regime shifts in forests (*29*, *31*).

Guided by the practice of explaining and modeling single regime shifts as emergent dynamics from fast and slow processes (*2*, *8*, *11*, *20*, *23*–*25*), we hypothesized that cascading effects between regime shift couplings were determined by cross-scale interactions. For domino effects, we only found support of cross-scale interactions in time but not in space. For hidden feedbacks, we found evidence of matching in space and time. Together, these results show that the likelihood of regime shift coupling depends on cross-scale interactions but differs for each cascading effect type. Lack of evidence for interactions across spatial scales for domino effects suggests that stochastic and transient dynamics might be playing an important role in regime shifts (*32*) and their cascading effects. A major role of stochastic and transient dynamics in regime shift–couplings limits the applicability of early warning signals (*10*, *21*) to predict cascading effects (*25*). Developing early warning signals for coupled regime shifts is therefore a research need.

Synchronization of regime shifts in time or space is a subject of debate (*19*, *33*–*35*). Temporal correlations—typically induced by driver sharing—can be broken by spatial heterogeneity (*19*), indicating that context matters for correlations to emerge. Spatial heterogeneity can smooth out critical transitions (*36*, *37*). Yet, identifying common drivers is useful for designing management strategies that target bundles of drivers instead of well-studied variables independently, increasing the chances that managers will avoid several regime shifts under the influence of the same sets of drivers (*13*, *38*). For example, management options for drivers such as sedimentation, nutrient leakage, and fishing can reduce the likelihood of regime shifts such as eutrophication and hypoxia in coastal brackish lagoons as well as coral transitions in adjacent coral reefs.

Our results complement previous findings (table S1) by offering a wide spectrum of causal hypotheses about how regime shifts can be coupled. However, the limitations of our method need to be acknowledged. Regime shifts were represented as static networks, and the cascading effects were identified by matching two pieces of information: variable names and positions within the causal diagram. Therefore, the method identifies structural dependencies but cannot predict how the dynamics will unfold in space or time. For example, if a connection between mangrove collapse and coral transitions is found through protection against coastal erosion, geographical distance between the two systems or the direction of oceanic currents can change or even cancel out the coupling strength. In fact, coupling strength is expected to change from one place to another. Hence, our method identifies plausible connections between regime shifts, but identifying the conditions that change plausible to probable requires more detailed understanding of regime shift mechanisms. Empirical studies and modeling syntheses are required to translate our identification of possible mechanisms into context-sensitive forecasts. Dynamic models of these types of dynamics require careful assumptions about parameter values and the functional form of the system equations. Generalized modeling is a promising technique that does not require particular assumptions, allowing the researcher to reach more general conclusions based on stability properties of the system (*39*, *40*). Another potential avenue for future research is looking at how transport mechanisms couple physically distant ecosystems—for example, through the moisture-recycling feedback (*41*) or international trade (*18*). A key lesson from our study is that regime shifts can be interconnected. Regime shifts should not be studied in isolation under the assumption that they are independent systems. Methods and data collection need to be further developed to account for the possibility of cascading effects.

Our finding that ~45% of regime shift couplings can have structural dependence suggests that current approaches to environmental management and governance underestimate the likelihood of cascading effects. More attention should be paid to how Earth is social-ecologically connected (*18*), how those connections should be managed, and how to best prepare for regime shifts. Our research suggests that regional ecosystems can be transformed by ecosystem management far away and, conversely, can themselves drive the transformations of other distant ecosystems. Decisions made in one place can undermine the achievement of sustainable development goals in other places. For example, it has been shown that many Arctic regime shifts have the potential to affect non-Arctic ecosystems far away and the provision of their ecosystem services (*30*, *42*, *43*). It implies that whoever does make decisions on management is not necessarily the one who has to deal with the impacts. This issue is evident in governance of water-transport systems, whether run-off or atmospheric transport, but it is applicable to other dynamics that connect faraway ecosystems through other mechanisms, such as climate change, fire, nutrient inputs, or trade. Our results highlight variables that are key for domino effects and hidden feedbacks, such as climate, agriculture, transport of nutrients, and water. They are also good observables for monitoring early-warning indicators of the strengthening of regime shift coupling. How and when nonlinear change can be transmitted across space and time in the Earth system should be considered in assessments and management of future environmental change.

REFERENCES AND NOTES

1. M. Scheffer, S. Carpenter, *Trends Ecol. Evol.* **18**, 648–656 (2003).
2. M. Scheffer, S. Carpenter, J. A. Foley, C. Folke, B. Walker, *Nature* **413**, 591–596 (2001).
3. R. Biggs, G. Peterson, J. Rocha, *Ecol. Soc.* **23**, art9 (2018).
4. C. Boettiger, A. Hastings, *Nature* **493**, 157–158 (2013).
5. A. Hastings, D. B. Wysham, *Ecol. Lett.* **13**, 464–472 (2010).
6. S. R. Carpenter *et al*., *Proc. Natl. Acad. Sci. U.S.A.* **106**, 1305–1312 (2009).
7. R. May, *Nature* **269**, 471–477 (1977).
8. C. S. Holling, *Annu. Rev. Ecol. Syst.* **4**, 1–23 (1973).
9. C. Folke *et al*., *Annu. Rev. Ecol. Evol. Syst.* **35**, 557–581 (2004).
10. M. Scheffer *et al*., *Science* **338**, 344–348 (2012).
11. R. V. Solé, *Phase Transitions* (Princeton Univ. Press, 2011).
12. M. Scheffer, *Critical Transitions in Nature and Society* (Princeton Univ. Press, 2009).
13. J. C. Rocha, G. D. Peterson, R. Biggs, *PLOS ONE* **10**, e0134639 (2015).
14. S. Drijfhout *et al*., *Proc. Natl. Acad. Sci. U.S.A.* **112**, E5777–E5786 (2015).
15. W. Steffen *et al*., *Proc. Natl. Acad. Sci. U.S.A.* **115**, 8252–8259 (2018).
16. R. J. Díaz, R. Rosenberg, *Science* **321**, 926–929 (2008).
17. A. H. Altieri *et al*., *Proc. Natl. Acad. Sci. U.S.A.* **114**, 3660–3665 (2017).
18. J. Liu *et al*., *Science* **347**, 1258832 (2015).
19. T. P. Hughes, S. Carpenter, J. Rockström, M. Scheffer, B. Walker, *Trends Ecol. Evol.* **28**, 389–395 (2013).
20. S. R. Carpenter, *Regime Shifts in Lake Ecosystems: Pattern and Variation* (International Ecology Institute, 2003).
21. M. Scheffer *et al*., *Nature* **461**, 53–59 (2009).
22. J. C. Rocha, thesis, Stockholm Resilience Centre, Stockholm University (2010).
23. A.-S. Crépin, *Environ. Resour. Econ.* **36**, 191–213 (2006).
24. Y. Kuznetsov, *Elements of Applied Bifurcation Theory* (Springer, 2004).
25. M. M. Dekker, A. S. von der Heydt, H. A. Dijkstra, *Earth Sys. Dyn. Discuss.* **9**, 1243–1260 (2018).
26. A. Kinzig *et al*., *Ecol. Soc.* **11**, art20 (2006).
27. Materials and methods are available as supplementary materials.
28. P. N. Krivitsky, *Electron. J. Stat.* **6**, 1100–1128 (2012).
29. C. Gaucherel, V. Moron, *Int. J. Climatol.* **37**, 399–408 (2016).
30. G. Peterson, J. Rocha, *Arctic Resilience Report*, M. Carson, G. Peterson Eds. (Stockholm Environment Institute and Stockholm Resilience Centre, 2016).
31. V. Brovkin, T. Raddatz, C. H. Reick, M. Claussen, V. Gayler, *Geophys. Res. Lett.* **36**, 1 (2009).
32. A. Hastings *et al*., *Science* **361**, eaat6412 (2018).
33. E. J. Defriez, D. C. Reuman, *Glob. Ecol. Biogeogr.* **26**, 878–888 (2017).
34. K. T. Frank, B. Petrie, W. C. Leggett, D. G. Boyce, *Proc. Natl. Acad. Sci. U.S.A.* **113**, 8248–8253 (2016).
35. G. Beaugrand *et al*., *Philos. Trans. R. Soc. London B Biol. Sci.* **370**, 1 (2015).
36. P. Villa Martín, J. A. Bonachela, S. A. Levin, M. A. Muñoz, *Proc. Natl. Acad. Sci. U.S.A.* **112**, E1828–E1836 (2015).
37. E. S. Medeiros, I. L. Caldas, M. S. Baptista, U. Feudel, *Sci. Rep.* **7**, 42351 (2017).
38. J. Rocha, J. Yletyinen, R. Biggs, T. Blenckner, G. Peterson, *Philos. Trans. R. Soc. London B Biol. Sci.* **370**, 1 (2015).
39. T. Gross, L. Rudolf, S. A. Levin, U. Dieckmann, *Science* **325**, 747–750 (2009).
40. S. J. Lade, A. Tavoni, S. A. Levin, M. Schlüter, *Theor. Ecol.* **6**, 359–372 (2013).
41. P. W. Keys *et al*., *Biogeosciences* **9**, 733–746 (2012).
42. I. Cvijanovic *et al*., *Nat. Commun.* **8**, 1947 (2017).
43. J. Huang *et al*., *Nat. Clim. Chang.* **7**, 875–879 (2017).

ACKNOWLEDGMENTS

We are grateful to the contributors, reviewers, and developers of the regime shifts database. **Funding:** This work was supported by FORMAS grant 942-2015-731 to J.C.R. and National Science Foundation grant OCE-1426746 to S.L. **Author contributions:** J.C.R. designed the research; J.C.R. and G.P. curated the data; J.C.R. wrote the code and ran the analysis, with guidance from G.P., Ö.B., and S.L.; and J.C.R., G.P., Ö.B., and S.L. wrote the paper. **Competing interests:** The authors declare no competing interests. **Data and materials availability:** Data from the regime shifts database are publicly available at www.regimeshifts.org. The version of the database used and curated causal networks are available in both the regime shifts database and at https://doi.org/10.6084/m9.figshare.7265096.v1. The development version of the code is available at https://github.com/juanrocha/Domino.

SUPPLEMENTARY MATERIALS

www.sciencemag.org/content/362/6421/1379/suppl/DC1
Materials and Methods
Supplementary Text
Figs. S1 to S5
Tables S1 to S5
References (*44*–*78*)

10 July 2018; accepted 30 October 2018
10.1126/science.aat7850

REPORTS

EXOPLANET ATMOSPHERES

Spectrally resolved helium absorption from the extended atmosphere of a warm Neptune-mass exoplanet

R. Allart[1]*, V. Bourrier[1], C. Lovis[1], D. Ehrenreich[1], J. J. Spake[2], A. Wyttenbach[1,3], L. Pino[1,4,5], F. Pepe[1], D. K. Sing[2,6], A. Lecavelier des Etangs[7]

Stellar heating causes atmospheres of close-in exoplanets to expand and escape. These extended atmospheres are difficult to observe because their main spectral signature—neutral hydrogen at ultraviolet wavelengths—is strongly absorbed by interstellar medium. We report the detection of the near-infrared triplet of neutral helium in the transiting warm Neptune-mass exoplanet HAT-P-11b by using ground-based, high-resolution observations. The helium feature is repeatable over two independent transits, with an average absorption depth of 1.08 ± 0.05%. Interpreting absorption spectra with three-dimensional simulations of the planet's upper atmosphere suggests that it extends beyond 5 planetary radii, with a large-scale height and a helium mass loss rate of $\lesssim 3 \times 10^5$ grams per second. A net blue-shift of the absorption might be explained by high-altitude winds flowing at 3 kilometers per second from day to night-side.

HAT-P-11b is a transiting, warm Neptune-class exoplanet (27.74 ± 3.11 Earth masses, 4.36 ± 0.06 Earth radii) that orbits its star in 4.89 days (*1*–*3*). Its orbit is near the edge of the evaporation desert, a region at close orbital distances characterized by a lack of observed Neptune-mass exoplanets (*4*, *5*). The evaporation desert can be explained as the result of heating planetary atmospheres through stellar radiative flux: Planets that are insufficiently massive lose their gaseous atmospheres through its expansion and hydrodynamic escape (*6*, *7*). The upper atmosphere of planets in mild conditions of irradiation, such as HAT-P-11b, could extend without being subjected to substantial loss and yield deep transit. The low density of HAT-P-11b and the detection of water in its atmosphere (*8*) suggest a hydrogen-helium–rich atmosphere clear of aerosols down to an altitude corresponding to 1 mbar atmospheric pressure.

We observed two transits of HAT-P-11b with the CARMENES (Calar Alto high-Resolution search for M dwarfs with Exoearths with Near-infrared and optical Échelle Spectrographs) (*9*) instrument on the Calar Alto 3.5 m telescope on 7 August 2017 (visit 1) and 12 August 2017 (visit 2). CARMENES consists of two high-resolution spectrographs covering parts of the visible (5200 to 9600 Å) and near-infrared (9600 to 17,100 Å) domains with spectral resolving powers of ~95,000 and ~80,000, respectively. We analyzed data from the near-infrared channel. The data are automatically reduced with the CARMENES Reduction and Calibration pipeline (*10*), which applies a bias, flat-field, and cosmic ray correction to the raw spectra. A flat-relative optimal extraction (FOX) (*11*) and wavelength calibration (defined in vacuum) were then applied to the spectra (*12*). We observed HAT-P-11 for 6 and 5.8 hours in visits 1 and 2, respectively, in 53 and 51 exposures, each of 408 s. Among these spectra, 19 and 18 were obtained during the 2.4-hour duration of the planetary transit in visits 1 and 2, respectively (*13*).

During a transit, the atmosphere of a planet blocks a fraction of the stellar light at a given wavelength, depending on its structure and composition. We retrieved the near-infrared transmission spectrum of the exoplanet atmosphere by calculating the ratio between the in-transit spectra and an out-of-transit master spectrum (fig. S1), representing the unocculted star. The out-of-transit master for each visit was determined by co-adding spectra taken before and after transit (*13*). Because of the change in radial velocity arising from the planet's motion, the spectrum of its atmosphere experiences a spectral shift during the transit. Transmission spectra were calculated for each in-transit exposure, offset in wavelength to the planet's rest frame, and co-added (*14*–*16*) to search for absorption from the planet atmosphere. HAT-P-11b has an eccentric orbit [eccentricity (e) = 0.26] that causes the planetary radial velocity to increase from $-36\ \mathrm{km \cdot s^{-1}}$ to $-24\ \mathrm{km \cdot s^{-1}}$ during the transit. As a result, any absorption signatures from the planet atmosphere are expected to be blue-shifted with respect to their rest wavelengths in the stellar reference frame. This helps to distinguish between signals with stellar or planetary origins. The signal-to-noise ratio also increases because the planet absorption is offset from the equivalent stellar line, unlike planets on circular orbits (fig. S2) (*13*). A search for atmospheric absorption features in excess of the planetary continuum absorption signal, optical transit depth ~3400 ppm, revealed absorption in the near-infrared He I triplet (10,832.06, 10,833.22, and 10,833.31 Å in vacuum) (Figs. 1 and 2). The He I triplet originates from a transition between the 2^3P state and the metastable 2^3S state, which can be populated by recombination from the singly ionized state or by collisional excitation from the ground state (*17*). The triplet is spectrally and temporally resolved during the transit owing to the high spectral resolution and fast cadence of the observations. The two strongest lines of the triplet are blended, whereas the third, weakest (and bluest) line is resolved from the two others. These transitions occur in a spectral region devoid of strong water absorption lines or OH emission lines from Earth's atmosphere (*13*). The spectral region is also devoid of strong stellar absorption features (fig. S1) (*13*).

Absolute fluxes cannot be determined from ground-based high-resolution spectra because of the variability of Earth's atmosphere and light losses at the spectrograph entrance. Although this does not prevent the detection of spectrally localized absorption features arising from the planet atmosphere, it does mean that these observations are not sensitive to any continuum occultation by the atmosphere. To highlight the excess atmospheric He I absorption from HAT-P-11b and to allow comparison with simulations, we rescaled the continuum of each individual transmission spectrum using the theoretical transit white light curve of the planet (table S1) (*13*). The rescaled transit light curve integrated over the spectral range 10,832.84 to 10,833.59 Å is shown in Fig. 2, including the most significant excess atmospheric absorption of 1.08 ± 0.05% (21σ, where σ is the standard deviation). The absorption signature is centered on the He I triplet in the planet reference frame, occurs during the planet transit, and is repeatable over two visits (0.82 ± 0.09% in visit 1 and 1.21 ± 0.06% in visit 2), so it arises from helium in the atmosphere of HAT-P-11b (Fig. 1 and fig. S2). The difference in absorption between the two visits could arise from variability in the size of the atmosphere or its helium density. The peak of the resolved helium absorption profile reaches ~1.2%, corresponding to an equivalent opaque radius of ~2.29 planetary radii (R_p).

We interpreted the observations of HAT-P-11b using three-dimensional (3D) simulations of its

[1]Observatoire Astronomique de l'Université de Genève, Université de Genève, Chemin des Maillettes 51, 1290 Versoix, Switzerland. [2]Astrophysics Group, School of Physics, University of Exeter, Stocker Road, Exeter EX4 4QL, UK. [3]Leiden Observatory, Leiden University, Postbus 9513, 2300 RA Leiden, Netherlands. [4]Dipartimento di Fisica e Astronomia "Galileo Galilei," Univ. di Padova, Vicolo dell'Osservatorio 3, Padova I-35122, Italy. [5]Anton Pannekoek Institute for Astronomy, University of Amsterdam, Science Park 904, 1098 XH Amsterdam, Netherlands. [6]Department of Earth and Planetary Sciences, Johns Hopkins University, Baltimore, MD, USA. [7]Institut d'Astrophysique de Paris, CNRS, UMR 7095, Sorbonne Université, 98 bis boulevard Arago, Paris F-75014, France.
*Corresponding author. Email: romain.allart@unige.ch

atmosphere using the EVaporating Exoplanets (EVE) code (*18*, *19*) [a detailed description is provided in (*13*)]. EVE was used to generate theoretical spectra after absorption by the planet and its upper atmosphere, accounting for limb-darkening, for the partial occultation of the stellar disk during ingress/egress, and for 3D effects linked to the atmospheric structure. The upper atmosphere consists of the thermosphere, the layer heated by the stellar irradiation, and the exosphere, the above layer in which the gas becomes collisionless (*13*). The thermosphere is parameterized with an isotropic, hydrostatic density profile defined by the ratio between the temperature of the thermosphere and its mean atomic weight, T_{th}/μ. We included a constant upward velocity v_{th} to account for the bulk expansion of the thermosphere driven by the stellar extreme ultraviolet (XUV) irradiation. This expansion can lead to substantial mass loss, so we modeled the exosphere of HAT-P-11b by releasing metastable helium atoms at the top of the thermosphere (*13*). The altitude of the thermopause (the thermosphere/exosphere boundary, also known as the exobase) (R_{trans}) is a free parameter in the fitting, as is the mass loss rate of metastable helium $\dot{M}_{He*}$. Monte Carlo particle simulations are used to compute the dynamics of the atmosphere under the influence of the planet and star gravity, and the stellar radiation pressure. The density profile of metastable helium in the thermosphere is scaled so that it matches the density of exospheric metaparticles at the thermopause. We assume that the low densities in the collisionless exosphere prevent the formation of additional metastable helium atoms or their de-excitation through collisions (*17*).

The theoretical spectra were oversampled in time and wavelength compared with the CARMENES observations. We therefore convolved the output with the instrumental response, resampled over the CARMENES wavelength scale, and averaged within the time windows of each observed exposure. The theoretical and observed time-series spectra were compared over visits 1 and 2 together (103 exposures), limiting the fitting to the spectral range 10,826 to 10,834 Å (139 pixels, defined in the star rest frame) to avoid contamination by Earth atmosphere. We calculated a grid of simulations as a function of the four free parameters in the model, using χ^2 as the merit function (fig. S4).

The exploration of the model parameter space reveals a broad χ^2 minimum ($\chi^2 \sim 6130$ for 14,178 data points). The best-fitting thermopause altitudes extend between 5 R_p and the Roche Lobe (the limit of the gravitational influence of the planet, at 6.5 R_p). The T_{th}/μ values indicate high temperatures and/or low mean atomic weight ($T_{th}/\mu \geq 24{,}000$ K·amu^{-1}), suggesting a large fraction of ionized gas and free electrons. The width of the absorption signature is dominated by thermal broadening, but the upward expansion of the thermosphere could play a role with v_{th} up to 10 km·s^{-1}, which is in the range of values predicted for HAT-P-11b (*20*). Comparison between our best-fitting signature from a radially expanding thermosphere and the observed absorption profile reveals that it is symmetrical but blue-shifted (Fig. 3). Including zonal winds flowing from day- to night-side in our best-fitting models provides a better match to the observed absorption profile ($\chi^2 = 6121$) for velocities of ~3 km·s^{-1} (fig. S4). 2D hydrodynamical simulations (*21*) have shown that such winds can form at high altitudes in the extended atmospheres of giant planets.

Our results suggest a negligible contribution from the exosphere, with $\dot{M}_{He*}$ below 3×10^5 g·s^{-1}. This is consistent with the spectral symmetry of the observed absorption profile near the He I triplet and the symmetry of the time series absorption around the transit center (Fig. 2). These properties demonstrate that absorption from HAT-P-11b arises mostly from spherical layers of gas likely to be still gravitationally bound to the planet. The absence of post-transit absorption, or a strong absorption signal blueward of the helium transitions, rule out an extended tail of helium trailing the planet. This is unlike the elongated hydrogen exosphere detected around GJ 436 b (*22*, *23*), a warm Neptune with similar density to that of HAT-P-11b. Our best-fitting models yield densities of metastable helium ~10 cm^{-3} at altitudes between 5 and 6.5 R_p, within the range of values simulated for GJ 436 b at similar altitudes (17).

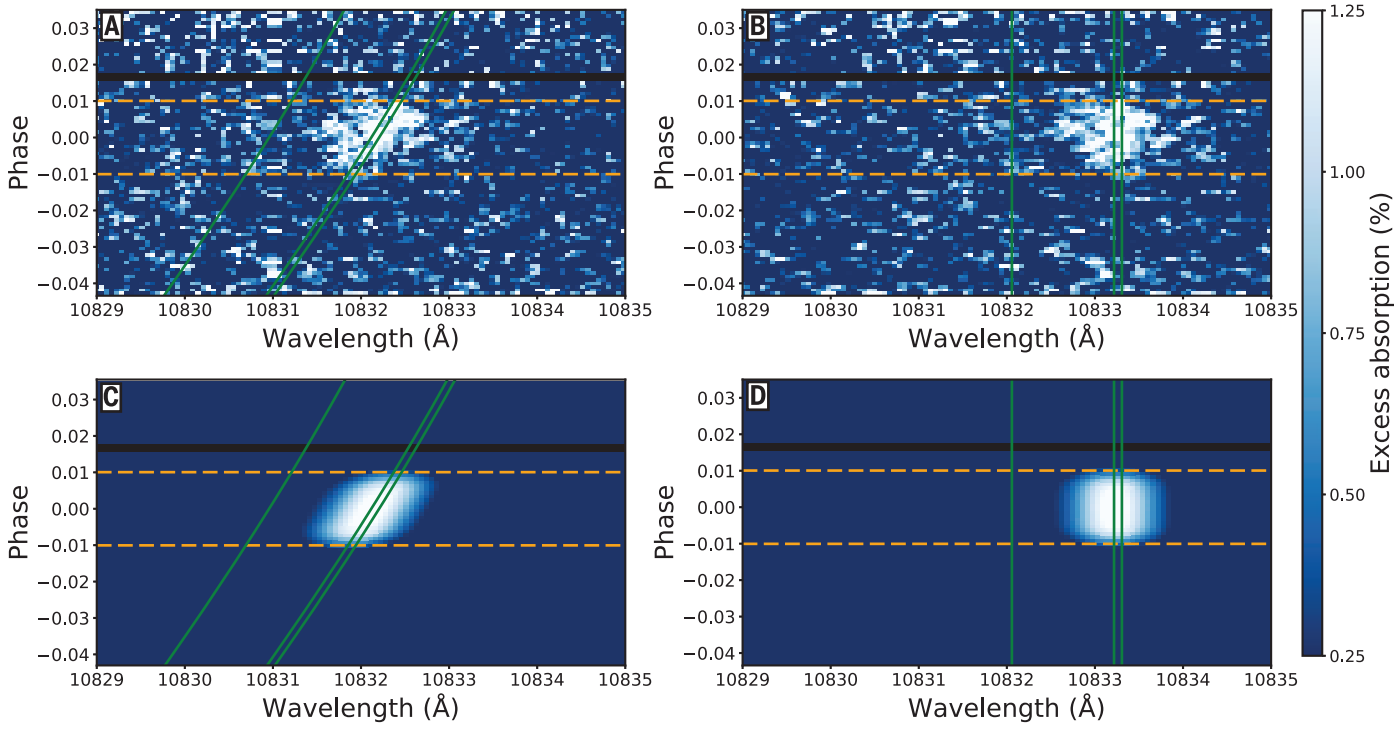

Fig. 1. He I transmission spectra of HAT-P-11b as a function of orbital phase. (**A**) Plotted in the star rest frame. (**B**) Plotted in the planet rest frame. Horizontal orange dotted lines correspond to the beginning and end of transit. Green lines show the three He I transitions in the planet rest frame. Excess atmospheric absorption is visible as a white signal centered on the He I transitions, following the planetary motion, and occurring only during the transit. (**C** and **D**) The equivalent simulated maps for our best-fitting atmospheric model (*13*).

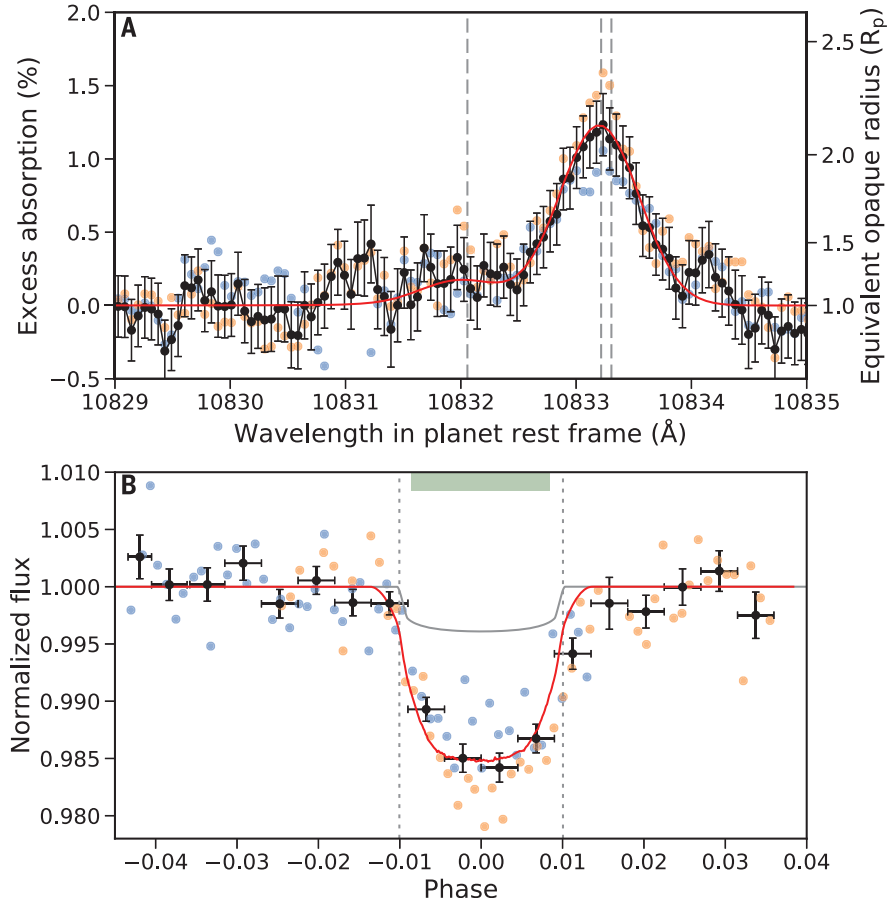

Fig. 2. Average He I transmission spectrum of HAT-P-11b in the planetary rest frame and transit light curve. (**A**) Transmission spectra in visit 1 (blue) and visit 2 (orange), showing the absorption signature centered on the He I triplet (rest wavelengths shown as dashed gray lines). The black points show the weighted average over the two visits, and the red line is our best-fitting model. Wavelengths are in the planet rest frame. (**B**) Light curves derived from the spectra in (A) normalized to the expected planetary continuum absorption and integrated over 10,832.84 to 10,833.59 Å. Plotting symbols are the same as in (A), and the theoretical planet light curve without helium absorption is shown in gray. The black light curve was binned in phase. The green band is the time window (−1 hour to +1 hour) used to produce the average spectrum in (A). Vertical gray dashed lines correspond to the beginning and end of the transit.

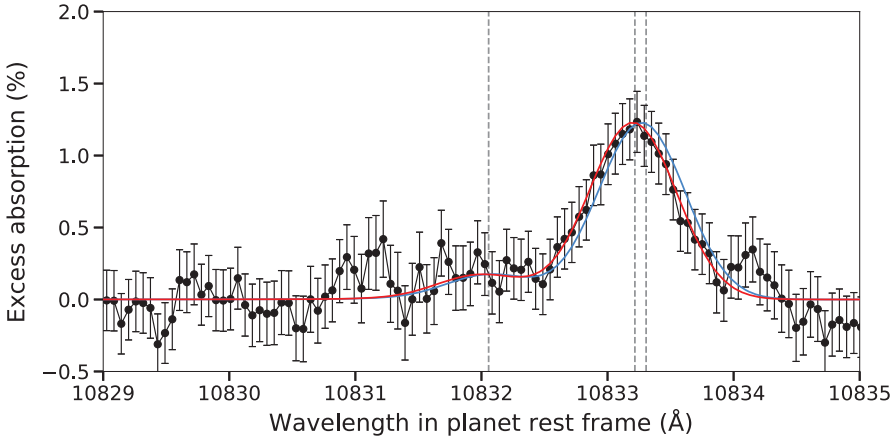

Fig. 3. Contribution of zonal winds to the He I absorption signature from HAT-P-11b. The black points are the observed average over the two nights, as shown in Fig. 2A. The blue curve corresponds to a radially expanding thermosphere, and the red curve (shown in Fig. 2A) is blue-shifted by the additional contribution of zonal winds flowing from day- to night-side at 3 km·s^{-1}.

Our best-fitting simulation in Fig. 4 and fig. S5 illustrates how the radiative environment from the host star (spectral type K4) influences the exosphere of HAT-P-11b. Helium atoms in the shadow of the planet keep moving on their original escape trajectory (determined by the orbital velocity of the planet when they escaped), until they radiatively de-excite with a lifetime of 131 min (*24*). Outside of the planet shadow, helium atoms are blown away faster than this lifetime by the strong stellar radiation pressure. It is much stronger at the helium triplet wavelength (~10,833 Å) than for the hydrogen Lyman-α wavelength (1215.7 Å) because of the brighter near-infrared continuum. Radiation pressure on metastable helium atoms escaping HAT-P-11b is higher than the gravitational pull of the star by a factor of ~90, whereas it reaches a maximum of ~5 for the hydrogen exospheres of planets around G- and K-type stars (*18*). However, the low photoionization threshold of metastable helium atoms implies that their lifetime is only 2.4 min at the orbital distance of HAT-P-11b, which explains why we do not observe an extended comet-like tail trailing the planet. There are, therefore, extended upper atmospheres around both warm Neptunes HAT-P-11b and GJ 436 b. Although they have similar mass and radius, the different spectral types and XUV emission of their host stars (K- and M-type, respectively) are expected to produce different structures for their upper atmospheres. The presence of helium at high altitudes around HAT-P-11b nonetheless suggests that large amounts of hydrogen could be escaping into its exosphere.

Theoretical models (*17*, *25*) have predicted that the metastable He I triplet can be used to trace

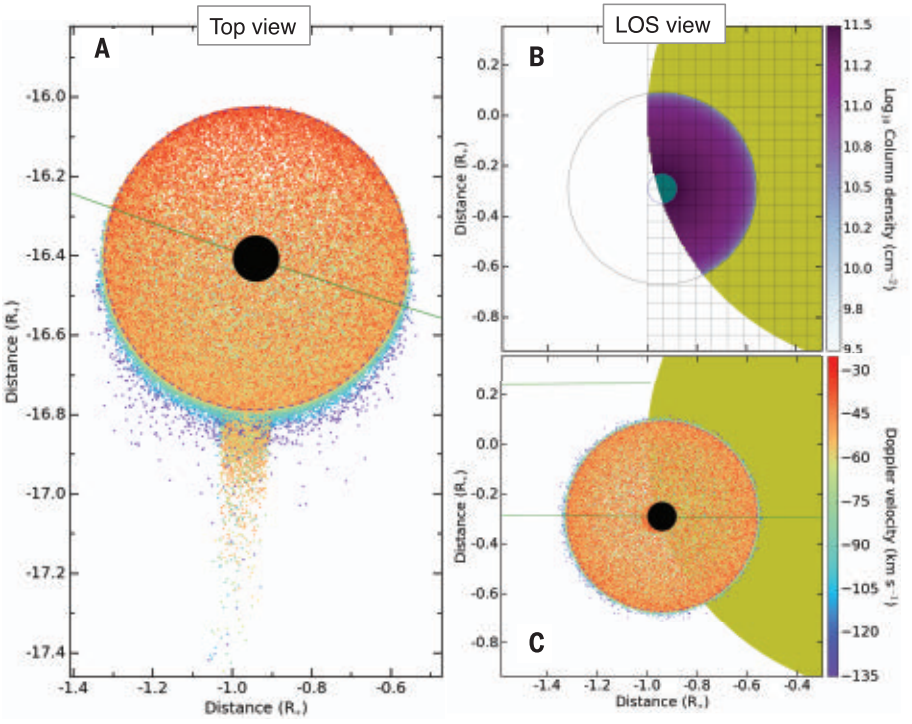

Fig. 4. The best-fitting EVE simulation of the HAT-P-11b helium absorption time series. The system is shown during transit ingress; egress and mid-transit are shown in fig. S5. Distances are defined with respect to the star center. (**A**) View of the exosphere from above the planet. Metastable helium atoms are colored as a function of their radial velocity in the stellar rest frame (color bar). The dashed circle is the projected transition between the exosphere and thermosphere regimes. All particles in this projected view are outside of the thermosphere. The eccentric orbit of HAT-P-11b (black disk, plotted above the exosphere for the sake of clarity) is shown as a green curve. The tail is due to particles in the planet shadow being protected from photo-ionization. (**B** and **C**) View along the LOS (line of sight) toward Earth, showing the (B) thermospheric and (C) exospheric regimes separately. (B) The thermosphere is colored as a function of the column density of metastable helium. (C) Particles in the exosphere are colored as in (A). (B) shows the grids discretizing the stellar disk, the thermosphere, and the planetary disk.

atmospheric evaporation. Because the 10,833-Å He I triplet is not absorbed by the interstellar medium, it allows probing planetary systems farther from Earth than the H I Lyman-α at 1215 Å (*26*). Although early searches were unsuccessful because of instrumental limitations (*27*), an unresolved detection of metastable helium on the inflated gas giant WASP-107b has been achieved with the Hubble Space Telescope (HST) (*28*). Because of the low spectral resolution of HST, the helium triplet in WASP-107b was covered with just 1 pixel. We have calculated that observations of HAT-P-11b helium atmosphere with the James Webb Space Telescope (JWST) would measure the triplet with a high sensitivity but over just 2 pixels (*13*). High-resolution spectrographs have the ability to spectrally resolve the He I transitions, aiding in the separation of planetary from stellar signals. As shown by our results (Fig. 2) (*29*), resolved observations of the He I triplet provide additional constraints on the extended atmospheres of exoplanets, from their thermosphere to exosphere.

REFERENCES AND NOTES

1. G. Á. Bakos *et al*., *Astrophys. J.* **710**, 1724–1745 (2010).
2. D. Deming *et al*., *Astrophys. J.* **740**, 33 (2011).
3. K. F. Huber, S. Czesla, J. H. M. M. Schmitt, *Astron. Astrophys.* **597**, A113 (2017).
4. A. Lecavelier des Etangs, *Astron. Astrophys.* **461**, 1185–1193 (2007).
5. C. Beaugé, D. Nesvorný, *Astrophys. J.* **763**, 12 (2013).
6. A. Vidal-Madjar *et al*., *Nature* **422**, 143–146 (2003).
7. E. D. Lopez, J. J. Fortney, N. Miller, *Astrophys. J.* **761**, 59 (2012).
8. J. Fraine *et al*., *Nature* **513**, 526–529 (2014).
9. A. Quirrenbach *et al*., *SPIE* **9147**, 91471F (2014).
10. J. A. Caballero *et al*., *SPIE* **9910**, 99100E (2016).
11. M. Zechmeister, G. Anglada-Escudé, A. Reiners, *Astron. Astrophys.* **561**, A59 (2014).
12. F. F. Bauer, M. Zechmeister, A. Reiners, *Astron. Astrophys.* **581**, A117 (2015).
13. Material and Methods are available as supplementary materials.
14. A. Wyttenbach, D. Ehrenreich, C. Lovis, S. Udry, F. Pepe, *Astron. Astrophys.* **577**, A62 (2015).
15. A. Wyttenbach *et al*., *Astron. Astrophys.* **602**, A36 (2017).
16. R. Allart *et al*., *Astron. Astrophys.* **606**, A144 (2017).
17. A. Oklopčić, C. M. Hirata, *Astrophys. J.* **855**, L11 (2018).
18. V. Bourrier, A. Lecavelier des Etangs, *Astron. Astrophys.* **557**, A124 (2013).
19. V. Bourrier, D. Ehrenreich, A. Lecavelier des Etangs, *Astron. Astrophys.* **582**, A65 (2015).
20. M. Salz, S. Czesla, P. C. Schneider, J. H. M. M. Schmitt, *Astron. Astrophys.* **586**, A75 (2016).
21. J. H. Guo, *Astrophys. J.* **766**, 102 (2013).
22. D. Ehrenreich *et al*., *Nature* **522**, 459–461 (2015).
23. B. Lavie *et al*., *Astron. Astrophys.* **605**, L7 (2017).
24. G. W. Drake, *Phys. Rev. A* **3**, 908–915 (1971).
25. S. Seager, D. D. Sasselov, *Astrophys. J.* **537**, 916–921 (2000).
26. N. Indriolo, L. M. Hobbs, K. H. Hinkle, B. J. McCall, *Astrophys. J.* **703**, 2131–2137 (2009).
27. C. Moutou, A. Coustenis, J. Schneider, D. Queloz, M. Mayor, *Astron. Astrophys.* **405**, 341–348 (2003).
28. J. J. Spake *et al*., *Nature* **557**, 68–70 (2018).
29. L. Nortmann *et al*., *Science* **362**, 1388–1391 (2018).
30. R. Allart *et al*., Spectrally resolved helium absorption from the extended atmosphere of a warm Neptune exoplanet. Zenodo (2018); doi:105281/zenodo.1473463

ACKNOWLEDGMENTS

We acknowledge the Geneva exoplanet atmosphere group for fruitful discussions and the support of X. Dumusque for the DACE platform. **Funding:** This work was based on observations collected at the Centro Astronómico Hispano Alemán (CAHA), operated jointly by the Max-Planck Institut für Astronomie and the Instituto de Astrofisica de Andalucia (CSIC) under OPTICON program 2017B/026, "Multi-wavelength observations of the warm Neptune HAT-P-11b: A journey across the atmosphere." This project has received funding from the European Union's Horizon 2020 research and innovation program under grant agreement 730890. This material reflects only the authors views, and the Commission is not liable for any use that may be made of the information contained therein. This work has been carried out in the frame of the National Centre for Competence in Research "PlanetS" supported by the Swiss National Science Foundation (SNSF). R.A., V.B., D.E., C.L., L.P., F.P., and A.W. acknowledge the financial support of the SNSF. A.W. acknowledges the financial support of the SNSF through the grant P2GEP2_178191. A.L.d.E. thanks the CNES for financial support. This project has received funding from the European Research Council (ERC) under the European Union's Horizon 2020 research and innovation program (project FOUR ACES; grant agreement 724427). This project has also received funding from the European Research Council (ERC) under the European Union's Seventh Framework Programme (Fp7/2007-2013)/ERC grant agreement 337592. **Author contributions:** R.A. coordinated the study, performed the data reduction, and analyzed the results. V.B. developed the EVE code, based on previous code written by V.B. and A.L.d.E.; R.A. and V.B. performed the EVE simulations and wrote the paper. J.J.S. performed the HST and JWST simulations. R.A., V.B., C.L., D.E., L.P., A.W., and F.P. wrote the OPTICON proposal. All authors participated in the discussion and interpretation of the results, and commented on the manuscript. **Competing interests:** The authors declared no competing interests. **Data and materials availability:** The CARMENES raw and reduced data can be obtained from the Calar Alto Observatory archive at http://caha.sdc.cab.inta-csic.es/calto/jsp/searchform.jsp under program number 051. The data and simulation outputs used to produce each figure are available at (*30*). The EVE code is described in (*13*, *18*, *28*) and available at https://github.com/RomainAllart/Science_Allart_HAT-P-11b.

SUPPLEMENTARY MATERIALS

www.sciencemag.org/content/362/6421/1384/suppl/DC1
Materials and Methods
Tables S1 and S2
Figs. S1 to S6
References (*31*–*45*)

14 March 2018; accepted 8 November 2018
Published online 6 December 2018
10.1126/science.aat5879

EXOPLANET ATMOSPHERES

Ground-based detection of an extended helium atmosphere in the Saturn-mass exoplanet WASP-69b

Lisa Nortmann[1,2]*, Enric Pallé[1,2], Michael Salz[3], Jorge Sanz-Forcada[4], Evangelos Nagel[3], F. Javier Alonso-Floriano[5], Stefan Czesla[3], Fei Yan[6], Guo Chen[1,2,7], Ignas A. G. Snellen[5], Mathias Zechmeister[8], Jürgen H. M. M. Schmitt[3], Manuel López-Puertas[9], Núria Casasayas-Barris[1,2], Florian F. Bauer[8,9], Pedro J. Amado[9], José A. Caballero[4], Stefan Dreizler[8], Thomas Henning[6], Manuel Lampón[9], David Montes[10], Karan Molaverdikhani[6], Andreas Quirrenbach[11], Ansgar Reiners[8], Ignasi Ribas[12,13], Alejandro Sánchez-López[9], P. Christian Schneider[3], María R. Zapatero Osorio[14]

Hot gas giant exoplanets can lose part of their atmosphere due to strong stellar irradiation, and these losses can affect their physical and chemical evolution. Studies of atmospheric escape from exoplanets have mostly relied on space-based observations of the hydrogen Lyman-α line in the far ultraviolet region, which is strongly affected by interstellar absorption. Using ground-based high-resolution spectroscopy, we detected excess absorption in the helium triplet at 1083 nanometers during the transit of the Saturn-mass exoplanet WASP-69b, at a signal-to-noise ratio of 18. We measured line blueshifts of several kilometers per second and posttransit absorption, which we interpret as the escape of part of the atmosphere trailing behind the planet in comet-like form.

In recent years, high-resolution spectroscopy has become a frequently used tool for investigating exoplanet atmospheres (*1*–*4*). Numerous stable high-resolution spectrographs have been deployed on telescopes specifically for exoplanetary science (*5*–*8*). One of these spectrographs is CARMENES (Calar Alto high-Resolution search for M dwarfs with Exoearths with Near-infrared and optical Échelle Spectrographs) (*8*) at the 3.5-m telescope of the Calar Alto Observatory. The spectrograph simultaneously covers the visible wavelength range from 0.52 to 0.96 μm and the near-infrared range from 0.96 to 1.71 μm. The near-infrared coverage provides access to exoplanet atmospheric features that cannot be observed in the visible range, including the triplet of metastable He I lines around 1083 nm. This feature has been proposed as a tracer for atmospheric evaporation (*9*), a process whereby intense x-ray (~0.5 to 10.0 nm) and extreme ultraviolet (EUV) (10.0 to 92.0 nm) irradiation from a host star causes atmospheres of hot gas exoplanets to expand, resulting in a bulk mass flow away from the planet. The continuous mass loss most strongly affects small sub-Neptune–sized planets and may be capable of removing their entire volatile atmosphere (*10*). Helium absorption at 1083 nm is sensitive to the low-density gas in an evaporating atmosphere (*9*, *11*, *12*), and its observation is not affected by absorption in the foreground interstellar medium, which hampers studies of the neutral hydrogen Lyman-α (Lyα) line (*9*). He I absorption has been detected in a transmission spectrum of the exoplanet WASP-107b using data from the Hubble Space Telescope (*13*). However, the low resolution prevented a detailed study of the line triplet, including its shape, depth, and temporal behavior.

The Saturn-mass exoplanet WASP-69b orbits an active star with a period of 3.868 days (*14*). It is a suitable target for atmospheric studies, due to its large atmospheric scale height and high planet-to-star radius ratio, facilitating the detection of 5.8 ± 0.3% excess absorption in the Na D line (*15*). We used the CARMENES spectrograph to observe two transits of WASP-69b on 22 August 2017 and 22 September 2017 (night 1 and night 2, respectively) (see table S1 for the observing log). The observations spanned approximately 4 hours for each epoch, which covered the full transit and provided a before- and after-transit baseline. In total, 66 spectra were recorded, 31 of them out-of-transit spectra.

The wavelength region surrounding the He I feature is affected by emission and water vapor absorption lines originating from within Earth's atmosphere (fig. S1). Although these lines are spectrally separated from the He I triplet, we corrected for the effect of water absorption using the European Southern Observatory (ESO) tool Molecfit (*16*) and for the sky emission lines using an empirical model derived from the data (*17*). After this correction, we performed continuum normalization and brought the spectra to the stellar velocity rest frame. We then computed a master out-of-transit spectrum (F_{out}), which was used to normalize all spectra, following

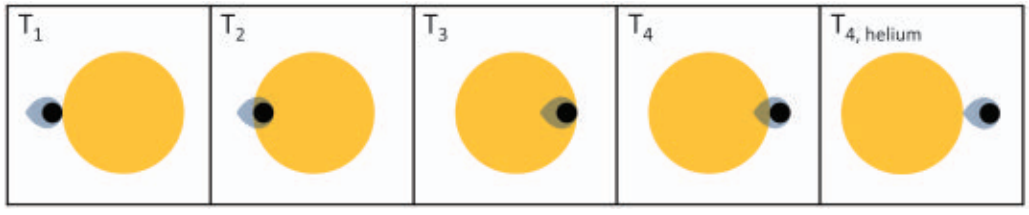

Fig. 1. Illustration of the exoplanet WASP-69b (black) and its extended helium atmosphere (gray-blue) at the different contact points. Shown are the first (T_1), second (T_2), third (T_3), and fourth (T_4) contacts of the broadband planet transit and also the moment when the tail has passed the stellar disk, $T_{4,\ helium}$, 22 ± 3 min after T_4.

[1]Instituto de Astrofísica de Canarias, Vía Láctea s/n, 38205 La Laguna, Tenerife, Spain. [2]Departamento de Astrofísica, Universidad de La Laguna, 38206 La Laguna, Tenerife, Spain. [3]Hamburger Sternwarte, Universität Hamburg, Gojenbergsweg 112, 21029 Hamburg, Germany. [4]Centro de Astrobiología, Consejo Superior de Investigaciones Científicas—Instituto Nacional de Técnica Aeroespacial (CSIC-INTA), European Space Astronomy Centre campus, Camino bajo del castillo s/n, 28692 Villanueva de la Cañada, Madrid, Spain. [5]Leiden Observatory, Leiden University, Postbus 9513, 2300 RA, Leiden, Netherlands. [6]Max-Planck-Institut für Astronomie, Königstuhl 17, 69117 Heidelberg, Germany. [7]Key Laboratory of Planetary Sciences, Purple Mountain Observatory, Chinese Academy of Sciences, Nanjing 210008, China. [8]Institut für Astrophysik, Georg-August-Universität, 37077 Göttingen, Germany. [9]Instituto de Astrofísica de Andalucía, Consejo Superior de Investigaciones Científicas (CSIC), Glorieta de la Astronomía s/n, 18008 Granada, Spain. [10]Departamento de Astrofísica y Ciencias de la Atmósfera, Facultad de Ciencias Físicas, Universidad Complutense de Madrid, 28040 Madrid, Spain. [11]Landessternwarte, Zentrum für Astronomie der Universität Heidelberg, Königstuhl 12, 69117 Heidelberg, Germany. [12]Institut de Ciències de l'Espai, Consejo Superior de Investigaciones Científicas (CSIC), Campus Universitat Autònoma de Barcelona, c/ de Can Magrans s/n, 08193 Bellaterra, Barcelona, Spain. [13]Institut d'Estudis Espacials de Catalunya, 08034 Barcelona, Spain. [14]Centro de Astrobiología, Consejo Superior de Investigaciones Científicas—Instituto Nacional de Técnica Aeroespacial (CSIC-INTA), Crta. de Ajalvir km 4, E-28850 Torrejón de Ardoz, Madrid, Spain.
*Corresponding author. Email: nortmann.astro@gmail.com

standard analysis methods (*1*, *15*). The resulting residual spectra contain the exoplanet absorption signal (fig. S2). We shifted them into the planetary rest frame and computed the transmission spectrum by co-adding all residual in-transit spectra (F_{in}/F_{out}) obtained between second and third contact (Fig. 1), i.e., when the planet disk was fully in front of the stellar disk.

The combined transmission spectrum for the two nights is shown in Fig. 2. An excess absorption in the He I line at the level of 3.59 ± 0.19% was detected. The given uncertainty corresponds to 1 standard deviation (1σ) of the continuum flux. The signal was detected separately in each visit at 3.96 ± 0.25% (1σ) and 3.00% ± 0.31% (1σ) for nights 1 and 2, respectively (fig. S3). We modeled the transmission spectrum with three Gaussian functions with fixed amplitude ratios and relative wavelengths according to theoretical values for the He I triplet (*18*, *19*). We fitted a common line width, Doppler shift, and intensity of the lines (*17*) and determined parameter uncertainties by Markov chain Monte Carlo sampling (fig. S4). The best-fitting model indicates a net blueshift of −3.58 ± 0.23 km s^{-1} (where the uncertainty corresponds to the standard deviation of the posterior probability distribution).

To examine the behavior of the helium absorption over time, we constructed a light curve by summing the flux within a 0.04-nm-wide passband centered on the blueshifted core of the He I feature for each residual spectrum in the planet rest frame (*15*). The resulting light curves for each of the two nights are shown in Fig. 3. The helium absorption began shortly after the planet ingress, with no observable pretransit absorption, and lasted for 22 ± 3 min after the transit ended (fig. S5). This light curve behavior does not depend on the width of the chosen passband. By fitting the Rossiter-McLaughlin effect (RME), a deformation of the stellar lines caused by the planet occulting different parts of the rotating stellar surface during transit, for our visible channel radial velocity data (*17*) (fig. S6), we obtained midtransit times consistent with the known planet orbit. The signal of the RME corresponded with the predicted broadband transit duration of 2.23 hours (*14*), so we can be confident that the observed post-transit helium absorption is real. We used the RME curve to estimate the potential contamination of the transmission spectrum by the corresponding deformation of the stellar lines during transit; we found that the impact was negligible (*17*) (fig. S7). The He I D_3 line at 587.6 nm and the Ca II infrared triplet (IRT) at 849.8, 854.2, and 866.2 nm, both indicators of stellar activity, showed no sign of active regions (*17*) (fig. S8). The time delay of the helium ingress and egress indicates that the distribution of helium around the planet is asymmetrical and that a cloud of gas is trailing the planet along its orbit (Fig. 1). We calculated the length of this tail as ~170,000 km, i.e., 2.2 times the planet radius (longer if tilted with respect to the planet's orbit). Acceleration of the tail material away from the planet could be the cause of the blueshifted absorption. This hypothesis is supported by the larger measured net blueshift of −10.69 ± 1.00 km s^{-1} when only the helium tail is occulting the stellar disk (fig. S9). The tail length and velocities suggest that helium is escaping the planet (*17*).

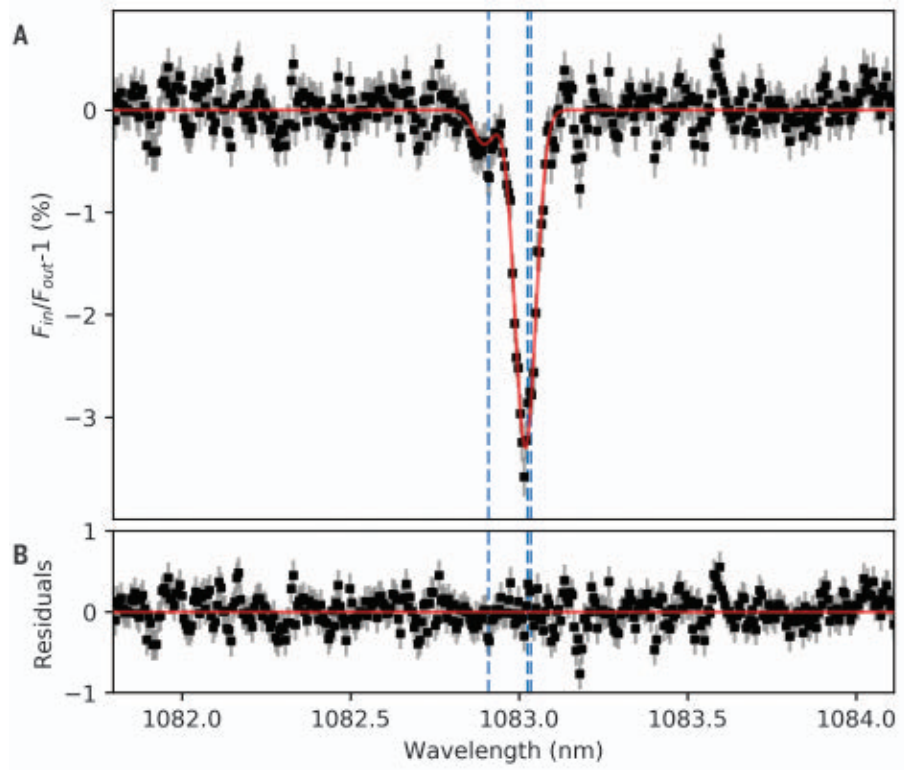

Fig. 2. Transmission spectrum between the second and third contacts of WASP-69b, showing planetary absorption in the He I triplet at 1083 nm. (**A**) The excess absorption of helium in the weighted-mean averaged transmission spectrum (black points) from two transit observations of WASP-69b (22 August 2017 and 22 September 2017) (see Fig. 1). The best-fitting model (red line) shows a net blueshift of −3.58 ± 0.23 km s^{-1}. The predicted positions of the helium triplet lines (1082.909 nm, 1083.025 nm, and 1083.034 nm) are indicated as vertical dashed blue lines. (**B**) The residuals of the data after subtraction of the model are shown in black, and the red line indicates the zero level.

We also analyzed CARMENES transit observations of the hot Jupiter-mass exoplanets HD 189733b and HD 209458b, the extremely hot planet KELT-9b, and the warm Neptune-sized exoplanet GJ 436b (fig. S10). GJ 436b and HD 209458b both show evaporation of hydrogen in the Lyα line (*20*, *21*), and KELT-9b is surrounded by a large cloud of evaporating hydrogen absorbing in the Balmer Hα line at 656.28 nm (*22*). GJ 436b and HD 209458b are predicted to have large absorption depths in the He I line (~8% and ~2%, respectively) (*9*), although a previous study of HD 209458b did not detect any absorption (*23*). We did not detect He I absorption for most of these planets, with 90% confidence upper limits of 0.41% for GJ 436b, 0.84% for HD 209458b [i.e., in disagreement with the predicted levels (*9*)], and 0.33% for KELT-9b (fig. S10). However, we did detect helium absorption in HD 189733b at the level of 1.04 ± 0.09% (*24*). A companion paper reports a similar detection of helium absorption for the warm Neptune-sized planet HAT-P-11b (*25*). For our detections, we calculated the equivalent height of the He I atmosphere δ_{Rp}, i.e., the height of an opaque atmospheric layer that would produce the observed absorption signal (table S2). For both WASP-69b and HD 189733b, we found δ_{Rp} to be ~80 times as large as the atmospheric scale height H_{eq} calculated for the respective planet's deep atmosphere, i.e., in hydrostatic equilibrium (*17*). For the other three planets, our upper limits correspond to no detections of features above ~40 H_{eq}.

Why do similar hot gas exoplanets show such a range of helium absorption values? The expansion of the escaping planetary atmosphere depends on parameters like the EUV irradiation and the planetary density (*26*), but the population of the helium triplet state depends on the irradiation at wavelengths <50.4 nm (*9*). Whereas GJ 436b and HD 209458b orbit very quiet stars (*27*, *28*), the hosts of the planets in which helium is detected, i.e., WASP-69, HD 189733, HAT-P-11, and WASP-107, are all relatively active stars (*14*, *15*, *29*, *30*). For Fig. 4A, we plotted the

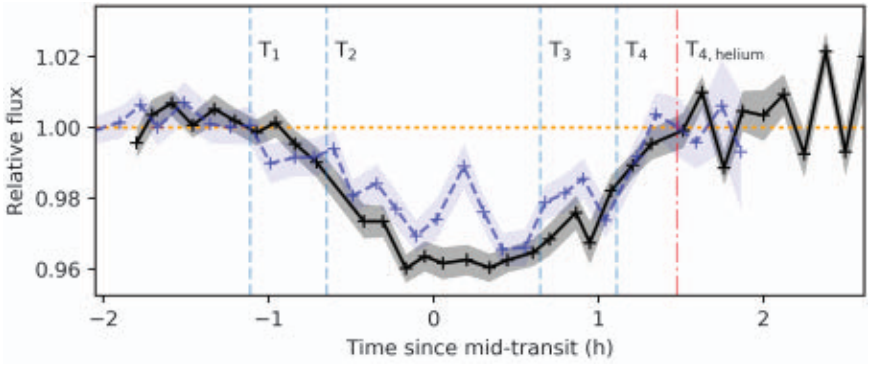

Fig. 3. Spectrophotometric transit light curves of WASP-69b. We integrated the spectral flux in a 0.04-nm-wide bin around the core of the planetary He I line for every observed spectrum over two transits, normalized by the continuum flux outside of the absorption feature. The first (T_1), second (T_2), third (T_3), and fourth (T_4) contacts of the planet transit are marked by dashed vertical lines. Two individual transit light curves are shown in black (night 1) and blue (night 2). The drop in flux from the continuum transit has already been removed, leaving the excess absorption due to helium. The continuum behavior is indicated by the horizontal yellow dotted line. The 1σ uncertainty intervals are shown as light blue and gray shaded regions. The excess absorption lasts until well after the stellar occultation by the planet has ended (T_4), indicating that absorbing material is still in front of the star. We find the excess absorption ends 22 ± 3 min after the planet's egress ($T_{4,\ helium}$, vertical red dash-dotted line).

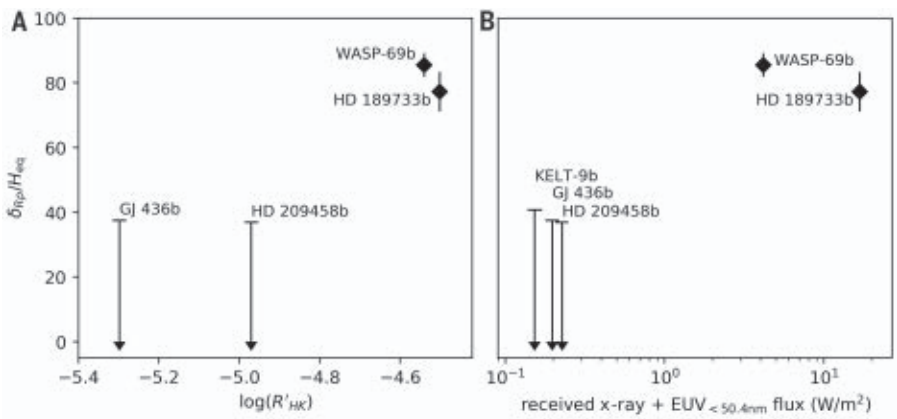

Fig. 4. Detected signals as a function of host star activity and received XUV_{He} irradiation. The equivalent heights of the He I atmosphere δ_{Rp}, normalized by one atmospheric scale height of the respective planet's lower atmosphere H_{eq}, are shown. For the two detections we plotted 1σ error bars, and for the nondetections we plotted upper limits corresponding to a 90% confidence level. (**A**) δ_{Rp}/H_{eq} as a function of the host star activity index $\log(R'_{HK})$, where larger values indicate stronger stellar activity (*31*). The KELT-9 system is not plotted, because its $\log(R'_{HK})$ is not known. (**B**) δ_{Rp}/H_{eq} as a function of stellar flux with a wavelength <50.4 nm at the distance of the planet orbit. The two strong detections of an extended helium atmosphere occur for the two planets having more active host stars and higher planetary XUV_{He} irradiation.

normalized absorption altitude of helium δ_{Rp}/H_{eq} against the stellar activity index $\log(R'_{HK})$ (*31*). Our sample size was limited, but the detections succeeded for the planets with the more active stellar hosts, hinting at a relation between He I detectability and host star activity.

Low-mass stars (F-, G-, K-, and M-types) have a convective layer that, in combination with stellar rotation, produces phenomena associated with magnetic activity. The exterior layers of low-mass stars are (from inside to outside) photosphere, chromosphere, transition region, and corona. In general, activity in the chromosphere is detected in spectral features such as the activity indicator Ca II H and K doublet lines at 393.4 and 396.8 nm, whereas the transition region and the corona produce emission in x-ray and EUV. The metastable 2^3S helium triplet state, which is the lower level of the observed absorption lines, is populated via radiative ionization of He I by photons with wavelengths <50.4 nm followed by recombination (*32*). Thus, a higher x-ray and EUV (<50.4 nm, hereafter XUV_{He}) irradiation level should enhance the formation of the He I triplet in atmospheres of hot gas planets. We calculated the XUV_{He} flux received by all discussed planets (table S3) at the separation of their orbit (*17*) (table S4). For Fig. 4B, we plotted the normalized He I atmospheric altitude δ_{Rp}/H_{eq} for our measurements as a function of the XUV_{He} flux. The line is detected for the planets receiving the largest combined XUV_{He} irradiation. These results indicate a dependence of the detectability of He I in planetary atmospheres on intense x-ray and EUV emission from the parent star.

REFERENCES AND NOTES

1. I. A. G. Snellen, R. J. de Kok, E. J. W. de Mooij, S. Albrecht, *Nature* **465**, 1049–1051 (2010).
2. M. Brogi *et al.*, *Nature* **486**, 502–504 (2012).
3. A. C. Lockwood *et al.*, *Astrophys. J.* **783**, L29 (2014).
4. M. Brogi *et al.*, *Astron. Astrophys.* **615**, A16 (2018).
5. E. Oliva *et al.*, in *Proceedings of the Society of Photo-Optical Instrumentation Engineers Conference Series*, I. S. McLean, M. Iye, Eds. (SPIE, 2006), vol. 6269, p. 626919.
6. S. Mahadevan *et al.*, in *Ground-Based and Airborne Instrumentation for Astronomy IV*, I. S. McLean, S. K. Ramsay, H. Takami, Eds. (SPIE, 2012), vol. 8446, p. 84461S.
7. É. Artigau *et al.*, in *Ground-Based and Airborne Instrumentation for Astronomy V*, S. K. Ramsay, I. S. McLean, H. Takami, Eds. (SPIE, 2014), vol. 9147, p. 914715.
8. A. Quirrenbach *et al.*, in *Ground-Based and Airborne Instrumentation for Astronomy V*, J. Evans, L. Simard, H. Takami, Eds. (SPIE, 2014), vol. 9147, p. 91471F.
9. A. Oklopčić, C. M. Hirata, *Astrophys. J.* **855**, L11 (2018).
10. M. S. Lundkvist *et al.*, *Nat. Commun.* **7**, 11201 (2016).
11. S. Seager, D. D. Sasselov, *Astrophys. J.* **537**, 916–921 (2000).
12. J. D. Turner, D. Christie, P. Arras, R. E. Johnson, C. Schmidt, *Mon. Not. R. Astron. Soc.* **458**, 3880–3891 (2016).
13. J. J. Spake *et al.*, *Nature* **557**, 68–70 (2018).
14. D. R. Anderson *et al.*, *Mon. Not. R. Astron. Soc.* **445**, 1114–1129 (2014).
15. N. Casasayas-Barris *et al.*, *Astron. Astrophys.* **608**, A135 (2017).
16. A. Smette *et al.*, *Astron. Astrophys.* **576**, A77 (2015).
17. Materials and methods are available as supplementary materials.
18. A. Kramida, Y. Ralchenko, J. Reader, NIST ASD Team, NIST Atomic Spectra Database, version 5.5.2 (National Institute of Standards and Technology, 2018); https://physics.nist.gov/asd [accessed 2 March 2018].
19. G. Drake, *High Precision Calculations for Helium* (Springer New York, 2006), pp. 199–219.
20. D. Ehrenreich *et al.*, *Nature* **522**, 459–461 (2015).
21. A. Vidal-Madjar *et al.*, *Nature* **422**, 143–146 (2003).
22. F. Yan, T. Henning, *New Astron.* **2**, 714–718 (2018).
23. C. Moutou, A. Coustenis, J. Schneider, D. Queloz, M. Mayor, *Astron. Astrophys.* **405**, 341–348 (2003).
24. M. Salz *et al.*, *Astron. Astrophys.* 10.1051/0004-6361/201833694 (2018).
25. R. Allart *et al.*, *Science* **362**, 1384–1387 (2018).
26. N. V. Erkaev *et al.*, *Astron. Astrophys.* **472**, 329–334 (2007).
27. R. P. Butler *et al.*, *Astrophys. J.* **617**, 580–588 (2004).
28. S. Czesla, M. Salz, P. C. Schneider, M. Mittag, J. H. M. M. Schmitt, *Astron. Astrophys.* **607**, A101 (2017).
29. H. A. Knutson, A. W. Howard, H. Isaacson, *Astrophys. J.* **720**, 1569–1576 (2010).
30. B. M. Morris *et al.*, *Astrophys. J.* **848**, 58 (2017).
31. R. W. Noyes, L. W. Hartmann, S. L. Baliunas, D. K. Duncan, A. H. Vaughan, *Astrophys. J.* **279**, 763 (1984).
32. J. Sanz-Forcada, A. K. Dupree, *Astron. Astrophys.* **488**, 715–721 (2008).

ACKNOWLEDGMENTS

Parts of the results shown are based on observations obtained with XMM-Newton, an ESA science mission with instruments and contributions directly funded by ESA Member States and NASA.

We acknowledge the XMM-Newton Project Scientist for the quick and positive reaction to our request for a director's discretionary time observation of WASP-107. We thank the anonymous reviewers for their contribution to this paper. **Funding:** CARMENES is an instrument for the Centro Astronómico Hispano-Alemán de Calar Alto (CAHA, Almería, Spain). CARMENES is funded by the German Max-Planck-Gesellschaft (MPG), the Spanish Consejo Superior de Investigaciones Científicas (CSIC), the European Union through FEDER/ERF FICTS-2011-02 funds, and the members of the CARMENES Consortium (Max-Planck-Institut für Astronomie, Instituto de Astrofísica de Andalucía, Landessternwarte Königstuhl, Institut de Ciències de l'Espai, Insitut für Astrophysik Göttingen, Universidad Complutense de Madrid, Thüringer Landessternwarte Tautenburg, Instituto de Astrofísica de Canarias, Hamburger Sternwarte, Centro de Astrobiología, and Centro Astronómico Hispano-Alemán), with additional contributions by the Spanish Ministry of Economy, the German Science Foundation through the Major Research Instrumentation Programme and Deutsche Forschungsgesellschaft (DFG) Research Unit FOR2544 "Blue Planets around Red Stars," the Klaus Tschira Stiftung, the states of Baden-Württemberg and Niedersachsen, and by the Junta de Andalucía. We acknowledge funding from the Spanish Ministry of Economy and Competitiveness (MINECO) and the Fondo Europeo de Desarrollo Regional (FEDER) through grants ESP2016-80435-C2-1-R, ESP 2016-76076-R, ESP2014-54362-P, ESP 2014-54062-R, AYA2016-79425-C3-2-P, AYA2016-79425-C3-1-P, AYA2016-79425-C3-2-P, AYA2014-54348-C3-1-R, and AYA2016-79425-C3-3-P. We also acknowledge funding through the DFG through grants DFG DR281/32-1, RE 1664/14-1, DFG SFB 676, and DFG SCHM 1032/57-1 and by the Deutsches Zentrum für Luft und Raumfahrt (DLR) through grants DLR 50 OR 1710, DLR 50 OR 1307, and BMWi50OR1505, as well as the support of the Generalitat de Catalunya/CERCA program. I.A.G.S. and F.J.A.-F. acknowledge funding from the research program VICI 639.043.107 funded by the Dutch Organisation for Scientific Research (NWO) and funding from the European Research Council (ERC) under the European Union's Horizon 2020 research and innovation program under grant agreement 694513. G.C. acknowledges support by the National Natural Science Foundation of China (grant 11503088) and the Natural Science Foundation of Jiangsu Province (grant BK20151051). **Author contributions:** L.N. performed data acquisition including proposal writing and preparation of observations (DAQ), data analysis (DA), and science interpretation (SI). F.J.A.-F., F.Y., and I.A.G.S. performed DAQ, DA, and SI. E.P. and S.C. performed DAQ and SI. M.S., M.L.-P., A.S.-L., D.M., K.M., and N.C.-B. performed DA and SI. J.S.-F. performed x-ray and EUV flux modeling and calculations, DAQ, and SI. E.N. performed telluric absorption line modeling and correction. M.Z. performed DA, instrument design (ID), and official instrument pipeline design (PD). F.F.B. performed DA and PD. A.R. performed DA, ID, PD, and SI. I.R. performed ID, DAQ, and SI. A.Q. performed ID and SI. J.A.C. performed ID and DAQ. G.C. performed planet scale height calculations, DAQ, and SI. J.H.M.M.S., P.J.A., S.D., T.H., M.L., K.M., P.C.S., and M.R.Z.O. performed SI. **Competing interests:** The authors have no competing interests to declare. **Data and materials availability:** The CARMENES data are available at Centro de Astrobiología (INTA-CSIC) in the Calar Alto (CAHA) archive at http://caha.sdc.cab.inta-csic.es/calto/jsp/searchform.jsp using the following identifiers and observation dates: WASP-69: 22-23.Aug.2017 (CAHA_IDs 261990 to 262072), 22.Sep.2017 (CAHA_IDs 263371 to 263467). KELT-9b: 06-07.August.2017 (CAHA_IDs 259314 to 259424). HD209458: 16-17.Sep.2016 (CAHA_IDs 249262 to 249415) and 08.11.2016 (CAHA_IDs 251027 to 251198). The CARMENES data for GJ 436 are not yet available in the CAHA archive, so their echelle order 56, containing the He I line, is provided at http://carmenes.cab.inta-csic.es/gto/jsp/nortmannetal2018.jsp. The XMM-Newton data are archived at http://nxsa.esac.esa.int/nxsa-web/#home with the observation IDs listed in the supplementary materials. Software scripts written for the manuscript are provided in data S1.

SUPPLEMENTARY MATERIALS

www.sciencemag.org/content/362/6421/1388/suppl/DC1
Materials and Methods
Figs. S1 to S10
Tables S1 to S4
References (*33*–*74*)
Data S1

14 March 2018; accepted 16 November 2018
Published online 6 December 2018
10.1126/science.aat5348

PLASMA ASTROPHYSICS

Electron-scale dynamics of the diffusion region during symmetric magnetic reconnection in space

R. B. Torbert[1,2]*, J. L. Burch[2], T. D. Phan[3], M. Hesse[2,4], M. R. Argall[1], J. Shuster[5], R. E. Ergun[6], L. Alm[7], R. Nakamura[8], K. J. Genestreti[8], D. J. Gershman[5], W. R. Paterson[5], D. L. Turner[9], I. Cohen[10], B. L. Giles[5], C. J. Pollock[5], S. Wang[11], L.-J. Chen[5,11], J. E. Stawarz[12], J. P. Eastwood[12], K. J. Hwang[2], C. Farrugia[1], I. Dors[1], H. Vaith[1], C. Mouikis[1], A. Ardakani[1], B. H. Mauk[10], S. A. Fuselier[2,13], C. T. Russell[14], R. J. Strangeway[14], T. E. Moore[5], J. F. Drake[11], M. A. Shay[15], Yuri V. Khotyaintsev[7], P.-A. Lindqvist[16], W. Baumjohann[8], F. D. Wilder[6], N. Ahmadi[6], J. C. Dorelli[5], L. A. Avanov[5], M. Oka[3], D. N. Baker[6], J. F. Fennell[9], J. B. Blake[9], A. N. Jaynes[17], O. Le Contel[18], S. M. Petrinec[19], B. Lavraud[20], Y. Saito[21]

Magnetic reconnection is an energy conversion process that occurs in many astrophysical contexts including Earth's magnetosphere, where the process can be investigated in situ by spacecraft. On 11 July 2017, the four Magnetospheric Multiscale spacecraft encountered a reconnection site in Earth's magnetotail, where reconnection involves symmetric inflow conditions. The electron-scale plasma measurements revealed (i) super-Alfvénic electron jets reaching 15,000 kilometers per second; (ii) electron meandering motion and acceleration by the electric field, producing multiple crescent-shaped structures in the velocity distributions; and (iii) the spatial dimensions of the electron diffusion region with an aspect ratio of 0.1 to 0.2, consistent with fast reconnection. The well-structured multiple layers of electron populations indicate that the dominant electron dynamics are mostly laminar, despite the presence of turbulence near the reconnection site.

Magnetic reconnection, a large-scale plasma process that converts electromagnetic energy to particle energy, is the dominant mechanism by which solar wind energy enters Earth's magnetosphere. This energy is subsequently dissipated by geomagnetic substorms and aurorae (*1*, *2*). Although the consequences of reconnection are large-scale, the process starts at the small ion scale, and even smaller, the electron-scale diffusion region (EDR). Studying the physical processes that cause magnetic reconnection requires determining structures and dynamics inside the EDR with sufficiently high-resolution plasma and field measurements (*3*), beyond the capabilities of previous spacecraft missions that have encountered the EDR (*4*–*6*).

The Magnetospheric Multiscale (MMS) mission focuses on investigating two reconnection regions known to exist around Earth: the dayside magnetopause and the nightside magnetotail, which host very different plasma parameter regimes. During its first phase (2015–2016), the four MMS spacecraft investigated reconnection in the dayside magnetopause (*3*), where the inflow conditions are highly asymmetric, with different plasma and magnetic pressures in the two inflow regions. In dayside reconnection, magnetic energy conversion processes occur in two separated regions: the X-line, where the magnetic field reverses, and the electron flow stagnation point (*7*, *8*). In its second phase (2017), MMS explored the kinetic processes of reconnection in Earth's magnetotail where the inflow conditions are nearly symmetric, the available magnetic energy per particle is more than an order of magnitude higher than on the dayside, and the X-line and stagnation point are coincident (*9*). The amount of magnetic energy per particle in the magnetotail is comparable to that of the solar corona, where magnetic reconnection also occurs.

On 11 July 2017 at ~22:34 Universal Time (UT), MMS encountered an EDR when it detected tailward-directed ion and electron jets (negative ion and electron bulk velocities, V_{iL} and V_{eL}; Fig. 1, F and G) followed by earthward-directed jets, spanning a reversal of essentially the north-south component of the magnetotail magnetic field B_N (Fig. 1D) in an intense current sheet (large out-of-plane electron velocity V_{eM}). We adopt an *LMN* coordinate system to orient the data to the usual 2D view of the magnetic field near a reconnection X-line (Fig. 1J), with *L* in the outflow direction, *M* along the X-line, and *N* normal to the current sheet (*10*). The out-of-plane guide field ratio, B_M/B_L, for this event is estimated to be small (<10%) (*10*). The spacecraft were in the magnetotail at a radial distance from Earth of 22 Earth radii.

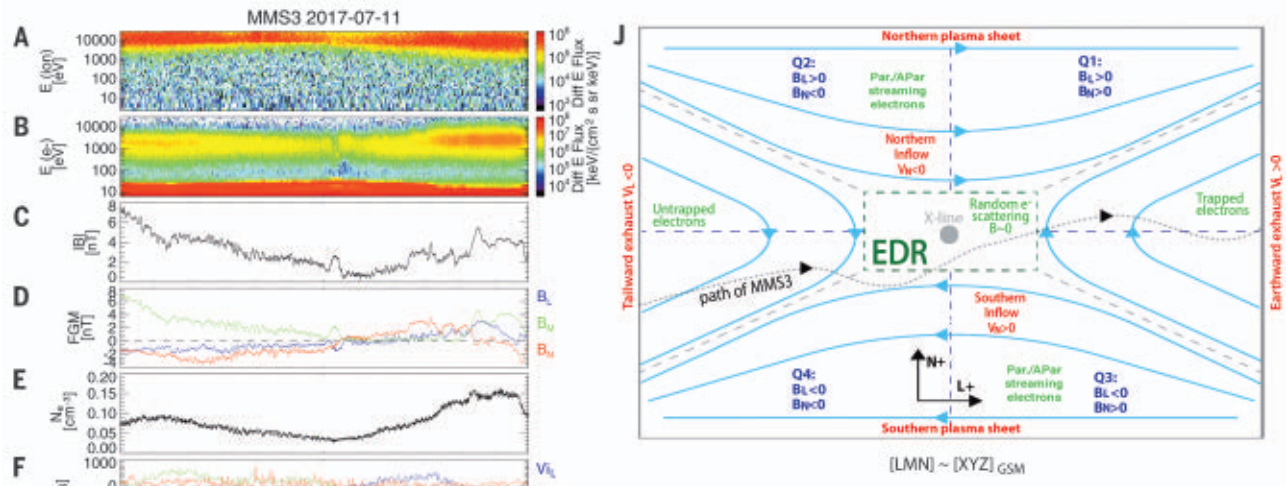

Fig. 1. MMS3 summary data near the crossing of the EDR at 22:34:03 on 11 July 2017. (**A** and **B**) Energy-time spectrograms of ion and electron energy flux, respectively. (**C**) Magnetic field magnitude. (**D**) Components in the *LMN* coordinate system, which is very close to the usual Geocentric Solar Magnetospheric (GSM) system (*10*). (**E**) Electron density. (**F**) Ion bulk velocity vector. (**G**) Electron bulk velocity vector. (**H**) The *L* component of ion and electron flow perpendicular to **B**, and of $\mathbf{E} \times \mathbf{B}/B^2$. (**I**) Electric field. (**J**) Illustration of a typical symmetric EDR in the *LMN* coordinate system, and the expected properties in various quadrants (Q1 to Q4), together with the inferred relative path of the MMS satellites as the X-line retreated tailward.

Four-spacecraft timing of the flow and field reversals indicate that the structure moved away from Earth with velocity V_L ~ −170 km/s. These are signatures of a tailward retreat of the reconnection X-line past the spacecraft, as indicated by the MMS path in Fig. 1J (*5*, *6*, *11*–*16*). Except for a brief excursion to the edge of the inflow region, seen in a small perturbation in magnetic field components beginning at 22:34:00 UT (due to a flapping of the current sheet), the spacecraft stayed close to the neutral sheet (B_L = 0 plane), indicated by small values of $|B_L|$ (~0 to 2 nT), during the flow and field reversal. These observations are consistent with crossing both ion and electron diffusion regions—an identification that is supported by the profiles of the ion and electron flows: V_{eM} peaked at ~ −15,000 km/s, within an order of magnitude of the electron Alfvén speed $B/\sqrt{2\mu_0 m_e n_e}$ (where m_e and n_e are electron mass and density), approximately 20,000 to 25,000 km/s. Starting from the X-line (at the $\mathbf{V}_{eL}$ and $\mathbf{B}$ reversal location) and going left and right in Fig. 1H, the electron perpendicular outflow speed $|V_{e\perp L}|$ increased and greatly exceeded the ion speed. While the ion outflow speed ($|V_{iL}|$; Fig. 1F) increased with increasing distance from the X-line, $|V_{e\perp L}|$ reached a peak (~7000 km/s) before slowing and approaching the ion flow speed at ~22:33:50 before, and ~22:34:20 after, the X-line. Thus, the ends of the ion diffusion region, where the ion and electron outflow velocities are expected to match, are likely encountered near these times. The end of the electron diffusion region, on the other hand, marked by the departure of $V_{e\perp}$ from $\mathbf{E} \times \mathbf{B}/B^2$, was confined to a much smaller interval around the X-line, where the electron density reached a symmetric minimum of 0.03 cm^{-3} (electron inertial length d_e ~ 30 km).

Figure 2, A to J, and Fig. 3, A to E, display data from one of the spacecraft, MMS3, in and around the EDR, again in *LMN* coordinates. Figure 2, K to N, shows reduced electron distribution functions (DFs) during the strong reconnecting current (J_M) at times before and during the peak of the quantity $\mathbf{J} \cdot \mathbf{E}'$ (where $\mathbf{E}' = \mathbf{E} + \mathbf{V}_e \times \mathbf{B}$), which is the electromagnetic energy conversion rate in the plasma frame, a signature of the EDR (*15*). Although $\mathbf{J} \cdot \mathbf{E}'$ is mostly positive throughout the period shown in Fig. 2, there are some regions with negative values, indicating that the electrons are transferring energy to the electromagnetic field, as seen also in simulations (*17*–*19*). Figure 3C shows that at all spacecraft, the signs of E_N and B_L were opposite, consistent with E_N converging toward the neutral sheet (B_L = 0) from both hemispheres, as expected for symmetric reconnection with a minimal guide field (*13*, *15*, *20*, *21*). MMS2 and MMS4 remained below the neutral sheet (B_L < 0 and E_N > 0) in the vicinity of the EDR crossing, whereas MMS1 and MMS3, located at higher *N*, made excursions above the sheet, where B_L > 0 and E_N < 0. This E_N field accelerates the neutral sheet electrons toward the inflow region, where they are accelerated along meandering trajectories (*22*) by the reconnection field,

[1]University of New Hampshire, Durham, NH, USA. [2]Southwest Research Institute (SwRI), San Antonio, TX, USA. [3]University of California, Berkeley, CA, USA. [4]University of Bergen, Bergen, Norway. [5]NASA Goddard Space Flight Center, Greenbelt, MD, USA. [6]University of Colorado Laboratory for Atmospheric and Space Physics, Boulder, CO, USA. [7]Swedish Institute of Space Physics, Uppsala, Sweden. [8]Space Research Institute, Austrian Academy of Sciences, Graz, Austria. [9]Aerospace Corporation, El Segundo, CA, USA. [10]Johns Hopkins University Applied Physics Laboratory, Laurel, MD, USA. [11]University of Maryland, College Park, MD, USA. [12]Blackett Laboratory, Imperial College London, London, UK. [13]University of Texas, San Antonio, TX, USA. [14]University of California, Los Angeles, CA, USA. [15]University of Delaware, Newark, DE, USA. [16]Royal Institute of Technology, Stockholm, Sweden. [17]University of Iowa, Iowa City, IA, USA. [18]Laboratoire de Physique des Plasmas, CNRS/Ecole Polytechnique/Sorbonne Université/Univ. Paris Sud/Observatoire de Paris, Paris, France. [19]Lockheed Martin Advanced Technology Center, Palo Alto, CA, USA. [20]Institut de Recherche en Astrophysique et Planétologie, CNRS, Centre National d'Etudes Spatiales, Université de Toulouse, Toulouse, France. [21]Institute for Space and Astronautical Sciences, Sagamihara, Japan.
***Corresponding author. Email: roy.torbert@unh.edu**

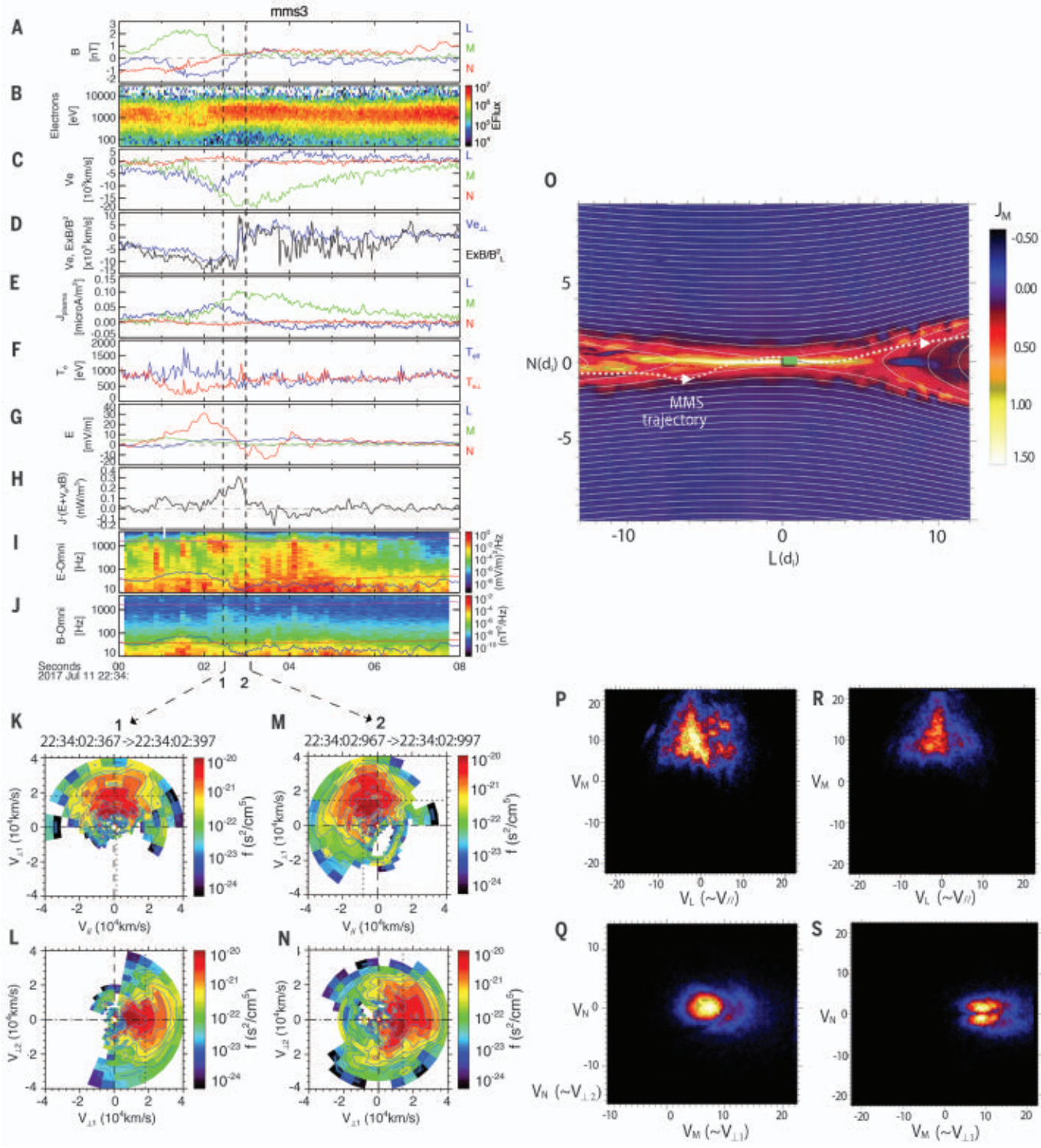

Fig. 2. MMS3 plasma and field data for the interval 22:34:00 to 22:34:08 on 11 July 2017. (**A**) Magnetic field components in *LMN* coordinate system. (**B**) Electron omnidirectional spectrogram, with minimum energy set at 50 eV to avoid the lower-energy spacecraft photoelectrons seen in Fig. 1B. (**C**) Electron bulk velocity. (**D**) *L* components of $\mathbf{V}_{e\perp}$ and $\mathbf{E} \times \mathbf{B}/B^2$. (**E**) Current from plasma measurements. (**F**) $T_{e||}$ and $T_{e\perp}$. (**G**) Electric field. (**H**) $\mathbf{J} \cdot \mathbf{E}'$. (**I** and **J**) Electric and magnetic omnidirectional frequency spectrograms, respectively, showing the power spectral density of electric and magnetic field fluctuations. (**K** to **N**) Electron velocity distribution functions at the times indicated. $V_{\perp 1}$ is (**b** × **v**) × **b**, where **b** and **v** are unit vectors of **B** and $\mathbf{V}_e$; $V_{\perp 2}$ = **v** × **b**; and $V_{||}$ is the parallel electron velocity. $V_{\perp 1}$ is essentially the **E** × **B** direction, and the bulk flow component in that direction is indicated by the dashed vertical lines. (**O**) Magnetic configuration of a computer simulation (*10*, *31*), with color-coded reconnection current (J_M) and the inferred MMS trajectory overlain. (**P** to **S**) Reduced distribution f_e near the green box in (O) from that simulation, with velocity axes (in ion Alfvén speed units) corresponding to those of the data in (K) to (N). The color code is the same as in (O), but with simulation units representing phase-space density, like those of (K) to (N).

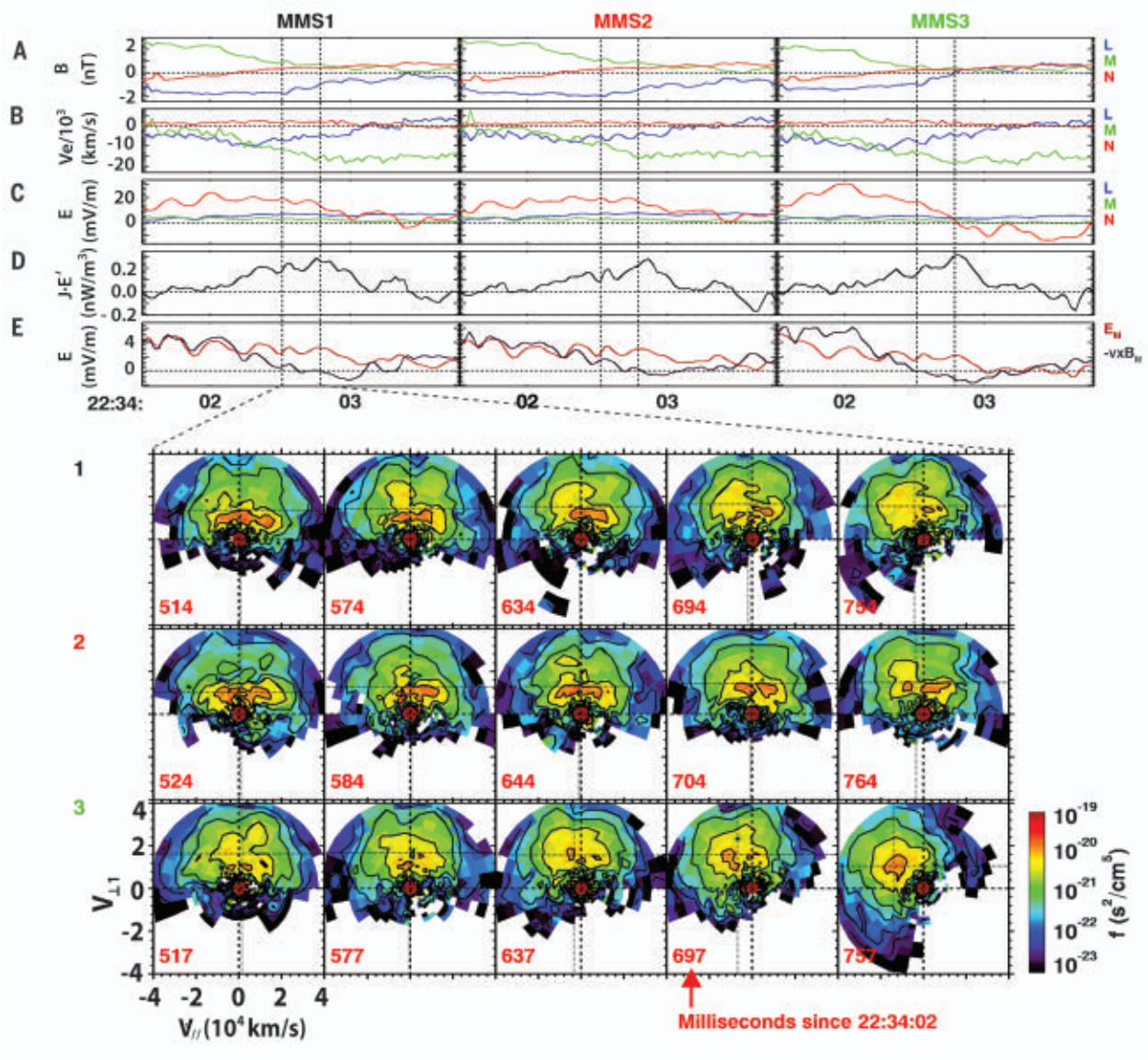

Fig. 3. Field data and electron DFs for three MMS spacecraft on 11 July 2017 for ~2 s around the EDR. Upper panels, for each spacecraft: (**A**) Components of **B**. (**B**) Electron bulk velocity. (**C**) **E**, where the reversal in E_N is seen on MMS3 and briefly MMS1, but not MMS2. (**D**) **J**·**E**′. (**E**) *M* component of **E** and −(**V**$_e$ × **B**). Lower panels from 2.604 s to 2.784 s are the reduced (summed over $V_{\perp 2}$) electron 30-ms DFs in ($V_{||}$, $V_{\perp 1}$) for each spacecraft at the times between the dotted lines in the upper panels.

E_M ~ 1 to 2 mV/m (Fig. 3, C and E) (*10*). The electrons were eventually turned toward the *L*, or exhaust, direction by B_N as they exited the EDR, forming the electron jet seen in Figs. 2C and 3B on either side of the X-line.

The electron temperature profile in Fig. 2F shows strong anisotropy from 22:34:01.0 to 22:34:02.8 due to magnetic field–aligned electrons in the inflow region (*4*). During the EDR crossing, there was only a small rise (a few hundred eV) in parallel or perpendicular temperature (the parallel or perpendicular pressure divided by n_e), unlike the case of asymmetric reconnection (*3*), implying that a substantial fraction of the energy conversion went into the strong electron flows in the *M* and *L* directions.

The aspect ratio of the EDR is an approximate measure of the reconnection rate that has not been determined experimentally but has been studied theoretically and with simulations (*4*, *20*, *23*). Four-spacecraft timing analysis of the B_N reversal near 22:34:02.2 (see Fig. 2A) indicates that the X-line structure was moving tailward (V_{XL}, *L* component of the X-line velocity, ~ −170 km/s). The EDR length can be estimated by multiplying V_{XL} by the 1/e width of V_{eM} (~3 s; Fig. 2C), or by the $|V_{eL}|$ peak-to-peak time (~2 s; Fig. 2D), yielding a full length of 350 to 500 km (12 to 17 d_e). MMS also made a brief excursion into the EDR inflow region (beginning at ~22:34:01.0), indicated by the increase in $|B_L|$ and confirmed by the cooler electrons (Fig. 2B). By 22:34:02.2, the change in B_L and the timing analysis (V_{XN} ~ −70 km/s) show the structure moving southward, giving MMS also a normal motion into the EDR, reaching the neutral sheet and the peak of the cross-tail current by 22:34:03.0. Using Ampere's law (*10*), dividing the change in B_L during this normal motion into the EDR (Fig. 2A, ~22:34:02.0 to 22:34:03.0) by the average of J_M, yields a simple estimate of the normal half-width of 30 km, ~1 d_e (*10*). Thus, the aspect ratio is ~0.1 to 0.2, implying a reconnection rate consistent with fast reconnection (*24*).

Multiple crescent- and triangular-shaped features in the DFs (Fig. 2, K to N, and lower panels of Fig. 3) are the result of electron meandering motion in the electromagnetic field structure of the EDR. Figure 2L shows a DF taken at a location below (in *N*) the EDR, which features multiple crescents, seen as enhanced phase-space density at increasing velocities, similar to predictions (*25*–*27*) and shown in Fig. 2Q from the simulation of Fig. 2O (*10*). Contrary to magnetopause observations and models (*3*, *28*), we find more than one crescent. The observations show that crescents at higher $V_{\perp 1}$ are broader in $V_{\perp 2}$ than models predict; that is, particles with a larger range of $V_{\perp 2}$ bounce more than predicted by the model by a factor of 2. A likely explanation is that the current sheet electron distribution is more energetic than in the model, but the distributions may be sensitive to even a very small guide field (*29*). Models show that these crescents are generated by the interaction of bouncing electrons with both the normal (E_N) and the reconnection electric field (E_M), and their existence is consistent with canonical momentum conservation. The observation of multiple crescents indicates that the rather complex electron orbits are relatively unperturbed by high-frequency fluctuations in the electromagnetic fields. This implies that turbulent effects, which would scatter electrons and hence eliminate distinct phase-space features such as crescents, do not dominate the particle dynamics in the EDR.

Figure 2, M and N, displays a second DF, taken near the X point, which features a pronounced triangular shape in the plane containing *B*, broader at higher energies. Figure 2N shows two enhancements at lower $V_{\perp 1}$ (seen at $\pm V_{\perp 2}$, which is within ~20° of V_N) corresponding to inflowing populations from both above and below the X-line. These enhancements are similar to those that appear in the simulation shown in Fig. 2, O to S. In Fig. 2M, the triangular shape narrows in width as the energy increases, which also appears in the simulation (Fig. 2R). Bouncing electrons account for this feature: For each bounce, electrons gain successively more energy from acceleration by the reconnection electric field. If electrons have a finite V_L, they eventually interact with the magnetic field in the outflow and are ejected from the immediate vicinity of the X-line. The acceleration by the reconnection electric field and this ejection explain the triangular shape of the distribution: Only electrons with very small V_L remain near the X-line long enough to execute multiple bounces and be accelerated to higher energies.

The electron DFs of Fig. 3 (lower panels) show the evolution of the above features as MMS entered the EDR. From signatures of the inflow region (*4*), with DFs elongated along *B* (MMS1 and MMS2, first column, at 22:34:02.514), the spacecraft, with MMS3 leading, penetrated farther into the current layer and saw accelerated and gyrating electrons growing in energy as time (and *N* position) increased, showing a perpendicular crescent with energy >1 keV (2×10^4 km/s). By 22:34:02.724, all spacecraft were showing the perpendicular crescents, enhanced flow along the $\mathbf{E} \times \mathbf{B}$ direction, and also beaming features in the parallel directions. The parallel beams may be responsible for the high-frequency electrostatic noise near the upper hybrid frequency (~1200 Hz), seen at this time in Fig. 2I (*30*). When the spacecraft were fully within the reconnecting current layer (Fig. 2B, 22:34:02.694 to 22:34:02.757), there were higher-energy features rotating into both the $V_{\perp 1}$ (~*M*) and $V_{||}$ directions along with persistent counterstreaming, low-energy (~10,000 km/s) field-aligned beams. By 22:34:02.757, MMS3, which was deepest in the EDR, saw very energetic electrons in $V_{\perp 1}$ and also in the $-V_{||}$ direction; that is, these accelerated electrons were rapidly leaving the EDR region. The evolution of many such features can be seen in movie S1.

MMS observations of the magnetotail reconnection electron diffusion region show that it differs from that on the dayside because it involves symmetric inflow. The aspect ratio of the diffusion region (0.1 to 0.2), determined by MMS, is consistent with simulations of fast reconnection (*7*, *15*, *17*, *24*). MMS observations of electron dynamics in the diffusion region match predictions made by one class of theories and models: nearly laminar ones that assume that the effects of turbulence and associated fluctuations on the electron dynamics are small. Unlike the magnetopause results (*3*), we find that electrons can be accelerated up to three successive times by the reconnection electric field, possibly as a consequence of longer confinement in the symmetric magnetic structure. Taken together with MMS observations at the magnetopause, these results provide confirmation that reconnection is an efficient mechanism for the release of magnetic energy, for both geomagnetic substorms and auroral phenomena, and also discriminate between competing theories of reconnection. The energy width of the electron crescents differs from model predictions.

REFERENCES AND NOTES

1. T. Nagai *et al*., *J. Geophys. Res.* **103**, 4419–4440 (1998).
2. V. Angelopoulos *et al*., *Science* **321**, 931–935 (2008).
3. J. L. Burch *et al*., *Science* **352**, aaf2939 (2016).
4. L. J. Chen *et al*., *J. Geophys. Res.* **113**, 1–19 (2008).
5. T. I. Nagai *et al*., *J. Geophys. Res.* **116**, A04222 (2011).
6. M. Oka, T.-D. Phan, M. Øieroset, V. Angelopoulos, *J. Geophys. Res.* **21**, 1955–1968 (2016).
7. J. L. Burch, T. D. Phan, *Geophys. Res. Lett.* **43**, 8327–8338 (2016).
8. K. J. Genestreti *et al*., *J. Geophys. Res.* **122**, 11342–11353 (2017).
9. P. A. Cassak, M. A. Shay, *Phys. Plasmas* **14**, 102114 (2007).
10. See supplementary materials.
11. M. Øieroset, T. D. Phan, M. Fujimoto, R. P. Lin, R. P. Lepping, *Nature* **412**, 414–417 (2001).
12. A. Runov *et al*., *Geophys. Res. Lett.* **30**, 1579 (2003).
13. A. L. Borg *et al*., *Geophys. Res. Lett.* **32**, 32–35 (2005).
14. V. Angelopoulos *et al*., *Science* **321**, 931–935 (2008).
15. J. P. Eastwood, T. D. Phan, M. Øieroset, M. A. Shay, *J. Geophys. Res.* **115**, A08215 (2010).
16. D. N. Baker *et al*., *Geophys. Res. Lett.* **29**, 2190 (2002).
17. S. Zenitani, M. Hesse, A. Klimas, M. Kuznetsova, *Phys. Rev. Lett.* **106**, 195003 (2011).
18. M. A. Shay *et al*., *Geophys. Res. Lett.* **43**, 4145–4154 (2016).
19. P. A. Cassak *et al*., *J. Geophys. Res.* **122**, 11523–11542 (2017).
20. M. A. Shay, J. F. Drake, R. E. Denton, D. Biskamp, *J. Geophys. Res.* **103**, 9165–9176 (1998).
21. J. R. Wygant *et al*., *J. Geophys. Res.* **110**, A09206 (2005).
22. R. Horiuchi, T. Sato, *Phys. Plasmas* **1**, 3587–3597 (1994).
23. P. A. Sweet, in *Electromagnetic Phenomena in Cosmical Physics*, B. Lehnert, Ed. (Cambridge Univ. Press, 1958), pp. 123–134.
24. H. E. Petschek, *NASA Spec. Publ.* **50**, 425 (1964).
25. J. Ng, J. Egedal, A. Le, W. Daughton, L.-J. Chen, *Phys. Rev. Lett.* **106**, 065002 (2011).
26. N. Bessho, L.-J. Chen, J. R. Shuster, S. Wang, *Geophys. Res. Lett.* **41**, 8688–8695 (2014).
27. J. R. Shuster *et al*., *Geophys. Res. Lett.* **42**, 2586–2593 (2015).
28. M. Hesse, N. Aunai, D. Sibeck, J. Birn, *Geophys. Res. Lett.* **41**, 8673–8680 (2014).
29. J. Ng, J. Egedal, A. Le, W. Daughton, *Phys. Plasmas* **19**, 112108 (2012).
30. W. M. Farrell, M. D. Desch, K. W. Ogilvie, M. L. Kaiser, K. Goetz, *Geophys. Res. Lett.* **30**, 2259 (2003).
31. M. Hesse *et al*., *Phys. Plasmas* **25**, 032901 (2018).

ACKNOWLEDGMENTS

The dedicated efforts of the entire MMS team are greatly appreciated. We are especially grateful to the leadership of the GSFC project manager, the late Craig Tooley; the deputy project manager, B. Robertson, and the SwRI payload project manager, R. Black. **Funding:** Supported by NASA prime contract NNG04EB99C at SwRI; STFC(UK) grant ST/N000692/1; CNES, CNRS-INSIS, and CNRS-INSU in France; the Austrian Research Promotion Agency FFG; NASA grant NNX14AC78G at the University of Maryland; NASA grant NNX08A083G-MMS IDS at the University of California and the University of Delaware; and the Swedish National Space Board. **Author contributions:** Analysis and writing, R.B.T., J.L.B., T.D.P., M.H., and M.R.A.; analysis, J.S., R.E.E., L.A., R.N., K.J.G., D.L.T., S.W., L.-J.C., J.E.S., J.P.E., K.J.H., C.F., I.D., C.M., A.A., C.T.R., R.J.S., T.E.M., J.F.D., M.A.S., Y.V.K., M.O., A.N.J., and S.M.P.; electric field data, R.B.T., R.E.E., H.V., P.-A.L., Y.V.K., F.D.W., and N.A.; plasma data, D.J.G., W.R.P., B.L.G., C.J.P., L.-J.C., S.A.F., J.C.D., L.A.A., B.L., and Y.S.; magnetic field data, C.T.R., R.J.S., W.B., O.L.C., H.V., and R.B.T.; energetic particle data, D.L.T., I.C., B.H.M., D.N.B., J.F.F., J.B.B., and A.N.J. **Competing interests:** The authors declare that there are no competing interests. **Data and materials availability:** The MMS data are archived at https://lasp.colorado.edu/mms/sdc/public/. We used data from the period 22:29 to 22:37 UT on 11 July 2017, modified as described in (*10*).

SUPPLEMENTARY MATERIALS

www.sciencemag.org/content/362/6421/1391/suppl/DC1
Materials and Methods
Supplementary Text
Figs. S1 to S4
Movie S1
Reference (*32*)

12 February 2018; accepted 6 November 2018
Published online 15 November 2018
10.1126/science.aat2998

QUASICRYSTALS

Single-component quasicrystalline nanocrystal superlattices through flexible polygon tiling rule

Yasutaka Nagaoka[1], Hua Zhu[1], Dennis Eggert[2,3], Ou Chen[1]*

Quasicrystalline superlattices (QC-SLs) generated from single-component colloidal building blocks have been predicted by computer simulations but are challenging to reproduce experimentally. We discovered that 10-fold QC-SLs could self-organize from truncated tetrahedral quantum dots with anisotropic patchiness. Transmission electron microscopy and tomography measurements allow structural reconstruction of the QC-SL from the nanoscale packing to the atomic-scale orientation alignments. The unique QC order leads to a tiling concept, the "flexible polygon tiling rule," that replicates the experimental observations. The keys for the single-component QC-SL formation were identified to be the anisotropic shape and patchiness of the building blocks and the assembly microscopic environment. Our discovery may spur the creation of various superstructures using anisotropic objects through an enthalpy-driven route.

A quasicrystalline (QC) order possesses a striking rotational symmetricity, yet it has no transitional periodicity (*1*, *2*). The first experimental discovery of a QC structure was made by Shechtman *et al*., who observed a selected-area electron diffraction pattern of Al-Mn alloys with a 10-fold rotational symmetry, which was strictly forbidden for periodic crystals (*1*). Soon after, scientists discovered 8-, 10-, and 12-fold two-dimensional (2D) polygonal QC structures and 3D icosahedral quasicrystals in a variety of intermetallic alloys (*3*). Subsequently, these findings led to studies that spread over a wide spectrum of research fields, including chemistry, materials science, mathematics, and even the arts (*3*–*6*).

Superstructures created by self-assembling objects at different length scales have attracted a great deal of scientific attention (*7*–*11*). Seminal discoveries of these fascinating structures have been presented using molecular and nanoscale building objects (*12*–*17*). However, examples of QC structures and their approximant orders created through bottom-up assemblies are still rare because of their metastability and high structural complexity. Wasio *et al.* reported a supramolecular assembly of a ferrocene derivative with a 10-fold QC order (*7*). Designed polymers have proved to be capable of self-organizing into 12-fold QC orders (*18*, *19*). Talapin *et al.* pioneered the work of assembling inorganic colloidal nanocrystals (NCs) into 12-fold QC superlattices (SLs) using two different kinds of NCs with well-controlled size ratios (*8*). In the similar binary NC systems, Murray and co-workers proposed new partial matching rules for generating QC-SLs with structural consistency over a large area (*10*). We reported 2D QC-approximant SLs and 3D cluster-based supercrystals assembled from truncated tetrahedral quantum dots (TTQDs) (*9*). In addition to the experimental efforts, computer simulations have had a role in theorizing QC order formations (*10*, *20*–*22*). Molecular dynamics computer simulations found a strong tendency of QC order formations from single-component colloids (*20*–*22*). Glotzer and colleagues showed that roughly spherical solids could be assembled into structures as complex as a 3D icosahedral quasicrystal (*20*, *21*). Despite these advances, QC structures from single-component NC building blocks were not explored experimentally, leaving NC assemblies behind atomic crystals and computer simulations.

Here, we report the formation of large-area, 10-fold QC-SLs assembled from single-component TTQDs. Transmission electron microscopy (TEM) and tomography reconstruction allowed us to make direct observations of the QC structures, from the NC packing to the atomic orientations of the individual particles in real space. In conjunction with small-angle electron diffraction (SA-ED) and fast Fourier transform (FFT) analysis in reciprocal space, we found that the SL possessed a unique type of QC order. This discovery led us to propose a tiling concept that we call the "flexible polygon tiling rule." Mechanistic studies demonstrated that the anisotropic surface tethers induced enthalpic patchiness of the TTQDs, which, combined with molecular microscopic environments at the assembly site, were responsible for the 10-fold QC-SL formation. Our discovery shows the possibility of creating superstructural materials, otherwise inaccessible through isotropic counterparts, from anisotropic building blocks even without the guidance of a unit cell.

We synthesized wurtzite (WZ) TTQDs with a truncated tetrahedron shape, in which the three $\{10\bar{1}1\}_{WZ}$ major facets were coated with oleic acid and one $\{0002\}_{WZ}$ facet was passivated by octadecylphosphonic acid (ODPA) (Fig. 1A and figs. S1 and S2) (*23*). The inorganic height of the TTQD was 6.7 ± 0.4 nm along the $[0002]_{WZ}$ crystal direction. We assembled the TTQDs by a liquid/air interface method (*24*), in which we slowly evaporated (~6 hours) a cyclohexane solution that contained TTQDs (5.0 mg/ml) on the surface of an ethylene glycol (EG) liquid subphase (Fig. 1B). TEM measurements of the resulting thin films indicated continuous SLs with lateral dimensions up to ~50 μm (Fig. 1B and figs. S3 and S4), but we did not identify translational periodicity (Fig. 1C). The SA-ED measurements we conducted were consistent with the real-space observations (Fig. 1C and figs. S3 to S5) as they displayed a diffraction spot pattern with a 10-fold rotational symmetry, suggesting a QC order. Detailed analysis of the ED pattern indicated that the major ED signals were located at 10-basis vectors of $[\cos(2\pi n/10), \sin(2\pi n/10)]$ (Fig. 1C, pink, and fig. S5) with an expanded pentagon at a "golden ratio" of $(1+\sqrt{5})/2 = 1.62$ (fig. S5 and table S1). We observed two sets of weak satellite peaks at 10-basis (Fig. 1C, orange) and 20-basis (Fig. 1C, blue) vectors of $[\cos(2\pi n/10 + 2\pi/20), \sin(2\pi n/10 + 2\pi/20)]$ and $[\cos(2\pi n/20 + 2\pi/40), \sin(2\pi n/20 + 2\pi/40)]$, respectively (fig. S5 and table S1). This 10-fold symmetrical diffraction pattern with the presence of higher-order electron reflections of the SL confirmed the QC order with a long-range structural consistency (Fig. 1C). Furthermore, the same QC superstructure was generated when using larger TTQD building blocks with an inorganic NC height of 8.5 ± 0.4 nm (figs. S6 and S7), proving the reliability of the formation of QC-SLs.

In-depth examinations showed that the QC-SLs we observed were patterned with decagon-derivative polygonal units (Fig. 1C). We used high-resolution TEM (HRTEM) to determine the atomic orientations of individual TTQDs in one polygonal unit. In addition to the 10 different atomic domains that we identified along the polygonal framework, there were two overlapping TTQD atomic orientations in the center (Fig. 1D, fig. S8, and table S2). The HRTEM results and particle orientation simulations allowed us to reconstruct the TTQD packing model in each polygonal unit (Fig. 1E and fig. S8). In the model, the polygonal framework was formed by ring tetrahelices with ramifications (*9*), and the center was stacked vertically by two TTQDs (figs. S9 and S10). We found that all the TTQDs in the model had the preferred facet-to-facet alignment (i.e., $\{0002\}_{WZ}$-to-$\{0002\}_{WZ}$ and $\{10\bar{1}1\}_{WZ}$-to-$\{10\bar{1}1\}_{WZ}$) (Fig. 1E and figs. S9 and S10). These results suggested that the formation of single-component 10-fold QC-SLs was induced by the anisotropic patchiness of the TTQDs (induced by the different surface molecular coatings and the intrinsic crystal dipole), where directional enthalpic forces were in play for the nucleation and growth of the QC-SLs (*9*).

[1]Department of Chemistry, Brown University, Providence, RI 02912, USA. [2]Max Planck Institute for the Structure and Dynamics of Matter, Hamburg 22761, Germany. [3]Heinrich Pette Institute–Leibniz Institute for Experimental Virology, Hamburg 20251, Germany.
*Corresponding author. Email: ouchen@brown.edu

To better identify the TTQD packing in three dimensions, we used electron tomography measurements and computational 3D reconstructions to resolve the geometrical positions of individual TTQDs inside the SL (movies S1 and S2). The left panels of Fig. 2, A to F, show six representative horizontal slices of the measured QC-SL at different vertical positions. Although the 10-fold rotational symmetry was retained across all of the reconstructed slices, a unique transition of the particle packing pattern was captured from the top to the bottom of the SL (fig. S11 and movies S1 and S2). The magnified reconstruction images (highlighted areas in the left panels of Fig. 2, A to F) show that the SL area contained six interconnected decagon-derivative units (the centers of each polygon units labeled by magenta color, Fig. 2G). In contrast to the appearance of the center particles in all slices, the surrounding polygonal framework pattern alternated from top to bottom as follows: 5-TTQD-pentagon in the top (first) slice (Fig. 2A), 10-TTQD-decagon in the second slice (Fig. 2B), and 5-TTQD-pentagon with a clockwise rotation of 36° with respect to the top pentagon (first slice) in the third slice (Fig. 2C). The same alternating pattern was repeated in the fourth to sixth slices (Fig. 2, D to F), indicating an identical second deck of the assembled structure along the vertical direction of the SLs (Fig. 2H). We further confirmed this double-decker structure by the vertical reconstruction (side view) of the QC-SLs (Fig. 2I and movie S3), which displayed a four-layer TTQD stacking (two layers in each deck). On the basis of the TEM and electron tomographic results, we constructed a 3D computer model of the six interconnected, decagon-derivative polygons to represent the unique architecture of the assembly (Fig. 2, G and H). Both the horizontal and vertical slices obtained from the computer model proved the model's correctness by matching the tomographic images perfectly (Fig. 2 and fig. S12).

The 10-fold QC order that we observed does not fall into any category of reported decagonal QC orders. Thus, to better understand the observed QC order, we introduced a "flexible polygon tiling rule" tiling method. Analogous to the "phason flip" mechanism (*25*), in which the whole system gains additional stability through local configuration changes at the interface (*25*), the flexible polygon tiling imparts local stability by having a flexible interface. In detail, the rule is constituted as follows: (i) Orientationally rigid regular polygons with an even number (n) of edges shall be packed densely in a 2D space; (ii) when packing, two neighboring polygons may overlap with one or two edges, but no more than two edges; (iii) when no edge or one edge is overlapping, the two polygons remain intact; (iv) when overlapping with two edges, the overlapped edges shall become flexible and transform into one straight edge (denoted as a "flexible edge"); (v) each polygon must have at least one flexible edge and at most $n/2$ flexible edges; and (vi) the generated tiling pattern has a QC order with n-fold rotational symmetry (Fig. 3, A and B, and fig. S13). Note that because edge sharing while maintaining orientational rigidity is impossible for the polygons with an odd number of edges, this tiling rule is limited to the even-number–edge polygons. We verified this rule by using octagons, decagons, dodecagons, and tetradecagons as building units. We successfully obtained 8-, 10-, 12-, and 14-fold QC orders, respectively, as confirmed by the corresponding FFT patterns (figs. S14 to S17).

To apply this proposed QC tiling rule, we first extracted the center of each polygon in a 10-fold QC-SL TEM image, and then quantified the nearest (Fig. 3C, yellow lines) and the second nearest (Fig. 3C, blue lines) inter–polygon center distances to be 16.6 ± 0.4 nm and 19.5 ± 0.5 nm, respectively (Fig. 3D). This distance ratio was matched by the geometry-determined ratio of $(\cos 2\pi/10)/(\cos 2\pi/20) = 0.8507$ for the decagonal center-to-center distances of one-edge (sharing one regular decagon edge) and two-edge (sharing one "flexible edge") overlapping scenarios (Fig. 3A and fig. S18). Consequently, the center of each polygon with m "flexible edges"

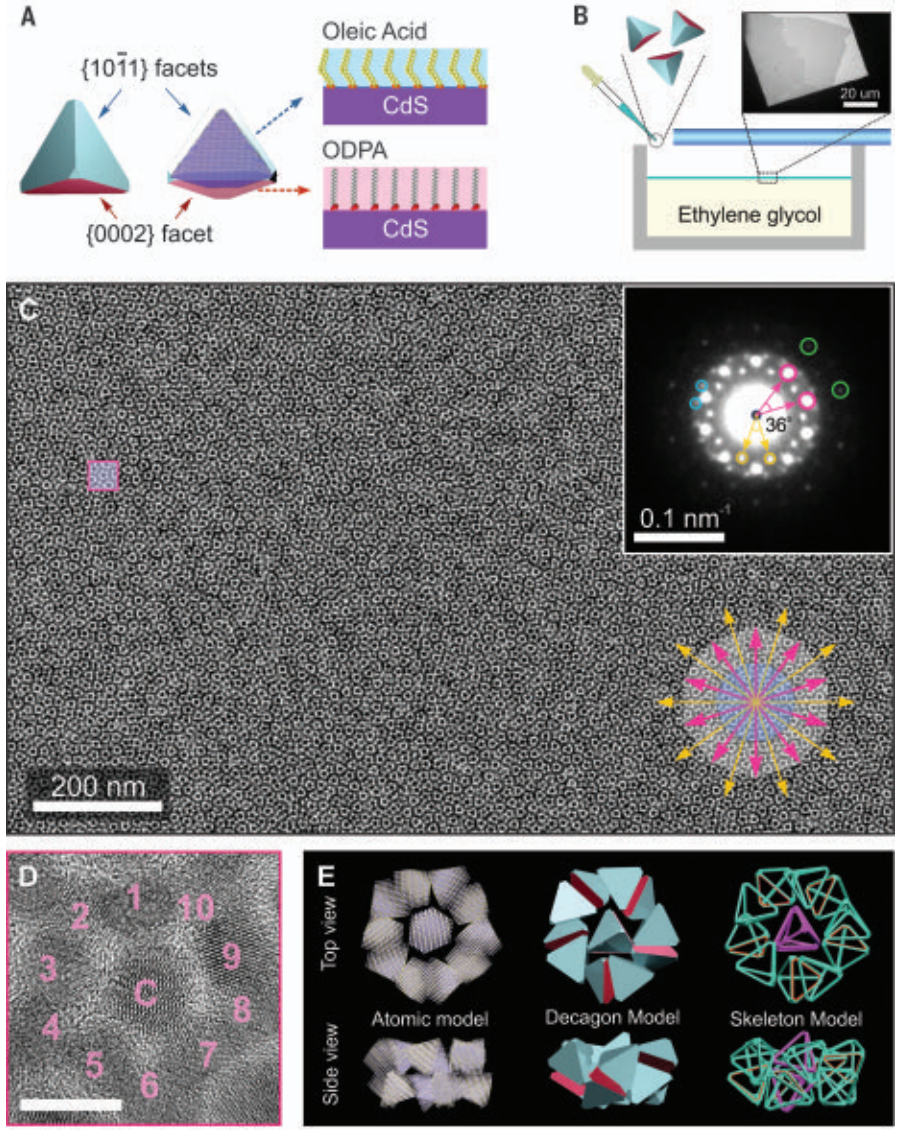

Fig. 1. 10-fold QC-SLs assembled from TTQDs. (**A**) Schematic illustration of an effective tetrahedral shape of a TTQD. The TTQD exhibits three major {10$\bar{1}$1} facets coated with oleic acid (blue) and one {0002} facet coated with ODPA (red). (**B**) Schematic illustration of the QC-SL formation at the liquid/air interface. (**C**) Representative TEM image of 10-fold QC-SLs and the corresponding SA-ED pattern (inset: pink, orange, and green cycles indicate 10-basis vectors; blue cycles indicate 20-basis vectors). (**D**) HRTEM image of a decagon-derivative unit [square highlighted in (C)] with 10 atomic domains on the framework and 2 in the center. Scale bar, 10 nm. (**E**) Computer-generated models (top and side views) of a decagon-derivative unit.

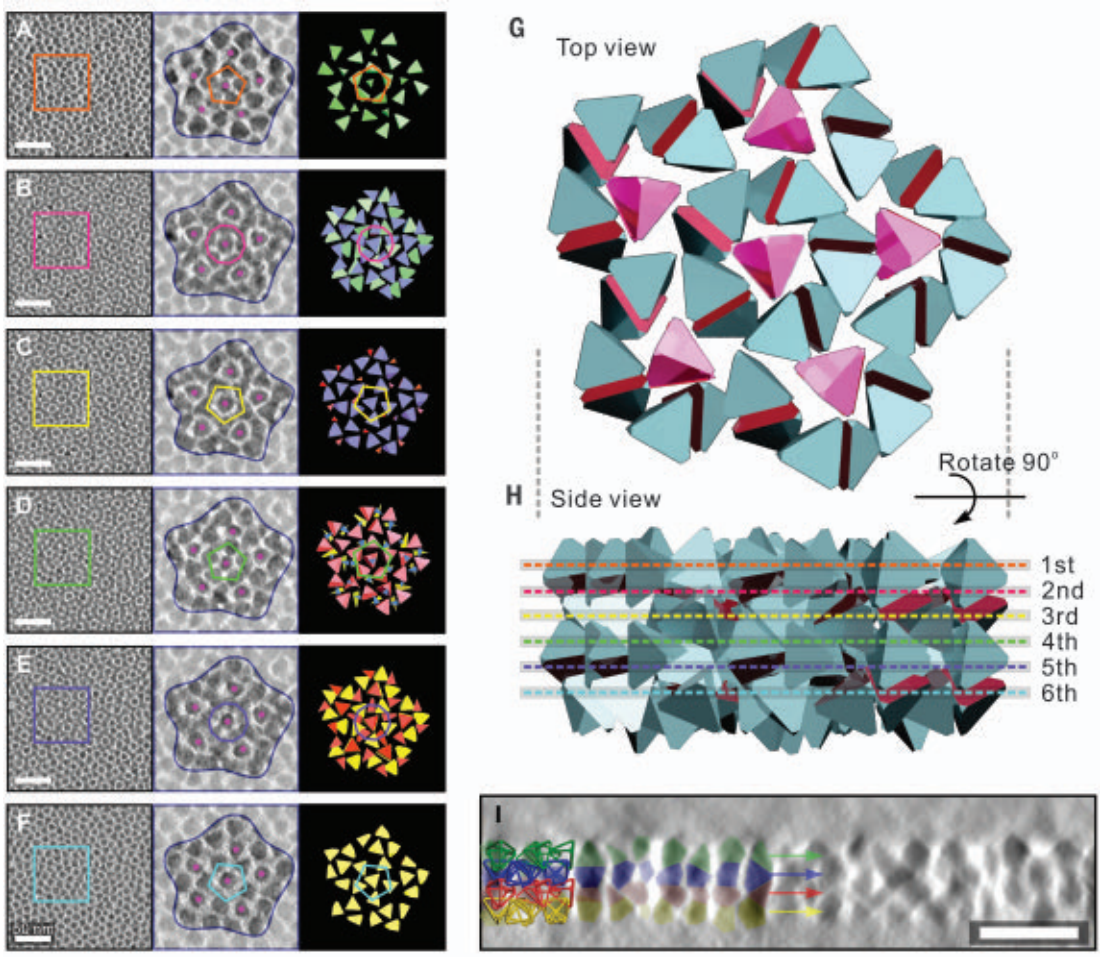

Fig. 2. Tomography reconstruction of the QC-SL with a double-decker stacking. (**A** to **F**) Horizontal slices at six different vertical positions showing the NC arrangement within the first to sixth layers shown in (H). Left: Snapshots of the tomographic movie. Center: Zoom-in images of the square-highlighted areas in left panels. Right: The corresponding horizontal slices from the computer-generated model shown in (G) and (H). (**G** and **H**) A computer-generated model of a double-decker QC-SL with six interconnected decagon-derivative units shown from a top view (G) and a side view (H). The centers of each polygon unit are labeled in magenta. (**I**) A vertical reconstruction slice of a double-decker QC-SL showing a four-layer TTQD stacking in the vertical direction (from top to bottom: green, blue, red, and yellow). Scale bar, 30 nm.

would be tiled by a $(10 - m)$-edge polygon with a uniform orientation. Following this procedure, a 2D TEM image of the QC-SLs was tiled by "flexible" polygons with five to nine edges (Fig. 3C and fig. S19). Consistently, the FFT of the obtained tiling pattern showed a high degree of consistency with the measured SA-ED pattern and the FFT pattern of the corresponding TEM image (Fig. 3, E to G). In addition, we analyzed the angle distributions of the inter–polygon center directions. The angle distributions for both cases (one-edge and two-edge overlapping cases) showed a 10-fold rotational symmetry (Fig. 3H), yet there was an angle offset of 18.0° ± 1.8° between the two cases (Fig. 3H and fig. S20). This angle analysis statistic was consistent with an overall 10-fold symmetry of the obtained TTQD assembled QC-SLs, which further validated our flexible polygon tiling rule.

Studies using silica microbeads have shown that patchy colloids, as a result of their unique energetic characteristics (vibrational and rotational entropies), can self-organize into unconventional structures more favorably than conventional lattices with equivalent potential energy upon crowding (*26*, *27*). In our case, the shape of the particles and their associated anisotropic surface patchiness (i.e., ODPA on $\{0002\}_{WZ}$ and oleic acid on $\{10\bar{1}1\}_{WZ}$) proved to be mandatory in order to form the observed QC-SLs (*9*). When assembling the isotropic analogs (oleic acid–coated spherical QDs) with the same single-particle volume, a regular face-centered cubic SL was obtained (fig. S21). In addition, the selection of the liquid subphase was found to be vital (*24*, *28*). In contrast to the 10-fold QC-SLs, a stack of monolayer hexagonal SLs was generated when EG was replaced with diethylene glycol (DEG) (figs. S22 to S24 and movies S4 and S5). This likely was due to the differences in their molecular structures; only the hydroxyl group is present in EG, whereas DEG contains an additional ether group, which provided a higher aliphatic Hansch hydrophobicity (π = −0.71 for $-COCH_3$ versus −1.16 for −OH) (*29*, *30*). The smaller π value for EG resulted in a lower interfacial surface energy (i.e., lower intermolecular affinity) between the solvent (cyclohexane) and the substrate (EG) (*31*), leading to a higher receding angle at the evaporation microsite (i.e., the SL formation site; see supplementary text) (*32*, *33*). Consequently, the TTQDs could interact with each other freely in space, forming the 10-fold QC-SLs in a process that largely was driven by the directional enthalpic patchiness (Fig. 4, i) (*9*, *27*). However, changing the liquid subphase to DEG resulted in a larger π value and thus a lower receding angle at the evaporation site, which limited the assembly space in the vertical dimension, thereby diminishing the interparticle enthalpic interactions. In addition, the same larger π value translated to a stronger attractive Derjaguin-Landau-Verwey-Overbeek force, thereby inducing a higher affinity between the ligand molecules on the surfaces of the TTQDs (i.e., oleic acid or ODPA) and the DEG liquid subphase, further minimizing the inter-TTQD interactions. Together, the formation of a hexagonal TTQD monolayer, dominantly driven by entropy, was favored (Fig. 4, ii). Consequently, upon further stacking, multilayer hexagonal SL generation was obtained (Fig. 4, ii, and fig. S25) (*32*, *33*). Likewise, 10-fold QC-SLs were formed on the surface of the glycerol, whereas a stack of monolayer hexagonal SLs was generated on top of the tri- and tetra-EG, thereby validating the reliability of the formation mechanism (fig. S25).

Our findings show that high-complexity superstructures can be obtained from single-component NC building blocks when anisotropic kinetic factors are fueled. We anticipate that the newly discovered QC-SLs and the proposed "flexible polygon" aperiodic tiling rule will spur other interesting

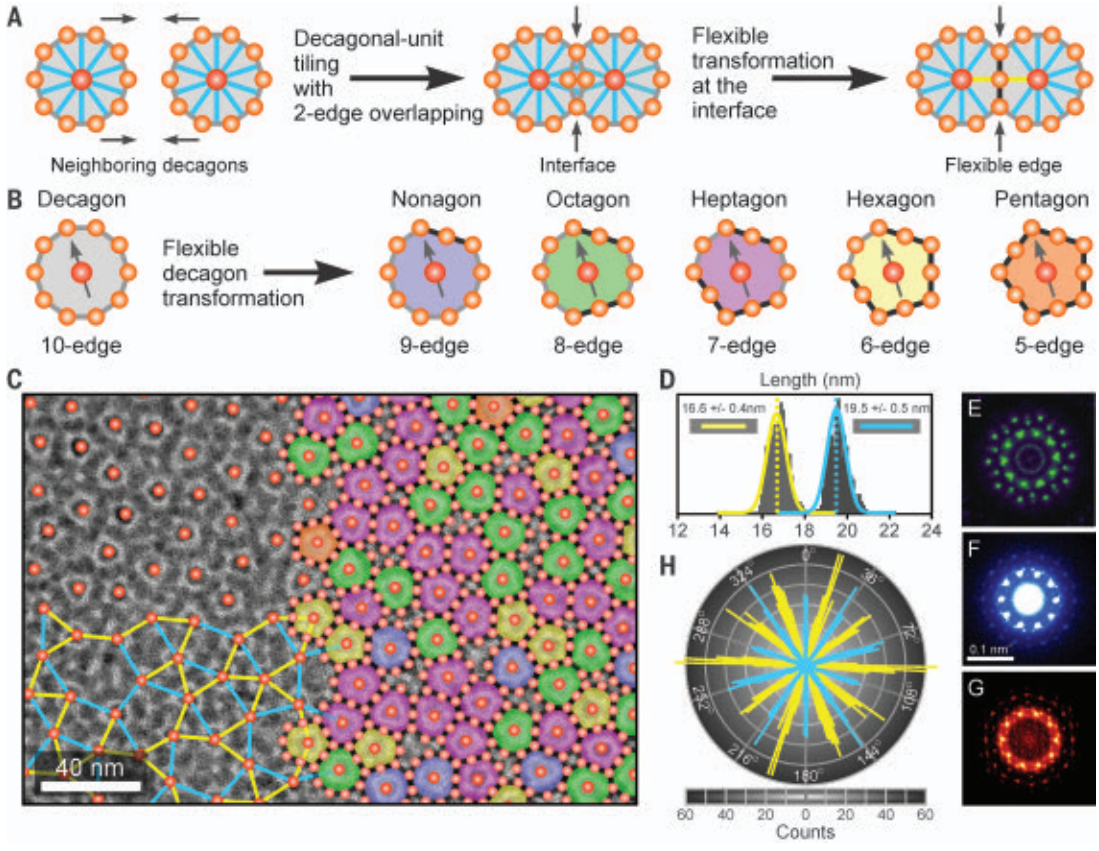

Fig. 3. QC order generated through a flexible polygon tiling rule. (**A**) Schematic illustration of the flexible edge transformation process for two-edge overlapping between two regular decagons. (**B**) Schematic demonstration of a flexible decagon transforming into possible orientational rigid polygons with nine to five edges. (**C**) A TEM image showing the flexible polygon tiling steps. Larger orange spheres at top left indicate the centers of each polygon; the yellow and blue lines connect the two polygon centers with the nearest and second nearest inter–polygon center distance, respectively; the right side of the image is tiled by color-coded flexible polygons [same color coding as in (B)]. (**D**) Histograms of the length distributions of the nearest (yellow lines) and second nearest (blue lines) inter–polygon center distances. (**E**) FFT pattern of an artificial QC order generated from flexible polygon tiling as shown in (C). (**F**) SA-ED pattern obtained from the TTQD QC-SLs. (**G**) FFT pattern of a 10-fold QC-SL TEM image. (**H**) Angle distributions of the nearest (yellow) and second nearest (blue) inter–polygon center directions.

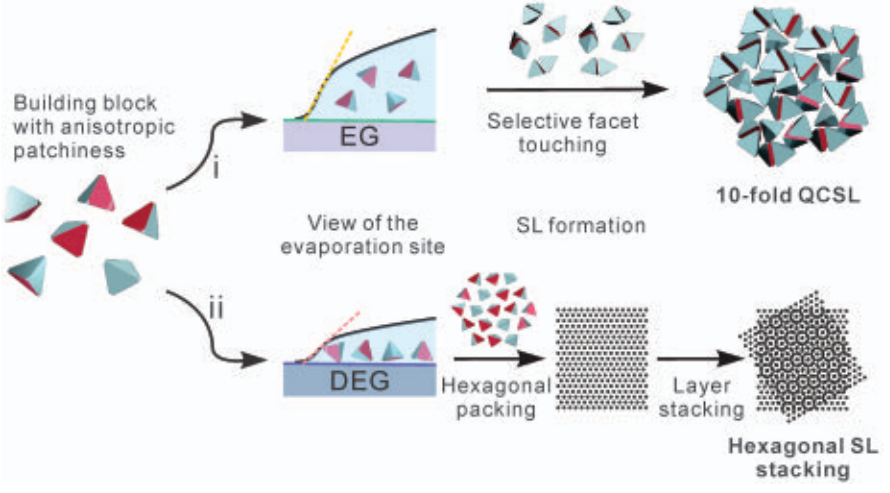

Fig. 4. Schematic representation of the TTQD assembly pathways. (i) 10-fold QC-SL formation on top of EG; (ii) hexagonal SL stacking formation on top of DEG.

superstructural assemblies from a spectrum of anisotropic building blocks of various length scales.

REFERENCES AND NOTES

1. D. Shechtman, I. Blech, D. Gratias, J. W. Cahn, *Phys. Rev. Lett.* **53**, 1951–1953 (1984).
2. D. L. D. Caspar, E. Fontano, *Proc. Natl. Acad. Sci. U.S.A.* **93**, 14271–14278 (1996).
3. A. Yamamoto, *Acta Crystallogr. A* **52**, 509–560 (1996).
4. W. N. Man, M. Megens, P. J. Steinhardt, P. M. Chaikin, *Nature* **436**, 993–996 (2005).
5. W. Steurer, *Chem. Soc. Rev.* **41**, 6719–6729 (2012).
6. P. J. Lu, P. J. Steinhardt, *Science* **315**, 1106–1110 (2007).
7. N. A. Wasio *et al.*, *Nature* **507**, 86–89 (2014).
8. D. V. Talapin *et al.*, *Nature* **461**, 964–967 (2009).
9. Y. Nagaoka *et al.*, *Nature* **561**, 378–382 (2018).
10. X. Ye *et al.*, *Nat. Mater.* **16**, 214–219 (2017).
11. Z. J. Yang, J. J. Wei, P. Bonville, M. P. Pileni, *J. Am. Chem. Soc.* **137**, 4487–4493 (2015).
12. H. X. Lin *et al.*, *Science* **355**, 931–935 (2017).
13. M. P. Boneschanscher *et al.*, *Science* **344**, 1377–1380 (2014).
14. M. Yang *et al.*, *Nat. Chem.* **9**, 287–294 (2017).
15. Z. J. Yang, J. J. Wei, Y. I. Sobolev, B. A. Grzybowski, *Nature* **553**, 313–318 (2018).
16. K. Miszta *et al.*, *Nat. Mater.* **10**, 872–876 (2011).
17. R. M. Choueiri *et al.*, *Nature* **538**, 79–83 (2016).
18. X. B. Zeng *et al.*, *Nature* **428**, 157–160 (2004).
19. K. Hayashida, T. Dotera, A. Takano, Y. Matsushita, *Phys. Rev. Lett.* **98**, 195502 (2007).
20. A. Haji-Akbari *et al.*, *Nature* **462**, 773–777 (2009).
21. M. Engel, P. F. Damasceno, C. L. Phillips, S. C. Glotzer, *Nat. Mater.* **14**, 109–116 (2015).
22. T. Dotera, T. Oshiro, P. Ziherl, *Nature* **506**, 208–211 (2014).
23. R. Tan *et al.*, *Chem. Mater.* **29**, 4097–4108 (2017).
24. A. Dong, J. Chen, P. M. Vora, J. M. Kikkawa, C. B. Murray, *Nature* **466**, 474–477 (2010).
25. M. Engel, H.-R. Trebin, *Phys. Rev. Lett.* **98**, 225505 (2007).
26. Q. Chen, S. C. Bae, S. Granick, *Nature* **469**, 381–384 (2011).
27. V. N. Manoharan, *Science* **349**, 1253751 (2015).
28. B. T. Diroll, N. J. Greybush, C. R. Kagan, C. B. Murray, *Chem. Mater.* **27**, 2998–3008 (2015).
29. D. Guo, C. Li, Y. Wang, Y. Li, Y. Song, *Angew. Chem. Int. Ed.* **56**, 15348–15352 (2017).
30. A. Leo, C. Hansch, D. Elkins, *Chem. Rev.* **71**, 525–616 (1971).

31. F. M. Menger, M. E. Chlebowski, *Langmuir* **21**, 2689–2695 (2005).
32. S. Šikalo, H. D. Wilhelm, I. V. Roisman, S. Jakirlic, C. Tropea, *Phys. Fluids* **17**, 062103 (2005).
33. R. Bhardwaj, X. H. Fang, P. Somasundaran, D. Attinger, *Langmuir* **26**, 7833–7842 (2010).

ACKNOWLEDGMENTS

O.C. thanks S. Zhao for valuable discussion. The TEM measurements were performed at the Electron Microscopy Facility in the Institute for Molecular and Nanoscale Innovation (IMNI) at Brown University. **Funding:** Supported by the Brown University Startup Fund and the IMNI Seed Fund (O.C.). **Author contributions:** Y.N. and O.C. conceived and designed the experiments; Y.N. and H.Z. conducted the synthesis and material characterizations; Y.N. performed the data analysis; D.E. performed electron tomography measurement and computer reconstruction; O.C. supervised the entire project; and Y.N. and O.C. wrote the manuscript. All authors discussed the results and commented on the manuscript. **Competing interests:** The authors declare no competing financial interest. **Data and materials availability:** All data are available in the main text or the supplementary materials.

SUPPLEMENTARY MATERIALS

www.sciencemag.org/content/362/6421/1396/suppl/DC1
Materials and Methods
Supplementary Text
Figs. S1 to S25
Tables S1 and S2
Movies S1 to S5
References (*34*–*41*)

15 August 2018; accepted 24 October 2018
10.1126/science.aav0790

MOLECULAR MAGNETS

Magnetic hysteresis up to 80 kelvin in a dysprosium metallocene single-molecule magnet

Fu-Sheng Guo[1], Benjamin M. Day[1,2], Yan-Cong Chen[3], Ming-Liang Tong[3]*, Akseli Mansikkamäki[4]*, Richard A. Layfield[1]*

Single-molecule magnets (SMMs) containing only one metal center may represent the lower size limit for molecule-based magnetic information storage materials. Their current drawback is that all SMMs require liquid-helium cooling to show magnetic memory effects. We now report a chemical strategy to access the dysprosium metallocene cation $[(Cp^{iPr5})Dy(Cp^*)]^+$ (Cp^{iPr5}, penta-iso-propylcyclopentadienyl; Cp*, pentamethylcyclopentadienyl), which displays magnetic hysteresis above liquid-nitrogen temperatures. An effective energy barrier to reversal of the magnetization of U_{eff} = 1541 wave number is also measured. The magnetic blocking temperature of T_B = 80 kelvin for this cation overcomes an essential barrier toward the development of nanomagnet devices that function at practical temperatures.

The observation of slow magnetic relaxation in coordination compounds that contain a single lanthanide ion stimulated considerable interest in monometallic single-molecule magnets (SMMs) (*1*). This family of materials shows magnetic hysteresis properties that arise from the electronic structure at the molecular level rather than interactions across comparatively large magnetic domains (*2*–*4*). In addition to the considerable fundamental interest in SMMs and related magnetic molecules, their magnetic memory properties have inspired proposals for applications as spin qubits (*5*) and in nanoscale spintronic devices (*6*). A key performance parameter of an SMM is the magnetic blocking temperature, T_B, one description of which refers to the maximum temperature at which it is possible to observe hysteresis in the field dependence of the magnetization, subject to the field sweep rate. The blocking temperature provides a means of comparing different SMMs and, to date, the vast majority that show any hysteresis at all require liquid-helium cooling to do so (*7*, *8*). A few notable examples have emerged from the extreme cold to set record blocking temperatures above the liquid-helium regime (*9*–*12*), including the dysprosium metallocene $[(Cp^{ttt})_2Dy][B(C_6F_5)_4]$ (Cp^{ttt}, 1,2,4-tri-*tert*-butylcyclopentadienyl), which showed magnetic hysteresis with coercivity up to 60 K (*13*–*15*); however, this threshold still falls markedly short of the more practically accessible 77 K temperature at which nitrogen liquefies. We now show that by designing the ligand framework so that two key structural parameters—that is, the Dy-Cp_{cent} distances (cent refers to the centroid of the Cp ligand) and the Cp-Dy-Cp bending angle—are rendered short and wide, respectively, we achieve an axial crystal field of sufficient strength to furnish an SMM that shows hysteresis above 77 K.

A dysprosium metallocene cation was targeted with cyclopentadienyl substituents of sufficient bulk to produce a wide Cp-Dy-Cp angle, but not too bulky to preclude close approach of the ligands. Thus, the borohydride precursor complex $[(\eta^5\text{-}Cp^{iPr5})Dy(\eta^5\text{-}Cp^*)(BH_4)]$ (**2**) (Cp^{iPr5}, penta-iso-propylcyclopentadienyl; **Cp***, pentamethylcyclopentadienyl) was synthesized by treating $[Dy(\eta^5\text{-}Cp^{iPr5})(BH_4)_2(THF)]$ (**1**) with KCp* (Fig. 1). The molecular structures of **1** and **2** were determined by x-ray crystallography (figs. S4 and S5 and tables S1 to S3). The target compound $[(\eta^5\text{-}Cp^*)Dy(\eta^5\text{-}Cp^{iPr5})][B(C_6F_5)_4]$ (**3**), hereafter abbreviated [Dy-5*][$B(C_6F_5)_4$], was then isolated in 60% yield by treating **2** with the superelectrophile $[(Et_3Si)_2(\mu\text{-}H][B(C_6F_5)_4]$ (Et, ethyl) (*16*). An x-ray crystallographic analysis of the molecular structure of **3** at 150 K (Fig. 1, figs. S6 and S7, and tables S1 and S4) revealed that the Dy-5* cation features Dy-Cp* and Dy-Cp^{iPr5} distances of 2.296(1) and 2.284(1) Å, respectively, which are, on average, 0.026 Å shorter than the analogous distances of 2.32380(8) and 2.30923(8) Å determined for $[(Cp^{ttt})_2Dy]^+$ (*13*). Furthermore, the Cp-Dy-Cp angle in Dy-5* is 162.507(1)° and hence almost 9.7° wider than the angle of 152.845(2)° found in $[(Cp^{ttt})_2Dy]^+$. On the basis of these structural parameters, the crystal field in Dy-5* should be stronger and more axial than in $[(Cp^{ttt})_2Dy]^+$, and hence, an improvement in the SMM properties can be expected.

The dc molar magnetic susceptibility (χ_M) was measured for compounds **1** to **3** in the temperature range of 2 to 300 K using an applied field of 1000 Oe, and the field dependence of the magnetization for **1** and **2** was measured at T = 2 and 5 K using fields up to 70 kOe (figs. S8 to S12). A description of the properties of **1** and **2** is provided in the supplementary materials. For **3**, the $\chi_M T$ value was measured to be 13.75 cm^3 K mol^{-1} at 300 K and then manifested a steady decrease down to 75 K. At lower temperatures, a sharp drop in $\chi_M T$ was observed, indicating the onset of magnetic blocking, with a value of 0.94 cm^3 K mol^{-1} reached at 2 K. Overall, the dc magnetic properties of compounds **1** to **3** are typical for a monometallic complex of Dy^{3+} with a $^6H_{15/2}$ ground multiplet (*17*). The SMM properties of compounds **1** to **3** were then established through measurements of the in-phase (the real component, χ') and the out-of-phase (the imaginary component, χ'') ac susceptibilities as functions of the ac frequency (ν) and temperature, using an oscillating field of 5 Oe and zero applied dc field (figs. S13 to S28 and tables S5 to S7). Focusing again on **3**, the $\chi''(\nu)$ isotherms show well-defined maxima up to 130 K (Fig. 2). The $\chi'(\nu)$ and $\chi''(\nu)$ data were then used to derive Cole-Cole plots of $\chi''(\chi')$ for relaxation in the temperature range of 82 to 138 K in intervals of 2 K, with each plot adopting a parabolic shape (figs. S26 to S28). Accurate fits of the ac susceptibility plots were obtained using equations

[1]Department of Chemistry, School of Life Sciences, University of Sussex, Falmer BN1 9QJ, UK. [2]School of Chemistry, The University of Manchester, Oxford Road, Manchester M13 9PL, UK. [3]Key Laboratory of Bioinorganic and Synthetic Chemistry of the Ministry of Education, School of Chemistry, Sun-Yat Sen University, Guangzhou 510275, People's Republic of China. [4]Department of Chemistry, Nanoscience Centre, University of Jyväskylä, P.O. Box 35, FI-40014 Jyväskylä, Finland.
***Corresponding author. Email: tongml@mail.sysu.edu.cn (M.-L.T.); akseli.mansikkamaki@jyu.fi (A.M.); r.layfield@sussex.ac.uk (R.A.L.)**

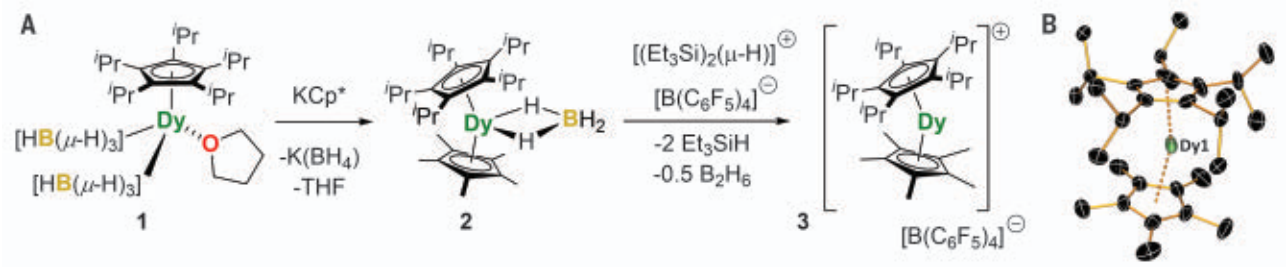

Fig. 1. Synthesis and molecular structures. (**A**) Reaction scheme for the synthesis of **3**. (**B**) Thermal ellipsoid representation (50% probability) of the molecular structure of the Dy-5* cation in **3**, as determined by x-ray crystallography {for clarity, the hydrogen atoms and $[B(C_6F_5)_4]^-$ counter anion are omitted}.

describing χ' and χ'' in terms of frequency, the isothermal susceptibility (χ_T), adiabatic susceptibility (χ_S), the relaxation time (τ), and the fitting parameter α to represent the distribution of relaxation times (eqs. S1 and S2) (*18*).

The resulting values of α = 0 to 0.027 indicate a very narrow range of relaxation times in the high-temperature regime. The relaxation times at temperatures in the range of 2 to 83 K were determined in intervals of about 5 K from plots of the magnetization decay versus time (figs. S29 to S48 and table S8). These data show, for example, that the magnetization in **3** decays almost to zero over a 50-s time period at 77 K, increasing to about 500 min at 15 K. The temperature at which τ = 100 s is 65 K. The relaxation times determined from the ac and dc measurements were then combined to obtain further insight into the magnetic relaxation by plotting τ as a function of T^{-1} (Fig. 2), which revealed a strong, linear dependence of the relaxation time on temperature in the range of 55 to 138 K. The $\tau(T^{-1})$ plot in the range of 10 to 55 K is curved in nature and represents an intermediate regime before purely temperature-independent relaxation is observed below 10 K. The relaxation time can be expressed as $\tau^{-1} = \tau_0^{-1}e^{-U_{eff}/k_BT} + CT^n + \tau_{QTM}^{-1}$, in which the first term represents Orbach relaxation with U_{eff} as the effective energy barrier to relaxation of the magnetization (k_B, Boltzmann constant), the second term represents the contribution from Raman processes (C, the Raman coefficient; n, the Raman exponent), and the third term represents the rate of quantum tunneling of the magnetization (QTM). Using this equation, an excellent fit [adjusted coefficient of determination (R^2) = 0.99958] of the data was obtained with $\tau_0 = 4.2(6) \times 10^{-12}$ s; U_{eff} = 1541(11) cm^{-1}; $C = 3.1(1) \times 10^{-8}$ s^{-1} K^{-n} and n = 3.0(1); and $\tau_{QTM} = 2.5(2) \times 10^4$ s. The U_{eff} value determined for **3** exceeds the value of 1277 cm^{-1} determined for $[(Cp^{ttt})_2Dy][B(C_6F_5)_4]$ by about 20% (*13*).

Potential applications of SMMs in information storage devices rely on the occurrence of magnetic remanence and coercivity; therefore, the hysteresis is a critical consideration (*19*). For **3**, using a relatively fast field sweep rate of 200 Oe s^{-1} revealed $M(H)$ hysteresis from 2 up to 85 K, with the loops gradually closing as the temperature increased (Fig. 3, A and B). At these temperature limits, coercive fields (H_c)

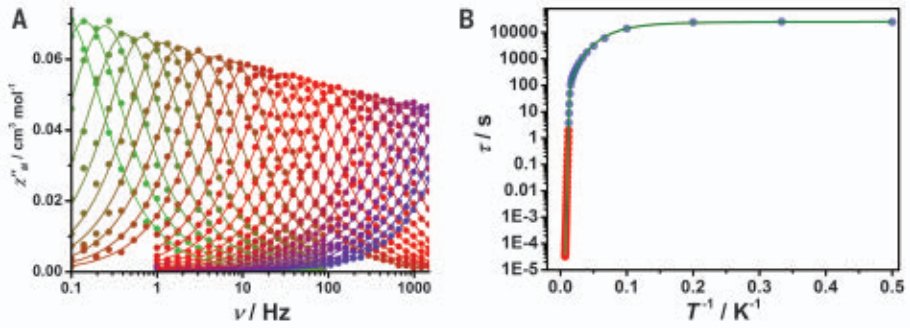

Fig. 2. Dynamic magnetic properties. (**A**) Frequency dependence of the out-of-phase χ''_M molar magnetic susceptibility for **3**, collected in zero dc field at ac frequencies of ν = 0.1 to 1488 Hz from 82 K (green trace) to 138 K (purple trace) in 2 K intervals. Solid lines represent fits to the data using eqs. S1 and S2, with adjusted R^2 = 0.99823 to 0.99988. (**B**) Temperature dependence of the relaxation time for **3**. The red points are from the ac susceptibility data, and the blue points are from measurements of the dc magnetic relaxation time. The solid green line is the best fit to $\tau^{-1} = \tau_0^{-1}e^{-U_{eff}/k_BT} + CT^n + \tau_{QTM}^{-1}$, using the parameters stated in the text.

of 50 kOe and 210 Oe (5.0 T and 21 mT), respectively, were measured (Fig. 3C, fig. S49, and table S9). Fixing the temperature at 77 K, a reduction in the sweep rate resulted in the coercive field approximately halving with the rate, that is, H_c = 5802 Oe at 700 Oe s^{-1}, 2946 Oe at 350 Oe s^{-1}, 1688 Oe at 200 Oe s^{-1}, 825 Oe at 100 Oe s^{-1}, 398 Oe at 50 Oe s^{-1}, and 191 Oe at 25 Oe s^{-1} (fig. S50 and table S10). The observation of coercivity in **3** at 25 Oe s^{-1} is notable because this sweep rate is slower than the 39 Oe s^{-1} used to determine the blocking temperature of 60 K for $[(Cp^{ttt})_2Dy][B(C_6F_5)_4]$ (*13*). At 80 K and 25 Oe s^{-1}, a coercive field of 63 Oe was measured (Fig. 3D), and the loops were completely closed at higher temperatures. Consistent with this finding, the field-cooled and zero-field-cooled magnetic susceptibilities for **3** diverged at 78 K (fig. S51). By analogy with the development of high-temperature (high-T_C) superconductors, we propose to designate the Dy-5* cation in **3** as a high-temperature, or high-T_B, SMM.

The importance of the strong axial crystal field in the Dy-5* cation combined with the absence of an equatorial field is illustrated further by comparing the U_{eff} and T_B values for **3** with those of the precursors **1** and **2**. In the case of **1**, the Cp^{iPr5} ligand provides a strong axial field, but the pseudo-octahedral coordination geometry introduces a non-negligible equatorial field and, although slow magnetic relaxation in zero field is observed with this system, the positions of the maxima in $\chi''(\nu)$ are temperature-independent up to 10 K and only observed up to 30 K (figs. S13 to S16). The resulting energy barrier of 241(7) cm^{-1} is comparatively small, and the rate of QTM is, at 5.0(1) $\times 10^{-3}$ s (fig. S17), some seven orders of magnitude faster than found with **3**. The competing equatorial field in **2** is more prominent, because the maxima in $\chi''(\nu)$ are very weakly temperature-dependent from 3 to 20 K, with the resulting energy barrier a negligible 7(1) cm^{-1} (figs. S19 to S22). In both **1** and **2**, the $M(H)$ hysteresis loops collected at 2 K and 200 Oe s^{-1} are waist-restricted, with no coercivity and only small openings as the field magnitude increases (figs. S18 and S23).

Ab initio calculations have enabled quantitative analysis of the properties of SMMs on a microscopic scale (*20*), particularly systems with η^n-bonded organometallic ligands (*21*–*30*). Calculations on the Dy-5* cation were performed at the XMS-CASPT2//SA-CASSCF/RASSI level (*31*, *32*): The resulting energies, principal components of the g-tensors, and the principal magnetic axes of the eight lowest Kramers' doublets in Dy-5* corresponding to the crystal-field (CF) states of the $^6H_{15/2}$ ground multiplet are listed in table S11. The principal magnetic axis in the ground doublet of Dy-5* (Fig. 4) is projected toward the

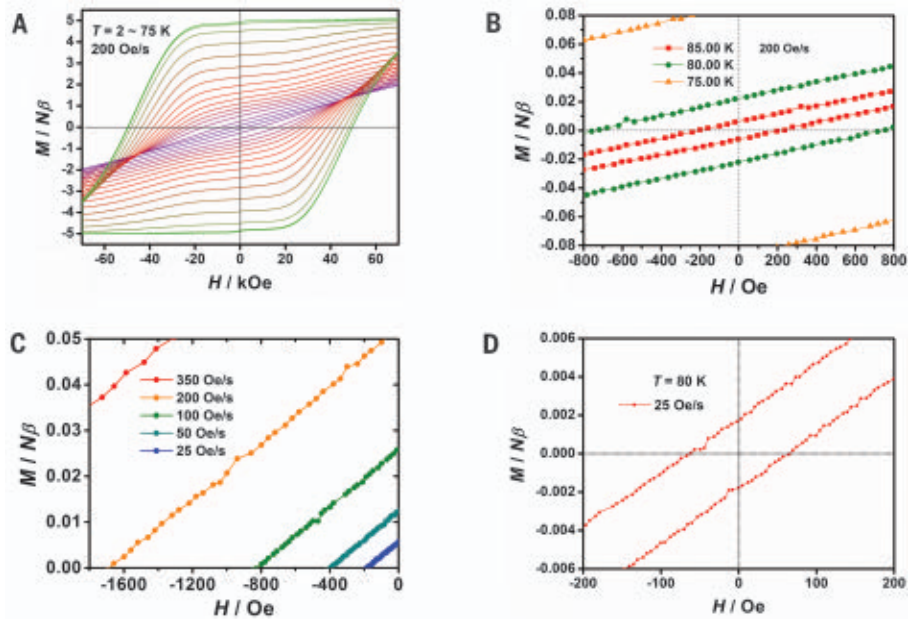

Fig. 3. Magnetic hysteresis properties of 3. (**A** and **B**) Magnetization versus field hysteresis loops in the temperature ranges of 2 to 75 K (A) and 75 to 85 K (B) using a field sweep rate of 200 Oe s^{-1}. (**C**) Expansion of the hysteresis loops at 77 K showing the coercive fields. (**D**) Hysteresis loops at 80 K using a field sweep rate of 25 Oe s^{-1}.

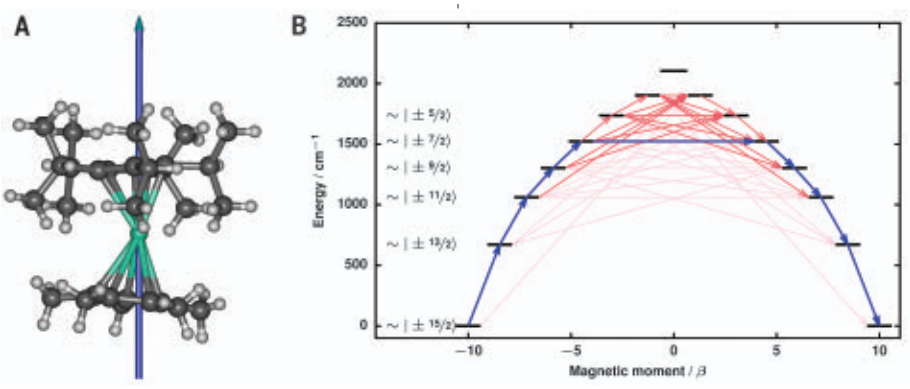

Fig. 4. Magnetic relaxation in the Dy-5* cation. (**A**) The principal magnetic axis of the ground Kramers' doublet. (**B**) Relaxation mechanism for Dy-5*. Blue arrows show the most probable relaxation route, and red arrows show transitions between states with less probable, but non-negligible, matrix elements; darker shading indicates a higher probability.

centroids of the two cyclopentadienyl ligands, with the principal axes of the next six doublets almost collinear and the largest deviation angle 5.3° with the fifth doublet. The highest doublet is perpendicular to the ground doublet.

The ***g***-tensor of the ground doublet is calculated to be perfectly axial, that is, $g_x = g_y = 0.000$ and $g_z = 20.000$ (table S11), which is consistent with the experimental hysteresis measurements in which QTM is completely blocked at zero field. In the six lowest doublets, the CF is highly axial, and each state can be assigned to a definite projection (greater than 96% character) of the total angular momentum, M_J (table S12). The transverse components of the ***g***-tensors increase roughly by an order of magnitude in each doublet upon moving to higher energy. In the fifth doublet, the transverse components are non-negligible, and in the sixth doublet, the transverse components are large enough to allow considerable tunneling. In the two highest states, the axiality is weaker and considerable mixing occurs under the CF, which most likely results from the asymmetry of the coordination environment.

The ab initio CF parameters were calculated for the Dy-5* cation following a previously established methodology (*33*, *34*) and are listed in table S13. The off-diagonal elements of the CF operator clearly have non-negligible elements owing to the low C_1 point symmetry of Dy-5*; however, the axial second-rank parameter B_2^0 is at least two orders of magnitude larger than any other parameter. This creates a highly axial CF environment despite the absence of point symmetry (or pseudosymmetry) that would be needed for a strictly axial CF. The off-diagonal elements of the CF play some role, and, in the higher-lying doublets of the ground multiplet, the axial nature of the CF is lost (vide infra). This demonstrates that strict point symmetry is not required to achieve a highly axial CF, provided that the axial parameters are sufficiently strong in comparison to the other CF parameters arising from the low-symmetry components of the CF.

The magnetic relaxation in the Dy-5* cation was studied further by constructing a qualitative relaxation barrier from the ab initio results, which follows a methodology in which the transition magnetic moment between the different states was calculated and the relaxation pathway follows the largest matrix elements (Fig. 4B and table S14) (*35*). The results predict that the barrier is crossed at the fourth excited doublet, corresponding to a U_{eff} value of 1524 cm^{-1} for the Orbach process, which is consistent with the calculated ***g***-tensors for this doublet and is in excellent agreement with the experimentally determined barrier height of 1541(11) cm^{-1}. To gain deeper insight into the nature of the spin-phonon relaxation, the first-order spin-phonon couplings with the optical phonons (approximated as the molecular vibrations) were evaluated from first-principles calculations (tables S15 to S18). In earlier work on $[(Cp^{ttt})_2Dy]^+$ (*14*), vibrations of the C–H oscillators in the Cp rings were recognized as the most important contribution to the Orbach relaxation, because they initiated the transition from the ground doublet to the first excited doublet. In the case of Dy-5**, these oscillators are absent, and the analogous transition from the ground to the first excited doublet is most likely initiated by out-of-plane vibrations of the Cp* ligand when comparing the frequency of these modes (632.9 and 640.5 cm^{-1}) to the calculated gap between the ground and first excited doublets (672 cm^{-1}) (see movies S1 to S7). Because the out-of-plane vibrations couple strongly to vibrations of the Cp* methyl groups, it is conceivable that their energies can be tuned by choosing ligand substituents that would bring the vibrational modes out of resonance with the excitation gap. Such an approach should lead to further improvements in SMM performance beyond those of the Dy-5* cation and therefore enhance their potential for applications in magnetic information storage materials.

Note added in proof: A study describing the properties of related cationic dysprosium metallocenes was recently published by Long, Harvey, and others (*36*).

REFERENCES AND NOTES

1. N. Ishikawa, M. Sugita, T. Ishikawa, S. Y. Koshihara, Y. Kaizu, *J. Am. Chem. Soc.* **125**, 8694–8695 (2003).
2. B. M. Day, F.-S. Guo, R. A. Layfield, *Acc. Chem. Res.* **51**, 1880–1889 (2018).
3. J.-L. Liu, Y.-C. Chen, M.-L. Tong, *Chem. Soc. Rev.* **47**, 2431–2453 (2018).

4. J. M. Frost, K. L. M. Harriman, M. Murugesu, *Chem. Sci.* **7**, 2470–2491 (2016).
5. M. Shiddiq *et al.*, *Nature* **531**, 348–351 (2016).
6. S. Thiele *et al.*, *Science* **344**, 1135–1138 (2014).
7. D. N. Woodruff, R. E. P. Winpenny, R. A. Layfield, *Chem. Rev.* **113**, 5110–5148 (2013).
8. P. Zhang, L. Zhang, J. Tang, *Dalton Trans.* **44**, 3923–3929 (2015).
9. J. D. Rinehart, M. Fang, W. J. Evans, J. R. Long, *J. Am. Chem. Soc.* **133**, 14236–14239 (2011).
10. Y.-C. Chen *et al.*, *J. Am. Chem. Soc.* **138**, 2829–2837 (2016).
11. S. K. Gupta, T. Rajeshkumar, G. Rajaraman, R. Murugavel, *Chem. Sci.* **7**, 5181–5191 (2016).
12. F. Liu *et al.*, *Nat. Commun.* **8**, 16098 (2017).
13. F.-S. Guo *et al.*, *Angew. Chem. Int. Ed.* **56**, 11445–11449 (2017).
14. C. A. P. Goodwin, F. Ortu, D. Reta, N. F. Chilton, D. P. Mills, *Nature* **548**, 439–442 (2017).
15. C. A. P. Goodwin, D. Reta, F. Ortu, N. F. Chilton, D. P. Mills, *J. Am. Chem. Soc.* **139**, 18714–18724 (2017).
16. S. J. Connelly, W. Kaminsky, D. M. Heinekey, *Organometallics* **32**, 7478–7481 (2013).
17. C. Benelli, D. Gatteschi, *Introduction to Molecular Magnetism: From Transition Metals to Lanthanides* (Wiley-VCH, 2015).
18. Y.-N. Guo, G.-F. Xu, Y. Guo, J. Tang, *Dalton Trans.* **40**, 9953–9963 (2011).
19. S. Demir, M. I. Gonzalez, L. E. Darago, W. J. Evans, J. R. Long, *Nat. Commun.* **8**, 2144 (2017).
20. L. Ungur, L. F. Chibotaru, *Inorg. Chem.* **55**, 10043–10056 (2016).
21. L. Ungur, J. J. Le Roy, I. Korobkov, M. Murugesu, L. F. Chibotaru, *Angew. Chem. Int. Ed.* **53**, 4413–4417 (2014).
22. J. J. Le Roy, L. Ungur, I. Korobkov, L. F. Chibotaru, M. Murugesu, *J. Am. Chem. Soc.* **136**, 8003–8010 (2014).
23. J. J. Le Roy *et al.*, *J. Am. Chem. Soc.* **135**, 3502–3510 (2013).
24. K. L. M. Harriman *et al.*, *Chem. Sci.* **8**, 231–240 (2017).
25. T. P. Latendresse, N. S. Bhuvanesh, M. Nippe, *J. Am. Chem. Soc.* **139**, 14877–14880 (2017).
26. T. Pugh, N. F. Chilton, R. A. Layfield, *Angew. Chem. Int. Ed.* **55**, 11082–11085 (2016).
27. T. Pugh *et al.*, *Nat. Commun.* **6**, 7492 (2015).
28. T. Pugh, V. Vieru, L. F. Chibotaru, R. A. Layfield, *Chem. Sci.* **7**, 2128–2137 (2016).
29. T. Pugh, N. F. Chilton, R. A. Layfield, *Chem. Sci.* **8**, 2073–2080 (2017).
30. A. F. R. Kilpatrick *et al.*, *Chem. Commun. (Camb.)* **54**, 7085–7088 (2018).
31. L. Ungur, L. F. Chibotaru, *Computational Modelling of Magnetic Properties of Lanthanide Compounds in Lanthanide and Actinides* in *Molecular Magnetism*, R. A. Layfield, M. Murugesu, Eds. (Wiley-VCH, 2015).
32. T. Shiozaki, W. Győrffy, P. Celani, H.-J. Werner, *J. Chem. Phys.* **135**, 081106 (2011).
33. L. Ungur, L. F. Chibotaru, *Chemistry* **23**, 3708–3718 (2017).
34. L. F. Chibotaru, in *Ab Initio Methodology for Pseudospin Hamiltonians of Anisotropic Magnetic Complexes*, S. A. Rice, A. R. Dinner, Eds. (Advances in Chemical Physics Series, Wiley, 2013), vol. 153, pp. 397–519.
35. L. Ungur, M. Thewissen, J.-P. Costes, W. Wernsdorfer, L. F. Chibotaru, *Inorg. Chem.* **52**, 6328–6337 (2013).
36. K. R. McClain *et al.*, *Chem. Sci. (Camb.)* **9**, 8492–8503 (2018).

ACKNOWLEDGMENTS

The authors thank the CSC-IT Center for Science in Finland, the Finnish Grid and Cloud Infrastructure (persistent identifier urn:nbn:fi:research-infras-2016072533), and H. M. Tuononen (University of Jyväskylä) for providing computational resources. **Funding:** The authors thank the European Research Council (CoG grant 646740), the EPSRC (EP/M022064/1), the NSF China (projects 21620102002 and 91422302), the National Key Research and Development Program of China (2018YFA0306001), and the Academy of Finland (projects 282499 and 289172). **Author contributions:** R.A.L. conceived the original idea and formulated the research aims. Synthetic and crystallographic work was carried out by F.-S.G. and B.M.D. Magnetic measurements were conducted by Y.-C.C. and M.-L.T. The theoretical analysis was carried out by A.M. All authors analyzed the data. R.A.L. wrote the manuscript, with contributions from all authors. **Competing interests:** The authors declare no competing interests. **Data and materials availability:** Metrical data for the solid-state structures of **1** to **3** are available free of charge from the Cambridge Crystallographic Data Centre under reference numbers CCDC 1854466 to 1854468. All other data are in the main text or supplementary materials.

SUPPLEMENTARY MATERIALS

www.sciencemag.org/content/362/6421/1400/suppl/DC1
Materials and Methods
Figs. S1 to S51
Tables S1 to S18
References (*37*–*77*)
Movies S1 to S7
Data S1 to S3

13 August 2018; accepted 9 October 2018
Published online 18 October 2018
10.1126/science.aav0652

MARINE PROTECTED AREAS

Elevated trawling inside protected areas undermines conservation outcomes in a global fishing hot spot

Manuel Dureuil[1,2]*, Kristina Boerder[1], Kirsti A. Burnett[2], Rainer Froese[3], Boris Worm[1]

Marine protected areas (MPAs) are increasingly used as a primary tool to conserve biodiversity. This is particularly relevant in heavily exploited fisheries hot spots such as Europe, where MPAs now cover 29% of territorial waters, with unknown effects on fishing pressure and conservation outcomes. We investigated industrial trawl fishing and sensitive indicator species in and around 727 MPAs designated by the European Union. We found that 59% of MPAs are commercially trawled, and average trawling intensity across MPAs is at least 1.4-fold higher as compared with nonprotected areas. Abundance of sensitive species (sharks, rays, and skates) decreased by 69% in heavily trawled areas. The widespread industrial exploitation of MPAs undermines global biodiversity conservation targets, elevating recent concerns about growing human pressures on protected areas worldwide.

In light of mounting anthropogenic pressures, spatial protection of sensitive habitats and species has emerged as a leading strategy to halt ongoing biodiversity loss, both on land and in the sea (*1*). However, it has been shown recently that about one-third of terrestrial protected areas experience intense human pressure, potentially undermining global conservation targets and sustainable development goals (*2*). We asked to which extent this conflict may also occur in the ocean, using newly available satellite sensors that allow fine-scale, real-time quantification of industrial fishing effort from space (*3*). We focused on Europe, which is both a global hot spot of industrial fishing (*3*) and features extensive marine protected area (MPA) networks that cover 29% of European Union (EU) territorial waters (*4*).

According to International Union for the Conservation of Nature (IUCN) guidelines, MPAs should be managed primarily for biodiversity conservation objectives (*5*) and exclude environmentally damaging industrial activities in any of their six protected-area categories (table S1) (*6*). With respect to commercial fisheries in MPAs, recent IUCN guidelines clarify that "any fishing gear used should be demonstrated to not significantly impact other species or other ecological values" (*7*). In the EU, a variety of different MPA types exist; although they may or may not adhere to nonbinding IUCN criteria (table S1), all feature biodiversity protection as a cross-cutting objective (table S2) and contribute toward international conservation targets (*8*). Yet, many MPA types do not address commercial fisheries, which are often regulated under the EU Common Fisheries Policy (table S2).

By far the most common industrial fishing method in Europe is trawling (*3*), which targets mainly bottom-associated fishes, often with a high rate of unwanted bycatch (fig. S1). This fishing technique has been identified as a threat to many endangered species in Europe, including most elasmobranchs (sharks, rays, and skates) (*9*), and has well-documented impacts on seafloor biodiversity (*10*), sensitive habitats, and indicator species (*11*). We directly quantified the extent of commercial trawling in the EU with respect to MPAs. We investigated associated changes in biodiversity using elasmobranchs as indicator species because they are particularly vulnerable to industrial exploitation and bycatch (*12*, *13*), have one of the highest extinction risk among marine fishes in Europe (*13*, *14*), and are generally not targeted by EU MPAs (table S2).

We quantified commercial trawling effort in the EU from automatic identification system (AIS) vessel tracking data at grid cells of 0.01° by 0.01° resolution for the year 2017, using a

[1]Department of Biology, Dalhousie University, Halifax, NS B3H 4R2, Canada. [2]Sharks of the Atlantic Research and Conservation Centre, Halifax, NS B3L 2Y5, Canada. [3]GEOMAR Helmholtz Centre for Ocean Research, 24105 Kiel, Germany.
*Corresponding author. Email: manuel.dureuil@dal.ca

neural network algorithm with 98% precision when run on test data (*3*). AIS is legally required for all EU industrial fishing vessels larger than 15 m, accounting for 94% of commercial trawling effort in our data. AIS data may miss some fraction of smaller artisanal boats, rendering our estimates of trawling effort conservative. All 727 MPAs included in our study were classified as 100% marine (no terrestrial components), were designated before 2017, and are registered in the World Database on Protected Areas, thus counting toward international biodiversity conservation targets.

We found that trawling efforts concentrated along coastlines of continental Europe and the United Kingdom (Fig. 1A), a pattern that is consistent with other data sources (*15*–*17*). Aggregate commercial effort exceeded 1 million hours of trawling in 2017, with more than 225,000 hours occurring inside MPAs (Table 1). Trawling intensity (hours per square kilometer) across the entire MPA network was 38% higher inside MPAs compared with unprotected areas (Fig. 1A and Table 1) and 46% higher inside MPAs when

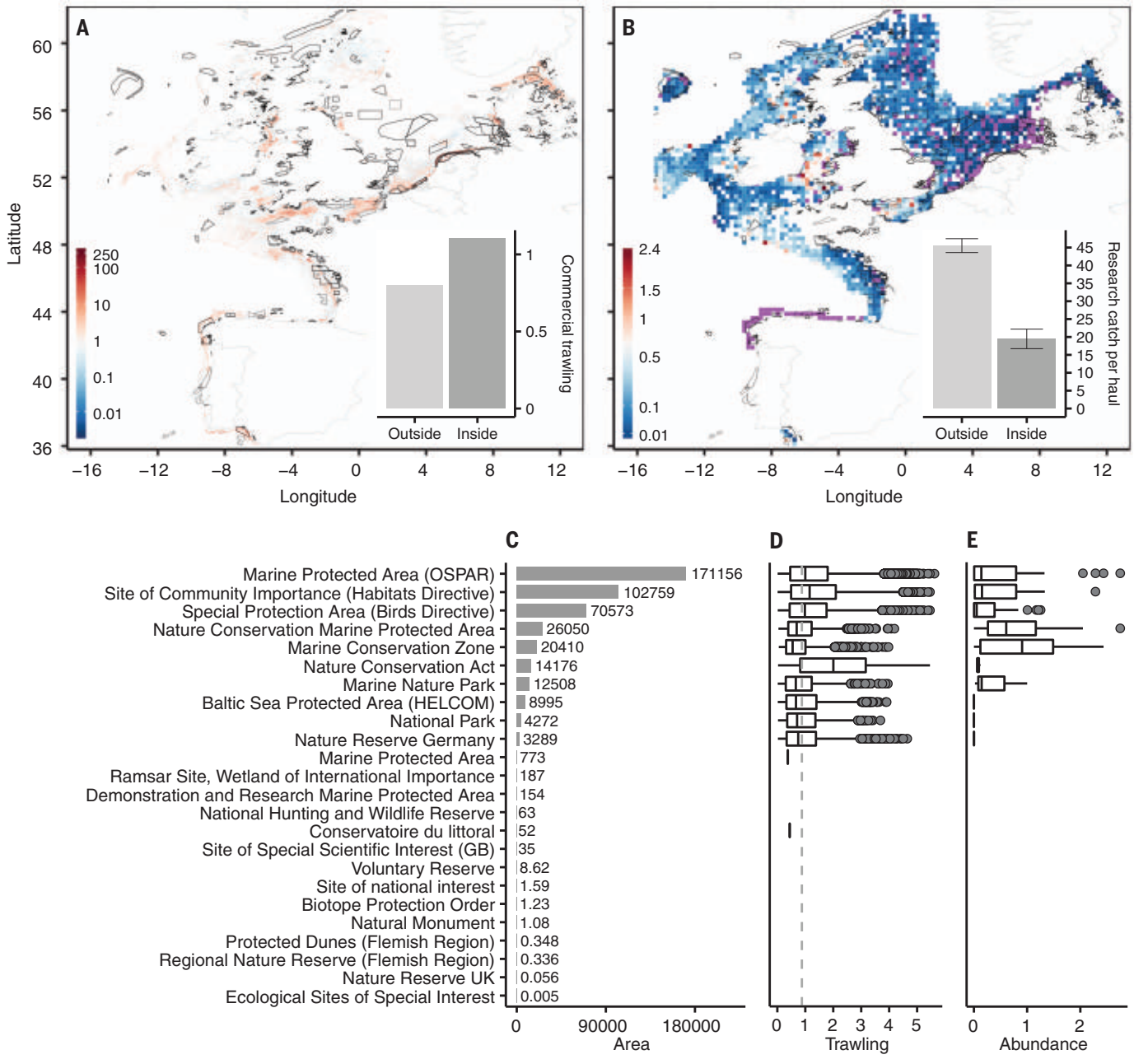

Fig. 1. Spatial distribution of marine protected areas, commercial trawling, and elasmobranchs in the European Union. (**A**) Commercial trawl fishing hours per 0.01° × 0.01° grid cell in 2017 (log_{10} color scale). Existing MPAs as of 2016 are outlined with black borders. (Inset) Aggregate commercial trawling intensity (hours per square kilometer) across MPAs versus unprotected areas. (**B**) Elasmobranchs scientific survey abundance expressed as normalized multispecies catch per unit effort per 0.25° × 0.25° grid cell (square-root transformed color scale). Grid cells in purple were surveyed, but no elasmobranchs were present. (Inset) The total elasmobranch research catch per haul inside versus outside MPAs, with 95% confidence limits. (**C**) MPA area (square kilometers), (**D**) commercial trawling intensity per trawled area (log_e hours per square kilometer trawled), and (**E**) elasmobranch abundance index for each MPA type. The gray dotted line in (D) indicates the median commercial trawling intensity in nonprotected areas for reference. No data in (E) indicates MPA types that were not scientifically surveyed.

comparing trawling intensity per trawled area (Table 1). This suggests that MPAs do not reduce fishing pressure under current management.

Elevated trawling intensity inside MPAs was especially pronounced in large-scale EU-wide MPA types, whereas untrawled MPAs were often small and designated by individual countries (Fig. 1, C and D, and fig. S2). Of all 727 MPAs, 489 were located in territorial waters (inside 12 nautical miles, 67%).

The MPAs with highest commercial trawling effort were typically located along the continental coastline (fig. S3), were recently designated, and in IUCN categories II or V (fig. S4). No trawling effort was detected in 295 of the 727 MPAs considered in this study, implying that at least 59% of MPAs experienced commercial trawling. Of these 295 MPAs, 171 were located in territorial waters. MPAs with no commercial trawling were generally smaller and older and had some IUCN category assigned, yet only 40% had management plans, compared with 60% of commercially trawled MPAs (table S3).

We addressed the cited IUCN criterion regarding fishing impacts on other species and ecological values (*7*) by assessing elasmobranchs inside and outside of MPAs and over time. We used randomized scientific trawl surveys by the International Council for the Exploration of the Sea (ICES) to estimate relative abundance for 20 elasmobranch species (table S4) from 1997 to 2016. Only surveys with gear types and depth appropriate to catch these species were considered. Data were normalized to avoid any one species dominating aggregate indices.

Elasmobranchs were generally rare across the study area, particularly in heavily trawled areas (Fig. 1B). The primary aggregations west and south of the British Isles are in agreement with previously described hot spots (*18*), and British MPAs also had the highest abundance of elasmobranchs (Fig. 1E and fig. S5). Elasmobranchs were caught in 141 (79%) of the 178 MPAs scientifically surveyed by ICES. Total elasmobranch catch per research haul was 2.3-fold higher outside MPAs than inside (Fig. 1B and Table 1), and a normalized multispecies abundance index was

Table 1. Commercial trawling effort and elasmobranch catch from research surveys inside and outside of MPAs. Commercial trawling is given in hours for the year 2017. Grid cells encompass 0.01° longitude by 0.01° latitude. Research catch from scientific surveys is given for the years 1997 to 2016 in total number of elasmobranch specimens per 60-min haul duration. The abundance index is given as normalized total multispecies catch per unit effort (msCPUE). Area (square kilometers) and commercial trawling hours for MPAs were calculated by subtracting the nonprotected area or hours from the total study area or hours, to avoid multiple counts for MPA types whose areas overlap.

	Outside MPAs	Inside MPAs	Total study area
Commercial trawling hours	848,703	227,718	1,0764,21
Area (km^2)	1,063,533	206,674	1,270,207
Number of 0.01° cells commercially trawled	335,167	57,085	392,252
Commercially trawled area (km^2)	252,886	43,812	296,698
Commercial trawling (hour km^{-2})	0.80	1.10	0.85
Commercial trawling (hour 0.01° $cell^{-1}$)	2.53	3.99	2.74
Commercial trawling (hour km^{-2} trawled area)	3.56	5.20	3.63
Research catch (number of elasmobranchs)	1,142,533	94,419	1,236,952
Research effort (number of hauls)	25,092	4,850	29,942
Total research catch per haul	45.53	19.47	41.31
Abundance index (msCPUE)	15.76	12.70	28.46

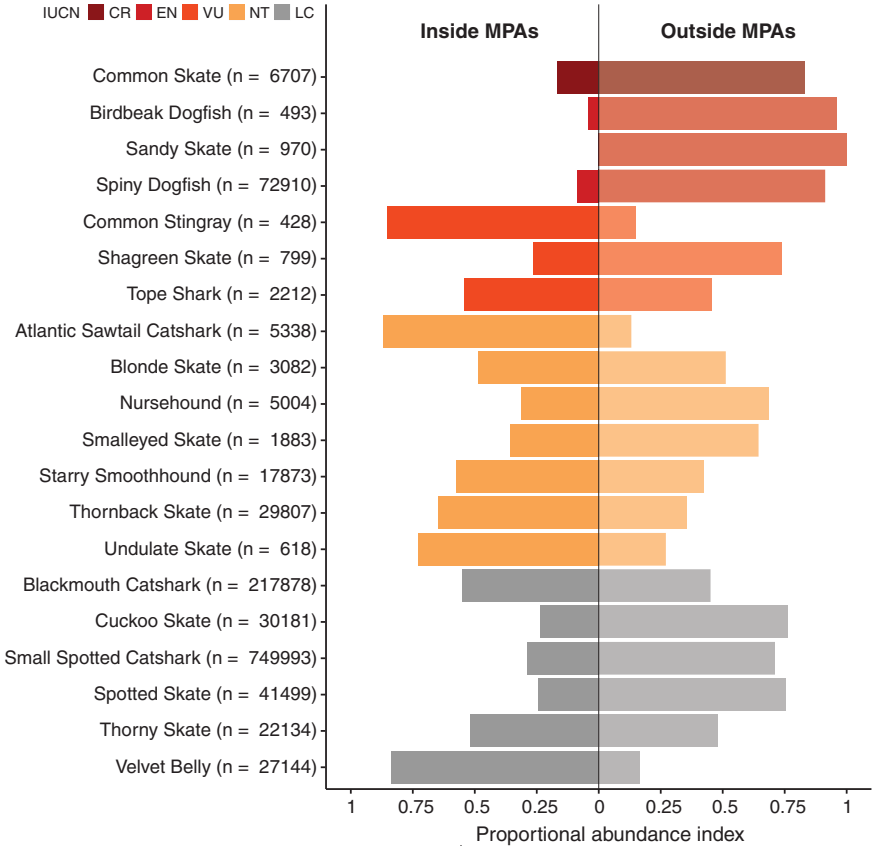

Fig. 2. Abundance of threatened species in relation to MPAs. Proportional scientific survey catch per unit effort is given for each elasmobranch species inside versus outside MPAs. The sample size for each species is given in brackets. Colors represent the IUCN Red List status per species. CR, critically endangered; EN, endangered; VU, vulnerable; NT, near threatened; LC, least concern.

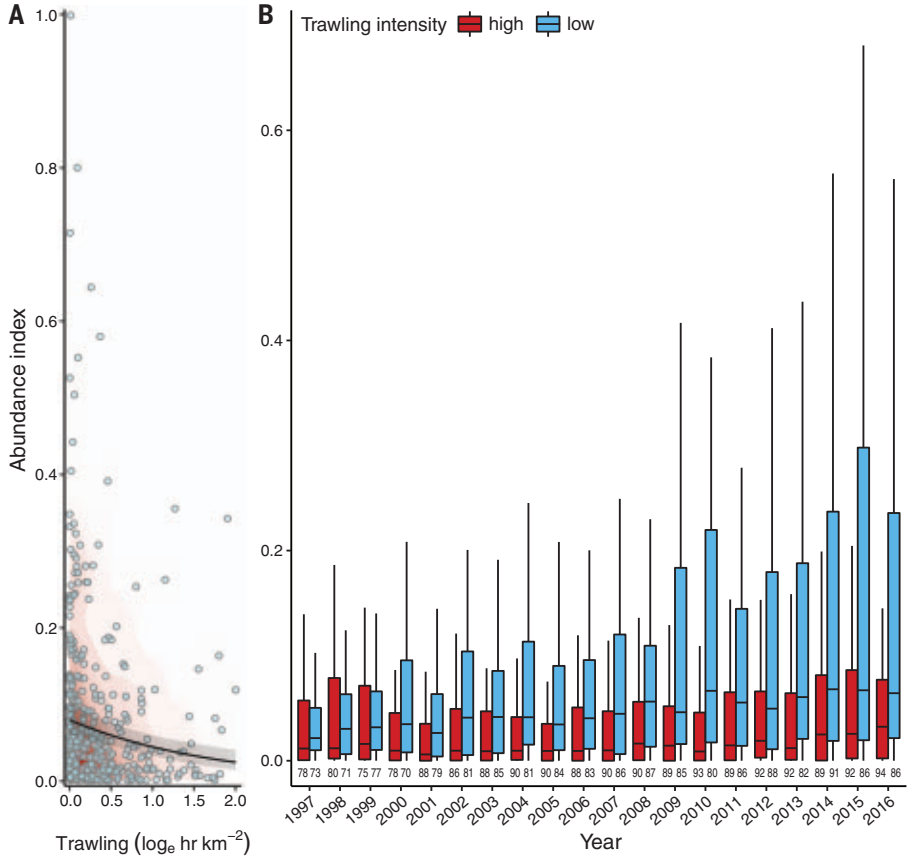

Fig. 3. Relationship between elasmobranch abundance and commercial trawling. (**A**) Elasmobranch abundance index (scaled multispecies catch per unit effort) versus commercial trawling intensity (log_e +1 hour km^{-2}) for all 392 ICES statistical management areas scientifically surveyed over the study area. The black line shows the predicted relationship of relative abundance and commercial trawling intensity for the average temperature and depth across management areas, with 95% confidence limits in gray (table S5). Red shading visualizes the density distribution of data points. (**B**) The temporal trend of elasmobranch mutispecies catch per unit effort is shown in ICES statistical management areas, with high (upper quartile, ≥0.616 hours km^{-2}) versus low (lower quartile, ≤0.037 hours km^{-2}) commercial trawling intensity. Sample size of ICES statistical areas for each year is indicated below.

24% higher outside of MPAs (Table 1). This conservation paradox was especially pronounced for endangered and critically endangered species, which were all ≥5-fold more abundant outside MPAs (Fig. 2).

Size, age, and management attributes of MPAs are all thought to drive conservation outcomes (*19*). Yet under current fishing pressure, only MPA size showed a positive trend with relative elasmobranch abundance in our study area (fig. S6). No clear pattern emerged between elasmobranch abundance and the age of the MPA, whether it was classified according to the IUCN categories or had a management plan (fig. S7). Of the 178 MPAs scientifically surveyed, only 24 (or 13%) had no commercial trawling present, and in 10 of those MPAs, elasmobranchs have been reported. These untrawled MPAs had indeed higher average elasmobranch abundance as compared with those of commercially trawled MPAs (fig. S8). Overall, elasmobranch abundance decreased with increasing trawling intensity both inside (fig. S9) and outside MPAs (fig. S10).

After controlling for spatial autocorrelation and potentially confounding effects of habitat and climate, we found that commercial trawling was the strongest predictor of elasmobranch relative abundance across the study area ($P < 0.001$) (Fig. 3A and table S5), with an average decrease of 69% across the observed gradient of trawling intensity (0 to 6.4 hours km^{-2}). Analyzing this relationship over time, we detected no trend in relative elasmobranch abundance in areas with high trawling intensity but detected higher and increasing abundance in areas with low trawling intensity (Fig. 3B). These results further support the notion that elevated trawling effort in MPAs negatively affects sensitive species and ecological values and is thus conflicting with IUCN criteria.

These data demonstrate that simply designating areas as MPAs has little benefit for those species that require protection the most. That most major EU MPA types exhibit high trawling intensity (Fig. 1D and fig. S2) and do not address industrial fishing (table S2) leaves protected zones vulnerable to fishing effort aggregation and associated biodiversity impacts documented here. Our finding that 59% of studied MPAs are fished industrially exceeds recently documented shortfalls on land, where 33% of protected areas are exposed to undue human pressures (*2*). A sectoral approach in which marine conservation measures are implemented by EU member states, but fisheries are managed by a Common Fisheries Policy, may drive this apparent disconnect. Last, the lack of transparent international MPA standards may further exacerbate this; we found that of 727 EU MPAs studied here, >50% do not report a management plan, >90% are not classified according to IUCN criteria, and >99% have no information on no-take areas, according to the World Database on Protected Areas. We suggest that better reporting and independent vetting of MPA standards is needed to assess the true value of the world's increasing MPA coverage.

Our results suggest that much of the EU's spatially impressive MPA network is being affected more heavily than nonprotected areas by industrial fishing and, as such, provides a false sense of security about positive conservation actions being taken. This is not an isolated occurrence, as data from terrestrial protected areas (*2*) and marine case studies from elsewhere suggest (*20*, *21*). Hence, internationally agreed-upon conservation targets under the Convention on Biological Diversity might be undermined by increasing human pressure, both on land and in the sea. Considerable work remains to be done to improve MPA policy, to develop and enforce minimum standards for MPA designation and classification, and to make MPA regulations and management stronger and more transparent. This would help to ensure that international targets for increased protected area coverage translate into tangible benefits for biodiversity conservation and the recovery of threatened marine wildlife.

REFERENCES AND NOTES

1. B. Worm, *Nature* **543**, 630–631 (2017).
2. K. R. Jones *et al.*, *Science* **360**, 788–791 (2018).
3. D. A. Kroodsma *et al.*, *Science* **359**, 904–908 (2018).
4. European Union, *The EU in the World 2016 Edition* (European Union, 2016).

5. J. Day *et al.*, *Guidelines for Applying the IUCN Protected Area Management Categories to Marine Protected Areas* (IUCN, 2012).
6. WCC-2016-Rec-102-EN, "Protected areas and other areas important for biodiversity in relation to environmentally damaging industrial activities and infrastructure development" (2016); https://portals.iucn.org/library/sites/library/files/resrecfiles/wcc_2016_rec_102_en.pdf.
7. International Union for Conservation of Nature, "Applying IUCN's Global Conservation Standards to Marine Protected Areas (MPA)" (2018); https://www.iucn.org/sites/dev/files/content/documents/applying_mpa_global_standards_v120218_nk_v2.pdf.
8. European Environment Agency, "Marine protected areas in Europe's seas An overview and perspectives for the future" (EEA, Copenhagen, 2015).
9. International Union for Conservation of Nature, The IUCN red list of threatened species version 3 (2017); www.iucnredlist.org.
10. S. F. Thrush, P. K. Dayton, *Annu. Rev. Ecol. Syst.* **33**, 449–473 (2002).
11. R. Cook *et al.*, *PLOS ONE* **8**, e69904 (2013).
12. N. K. Dulvy *et al.*, *eLife* **3**, e00590 (2014).
13. P. G. Fernandes *et al.*, *Nat. Ecol. Evol.* **1**, 0170 (2017).
14. A. Nieto *et al.*, *European Red List of Marine Fishes* (European Union, 2015).
15. International Council for the Exploration of the Sea, "Report of the Workshop on guidance on how pressure maps of fishing intensity contribute to an assessment of the state of seabed habitats (WKFBI)" (ICES, 2016).
16. O. R. Eigaard *et al.*, *ICES J. Mar. Sci.* **74**, 847–865 (2017).
17. International Council for the Exploration of the Sea, "EU request on indicators of the pressure and impact of bottom-contacting fishing gear on the seabed, and of trade-offs in the catch and the value of landings" (ICES, sr.2017.13, 2017).
18. J. R. Ellis, A. Cruz-Martínez, B. D. Rackham, S. I. Rogers, *J. Northwest Atl. Fish. Sci.* **35**, 195–213 (2005).
19. G. J. Edgar *et al.*, *Nature* **506**, 216–220 (2014).
20. J. E. Cramp, C. A. Simpfendorfer, R. L. Pressey, *Science* **360**, 723 (2018).
21. R. A. Magris, R. L. Pressey, *Science* **360**, 723–724 (2018).

ACKNOWLEDGMENTS

We are grateful for support by the Transatlantic Ocean System Science and Technology program that made this collaboration possible. Special thanks to T. Werner (Nature and Biodiversity Conservation Union) for very helpful comments and suggestions throughout the study. All authors gratefully acknowledge the open data policy and help from Global Fishing Watch, WDPA, and ICES. **Funding:** M.D. acknowledges support from the Sobey Fund for Oceans, the Nova Scotia Innovation and Research Entrance Graduate Scholarship, and Dalhousie University Department of Biology. Additional funding was provided by the Natural Science and Engineering Research Council of Canada and Google Earth Engine. **Author contributions:** All authors designed the study. M.D. compiled and analyzed elasmobranch data; K.B. compiled trawling data, which was analyzed by M.D. and K.B. M.D., K.B., and K.A.B. compiled and analyzed MPA data. All authors discussed the results and jointly wrote the manuscript. **Competing interests:** The authors declare no competing financial interests. **Data and materials availability:** All data are publicly available via the permanent web links provided in the supplementary materials.

SUPPLEMENTARY MATERIALS

www.sciencemag.org/content/362/6421/1403/suppl/DC1
Materials and Methods
Figs. S1 to S32
Tables S1 to S6
References (*22*–*33*)

2 May 2018; accepted 7 November 2018
10.1126/science.aau0561

PLANT SCIENCE

Root branching toward water involves posttranslational modification of transcription factor ARF7

Beatriz Orosa-Puente[1]*†, Nicola Leftley[2]†, Daniel von Wangenheim[2]†, Jason Banda[2], Anjil K. Srivastava[1], Kristine Hill[2]‡, Jekaterina Truskina[2,3], Rahul Bhosale[2], Emily Morris[2], Moumita Srivastava[1], Britta Kümpers[2], Tatsuaki Goh[2,4]§, Hidehiro Fukaki[4], Joop E. M. Vermeer[5,6], Teva Vernoux[3], José R. Dinneny[7], Andrew P. French[2,8], Anthony Bishopp[2], Ari Sadanandom[1]¶, Malcolm J. Bennett[2]¶

Plants adapt to heterogeneous soil conditions by altering their root architecture. For example, roots branch when in contact with water by using the hydropatterning response. We report that hydropatterning is dependent on auxin response factor ARF7. This transcription factor induces asymmetric expression of its target gene *LBD16* in lateral root founder cells. This differential expression pattern is regulated by posttranslational modification of ARF7 with the small ubiquitin-like modifier (SUMO) protein. SUMOylation negatively regulates ARF7 DNA binding activity. ARF7 SUMOylation is required to recruit the Aux/IAA (indole-3-acetic acid) repressor protein IAA3. Blocking ARF7 SUMOylation disrupts IAA3 recruitment and hydropatterning. We conclude that SUMO-dependent regulation of auxin response controls root branching pattern in response to water availability.

The soil resources plants require, such as water, are often distributed heterogeneously (*1*). To aid foraging, root development is responsive to the spatial availability of soil signals (*2*, *3*). Microcomputed tomography imaging revealed that soil-water contact affects root architecture, causing lateral roots (LRs) to form when roots are in direct contact with moisture (*4*, *5*). This adaptive branching response is termed hydropatterning (*4*, *5*). In this current study, we report the molecular mechanism controlling hydropatterning, revealing that core components of the auxin response machinery are targets for posttranslational regulation.

The hydropatterning response can be mimicked in vitro by growing seedling roots vertically on the surface of agar plates (*4*). Opposite sides of a root are either in contact with moisture (directly with the plate or via the meniscus) or exposed to air (fig. S1). To visualize whether primordia preferentially form on the side in contact with moisture, we transferred a root, including the gel it was growing on, into a light sheet fluorescence microscope to image young primordia and measure their angle of outgrowth with respect to the agar surface (fig. S1). This revealed that LRs preferentially emerge from the side of the root in contact with moisture (Fig. 1A).

What causes new primordia to form on the water-contact side of a root? Seedlings exposed to a hydropatterning stimulus exhibit an auxin response gradient across the root radius (*4*). Auxin regulates LR development (*6*). Auxin-responsive gene expression is regulated by a family of transcription factors termed auxin response factors (ARFs) (*7*). The model plant *Arabidopsis thaliana* contains five *ARF* transcriptional activating genes termed *ARF5*, *-6*, *-7*, *-8*, and *-19* (*8*). To determine which ARF gene(s) controls hydropatterning, we phenotyped loss-of-function alleles. ARF7 mutants (*8*, *9*) were all impaired (Fig. 1, A to C, and fig. S2), whereas hydropatterning was normal in mutants of other ARF family members tested (fig. S3). Hence, hydropatterning appears ARF7 dependent.

ARF7 regulates LR initiation (*6*, *8*, *10*, *11*). Network inference, chromatin immunoprecipitation–polymerase chain reaction (ChIP-PCR) validation, and transcriptomic studies have revealed that ARF7 controls the auxin-dependent expression of LR regulatory genes such as *LBD16* (fig. S4) (*12*). Like *ARF7*, *LBD16* loss-of-function alleles *lbd16-1* and *lbd16-2* exhibit a hydropatterning defect (fig. S5). ARF7 may therefore control hydropatterning in an *LBD16*-dependent

[1]Department of Biosciences, University of Durham, Durham DH1 3LE, UK. [2]Plant and Crop Sciences, School of Biosciences, University of Nottingham, Sutton Bonington LE12 5RD, UK. [3]Laboratoire Reproduction et Développement des Plantes, Univ Lyon, ENS de Lyon, F-69342, Lyon, France. [4]Department of Biology, Graduate School of Science, Kobe University, Kobe 657-8501, Japan. [5]Department of Plant and Microbial Biology, University of Zurich, CH-8008 Zurich, Switzerland. [6]Developmental Biology, Wageningen University and Research, Wageningen, Netherlands. [7]Department of Biology, Stanford University, Stanford, CA 94305, USA. [8]School of Computer Science, Jubilee Campus, University of Nottingham, Nottingham NG8 1BB, UK.
*Present address: School of Biological Sciences, University of Edinburgh, Edinburgh EH9 3FF, UK. †These authors contributed equally to this work. ‡Present address: Center for Plant Molecular Biology – ZMBP, University of Tübingen, D - 72076 Tübingen, Germany. §Present address: Graduate School of Science and Technology, Nara Institute of Science and Technology, 8916-5 Takayama, Ikoma 630-0192, Japan.
¶Corresponding author. Email: ari.sadanandom@durham.ac.uk (A.S.); malcolm.bennett@nottingham.ac.uk (M.J.B.)

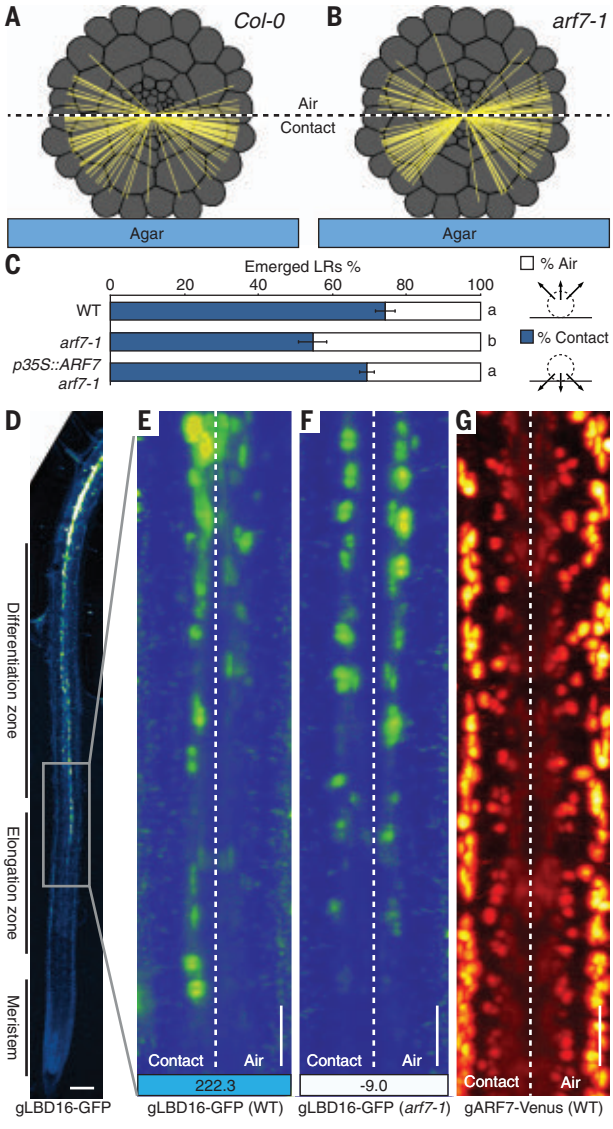

Fig. 1. *Arabidopsis* root branching toward water is ARF7 dependent. (**A** and **B**) Cross-section schematic of a root growing on agar. The LR primordia outgrowth angle (yellow lines) in respect to the agar surface is quantified from 3D light sheet microscopy images of WT (A) and *arf7-1* (B) plants. (**C**) Hydropatterning bioassay of WT, *arf7*, and *arf7* overexpressing ARF7 (*p35S::ARF7*). Data shown are mean values ± SE. Statistical differences were analyzed on the percent of emerged LRs emerging toward either contact or air using an analysis of variance, Tukey's HSD test ($P < 0.05$); statistically similar groups are indicated using the same letter. (**D**) Confocal image of *Arabidopsis* root tip expressing *gLBD16-GFP*. Gray boxed area highlights onset of *LBD16-GFP* expression in the elongation zone. (**E** to **G**) Maximum intensity projections of radial reslices obtained from light sheet fluorescent microscopy–multiview imaging show the gene expression pattern of *LBD16-GFP* in WT (E), *arf7* (F), and *ARF7::ARF7-Venus* (G) on the contact versus air sides. The numbers at the bottom of (E) and (F) display the index of asymmetry. Positive values correspond to an earlier expression beginning on the contact side; negative values show asymmetry toward the air side. Details are explained in figs. S1 and S6 to S8. Scale bars, 50 μm.

manner. *LBD*-like genes are differentially expressed in maize during hydropatterning (*5*). To determine whether *LBD16* is differentially expressed in response to a hydropatterning stimulus by ARF7, we monitored spatial expression of a *gLBD16–green fluorescent protein* (*GFP*) reporter (*13*). *LBD16-GFP* was first detected in the elongation zone (Fig. 1D and movie S1) in a subset of cells [termed xylem pole pericycle (XPP) founder cells, from which primordia originate], consistent with this reporter being an early marker for LR development (*13*). In *Arabidopsis*, LRs originate from pericycle cells positioned above either xylem pole (*6*). We tested whether *gLBD16-GFP* was differentially expressed in XPP cell files closest to the agar. To mark which side of a root was exposed to air, we overlaid samples with agar with a low melting point and containing fluorescent beads and then imaged from multiple angles using light sheet microscopy (figs. S6 to S8). Reconstructed root images revealed preferential *gLBD16-GFP* expression in XPP cell nuclei earlier on one side of wild-type (WT) roots (Fig. 1E). Asymmetric *gLBD16-GFP* expression was disrupted in *arf7-1* (Fig. 1F), consistent with the mutant's hydropatterning defect (Fig. 1C). Quantification of *LBD16-GFP* distribution in WT and *arf7-1* revealed this reporter was differentially expressed in an ARF7-dependent manner (fig. S8, A to D and F). To test whether asymmetric *LBD16* expression is essential for hydropatterning, the constitutive 35S promoter was used to drive *LBD16* expression in *lbd16* (fig. S9). Expression of *35S:LBD16* failed to rescue the *lbd16* hydropatterning defect (in contrast to *LBD16:LBD16-GFP*). Hence, asymmetric *LBD16* expression is essential for hydropatterning.

We next tested whether LBD16-dependent hydropatterning was controlled by means of differential ARF7 expression by using transcriptional and translational *ARF7pro::ARF7-VENUS* reporters (figs. S10 and S11). In contrast to *gLBD16-GFP* (Fig. 1, E and F), ARF7 reporters did not exhibit differential expression in LR stem cells (Fig. 1G). To test whether ARF7 was a target of posttranslational regulation, ARF7 was constitutively expressed (using the 35S promoter) in *arf7-1*. This revealed *35S:ARF7* could rescue *arf7-1* hydropatterning (Fig. 1C and fig. S12). Hence, ARF7 appears to control hydropatterning by means of a posttranslational (rather than transcriptional) mechanism.

ARF7 contains posttranslational regulatory motifs including four putative sites for addition of small ubiquitin-like modifier (SUMO) proteins at lysine residues (K104, K151, K282, and K889) (Fig. 2A). SUMO, unlike ubiquitin, can modify the function (rather than abundance) of target proteins (*14*). We confirmed ARF7 is a target for SUMOylation by coexpressing GFP- and hemagglutinin (HA) epitope–tagged ARF7 and SUMO sequences (Fig. 2B). Addition of SUMO to ARF7 is abolished after replacing lysine with arginine in all four ARF7 SUMOylation motifs (in *gARF7-*$^{4K/R}$; Fig. 2B).

To test the importance of ARF7 SUMOylation for LR development and hydropatterning, we expressed SUMOylatable gARF7 and non-SUMOylatable *gARF7-*$^{4K/R}$ transgenes in *arf7-1*. Bioassays revealed *arf7* hydropatterning could be rescued by WT *gARF7* (Fig. 2, C and D, and fig. S13) but not by *gARF7-*$^{4K/R}$ (Fig. 2, E and F, and fig. S14). Nevertheless, *gARF7-*$^{4K/R}$ (like *gARF7*) remained capable of restoring *arf7* LR density to a WT level (Fig. 2F). Hence, ARF7-$^{4K/R}$ remained functional but unable to regulate hydropatterning. Quantification of *LBD16-GFP* distribution in *gARF7* versus *gARF7-*$^{4K/R}$ *arf7-1* revealed that this reporter was differentially expressed only in the presence of SUMOylatable ARF7 (fig. S8, A to C and E and G). We conclude ARF7 SUMOylation is required for hydropatterning.

How does SUMOylation modify ARF7 activity? ARF7 is rapidly SUMOylated after auxin treatment (Fig. 2G). One ARF7 SUMOylation site (K151) is located within the DNA binding domain (Fig. 2A) (*15*). SUMOylation may attenuate auxin-induced ARF7 DNA binding activity. Time course ChIP-PCR analysis revealed ARF7 transiently interacts with the *LBD16* promoter after auxin treatment (fig. S15). Furthermore, ChIP-PCR assays performed on *LBD16* and *LBD29* target promoters detected higher DNA binding by ARF7-$^{4K/R}$-GFP than WT ARF7-GFP (fig. S16). Hence, SUMOylation negatively regulates ARF7 DNA binding activity.

ARF7 transcriptional activity is negatively regulated by Aux/IAA (indole-3-acetic acid) repressor proteins (*16*). Aux/IAA proteins such as IAA3/SHY2 and IAA14/SLR control ARF7 activity during LR development (*16*, *17*). Like *arf7-1*, *IAA3* loss-of-function allele *shy2-31* causes an LR hydropatterning defect (Fig. 3A and fig. S17). Thus, we tested whether interactions among ARF7, IAA3/SHY2, and IAA14/SLR were SUMO

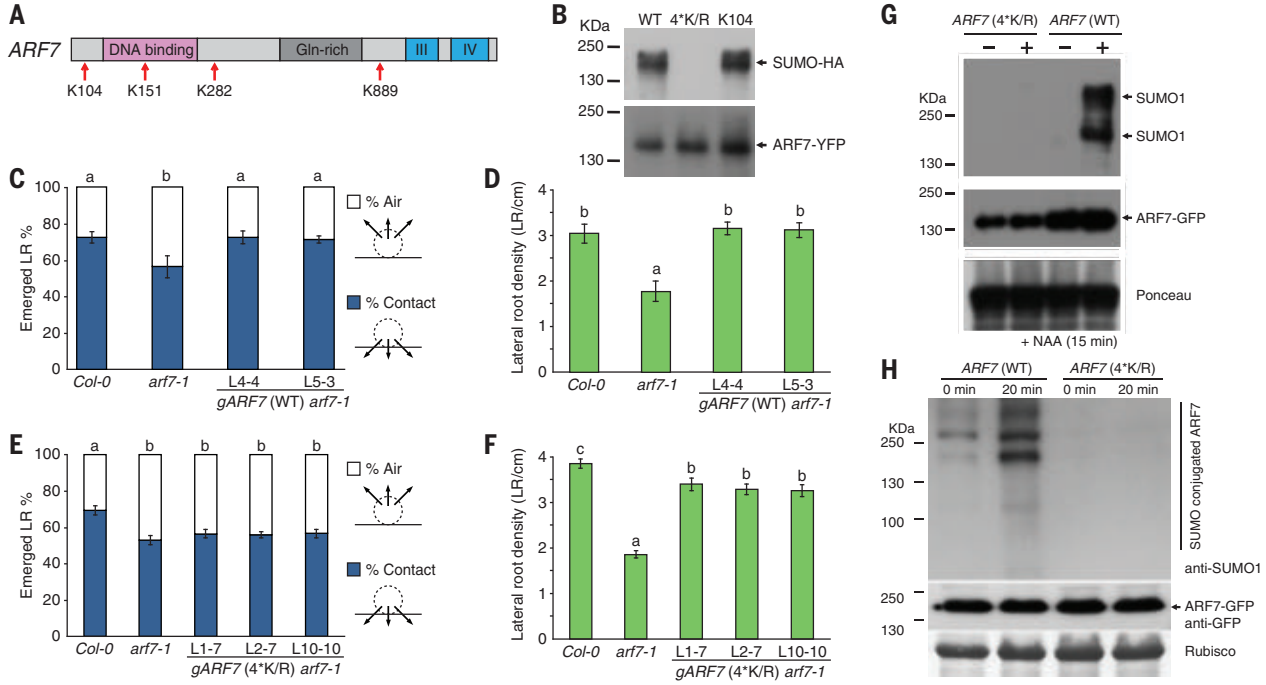

Fig. 2. ARF7 SUMOylation regulates hydropatterning and DNA binding affinity. (**A**) Schematic of ARF7 domains and four predicted SUMO sites K104, K151, K282, and K889. (**B**) Replacing all ARF7 SUMO site lysine with arginine residues in ARF7-GFP(4*K/R) blocks SUMOylation with HA-SUMO1 (but not WT ARF7 or single SUMO K104) in transient expression assays. YFP, yellow fluorescent protein. (**C** and **D**) Bioassays reveal that two independent transgenic lines expressing WT gARF7 can rescue *arf7-1* hydropatterning (C) and LR density defects (D). *n* LR = 196 (Col-0), 78 (arf7-1), 292 (L4-4), and 231 (L5-3); *n* plants = 7 (Col-0), 5 (arf7-1), 10 (L4-4), and 9 (L5-3). (**E** and **F**) Bioassays reveal that three independent transgenic lines expressing gARF7(4*K/R) cannot rescue *arf7-1* hydropatterning (E) but do restore LR density (F). *n* LR = 374 (Col-0), 268 (arf7-1), 198 (L1-7), 286 (L2-7), and 206 (L10-10); *n* plants = 12 (Col-0), 16 (arf7-1), 8 (L4-4), 11 (L5-3), and 8 (L10-10). Data are mean values ± SE, and statistics were performed as in Fig. 1C. (**G**) Immunoprecipitation reveals that ARF7-GFP [but not ARF7-GFP(4*K/R)] is rapidly SUMOylated 15 min after naphthaleneacetic acid (NAA) treatment. (**H**) Immunoprecipitation reveals that ARF7-GFP [but not ARF7-GFP(4*K/R)] is rapidly SUMOylated 20 min after seedlings were removed from their agar plates.

Fig. 3. SHY2 interacts with ARF7 in a SUMO-dependent manner to control hydropatterning. (**A**) Bioassay reveals that *IAA3/SHY2* mutant allele *shy2-31* does not exhibit a hydropatterning response. Data shown are mean ± SE. Letters indicate a significant difference compared with WT (*Ler*) roots based on Student's *t* test ($P < 0.05$). *n* LR = 208 (Ler) and 604 (shy2-31); *n* plants = 7 (Ler) and 19 (shy2-31). (**B**) The *IAA3* (but not *IAA14*) sequence contains a putative SIM, suggesting that IAA3 could bind SUMOylated ARF7. (**C**) Transient expression of IAA3/SHY2–HA (WT-SIM) or IAA3/SHY2–HA (SIM mutant) with ARF7-GFP or ARF7-GFP(4*K/R), followed by immunoprecipitation and western analysis, revealed that IAA3 interacts with ARF7 in a SIM- and SUMO-dependent manner. (**D**) Phenotyping *Arabidopsis* seedlings expressing *shy2-2* ± SIM by using the endodermal *CASP1* promoter revealed *CASP1:shy2-2* (WT) blocks LR branching (top), whereas *CASP1:shy2-2* (non-SIM) branch normally (bottom). Seedlings are from six independent lines termed SIM-containing *CASP1:shy2-2* (WT L1, L2, and L3) and non–SIM-containing *CASP1:shy2-2* (SIML1, L2, and L3). (**E**) Schematic summarizing the SUMO-dependent ARF7 model for hydropatterning, in which ARF7 is SUMOylated on the air side of the root, resulting in an interaction with IAA3 that inhibits LR initiation. On the contact side of the root, ARF7 is not SUMOylated, enabling the transcriptional factor to activate expression of genes involved in LR initiation.

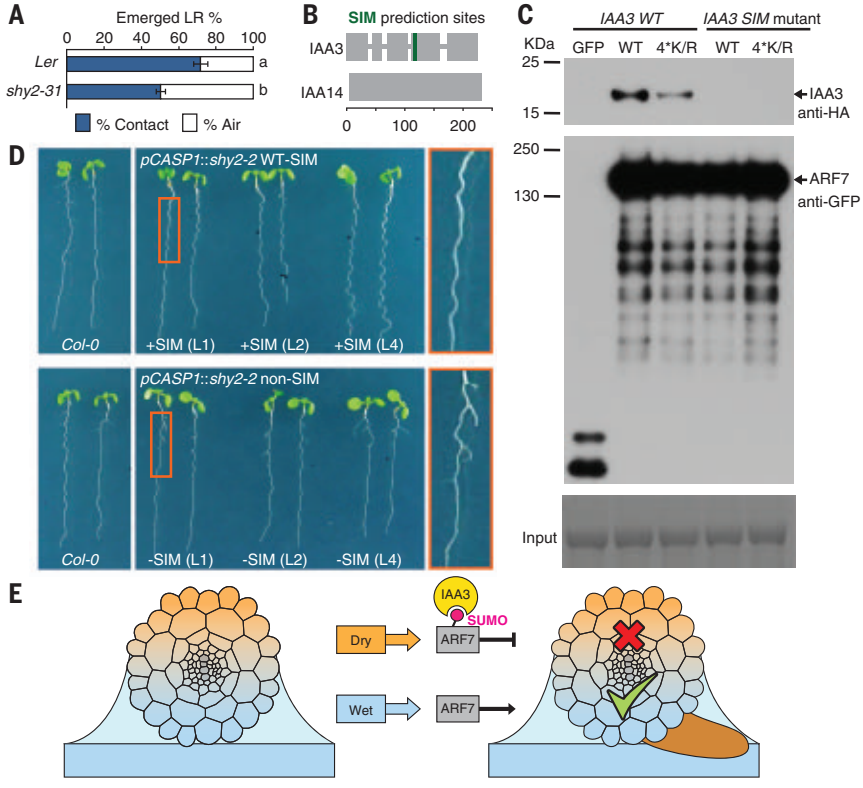

dependent. Pull-down assays revealed that ARF7-GFP interacted with IAA3/SHY2 and IAA14/SLR proteins (fig. S18). In contrast, non-SUMOylatable ARF7-$^{4K/R}$ largely failed to pull down IAA3/SHY2. However, both forms of ARF7 interacted with IAA14/SLR (fig. S19). Hence, interaction between ARF7 and IAA3/SHY2 (but not IAA14/SLR) depends on the residues that regulate ARF7 SUMOylation.

Bioinformatic analysis revealed that *IAA3/SHY2* (but not *IAA14/SLR*) contained a SUMO interaction motif (SIM) (Fig. 3B). With its SIM domain mutated, interaction between IAA3 and WT ARF7 was abolished (Fig. 3C). Nevertheless, the IAA3 SIM mutant protein could interact with the TIR1 auxin receptor and TPL transcriptional repressor (figs. S19 and S20). Hence, mutating the SIM site differentially affects IAA3's ability to interact with SUMOylated ARF7 but not with other partners.

To assess the functional importance of the *IAA3* SIM sequence in planta, we engineered transgenic plants overexpressing *shy2-2* with or without SIM sequences. We examined the impact of the SIM sequence on the suppression of root branching characteristic of *shy2-2* mutant plants (*18*), a phenotype not dependent on hydropatterning. We drove overexpression of the *shy2-2* gene with the endodermal-specific CASP promoter. More root branching is evident in roots of plants expressing p*CASP:shy2-2* without the SIM sequence than in plants expressing p*CASP:shy2-2* with the SIM sequence (Fig. 3D). Thus, overexpression of shy2-2 in endodermis can block ARF7-dependent LR development, but only if the SIM sequence is included.

SUMO modifiers are added and removed from target proteins by E3 ligases and SUMO proteases, respectively. In *Arabidopsis*, OTS1 and OTS2 proteases cleave off SUMO from nuclear localized proteins (*19*). Pull-down assays revealed ARF7 is a direct target for OTS1 (fig. S21). Our bioassays revealed that the *ots1 ots2* mutant exhibits a hydropatterning defect (fig. S22). Hence, hydropatterning appears dependent on OTS1 and OTS2 function. These SUMO proteases are labile when plants are exposed to abiotic stress, causing their SUMOylated target proteins to accumulate (*19*, *20*). Indeed, transiently exposing *gARF7-GFP* seedlings to 20 minutes outside an agar plate resulted in a rapid increase in ARF7 SUMOylation (Fig. 2H). Hence, the absence (rather than the presence) of water stimulates this posttranslational response. Modeling suggests a substantial differential in water potential is generated across the air and contact axis of the root (*5*). We hypothesize that this triggers SUMOylated ARF7 on the air side of roots to recruit IAA3 and create a transcriptional repressor complex, thereby blocking auxin-responsive gene expression associated with LR initiation (Fig. 3E). Conversely, because IAA3 cannot be recruited by non-SUMOylated ARF7 in root cells on the contact side, this population of transcription factors can induce expression of genes like *LBD16* to trigger organ initiation (Fig. 3E).

Our study has revealed how environmental inputs modulate the auxin response machinery. The SUMO-mediated posttranslational regulation of auxin signaling operates on top of the specificity provided from distribution of the hormone itself and the expression patterns of individual regulatory components. Thus, auxin regulation controls root branching pattern in response to water availability, building a root architecture that optimizes access to water.

REFERENCES AND NOTES

1. A. Hodge, *New Phytol.* **162**, 9–24 (2004).
2. B. D. Gruber, R. F. H. Giehl, S. Friedel, N. von Wirén, *Plant Physiol.* **163**, 161–179 (2013).
3. E. C. Morris *et al.*, *Curr. Biol.* **27**, R919–R930 (2017).
4. Y. Bao *et al.*, *Proc. Natl. Acad. Sci. U.S.A.* **111**, 9319–9324 (2014).
5. N. E. Robbins 2nd, J. R. Dinneny, *Proc. Natl. Acad. Sci. U.S.A.* **115**, E822–E831 (2018).
6. J. Lavenus *et al.*, *Trends Plant Sci.* **18**, 450–458 (2013).
7. T. Ulmasov, J. Murfett, G. Hagen, T. J. Guilfoyle, *Plant Cell* **9**, 1963–1971 (1997).
8. Y. Okushima *et al.*, *Plant Cell* **17**, 444–463 (2005).
9. R. M. Harper *et al.*, *Plant Cell* **12**, 757–770 (2000).
10. M. A. Moreno-Risueno *et al.*, *Science* **329**, 1306–1311 (2010).
11. B. Péret *et al.*, *Nat. Cell Biol.* **14**, 991–998 (2012).
12. J. Lavenus *et al.*, *Plant Cell* **27**, 1368–1388 (2015).
13. T. Goh, S. Joi, T. Mimura, H. Fukaki, *Development* **139**, 883–893 (2012).
14. E. S. Johnson, *Annu. Rev. Biochem.* **73**, 355–382 (2004).
15. D. R. Boer *et al.*, *Cell* **156**, 577–589 (2014).
16. T. Goh, H. Kasahara, T. Mimura, Y. Kamiya, H. Fukaki, *Philos. Trans. R. Soc. Lond. B Biol. Sci.* **367**, 1461–1468 (2012).
17. K. Swarup *et al.*, *Nat. Cell Biol.* **10**, 946–954 (2008).
18. J. E. M. Vermeer *et al.*, *Science* **343**, 178–183 (2014).
19. L. Conti *et al.*, *Dev. Cell* **28**, 102–110 (2014).
20. L. Conti *et al.*, *Plant Cell* **20**, 2894–2908 (2008).

ACKNOWLEDGMENTS

We acknowledge T. Guilfoyle for insightful discussions and dedicate this manuscript in his memory. We thank J. Dewick for assisting with the submission of this manuscript and C. Testerink for providing seed for the *lbd16-2* mutant allele. **Funding:** This work was supported by awards from the Biotechnology and Biological Sciences Research Council (grants no. BB/G023972/1, BB/R013748/1, BB/L026848/1, BB/M018431/1, BB/P016855/1, BB/M001806/1, BB/M012212); European Research Council (ERC) FUTUREROOTS Advanced grant 294729; ERC SUMOrice Consolidator grant 310235; Leverhulme Trust grant RPG-2016-409; ANR 2014-CE11-0018 Serrations grant; AuxID PICS grant from the CNRS; a joint INRA/University of Nottingham PhD grant to J.T.; J.E.M.V. is supported by the Swiss National Science Foundation (PP00P3_157524 and 316030_164086) and the Netherlands Organization for Scientific Research (NWO 864.13.008). H.F. was supported by a Grant-in-Aid for Scientific Research on Priority Areas (19060006) from the MEXT, Japan. **Author contributions:** B.O.-P., N.L., D.v.W., J.B., K.H., H.F., J.E.M.V., T.V., J.R.D., A.P.F., A.B., A.S., and M.J.B. designed experiments; B.O.-P., N.L, D.v.W., J.B., A.K.S., K.H., J.T., R.B., E.M., M.S., B.K., and T.G. performed experiments; and B.O.-P., N.L., D.v.W., A.B., A.S., and M.J.B. wrote the manuscript. **Competing interests:** Authors declare no competing interests. **Data and materials availability:** No restrictions are placed on materials, such as materials transfer agreements. Details of all data, code, and materials used in the analysis are available in the main text or the supplementary materials.

SUPPLEMENTARY MATERIALS

www.sciencemag.org/content/362/6421/1407/suppl/DC1
Materials and Methods
Figs. S1 to S22
Tables S1 to S3
References (*21*–*28*)
Movie S1

19 June 2018; accepted 6 November 2018
10.1126/science.aau3956

SOCIAL NETWORKS

The strength of long-range ties in population-scale social networks

Patrick S. Park[1]*, Joshua E. Blumenstock[2], Michael W. Macy[3,4]*

Long-range connections that span large social networks are widely assumed to be weak, composed of sporadic and emotionally distant relationships. However, researchers historically have lacked the population-scale network data needed to verify the predicted weakness. Using data from 11 culturally diverse population-scale networks on four continents—encompassing 56 million Twitter users and 58 million mobile phone subscribers—we find that long-range ties are nearly as strong as social ties embedded within a small circle of friends. These high-bandwidth connections have important implications for diffusion and social integration.

Over the last 40 years, the social sciences have embraced the counterintuitive thesis that individuals are more likely to acquire new information from a weak social tie to an acquaintance than from a strong tie with a close friend or family member (*1*). The reason is straightforward: Information that one acquires from within a "small circle of friends" is more likely to be redundant than information acquired from an acquaintance in a distant region of a social network. Thus, the prevailing consensus, dating back to Granovetter's seminal thesis (*1*), is that there is a trade-off between the diversity of information acquired through weak bridging ties (linking individuals whose social circles do not overlap) and the volume of information, or bandwidth, acquired through strong, structurally embedded ties (between

[1]Ross School of Business, University of Michigan, Ann Arbor, MI 48109, USA. [2]School of Information, University of California, Berkeley, Berkeley, CA 94720, USA. [3]Information Science Department, Cornell University, Ithaca, NY 14853, USA. [4]Department of Sociology, Cornell University, Ithaca, NY 14853, USA.
***Corresponding author. Email: patpark@umich.edu (P.P.); mwm14@cornell.edu (M.M.)**

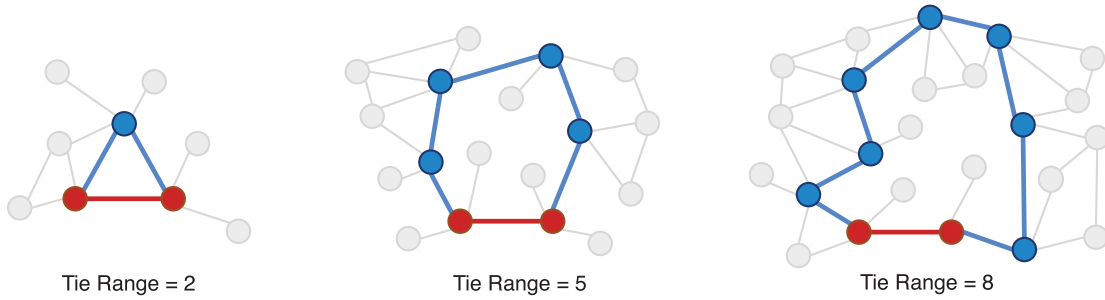

Fig. 1. Tie range is defined as the second-shortest (blue) path length between two connected (red) nodes.

individuals with at least one friend in common) (*2*–*4*).

This diversity-bandwidth trade-off is empirically supported by studies showing that tie strength decreases as social ties become less embedded, i.e., as they connect individuals with fewer network "neighbors" in common (*5*). By extrapolation, tie strength should decrease further between individuals who do not even have "neighbors of neighbors" in common; that is, as the network distance, or range of the tie, increases. Tie range is defined as the second-shortest path length, i.e., the number of intermediary ties required to reach from an individual node to its neighbor if their direct tie were removed (*1*, *6*) (Fig. 1).

The diversity-bandwidth trade-off has been widely tested and confirmed for small networks with embedded and unembedded short-range ties (*2*). Until recently, however, it has been difficult to empirically test whether the trade-off applies to long-range ties because of the inability to obtain data for the population-scale social networks in which long-range ties can be found. In theory, a long-range tie could be found in a relatively small ring lattice. However, the tendency for social networks to be highly clustered means that long range-ties are rarely observed in networks with no more than a few thousand nodes, such as villages, schools, and workplaces. Thus, the existence of long-range ties has been largely a postulate of the "small world" puzzle of "six degrees of separation," which refers to the minimum number of intermediate ties between any two people on the planet. Watts and Strogatz (*7*) used simulations to show that the six degrees phenomenon could be explained by long-range ties, but the ties themselves were never directly observed. Since then, several studies have confirmed the six (or fewer) degrees of separation in a variety of contexts, including email networks (*8*), MSN Messenger (*9*), and Facebook (*10*). Although these results are consistent with the postulated existence of long-range ties, their prevalence and strength have not been directly measured, and other studies demonstrate that heavy-tailed degree distributions could also account for six degrees, even in the absence of long-range ties (*11*, *12*).

We report direct evidence of long-range ties in social networks, made possible by analyzing 11 population-scale communication networks from culturally and economically diverse populations spanning four continents: three independent nationwide phone networks (in Afghanistan, Rwanda, and a large European country), as well as 56 million Twitter users in eight countries (fig. S1) with relatively high Twitter penetration (United States, United Kingdom, France, Netherlands, Japan, South Korea, Singapore, and Turkey). Details of data collection and measurement are provided in supplementary materials (SM) section 1.

The data confirmed, at a global scale, previous findings that social ties tend to be weaker (lower call volume and fewer tweet exchanges) when people share fewer common neighbors (*1*, *5*, *13*). This was evident in all 11 networks (fig. S2). However, our focus was on testing whether tie strength declined with tie range. Tie strength declined as range increased from two (the theoretical lower bound) to four (the upper bound on what is likely to be observable in small local networks) in all three phone networks and most of the Twitter networks (Fig. 2).

What happened above range four, the region that is difficult to observe without population-scale networks, was especially notable. Instead of declining further, tie strength increased with the network distance spanned, especially in the phone networks (Fig. 2B). Figure S3 shows that ties with range six or greater were approximately as strong as embedded ties with one common neighbor in all three phone networks and in three out of the eight Twitter networks (Japan, South Korea, and the Netherlands).

We refer to these high-bandwidth long-range ties as network "wormholes," borrowing the term from cosmology to capture the possibility that, though relatively rare (fig. S4), long-range ties can provide high-bandwidth shortcuts across vast reaches of network space. To illustrate, Fig. 3 depicts Singapore's Twitter network (the smallest of the networks), in which a tie is composed of one or more reciprocated @mentions. The wormholes, defined here as ties above range six and above median tie strength, are shown with curved yellow edges and represent only 0.46% of all ties. The inset shows how network wormholes can substantially shrink networks by directly linking nodes that would otherwise be connected by a long chain of intermediary links.

The unexpected strength of long-range ties has implications for two related puzzles on the diffusion of new information. Figure 4 addresses these puzzles by decomposing Fig. 2 into the within- and between-individual variation. The within-individual analysis compares the strength of each individual's short- and long-range ties. This analysis addresses Granovetter's (*1*) original puzzle: From whom are we more likely to receive new information? By contrast, the between-individual analysis compares the average tie strength between people who have mostly long-range ties with those whose ties are mostly short-range. This corresponds more closely to the follow-up puzzle posed by Aral and Van Alstyne (*2*): Who is more likely to receive new information? The U-shape pattern was more pronounced in the within-individual analysis than the overall results in Fig. 2; across all 11 networks, people interacted with their most socially distant neighbors nearly as much as they did with their embedded neighbors. The between-individual U-shape was less consistent across networks (see SM section 2).

To verify the robustness of these findings, we ran a battery of tests, described in detail in SM section 3. To begin, Fig. 2 reports the generality of our results across alternative communication platforms and across countries with widely divergent cultural and economic conditions. Twitter and phone networks differ fundamentally in user demographics, relational structure (multilateral distribution versus dyadic conversation), mode of expression (text versus voice), population penetration (partial versus full), openness (public versus private), and incremental cost (free versus paid). Despite these differences, we nevertheless observed the same phenomenon: strong ties that span extreme network distances. This ubiquity suggests that the result does not reflect an idiosyncrasy of the country or communication platform, such as the opportunity on Twitter to form strong relationships with erstwhile strangers, a preference for unembedded relationships in individualistic cultures, or demographic biases in technology use.

We also tested robustness across several alternative measures of tie strength (SM sections 3.2 to 3.4): the mean duration and frequency of calls on the phone networks (fig. S5), the affective strength of message content (fig. S6), and the reciprocity of @mentions (fig. S7) on Twitter (*1*, *14*). In all instances, we observed that tie strength eventually increased with range, confirming the pattern in Fig. 2. Finally, we found little support for the possibility that the results were an artifact of missing data (see SM section 3.5). In principle, strong embedded ties could be incorrectly measured as network wormholes if data were missing on common neighbors. This possibility is mitigated by the existence of

network wormholes in all 11 observed networks despite differences in population coverage, from approximately 3.5% of the 2014 French internet population on Twitter, to more than 90% of all phone lines in the European phone network. Nevertheless, we tested the effects of missing data by randomly removing nodes and edges from the observed networks. We found that missing data do not explain the strength of long-range ties (fig. S8) or cause embedded ties to appear to be long-range (figs. S9 and S10). The reason is straightforward: For a range two tie to appear to be range three because of missing data, all common neighbors would need to be missing; if even a single common neighbor were observed, the tie would remain range two. For the range to appear longer than three, the number of necessary missing neighbors or missing ties increases exponentially.

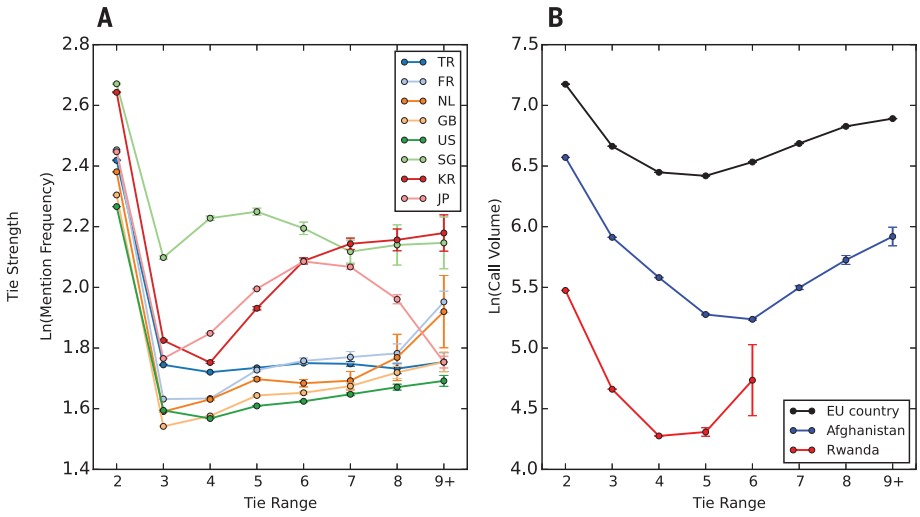

Fig. 2. The strength of social ties by tie range. Results are shown for eight Twitter networks (**A**) and three phone networks (**B**). Tie strength [mean and 99% confidence interval (CI)] is measured as the log of the frequency of bidirected @mentions (A) and the log of total bidirected call volume in seconds (B).

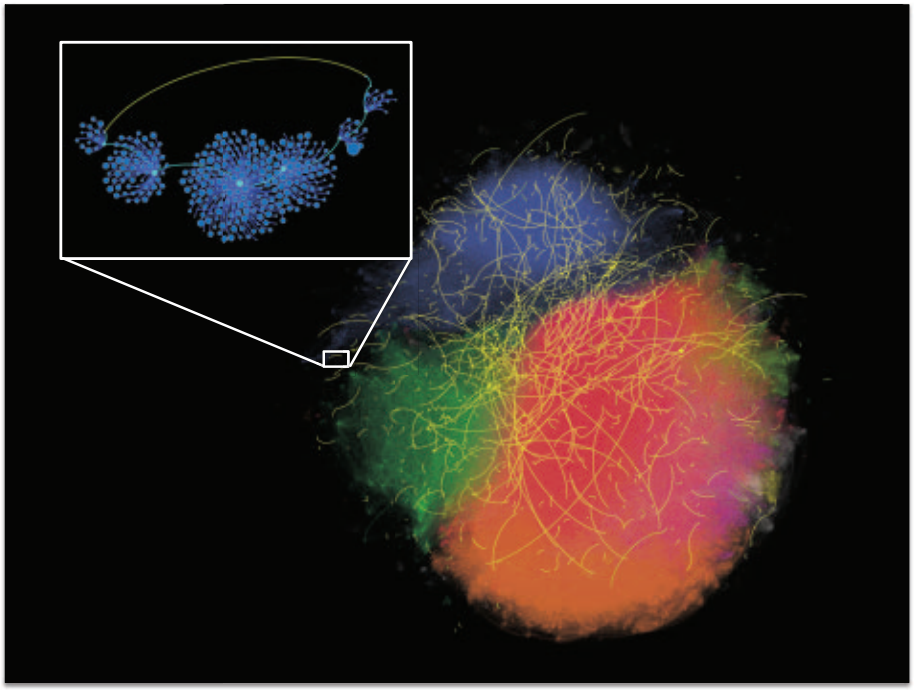

Fig. 3. Network wormholes in Singapore's Twitter network. Each dot represents an individual, and each edge represents a bidirected @mention. Nodes and edges are colored according to membership in distinct network communities (*31*). A sample of network wormholes (with range six or above and above-median tie strength) is shown in yellow. The inset highlights a single wormhole of range eight, i.e., the second-shortest path between the yellow nodes requires traversing eight intermediary ties (blue edges). The sizes of the nodes in the inset are proportional to the number of network neighbors.

The discovery of high-bandwidth ties that span vast network distances poses intriguing puzzles that call for further research into their formation and surprising strength. Although a comprehensive investigation is beyond the scope of this report, SM section 4 explores the cultural context, spatial distance, social function, and personal attributes of these ties to look for possible clues, which we briefly summarize.

First, the content of the messages exchanged over strong, long-range Twitter ties displayed no single characteristic pattern; see table S1 for a few example conversations. Topic modeling of message content suggested that network wormholes frequently involved religious and cultural topics (tables S2 to S4) as well as social process words (e.g., "buddy," "talk"), but very few work-related words (e.g., "job", "boss"). See SM section 4 and fig. S11 for details.

Second, temporal analysis suggested that network wormholes were more likely to be interpersonal social relationships rather than instrumental or work-related (e.g., between a service provider and client). In particular, the increase in tie strength with longer range was driven by ties that were active during non–working hours (fig. S12).

Finally, the strength of long-range ties was not a byproduct of physical distance (SM section 4.3). Prior work has shown that tie probability declines with geographic distance (*15*–*18*), which may have helped promote the widely held but historically untestable assumption that tie strength decreases with range. Figures S13 and S14 show that physical and network distances were conceptually and empirically distinct dimensions. Results were consistent with previous findings that tie strength generally decreases with spatial distance, but the pattern was the opposite for network distance. Notably, the change in tie strength with range largely followed the patterns in Fig. 2, even among ties with shorter spatial distance.

Future research should target three possible explanations for the formation and strength of long-range ties. First, long-range ties frequently connected low-degree nodes on the periphery of the network (fig. S15). This may indicate that limited time or attention induced people to choose between a small number of close friends and many weakly tied acquaintances (*19*), and those with few neighbors had fewer chances to have neighbors (or neighbors of neighbors) in common. Second, Burt (*20*) found that weak ties are more likely to break over time. If social and spatial mobility breaks weaker ties, the stronger ones that remain become longer range as weaker indirect paths erode (see SM section 4.4). For example, in a book about his friendship with his high school calculus teacher, Strogatz (*21*) tells

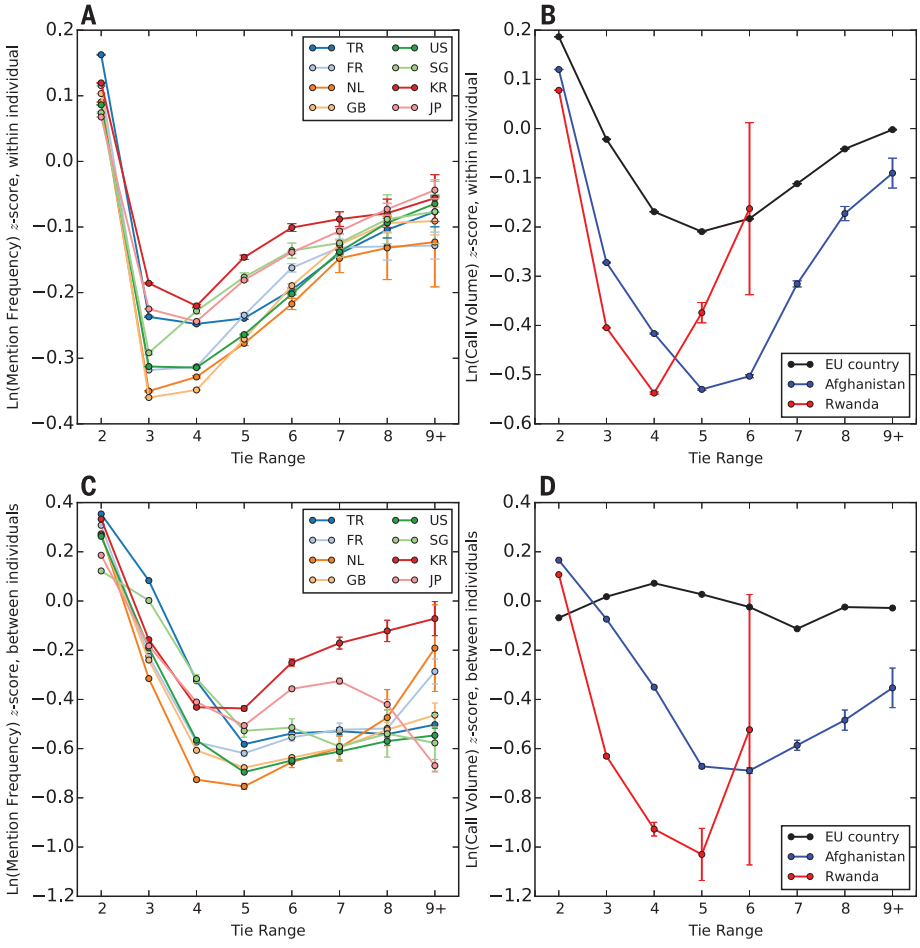

Fig. 4. Within-individual and between-individual decomposition of tie strength (mean and 99% CI) by tie range. The first row shows the within-individual relationship for Twitter (**A**) and phone networks (**B**), where the z-score is calculated by standardizing each tie with the individual's average and standard deviation of tie strength. The second row shows the between-individual relationship for Twitter (**C**) and phone networks (**D**), where the z-score is calculated by standardizing each individual's average tie strength with the grand mean and standard deviation of the entire network. The tie range in the second row represents the average range of each individual's ties, rounded to the nearest integer.

the story of their strong tie that remained strong despite the increasing separation of their evolving social networks over time. This winnowing process might also explain the heavy-tailed range distribution (fig. S16). Finally, research on multiplexity and multidimensional homophily (*22*) indicates that social networks tend to be composed of many different types of relationships (friendship, kinship, work, politics, religion, hobbies, etc.). The discovery of network wormholes suggests that these layers may not be fully integrated, e.g., a strongly tied religious or political neighbor might not be introduced to one's workplace colleagues (*23*).

The surprising strength of long-range ties was found in a wide range of cultures, communication platforms, and measures of network structure and survived a battery of robustness tests. But do these network wormholes matter, given their relative rarity? SM section 5 presents a counterfactual experiment that compares the observed Singapore network with an otherwise identical network in which tie strengths were permuted inversely with range (as would be expected with a diversity-bandwidth trade-off). The counterfactual network greatly increased the average shortest path length (i.e., the mean strength-weighted geodesic distance) between two random nodes, relative to the observed network with wormholes (fig. S17). In simulation experiments, contagions also spread more slowly and reached fewer nodes when wormholes were removed from the network (fig. S18). These effects, combined with the tendency for network wormholes to link peripheral nodes, support recent studies that question the dependence of diffusion on "hubs" (*24*, *25*). Finally, the stronger emotional affect observed in longer-range Twitter ties highlights the potential implications for the spread of emotional contagions (*13*, *26*) such as moral indignation, political celebration, ideological fervor, happiness, and value judgments (*27*) that in turn may influence voting (*28*), participation in risky social movements, and health (*29*, *30*).

REFERENCES AND NOTES

1. M. S. Granovetter, *Am. J. Sociol.* **78**, 1360–1380 (1973).
2. S. Aral, M. Van Alstyne, *Am. J. Sociol.* **117**, 90–171 (2011).
3. R. Reagans, B. McEvily, *Adm. Sci. Q.* **48**, 240–267 (2003).
4. A. Tiwana, *Strateg. Manage. J.* **29**, 251–272 (2008).
5. J.-P. Onnela *et al.*, *Proc. Natl. Acad. Sci. U.S.A.* **104**, 7332–7336 (2007).
6. G. Kossinets, D. J. Watts, *Science* **311**, 88–90 (2006).
7. D. J. Watts, S. H. Strogatz, *Nature* **393**, 440–442 (1998).
8. P. S. Dodds, R. Muhamad, D. J. Watts, *Science* **301**, 827–829 (2003).
9. J. Leskovec, E. Horvitz, in *Proceeding of the 17th international conference on World Wide Web - WWW '08* (ACM Press, New York, 2008), pp. 915–924.
10. L. Backstrom, P. Boldi, M. Rosa, J. Ugander, S. Vigna, in *Proceedings of the 3rd Annual ACM Web Science Conference on - WebSci '12* (ACM Press, New York, 2012), pp. 33–42.
11. A.-L. Barabási, R. Albert, *Science* **286**, 509–512 (1999).
12. L. A. Amaral, A. Scala, M. Barthelemy, H. E. Stanley, *Proc. Natl. Acad. Sci. U.S.A.* **97**, 11149–11152 (2000).
13. A. D. I. Kramer, J. E. Guillory, J. T. Hancock, *Proc. Natl. Acad. Sci. U.S.A.* **111**, 8788–8790 (2014).
14. E. Gilbert, K. Karahalios, in *Proceedings of the 27th international conference on Human factors in computing systems - CHI 09* (ACM Press, New York, 2009), pp. 211–220.
15. G. Daraganova *et al.*, *Soc. Networks* **34**, 6–17 (2012).
16. R. Lambiotte *et al.*, *Physica A* **387**, 5317–5325 (2008).
17. D. Liben-Nowell, J. Novak, R. Kumar, P. Raghavan, A. Tomkins, *Proc. Natl. Acad. Sci. U.S.A.* **102**, 11623–11628 (2005).
18. P. Preciado, T. A. B. Snijders, W. J. Burk, H. Stattin, M. Kerr, *Soc. Networks* **34**, 18–31 (2012).
19. J. Saramäki *et al.*, *Proc. Natl. Acad. Sci. U.S.A.* **111**, 942–947 (2014).
20. R. S. Burt, *Soc. Networks* **22**, 1–28 (2000).
21. S. Strogatz, *The Calculus of Friendship* (Princeton Univ. Press, 2009).
22. M. McPherson, L. Smith-Lovin, J. Cook, *Annu. Rev. Sociol.* **27**, 415–444 (2001).
23. P. Block, T. Grund, *Netw. Sci. (Camb Univ Press)* **2**, 189–212 (2014).
24. S. González-Bailón, *Decoding the Social World: Data Science and the Unintended Consequences of Communication* (MIT Press, 2017).
25. P. Barberá *et al.*, *PLOS ONE* **10**, e0143611 (2015).
26. J. H. Fowler, N. A. Christakis, *BMJ* **337**, a2338 (2008).
27. L. Muchnik, S. Aral, S. J. Taylor, *Science* **341**, 647–651 (2013).
28. R. M. Bond *et al.*, *Nature* **489**, 295–298 (2012).
29. D. McAdam, *Am. J. Sociol.* **92**, 64–90 (1986).
30. D. Centola, *Science* **329**, 1194–1197 (2010).
31. V. D. Blondel, J.-L. Guillaume, R. Lambiotte, E. Lefebvre, *J. Stat. Mech. Theory Exp.* **2008**, P10008 (2008).
32. P. S. Park, J. E. Blumenstock, M. W. Macy, Replication Data for: "The Strength of Long-Range Ties in Population-Scale Social Networks," Harvard Dataverse, Version 1 (2018); https://doi.org/10.7910/DVN/NPRNCC

ACKNOWLEDGMENTS

We are especially grateful to N. Eagle, who provided access to phone data for this study. We thank I. Kloumann, B. Lee, and M. Park for helpful feedback and N. Bhat, M. Flashman, X. Ma, S. Ogden, and Y. Zhao for research assistance. **Funding:** This study was supported by the U.S. National Science Foundation (SES-1226483 and SES-1434164), the Air Force Office of Scientific Research (FA9550-15-1-0036), and the Defense Advanced Research Project Agency (HR0011-18-C0049). **Author contributions:** M.W.M. and P.S.P. designed the study; J.E.B., M.W.M., and P.S.P. collected the data; P.S.P. analyzed the data; and J.E.B., M.W.M., and P.S.P. wrote the manuscript. **Competing interests:** All authors declare no competing interests. **Data and materials availability:** The de-identified edgelists with edge weight, tie range, and geographic distance to construct the eight Twitter networks and related scripts are available at (*32*).

SUPPLEMENTARY MATERIALS

www.sciencemag.org/content/362/6421/1410/suppl/DC1
Materials and Methods
Figs. S1 to S18
Tables S1 to S4
References (*33*–*55*)

2 August 2018; accepted 6 November 2018
10.1126/science.aau9735

PALEOBOTANY

A hidden cradle of plant evolution in Permian tropical lowlands

Patrick Blomenkemper[1], Hans Kerp[1], Abdalla Abu Hamad[2], William A. DiMichele[3], Benjamin Bomfleur[1]*

The latitudinal biodiversity gradient today has deep roots in the evolutionary history of Earth's biota over geologic time. In the marine realm, earliest fossil occurrences at low latitudes reveal a tropical cradle for many animal groups. However, the terrestrial fossil record—especially from drier environments that are thought to drive evolutionary innovation—is sparse. We present mixed plant-fossil assemblages from Permian equatorial lowlands in present-day Jordan that harbor precocious records of three major seed-plant lineages that all became dominant during the Mesozoic, including the oldest representative of any living conifer family. These finds offer a glimpse of the early evolutionary origins of modern plant groups in disturbance-prone tropical habitats that are usually hidden from observation.

Tropical regions today harbor the greatest biodiversity on our planet, with species richness decreasing toward the poles (*1*). Explanations for this phenomenon lie not only in present-day climate gradients and continent configurations, but also in the deep evolutionary histories of organism groups over geologic time (*2*, *3*). One hypothesis is that equatorial ecosystems function as "evolutionary cradles"—a term introduced by botanist G. Ledyard Stebbins (*4*)—that generate new lineages at higher rates than extratropical regions. Earliest originations in such equatorial cradles have been well documented for marine organisms (*2*, *3*, *5*, *6*). To what degree the evolution of terrestrial biota follows a similar pattern, however, remains controversial (*3*, *7*); paleobotanical evidence in particular (*8*–*10*) is subject to strong preservation bias, partly because drought-prone equatorial habitats that are thought to spawn plant evolutionary innovations rarely preserve fossils (*3*, *11*, *12*). Here, we report a Permian flora from the Middle East that holds the earliest records of three major seed-plant lineages, among these the oldest fossil record of any living family of conifers.

Toward the end of the Paleozoic, the vegetation of the supercontinent Pangea differentiated into four major floristic regions: the hot and dry equatorial expanse of central Pangea (Euramerica); a realm of humid tropical rainforest stretching mainly across the large island chains in the eastern Tethys (Cathaysia); and two temperate to cool realms in the northern (Angara) and southern (Gondwana) mid- to high latitudes (*12*). Permian plant-bearing deposits from coastal tropical lowlands, however, yield mixed floras with typical members from different floral provinces (*12*–*14*), indicating that these seemingly separate geographic realms were climate-controlled biomes with plant communities adapted to local habitat conditions (*12*, *13*). From a macro-evolutionary perspective, the xeromorphic, drought-tolerant components of such mixed floras are especially interesting because these assemblages occasionally contain so-called "Methuselah taxa" (*12*)—rare and unexpectedly early occurrences that reveal new lineages and evolutionary innovations to be much older than previously thought and that normally elude detection in the fossil record because they thrived in drier environments with very limited preservation potential (*11*, *12*, *15*).

We collected plant-fossil assemblages from the Umm Irna Formation, an up to ~85-m-thick succession of Permian alluvial deposits exposed along the eastern shore of the Dead Sea in Jordan (fig. S1 and table S1). What makes these fossil assemblages notable among coeval mixed floras is the quality of preservation; many of the fossils are mummified with pristinely preserved cuticles (*14*, *16*), the microscopic diagnostic features of which enable a systematic placement even in the absence of fertile organs (*17*). The Umm Irna Formation is intercalated with erosional contacts between the Cambrian Umm Ishrin Sandstone Formation below and the basal Triassic Ma'in Formation above. Independent evidence from plant macro- and microfossils (*14*, *16*), from conodont and foraminifer biostratigraphy (*18*), from sequence stratigraphy (*18*), and from lithostratigraphic correlation with other well-dated successions on the Arabian Plate (*16*) together provides a robust age framework (*19*). The Permian-Triassic boundary occurs at or immediately above the base of the Ma'in Formation, and the underlying Umm Irna Formation is Lopingian (Late Permian), most likely Changhsingian (latest Permian), in age (*18*, *19*). During that time, the region was an equatorial coastal lowland along the western Tethys margin at a latitude of about 15°S and had a hot, subhumid climate with pronounced dry seasons (*14*, *16*, *18*, *19*). The depositional environment was a richly structured riverscape that harbored varied plant communities, depending on local habitat conditions (*19*). As a result, different sedimentary subenvironments have preserved distinct plant-fossil assemblages (*19*) (table S1).

Of particular note are fossil assemblages from point-bar and abandoned-channel deposits (*19*) that contain diverse accumulations of plant remains washed in from surrounding riparian forests and from drier habitats. These assemblages have now yielded the earliest bona fide records of three major seed-plant lineages that became dominant in the Mesozoic: Corystospermales, Bennettitales, and Podocarpaceae (Fig. 1). Previous reports of *Dicroidium*, a type of corystospermalean foliage, from the Umm Irna Formation remained controversial because the genus is traditionally regarded as an index fossil for the Gondwanan Triassic and because fertile organs were lacking (*20*). New material, including numerous large frond fossils (Fig. 1A) and the affiliated fertile organs (Fig. 1C), now unequivocally confirms the presence of corystosperms in the Permian of Jordan. So far, at least six *Dicroidium* species can be distinguished. Bennettitales is an extinct group of seed plants with a cycadlike growth habit and compound flowerlike reproductive organs. These plants have been known mainly from the Mesozoic, the earliest record being from the Middle Triassic (*21*). Because of their sophisticated mode of sexual reproduction, which in many ways resembled that of modern angiosperms, some authors consider Bennettitales to be basal members of the group of plants that gave rise to crown-group angiosperms more than 100 million years later (*22*, *23*). We collected large fragments of entire-margined *Nilssoniopteris* leaves and of pinnate *Pterophyllum* fronds (Fig. 1, D and I), as well as dispersed cuticle pieces, all showing the syndetocheilic type of stomata (Fig. 1, J to M) diagnostic of Bennettitales (*17*, *21*).

Podocarpaceae is the second-largest extant family of conifers and was an important component of Mesozoic floras worldwide (*17*, *24*). Before now, the earliest records of the group were from the Lower Triassic (*24*). Conifer twigs from Jordan bear helically arranged, single-veined needles that are twisted near the base to become flattened into a single plane (Fig. 1, E, N, and O). Their cuticles (Fig. 1, F to H) show overall smooth outer surfaces and longitudinally oriented, paratetracytic stomata in rows and tight chains (Fig. 1, G and H), a combination of macro- and micromorphological features that is diagnostic of Podocarpaceae (*25*). Other single-veined but shorter-leafed forms (Fig. 1, N and O) similar to the common Mesozoic foliage taxon *Elatocladus* may also belong to Podocarpaceae or to another modern conifer family (*24*). Further unexpected finds are various remains of zamiinean cycads such as *Ctenis* (Fig. 1, P and Q) and *Pseudoctenis* (Fig. 1, R and S), including leaflets whose characteristic epidermal anatomy (Fig. 1, R and S) agrees closely with

[1]Palaeobotany Research Group, Institute of Geology and Palaeontology, University of Münster, Münster, Germany. [2]Department of Applied and Environmental Geology, The University of Jordan, Amman, Jordan. [3]Department of Paleobiology, NMNH Smithsonian Institution, Washington, DC, USA.
*Corresponding author. Email: bbomfleur@uni-muenster.de

those of Late Triassic forms (*17*, *26*). Notably, however, all these precocious occurrences of typically post-Paleozoic seed-plant lineages occur intermixed with characteristic Paleozoic plant taxa, such as Noeggerathiales (*Discinites*), Nystroemiales (*Nystroemia*), rare gigantopterids, Laurasian Permian conifers (*Quadrocladus* and *Otovicia*), and putative ginkgophytes (*Rhipidopsis*) (fig. S2 and table S1) (*17*).

Plant assemblages from deposits representing permanently waterlogged back-swamp environments that occur locally in the Umm Irna Formation (*19*) are, by contrast, dominated by plants characteristic of the tropical ever-wet Cathaysian flora, including various gigantopterid seed ferns (*Gigantopteris*, *Gigantonoclea*, and *Fascipteris*), the sphenophyte *Lobatannularia*, and putative ginkgophytes (*Saportaea* and *Rhipidopsis*) (fig. S2 and table S1), with occasional occurrences of small *Glossopteris* leaves (fig. S2)—the classical index fossil of the Permian southern Gondwana flora (*13*, *17*).

Altogether, the peculiar plant-fossil record of the Umm Irna Formation not only reveals a melting pot of plant communities considered typical of different Paleozoic floristic regions, but also yields precocious records of three major seed-plant lineages: the chiefly Mesozoic groups Bennettitales and Corystospermales, as well as Podocarpaceae, which marks the earliest fossil record of any living group of conifers. Before the discoveries from the Umm Irna Formation, all three groups were thought to have first appeared some time during the Early or Middle Triassic in the wake of the end-Paleozoic mass extinction (*14*, *16*, *17*, *21*, *24*).

The unexpectedly early fossil records for these groups will aid in calibrating the age framework of seed-plant phylogenies and push back divergence-age estimates for major lineages still deeper into the Paleozoic. Moreover, the biostratigraphic ranges of Bennettitales, Corystospermales, and Podocarpaceae alike can now be traced back across the Permian-Triassic boundary––the date that marks the greatest mass extinction of animal groups in Earth's history (*27*). From a bottom-up perspective, our finds thus add at least three groups to the growing list of major plant lineages that did not vanish at the end of the Paleozoic, confirming that land plants—and perhaps terrestrial biotas as a whole—were less affected by global biotic crises than previously thought (*28*). Instead of a sudden, catastrophic extinction followed by a restoration of ecosystems with entirely new groups, the vegetation changes across the Permian-Triassic boundary appear more and more to reflect the gradual demise of particular groups and the takeover of vacated resource spaces by others that had already existed long before, but under conditions unfavorable for fossilization. In this respect, the later evolutionary trajectories of the various plant groups that occur side by side in the Umm Irna Formation reveal a distinct pattern of extinction selectivity: Competitively favored groups that dominated wetland floras in stable, mesic environments—including both Cathaysian (gigantopterid) and Gondwanan (glossopterid) taxa—would vanish with the warming climates in the aftermath of the end-Permian biotic crisis (*29*). More stressed and disturbance-prone habitats, by contrast, sheltered the evolutionary cradles for highly adaptable seed-plant groups that would not only persist through the crisis interval, but also emerge to become some of the most iconic plant groups of the Mesozoic. Bennettitales, Cycadales, and podocarp conifers persisted in equatorial latitudes and expanded their ranges "out of the tropics" (*5*, *6*) during the Triassic, reaching worldwide distribution during the later Mesozoic (*17*, *24*). The *Dicroidium* plants even appear to have abandoned their tropical cradle. They migrated southward and became the dominant canopy trees in temperate forests across the mid- to high-latitude regions of Gondwana during the Triassic (*14*, *16*, *17*), before they themselves would eventually disappear in the Jurassic and leave their youngest-known fossil remains in polar refugia of present-day Antarctica (*30*).

The Umm Irna Formation allows a glimpse into a rich evolutionary cradle of modern seed-plant lineages. The geological and paleoenvironmental setting of this fossil deposit renders a more precise search image for future paleontological exploration. We anticipate that targeted search in similar

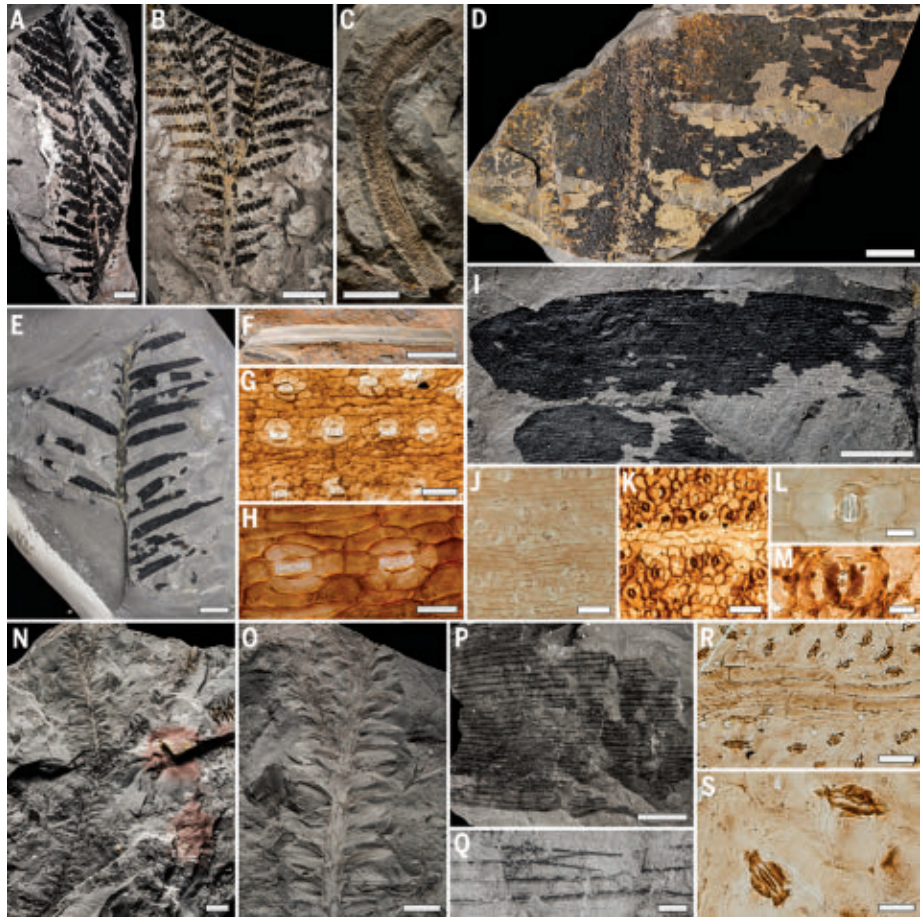

Fig. 1. Selected precocious records of iconic Mesozoic plant groups in the Late Permian Umm Irna Formation, Jordan. Pictured are Corystospermales (**A** to **C**), Bennettitales (**D** and **I** to **M**), Podocarpaceae (**E** to **H**), *Elatocladus* twigs (**N** and **O**), and zamiinean cycads (**P** to **S**). [(A) and (B)] Almost complete fronds of *Dicroidium robustum* (A) (sample JO15-4-120) and *D. irnense* (B) (JO15-4-4); (C) a *Pteruchus* pollen organ (JO17-7-63); [(D) and (I)] frond fragments of *Pterophyllum* [(D) JO15-5-115 and (I) JO15-5-71]; [(E) to (H)] a shoot fragment (E) (JO15-5-39), an isolated needle (F) (JO17-5-6), and in situ cuticles [(G) and(H)] (JO17-5-6SL-001 and -002) of an undescribed podocarp; [(J) and (L)] a bennettitalean cuticle with characteristic syndetocheilic stomata [(L) JO17-4B-92/94SL-001 to -005], obtained in situ from a *Pterophyllum* leaflet (JO17-4B-92); [(K) and (M)] a dispersed bennettitalean cuticle with syndetocheilic stomata (M) found among residues of bulk-macerated rock samples (JO15-5A-50SL-011, -SL-013, and -SL-014); [(N) and (O)] part and counterpart detail of an *Elatocladus*-type conifer branch [(N) JO15-5-52 and (O) JO15-5-71]; [(P) and (Q)] *Ctenis*-like cycad leaf with anastomosing veins (Q) (JO17-5A-27); [(R) and (S)] dispersed *Pseudoctenis* cuticles found among residues of bulk-macerated rock sample (JO15-5-52SL-003 and -005). Scale bars, [(A) and (B)], 2 cm; [(C) to (F), (I), and (N) to (P)], 1 cm; (Q), 1 mm; [(G), (J), (K), and (R)], 100 μm; (H), 50 μm; [(L), (M), and (S)], 20 μm.

paleo-equatorial lowland settings will help uncover the early origins of evolutionary innovation.

REFERENCES AND NOTES

1. K. J. Gaston, *Nature* **405**, 220–227 (2000).
2. D. Jablonski, *Nature* **364**, 142–144 (1993).
3. P. D. Mannion, P. Upchurch, R. B. J. Benson, A. Goswami, *Trends Ecol. Evol.* **29**, 42–50 (2014).
4. G. L. Stebbins, *Flowering Plants: Evolution above the Species Level* (Belknap Press, 1974).
5. D. Jablonski, K. Roy, J. W. Valentine, *Science* **314**, 102–106 (2006).
6. D. Jablonski *et al*., *Proc. Natl. Acad. Sci. U.S.A.* **110**, 10487–10494 (2013).
7. J. T. Weir, D. Schluter, *Science* **315**, 1574–1576 (2007).
8. P. R. Crane, S. Lidgard, *Science* **246**, 675–678 (1989).
9. S. L. Wing, L. D. Boucher, *Annu. Rev. Earth Planet. Sci.* **26**, 379–421 (1998).
10. L.-M. Lu *et al*., *Nature* **554**, 234–238 (2018).
11. H. J. Falcon-Lang *et al*., *Geology* **37**, 923–926 (2009).
12. C. V. Looy, H. Kerp, I. A. P. Duijnstee, W. A. DiMichele, *Sediment. Rec.* **12**, 4–10 (2014).
13. M. Berthelin *et al*., *Palaeogeogr. Palaeoclimatol. Palaeoecol.* **196**, 85–98 (2003).
14. H. Kerp, A. Abu Hamad, B. Vörding, K. Bandel, *Geology* **34**, 265–268 (2006).
15. R. A. Gastaldo, T. M. Demko, in *Topics in Geobiology*, vol. 32, *Taphonomy*, P. A. Allison, D. J. Bottjer, Eds. (Springer, 2011), pp. 249–285.
16. A. Abu Hamad, H. Kerp, B. Vörding, K. Bandel, *Rev. Palaeobot. Palynol.* **149**, 85–130 (2008).
17. T. N. Taylor, E. L. Taylor, M. Krings, *Paleobotany: The Biology and Evolution of Fossil Plants* (Elsevier, 2009).
18. J. H. Powell *et al*., *Riv. Ital. Paleontol. Statigr.* **122**, 23–39 (2016).
19. Supplementary materials.
20. G. A. Pattemore, J. F. Rigby, G. Playford, *Bol. Geol. Min.* **126**, 689–722 (2015).
21. S. McLoughlin, C. Pott, I. H. Sobbe, *Palaeobiodivers. Palaeoenviron.* **98**, 71–95 (2018).
22. P. R. Crane, E. M. Friis, K. R. Pedersen, *Nature* **374**, 27–33 (1995).
23. E. M. Friis *et al*., *Nature* **450**, 549–552 (2007).
24. C. N. Miller, *Bot. Rev.* **43**, 217–280 (1977).
25. M. Pole, *J. R. Soc. N. Z.* **28**, 375–403 (1998).
26. C. Pott, H. Kerp, M. Krings, *Ann. Naturhist. Mus. Wien* **109A**, 1–17 (2007).
27. D. H. Erwin, *Nature* **367**, 231–236 (1994).
28. A. Traverse, *Hist. Biol.* **1**, 277–301 (1988).
29. J. C. McElwain, S. W. Punyasena, *Trends Ecol. Evol.* **22**, 548–557 (2007).
30. B. Bomfleur, P. Blomenkemper, H. Kerp, S. McLoughlin, in *Transformative Palaeobotany*, M. Krings, C. J. Harper, N. R. Cúneo, G. W. Rothwell, Eds. (Academic Press, ed. 1, 2018), pp. 593–611.

ACKNOWLEDGMENTS

We thank the University of Jordan (Amman) for support; N. S. and H. S. Badandi (Irbid, Jordan), F. Scholze and J. W. Schneider (Freiberg, Germany), and S. Voigt (Thallichtenberg, Germany) for fieldwork assistance; and S. McLoughlin (Stockholm, Sweden), M. Pole (Toowong, Australia), C. Pott (Münster, Germany), and three anonymous reviewers for helpful discussion. **Funding:** Financial support was provided by the German Science Foundation (DFG Emmy Noether grant BO3131/1-1, "Latitudinal Patterns in Plant Evolution," to B.B. and DFG grants KE584/11-1+2 and KE584/20-1 to H.K.). **Author contributions:** All authors contributed equally to the work. **Competing interests:** The authors declare no competing interests. **Data and materials availability:** All data are available in the main text and the supplementary materials; all fossil material is housed in the palaeobotanical collections at the Institute of Geology and Palaeontology of the Westfälische Wilhelms-Universität (Münster, Germany).

SUPPLEMENTARY MATERIALS

www.sciencemag.org/content/362/6421/1414/suppl/DC1
Materials and Methods
Supplementary Text
Figs. S1 and S2
Table S1
References (*31*–*63*)

11 June 2018; accepted 8 November 2018
10.1126/science.aau4061

CANCER

NK cell–mediated cytotoxicity contributes to tumor control by a cytostatic drug combination

Marcus Ruscetti[1]*, Josef Leibold[1]*, Matthew J. Bott[1]*, Myles Fennell[1], Amanda Kulick[2], Nelson R. Salgado[1], Chi-Chao Chen[1], Yu-jui Ho[1], Francisco J. Sanchez-Rivera[1], Judith Feucht[3], Timour Baslan[1], Sha Tian[1], Hsuan-An Chen[1], Paul B. Romesser[1], John T. Poirier[2,4], Charles M. Rudin[2,4], Elisa de Stanchina[2], Eusebio Manchado[1], Charles J. Sherr[5,6], Scott W. Lowe[1,6]†

Molecularly targeted therapies aim to obstruct cell autonomous programs required for tumor growth. We show that mitogen-activated protein kinase (MAPK) and cyclin-dependent kinase 4/6 inhibitors act in combination to suppress the proliferation of KRAS-mutant lung cancer cells while simultaneously provoking a natural killer (NK) cell surveillance program leading to tumor cell death. The drug combination, but neither agent alone, promotes retinoblastoma (RB) protein-mediated cellular senescence and activation of the immunomodulatory senescence-associated secretory phenotype (SASP). SASP components tumor necrosis factor–α and intercellular adhesion molecule–1 are required for NK cell surveillance of drug-treated tumor cells, which contributes to tumor regressions and prolonged survival in a KRAS-mutant lung cancer mouse model. Therefore, molecularly targeted agents capable of inducing senescence can produce tumor control through non–cell autonomous mechanisms involving NK cell surveillance.

The KRAS oncogene is frequently mutated in several human cancers. It drives tumorigenesis by constitutively activating growth factor signaling pathways that promote uncontrolled proliferation, namely the mitogen-activated protein kinase (MAPK) or phosphoinositide 3-kinase pathways. Although much effort has been placed on targeting KRAS or its downstream effectors, to date, most therapeutic agents have failed, owing to an inability to sustain inhibition of RAS-driven signaling (*1*, *2*). Combinatorial strategies are being developed to circumvent these effects, for example, by combining MAPK kinase (MEK) inhibitors with upstream receptor tyrosine kinase inhibitors to thwart adaptive resistance mechanisms (*3*, *4*). Another approach involves combining MEK inhibitors with downstream cyclin-dependent kinase 4 and 6 (CDK4/6) inhibitors that, in principle, could more potently block the proliferation of KRAS-mutant cells by simultaneously reducing MAPK-regulated cyclin D levels and directly targeting CDK4 kinase activity (*5*). In addition to the intrinsic effects on tumor cell proliferation, both MEK and CDK4/6 inhibitors can modulate T cell function as single agents or in combination with T cell checkpoint blockade (*6*–*8*).

We explored the cell autonomous and non–cell autonomous effects of combining MEK and CDK4/6 inhibitors using KRAS-mutant tumor models. We first tested a number of highly selective CDK4/6 inhibitors (palbociclib, abemaciclib, ribociclib) in combination with the U.S. Food and Drug Administration–approved MEK inhibitor trametinib in human KRAS-mutant lung and pancreatic cancer cell lines. Compared with treatment with either single agent, the two-drug combination was substantially more effective at inhibiting proliferation as well as phosphorylation of the retinoblastoma (RB) protein, a direct CDK4 and 6 target (Fig. 1A and fig. S1). Accordingly, the combination of trametinib and palbociclib was more effective at impairing tumor growth and inducing tumor stasis in mice harboring a KRAS-mutant lung cancer patient-derived xenograft (PDX), when treated at the maximally tolerated dose for each agent (Fig. 1B) (*9*, *10*). Similar results were also observed in other KRAS-mutant PDX models treated at lower doses (Fig. 1C and fig. S2, A and B), confirming that the combination produces biological effects that neither drug can achieve alone.

These human xenograft studies require the use of immunodeficient NOD-scid IL2Rg^{null} (NSG) mice. To assess whether and to what extent tumor cell responses are altered by the immune system, we made use of an established syngeneic transplant mouse model of lung cancer. Mouse tumor cells derived from a *Kras*$^{G12D/+}$;*Trp53*$^{-/-}$

[1]Department of Cancer Biology and Genetics, Sloan Kettering Institute, Memorial Sloan Kettering Cancer Center, New York, NY 10065, USA. [2]Department of Molecular Pharmacology, Sloan Kettering Institute, Memorial Sloan Kettering Cancer Center, New York, NY 10065, USA. [3]Center for Cell Engineering and Immunology Program, Memorial Sloan Kettering Cancer Center, New York, NY 10065, USA. [4]Department of Medicine, Memorial Sloan Kettering Cancer Center, New York, NY 10065, USA. [5]Department of Tumor Cell Biology, St. Jude Children's Research Hospital, Memphis, TN 38105, USA. [6]Howard Hughes Medical Institute, Chevy Chase, MD 20815, USA.
*These authors contributed equally to this work.
†Corresponding Author. Email: lowes@mskcc.org

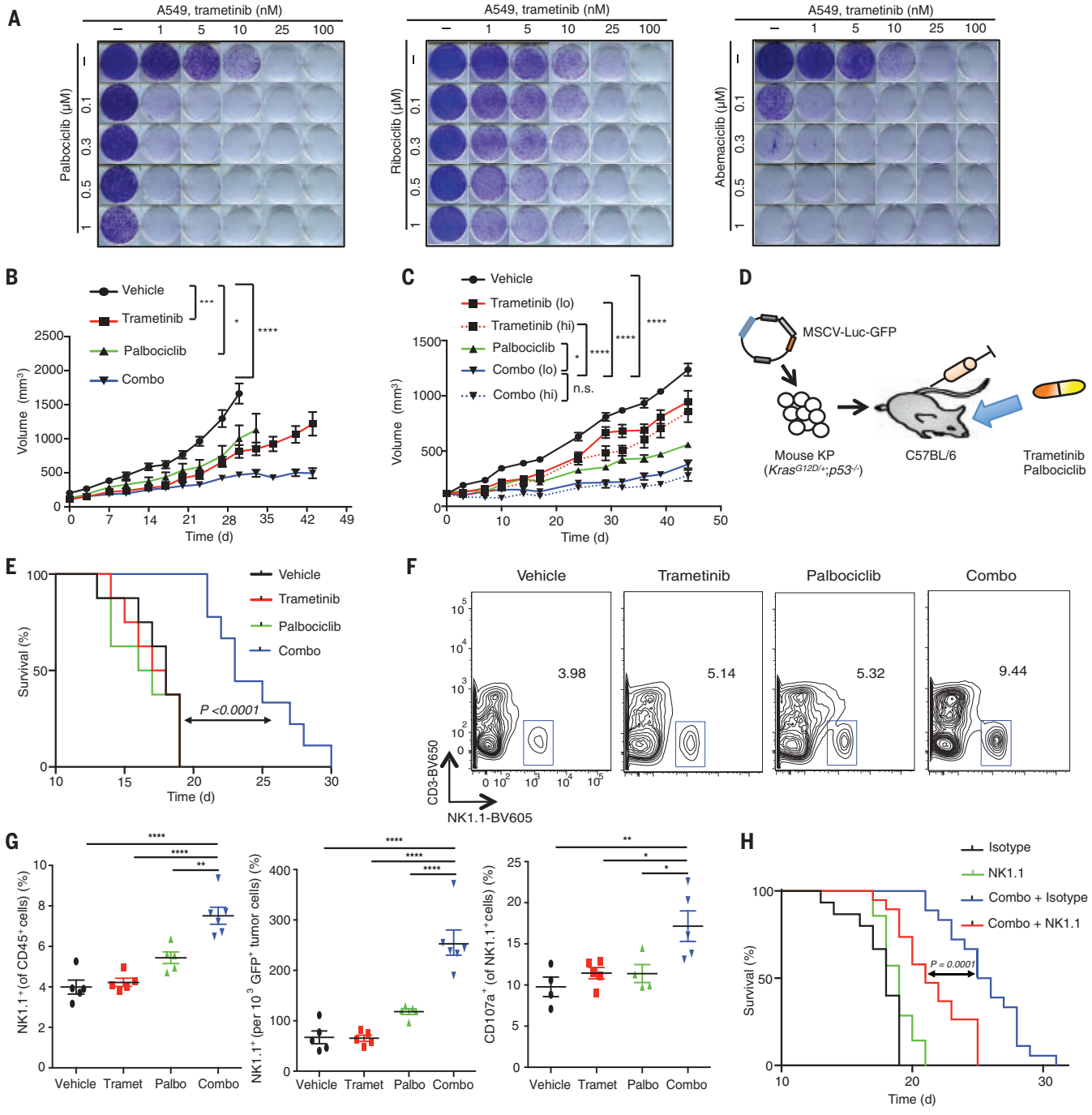

Fig. 1. NK cell immunity is required for the efficacy of combination MEK and CDK4/6 inhibitor therapy. (**A**) Clonogenic assay of A549 lung cancer cells treated with MEK (trametinib) and/or various CDK4/6 inhibitors (palbociclib, ribociclib, abemaciclib); representative of three biological replicates. (**B**) Tumor volumes of mice bearing KRAS-mutant MSK-LX27 PDX lung tumors treated with vehicle, trametinib (3 mg/kg body weight), palbociclib (150 mg/kg body weight), or both in combination (Combo) for indicated times (n = 5 mice per group). (**C**) Tumor volumes of mice bearing KRAS-mutant MSK-LX68 PDX lung tumors treated with vehicle, trametinib [1 mg/kg (lo) or 3 mg/kg (hi) body weight], palbociclib (150 mg/kg body weight), or both in combination for indicated times (n = 8 mice per group). n.s., not significant. (**D**) Syngeneic KP transplant lung cancer model. (**E**) Kaplan-Meier survival curve of KP transplant mice treated with vehicle, trametinib (1 mg/kg body weight), palbociclib (100 mg/kg body weight), or both in combination ($n \geq 8$ per group) (log-rank test). (**F**) Representative flow cytometry plots of NK cell populations in lung tumors from KP transplant mice treated for 1 week as in (E). (**G**) Percentage of NK cells within the CD45$^+$ population (left), total NK cells relative to tumor cell number (middle), and percentage of CD107a$^+$ degranulating NK cells (right) ($n \geq 4$ mice per group). Palbo, palbociclib; Tramet, trametinib. (**H**) Kaplan-Meier survival curve of KP transplant mice treated with vehicle or combined trametinib (1 mg/kg body weight) and palbociclib (100 mg/kg body weight) and either an isotype control antibody (C1.18.4) or NK1.1-depleting antibody (PK136) ($n \geq 8$ per group) (log-rank test). (B and C) Two-way ANOVA. (G) One-way ANOVA. Error bars, mean ± SEM. *P < 0.05, **P < 0.01, ***P < 0.001, ****P < 0.0001.

(KP) lung tumor (*11*) were engineered to express luciferase and green fluorescent protein (GFP) and tested for drug sensitivity in vitro or after intravenous injection into C57BL/6 immunocompetent mice (Fig. 1D), where they produced aggressive lung adenocarcinomas by 1-week post transplantation. As in the human models, the trametinib plus palbociclib combination synergistically suppressed the growth of cultured KP tumor cells (fig. S2C) and significantly increased the survival of lung tumor–bearing animals (Fig. 1E). This effect was substantially impaired when the same cells were transplanted into immunodeficient NSG mice (fig. S2D and E), suggesting that the immune system might contribute to treatment efficacy.

Immune profiling of lung tumors after 1 week of combination treatment revealed a general influx of $CD45^+$ immune cells compared with single-agent treatment (fig. S3A). Whereas there was no change in B cell or macrophage numbers in tumors after treatment, there was an increased infiltration of $CD4^+$ and $CD8^+$ T cells in the lungs and spleens of both tumor-bearing and naïve (tumor-free) mice after either single-agent or combination therapy. However, changes in $CD4^+$ or $CD8^+$ T cell activation were not observed, as assessed by staining for CD69, KLRG1, and CD107a, a marker of lymphocyte degranulation (figs. S3, B to D; S4, A and B; and S5, A to D). Thus, the drug combination does not appear to produce selective activation of T cells in this lung cancer model.

By contrast, combined treatment with trametinib and palbociclib triggered the selective accumulation of natural killer (NK) cells and a decrease in $Gr\text{-}1^{hi}CD11b^+$ myeloid-derived suppressor cells (MDSCs) in the lungs of tumor-bearing mice compared with treatment with either agent alone (Fig. 1, F and G; and figs. S3, E and F; S4, C and D; and S5F). NK cells derived from combination-treated tumors appeared activated and more mature, as indicated by cell surface expression of CD107a and other activating receptors and altered transcriptional profiles showing a reduction in proliferation-associated genes and an increase in expression of genes linked to NK cell maturation and cytotoxicity (Fig. 1G and figs. S4C, S5E, and S6). Combined treatment also led to NK cell accumulation (but not activation) and a decrease in MDSCs in the spleens of tumor-bearing mice but not in the lungs or spleens of naïve mice (figs. S3, F to H, and S5, E to G), suggesting that this immune effect is tumor dependent.

To determine whether specific immune cells contribute to the outcome of combination therapy, we assessed the impact of perturbing immune cell function on the survival of tumor-bearing (immunocompetent) mice after vehicle or trametinib and palbociclib therapy. Neither depletion of macrophages, $Gr\text{-}1^+$ granulocytes/MDSCs, and $CD4^+$ and $CD8^+$ T cells using blocking antibodies nor anti–PD-1 immunotherapy (to stimulate exhausted T cells) had any impact on the survival of vehicle or combination-treated mice (figs. S7, A to D, and S8). By contrast, depletion of NK cells using an anti-NK1.1 antibody (PK136) significantly reduced the survival advantage produced by combination therapy while having no effect on cohorts treated with vehicle or single agents (Fig. 1H and figs. S7E and F, and S8). This effect was independent of the MDSC reduction after treatment (fig. S3F), as Gr-1 depletion did not influence the survival of combination-treated mice in the presence or absence of NK cells (fig. S7B). Hence, in this model, the trametinib and palbociclib combination triggers a potent and selective NK cell–mediated response that contributes to treatment efficacy.

We found the contribution of immune surveillance to the action of an apparently cytostatic drug combination intriguing and set out to study the underlying mechanisms in more detail. CDK4 and 6–mediated phosphorylation of RB (the intended target of trametinib and palbociclib treatment) cancels its growth-suppressive action to facilitate E2F-mediated G_1-S progression (*5*). We confirmed in all our models that combination therapy produced a more potent reduction in RB phosphorylation and proliferation without inducing apoptosis (fig. S9). Besides its role in modulating cell cycle progression, RB plays a crucial role in mediating cellular senescence, a tumor-suppressive program that involves a stable (if not permanent) cell cycle arrest program coupled to an immune modulatory component (*12*–*14*). Specifically, senescent cells display an RB-dependent down-regulation of proliferation genes (*15*, *16*) and a concomitant up-regulation of genes encoding a wide range of secretory proteins and other factors that modulate the microenvironment (*17*). Of note, this secretory program, often referred to as the senescence-associated secretory phenotype (SASP), can have either tumor-suppressive or tumor-promoting functions, depending on context (*18*–*23*). In its tumor-suppressive role, RB often collaborates with the p53 tumor suppressor to limit the proliferation of premalignant cells (*24*), and disruption of both genes is linked to senescence escape during tumorigenesis (*25*).

To test whether trametinib and/or palbociclib treatment induced senescence in human or mouse KRAS-mutant lung cancer cells, we evaluated a series of markers and functional properties associated with the senescent state (*14*, *26*). Only combination treatment resulted in significant senescence-associated beta-galactosidase (SA-β-gal) activity, the accumulation of senescence-associated heterochromatin foci, loss of the nuclear envelope protein Lamin B1, and increased expression of *DEC1*, *DCR2*, and *CDKN2B* (Fig. 2A and fig. S10).

Colony-forming assays revealed that many KRAS-mutant cell lines treated with either palbociclib or trametinib alone resumed proliferation upon drug washout, whereas combination-treated cells did not (Fig. 2B and fig. S11, A to B). This durable, senescent-like arrest was RB dependent and did not occur in tumor cells harboring RB genomic loss (Fig. 2B and figs. S11 and S12). Both human and murine KRAS-mutant tumor cells lacking p53 also displayed senescence markers in response to the trametinib and palbociclib combination (Fig. 2B and figs. S11 and S12). Therefore, this treatment can restore senescence to tumor cells that have escaped p53 tumor suppressive programs during tumor evolution provided that RB function is retained.

The senescence program provoked by combined trametinib and palbociclib treatment was also associated with a potent SASP induction. RNA sequencing (RNA-seq) analysis of human KRAS-mutant tumor cell lines after drug treatment revealed that the drug combination produced a greater reduction in proliferation genes and increase in SASP factor expression compared with either treatment alone (Fig. 2C, fig. S13B, and tables S1 and S2). Among the immune modulatory genes that were induced and secreted were chemokines involved in NK cell recruitment (CCL2, CCL4, CCL5, CXCL10, CX3CL1), as well as cytokines that promote NK cell proliferation and activation [interleukin-15 (IL-15), IL-18, tumor necrosis factor–α (TNF-α)] (Fig. 2D and fig. S13, A and C). Many of these same SASP factors were also induced in murine KP lung cancer cells and a PDX lung cancer model in vivo (fig. S13, D and E). Gene Set Enrichment Analysis revealed that signatures linked to oncogene-induced and replicative senescence (*22*, *27*), nuclear factor κB (NF-κB) and TNF-α signaling, and NK cell–mediated cytotoxicity were also selectively enriched in the transcriptional profiles of combination treated cells (fig. S13, F to H). Although not secretory per se, NK cell ligands (which are required for activation of NK cell cytotoxicity and tumor cell targeting) are part of the transcriptional module linked to the SASP (*28*, *29*). We found that intercellular adhesion molecule–1 (ICAM-1) and the NKG2D ligands ULBP2 and MICA were induced after combination treatment in human KRAS-mutant tumor cells, PDXs, and murine KP lung tumor cells (Fig. 2E and fig. S14). Overall, these data suggest that, in addition to a more stable cell cycle arrest conferred by RB-mediated senescence, combined MEK and CDK4/6 inhibition may promote tumor cell immune surveillance through induction of the SASP program.

To explore this possibility, we tested whether NK cells could functionally target tumor cells after combined trametinib and palbociclib treatment. Using an in vitro NK cell coculture assay that quantitatively measures both NK cell–tumor cell interactions and cytotoxicity, we observed that treatment with the drug combination, but not with single agents, triggered the rapid association and eventual killing of KRAS-mutant tumor cells by the human YT NK cell line even in the presence of the drugs (Fig. 2F; fig. S15, A and B; and movies S1 to S4). These results were corroborated using freshly isolated primary human NK cells (fig. S15, C and D) and using the murine system, in which senescent KP cells treated with the drug combination were sufficient to induce degranulation and cytotoxicity in drug-treated splenic NK cells upon coculture

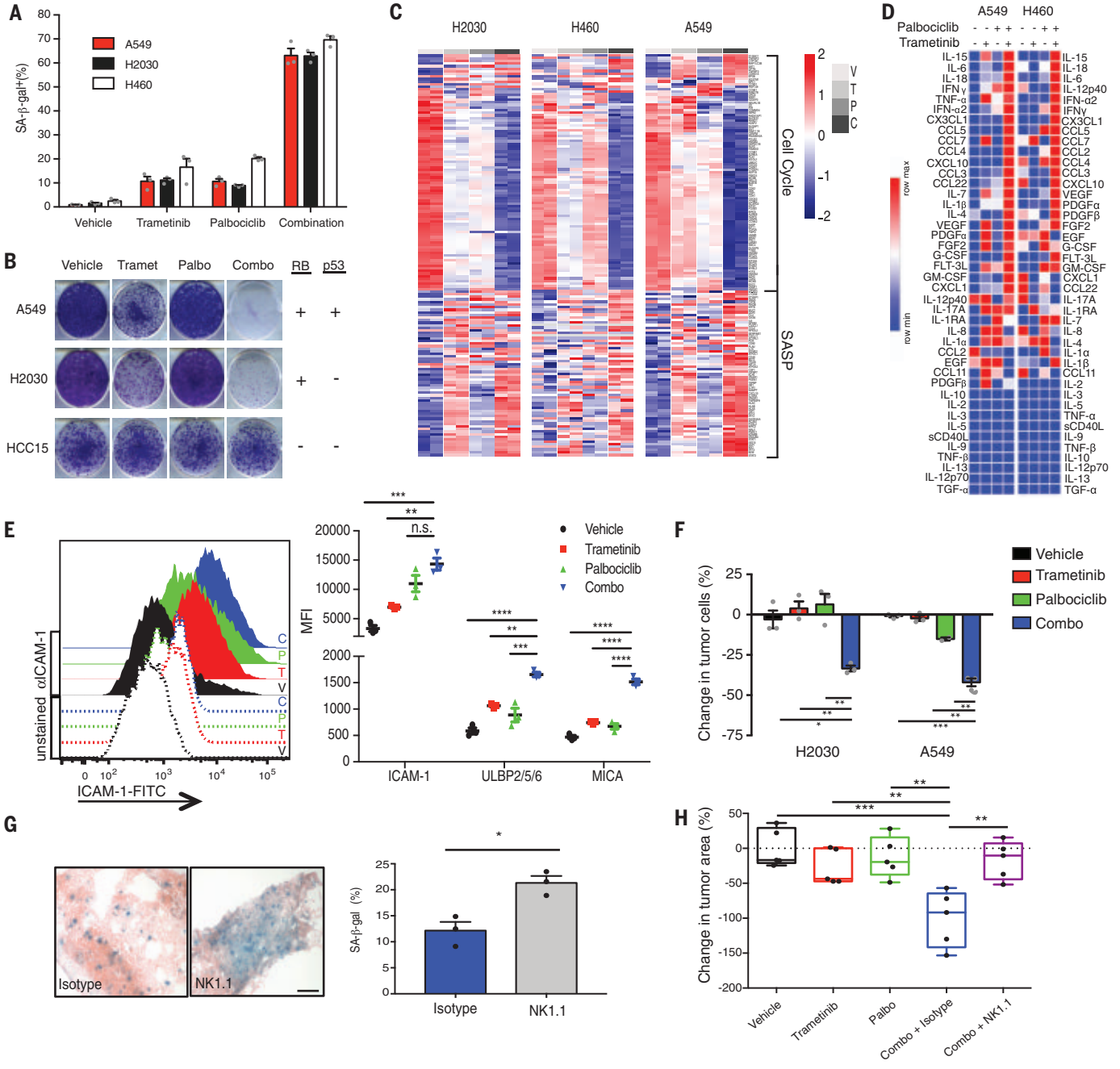

Fig. 2. Senescence and SASP induction after combination MEK and CDK4/6 inhibitor therapy induces NK cell immune surveillance. (**A**) Quantification of SA-β-gal$^+$ cells in human KRAS-mutant lung tumor cell lines after 8-day treatment with trametinib (25 nM) and/or palbociclib (500 nM). Mean of three biological replicates is plotted. (**B**) Clonogenic assay of human KRAS-mutant lung cancer cells replated in the absence of drugs after 8-day pretreatment as in (A); representative of three biological replicates. *RB* and *p53* genomic status is indicated on right. (**C**) Heat map of senescence-associated cell cycle and SASP gene expression in human KRAS-mutant lung cancer cell lines after treatment as in (A), as assessed by RNA-seq. Two biological replicates per cell line are shown. C, combination; P, palbociclib; T, trametinib; V, vehicle. (**D**) Heat map of cytokine array results from human KRAS-mutant lung tumor cells treated with trametinib (25 nM) and/or palbociclib (500 nM) for 8 days. Data are presented as mean of three biological replicates. (**E**) Flow cytometry analysis of ICAM-1 expression and levels of other NK cell–activating ligands after 8-day treatment of A549 lung tumor cells as described in (A). Quantification of mean fluorescence intensity (MFI) from three biological replicates is shown on the right. (**F**) Quantification of NK cell cytotoxicity (by live cell imaging) after pretreatment of A549 and H2030 lung tumor cell lines with indicated drugs for 8 days and coculturing with the YT NK cell line at a 10:1 effector to target cell (E:T) ratio for 20 hours in the presence or absence of indicated drugs. Change in tumor cells is normalized to control wells lacking NK cells. Mean of three biological replicates is plotted. (**G**) Representative SA-β-gal staining of KP transplant lung tumors after 1-week treatment with combined trametinib (1 mg/kg body weight) and palbociclib (100 mg/kg body weight) and either an isotype control antibody (C1.18.4) or NK1.1 depleting antibody (PK136) (scale bar, 50 μm). Quantification shown on right (n = 3 mice per group). (**H**) Effect of 1-week treatment as in (G) on lung tumor burden (relative to vehicle) (n = 5 mice per group). (E, F, and H) One-way ANOVA. (G) Unpaired two-tailed t test. Error bars, mean ± SEM. *P < 0.05, **P < 0.01, ***P < 0.001, ****P < 0.0001.

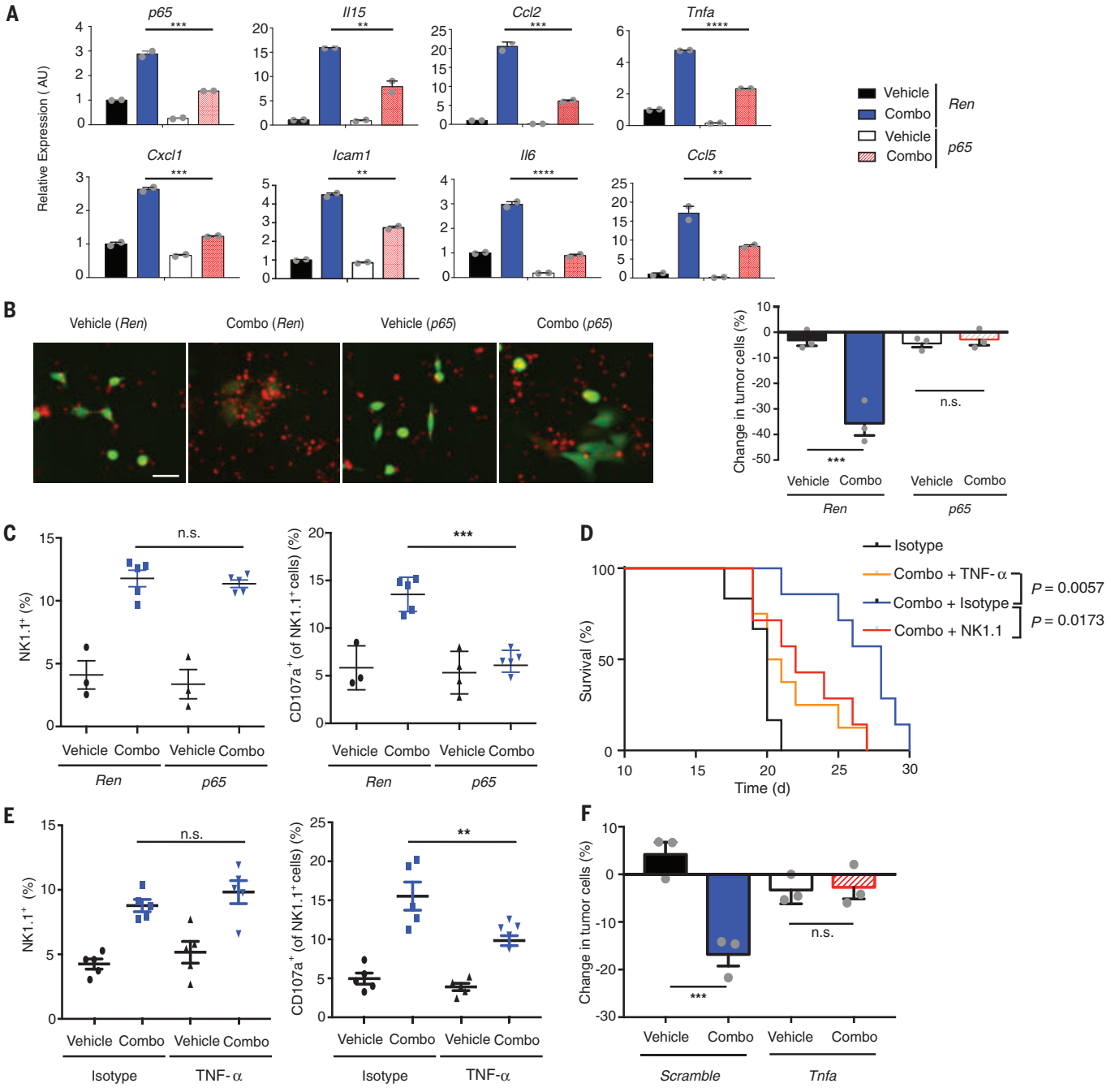

Fig. 3. NF-κB-mediated SASP and TNF-α secretion is required for treatment-induced NK cell activity. (**A**) Quantitative reverse transcription polymerase chain reaction analysis of SASP gene expression in KP tumor cells transduced with indicated shRNAs after treatment with vehicle or trametinib (25 nM) and palbociclib (500 nM) for 8 days. Mean of two biological replicates associated with three technical replicates is plotted. AU, arbitrary units. (**B**) Representative images of KP tumor cells with indicated shRNAs (green) pretreated as in (A) and cocultured with primary murine splenic NK cells (red) at a 20:1 E:T ratio for 20 hours in the presence or absence of indicated drugs (scale bar, 25 μm). Quantification of NK cell cytotoxicity (by live cell imaging) is shown on the right. Change in tumor cells is normalized to control wells lacking NK cells. Mean of three biological replicates is plotted. (**C**) Flow cytometry analysis of total and CD107a$^+$ degranulating NK cells within the CD45$^+$ population in the lungs after 1-week treatment of mice transplanted with KP tumor cells containing control *Renilla* (*Ren*) or *p65* shRNAs with vehicle or combined trametinib (1 mg/kg body weight) and palbociclib (100 mg/kg body weight) ($n \geq 3$ mice per group). (**D**) Kaplan-Meier survival curve of KP transplant mice treated with vehicle or combined trametinib (1 mg/kg body weight) and palbociclib (100 mg/kg body weight) and either an isotype control (HRPN), NK1.1 (PK136), or TNF-α (XT3.11) targeting antibody ($n \geq 6$ per group) (log-rank test). (**E**) Flow cytometry analysis as in (C) after 1-week treatment of KP transplant mice with vehicle or combined trametinib (1 mg/kg body weight) and palbociclib (100 mg/kg body weight) and either an isotype control (HRPN) or TNF-α (XT3.11) targeting antibody ($n = 5$ per group). (**F**) Quantification of NK cell cytotoxicity (by live cell imaging) toward KP tumor cells with indicated shRNAs pretreated as in (B) and cocultured with primary murine splenic NK cells at a 20:1 E:T ratio for 20 hours in the presence or absence of indicated drugs. (A to C and E and F) One-way ANOVA. Error bars, mean ± SEM. $^{**}P < 0.01$, $^{***}P < 0.001$, $^{****}P < 0.0001$.

(fig. S15, E and F). In vivo, NK cells also appeared to preferentially target senescent cells, as tumors in NK cell–depleted mice that received the trametinib and palbociclib combination were significantly larger and retained more SA-β-gal$^+$ cells compared with those in control mice with NK cells intact (Fig. 2, G and H, and fig. S15G). NK cells are therefore capable of eliminating senescent tumor cells after combined trametinib and palbociclib treatment.

We performed a genetic experiment to disable the SASP program in KP tumor cells. The transcription factor NF-κB is a master regulator of the SASP program but plays only a limited role in senescence-induced cell cycle arrest (*30*–*32*). KP tumor cells expressing a well-characterized short hairpin RNA (shRNA) targeting the p65 subunit of NF-κB underwent growth arrest in response to the drug combination but displayed a reduction in many SASP factors and were not targeted by spleen-derived murine NK cells in vitro (Fig. 3, A and B, and fig. S16, A to D). In vivo, tumors derived from p65-suppressed KP cells showed similar levels of NK cell accumulation as tumors expressing a control shRNA targeting the nonexpressed gene *Renilla* luciferase after combination therapy; however, these infiltrating NK cells were not activated, and the treatment was not as effective (Fig. 3C and fig. 16E). Thus, the SASP appears necessary for therapy-induced NK cell surveillance and the efficacy of the drug combination in vivo.

To pinpoint SASP factors needed for NK cell attack, we tested a range of neutralizing antibodies against NF-κB-regulated SASP factors (IL-15, IL-18, TNF-α, CCL2, CCL5) for their ability to alter survival in KP transplant mice treated with the trametinib and palbociclib combination. Only TNF-α depletion reduced animal survival, which was similar in magnitude to that produced by NK cell depletion (Fig. 3D and fig. S16, F and G) and was associated with a reduction in activated NK cells present in the treated tumors (Fig. 3E). This effect was in part due to tumor cell–derived TNF-α, as shRNAs capable of suppressing *Tnfa* in combination-treated KP cells markedly inhibited NK cell cytotoxicity in vitro (Fig. 3F and fig. S17, A to D). Still, *Tnfa* suppression (fig. S17E) was not as effective as *p65* depletion (fig. S16E) at impairing the survival of tumor-bearing mice after combination treatment, indicating that an interplay between multiple SASP factors is required for NK cell surveillance in vivo.

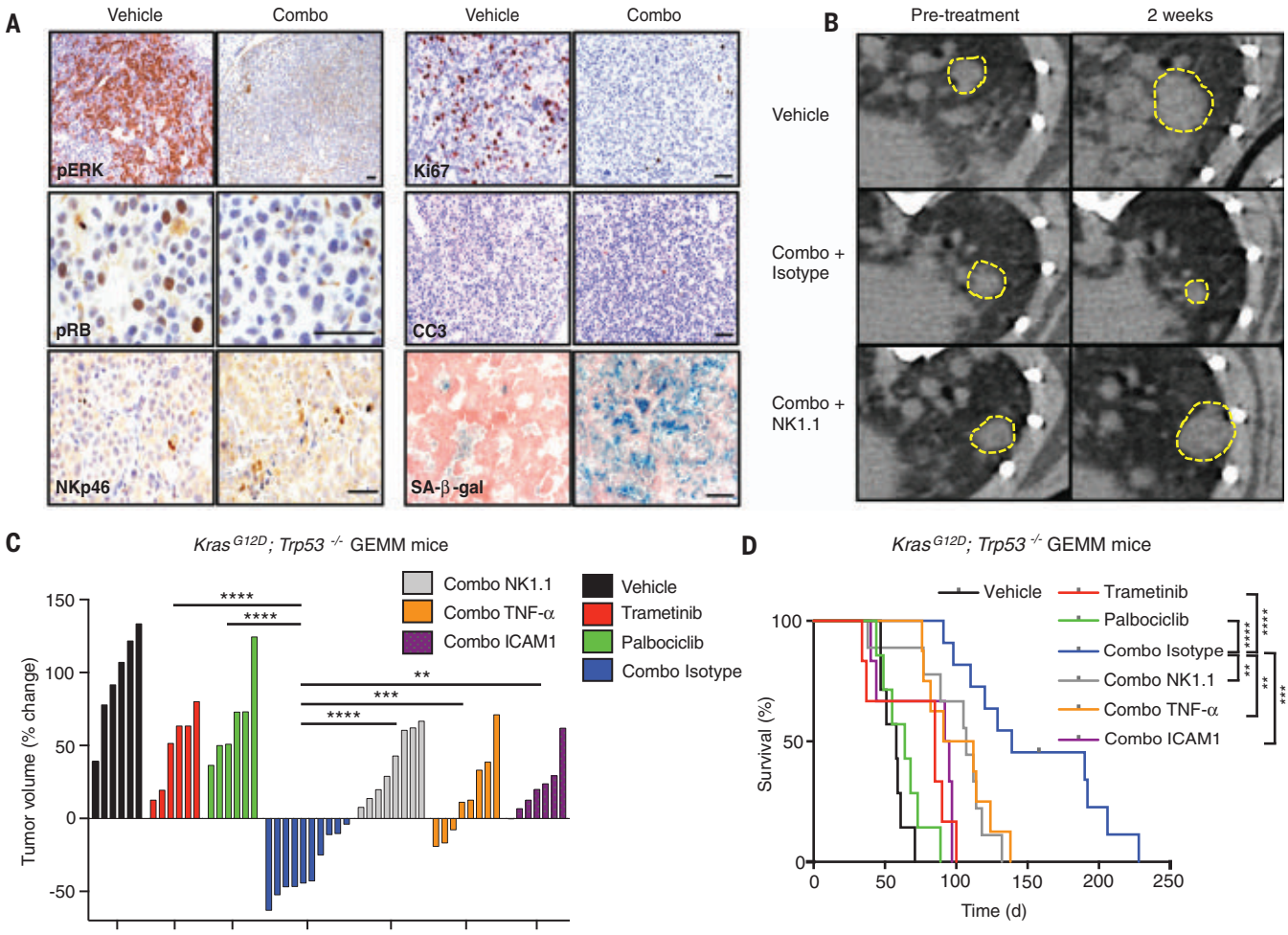

Fig. 4. Combination trametinib and palbociclib treatment drives NK cell–mediated lung tumor regressions in genetically engineered mice. (**A**) Immunohistochemical staining of KP GEMM tumors treated with vehicle or combined trametinib (1 mg/kg body weight) and palbociclib (100 mg/kg body weight) for 2 weeks (scale bar, 50 μm). CC3, cleaved caspase-3; pERK, phosphorylated extracellular signal–regulated kinase. (**B**) Representative μCT images of KP GEMM lung tumors prior to treatment and after 2 weeks of treatment with vehicle or combined trametinib (1 mg/kg body weight) and palbociclib (100 mg/kg body weight) and either an isotype control antibody (C1.18.4) or NK1.1 depleting antibody (PK136). Yellow boxes indicate lung tumors. (**C**) A waterfall representation of the response of each tumor after 2 weeks of treatment with vehicle, trametinib (1 mg/kg body weight), palbociclib (100 mg/kg body weight), or both, and either an isotype control (C1.18.4), NK1.1 (PK136), TNF-α (XT3.11), or ICAM-1 (YN1/1.7.4) blocking antibody ($n \geq 6$ per group). (**D**) Kaplan-Meier survival curve of KP GEMM mice treated as in (C) ($n \geq 6$ per group) (log-rank test). (C) One-way ANOVA. *$P < 0.05$, **$P < 0.01$, ***$P < 0.001$, ****$P < 0.0001$.

We also explored potential mechanisms by which NK cells target tumor cells undergoing therapy-induced senescence. Cell surface NK cell ligands and adhesion molecules are up-regulated along with the SASP during many forms of senescence (*29*). We found that both ICAM-1 and members of the MICA/B, ULBP, Rae-1, and H60 family of NKG2D ligands were increased after combination therapy in an NF-κB-dependent or independent manner, respectively (Figs. 2E and 3A and figs. S14 and 16D). Furthermore, blocking ICAM-1 and its receptor LFA-1 (and to a lesser extent NKG2D) blunted NK cell cytotoxicity in combination-treated tumor cells in live cell imaging and chromium release assays and significantly reduced the survival of combination-treated KP transplant mice in vivo (figs. S15, C and D, and S17, F to H). Therefore, the SASP transcriptional module contributes both secreted (i.e., TNF-α) and cell surface (i.e., ICAM-1) factors to facilitate NK cell surveillance.

The orthotopic KP model represents a flexible syngeneic experimental system but is extraordinarily aggressive with tumors disseminated throughout the lungs, making assessment of tumor response to therapy challenging. To examine the impact of this senescence-inducing therapy on NK cell immune surveillance and tumor progression in a more physiologically relevant setting, we utilized an autochthonous model of KRAS-mutant lung cancer. Genetically engineered $Kras^{LSL\text{-}G12D/wt}$;$Trp53^{flox/flox}$ (KP GEMM) mice were infected intratracheally with an adenovirus expressing Cre recombinase to induce endogenous lung tumor formation (*33*), leading to the development of focal KRAS-driven tumors that could be monitored using microcomputed tomography (μCT). Consistent with our findings in the syngeneic transplant model, combined trametinib and palbociclib treatment after endogenous tumor formation led to a significant reduction in RB phosphorylation and tumor cell proliferation, accumulation of SA-β-gal$^+$ senescent tumor cells, induction of SASP factors including TNF-α and ICAM-1, and subsequent recruitment of NK cells within lung adenocarcinomas of KP GEMM mice (Fig. 4A and fig. S18, A to D).

The contribution of NK cells to the activity of the combination therapy was marked. Two weeks post treatment, we observed tumor regressions in mice treated with the combination therapy and an isotype control antibody but not in those mice receiving an NK1.1-depleting antibody or single-agent trametinib or palbociclib whose tumors continued to progress (Fig. 4, B and C). Moreover, the overall survival of mice treated with trametinib plus palbociclib, which included a notable number of long-term survivors, was significantly longer than mice receiving single-agent treatment or the combination treatment in the context of NK cell depletion (Fig. 4D). Antibody-mediated blockade of SASP factors TNF-α or ICAM-1 also prevented tumor regressions and blunted the survival benefit of the drug combination (Fig. 4, C and D). Therefore, senescence-inducing targeted therapies can lead to tumor control in KRAS-mutant lung tumors, with SASP-provoked and NK cell–mediated immune surveillance facilitating tumor regression and prolonged survival.

Leveraging immunocompetent mouse models of KRAS-mutant lung cancer, we explored the non–cell autonomous effects of combined MEK and CDK4/6 inhibitor therapy, revealing an immune modulatory component to the antitumor response. Complementary to previous work in other systems demonstrating activation of T cell responses using similar monotherapies (*6*, *7*), our studies highlight a distinct mechanism of innate immune attack by NK cells, which act as a natural senolytic to eliminate tumor cells in combination drug–treated mice harboring autochthonous tumors. The ability of NK cells to target drug-treated tumor cells requires the induction of RB-mediated cellular senescence and acquisition of an NF-κB–dependent SASP program that culminates in the secretion of proinflammatory cytokines (e.g., TNF-α) and surface expression of NK cell–activating molecules (e.g., ICAM-1) (fig. S18E). Thus, whereas developing tumors evade both senescence and immune surveillance to become fully malignant, these processes can be reestablished in tumor cells by certain targeted cancer therapies. Although chronic SASP induction can have deleterious consequences in some settings (*17*, *34*), the timely clearance of senescent cells by NK cells in this model establishes senescence induction as a beneficial outcome of targeted therapy, and explains how some cytostatic agents can be cytotoxic in vivo. Because NK cells do not require neoantigen recognition to target tumor cells (*28*), strategies to exploit and enhance this form of immune surveillance may complement existing efforts to harness adaptive immune surveillance by means of T cell checkpoint blockade immunotherapies.

REFERENCES AND NOTES

1. A. A. Samatar, P. I. Poulikakos, *Nat. Rev. Drug Discov.* **13**, 928–942 (2014).
2. P. Lito *et al.*, *Cancer Cell* **25**, 697–710 (2014).
3. E. Manchado *et al.*, *Nature* **534**, 647–651 (2016).
4. A. Prahallad *et al.*, *Nature* **483**, 100–103 (2012).
5. C. J. Sherr, D. Beach, G. I. Shapiro, *Cancer Discov.* **6**, 353–367 (2016).
6. J. Deng *et al.*, *Cancer Discov.* **8**, 216–233 (2018).
7. S. Goel *et al.*, *Nature* **548**, 471–475 (2017).
8. P. J. R. Ebert *et al.*, *Immunity* **44**, 609–621 (2016).
9. D. W. Fry *et al.*, *Mol. Cancer Ther.* **3**, 1427–1438 (2004).
10. A. G. Gilmartin *et al.*, *Clin. Cancer Res.* **17**, 989–1000 (2011).
11. N. Dimitrova *et al.*, *Cancer Discov.* **6**, 188–201 (2016).
12. J. W. Shay, O. M. Pereira-Smith, W. E. Wright, *Exp. Cell Res.* **196**, 33–39 (1991).
13. T. Kuilman, C. Michaloglou, W. J. Mooi, D. S. Peeper, *Genes Dev.* **24**, 2463–2479 (2010).
14. N. E. Sharpless, C. J. Sherr, *Nat. Rev. Cancer* **15**, 397–408 (2015).
15. A. Chicas *et al.*, *Cancer Cell* **17**, 376–387 (2010).
16. M. Narita *et al.*, *Cell* **113**, 703–716 (2003).
17. J. P. Coppé *et al.*, *PLOS Biol.* **6**, e301 (2008).
18. T. Eggert *et al.*, *Cancer Cell* **30**, 533–547 (2016).
19. T. W. Kang *et al.*, *Nature* **479**, 547–551 (2011).
20. V. Krizhanovsky *et al.*, *Cell* **134**, 657–667 (2008).
21. W. Xue *et al.*, *Nature* **445**, 656–660 (2007).
22. N. Tasdemir *et al.*, *Cancer Discov.* **6**, 612–629 (2016).
23. J. P. Coppé, P. Y. Desprez, A. Krtolica, J. Campisi, *Annu. Rev. Pathol.* **5**, 99–118 (2010).
24. M. Serrano, A. W. Lin, M. E. McCurrach, D. Beach, S. W. Lowe, *Cell* **88**, 593–602 (1997).
25. S. W. Lowe, C. J. Sherr, *Curr. Opin. Genet. Dev.* **13**, 77–83 (2003).
26. M. Collado, M. Serrano, *Nat. Rev. Cancer* **6**, 472–476 (2006).
27. A. L. Fridman, M. A. Tainsky, *Oncogene* **27**, 5975–5987 (2008).
28. M. G. Morvan, L. L. Lanier, *Nat. Rev. Cancer* **16**, 7–19 (2016).
29. A. Sagiv *et al.*, *Aging (Albany NY)* **8**, 328–344 (2016).
30. J. C. Acosta *et al.*, *Cell* **133**, 1006–1018 (2008).
31. A. V. Orjalo, D. Bhaumik, B. K. Gengler, G. K. Scott, J. Campisi, *Proc. Natl. Acad. Sci. U.S.A.* **106**, 17031–17036 (2009).
32. Y. Chien *et al.*, *Genes Dev.* **25**, 2125–2136 (2011).
33. E. L. Jackson *et al.*, *Genes Dev.* **15**, 3243–3248 (2001).
34. B. G. Childs, M. Durik, D. J. Baker, J. M. van Deursen, *Nat. Med.* **21**, 1424–1435 (2015).

ACKNOWLEDGMENTS

We thank H. Varmus, T. Jacks, and J. P. Morris IV for sharing cell lines; A. Banito, X. Li, D. Alonso-Curbelo, V. Low, H. C. Chen, L. Zamechek, W. Luan, F. Luna, and M. Rowicki for technical assistance and advice; N. Adams and J. Sun for graciously providing murine NKG2D-Fc antibodies and helpful comments on the manuscript; J. Boudreau and K. Hsu for insights concerning in vitro NK cell assays; and other members of the Lowe laboratory for insightful discussions. **Funding:** We thank W. H. Goodwin and A. Goodwin and the Commonwealth Foundation for Cancer Research for research support. This work was supported by three grants from the National Cancer Institute (PO1 CA129243-06, P30 CA008748-S5, and U54 OD020355-01), a grant from the Center of Experimental Therapeutics of Memorial Sloan Kettering Cancer Center (MSKCC), and an MSKCC-Parker Institute for Cancer Immunotherapy pilot grant. M.R. was supported by an MSKCC Translational Research Oncology Training Fellowship (NIH T32-CA160001) and an American Cancer Society Postdoctoral Fellowship (129040-PF-16-115-01-TBG). J.L. was supported by a fellowship of the German Research Foundation (DFG). M.J.B. was supported by an American Association for Thoracic Surgery-Andrew Morrow Research Scholarship. T.B. was supported by the William C. and Joyce C. O'Neil Charitable Trust and Memorial Sloan Kettering Single Cell Sequencing Initiative. F.J.S.-R. is an HHMI Hanna Gray Fellow and was partially supported by an MSKCC Translational Research Oncology Training Fellowship (NIH T32-CA160001). P.B.R. was supported in part by a K12 Paul Calebresi Career Development Award for Clinical Oncology (K12 CA184746). E.d.S. received support through a U54 OD020355-01 NIH grant and the Geoffrey Beene Cancer Research Center. C.M.R. was supported by a Stand Up To Cancer grant from the American Association for Cancer Research. S.W.L. is the Geoffrey Beene Chair of Cancer Biology. S.W.L. and C.J.S. are Howard Hughes Medical Institute investigators. **Author contributions:** M.R. and J.L. conceived the project, performed and analyzed experiments, and wrote the paper with assistance from all authors. M.J.B., M.F., A.K., N.R.S., C.-C.C., Y.-j.H., F.J.S.-R., J.F., T.B., S.T., H.A.C., and E.M. performed and analyzed experiments. P.B.R., J.T.P., C.M.R., and E.d.S. provided patient-derived tumor specimens. C.J.S. and S.W.L. conceived the project, supervised experiments, and wrote the paper. **Competing interests:** P.B.R. is a shareholder of Pfizer and a consultant for EMD Serono and AstraZeneca and has received an honorarium from Corning. E.M. is an employee and share holder of Novartis. S.W.L. is a founder and scientific advisory board member of Blueprint Medicines and ORIC Pharmaceuticals and received an award and honorarium from Eli Lilly and Company. **Data and materials availability:** RNA-seq data presented in this study are deposited in the Gene Expression Omnibus database under accession number GSE110397.

SUPPLEMENTARY MATERIALS

www.sciencemag.org/content/362/6421/1416/suppl/DC1
Materials and Methods
Figs. S1 to S18
Movies S1 to S4
Tables S1 and S2
References (*35*–*41*)

4 January 2018; resubmitted 10 June 2018
Accepted 19 November 2018
10.1126/science.aas9090

CELL BIOLOGY

ATP-dependent force generation and membrane scission by ESCRT-III and Vps4

Johannes Schöneberg[1,2,3], Mark Remec Pavlin[2,4]*, Shannon Yan[1,2]*, Maurizio Righini[6]†, Il-Hyung Lee[1,2]‡, Lars-Anders Carlson[1,2]§, Amir Houshang Bahrami[3], Daniel H. Goldman[2,5,6]||, Xuefeng Ren[1,2], Gerhard Hummer[3,7], Carlos Bustamante[1,2,4,5,6,8,9]¶, James H. Hurley[1,2,4,9]¶

The endosomal sorting complexes required for transport (ESCRTs) catalyze reverse-topology scission from the inner face of membrane necks in HIV budding, multivesicular endosome biogenesis, cytokinesis, and other pathways. We encapsulated ESCRT-III subunits Snf7, Vps24, and Vps2 and the AAA+ ATPase (adenosine triphosphatase) Vps4 in giant vesicles from which membrane nanotubes reflecting the correct topology of scission could be pulled. Upon ATP release by photo-uncaging, this system generated forces within the nanotubes that led to membrane scission in a manner dependent upon Vps4 catalytic activity and Vps4 coupling to the ESCRT-III proteins. Imaging of scission revealed Snf7 and Vps4 puncta within nanotubes whose presence followed ATP release, correlated with force generation and nanotube constriction, and preceded scission. These observations directly verify long-standing predictions that ATP-hydrolyzing assemblies of ESCRT-III and Vps4 sever membranes.

Cellular membranes are constantly remodeled in the course of vesicular trafficking, cell division, the egress of HIV, and many other processes. Membranes can bud and be severed either toward or away from the cytosol. The latter is referred to as reverse-topology scission and is catalyzed by the endosomal sorting complexes required for transport (ESCRT) machinery, a set of ~18 proteins in yeast and ~28 in mammals (*1*–*4*). The core machinery of membrane scission by the ESCRTs consists of the ESCRT-III protein family. The most important components for membrane scission are Snf7, Vps24, and Vps2 (*5*, *6*). When recruited to membranes, ESCRT-III proteins assemble into flat spiral disks (*7*–*9*), helical tubes (*7*, *10*, *11*), or conical funnels (*11*–*13*). ESCRT filaments have a preferred curvature (*8*, *9*, *14*). When they are bent to curvatures of higher or lower values, ESCRT filaments act as springs that restore their own shape to the preferred value (*9*, *15*, *16*). This spring-like behavior has led to the prediction that ESCRTs exert measurable forces upon membranes, which we set out to test.

The AAA$^+$ ATPase Vps4 (*17*) is intimately associated with the ESCRT machinery and is essential for the membrane scission cycle. Vps4 is recruited to scission sites by Vps2 (*18*, *19*). Vps2 is thought to have a capping role whereby it inhibits Snf7 polymerization (*6*). By recycling Vps2 (*20*), Vps4 promotes Snf7 polymerization. Thus, Vps4 is critical for the recycling of ESCRT-III and the replenishment of the soluble cytoplasmic pool. Early attempts at in vitro reconstitution of ESCRT-mediated budding and scission using giant unilamellar vesicles (GUVs) suggested that the process was independent of Vps4 and ATP (*21*, *22*), except for the final postscission recycling step. Cell imaging studies, however, showed that Vps4 localization peaked prior to scission in HIV-1 budding and cytokinesis (*23*–*28*), consistent with its direct role in scission upon ATP hydrolysis. A second goal of this study was to determine if Vps4 and ATP hydrolysis are directly involved in membrane scission, as opposed to mere recycling.

We encapsulated into GUVs the minimal ESCRT-III-Vps4 module containing yeast Snf7, Vps24, Vps2, and Vps4 (referred to here as the module) (fig. S1) in a mixture of palmitoyloleoyl-phosphatidylcholine, palmitoyloleoyl-phosphatidylserine, and biotinyl–phosphatidylethanolamine (80:20:0.1) at near-physiological ionic strength (~150 mM NaCl) (Fig. 1, D to G). We used optical tweezers to pull nanotubes extending between the surface of a GUV held by suction on an aspiration pipette and the surface of a streptavidin-coated polystyrene bead held by an optical trap (Fig. 1, A to C). To fuel the AAA+ ATPase Vps4, we also encapsulated the caged ATP analog P3-(1-(2-nitrophenyl)ethyl)ester–ATP (NPE-ATP). An optical fiber was used to illuminate with UV one GUV at a time, so that experiments could be carried out sequentially on individual GUVs in the same microfluidic observation chamber. In control experiments, where all components were included except for ATP, UV illumination led to no change in the force exerted on the bead (Figs. 1H and 2B). In similar control experiments omitting only Vps4, UV illumination resulted in a slight drop in the pulling force (Figs. 1I and 2C), attributed to the generation of two product molecules upon NPE-ATP uncaging. Thus, in the absence of ESCRT activity, the membrane nanotube was stable. When ATP was uncaged in the presence of the complete ESCRT module, a large rise in retraction force was indeed observed (Figs. 1J and 2I and movie S1). Over ~2 to 10 min (Fig. 1J), the force exceeded the trap maximum of ~65 pN and pulled the bead out of the laser trap (movie S1). This showed that in the presence of ATP, the ESCRT module can exert forces on membranes.

We sought to determine which components of the ESCRT module were required for force generation (Fig. 2A). With Vps2 or Vps24 as the only ESCRT-III subunits, essentially no force was generated (Fig. 2, D and E). In the presence of Snf7, omission of Vps2 or Vps24 led to little or no force generation (Fig. 2, F and H), consistent with the role of Vps2 in coupling of ATP hydrolysis by Vps4 to ESCRT-III remodeling and a role of Vps24 in copolymerizing with Vps2. When both Vps2 and Vps24 were present, but Snf7 was missing, a force rise of up to 12 pN was produced, consistent with the ability of Vps24 and Vps2 to co-polymerize (*10*, *20*) (Fig. 2G). The inactivated mutant E233Q protein (Glu^{233}→Gln) of Vps4 (*17*) failed to generate force (Fig. 2J). Deletion of the Vps4-coupling MIM1 motif of Vps2 (Fig. 2K) (*18*, *19*), which is essential for biological function, abrogated force production. Thus, the ability of the ESCRT module to exert forces on nanotubes, in an ATP-dependent manner (Fig. 2, B and C), correlates closely with the presence of all the components that are crucial for ESCRT-mediated membrane scission and their individual integrity (Fig. 2I).

We integrated a confocal microscope with optical tweezing capability to image membrane nanotubes pulled from GUVs containing fluorophore-labeled ESCRTs (Fig. 3, A to E, and fig. S2). By pulling on bare membranes, we obtained the bending modulus κ and standardized the calculation of the membrane nanotube radius (fig. S3). To maximize the signal in these experiments, Snf7 was labeled with the photostable dye Lumidyne-550 and imaged with a resonant scanner and a gallium arsenide phosphide (GaAsP) detector. We quantitated Snf7, Vps4, and membrane intensity using Gaussian fitting to the diffraction-limited tube profile (fig. S4).

[1]Department of Molecular and Cell Biology, University of California, Berkeley, Berkeley, CA 94720, USA. [2]California Institute for Quantitative Biosciences, University of California, Berkeley, Berkeley, CA 94720, USA. [3]Department of Theoretical Biophysics, Max Planck Institute of Biophysics, 60438 Frankfurt am Main, Germany. [4]Graduate Group in Biophysics, University of California, Berkeley, Berkeley, CA 94720, USA. [5]Howard Hughes Medical Institute, University of California, Berkeley, Berkeley, CA 94720, USA. [6]Department of Chemistry, University of California, Berkeley, Berkeley, CA 94720, USA. [7]Institute of Biophysics, Goethe University, Frankfurt/M, Germany. [8]Department of Physics, University of California, Berkeley, Berkeley, CA 94720, USA. [9]Molecular Biophysics and Integrated Bioimaging Division, Lawrence Berkeley National Laboratory, Berkeley, CA 94720, USA.
*These authors contributed equally to this work. †Present addresses: Centrillion Technologies, Palo Alto, CA, USA. ‡Department of Chemistry, University of Puget Sound, Tacoma, WA, USA. §Department of Medical Biochemistry and Biophysics, Wallenberg Centre for Molecular Medicine, Umeå University, Umeå, Sweden. ||Department of Molecular Biology and Genetics, Johns Hopkins University School of Medicine, Baltimore, MD, USA.
¶Corresponding author. Email: jimhurley@berkeley.edu (J.H.H.); carlosb@berkeley.edu (C.B.)

We monitored the response of a total of 46 nanotubes pulled from ESCRT module-filled GUVs following UV illumination. The nanotubes manifested a force increase and accumulation of Snf7 and Vps4 (Fig. 3, F to I, and movie S2). Of the 46 trials, 38 (83%) led to scission (Fig. 3J) as judged by simultaneous disappearance of the tube, sudden decrease in the force to zero, and appearance of membrane-, Snf7-, and Vps4-containing remnants on the trapped bead (Fig. 3, H and I). Tube lifetimes were widely distributed (Fig. 3J), with a mean lifetime of 425 s before scission. The distributions of lifetimes were similar at the superphysiological concentration of 2 μM, which was used to facilitate visualization, and the near-physiological concentration of 200 nM (Fig. 3J). One to two diffraction-limited puncta of Snf7 intensity appeared at >7 SD in 11 of 17 events analyzed. Typically, the puncta nucleated at the tube-vesicle junction (Fig. 3, F and G, and movie S2). Subsequently, the puncta sometimes moved or disappeared within the tubes. Snf7 puncta were essentially always colocalized with Vps4 (Fig. 3, F and G). At 2 μM, puncta contained in the range of 100 to 600 copies of Snf7 (Fig. 3K), which could exceed the minimum needed for scission yet is also roughly consistent with estimates in yeast cells (*29*).

To understand the relationship between the observed force (Fig. 4, A and B) and bulk and microscopic properties of the system, we quantitated the nanotube radius over time. Nanotubes used in this study were typically of a radius (r) of ~20 nm prior to ATP release (Fig. 4, C and D). The tubes began to narrow almost immediately following ATP release. Narrowing was associated with an increase in the amount of Snf7 and Vps4 seen in the tubes (Fig. 4, E and F), while essentially no change was seen in the intensity of the GUV membrane or the amount of Snf7 and Vps4 associated with the GUV (Fig. 4, G and H). This behavior was consistent over 17 traces (Fig. 4, K to N). Final values of r reached 5 to 10 nm by the time of scission. The uncertainty in the final values of r was substantial, because the membrane fluorescence signal was weak when r was <10 nm. In the case of constant membrane tension σ and bending modulus κ, the initial

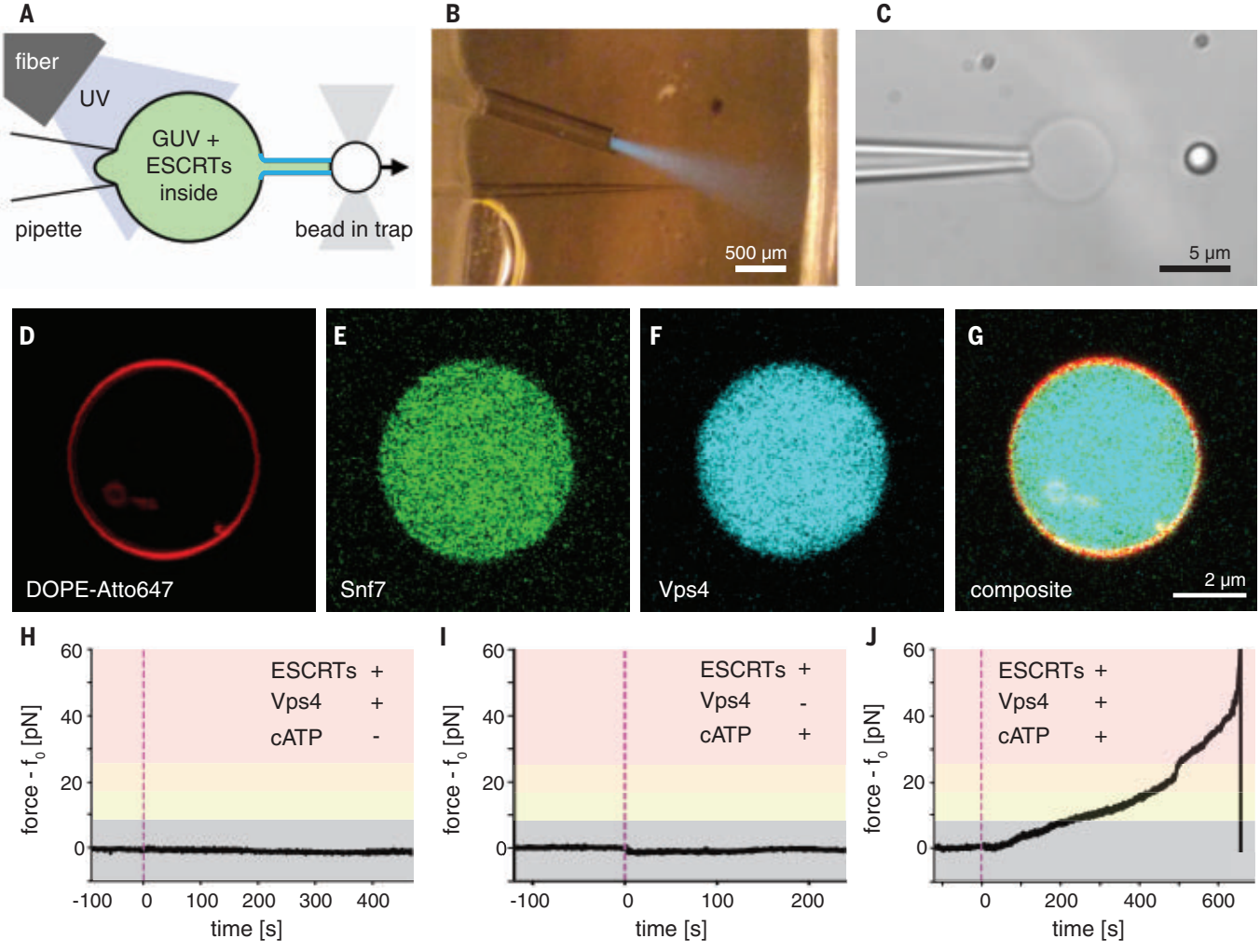

Fig. 1. ESCRT-III exerts an ATP-dependent force on membrane tubes. (**A**) Schematic of the experiment: a membrane tube (middle) is pulled out of a micropipette-aspirated GUV with a functionalized bead held in an optical trap, creating a reverse-curvature topology. Components of the ESCRT machinery and caged ATP are encapsulated in the lumen of the GUV. An optical fiber delivers UV light to uncage the ATP inside the vesicle and start the reaction. (**B**) Aspiration pipette, optical fiber, and UV light cone (blue) inside the microfluidic chamber for our experiments. (**C**) GUV (center) aspirated by the micropipette (left) and a tube-pulling bead (right). (**D** to **G**) Labeling different components of the ESCRT module [membrane label in (D), Snf7 in (E), Vps4 in (F); merged image in (G); 2 μM for all components] revealed a uniform distribution of proteins in the lumen of GUVs. (**H** to **J**) Force profiles over time detected by optical tweezers on a membrane tube pulled from a GUV that encapsulates components of the ESCRT module. (H) Control experiment on a full ESCRT module but with ATP omitted. No change in force could be measured. (I) Control experiment on a full ESCRT module but with Vps4 omitted. Apart from a minute dip in the force profile, which was due to small changes in osmolarity upon ATP uncaging, no effects were detected. (J) ATP uncaging (dashed line) in the presence of a full ESCRT module leads to a rise in force exerted on the tube, which is connected to the bead held by the optical trap. A large rise in force can overcome the trapping strength and pull the bead out of the trap.

and final force and radius are related to each other by the equations $f/f_o = (r/r_o + r_o/r)/2$ and $r/r_o = f/f_o - \sqrt{(f/f_o)^2 - 1}$. Figure 4, A to D, shows the values of f (Fig. 4, A and B) and r (Fig. 4, C and D) computed from the experimental values of r and f, respectively, with no adjustable parameters. The correlation between the measured and computed values was generally excellent (Fig. 4O). Consistent with an apparently constant κ, there was no accumulation of Snf7 on the GUV membrane over the course of the scission events (Fig. 4I). Consistent with a constant σ, the length of the membrane tongue in the pipette was typically constant (Fig. 4J). The formation of ESCRT puncta imposes nanotube radii smaller than the equilibrium radius r_o, which is associated with an increased pulling force, $f > f_o$. These findings are consistent with force generation by punctate microscopic assemblies of ESCRTs within the nanotubes, leading to the constriction of membrane tubes followed by scission.

It has been inferred that the core ESCRT-III proteins Snf7, Vps24, and Vps2, together with Vps4, comprise the minimal ATP-dependent scission machinery (*1*, *4*, *30*, *31*). Here, we directly confirmed this idea by visualizing scission in a minimal system that replicated a wide range of biologically validated structure–function relationships.

The most notable finding from the reconstituted system is that the core ESCRT-III proteins and Vps4 together exert an ATP-dependent axial force on the nanotube before severing. It was previously proposed (*8*) and then demonstrated (*9*) that Snf7 filaments have a preferred curvature and may exert forces when bent above or below their preferred value. It had also been hypothesized that breakage or remodeling of ESCRT filaments by Vps4 could contribute to force generation (*4*, *15*, *20*, *32*). Our observations now provide experimental confirmation that ESCRTs indeed can generate force from within a narrow membrane tube, and our results show that this force contributes to membrane constriction and is correlated with reverse-topology membrane scission.

ESCRTs (*7*, *10*, *11*) and the "normal topology" scission factor dynamin (*33*) have been visualized as cylindrical membrane coats, and Snf7 has also been seen in the form of large spirals of hundreds to thousands of copies (*9*). In the case of dynamin, extended coating of the tube is not needed, and one or a few rings appear capable of mediating scission (*34*). Our measurements of

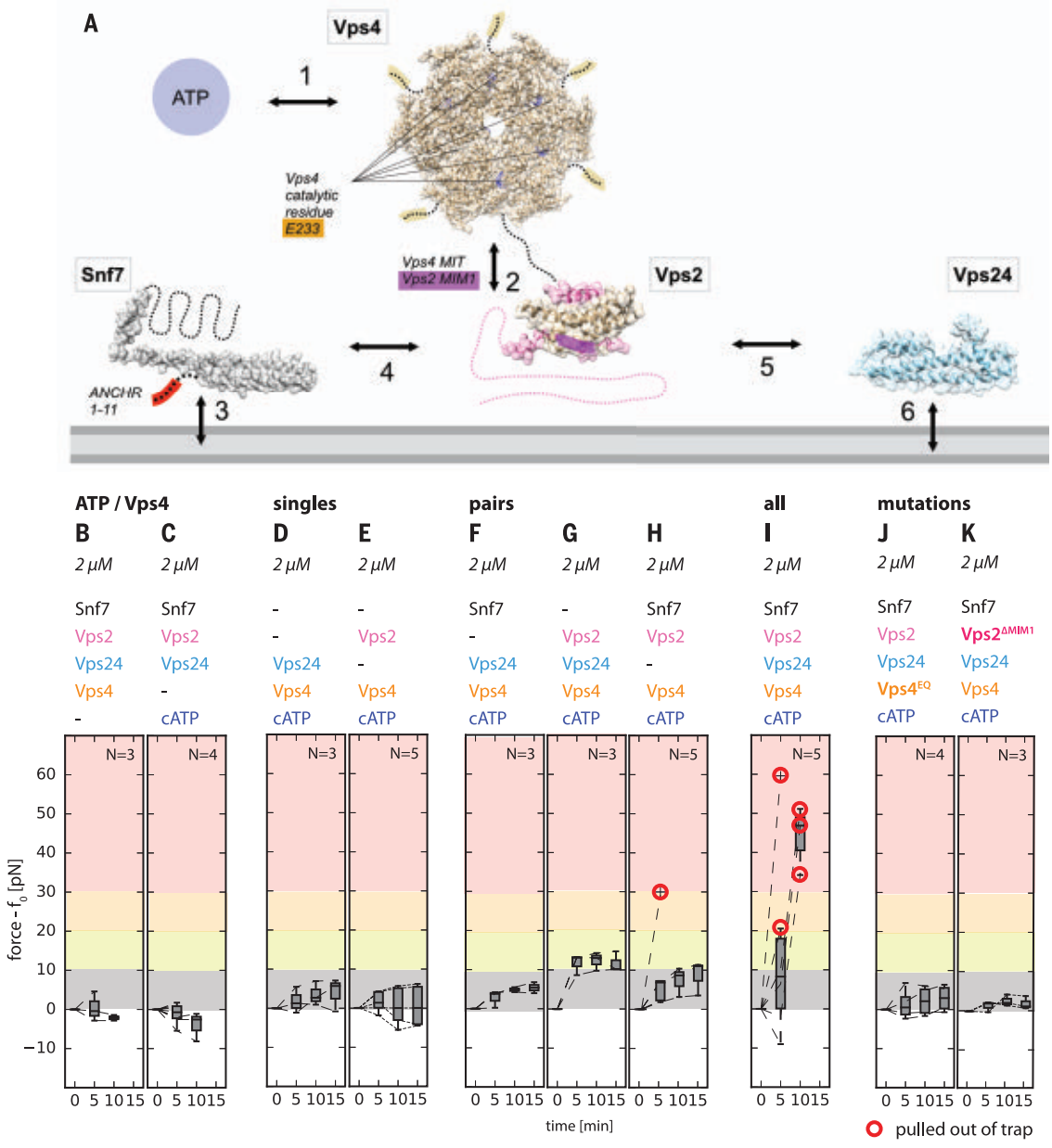

Fig. 2. Molecular determinants of force generation. (**A**) Interaction network of the ESCRT module. ESCRT proteins (space-filling structures and dashed lines) interact with the membrane (gray, bottom) as well as with each other. Key components (ATP), catalytic sites, and interacting motifs are highlighted in colors. (**B** to **K**) Individual components of the module contributed differently to the force exerted on membrane tubes: ATP and Vps4 were essential for force generation (B and C), and so was ATP hydrolysis (J, catalytically dead Vps4EQ mutant) and critical protein domains (K, Vps2 ΔMIM1). Only the full module (I), or pairings of Vps2 with Vps24 and Snf7 with Vps2 (G and H), led to significant force generation. Our data are consistent with the known interactions underpinning the activity of the ESCRT machinery.

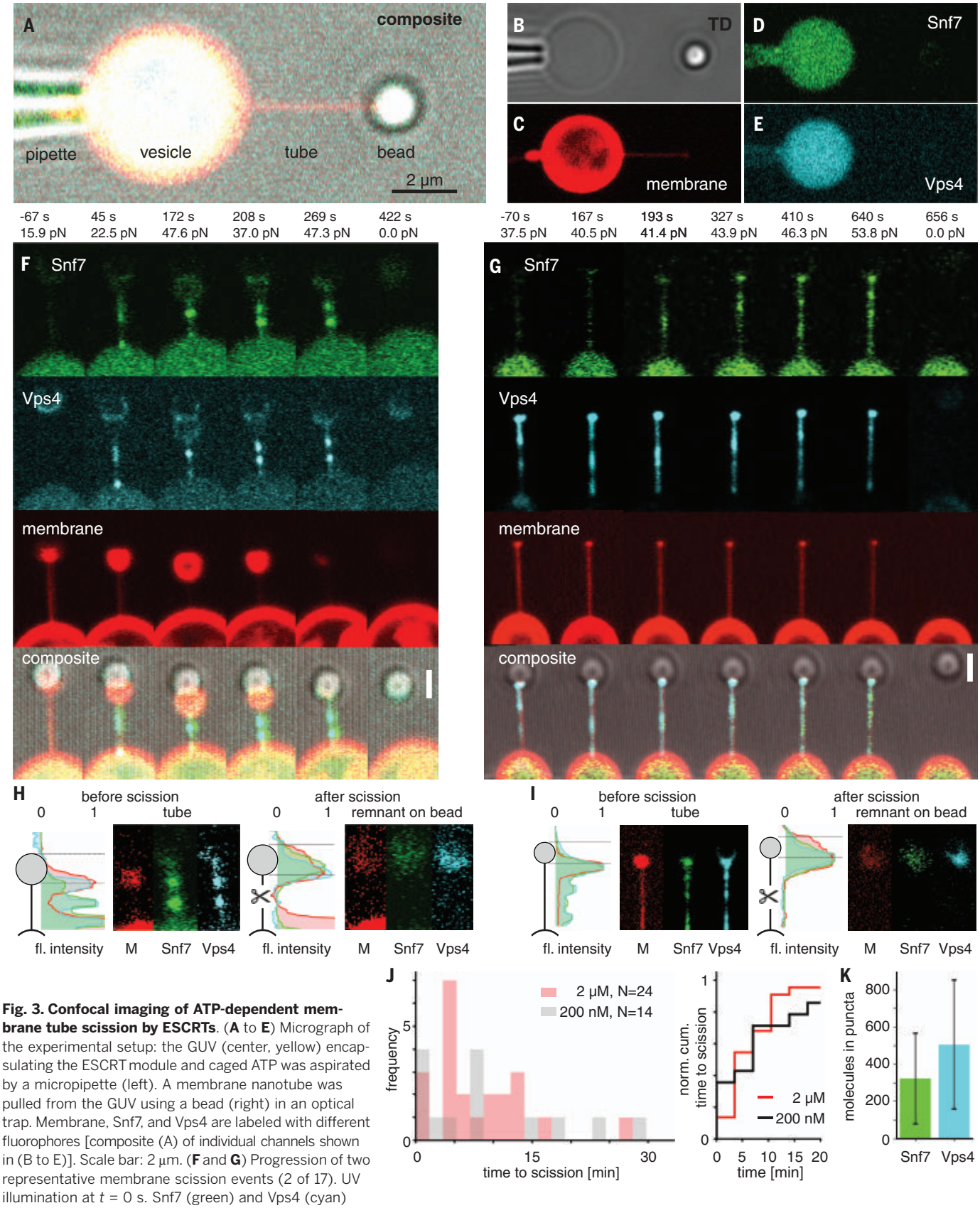

Fig. 3. Confocal imaging of ATP-dependent membrane tube scission by ESCRTs. (**A** to **E**) Micrograph of the experimental setup: the GUV (center, yellow) encapsulating the ESCRT module and caged ATP was aspirated by a micropipette (left). A membrane nanotube was pulled from the GUV using a bead (right) in an optical trap. Membrane, Snf7, and Vps4 are labeled with different fluorophores [composite (A) of individual channels shown in (B to E)]. Scale bar: 2 μm. (**F** and **G**) Progression of two representative membrane scission events (2 of 17). UV illumination at t = 0 s. Snf7 (green) and Vps4 (cyan) puncta became visible at the vesicle-tube junction and migrated into the tube. Scission happened at ~410 s and ~650 s, respectively. Scale bar: 1.5 μm. (**H** and **I**) Tube remnants on the bead identified scission in the middle of the tube. [Brightness adjusted compared to (F) and (G).] (**J**) Quantification of tube scission. (**K**) Protein copy numbers in puncta.

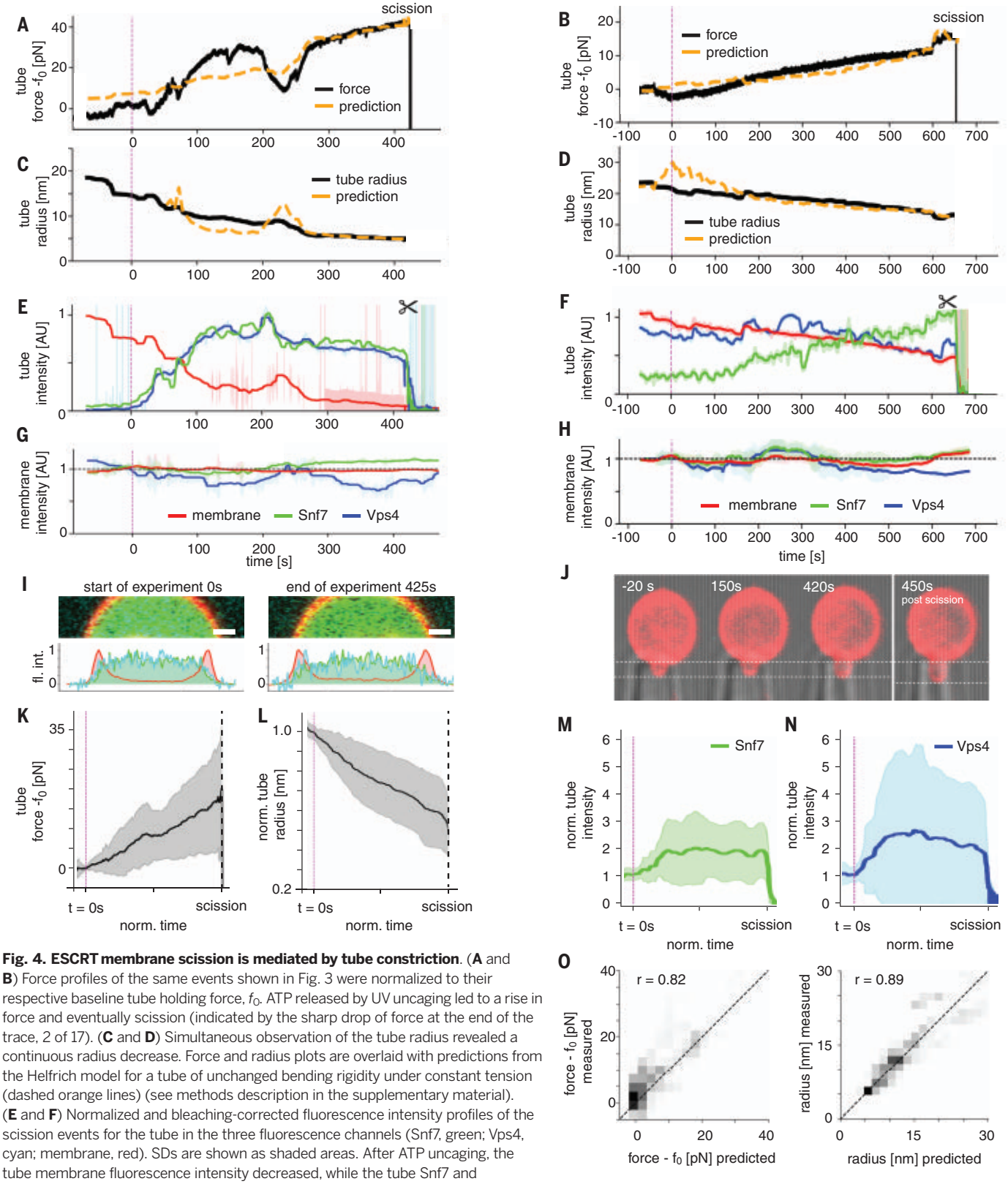

Fig. 4. ESCRT membrane scission is mediated by tube constriction. (**A** and **B**) Force profiles of the same events shown in Fig. 3 were normalized to their respective baseline tube holding force, f_0. ATP released by UV uncaging led to a rise in force and eventually scission (indicated by the sharp drop of force at the end of the trace, 2 of 17). (**C** and **D**) Simultaneous observation of the tube radius revealed a continuous radius decrease. Force and radius plots are overlaid with predictions from the Helfrich model for a tube of unchanged bending rigidity under constant tension (dashed orange lines) (see methods description in the supplementary material). (**E** and **F**) Normalized and bleaching-corrected fluorescence intensity profiles of the scission events for the tube in the three fluorescence channels (Snf7, green; Vps4, cyan; membrane, red). SDs are shown as shaded areas. After ATP uncaging, the tube membrane fluorescence intensity decreased, while the tube Snf7 and Vps4 intensities increased. (**G** and **H**) The GUV membrane fluorescence intensity profile over the time course of the scission event was essentially constant and showed no correlation with the force (Snf7, green; Vps4, cyan; membrane, red). SDs are shown as shaded areas. (**I**) Fluorescence intensity profiles of the GUV membrane at the start and at the end of the scission trace. No increase in protein fluorescence on the membrane was detected. (**J**) GUV aspiration projection at the beginning, middle, and end of the scission trace, showing essentially no change. (**K** to **N**) Averages (N = 17) ± SD of the force, radius, and tube fluorescence showed a consistent force rise, radius decrease, and fluorescence increase in the tube. (**O**) Correlation (r) between experiments and prediction for radius and force (N = 17).

scission by diffraction-limited puncta of Snf7 are consistent with imaging in cells (*29*) and with scission by rings or cones of molecular dimensions. The mechanical nature of constriction and force generation remains to be elucidated through structural approaches.

REFERENCES AND NOTES

1. J. McCullough, L. A. Colf, W. I. Sundquist, *Annu. Rev. Biochem.* **82**, 663–692 (2013).
2. Y. Olmos, J. G. Carlton, *Curr. Opin. Cell Biol.* **38**, 1–11 (2016).
3. C. Campsteijn, M. Vietri, H. Stenmark, *Curr. Opin. Cell Biol.* **41**, 1–8 (2016).
4. J. Schöneberg, I.-H. Lee, J. H. Iwasa, J. H. Hurley, *Nat. Rev. Mol. Cell Biol.* **18**, 5–17 (2017).
5. M. Babst, D. J. Katzmann, E. J. Estepa-Sabal, T. Meerloo, S. D. Emr, *Dev. Cell* **3**, 271–282 (2002).
6. D. Teis, S. Saksena, S. D. Emr, *Dev. Cell* **15**, 578–589 (2008).
7. P. I. Hanson, R. Roth, Y. Lin, J. E. Heuser, *J. Cell Biol.* **180**, 389–402 (2008).
8. Q.-T. Shen *et al*., *J. Cell Biol.* **206**, 763–777 (2014).
9. N. Chiaruttini *et al*., *Cell* **163**, 866–879 (2015).
10. S. Lata *et al*., *Science* **321**, 1354–1357 (2008).
11. J. McCullough *et al*., *Science* **350**, 1548–1551 (2015).
12. M. J. Dobro *et al*., *Mol. Biol. Cell* **24**, 2319–2327 (2013).
13. A. G. Cashikar *et al*., *eLife* **3**, e02184 (2014).
14. M. Lenz, D. J. G. Crow, J. F. Joanny, *Phys. Rev. Lett.* **103**, 038101 (2009).
15. L.-A. Carlson, Q.-T. Shen, M. R. Pavlin, J. H. Hurley, *Dev. Cell* **35**, 397–398 (2015).
16. N. Chiaruttini, A. Roux, *Curr. Opin. Cell Biol.* **47**, 126–135 (2017).
17. M. Babst, B. Wendland, E. J. Estepa, S. D. Emr, *EMBO J.* **17**, 2982–2993 (1998).
18. M. D. Stuchell-Brereton *et al*., *Nature* **449**, 740–744 (2007).
19. T. Obita *et al*., *Nature* **449**, 735–739 (2007).
20. B. E. Mierzwa *et al*., *Nat. Cell Biol.* **19**, 787–798 (2017).
21. T. Wollert, C. Wunder, J. Lippincott-Schwartz, J. H. Hurley, *Nature* **458**, 172–177 (2009).
22. T. Wollert, J. H. Hurley, *Nature* **464**, 864–869 (2010).
23. V. Baumgärtel *et al*., *Nat. Cell Biol.* **13**, 469–474 (2011).
24. N. Jouvenet, M. Zhadina, P. D. Bieniasz, S. M. Simon, *Nat. Cell Biol.* **13**, 394–401 (2011).
25. N. Elia, R. Sougrat, T. Spurlin, J. H. Hurley, J. Lippincott-Schwartz, *Proc. Natl. Acad. Sci. U.S.A.* **108**, 4846 (2011).
26. J. Guizetti *et al*., *Science* **331**, 1616–1620 (2011).
27. M. Bleck *et al*., *Proc. Natl. Acad. Sci. U.S.A.* **111**, 12211–12216 (2014).
28. M. A. Y. Adell *et al*., *J. Cell Biol.* **205**, 33–49 (2014).
29. M. A. Y. Adell *et al*., *eLife* **6**, e31652 (2017).
30. P. I. Hanson, A. Cashikar, *Annu. Rev. Cell Dev. Biol.* **28**, 337–362 (2012).
31. W. M. Henne, H. Stenmark, S. D. Emr, *Cold Spring Harb. Perspect. Biol.* **5**, a016766 (2013).
32. N. Elia, G. Fabrikant, M. M. Kozlov, J. Lippincott-Schwartz, *Biophys. J.* **102**, 2309–2320 (2012).
33. B. Antonny *et al*., *EMBO J.* **35**, 2270–2284 (2016).
34. A. V. Shnyrova *et al*., *Science* **339**, 1433–1436 (2013).

ACKNOWLEDGMENTS

We thank J.-Y. Lee, H. Aaron, S. Ruzin, and D. Schichnes for assistance with imaging; M. Vahey, D. Fletcher, and P. Lishko for advice on the aspiration pipette setup; A. Lee for assistance with the optical trap force calibration; and C. Glick for advice with the microfluidics. **Funding:** Research was supported by a Marie Skłodowska-Curie postdoctoral fellowship smStruct (J. S.), an NSF predoctoral fellowship (M.R.P.), NIH grant R56AI127809 and R01GM032543 (C.B.), DOE grant DE-AC02-05CH11231 (C.B.), the Howard Hughes Medical Institute (C.B.), NIH grant R01AI112442 (J.H.H.), the Max Planck Society (A.H.B. and G.H.), and the German Research Foundation CRC 807 (A.H.B. and G.H.). **Author contributions:** Conceptualization, J.S., M.R., D.H.G, S.Y., M.R.P., A.H.B., C.B., G.H., and J.H.H; methodology, J.S., S.Y., M.R., D.H.G, A.H.B., M.R.P., I.-H.L., and L.-A.C.; Confleezers, J.S., S.Y., and I.-H.L., software, J.S.; formal analysis, J.S. and A.H.B.; investigation, J.S., S.Y., M.R., M.R.P., A.H.B., and D.H.G; resources, J.S., S.Y., M.R., M.R.P., I.-H.L., L.-A.C., and X.R.; data curation, J.S; writing of original draft, J.S. and J.H.H; manuscript review and editing, J.S., S.Y., M.R., M.R.P., I.-H.L, L.-A.C, A.H.B., D.H.G., X.R., G.H., C.B., and J.H.H ; visualization, J.S.; supervision, G. H, C.B., and J.H.H. **Competing interests:** The authors declare no competing interests. **Data and materials availability:** All data are available in the main text or the supplementary materials. Code is available at https://github.com/JohSchoeneberg/Confleezers.

SUPPLEMENTARY MATERIALS

www.sciencemag.org/content/362/6421/1423/suppl/DC1
Materials and Methods
Figs. S1 to S4
References (*35*–*37*)
Movies S1 and S2

1 February 2018; resubmitted 17 September 2018
Accepted 7 November 2018
10.1126/science.aat1839

Polymer and Protein Molecular Weight Analyzer

The BI-MwA Molecular Weight Analyzer from Testa Analytical Solutions is a high-performance tool for studying synthetic and natural polymers in solution as well as investigating protein aggregation, oligomerization, and complex formation. Employing a 30-mW, 660-nm diode laser, the BI-MwA uses seven angles to determine the intensity of scattered light as a function of angle and polymer concentration. Using this information, the system software can quickly produce Zimm, Berry, and Debye plots from which weight average molecular weight (Mw), radius of gyration (Rg), and second viral coefficient (A2) data are calculated. The BI-MwA can be used in batch or flow mode, as part of a multidetector gel permeation chromatography/size-exclusion chromatography (GPC/SEC) system, or for following the kinetics of polymerization using the tunable diode laser absorption spectroscopy (TDLAS) technique.

Testa Analytical Solutions
For info: +49-30-864-24-076
www.testa-analytical.com

Automated Rotary Vial Washer

SP PennTech's RW-500 rotary vial washer is a small, automated system designed for low-to-medium output pharmaceutical and biotech applications. This washer has only two moving parts inside the washing chamber, and does not use needles, minimizing the chance of glassware damage and the possibility of a U.S. Food and Drug Administration (FDA) 483 notice for a product containing unintended particulates. Suitable for washing the full range of pharmaceutical vials from 2 mL–100 mL, the RW-500 combines effective vial washing with automatic tray loading, enabling outputs of up to 100 vials/min. Each vial format has a human–machine interface (HMI)-selected "recipe" with specific settings for variables such as spraying time and indexing time. Water for injection may optionally be recycled, filtered, and reused for early wash stages, and intermittent spraying further reduces water consumption.

SP PennTech
For info: 845-255-5000
sp-penntech.com/rw-500-vial-washer

CRISPR/Cas9 Gene Editing Kits

AMS Biotechnology (AMSBIO) offers CRISPR kits for almost any project type, including knockouts, knockins, point mutations, gene replacements, humanizations, tagging, and many more. CRISPR/Cas9 is a simple, efficient genome editing tool that allows for specific genome disruption and replacement, resulting in high specificity and low cell toxicity. The custom-designed CRISPR Complete Kit consists of CRISPR RNA (crRNA), transactivating crRNA (tracrRNA), Cas9 nuclease protein, and donor construct. The donor construct may be provided as oligonucleotide or plasmid, depending on project needs. AMSBIO also offers a comprehensive selection of CRISPR/Cas9 products for genome engineering—including Cas9 and guide RNA (gRNA) delivery systems in a flexible range of formats, homologous recombination donor vectors, and AAVS1 safe harbor targeting. This includes all-in-one Cas9/gRNA vectors, vectors for multiplex gRNA delivery, Cas9 messenger RNA and protein for transfection, and quantitative PCR primers and antibodies for Cas9 detection.

AMS Biotechnology
For info: 800-987-0985
www.amsbio.com/genome-editing-crispr-cas9.aspx

Custom High-Pressure Parallel Reactor

The Asynt High-Pressure Parallel Reactor can be custom configured to optimally suit applications including homogeneous and heterogeneous catalysis, hydrogenation, carbonylation, corrosion testing, parallel synthesis, and screening. Typically constructed from durable 316 stainless steel, this reactor is an affordable, compact unit that can be used to screen 10 mL × 30 mL reactions at pressures up to 200 bar and temperatures of 320°C. It can be used with a hotplate stirrer or customized for more rapid heating and/or multiple temperature zones. Several options are available, ranging from facilities for internal cell measurement, to sealed sample/additions valves, condenser jackets, electrical heating options, liquid charging systems, gas supply/mixing systems, air-driven stirrers, purged heating chambers, and more. Drawing upon skilled United Kingdom craftsmen, Asynt can also build these reactors from alternative materials, such as Hastelloy, Inconel, titanium, and alloy steels, allowing for greater heat capacity and use with particularly corrosive or caustic chemicals.

Asynt
For info: +44-(0)-1638-781-709
www.asynt.com/product/custom-high-pressure-parallel-reactors

hPSC Genetic Analysis Kit

Human pluripotent stem cells (hPSCs), including embryonic and induced pluripotent stem cells, acquire recurrent genetic abnormalities during prolonged culturing. These karyotypic abnormalities can alter the behavior of stem cells, jeopardizing the validity of a disease model, drug screen, or cell therapy. The hPSC Genetic Analysis Kit from STEMCELL Technologies contains all required components to detect over 70% of the most common karyotypic abnormalities reported in hPSC cultures. This quantitative PCR–based kit enables screening of multiple human stem cell lines in a rapid, cost-effective manner. It uses double-quenched probes, which give superior performance over single-quenched probes, and detects the copy number of the minimal critical regions of commonly mutated genetic loci with high specificity and sensitivity. By addressing an unmet need in the field, it empowers researchers to confirm stem-cell culture quality and have confidence in their data.

STEMCELL Technologies
For info: 800-667-0322
www.stemcell.com

Lyophilizer

The Ultra Lyophilizer from SP Scientific is a compact, free-standing freeze-drying system that can process bulk products, vials of all shapes and sizes, and large numbers of microplates. With the Ultra, you can specify up to 2.13 m^2 of useable shelf area in a footprint of only 1.13 m^2. The highly polished 316 stainless-steel product chamber, shelves, and smooth-walled condenser chamber ensure that best-processing conditions can be easily maintained and that the freeze dryer gives many years of trouble-free operation. Up to 15 shelves can be specified, and interspacing can be simply rearranged in most models. With shelf temperatures as low as –70°C and condenser temperatures down to –85°C, the Ultra supports a wide range of applications. Easy-defrost condensers enable fast turnaround between runs. A choice of condenser capacities of 35 L or 50 L allows you to select a high shelf-surface-to-condenser-surface ratio, which is most suitable for freeze-drying products requiring a very large amount of shelf area but containing less solvent, as is the case with many diagnostic kits and tissue-banking applications.

SP Scientific
For info: 845-255-5000
www.spscientific.com

Electronically submit your new product description or product literature information! Go to www.sciencemag.org/about/new-products-section for more information.

Newly offered instrumentation, apparatus, and laboratory materials of interest to researchers in all disciplines in academic, industrial, and governmental organizations are featured in this space. Emphasis is given to purpose, chief characteristics, and availability of products and materials. Endorsement by *Science* or AAAS of any products or materials mentioned is not implied. Additional information may be obtained from the manufacturer or supplier.

Science Careers

SCIENCE CAREERS ADVERTISING

For full advertising details, go to ScienceCareers.org and click For Employers, or call one of our representatives.

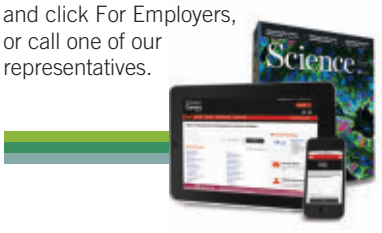

AMERICAS

+1 202 326-6577
+1 202 326-6578
advertise@sciencecareers.org

EUROPE, INDIA, AUSTRALIA, NEW ZEALAND, REST OF WORLD

+44 (0) 1223 326527
advertise@sciencecareers.org

CHINA, KOREA, SINGAPORE, TAIWAN, THAILAND

+86 131 4114 0012
advertise@sciencecareers.org

JAPAN

+81 3-6459-4174
advertise@sciencecareers.org

CUSTOMER SERVICE

AMERICAS

+1 202 326-6577

REST OF WORLD

+44 (0) 1223 326528

advertise@sciencecareers.org

ScienceCareers
FROM THE JOURNAL SCIENCE AAAS

ScienceCareers.org

POSITIONS OPEN

Northeast Ohio MEDICAL UNIVERSITY

Chondrocyte is the only cell type present in the cartilage and the response of chondrocytes to anabolic/catabolic stimuli is mediated by a wide variety of factors acting through specific receptors. Activation of these receptors leads, through cell signaling, transcriptional upregulation and post-transcriptional regulation, to a program of chondrocyte responses that determines the fate of the articular cartilage. Our laboratory is focused on identifying the novel transcriptional and post-transcriptional regulators of chondrocyte genes expression in diseased and healthy cartilage. Experience with animal models of OA will be a plus. Candidates with experience in RNA/miRNA biology will be given preference. Responsibilities include designing, conducting, and analyzing scientific experiments in her/his field; presenting research results in oral and written formats; developing and maintaining knowledge of the current scientific literature. Send applications to **thaqqi@neomed.edu**. Only short-listed candidates will be contacted for interview.

FACULTY POSITIONS IN MOLECULAR CARDIOVASCULAR BIOLOGY

Assistant, Associate or full Professor faculty positions are available for the Division of Molecular Cardiovascular Biology, within the Heart Institute, in the Department of Pediatrics at Cincinnati Children's Hospital Medical Center. These will be regular, tenure-track faculty appointments. The applicant should have a Ph.D., M.D. or M.D.-Ph.D. with a research program that investigates or can be applied to the investigation of the molecular biology of cardiac muscle, although applicants with a skeletal muscle research focus will also be considered. The successful applicant will receive a generous startup package and join a multidisciplinary, world-renowned faculty performing cutting-edge heart and skeletal muscle research with a strong emphasis on disease mechanisms. Cincinnati Children's Hospital Medical Center was named the second best children's hospital in the United States in the 2018 *U.S. News & World Report* and is the second-highest ranking recipient of research grants from the NIH among pediatric institutions. The Heart Institute has brought together clinical care, research and education programs, all directed at providing comprehensive care for children with heart and muscle disease and developing novel therapeutic avenues for treatment (https://www.cincinnatichildrens.org/research/divisions/h/heart).

A letter of interest, accompanied by a complete *curriculum vitae* and the names of three references should be electronically sent to email: **Jeff.Molkentin@cchmc.org**

In consideration of our children the Medical Center is committed to a smoke-free workplace. Children's Hospital Medical Center conducts pre-employment drug screening as part of a comprehensive program to maintain a drug-free workplace. Equal Opportunity Employer M/F. Minorities are encouraged to apply.

Call for Outstanding Scientists & Engineers

Advanced Innovation Center for Intelligent Robots and Systems

Beijing Institute of Technology

Beijing, China (Valid before Jan. 2020)

The Advanced Innovation Center for Intelligent Robots and Systems, Beijing Institute of Technology (BAICIRS) is recruiting outstanding scientists & engineers in areas including but not limited to:

- Mechanism design for legged robots
- Operating mechanism design
- Hydromechatronics drive
- Synthetic simulation system based on high-level architecture
- Vision processing algorithms
- Micro/nano device design
- Laser imaging sensor design
- EEG & EMG signal acquisition and processing
- Electromagnetic field signal collection and improved algorithm
- Neurophysiology of perception and motion control
- Biomaterial preparation and development
- Cell electrophysiological research
- Soft robot dynamics
- Prosthetic design and control
- Pneumatic artificial muscle
- EtherCAT communication
- SLAM
- MEMS device design
- Software/hardware design for embedded system
- Cerebral function imaging
- Human health indicators collection and processing
- Detection of mobile device inside human body cavities
- Artificial intelligence
- Cell communications and neural transmission
- Tissue engineering
- Three-dimensional dynamic simulation
- Robotic appearance design
- Animation design

Beijing Institute of Technology (BIT), founded in 1940, has always been a leading institution of science and technology in China. In 2016-2017, BIT was ranked among the Top 400 in QS World Universities Ranking, as well as the 15th among the Chinese universities in the above rankings. The fundamental research on engineering, material science, chemistry, physics, computer, mathematics and social science in BIT is among the top 1% in ESI ranking.

BAICIRS, as a secondary institute subordinated to BIT, was founded in August 2015 among the first batch of 13 advanced innovation centers accredited by Beijing Municipal Education Commission. Focusing on national major demands and the global research fronts in intelligent robots and systems, and with the objective to yield solutions for a series of major and frontier scientific issues, BAICIRS endeavors to make breakthroughs in theories and technologies of locomotion bionics, multiscale perception and manipulation, biomechatronic fusion and interaction, and system control and integration, through comprehensive and interdisciplinary integration of molecular bionics, bionic mechanics, multiscale perception and manipulation technologies, and multiple artificial intelligence technologies.

BAICIRS provides favorable research environment, including a spacious lab covering 8 different floors in one building in the modernized Science Park of BIT, with the floorage of 15,000 m^2 in total, and advanced research equipment and facilities, furnishing a world-class environment for research activities.

BAICIRS invites applications for the following positions:

1.Positions Supported by the National "Young Thousand Talents Program"

► Qualifications

- The applicants are required to hold a Ph.D. and have at least three years overseas research experience in world-class universities, research institutes, or top-ranking overseas companies. Applicants with overseas experience and who are now working in China for less than one year will also be considered.
- Under the age of 40. Exceptional candidates who have made outstanding research discoveries will be considered as individual cases.

► Benefits

- Professorship and Ph.D. supervisor, with special enrollment quotas for graduate students.
- A subsidy of CNY 2-6 million for research funding and laboratory space provided by BIT.
- Annual salary of CNY 420,000 (insurance and accumulation fund paid by BIT not included).
- Opportunity of buying a new flat of one sitting room and two bedrooms with a discount of CNY 1 million compared to the market price or a subsidy of CNY 2 million. Assistance of housing during the transition period will be provided.
- Assistance in placement of children and spouse for educational and job opportunities.
- International travel expenses will be covered for the interview, with recommendations to other positions if not recruited.

2.Tenure-Track Positions

► Qualifications

- The applicants are required to hold a Ph.D. and have more than 2 years' experience at world-class universities or research institutions, under the age of 35 for associate professor and 32 for assistant professor.
- The applicants are required to have expertise about the latest development in the research area with highly recognized research achievements, show potential for being future academic leaders to develop new research directions, and be supported by high-level papers as the first author or corresponding author.

► Benefits

- Professorship/associate-professorship and supervisor of Ph.D./master's degree students, with special enrollment quotas for graduate students.
- Annual salary of CNY 300,000-360,000 (Insurance and accumulation fund paid by BIT not included).
- Research start-up funds of CNY 400,000-600,000.
- Assistance in the placement of children's educational opportunities.

Application Instructions

Please send your resume, which includes:
- a list of publications (necessary) and
- a future research plan (preferable)

to the following two emails:
ninger1979@bit.edu.cn; rouer_dai@bit.edu.cn

Welcome to visit website http://baicirs.bit.edu.cn/english/

2018: A crucial year for China

The year 2018 is of special significance to China because it marks the 40th anniversary of the Reform and Opening-Up, and the fifth year since the Belt and Road Initiative started.

If the momentous economic changes that have taken place in this great East-Asian country over the last few decades were presented in motion pictures, they would appear as epic and magnificent. But what matters the most, and is really behind all of the country's recent prosperity, is the formation of a set of theories with uniquely Chinese characteristics. Because of these theories, China found that it no longer needed to blindly follow the so-called "truths" that underlie the patterns of development in other countries. The country has proved by its actions that the path it's walking on is the right one, and this path has become the driving force for its high-speed growth and the motivation for the Belt and Road.

As of July 2018, more than 100 countries and international organizations have signed agreements with China to work on the Belt and Road Initiative—countries ranging from Eurasia to Africa, Latin America, the Caribbean, and the South Pacific. And now the basic design of the Belt and Road has been completed, and all its supporting pillars have been built: The project has been included in the international discourse system and written into resolutions of the United Nations General Assembly and the United Nations Security Council. A three-part structure of international cooperation has emerged, which is (1) based on bilateral cooperation, (2) supported by a multilateral mechanism, and (3) led by summit forums. Under the Belt and Road, and based on the principles of equality, openness, and benefit-for-all, China has formed an open international system in which countries can work together toward their goals. It can be said that the domestic and international achievements represented by both the 40 years of the Reform and Opening-Up and the five years of the Belt and Road have rested on these same principles of cooperation and on a win-win spirit.

Of course, the economy isn't the only thing that has changed in China. Along with economic developments, significant evolution has occurred in the country's educational system.

Shixin Wang
Deputy Chief Editor of China Education Online, Chief Executive Editor of AcaBridge

The academic explosion in China

According to a recent report from Bloomberg News, Qingnan Xie of the Nanjing University of Science and Technology and Richard B. Freeman of Harvard University analyzed the total number of papers published in scientific fields from 2000 to 2016 in China. The research showed that, in the fields of physics, engineering, and mathematics, the proportion of papers published by Chinese scholars grew four-fold during this period. In 2016, this number exceeded the number of papers published by American authors. And when selecting Chinese authors rather than going by which country a paper was published in, the number rose even higher. More than 30% of all papers published in the fields of physics, engineering, and mathematics were written by Chinese scientists.

Before the research of Xie and Greenberg was completed, Science and Engineering Indicators 2018, released by the U.S. National Science Foundation at the beginning of this year, showed that 426,000 science and engineering papers were published in China during 2016, more than the 409,000 papers published in the United States during the same year.

China is catching up with the United States at an amazing speed, not only in terms of the number of scientific papers published, but also in terms of their quality. Papers published in 82 top science and technology journals were analyzed, and the result was published by the Nature Index (of Nature magazine). It shows that China has overtaken Europe, Japan, and South Korea and become second only to the United States, which ranks first. "Judging by the current trend, it's likely that China will replace the United States in terms of the quality of papers after seven to eight years, in around 2025," Nature predicted. Xie and Free-

man analyzed the authors whose papers were published in Nature and Science during 2016, and found that 20% of them were from China—and that percentage has doubled.

The "engine" that has propelled China to catch up with the United States at such an astonishing pace is ultimately powered by outstanding people—and of course, financial support. In terms of annual R&D expenditures, reported by the Science and Engineering Indicators 2018, the United States in 2015 led the world with USD 497 billion, accounting for 26% of the global total amount; China ranked next with USD 409 billion, accounting for 21%. However, as for the annual rate of growth for R&D expenditures, China's annual rate is 18%, which is more than four times that of the United States (4%).

Breaking the "Five-Only" standard

In October 2018, the Chinese Ministry of Science and Technology, along with the Ministry of Education (MOE) and other ministries, issued a notice implementing a new policy aimed at eliminating the "Four-Only" standard for academic evaluation, which "examines only the numbers of published papers, and judges people only by their titles, only by their degrees, and only by the awards they have received." In November, the MOE issued another notice that added an additional standard: "judges people only by their positions" (hereafter the "Four-Only" standard will be referred to as the "Five-Only" standard). The implementation of this new policy caused great shock and much heated discussion.

This directive is not only a correction of several problems that have long been criticized throughout Chinese academic circles, but also a challenge to some international practices and common rules.

Some observers believe that the purpose of eliminating the "Five-Only" standard is to deepen the reform of the educational system in China's colleges and universities, to encourage people to research and educate with the right moral values, to reverse the trend of applying unreasonable academic evaluation standards, and to encourage the practice of evaluating papers according to their quality, the scientific contributions they make, and the influence they have on their field. Such a system will inspire passion and a spirit of innovation, and will help create a more "level playing field" for people in all career paths.

Nevertheless, there are those who worry about how the new evaluation rules will be put in to practice after the old ones are gone, and how to define the line between what's "normal" and what's not. If these issues are not resolved, the result will be a chaotic academic evaluation system, and even the standards of "Double-First Class" universities will be affected.

However, those who are concerned have perhaps not considered the profound impact that bringing about these new standards will have. It's true that these issues are not only problematic in China, but also in other academically advanced countries. But one can see this new approach as an opportunity. There's an old saying in China that goes, "Great chaos promotes great solutions," which in this case means that if by resolving the old issues, a new set of academic evaluation standard is created that promotes innovation, it will greatly motivate China's progress in science and technology. The influence of these developments could be dramatic.

Establishment of Westlake University

On October 20, 2018, Westlake University was formally established. Five Nobel laureates, dozens of principals and representatives from home and abroad, and nearly 100 donors gathered in Hangzhou to celebrate the university's founding.

The opening of Westlake reflects China's progress, and is a real breakthrough. Internationally, elite schools are mainly private universities, while Chinese higher education is basically dominated by public colleges and universities. Though this pattern has demonstrated its advantages, it has also encountered a series of problems brought about by administrative difficulties and other reasons.

Westlake University is China's first privately funded research university, developed through the collaboration of many different groups and with the approval of the Chinese government. High hopes were placed on the university both from the international community and all sectors of society. These hopes are represented in the letter of congratulation sent by the MOE to Westlake University: "The establishment of Westlake is the positive attempt of social forces to establish research-based universities and is a positive action for servicing the national innovation-driven development strategy. It is of great significance to the reform and innovation of the Chinese higher-education system." From its proposal, submitted on March 11, 2015, to its founding on October 20, 2018, Westlake was established in only 1,319 days. This great speed is further evidence of the powerful support and tremendous encouragement flowing out from all sectors of Chinese society to this research-based university.

The university's greatest significance lies in its implementation in the mode of "universities established mainly by foundations." The School Board is the highest decision-making body at Westlake. Previously, Chinese universities were mainly funded by government (public, institutional) and only supplemented by market contributions (private, profit-making), while Westlake took a different path, to operate with private funding.

What's even more fascinating is the organizational concept and institutional arrangement behind Westlake University. All rules and regulations at Westlake University have been organized on the basis of full consideration of China's national conditions; they also follow international standards and fully reflect the changes characteristic of globalization, and are seen in the university's teaching and research, administrative services, logistical support, campus culture, and other aspects. For example, in terms of system design, the Principal Accountability System has been established under the leadership of the School Board, and the Party Committee of Westlake University has been organized to guarantee adherence to the accepted governance principles of teaching, administrative management, and academic guidance determining administrative services.

As for Westlake's specific institutional arrangement, there are many interesting facets to note: Vocational administrative services free teachers from the red tape of daily routines; efficient research platforms ensure the smooth progress of cutting-edge science; and teachers are responsible for formulating the rules and regulations of university governance and handing them over to Westlake's administrative teams and scientific research platforms for specific implementation.

In particular, Westlake University proposes to build an academic evaluation system that encourages innovation. "Neither the number and citation rate of academic papers nor the influencing factors of academic journals will be the main indicators of academic evaluation in Westlake University." Here, the academic evaluation of scientists depends mainly on whether their research is at the forefront of relevant fields and has the potential to make a substantive impact. The humanistic care and truly academic atmosphere generated by this new evaluation mechanism will become part of the unique campus culture of Westlake University.

If the groundbreaking pattern established by Westlake proves to be workable, then other private colleges and universities in China will hopefully follow suit.

State Key Laboratory of Microbial Technology, Shandong University:
To Fuel, Feed, Heal, and Clean the World with Microbial Technology

Youming Zhang, Ph.D.,
Director, Professor, SKLMT
Shengying Li, Ph.D.,
Professor, SKLMT

山东大学 SHANDONG UNIVERSITY

The program of microbiology at Shandong University has a long and brilliant history, where the earliest Doctor's and Master's degrees in Microbiology in China were awarded. As a pioneer of microbiology education in China's universities, this program has trained a large number of microbiology professionals since 1950s. On the basis of this program, the State Key Laboratory of Microbial Technology (SKLMT) was founded in 1987 at Shandong University.

Overview

Microbial technology is the core biotechnology and the central driving force for the development of life sciences. It plays essential roles in solving the major problems that "a community of shared future for mankind" is now facing, such as climate change, fuel shortage, food crisis, infectious and incurable diseases, and environmental disruption. To address these global challenges, SKLMT is dedicated to the development of innovative microbial technologies, with an emphasis on resources and environmental microbial technology, pharmaceutical microbial technology, industrial microbial technology, and marine microbial technology.

Over the past 30 years, SKLMT has fostered a growing number of cutting-edge researches including the Red/ET DNA recombineering and DNA direct cloning technology, industrial application of the cellulase over-producing *Penicillium* strains, the mechanisms of biogeochemical cycling driven by marine microorganisms, myxobacterial genetics and chemecology, and biomass-based bioproduction of high value-added chemicals, to name a few.

Global challenges call for global collaborations. SKLMT on one hand gathers international scholars to carry out joint researches, on the other hand contributes Chinese wisdom to accelerate the development of applicable microbial technology. For example, the Shandong University–Helmholtz Institute of Biotechnology, co-built by Shandong University (SDU), the Helmholtz Center for Infection Research (HZI) and the Institute for Drug Science (HIPS), was officially established in 2014. On this platform, international forums, exchanges of students and scholars, co-publication of high impact papers, and technology transfers are in bloom.

From land to ocean

Limited by the previous laboratory's location and the accessibility to marine microorganisms, the early research activities of SKLMT were focused on terrestrial microbial resources. The relocation of SKLMT in 2016 from inland Jinan to coastal Qingdao, which is the International Center for Marine Scientific Research and Education, paves the broadway to ocean for SKLMTers. Prof. Zixin Deng, an Academician of the Chinese Academy of Sciences as well as the Director of the SKLMT Academic Council, encourages more Chinese microbiologists to "Xia Hai" (pursue the studies on marine microorganisms). To date, SKLMTers have isolated and identified a large number of new species of marine microorganisms from deep sea and polar region, significantly enriching our knowledge on the underexplored marine microbial resources. The team led by Profs. Xiulan Chen and Yu-zhong Zhang keeps providing new molecular insights into diverse microbial enzymes for transformation of marine organic matters that are important participants in the global biogeochemical cycles of carbon, nitrogen, sulfur, and phosphorus. In the future, SKLMT will place a high premium on marine microbial resources and make greater efforts on exploring the solutions to the above-mentioned global challenges from the plethora of oceanic microorganisms.

Embracing synthetic biology

Born in the post-genomic era, synthetic biology has conceptually and technically been reshaping all aspects of life sciences including microbiology and biotechnology. SKLMT has been embracing the revolutionary changes brought by synthetic biology. Today, a number of SKLMTers are at the forefront of synthetic biology. Prof. Youming Zhang is the inventor of the Red/ET DNA recombineering technology, with which the large DNA fragments (> 100 kb) can be directly cloned from genomes. Combined with CRISPR-CAS, the upgraded Red/ET recombineering system has become more efficient and accurate, thus being applied for constructions of drug biosynthetic pathways, magnetic nanostructures, and humanized animal models for antibody production. This pioneering microbial technology is now widely used in global laboratories as well as pharmaceutical and biotechnology companies. Recently, Profs. Luying Xun and Lichuan Gu invented a "T5 exonuclease DNA assembly" (TEDA) method, which is simpler, cheaper, and more efficient than the existing Gibson assembly and the commercial In-Fusion method.

Besides these new enabling technologies, the world-class libraries of catalytic parts for diverse purposes in synthetic biology, such as the microbial P450 enzyme library, the redox partner protein library, the glycosidase library, the glycosyltransferase library, and the extreme enzyme library have been built at SKLMT. In addition, the teams led by Profs. Yuezhong Li, Qingsheng Qi, Yuemao Shen, Guanjun Chen, Lushan Wang, Xiang Gao, Shengying Li and others have made significant progresses on constructing diverse advanced microbial cell factories based on bacteria, myxobacteria, Streptomyces, yeasts, and filamentous fungi.

At present, SKLMT is globally recruiting young talents to join us in order to develop the disruptive microbial synthetic biology technologies such as "transparent chassis" and "smart P450 enzyme" to make our SKLMTers' voice in the world.

Nanjing Agricultural University Welcomes Talents from All Over the World

Nanjing Agricultural University (NAU) sincerely invites you to join us in teaching and research.

About us

Nanjing Agricultural University is a university under the administration of the Ministry of Education and has been selected and included in the National "Double World-Class" University Construction Initiative. In the fourth-round national first-level discipline evaluation in 2017, it had four disciplines listed in Class A+, ranking itself the 11th of the top universities in China. In the ESI rankings, it had seven disciplines ranked among the top 1% worldwide, and two of the disciplines, Agricultural Science and Plant & Animal Science, among the top 1‰. The US News 2018 has listed NAU the top 9 among the Best Global Universities of Agricultural Sciences.

Fields of research

The fields of research you are invited to join in are:

Agricultural Sciences including :

Crop Science, Horticulture, Agricultural Resources & Environment, Plant Protection, Animal Husbandry, Veterinary Science, Fisheries Science, and Grass Science;

Science and Technology including :

Biology, Ecology, Environmental Science & Engineering, Food Science & Engineering, Landscape Architecture, Agricultural Engineering, Bioinformatics, and Computer Science & Technology;

Humanities and Social Sciences including :

Management, Economics, Sociology, Legal Science, History, Literature, and Linguistics.

You are also welcome to join us in the following **Interdisciplinary Subjects :**

Genomics & Phenomics, Microorganism-Botany-Pest Interactions, Food Nutrition and Human Health, Agricultural Equipment Engineering, Agricultural Informatics, and so on.

Position requirements

Doctorate recipients from world famous universities; post-doctor researchers from famous research institutes; and talents with professional titles of associate professor, professor or other higher titles, from world-famous higher institutions or research institutes, and with outstanding teaching and research achievements.

NAU will offer you a benefits package which is competitive among the universities in the local area and which will be negotiated in person.

Talent introduction policy

You will enjoy a talent allowance equivalent to those for the Zhongshan Scholars of NAU who are Zhongshan Distinguished Professor, Zhongshan Professor, Zhongshan Fellow, and Zhongshan Young Scholar, according to your qualities for recruitment; or we may talk and agree on your annual salary.

Specific conditions of your research team, laboratory, graduate students to supervise, accommodation, and employment of your spouse are to be discussed in person.

Note: The Zhongshan Scholars is an NAU-developed open initiative to support career development and academic innovation for leading scientists of today and tomorrow, and it is a major initiative to construct a world-class university and to establish world-class disciplines, so as to realize NAU's strategy of rejuvenation by talents. Recruitment is divided into four categories:Zhongshan Distinguished Professor, Zhongshan Professor, Zhongshan Fellow and Zhongshan Young Scholar. Special talent allowance is provided for these outstanding scientists.

Application documents

Please prepare and email to rcb@njau.edu.cn the following documents for your qualification:

- a detailed CV, starting from your undergraduate education till the time of your application, including periods of continuous education, working experience, publications, research projects hosted or participated in, and certificates of awards.
- photocopies of diplomas, certificate of doctor's degree, and certificate of current employment
- Full texts of five representative papers published in the past five years.

Contacts:
Ms. Liu Hongmei
Telephone:
+86-25-84399039
Email address:
rcb@njau.edu.cn

Opportunities to shine at ShanghaiTech University

ShanghaiTech University is a young and dynamic higher education institution aiming for high-quality research and global influence. To address challenges faced by China and the world, it seeks innovative solutions in energy, materials, environment, human health, data science, artificial intelligence (AI), and electrical engineering. An integral part of the Zhangjiang Comprehensive National Science Center, the university is now leading several frontier research projects at large-scale facilities. For more information, please visit: **www.shanghaitech.edu.cn**.

To apply: using this format, please submit a cover letter (Firstname_Lastname_Cover_Letter.pdf), a research plan (Firstname_Lastname_Research_Plan.pdf), and a CV (Firstname_Lastname_CV.pdf) to **shanghaitechuniversity@gmail.com**.

We are now seeking talented researchers for multiple faculty positions at all ranks in the following fields:

School of Physical Science and Technology: energy, system materials, photon and condensed state, material biology, environmental science and engineering

School of Life Science and Technology: molecular and cell biology, structural biology, neuroscience, immunology, stem cells and regenerative medicine, system biology and biological data, molecular imaging, biomedical engineering

School of Information Science and Technology: computer science, electrical engineering, information engineering, artificial intelligence, network and communication, virtual reality, statistics, big data and data mining

School of Entrepreneurship and Management: economics, finance, accounting, management, marketing, strategy and entrepreneurship

School of Creativity and Art: Innovative Design, Filmmaking, Game Design, Tech-driven Art, Big Data Visualization, Creativity, Design Thinking

Shanghai Institute for Advanced Immunochemical Studies: antibody therapy, Immunotherapy, cell therapy, regeneration medicine

iHuman Institute: bio-imaging, biology, chemistry, computational biology, AI/ML

Institute of Mathematical Sciences: pure mathematics, theory of computing, applied mathematics

Successful applicants will have a doctoral degree, and are expected to establish a record for independent, internationally recognized research, supervise students and teach high-quality courses.

ShanghaiTech University will offer attractive compensation packages, including: **Initial research support package:** reasonable start-up funds, research associates and post-doctoral fellows, laboratory space to meet research needs

Compensation and benefits: highly competitive salary commensurate with experience and academic accomplishments, a comprehensive benefit package Subsidized housing: on-campus, 80/100/120 m^2 faculty apartments available at low rent for tenure and tenure-track faculty

Relocation & travel allowance: reimbursement of expenses for household relocation and family's one-way travel

Family assistance: support with children's education; affiliated kindergarten, primary and middle schools are under construction

香港中文大學(深圳)
The Chinese University of Hong Kong, Shenzhen

Professor/Associate Professor/Assistant Professor/Lecturer
The School of Science and Engineering

Located in the Longgang District of Shenzhen, The Chinese University of Hong Kong, Shenzhen (CUHK-Shenzhen) is a research-intensive university, established in 2014 through a Mainland–Hong Kong collaboration with generous support from the Shenzhen Municipal Government. It inherits the fine academic traditions of The Chinese University of Hong Kong and will develop its academic programmes in phases and offer courses in Schools of Science and Engineering, Management and Economics, and Humanities and Social Science. English is the main language for course instructions, and the students will receive degrees of The Chinese University of Hong Kong. At present, several research centers have been established in the School of Science and Engineering, including Arieh Warshel Institute of Computational Biology, Kobilka Institute of Innovative Drug Discovery, Hopcroft Institute for Advanced Study in Information Sciences, and Shenzhen Key Laboratory of Semiconductor Laser.

Post Specification
The School of Science and Engineering invites applications for multiple faculty positions at both senior and junior levels in the areas of Computer Science, Data Sciences, Electrical Engineering, New Energy Science and Engineering, Material Science and Engineering, Physics, Robotics, Chemistry and Organic Chemistry, Bioinformatics, Computational Biology, Molecular Simulation, Computational Chemistry, Cell Biology and Molecular Biology, Structural Biology (in particular G-protein couple receptors), Pharmacology, Stem Cell Biology, Regenerative Medicine, Biomedical Science and Engineering, Statistics, Mathematics, Financial Engineering, and Quantitative Finance. Applications in other areas will also be considered.

Junior applicants should have (i) a PhD degree (by the time of reporting for duty) in related fields; and (ii) high potential in teaching and research. Candidates for senior post (Associate and Full Professor) are expected to have demonstrated academic leadership and strong commitment to excellence in teaching, research, and services. Junior appointments will normally be made on contract basis for up to three years initially, leading to longer-term appointment or tenure later subject to review. Exceptional appointments with tenure will be considered for candidates of proven excellence. Applicants are encouraged to check out the details about the university at http://www.cuhk.edu.cn/en.

Salary and Fringe Benefits
Salary will be comparable to international standards, commensurate with experience and accomplishments. Appointments will be made under the establishment of CUHK-Shenzhen, and employee benefits will be provided according to the relevant labor laws of Mainland China as well as CUHK-Shenzhen regulations. Subsidies from various government sponsored talent programs will also be made available for eligible candidates http://www.cuhk.edu.cn/UploadFiles/talentsprogramoutline.pdf

Application package, including CV and contacts of three referees, as well as personal statements in teaching, research, and service, should be emailed to: Talents4SSE@cuhk.edu.cn. Applicants are required to specify the rank of the position in their letter of application. Applicants also need to ask three referees to send the letters directly to Talents4SSE@cuhk.edu.cn upon submitting application materials.

Recruitment of Global Talents for Guangdong Ocean University

Guangdong Ocean University (GDOU), located in a beautiful, southernmost coastal city, Zhanjiang, in mainland of China, is a key institution featured with Ocean Science and Fisheries Sciences. GDOU provides full range of academic programs at undergraduate and graduate level, including PhD programs in Fisheries Science, Food Science & Technology, and Ocean Science. Our main campus is located at the east side of Huguangyan International Geological Park (4A). This dream campus, 806 acres in total, a beautiful place facing sea and surrounded by mountains, is home to studying, teaching and research facilities. At GDOU more than 32,000 students from different countries come together to discover. Over 2,500 qualified and brilliant staff and faculty are contributing to teaching, researching and more at GDOU. GDOU is proud to have 16 key laboratories or Engineering Research Centers of Guangdong Province and 15 affiliated research institutes.

Due to the fast development, GDOU is now recruiting high-level faculty from China and abroad.

1. Disciplines
Science, Engineering, Agronomy, Economics, Management, Law, Literature, Education, marine-related disciplines, Art etc. Please find the details in GDOU website.

2. Job Description
Teaching and research in university

3. Job Requirements
(1) PhD from oversea or domestic universities/research institutes
(2) Be capable of teaching and researching in university

4. Contact Information
1. Applicants can send a detailed CV to gdouszkrcyj@163.com. Please detail your education, work experience, publications and research interests etc and use Applicant's Name + Profession (Field of Research) + Current Institution of Study or Work + Interest Recruit Type as the subject of the email.
2. Should you have any questions, please contact Dr. Jichang Jian or Ms. Xiaolei Li.

telephone: (+86)0759-2383281
email: gdouszkrcyj@163.com

3. GDOU Website: http://www.gdou.edu.cn, Recrutment: http://news.gdou.edu.cn/special/show.php?specialid=12

DISCOVER THE FUTURE

TWO LEADING POSITIONS AT SCILIFELAB

To further strengthen our research environment and complement research areas already present at SciLifeLab, we are now looking to recruit two outstanding young group leaders to new Fellows positions. As part of the SciLifeLab Fellows program, you become an associate at our research center, as well as contract a position at one of our host universities.

Read more at: www.scilifelab.se/fellows. Application deadline: January 15, 2018.

Stockholm University

Assistant Professor in Computational Biology

Studies of algorithms, modelling and methodology, with applications in life sciences

Stockholm University

Assistant Professor in Environmental Genomics

Genomic studies of all kinds of non-human biota and their relationships to the environment, focusing on structure and function of ancient or recent systems

About SciLifeLab

As a national hub for molecular biosciences in Sweden, SciLifeLab (Science for Life Laboratory) facilitates cutting-edge, multi-disciplinary life science research and promotes its translation to the benefit of society. The center focuses on both health and environmental research and is jointly operated by its four founder universities: KTH Royal Institute of Technology, Karolinska Institutet, Stockholm University, and Uppsala University. About 200 research groups, 1500 researchers and 40 national infrastructure facilities are associated with SciLifeLab.

SciLifeLab

University of Massachusetts Medical School

Tenure-Track Faculty Position in Virology

The Department of Microbiology and Physiological Systems (MaPS) at the University of Massachusetts Medical School (UMMS) (http://www.umassmed.edu/) invites applications for a tenure-track faculty position at the rank of **ASSISTANT PROFESSOR**. Depending on qualifications, candidates may be considered for an appointment at the rank of **ASSOCIATE or FULL PROFESSOR**. We seek candidates who are focused on studies of viral infection, including (but not limited to): molecular mechanisms of virus infection and pathogenesis; cell biology of infection; virus structure; viral evolution, and interactions of viruses with their hosts. Candidates will be expected to develop and maintain an innovative, externally funded research program. We offer competitive startup and ongoing support, highly competitive salaries, faculty mentoring, a centralized graduate program, and an exceptionally collaborative culture with abundant opportunities for basic and translational research.

UMMS is part of the unique, world-leading greater Boston biomedical research, clinical, and biotech community. Institutionally, traditional departments are complemented with interdepartmental centers and programs (www.umassmed.edu/about/department-and-centers/). The successful candidate will also be a founding member of the nascent UMMS Virology Center.

MaPS is located in the state-of-the-art Albert Sherman Center. Faculty research endeavors are supported with a wide array of departmental shared facilities as well as core facilities (https://www.umassmed.edu/research/cores/) and BSL-3 and ABSL-3 suites. Please use the following link to apply: **https://academicjobsonline.org/ajo/jobs/12777**. Applications will be reviewed on an ongoing basis. Direct questions to Timothy Kowalik, PhD (timothy.kowalik@umassmed.edu).

UMass Medical School values diversity, equity and inclusion. This is exemplified by our definition of diversity (https://www.umassmed.edu/dio/about/layers/), by recognizing the intrinsic relationship between diversity and excellence in all our endeavors, and by embracing open and equitable access to opportunities for learning and development as our obligation and goal.

NYU Winthrop Hospital

Assistant, Associate or Full Professors

The New York University Long Island School of Medicine (NYU LISoM) and its Research Institute and Diabetes and Obesity Research Center invite applicants from accomplished basic and physician scientists for tenure eligible Assistant, Associate or Full Professor positions. Applicants must have an M.D. and/or Ph.D. or equivalent degree and have demonstrated excellence in research. The successful candidates will have experience in related fields of diabetes, obesity and heart disease. We are also interested in researchers focused on islet cell biology including basic and translational studies. Responsibilities include establishing a vigorous and independently funded research program, supervising and mentoring students and postdoctoral fellows with diverse backgrounds, and contributing to medical school education. Scholarship that bridges disciplines is encouraged across departments with NYU's many schools, centers and institutes. In particular, there is a strong and growing set of collaborations with NYU School of Medicine's Division of Endocrinology, Diabetes and Metabolism. We seek individuals with strong records of independent creative accomplishments, who will interact productively with colleagues within the NYU LISoM and with NYU School of Medicine taking advantage of unique opportunities to translate basic science into clinical practice. The Center is located in a new Research and Academic Center Building with ample opportunities to collaborate with basic and clinical scientists. The Center is within easy commute to New York. Currently, research is being carried out by basic and clinical investigators in lipid disorders, renal, cardiovascular and central nervous system complications, and obesity interventions. We have a strong set of clinical and educational programs for collaborations between pre-clinical and clinical faculty.

Please submit a letter describing qualifications, along with a CV, a two page summary of current and proposed research, and names of referees to: Dr. Mahmood Hussain, Endowed Chair and Director, Diabetes and Obesity Research Center, NYU Winthrop, **dorc@nyulangone.org**.

The new NYU LISoM is located at the campus of NYU Winthrop Hospital in Mineola, in western Nassau County, just 25 miles from Manhattan and NYU SOM and a block from the Mineola LIRR Train Station.

ICBII outSMARTing CNS Diseases

PhD Scientists, Sr. Scientific Investigators, Principle Scientists, and Directors

ICB International, Inc., ("ICBII"), of La Jolla, California is dedicated to developing disease altering therapies for afflictions of the central nervous system (CNS) to ameliorate the sufferings of hundreds of millions of patients worldwide. Realizing that blood-brain barrier (BBB) has been an insurmountable barrier to developing diagnostics and curative therapies for brain diseases, ICBII made it a priority to deal with BBB challenges. We have developed novel antibody mimics, referred to SMART Molecules (SMs), proven, in transgenic mouse models of Alzheimer's and Parkinson's diseases ,not only to cross the BBB, but also to detect, quantify, and modulate the function of errant CNS proteins. To advance its science from laboratory to patients, ICBII is looking for PhD/MD candidates with a commitment to scientific excellence to eradicate CNS disorders with the energy, enthusiasm, and innovation to make a difference in patients' lives by avoiding mistakes of the past clinical studies. We are looking for scientists in the following categories:

- Protein Engineers experienced in phage display libraries.
- Neurobiologists experienced in quantification of CNS proteins and mechanisms of protein transport across the BBB.
- Immunologists experienced in developing mechanisms based inhibitors for proteins and enzymes involved in synaptic dysfunction.
- Pharmacologists experienced in PK, PD, and toxicology in animals and humans.
- Radiologists/radiochemist with experience in developing radiolabeled proteins and imaging animals using PET scanner.

Successful candidates will have a PhD/MD in relevant discipline and 3 to 5 years' experience working in the pharmaceutical and/or biotech industry as well as demonstrated track record of accomplishment in the form of publications in scientific journals and/or drug development. The position and salary will be commensurate with experience and accomplishments. These positions are open to US Citizens and permanent residents (Green Card holders) with a passion to work in the laboratory to combat neurodegenerative diseases. If you are a vibrant scientist with excellent interpersonal skills, please email your resume with a cover letter stating your interest and naming three references to **info@icbii.com**. We are an equal opportunity employer. All correspondence will be held in confidence.

Beth Israel Deaconess Medical Center

HARVARD MEDICAL SCHOOL TEACHING HOSPITAL

The Parikh laboratory at Harvard Medical School and Beth Israel Deaconess Medical Center in Boston is seeking a Postdoctoral Fellow who will lead a wholly NIH-funded project to understand the molecular processes regulating homeostasis of NAD+. NAD+ regulation in metabolically active organs may be pivotal both for cell-autonomous functions during acute stress and for generalized physiological disturbances such as impaired organ function. The successful applicant will apply systematic functional screens (e.g., CRISPR) to identify central control mechanisms for NAD+ balance and will lead vertically integrated experiments to evaluate metabolism and physiology across cellular and in vivo models of acute stress.

Candidates must be enthusiastic, passionate and self-motivated with a commitment to career development. You will have the support of an organized Departmental Postdoctoral training program including opportunities to present your work and bi-annual review of a personalized Individual Development Plan with your primary mentor and a co-mentor to ensure that you are meeting career goals. The candidate must be able to independently and efficiently manage concurrent projects and while possessing a strong commitment to contributing intellectually and interpersonally toward a positive and stimulating lab environment.

Essential Responsibilities:

1. Abides by the institutional policies of BIDMC relating to health and safety, equality of opportunity and data storage and management.
2. As a member of the research team, actively pursues research under the supervision of a principal investigator while developing skills for independent work.
3. Receives training in and performs duties contributing to the investigational work of the team including formulation of research questions and design, conduct of experiments, and evaluation of results.
4. Prepares and publishes scientific manuscripts under direction of PI.
5. Develops expertise in desired lab skills/informatics/physics/clinical research. Develops proficiency with research tools and equipment. Develops ability to work with more independence as the fellowship progresses.

Required Qualifications:

1. Doctoral degree required.
2. 0-1 years related work experience required.
3. Extensive experience in molecular biology, mammalian cell culture, manipulation of DNA and RNA in cells using CRISPR and RNAi.
4. Ability to produce complex documents, perform analysis and maintain databases. Prior experience reviewing, analyzing, and summarizing scientific literature.
5. Excellent attention to detail and interpersonal, organizational, writing, and project management skills.
6. Strong organizational and data management skills.
7. Advanced technical computer skills as required for technical support specific to functional area and related systems.

Competencies:

1. **Decision Making:** Ability to make decisions that are guided by general instructions and practices requiring some interpretation. May make recommendations for solving problems of moderate complexity and importance.
2. **Problem Solving:** Ability to address problems that are varied, requiring analysis or interpretation of the situation using direct observation, knowledge and skills based on general precedents.
3. **Independence of Action:** Ability to follow precedents and procedures. May set priorities and organize work within general guidelines. Seeks assistance when confronted with difficult and/or unpredictable situations. Work progress is monitored by supervisor/manager.
4. **Written Communications:** Ability to summarize and communicate in English moderately complex information in varied written formats to internal and external customers.
5. **Oral Communications:** Ability to comprehend and communicate complex verbal information in English to medical center staff, patients, families and external customers.
6. **Knowledge:** Ability to demonstrate in-depth knowledge of concepts, practices and policies with the ability to use them in complex varied situations.
7. **Team Work:** Ability to lead collaborative teams for larger projects or groups both internal and external to the Medical Center and across functional areas. Results have implications for the management and operations of multiple areas of the organization.
8. **Customer Service:** Ability to provide a high level of customer service and staff training to meet customer service standards and expectations for the assigned unit(s). Resolves service issues in the assigned unit(s) in a timely and respectful manner.

Physical Nature of the Job:

1. **Light work:** Exerting up to 20 pounds of force frequently to move objects. Some elements of the job are sedentary, but the employee will be required to stand for periods of time or move throughout the hospital campus

To apply:
Interested applicants should send a **single PDF file including:**

1. Cover letter (please state how you heard about the position)
2. CV demonstrating publication of impactful work
3. One-page statement of research interests
4. Contact information for three references

EOE M/F/VET/DISABILITY/GENDER IDENTITY/SEXUAL ORIENTATION.

By **Katarina Radošević**

Forced to change—for good

"Can't stop loving you … " My 3-year-old son was singing along with Phil Collins from his car seat. We were on our commute, spending a few hours of quality time in Dutch rush-hour traffic. But I was not in the mood to sing along. My manager at the biotech company where I had been working for a bit more than a year had just told me that, in spite of my excellent performance, he did not foresee giving me more responsibilities in the near future. I was working part time so that I could spend more time with my young children, and he believed the career growth I sought required a full-time employee. The message hit me hard. But it precipitated a change that, in the end, taught me the power of embracing opportunities, no matter where they come from.

My manager's decision planted a seed of self-doubt. Was he right? Was I asking for too much? But I reminded myself that I had already proved I could be an effective scientist on a part-time schedule. During my 7 years as a university researcher working part time—a common choice among working mothers in the Netherlands—my career had flourished. With rigorous time management and organization, I got at least as much good work done in 4 days a week as others did on full-time schedules.

When I left my university post for the biotech company, spurred by the desire for my work to reach patients, I expected that I would be able to grow professionally and advance my career there. I had the impression that the company valued performance and ambition. But now I was being told that I should be happy in my current role as a troubleshooter, rather than the project leader I aspired to be.

A friend suggested that I reach out to senior managers about opportunities in other departments. At first, I resolutely rejected that idea. Didn't he understand? I wanted to work on antibodies and nothing but antibodies! That was what I knew, where I felt I could add the most value. And yet, I did not want to leave this cool company just because of one unsupportive manager.

With little expectation that it would lead anywhere, I approached the three senior managers. One did not respond. One had nothing to offer. The third invited me to chat. He patiently listened to my story, asked what I was looking for, and then—in the blink of an eye—told me that I was welcome to join him in building a vaccine research unit. I stuttered that I knew nothing about vaccines. He waved nonchalantly and said, "You will learn. You are smart and willing to work hard. You will make it."

"When I step out of my comfort zone, I find my most creative, productive self."

The reassurance was exactly what I had been looking for, but I was still shaken by my manager's lack of confidence in me. Could I really handle a high-responsibility role in a completely new field?

A few sleepless nights later, I decided that taking a chance on the unknown was better than staying in a position that made me miserable. The worst thing that could happen was that I would fail. But I already felt like a failure, so why not try it?

I soon discovered a new passion. My career path within the company opened up. I took on more responsibilities, developed new skills, expanded my scientific horizons, worked with great people, and led fantastic projects—all because of a change that had felt forced on me. It had pushed me further than I was willing to go, further than I thought I could cope with, and taught me that when I step out of my comfort zone, I find my most creative, productive self.

More than 10 years later, antibodies—my scientific "first love"—crossed my path again in the form of an exciting, challenging position that demanded a major life change, complicated by my recent divorce. I would have to leave my home and community, start again in another country, and find a way to co-parent across borders. After many discussions, I asked my son whether he would go abroad with me. Without lifting his eyes from his *Minecraft* game, he responded, "*Pourquoi pas*?" I couldn't have said it better myself. ■

Katarina Radošević is global head of biologics research at Sanofi in Paris. *She thanks Andrea Dingemans for editorial support. Send your story to SciCareerEditor@aaas.org.*

ILLUSTRATION: ROBERT NEUBECKER

BIT Talents Recruitment
Give You the Most, To Show Your Best

北京理工大学
BEIJING INSTITUTE OF TECHNOLOGY

Beijing Institute of Technology (BIT), founded in 1940, is the first university of science and technology founded by the Communist Party of China and has always been the first batch of universities sponsored by China's Project 211, Project 985 and the "World-class University Construction Plan", category A. In 2016-2017, BIT was ranked among the Top 400 in QS World Universities Ranking, as well as the 15th among the Chinese universities in the above rankings. The fundamental research on engineering, material science, chemistry, physics, computer, mathematics and social science in BIT is among the top 1% in ESI ranking and engineering is among the top 1‰.

The university faculty includes more than 4300 teachers, 22 members of Chinese Academy of Sciences and members of Chinese Academy of Engineering, 49 selected in "Thousand Talents Plan" (the State Recruitment Program of Global Experts), 22 in "Ten Thousand Talents Plan", 39 Distinguished Professors of "Cheung Kong Scholar Program", 38 winners of China National Funds for Distinguished Young Scientists and 28 innovative teams such as Innovation Communities supported by Natural Science Foundation of China. BIT has now 9 State key laboratories (centers), 49 key laboratories of Peking or ministries. It has made a great contribution to the development of science and technology in the history of China, such as the first television transmitting and receiving device, the first secondary solid high-altitude rocket, the first light tank, the first low altitude altimetry radar, the first 20km remote camera, etc.

In recent years, BIT has attached great importance to talents recruitment and development. Under the BIT Talent Strategy, a series of programs have been launched, including the "Distinguished Academic Leader Plan", "Innovative Talent Special Support Program" and "Xu Teli Program for Young Scholars". In addition, BIT founded the Advanced Research Institute of Multi-disciplinary Science and carried out the "Green Channel for Talents" to provide a good development platform and excellent conditions. BIT has been recruiting academic leaders and distinguished middle-aged and young scholars from home and abroad.

I.Qualifications and Conditions

(I) Thousand Talents Plan for Young Scholars

1.Have an overseas scientific research experience of 36 months or above after obtaining a doctorate degree;
2.No more than 40 years old;
3.Work full time when successfully selected.

(II) Xu Teli Program for Young Scholars

1.Must have a Ph.D. degree and generally be not more than 40 years old; Work full-time at BIT;
2.Have a doctoral degree obtained from a world-renowned university or Have an overseas work experience of 2 years or above in well-known universities, scientific research institutions or R&D institutions of well-known enterprises abroad.

(III) The Excellent Young Teachers Program

Generally, have a research, learning, or work experience of over 2 years in well-known overseas universities or academic institutions;

(IV) Postdoctoral Support Program

1.Have obtained a full-time Ph.D. degree within the past 3 years and be not more than 35 years old;
2.If recruited, the applicant shall be able to work full-time in post-doctoral research (including the joint training of workstation).

(V) Distinguished Academic Leader Plan

Compensation, fund and relocation package will be discussed case by case.

II.We Offer

1.A competitive salary and welfare;
2.Adequate funding for scientific research;
3.Support for building academic team;
4.Office and laboratory arrangements;
5.Transitional housing;
6.Apply for permanent Beijing residence;
7.Assistance in solving life issues with family members;
8.Allowance for international round-trip travel expenses (Thousand Talents Plan for Young Scholars Candidates).

III.To Apply

Applicants please send CV, full copies of representative academic publications with citations and peer reviews, etc. via email to HR of BIT. Please specify the talent program you are applying for. You can also log on to the BIT Recruitment System (http://zhaopin.bit.edu.cn/) to apply online.

Contact us:

Distinguished Academic Leader Plan/ Thousand Talents Plan for Young Scholars/Xu Teli Program for Young Scholars
Ms. Xia, Mr. Fan
+8610-68914243/4546
bitrcb@bit.edu.cn

The Excellent Young Teachers Program
Ms. Zhang, Mr. Zhou
+8610-68918577
bitzhaopin@bit.edu.cn

Postdoctoral Support Program
Ms. Yu, Mr. Liu
+8610-68912338
bitbsh@bit.edu.cn

Know more, please visit http://www.bit.edu.cn

Do you have the next big idea in the life sciences?

Apply to lead a **new research area** at Janelia Research Campus.

Apply by **March 1, 2019**

More Information **janelia.org/new-research-area**

hhmi | janelia